A Synthetic Nitrogenase: Insights into the Mechanism of Nitrogen Fixation by a Single-Site Fe Catalyst

Thesis by
Niklas Bjarne Thompson

In Partial Fulfillment of the Requirements for the
Degree of
Doctor of Philosophy

CALIFORNIA INSTITUTE OF TECHNOLOGY
Pasadena, California

2018
Defended May 25, 2018

Niklas Bjarne Thompson
ORCID: 0000-0003-2745-4945

To K. K.-L.,

For helping me learn how to see.

To G. L. H.,

For teaching me how to understand.

ACKNOWLEDGEMENTS

The fundamental laws necessary for the mathematical treatment of a large part of physics and the whole of chemistry are thus completely known, and the difficulty lies only in the fact that application of these laws leads to equations that are too complex to be solved.

PAUL A. M. DIRAC

[E]ven the most difficult problems in chemical experimentation can be solved by the hands of a master.

J. F. W. ADOLF VON BAEYER

This will make him famous, even though he has no talent for chemistry.

J. F. W. ADOLF VON BAEYER

Conducting academic research is as rewarding as it can be disappointing. Day by day, if not hour by hour, my time as a graduate student could oscillate from exhilarating to crushing, a necessary evil that is the byproduct of intense and intellectually satisfying work. If I have learned, if I have grown as a scientist, it is only by virtue of the steadfastness of my research adviser, Jonas C. Peters. Over the past five years, Jonas has provided my anchor as a mentor, philosopher, and, I hope, as a colleague and a friend. My only regret is not visiting his office more often and taking full advantage of his experience.

I extend my lasting gratitude the the remainder of my thesis committee, Theodor Agapie, Gregory C. Fu, and Garnet K.-L. Chan. As chair, Theo has constantly pushed me with deep, even-handed criticism, which has been critical in my growth. Beyond this role, I have had the opportunity to collaborate with Theo's own students and postdocs, interactions that have broadened my scientific experience beyond the narrow focus of my dissertation work. Greg, too, has constantly reminded me to ask the important, soluble scientific questions, without which a researcher cannot hope to succeed. Although a more recent addition to my committee, Garnet has, both through his public seminars at Caltech, and through our own personal conversations, exposed me to a realm of chemical theory that has enriched my own worldview.

The success of a scientist is, to a large extent, determined by the quality of his peers, and in that respect I have had the privilege to work alongside outstanding colleagues at Caltech. Within his own group, Jonas has only ever attracted scientists of a high caliber, who are too numerous to give a justified account here. Nevertheless, I am deeply indebted to those who preceded me, particularly John S. Anderson and Marc-Etienne Moret, who laid the groundwork for all of the work I have accomplished in Jonas's laboratory. As mentors, Sid Creutz, Gaël Ung, and especially Jon Rittle have helped to forge me into the chemist I am today. Trevor Del Castillo has been a constant colleague and friend these past years, and I am proud to have co-authored my first scientific works together with a mind such as his. All of the loose ends I have left dangling from this thesis I leave up to those I have mentored in turn, Matt Chalkley, Dirk-Jan Schild, and Patricia Nance—good luck! To the rest of the group—thank you!

Outside of the Peters group, I have found collaborators and friends who are no less important. Graham de Ruiter, Tzu-Pin Lin, and Alice Chang have allowed me to participate in their own work, to the benefit of us all, I hope. Bryan Hunter has been an inspiration, not only as a dogged and insightful scientist, but also as a loyal and witty friend. Michael T. Green, first as an author and then as a colleague, has made me feel welcome in a larger community where I hope to continue dwelling. The same can be said of Daniel L. M. Suess, with whom I am eager to work again. Blake Daniels and Kareem Hannoun helped ease my transition to the strange state of California. Matt Bizjack, Peter Brown, Max Frank, Liz Lyon, Sam Rappeport, Kareem Sayegh, Ethan Tate, Katie Thomas, Harry Winkler, and many others, have, over the years, peeled me away from the box and bench, and I can only say I hope this becomes more frequent.

None of this work would be possible without the well-oiled machine that is CCE. Larry Henling, Mike Takase, David VanderVelde, among others, make it a pleasure to collect data at Caltech. Paul Oyala, who has suffered a concentrated dose of my chemical musings with grace, is a welcome addition to this cadre. Beyond these experimentalists, CCE employs an

efficient and caring administrative staff, without whom we would all be lost.

If we stand on the shoulders of giants, I have had the privilege to glimpse staggering heights. My parents, both as scientists and as humanitarians, have been a model I don't think I can ever hope to achieve. As my long, some 27-odd-year schooling comes, finally, to an end, words fail to impart my gratitude. Kajsa, I know that you have given up hopes on the Prize, but if it fails to come, it is not your failing, but the shortsightedness of the Committee that fails you. Although he will never see the fruits of his labor, Professor Hillhouse inculcated my hope that I could one day conquer the metal–ligand multiple bond. And while modern chemistry may descend from a long line of Scandinavian theorists, I am proud to have descended from a long line of Skånian artists, whose work, for me, is no less fundamental.

To Sam—it was never going to be easy, but we did it! If I can ever claim to have finished, it is because of your love.

ABSTRACT

Nitrogen fixation—specifically the conversion of molecular nitrogen (N_2) into ammonia (NH_3)—is a fundamental reaction necessary to support life. Our group has recently discovered the first family of well-defined iron complexes that catalyze the conversion of N_2 to NH_3. This thesis details mechanistic study of the nitrogen fixation chemistry these complexes. Chapter 1 presents an abbreviated overview of catalytic nitrogen fixation, which places our work in a larger context. Chapter 2 details the synthesis and N_2-to-NH_3 conversion activity of a series of cobalt complexes that are homologous to the known iron-based catalysts. The central goal of this work was to provide a structure-function study of the isostructural cobalt and iron complexes, in which the nature of the transition metal ion was changed in a fashion that predictably modulated the electronics of the system. Chapter 3 details in situ mechanistic studies of nitrogen fixation catalyzed by the iron complexes under the originally-reported reaction conditions. In this study, we were able to achieve a nearly order-of-magnitude improvement of catalyst turnover. Study of the reaction dynamics evidence a single-site mechanism for N_2 reduction, which is corroborated by in situ monitoring of catalytic reaction mixtures using freeze-quench ^{57}Fe Mössbauer spectroscopy. In Chapter 4, we study the key N–N bond cleavage step in the catalytic cycle for nitrogen fixation. In this chapter, we demonstrate that sequential reduction and low-temperature protonation of an iron catalyst results in the formation of NH_3 and a terminal Fe(IV) nitrido complex. This result provides a compelling proposal for the mechanism of the catalytic nitrogen fixation reaction. Finally, in Chapter 5 we present spectroscopic and computational studies detailing the electronic structures of a redox series of Fe(NNR_2) complexes that model key catalytic intermediates occurring prior to the N–N bond cleavage step. We evidence one-electron redox non-innocence of the "NNR_2" ligand, which resembles that of the classically non-innocent ligand, NO, and may have mechanistic implications for the divergent nitrogen fixation activity of the some of the iron complexes studied by our group.

PUBLISHED CONTENT AND CONTRIBUTIONS

(1) Del Castillo, T. J.; Thompson, N. B.; Peters, J. C. A Synthetic Single-Site Fe Nitrogenase: High Turnover, Freeze-Quench ^{57}Fe Mössbauer Data, and a Hydride Resting State. *J. Am. Chem. Soc.* **2016**, *138*, 5341–5350. N.B.T. participated in the design and execution of catalytic reactions, performed kinetic analyses, collected and analyzed freeze-quench Mössbauer spectra, and participated in the preparation of the manuscript, DOI: 10.1021/jacs.6b01706.

(2) Del Castillo, T. J.; Thompson, N. B.; Suess, D. L. M.; Ung, G.; Peters, J. C. Evaluating Molecular Cobalt Complexes for the Conversion of N_2 to NH_3. *Inorg. Chem.* **2015**, *54*, 9256–9262. N.B.T. prepared and characterized the complexes of the alkyl ligand, performed quantum-chemical calculations, and participated in the preparation of the manuscript, DOI: 10.1021/acs.inorgchem.5b00645.

(3) Thompson, N. B.; Green, M. T.; Peters, J. C. Nitrogen Fixation via a Terminal Fe(IV) Nitride. *J. Am. Chem. Soc.* **2017**, *139*, 15312–15315. N.B.T. conceived of and carried out all experiments, collected and analyzed Mössbauer spectra, analyzed X-ray absorption spectra, performed quantum-chemical calculations, and prepared the manuscript, DOI: 10.1021/jacs.7b09364.

TABLE OF CONTENTS

LIST OF FIGURES

LIST OF TABLES

NOMENCLATURE

β_e**.** The Bohr magneton.

12-c-4. 12-crown-4.

2-MeTHF. 2-methyltetrahydrofuran.

9-BBN. 9-Borabicyclo[3.3.1]nonane.

[BAr$^{F}_{4}$]$^{-}$. Tetrakis(3,5-bis(trifluoromethyl)phenyl)borate.

[OTf]$^{-}$. Trifluoromethanesulfonate.

[TBA]$^{+}$. Tetrabutylammonium.

***t*BuLi.** *tert*-butyllithium.

ADP. Adenosine Diphosphate.

atm. Atmospheres; 1 atm = 101.325 kPa = 1.01325 bar.

ATP. Adenosine Triphosphate.

BDE. Bond Dissociation Enthalpy.

CAS. Complete Active Space.

CASSCF. Complete Active Space Self Consistent Field.

CI. Configuration Interaction.

Cp. Cyclopentadienide.

Cp*. Pentamethylcyclopentadienide.

CPET. Concerted Proton-electron Transfer.

CW. Continuous Wave.

cyclam. 1,4,8,11-Tetraazacyclotetradecane.

DFT. Density Functional Theory.

DME. Dimethoxyethane.

dppe. 1,2-bis(diphenylphosphino)ethane.

ENDOR. Electron Nuclear Double Resonance.

EPR. Electron Paramagnetic Resonance.

EXAFS. Extended X-ray Absorption Fine Structure.

Fc. Ferrocene ($FeCp_2$).

HAT. Hydrogen Atom Transfer.

HER. Hydrogen Evolving Reaction.

HFC. Hyperfine Coupling.

HYSCORE. Hyperfine Sublevel Correlation.

MO. Molecular Orbital.

N[Si$_2$]. 2,2,5,5-tetramethyl-1-aza-2,5-disilacyclopentyl.

Na/Hg. Sodium–mercury amalgam.

NArP$_3$. Tris(2-diisopropylphosphino-4-methylphenyl)amine.

NC$_9$H$_{18}$. 2,2,6,6-tetramethylpiperidyl.

NEVPT2. N-electron Valence Perturbation Theory, of second order.

NMR. Nuclear Magnetic Resonance.

NOON. Natural orbital occupation number.

P$_3^B$. Tris(*o*-diisopropylphosphinophenyl)borane.

P$_3^C$. Tris(*o*-diisopropylphosphinophenyl)methide.

P$_3^{Si}$. Tris(*o*-diisopropylphosphinophenyl)silylide.

P$_i$. Phosphate (PO_4^{3-}).

PCET. Proton-coupled Electron Transfer.

PCET. Proton-coupled Electron Transfer.

PhBP$^R_3$. $[PhB(CH_2PR_2)_3]^-$.

PP$_3$. Tris(2-diphenylphosphinoethyl)phosphine.

Q-band. Approximately 34 GHz.

SQUID. Super-conducting Quantum Interference Device.

TD-DFT. Time-Dependent Density Functional Theory.

TfOH. Trifluoromethanesulfonic (triflic) acid.

Tg. Teragram (10^{12} g, or 1 million metric tons).

THF. Tetrahydrofuran.

TMS. Trimethylsilyl.

TOF. Turnover Frequency.

TON. Turnover Number.

TPP. *meso*-tetraphenyl-, *meso*-tetra-*p*-tolyl-, or *meso*-tetra-*p*-chlorophenyl porphyrin.

VN. Valence Number = (*Element valence*) − (*# nonbonding electrons*).

X-band. Approximately 9.4 GHz.

XANES. X-ray Absorption Near Edge Structure.

XAS. X-ray Absorption Spectroscopy.

Chapter 1

INTRODUCTION

1.1 Opening Remarks

The chemistry of nitrogen fixation, and the mechanisms by which transition metal ions—particularly iron—catalyze this fundamental transformation, form the leitmotif of this thesis. In principle, nitrogen fixation refers to any process by which molecular nitrogen—or dinitrogen (N_2)—is oxidized or reduced to a form that is sufficiently reactive to become biologically and industrially relevant. Oxidatively, this can be thought to occur via sequential oxygenation of N_2, first proceeding through nitrous oxide (N_2O), and thence cleavage of the N–N bond to produce nitric oxide (NO), nitrite (NO_2^-), and, finally nitrate (NO_3^-). While these chemicals are of industrial and biological importance, the direct oxygenation of N_2 constitutes a relatively small proportion of terrestrial nitrogen-fixing processes (accounting for roughly 10% of the 400 Tg or so of fixed N atoms per *annum*), mostly occurring as a by product of the combustion of carbon-based fuels and in the extreme ionizing conditions produced by lightning discharges.[1] By far more important for the global nitrogen cycle is nitrogen fixation via reduction, which, conceptually, but not necessarily mechanistically, proceeds through stepwise hydrogenation of N_2 to diazene (N_2H_2), hydrazine (N_2H_4), and, ultimately, ammonia (NH_3). Both N_2H_2 and N_2H_4 are extremely reactive[i] and in practice, if they are intermediates in the reduction of N_2, they are themselves generally reduced to NH_3.[ii] The 6 H^+/6 e^- reduction of N_2 to NH_3 accounts for about 90% of the global nitrogen fixed per *annum*.[1] Given its importance, this reaction is our object of study, and unless noted otherwise, we will use the term nitrogen fixation to refer exclusively to the conversion of N_2 to NH_3.

[i] N_2H_4, for example, finds use as a propellant in rocket fuel.

[ii] There are a handful of systems selectively catalyze the 4 H^+/4 e^- reduction of N_2 to N_2H_4,[2–4] but these appear to be the exception rather than the rule.

1.2 The Significance and Challenge of Nitrogen Fixation

Nitrogen is an abundant element, indeed, the 7th most abundant in the universe, and composes 78.1% of our atmosphere in its molecular form.[5] It is therefore unsurprising that all known forms of life contain nitrogen as a constitutive element, where it is found, for example, in all nucleic and amino acids, and therefore DNA, RNA, and proteins. Industrially, nitrogen is also an important element, found in commodity chemicals such as isocyanates (produced on a multi-Tg scale per *annum*[6]) and, perhaps more importantly, in fertilizers for food production.[1] However, despite its abundance, the remarkable chemical inertness of N_2 means that it cannot be used directly as a source of elemental nitrogen in chemical synthesis—hence, it must be "fixed" to a reactive form prior to incorporation into these important chemicals.

Much of the reactivity—or lack thereof—of N_2 can be rationlized in terms of its extremely strong N≡N triple bond. In terrestrial chemistry, the homolytic bond strength of the N_2 molecule is only surpassed by that of carbon monoxide (CO).[iii] However, whereas CO is a heterodiatomic gas, and is therefore dipolar, N_2 is symmetrical, possesses no dipole moment in the absence of an external electric field, and for that reason is far less reactive than CO despite its weaker chemical bond. As judged by the ionization potential, electron affinity, and proton affinity (Table 1.1), it is less favorable to oxidize, reduce, and protonate N_2 when compared with CO. Indeed, it is more favorable to protonate the C–H bond of methane than it is to protonate N_2. Thus, part of the challenge of N_2 fixation lies in the stability of the N≡N bond, which translates into large barriers towards its reduction in the absence of a catalyst.

However, the peculiar challenge of nitrogen fixation lies not only in the stability of the starting material (N_2), but in the nature of the products. Considering the thermodynamics of the direct hydrogenation of another typical example of a triply-bonded substrate, acetylene

[iii] The strongest chemical bond probably belongs to doubly-protonated N_2, the linear protodiazonium dication, $[HNNH]^{2+}$,[7] although the existence of this species is somewhat dubious.[8] The related diazonium cation, $[HN_2]^+$, features a similar bond strength, and can be detected in interstellar space.[9]

Table 1.1: Collected Physical Properties.[a]

	N≡N	C≡O	H_3C–H
BDE (kcal mol^{-1})	225	256	
Ionization Potenial (eV)	15.6	14.0	
Electron Affinity (eV)	−1.8	1.3	
Proton Affinity (eV)	5.1	6.2[b]	5.6

[a]Data taken from [3, 10, 11].
[b]For the C atom.

(C_2H_2), we see that after the complete reduction of the C≡C triple bond of C_2H_2 to form the C=C double bond of ethylene (C_2H_4), the overall process is rendered exothermic (Figure 1.1, left). This is not true for N_2 reduction, where every transfer of a H^+/e^- equivalent produces a nitrogen hydride intermediate that is unstable with respect to disproportionation to N_2 and molecular hydrogen (H_2). It is only when the N≡N triple is completely reduced to form two equivalents of NH_3 that the overall transformation becomes favorable (Figure 1.1, right). Thus the challenge of N_2 reduction can be understood to be due to the kinetic and thermodynamic stability of this unique molecule.

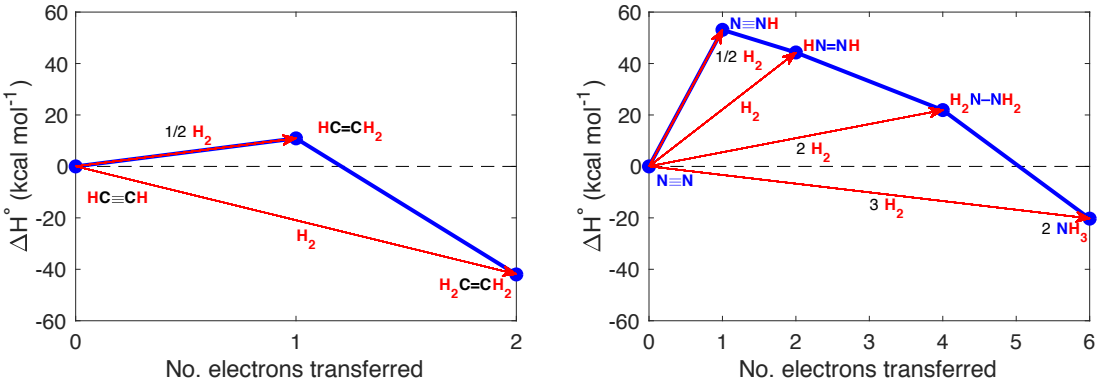

Figure 1.1: Thermodynamics of the reduction of C_2H_2 (left) and N_2 (right). Data taken from [3, 11].

For these reasons, systems capable of the catalytic fixation of N_2 are exceedingly rare. Over the millenia of evolution, only a single family of highly conserved enzymes emerged capable of catalyzing this transformation. Similarly, despite over a century of concerted efforts, only a single synthetic nitrogen fixation technology is practiced at an industrial

scale, and operates to this day on more-or-less the same principles as it did at the time of its discovery in 1909. This dearth has motivated chemists to unravel the mechanistic details of these paradigmatic nitrogen fixation systems, and continues to drive efforts directed at the development of novel synthetic catalysts for the reduction of N_2 to NH_3.

1.3 Catalytic Nitrogen Fixation—A Historical Perspective

1.3.1 The Haber–Bosch Process

Around the turn of the 20th century, the German chemical industry had a vested interest in devising a chemical synthesis of NH_3 from its elements, owing to worries that the outbreak of war may endanger the supply of nitrates for fertilizer (and munitions).[12] In 1909, Fritz Haber succeeded in demonstrating that a tube furnace containing a transition metal catalyst and a mixture of purified N_2 and H_2 could drive the small, equilibrium formation of NH_3 according to Equation 1.1. Industrially-useful reaction rates and single-pass conversion could be achieved at pressures of around 100 atm and temperatures around 500 °C. Under the direction of a second chemist, Carl Bosch, this laboratory-scale demonstration was ultimately commercialized by BASF in 1913. The key to Bosch's success lay in replacing Haber's rather expensive osmium catalyst with a cheaper version based on its 3d congener, Fe.

$$N_2 + 3\,H_2 \underset{\sim 100\text{ atm, }500\text{ °C}}{\overset{\text{catalytic M}}{\rightleftharpoons}} 2\,NH_3 \tag{1.1}$$

The importance of the Haber–Bosch process, as the industrial synthesis of NH_3 from N_2 and H_2 has come to be be known, cannot be overstated. The majority of terrestrial nitrogen is trapped as the inert gas N_2, and, as such, nitrogen is often a limiting nutrient in agroecosystems. The industrialization of NH_3 synthesis, and thus fertilizer, from N_2 has had a dramatic effect on global food security. It is estimated that approximately 50% of the world's population exists today as a result of the food production supported by industrial fertilizer.[13] For this achievment, Haber and Bosch both received Nobel Prizes, in 1918 and

1931, respectively.[iv]

Due to the pioneering surface studies of Gerhard Ertl, the mechanism of nitrogen fixation over Fe surfaces has been elucidated.[14,15] The key step in this mechanism is the rate-limiting dissociative adsorption of N_2 to produce surface-bound Fe nitrides (N*, Equation 1.2), which recombine in a stepwise fashion with surface-bound Fe hydrides (H*) to produce N–H bonds, culminating in the formation of two molecules of NH_3 which desorb from the catalyst (Equation 1.3). In part for his work on the Haber-Bosch process, Ertl, too, received a Nobel Prize in 2007.

$$N_2 \xrightarrow{Fe} 2\,N^* \tag{1.2}$$

$$N^* + 3H^* \rightleftarrows NH_3^* \xrightarrow[-Fe]{} NH_3 \tag{1.3}$$

While many improvements in the chemistry and engineering of the Haber-Bosch process have been made since 1909, including the synthesis of new, highly active catalysts based on the 4d congener of Group VIII, ruthenium,[12] NH_3 generation plants still require enormous energy inputs to operate. The typical input required is about 116 kcal mol^{-1} per molecule of NH_3 synthesized.[16] As a result, Haber-Bosch plants consume approximately 1 to 2% of the world's energy supply each year to to produce about 120 Tg of fixed nitrogen.[1,12] This also contributes to CO_2 emissions, as large amounts of natural gas are consumed to supply the H_2 required via steam reformation. As a large-scale NH_3 synthesis process, it is unlikely that Haber–Bosch will be replaced by emergent N_2-to-NH_3 conversion technologies. However, such technologies may ultimately have a role to play in small-scale, distributed energy infrastructures needed to meet intensifying global energy demands in a sustainable fashion.[17]

[iv] We should be careful not to lionize Fritz Haber, who, in addition to discovering the first catalytic synthesis of NH_3 from its elements, also invented chemical warfare during World War I.[12]

1.3.2 Biological Nitrogen Fixation

The fixation of N_2 to NO_x by lightning storms on prebiotic Earth may have provided the initial supply of fixed nitrogen upon which life evolved; however, because of the high nitrogen content of, for example, proteins (typically 15% nitrogen[5]), evolutionary pressure likely demanded a more efficient and reliable source of reactive nitrogen.[18] Ultimately, this drove the evolution of the nitrogenase family of enzymes, the only enzymatic system known to catalyze the conversion of N_2 to NH_3. The nitrogenases perform this herculean task at ambient pressures, using H^+ derived from water and e^- delivered at biological potentials to reduce N_2 to NH_3 via proton-coupled electron transfer (PCET), according to the (apparent) limiting stoichiometry shown in Equation 1.4.[19] Although the ATP-dependent nature of this reaction means that it, too, is quite costly in energetic terms,[v] the contrast in reaction conditions when compared with Haber-Bosch is remarkable.

$$N_2 + 8\,H^+ + 8\,e^- + 16\,\mathrm{MgATP} \rightarrow 2\,NH_3 + H_2 + 16\,\mathrm{MgADP} + 16\,P_i \qquad (1.4)$$

It was first recognized in 1930 that transition metals were required for nitrogen fixation by diazotrophic[vi] bacteria.[21] Since that time, our understanding of the mechanism of biological nitrogen fixation has matured considerably. Nitrogenase is a two-component system comprised of an obligate ferredoxin-like $[Fe_4S_4]$ protein (Fe protein) that serves as a nucleotide-dependent electron donor to a second component that reduces substrate (MFe protein).[22] In addition to a complex $[Fe_8S_7]$ electron-transfer cluster (P-cluster), the MFe protein features, as the active site of substrate binding and reduction, a complex [MFe_7S_9C-homocitrate] cluster (the FeM-cofactor, or FeMco). This cluster is composed of fused $[Fe_4S_4]$ and $[MFe_3S_4]$ cubanes, where M = V, Mo, or Fe, and a unique μ_6-C^{4-} ligand (Figure 1.2, top).[23,24] Biochemical studies of the Mo-dependent nitrogenase of *Klebsiella pneumoniae* have suggested a unified kinetic scheme, the Lowe-Thorneley (LT) cycle,

[v] The authors of [16] estimate ~60 kcal mol^{-1}, although this number is highly dependent on the free energy of hydrolysis of MgATP, which is sensitive to the precise conditions of the cellular environment.[20]

[vi] Literally, "dinitrogen eaters".

which circumscribes the catalytic cycle for N_2 fixation as a series of kinetically-distinct PCET events (Figure 1.2, bottom),[25,26] while site-directed mutagenesis studies on the Mo-dependent nitrogenase of *Azotobacter vinelandii* have implicated one or more of the Fe centers of FeMoco in bond-making and -breaking events.[27]

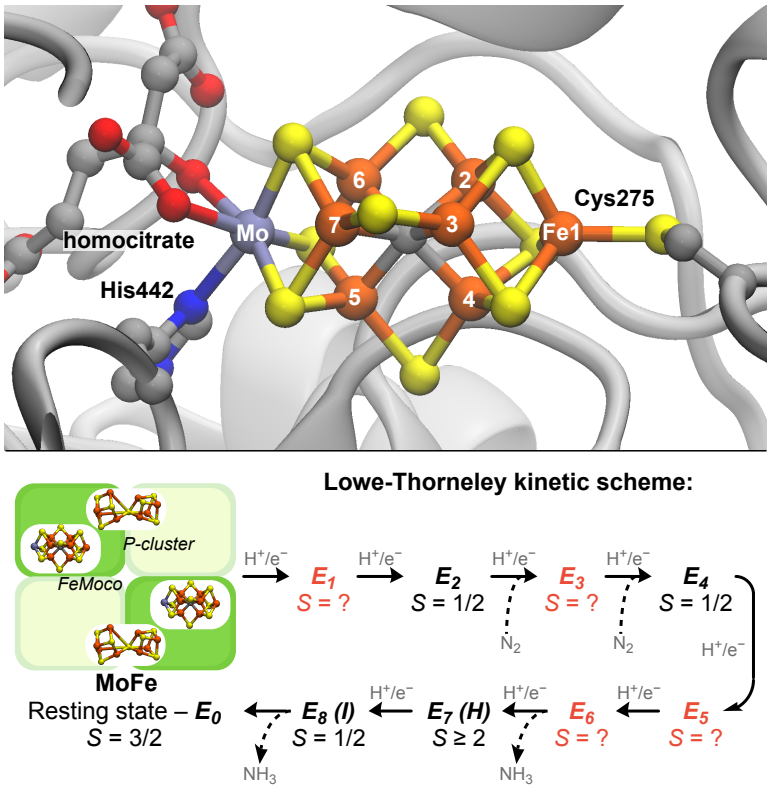

Figure 1.2: (Top) Structure of FeMoco bound in MoFe protein from *Azotobacter vinelandii* [23], along with the numbering scheme for the Fe atoms. (Bottom) Lowe-Thorneley kinetic model of the nitrogenase catalytic cycle, adopting the nomenclature of Hoffman and co-workers [28]. Proposed intermediates that have been the subject of EPR studies are shown in black, while those in red have not been observed.

Despite these advances, an atomically-precise mechanism for N_2 reduction by nitrogenase has yet to be described. For example, although Fe is now proposed to be the active site metal for initial N_2 coordination, even basic questions, such as number and geometry of the ligating Fe atoms, remain unanswered.[28] The central difficulty in studying the mechanism of nitrogenase lies in the fact that the enzyme is quite promiscuous with respect to its substrate, and is capable of reducing not just N_2, but also CN^-, CO, C_2H_2, and N_2O, among

others.[25,29] Even in the absence of these other substrates, nitrogenase will reduce H^+ (from water) to H_2, meaning that catalytic intermediates—of which there are myriad—can only be observed in situ at low temperatures.[28] This has motivated synthetic chemists to direct their efforts at the construction of structural and/or functional models of the active site cofactor, FeMco, both to expose the elementary reaction steps in the reduction of N_2 by molecular catalysts, as well as to develop novel nitrogen fixation technolgies operating via PCET (cf. Equation 1.4).

1.3.3 Synthetic Molecular Catalysts

The binding of N_2 to a discrete transition metal center was first observed in 1965 when Allen and Senoff synthesized the Ru ammine complex shown in Figure 1.3, A.[30] According to the classical Dewar-Chatt-Duncanson model, the binding of N_2 to a metal center should result in charge-transfer from the manifold of filled d_π-symmetry orbitals into the π^* orbitals of the N_2 moiety, polarizing the N–N bond, and disposing the distal N atom (N_β) toward functionalization by electrophiles.[vii] This principle was elegantly demonstrated by Chatt and co-workers in 1972, reporting the first well-defined[viii] example of the protonation of N_2 bound to a transition metal center (Figure 1.3, B).[32] Soon thereafter, many more transition metal systems, principally based off of the Group VI metals Mo and W, were discovered to promote N_2 functionalization, including the complete reduction of the N_2 ligand to N_2H_4 and NH_3.[33]

On the basis of these stoichiometric studies, Chatt and co-workers proposed the schemes shown in Figure 1.3, C for the catalytic reduction of N_2 mediated by a single-site transition metal catalyst.[33] In what has become to be known as the distal Chatt cycle (Figure 1.3, C, boxed reactions), a metal-bound N_2 moiety is sequentially reduced at N_β,

[vii] Other binding modes of N_2 are now known,[31] but the end-on, η^1 binding mode is most relevant to the catalytic nitrogen fixation systems considered here.

[viii] It should be noted that in 1971 Shilov and co-workers reported the reduction of N_2 to mixtures of NH_3 and N_2H_4 in the presence of transition metal salts. Even the catalytic reduction of N_2 to N_2H_4 was realized, although the active species in this system is ill-defined.[2]

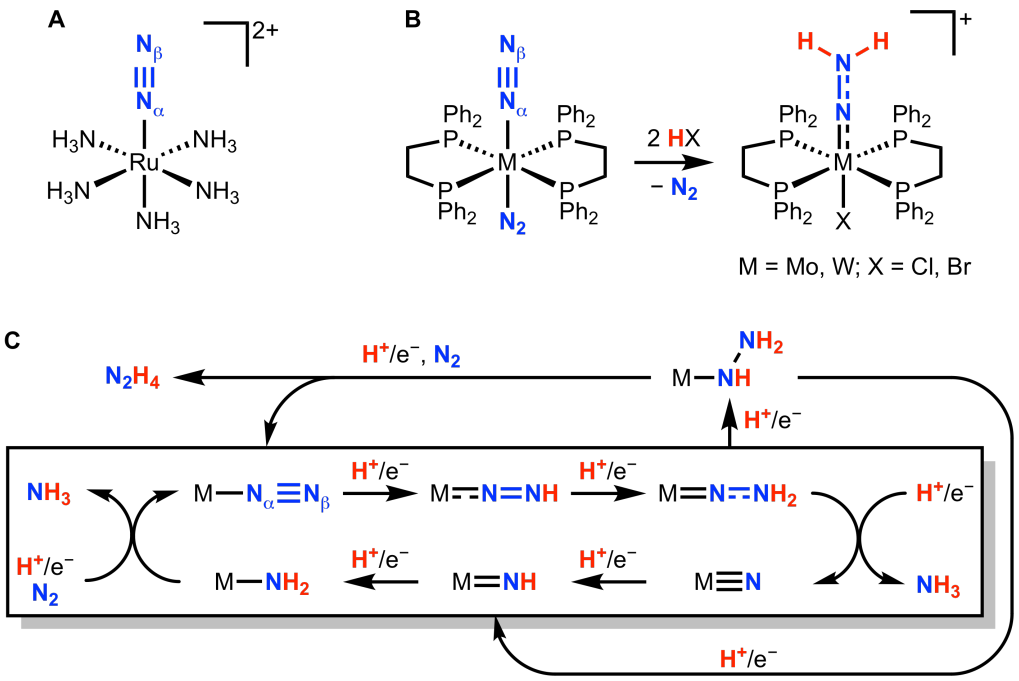

Figure 1.3: (A) The first example of a molecular transition metal compound that binds N_2. (B) The first well-defined example of the protonation of a transition metal bound N_2 ligand. (C) The Chatt cycles.

yielding metal diazenido, M(NNH), and hydrazido(2−), M(NNH_2), intermediates prior to the key N–N bond cleavage reaction to produce a terminal metal nitrido, M≡N,[ix] and the first equivalent of NH_3. The further 3 H^+/3 e^- reduction of this nitrido releases the second equivalent of NH_3 and recovers the low valent starting material in the presence of N_2.

Based on the observation that certain W(N_2) complexes promoted the reduction of the N_2 ligand to the hydrazido(1−) state, M($NHNH_2$), and could release this ligand as free N_2H_4 upon protonolysis, it was also proposed that the catalytic cycle could diverge at the M(NNH_2) state.[33] After α-functionalization to produce M($NHNH_2$), this hydrazido(1−) complex could either continue functionalization at N_α, leading to the release of N_2H_4, or undergo a similar N–N bond cleavage reaction as in the distal mechanism to produce a terminal metal imido intermediate, M=NH (Figure 1.3, C). A purely "alternating" cycle can also be envisioned—proceeding from M(NNH) to a metal diazene adduct, M(N_2H_2),

[ix] Potentially via the intermediacy of a triply β-functionalized hydrazidium species, M(NNH_3).

and thence to $M(NHNH_2)$.[x]

As an early proof-of-principle demonstration of the Chatt cycle, in 1985 Pickett and Talarmin reported a cyclic electrosynthesis of NH_3 from N_2 via stepwise protonation and reduction of *trans*-$(dppe)_2W(N_2)_2$ (Figure 1.4, A),[38] however subsequent attempts to render this process electrocatalytic have been unsuccessful.[39] Although the intervening years have seen numerous examples of the coordination, reduction, and functionalization of N_2 at Groups IV through IX metal centers,[40,41] the first catalytic nitrogen fixation reaction mediated by well-defined molecular complexes was only reported in 2003 by Schrock and co-workers.[42]

In the Schrock system, N_2 is reduced at room temperature and 1 atm in a heterogeneous mixture of $CrCp^*_2$ (Cp^* = pentamethylcyclopentadienide), $[LutH][BAr^F{}_4]$ ($[LutH]^+$ = 2,6-dimethylpyridinium; $[BAr^F{}_4]^-$ = tetrakis(3,5-bis(trifluoromethyl)phenyl)borate), and a catalytic amount of $[(HIPTN_3)Mo(N_xH_y)]^n$ (Figure 1.4, B). A variety of $(HIPTN_3)Mo$ complexes with nitrogenous ligands were shown to be effective precatalysts, and yields up to 8 equivalents of NH_3 per Mo atom were obtained. Remarkably, Schrock and co-workers isolated and characterized 9 of the 14 possible intermediates along a Chatt-like catalytic cycle, and demonstrated the stepwise interconversion of many of these species under catalytically-relevant conditions.[43–45] Along with theoretical studies,[46] these results argue strongly in favor of the distal Chatt cycle (Figure 1.3, C).

It took another 8 years before the second example of a catalytic nitrogen fixation reaction mediated by molecular transition metal complexes was reported by Nishibayashi and co-workers.[47] In this system, a family of dinuclear Mo complexes featuring PNP pincer ligands catalyze the reduction of N_2 to NH_3 at room temperature and 1 atm in a heterogeneous mixture of $CoCp_2$ (Cp = cyclopentadienide) and [LutH][OTf] ($[OTf]^-$ = trifluoromethanesulfonate), with yields of up to 26 equivalents of NH_3 per Mo atom

[x]There is compelling evidence that the recently-discovered catalytic reduction of N_2 to N_2H_4 by bisphosphine-supported Fe complexes might proceed via this mechanism.[4,34,35] For an example of initial α-functionalization, see [36, 37].

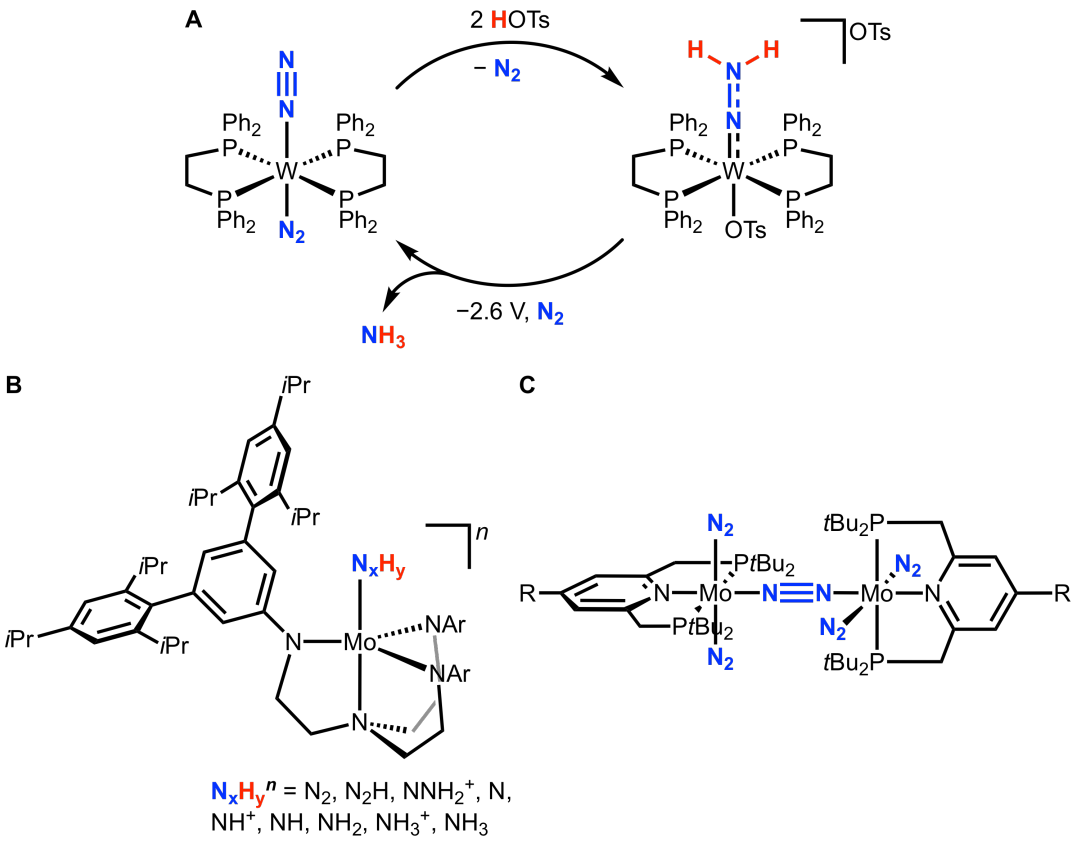

Figure 1.4: (A) Cyclic scheme for the electrosynthesis of NH_3 reported by Pickett and Talarmin; after three cycles, the maximum observed yield of NH_3 is 73%. (B) $[(HIPTN_3)Mo(N_xH_y)]^n$ complexes relevant to the catalytic nitrogen fixation reaction developed by Schrock and co-workers. (C) Dinuclear (PNP)Mo complexes reported by Nishibayashi and co-workers for catalytic nitrogen fixation.

(Figure 1.4, C).[47,48] The isolation of several Chatt-like intermediates in this system is also consistent with a distal mechanism, although the precise speciation of Mo (e.g., mono- versus dinuclear) under turnover conditions is unclear.[47,49]

Despite these slow beginnings, between 2014 and the present, the number of synthetic molecular catalysts for nitrogen fixation has expanded considerably; a comprehensive account can be found in Chapter 3. The field is therefore undergoing an exciting *naissance*, which motivates detailed mechanistic study of the most active catalysts. In addition to the academic merit of such study, elucidating the operating principles behind these catalysts may inform the design of novel nitrogen fixation technologies in the future.

1.4 A Synthetic Fe-based "Nitrogenase"

Because of the presence of Mo in the most efficient nitrogenase enzymes and the early success of synthetic Group VI complexes in stoichiometric N_2 reduction, much focus has been placed on the development of Mo-based nitrogen fixation catalysts (*vide supra*). However, the proposal that Fe is the substrate-binding site of FeMoco,[27] coupled with the fact that Fe is the only obligate metal of biological nitrogen fixation,[22] has motivated our group, among others,[50] to develop Fe-based nitrogen fixation catalysts.

Taking inspiration from the local trigonal symmetry of the so-called belt Fe atoms of FeMoco (Fe2 through Fe7, Figure 1.2), we have been interested in the chemistry of Fe phopshine complexes under C_3 symmetry. Under three-fold symmetry, the ($3d_{x^2-y^2}$, $3d_{xy}$) and ($3d_{xz}$, $3d_{yz}$) orbitals split into two doubly-degenerate e sets, the relative ordering of which is determined by the degree of pyramidalization about the metal center (Figure 1.5, A). We hypothesized that, in principle, this effect could modulate the π-basicity of the metal, allowing a single Fe center to support both π-acidic and π-basic nitrogenous moieties that may be sampled along a N_2 fixation pathway (Figure 1.3, C). Lending credence to this idea, early work using tris(phosphino)borate ligands demonstrated that a single pseudo-tetrahedral Fe center can support both N_2 and N^{3-} ligands and formal oxidation states ranging from Fe(0) to Fe(IV) (Figure 1.5, B).[51,52]

In recent years, we have focused on a family of Sacconi-type tetradentate ligands,[53] P_3^E (P_3^E = tris(*o*-diisopropylphosphinophenyl)-borane, -methide, or -silylide), in which three phosphine donors are bonded to a central atom through an *o*-phenylene linker (E = B, Si, C; Figure 1.5, C). With this ligand platform, the presence of the axial atom allows the metal to sample both trigonal bipyramidal and pseudo-tetrahedral geometries, the degree of pyramidalization depending on the flexibility of the M–E interaction. We have shown that (P_3^E)Fe complexes promote the binding and activation of N_2, as well as the functionalization of bound N_2 with various electrophiles.[54–59] In 2013, it was discovered that the (P_3^B)Fe platform could catalytically reduce N_2 to NH_3 using an extremely potent acid/reductant

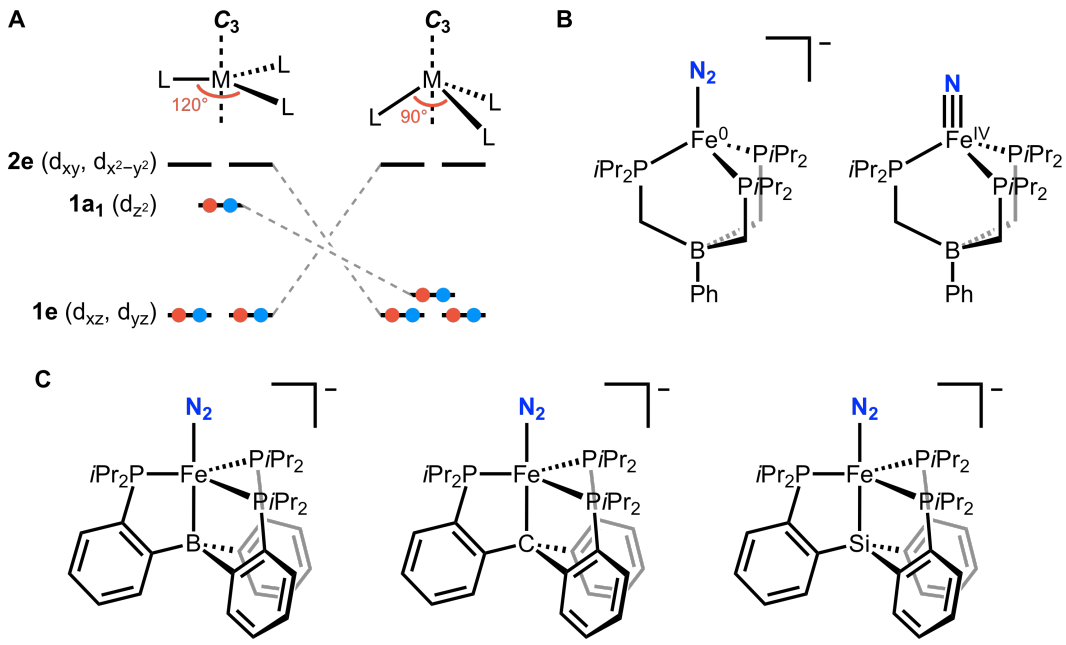

Figure 1.5: (A) Qualitative ligand field splitting diagrams for a metal center under idealized C_{3v} symmetry, showing the effect of pyramidalization on the relative energy of the d_δ and d_π e-symmetry orbitals. (B) Examples of $Fe^0(N_2)$ and $Fe^{IV}{\equiv}N$ complexes supported by the same tris(phosphino)borate ligand. (C) The $[(P_3{}^E)Fe(N_2)]^-$ complexes that are the subject of this thesis.

pair—$[H(OEt_2)_2][BAr^F{}_4]$ ($HBAr^F{}_4$) and KC_8—in Et_2O at −78 °C.[60] Soon thereafter, this catalysis was extended to the $(P_3{}^C)$Fe platform.[59] More recently, we have discovered that a much milder chemical reductant, $CoCp^*{}_2$, can also drive this catalysis.[61]

This discovery represents the third example of a synthetic molecular catalyst for nitrogen fixation, and the first using the biologically-relevant metal, Fe. As such, we turned our focus to mechanistic study of the $(P_3{}^E)$Fe system through the combination of synthetic, stoichiometric, and in situ studies. The body of this thesis details a portion of these efforts, as summarized below.

1.5 Chapter Summaries

Perhaps counter-intuitively, Chapter 2 details the synthesis and N_2-to-NH_3 conversion activity of a series of $(P_3{}^E)$Co complexes. However, the central goal of this work was to provide a structure-function study of $(P_3{}^E)$M complexes in which, rather than altering

the nature of the axial E ligand, the nature of the transition metal ion was changed in a fashion that predictably modulated the electronics of the system. After synthesizing a series of $[(P_3{}^E)Co(N_2)]^n$ complexes and subjecting them to the standard catalytic reaction conditions developed for the previously-reported Fe catalysts, it was found that only the borane complex $[(P_3{}^B)Co(N_2)]^-$ furnished super-stoichiometric yields of NH_3, suggesting that "$(P_3{}^B)Co$" serves as a molecular (pre)catalyst for N_2 fixation, and highlighting the importance of the *Z*-type M–B motif in N_2 fixation activity. Prior to this study, the only well-defined molecular systems (including nitrogenase enzymes) capable of directly mediating the catalytic conversion of N_2 to NH_3 contained either Mo or Fe ions. These results point to Group IX $M(N_2)$ complexes as targets for the development of novel N_2-fixing catalysts.

Chapter 3 details in situ mechanistic studies of nitrogen fixation catalyzed by $[(P_3{}^B)Fe(N_2)]^-$ under the originally-reported reaction conditions. In this study, we were able to achieve a nearly order-of-magnitude improvement of catalyst turnover, at the cost of lowered yields due to competitive catalyzed and uncatalyzed hydrogen evolving reactions (HER). Study of the reaction dynamics evidence a single-site mechanism for N_2 reduction, and the successful demonstration of electrolytic N_2-to-NH_3 conversion indicates that the active redox state during catalysis is $[(P_3{}^B)Fe(N_2)]^-$. In situ monitoring of catalytic reaction mixtures using freeze-quench ^{57}Fe Mössbauer spectroscopy suggests that a previously characterized borohydrido–hydrido species is an off-path resting state of the overall catalysis. This hydride species, which was previously posited to be primarily a catalyst sink, can instead re-enter the catalytic pathway via its conversion to catalytically active $[(P_3{}^B)Fe(N_2)]^-$. This observation underscores the importance of understanding hydride reactivity in the context of metal-mediated N_2 fixation. The observed HER activity may provide a viable strategy for recovering catalytically active states from the unavoidable generation of metal hydride intermediates.

In Chapter 4, we study the key N–N bond cleavage step in the catalytic cycle for N_2

reduction by $[(P_3{}^B)Fe(N_2)]^-$. Although we had proposed that this process might occur at a single Fe center in a heterolytic fashion to produce NH_3 and a terminal Fe nitride, such reactivity had never been confirmed experimentally for any $Fe(N_2)$ complex. In this chapter, we demonstrate that sequential reduction and low-temperature protonation of $[(P_3{}^B)Fe(N_2)]^-$ cleanly produces the (formally) hydrazido(2−) complex $(P_3{}^B)Fe(NNH_2)$. In turn, this species undergoes protonolysis of the N–N bond to produce the terminal nitrido $[(P_3{}^B)Fe{\equiv}N]^+$. Characterization of these highly reactive species was accomplished via freeze-quench ^{57}Fe Mössbauer and Fe *K*-edge X-ray absorption spectroscopy (XAS). This result validates the hypothesis above, and shows that the distal Chatt cycle is a plausible mechanism for catalytic nitrogen fixation by $[(P_3{}^B)Fe(N_2)]^-$. Spectroscopic and computational studies suggest that this reactivity is enabled by a buffering of the physical oxidation state range of the Fe via metal-ligand covalency. In this way, the redox behavior of the $(P_3{}^B)Fe$ unit crudely models that of a metallocluster, in which the potential range of multi-electron processes is compressed by delocalization of electrons/holes among many metals, a feature of potential relevance to biological N_2 fixation.

Finally, in Chapter 5 we present spectroscopic and computational studies detailing the electronic structures of a redox series of $Fe(NNR_2)$ complexes that model key catalytic intermediates occurring prior to the N–N bond cleavage step. Although two closed-shell configurations of the "NNR_2" ligand have been commonly considered in the literature—isodiazene and hydrazido(2−)—we present evidence suggesting that $[(P_3{}^E)Fe(NNR_2)]^n$ complexes contain an open-shell $[NNR_2]^{\bullet-}$ ligand coupled antiferromagnetically to the Fe center. This one-electron redox non-innocence resembles that of the classically non-innocent ligand, NO, and may have mechanistic implications for the divergent nitrogen fixation activity of the $(P_3{}^B)Fe$ and $(P_3{}^{Si})Fe$ platforms.

References

(1) Fowler, D. et al. *Phil. Trans. R Soc. B* **2013**, *368*, DOI: 10.1098/rstb.2013.0164.

(2) Shilov, A.; Denisov, N.; Efimov, O.; Shuvalov, N.; Shuvalova, N.; Shilova, A. *Nature* **1971**, *231*, 460–461.

(3) Bazhenova, T.; Shilov, A. *Coord. Chem. Rev.* **1995**, *144*, 69–145.

(4) Hill, P. J.; Doyle, L. R.; Crawford, A. D.; Myers, W. K.; Ashley, A. E. *J. Am. Chem. Soc.* **2016**, *138*, 13521–13524.

(5) Greenwood, N. N.; Earnshaw, A., *Chemistry of the Elements*, 2nd ed.; Elsevier Butterworth-Heinemann: New York, 1997.

(6) Six, C.; Richter, F. In *Ullmann's Encyclopedia of Industrial Chemistry*; Wiley-VCH: 2003.

(7) Kalescky, R.; Kraka, E.; Cremer, D. *J. Phys. Chem. A* **2013**, *117*, 8981–8995.

(8) Olah, G. A.; Prakash, G. K. S.; Molnár, A.; Sommer, J., *Superacid Chemistry*, 2nd ed.; Wiley: Hoboken, 2009.

(9) Caselli, P.; Myers, P. C.; Thaddeus, P. *Astrophys. J. Lett.* **1995**, *455*, L77.

(10) Chatt, J. *Pure Appl. Chem.* **1970**, *24*, 425–442.

(11) Siegbahn, P. E. M.; Westerberg, J.; Svensson, M.; Crabtree, R. H. *J. Phys. Chem. B* **1998**, *102*, 1615–1623.

(12) Smil, V., *Enriching the Earth: Fritz Haber, Carl Bosch, and the Transformation of World Food Production*; MIT Press: Cambridge, 2001.

(13) Erisman, J. W.; Sutton, M. A.; Galloway, J.; Klimont, Z.; Winiwarter, W. *Nat. Geosci.* **2008**, *1*, 636–639.

(14) Ertl, G. *J. Vac. Sci. Technol., A* **1983**, *1*, 1247–1253.

(15) Ertl, G. *Angew. Chem. Int. Ed.* **2008**, *47*, 3524–3535.

(16) Van der Ham, C. J. M.; Koper, M. T. M.; Hetterscheid, D. G. H. *Chem. Soc. Rev.* **2014**, *43*, 5183–5191.

(17) Jewess, M.; Crabtree, R. H. *ACS Sustainable Chem. Eng.* **2016**, *4*, 5855–5858.

(18) Navarro-González, R.; McKay, C. P.; Mvondo, D. N. *Nature* **2001**, *412*, 61–64.

(19) Simpson, F.; Burris, R. *Science* **1984**, *224*, 1095–1097.

(20) Nelson, D. L.; Cox, M. M., *Lehninger Principles of Biochemistry*, 5th ed.; W. H. Freeman and Co.: New York, 2008.

(21) Bortels, H. *Arch. Mikrobiol.* **1930**, *1*, 333–342.

(22) Rees, D. C.; Akif Tezcan, F.; Haynes, C. A.; Walton, M. Y.; Andrade, S.; Einsle, O.; Howard, J. B. *Phil. Trans. R. Soc. A* **2005**, *363*, 971–984.

(23) Spatzal, T.; Aksoyoglu, M.; Zhang, L.; Andrade, S. L. A.; Schleicher, E.; Weber, S.; Rees, D. C.; Einsle, O. *Science* **2011**, *334*, 940–940.

(24) Lancaster, K. M.; Roemelt, M.; Ettenhuber, P.; Hu, Y.; Ribbe, M. W.; Neese, F.; Bergmann, U.; DeBeer, S. *Science* **2011**, *334*, 974–977.

(25) Burgess, B. K.; Lowe, D. J. *Chem. Rev.* **1996**, *96*, 2983–3012.

(26) Wilson, P.; Nyborg, A.; Watt, G. *Biophys. Chem.* **2001**, *91*, 281–304.

(27) Dos Santos, P. C.; Igarashi, R. Y.; Lee, H.-I.; Hoffman, B. M.; Seefeldt, L. C.; Dean, D. R. *Acc. Chem. Res.* **2005**, *38*, 208–214.

(28) Hoffman, B. M.; Lukoyanov, D.; Yang, Z.-Y.; Dean, D. R.; Seefeldt, L. C. *Chem. Rev.* **2014**, *114*, 4041–4062.

(29) Hu, Y.; Lee, C. C.; Ribbe, M. W. *Science* **2011**, *333*, 753–755.

(30) Allen, A. D.; Senoff, C. V. *Chem. Commun.* **1965**, 621–622.

(31) Holland, P. L. *Dalton Trans.* **2010**, *39*, 5415–5425.

(32) Chatt, J.; Heath, G. A.; Richards, R. L. *J. Chem. Soc., Chem. Commun.* **1972**, 1010–1011.

(33) Chatt, J.; Dilworth, J. R.; Richards, R. L. *Chem. Rev.* **1978**, *78*, 589–625.

(34) Piascik, A. D.; Hill, P. J.; Crawford, A. D.; Doyle, L. R.; Green, J. C.; Ashley, A. E. *Chem. Commun.* **2017**, *53*, 7657–7660.

(35) Field, L. D.; Li, H. L.; Dalgarno, S. J.; Turner, P. *Chem. Commun.* **2008**, 1680–1682.

(36) Sellmann, D.; Weiss, W. *Angew. Chem. Int. Ed.* **1977**, *16*, 880–881.

(37) Sellmann, D.; Weiss, W. *Angew. Chem. Int. Ed.* **1978**, *17*, 269–270.

(38) Pickett, C. J.; Talarmin, J. *Nature* **1985**, *317*, 652–653.

(39) Pickett, C. J.; Ryder, K. S.; Talarmin, J. *J. Chem. Soc., Dalton Trans.* **1986**, 1453–1457.

(40) Fryzuk, M. D.; Johnson, S. A. *Coord. Chem. Rev.* **2000**, *200-202*, 379–409.

(41) Khoenkhoen, N.; de Bruin, B.; Reek, J. N. H.; Dzik, W. I. *Eur. J. Inorg. Chem. 2015*, 567–598.

(42) Yandulov, D. V.; Schrock, R. R. *Science* **2003**, *301*, 76–78.

(43) Yandulov, D. V.; Schrock, R. R. *J. Am. Chem. Soc.* **2002**, *124*, 6252–6253.

(44) Yandulov, D. V.; Schrock, R. R. *Inorganic Chemistry* **2005**, *44*, 1103–1117.

(45) Weare, W. W.; Dai, X.; Byrnes, M. J.; Chin, J. M.; Schrock, R. R.; Müller, P. *Proc. Natl. Acad. Sci.* **2006**, *103*, 17099–17106.

(46) Schrock, R. R. *Angew. Chem. Int. Ed.* **2008**, *47*, 5512–5522.

(47) Arashiba, K.; Miyake, Y.; Nishibayashi, Y. *Nat. Chem.* **2011**, *3*, 120–125.

(48) Kuriyama, S.; Arashiba, K.; Nakajima, K.; Tanaka, H.; Kamaru, N.; Yoshizawa, K.; Nishibayashi, Y. *J. Am. Chem. Soc.* **2014**, *136*, 9719–9731.

(49) Tanaka, H.; Arashiba, K.; Kuriyama, S.; Sasada, A.; Nakajima, K.; Yoshizawa, K.; Nishibayashi, Y. *Nat. Commun.* **2014**, *5*, 3737.

(50) Hazari, N. *Chem. Soc. Rev.* **2010**, *39*, 4044–4056.

(51) Betley, T. A.; Peters, J. C. *J. Am. Chem. Soc.* **2003**, *125*, 10782–10783.

(52) Betley, T. A.; Peters, J. C. *J. Am. Chem. Soc.* **2004**, *126*, 6252–6254.

(53) Stoppioni, P.; Mani, F.; Sacconi, L. *Inorg. Chim. Acta* **1974**, *11*, 227–230.

(54) Mankad, N. P.; Whited, M. T.; Peters, J. C. *Angew. Chem. Int. Ed.* **2007**, *46*, 5768–5771.

(55) Lee, Y.; Mankad, N. P.; Peters, J. C. *Nat. Chem.* **2010**, *2*, 558–565.

(56) Moret, M.; Peters, J. C. *Angew. Chem. Int. Ed.* **2011**, *50*, 2063–2067.

(57) Moret, M.-E.; Peters, J. C. *J. Am. Chem. Soc.* **2011**, *133*, 18118–18121.

(58) Anderson, J. S.; Moret, M.-E.; Peters, J. C. *J. Am. Chem. Soc.* **2013**, *135*, 534–537.

(59) Creutz, S. E.; Peters, J. C. *J. Am. Chem. Soc.* **2014**, *136*, 1105–1115.

(60) Anderson, J. S.; Rittle, J.; Peters, J. C. *Nature* **2013**, *501*, 84–87.

(61) Chalkley, M. J.; Del Castillo, T. J.; Matson, B. D.; Roddy, J. P.; Peters, J. C. *ACS Cent. Sci.* **2017**, *3*, 217–223.

Chapter 2

EVALUATING MOLECULAR COBALT COMPLEXES FOR THE CONVERSION OF N_2 TO NH_3

2.1 Introduction

Despite extensive study, there are many unanswered questions regarding the rational design of molecular N_2-to-NH_3 conversion catalysts. It may be that the ability of a complex to activate terminally bound N_2 (often taken to be reported by the IR-active N–N stretching frequency, ν_{NN}) relates to the propensity of that complex to functionalize the N_2 moiety. For example, $HCo(N_2)(PPh_3)_3$ (ν_{NN} = 2088 cm^{-1}) quantitatively releases N_2 upon treatment with acid, with no evidence of N_2 functionalization;[1,2] however, if this cobalt complex is deprotonated to generate the more activated complex $[Li(Et_2O)_3][(PPh_3)_3Co(N_2)]$ (ν_{NN} = 1900 cm^{-1}), treatment with acid does produce some NH_3 and N_2H_4 (0.21 and 0.22 equiv, respectively).[2] Extensive efforts have been made to study the activation and functionalization of N_2 bound to metal centers of varying electronic properties.[3–9] In some cases, systems have been shown to activate bound N_2 to the extent that the N–N bond is fully cleaved.[10–18] In other cases, it has been shown that the treatment of strongly activated N_2 complexes with acid or H_2 leads to reduced nitrogenous products.[1–9] However, this guiding principle alone has been insufficient in the design of synthetic species capable of catalyzing the conversion of N_2 to NH_3.[6,19–24] In this regard, it is prudent to study the few systems known to catalyze this reaction with an emphasis on identifying those properties critical to the observed N_2 reduction activity.

In 2013 we reported that $[(P_3{}^B)Fe(N_2)]^-$ catalyzes the conversion of N_2 to NH_3 at −78 °C.[21] We have postulated that the success of this system in activating N_2 stoichiometrically and mediating its catalytic conversion to NH_3 may arise from a highly flexible

Reproduced in part with permission from Del Castillo, T. J.; Thompson, N. B.; Suess, D. L.; Ung, G.; Peters, J. C. *Inorg. Chem.* **2015**, *54*, 9256–9262.

Fe–B interaction.[25,26] Such flexibility, *trans* to the N_2 binding site, may allow a single Fe center to access both trigonal bipyramidal and pseudo-tetrahedral coordination geometries, alternately stabilizing π-acidic or π-basic nitrogenous moieties sampled along an N_2 fixation pathway.[4] Consistent with this hypothesis, we have studied isostructural $P_3{}^E$-ligated Fe systems and found a measurable dependence of the nitrogen fixation activity on the identity of the E atom, with the least flexible E = Si system furnishing divergently low NH_3 yields and the more flexible E = C or B systems affording moderate yields of NH_3.[21,22] However, the lower NH_3 production by the E = Si precursor may alternatively be attributed to other factors. Potential factors include: (i) a lesser degree of N_2 activation than that observed in the E = C or B species (*vide infra*); (ii) faster poisoning of the E = Si system, for example, by more rapid formation of an inactive terminal hydride;[21,22] or (iii) faster degradation of the E = Si system, for example, by dechelation of the ligand.

To complement our previous ligand modification studies, here we instead alter the identity of the transition metal. Moving from Fe to Co predictably modulates the π basicity and electronic configuration of the metal center while maintaining the ligand environment. In principle, this allows the extrication of electronic effects, such as π backbonding, from structural features, such as geometric flexibility, via a comparison of the Fe and Co systems. We therefore sought to explore the N_2 reduction activity of Co complexes of the $P_3{}^E$ family of ligands. While correlating NH_3 yields with molecular structure is no doubt informative in terms of understanding the behavior of nitrogen-fixing systems, correlation does not imply causation, and the results described herein should be read with that in mind.

2.2 Results and Discussion

2.2.1 Synthesis and Structural Analysis

The previously reported complex $(P_3{}^B)Co(N_2)$ provides a logical entry point to study the N_2 chemistry of $(P_3{}^B)Co$ complexes (Figure 2.1).[27] The cyclic voltammogram of $(P_3{}^B)Co(N_2)$ in THF displays a quasi-reversible reduction wave at −2.0 V vs $Fc^{+/0}$ and

a feature corresponding to an oxidation process at −0.2 V vs $Fc^{+/0}$ (Figure 2.2). These features are reminiscent of the cyclic voltammogram of $(P_3{}^B)Fe(N_2)$, which shows a reduction event at −2.1 V vs $Fc^{+/0}$ and an oxidation event at −1.5 V vs $Fc^{+/0}$.[26]

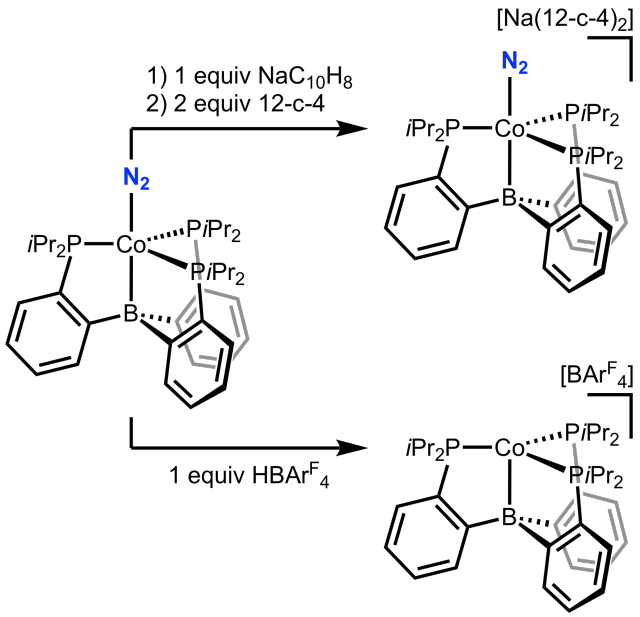

Figure 2.1: Chemical oxidation and reduction of $(P_3{}^B)Co(N_2)$.

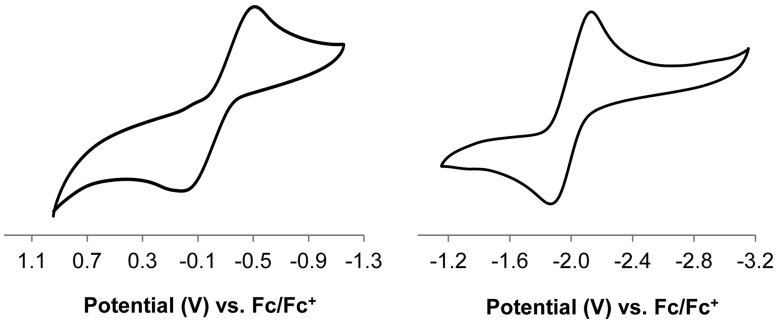

Figure 2.2: Cyclic voltammagrams of $(P_3{}^B)Co(N_2)$ scanning oxidatively (left) and reductively (right) at 100 mV s^{-1} in THF with a 0.1 M [TBA][PF_6] electrolyte.

Treatment of $(P_3{}^B)Co(N_2)$ with 1 equiv of $NaC_{10}H_8$ followed by 2 equiv of 12-crown-4 (12-c-4) generates diamagnetic $[Na(12\text{-c-}4)_2)][(P_3{}^B)Co(N_2)]$ as a red crystalline solid (Figure 2.1). The ν_{NN} stretch of $[(P_3{}^B)Co(N_2)]^-$ is lower in energy than that of $(P_3{}^B)Co(N_2)$ (Table 2.1), and the solid-state structure of $[(P_3{}^B)Co(N_2)]^-$ displays contracted Co–N, Co–B, and Co–P distances compared to $(P_3{}^B)Co(N_2)$, consistent with increased π/σ backbond-

ing to each of these atoms. The one-electron oxidation of $(P_3^B)Co(N_2)$ can be achieved by the addition of 1 equiv of $HBAr^F_4$ at low temperature followed by warming, which generates red-purple $[(P_3^B)Co][BAr^F_4]$ (Figure 2.1). The structure of $[(P_3^B)Co]^+$ (Figure 2.3) confirms that it does not bind N_2 in the solid state. The lack of N_2 binding at room temperature for $[(P_3^B)Co]^+$ is consistent with the behavior of the isostructural Fe complex $[(P_3^B)Fe][BAr^F_4]$.[28] SQUID magnetometry measurements indicate that $[(P_3^B)Co]^+$ is high spin ($S = 1$) in the solid state with no evidence for spin crossover.

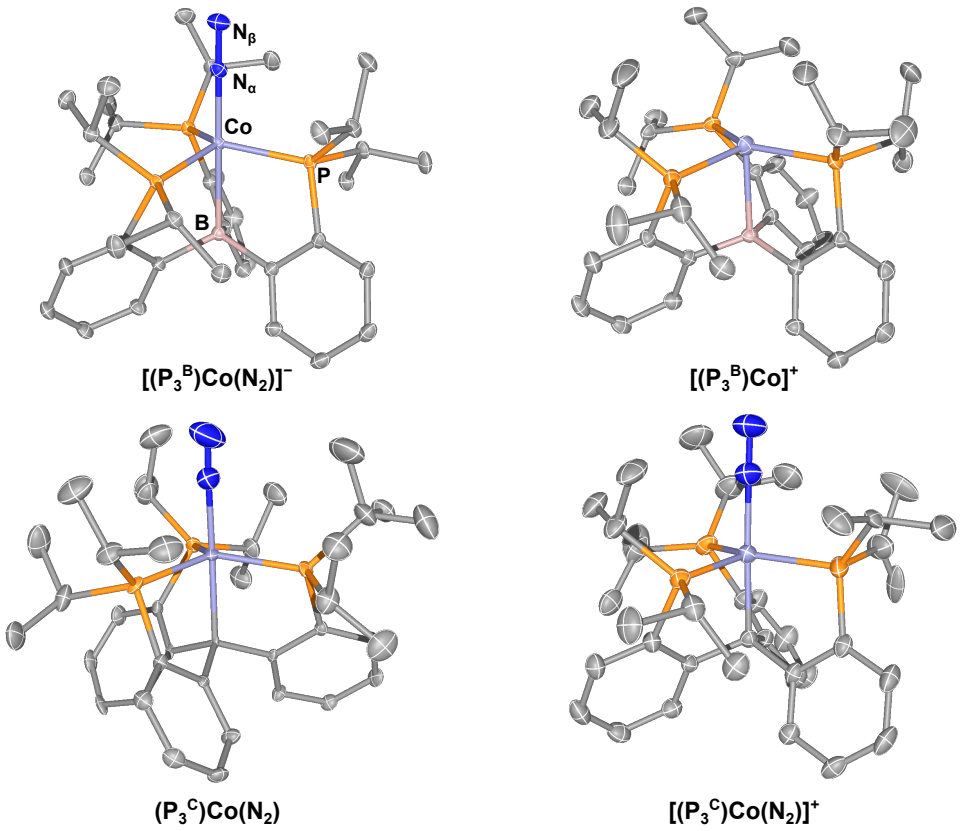

Figure 2.3: Solid-state structures of $[(P_3^B)Co(N_2)]^-$, $[(P_3^B)Co]^+$, $(P_3^C)Co(N_2)$, and $[(P_3^C)Co(N_2)]^+$ as determined by X-ray crystallography. Thermal ellipsoids are shown at 50% probability. Counterions, solvent molecules, and H atoms are omitted for clarity.

The synthesis of $(P_3^{Si})Co(N_2)$ was reported previously.[29] The isoelectronic alkyl species $(P_3^C)Co(N_2)$ was obtained in 83% yield as a deep-red solid from the reaction of $(P_3^C)H$, $CoCl_2 \cdot 1.5THF$, and MeMgCl under an N_2 atmosphere (Figure 2.4). $(P_3^C)Co(N_2)$

($\nu_{NN} = 2057\ cm^{-1}$) is diamagnetic, possesses C_3 symmetry in solution, and binds N_2, as confirmed by its solid-state structure (Figure 2.3). The cyclic voltammogram of $(P_3^C)Co(N_2)$ in THF displays a quasi-reversible oxidation wave at −1.1 V vs $Fc^{+/0}$ (Figure 2.5, left). Treatment of $(P_3^C)Co(N_2)$ with 1 equiv of $[Fc][BAr^F{}_4]$ at low temperature allowed for isolation of the one-electron oxidation product $[(P_3^C)Co(N_2)][BAr^F{}_4]$ (ν_{NN} = 2182 cm^{-1}) in 86% yield after recrystallization (Figure 2.4). The coordinated N_2 ligand of $[(P_3^C)Co(N_2)]^+$ is labile and can be displaced under vacuum (Figure 2.5, middle) to generate a vacant or possibly solvent-coordinated $[(P_3^C)Co(L)]^+$ species. The CW X-band EPR spectrum of $[(P_3^C)Co(N_2)]^+$ at 80 K under N_2 is consistent with an $S = 1/2$ species (Figure 2.5, right).

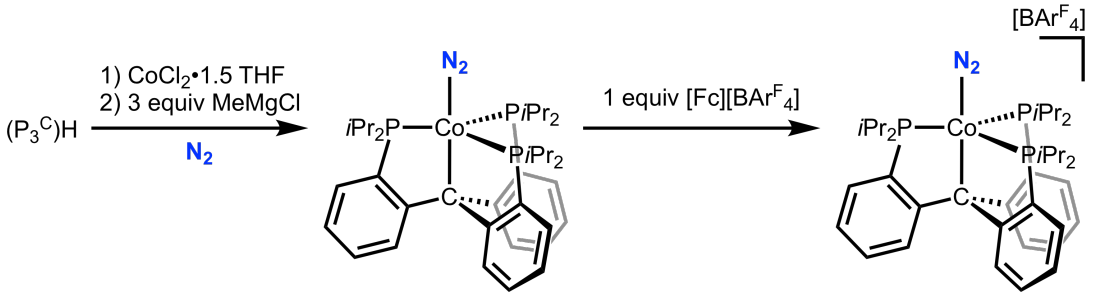

Figure 2.4: Synthesis and Oxidation of $(P_3^C)Co(N_2)$.

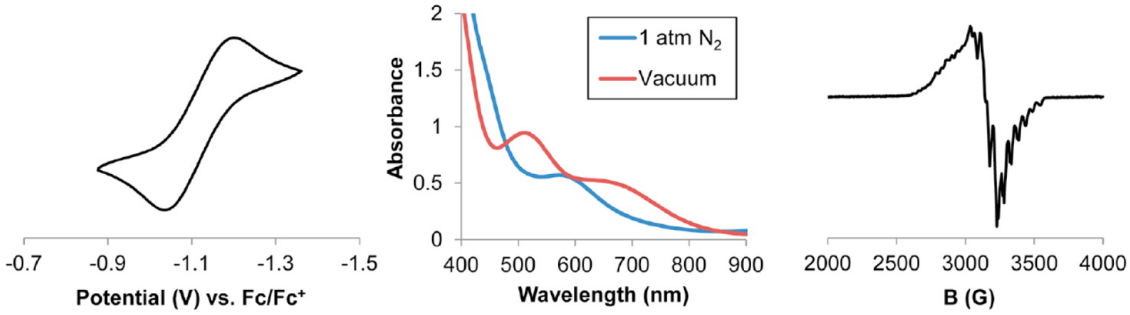

Figure 2.5: (Left) Cyclic voltammogram of $(P_3^C)Co(N_2)$ scanning oxidatively at 100 mV s^{-1} in THF with a 0.1 M $[TBA][PF_6]$ electrolyte. (Middle) UV–vis spectra of $[(P_3^C)Co(N_2)]^+$ under 1 atm of N_2 (solid line) and under static vacuum (dotted line; after three freeze–pump–thaw cycles). Spectra were collected on a 1 mM solution of $[(P_3^C)Co(N_2)]^+$ in THF at 298 K. (Right) CW X-band EPR spectrum of $[(P_3^C)Co(N_2)]^+$ collected under 1 atm of N_2 in 2-MeTHF at 77 K. No low-field features were detected.

With these complexes in hand, we have completed the synthesis of a family of isostructural $(P_3^E)M$ complexes of Fe and Co. Select physical data for these complexes are presented

in Table 2.1. A comparison between the Fe and Co complexes reveals trends which may be of relevance to the ability of these complexes to mediate the reduction of N_2 to NH_3. First, consideration of the M–E interatomic distances presented in Table 2.1 reveals that the ($P_3{}^B$)Co platform exhibits a significant degree of flexibility in the M–B interaction, similar to that observed for the ($P_3{}^B$)Fe platform. Within each platform, the M–B distance varies by > 0.16 Å between the neutral halide and anionic N_2 complexes. Likewise, the M–C interaction among ($P_3{}^C$)Co complexes exhibits flexibility comparable to that of the analogous iron series. For both platforms, the M–C distance increases by about 0.07 Å upon one-electron reduction of the cationic N_2 complexes.

A comparison of the trends in the interatomic distances between the isoelectronic redox series $[(P_3{}^B)Co(N_2)]^n$ and $[(P_3{}^C)Co(N_2)]^n$ reveals divergent geometric behavior. Upon reduction from ($P_3{}^B$)Co(N_2) to $[(P_3{}^B)Co(N_2)]^-$, the Co–B distance decreases by 0.02 Å, resulting in a significant decrease in the pyramidalization about Co ($\Delta\tau$ = 0.13).[30] The opposite is true for the reduction of $[(P_3{}^C)Co(N_2)]^+$ to ($P_3{}^C$)Co(N_2), which results in an increase in the Co–C distance and an increase in the pyramidalization by the opposite amount ($\Delta\tau$ = −0.13). A plausible rationale is that the *Z*-type borane ligand in ($P_3{}^B$)Co complexes enforces a trigonal bipyramidal geometry upon reduction by drawing the Co atom into the P_3 plane with an attractive Co–B interaction (Figure 2.6). The *X*-type alkyl ligand in ($P_3{}^C$)Co complexes instead causes a distortion away from a trigonal pyramidal geometry upon reduction, with a comparatively repulsive Co–C interaction forcing the Co atom above the P_3 plane. Across the $[(P_3{}^{Si})Fe(N_2)]^n$ redox series, the Fe–Si distance contracts by 0.06 Å upon reduction (Table 2.1), suggesting that a *Z*-type $[R_3Si]^+$ disconnection dominates over the typical *X*-type $[R_3Si{:}]^-$ (cf. Chapter 5).

We can also assess the relative abilities of these ligand platforms to activate bound N_2 toward further functionalization, as judged by ν_{NN}. Making comparisons between valence isoelectronic Fe (or valence isoelectronic Co complexes) in Table 2.1 indicates that, in terms of N_2-activating ability, the ligands lie in the series: $P_3{}^{Si} < P_3{}^C < P_3{}^B$. Indeed, on average,

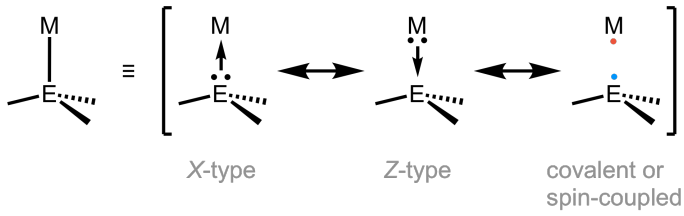

Figure 2.6: Possible valence bond resonance contributors to M–E bonding. Note that formal charges are not shown.

in a series of isoelectronic complexes ν_{NN} is 105 cm^{-1} lower in energy for the $P_3{}^B$ congener compared to the $P_3{}^{Si}$ complex, and 12 cm^{-1} lower in energy for the $P_3{}^C$ congener compared to the $P_3{}^{Si}$ complex.

At first glance, this appears inconsistent with the σ-accepting character of the borane ligand, which should render the metal center less basic. Indeed, the short M–B distances observed in $[(P_3{}^B)M(N_2)]^n$ complexes are indicative of such an interaction. However, this analysis is complicated by the differences in charge across each series, for the borane congener possesses one fewer proton in any isoelectronic series. Charge likely plays an important role in activating N_2 toward functionalization, given that charge delocalization via π backbonding will increase the basicity of N_β, by symmetry arguments (*vide infra*). If we now consider complexes with identical charge states, we see that ν_{NN} approximately follows the trend expected from the donor properties of the apical atom: $P_3{}^B < P_3{}^{Si} < P_3{}^C$. Although we have now removed an electron from the valence shell of the borane congener, such comparisons are reasonable considering that the HOMO for these species should be an orbital of $3_{dx^2-y^2}$ or $3d_{xy}$ parentage, which, by symmetry, has no overlap with the N_2 π^* orbitals.[31]

2.2.2 Evaluating N_2-to-NH_3 Conversion Activity

The reactivity of these $(P_3{}^E)Co$ complexes with sources of H^+ and e^- in the presence of N_2 was investigated. Similar to the anionic complex $[Na(12\text{-c-}4)_2][(P_3{}^B)Fe(N_2)]$,[21] treatment of a suspension of $[Na(12\text{-c-}4)_2][(P_3{}^B)Co(N_2)]$ in Et_2O at −78 °C with excess

Table 2.1: Select physical data for (P_3^E)M compounds (E = B, C, Si; M = Fe, Co)

	E =	Complex		ν_{NN} (cm^{-1})[a]	$E_{1/2}$ (V)[b]	S	d(M–E) (Å)	d(M–N_α) (Å)	d(M–P)$_{avg}$ (Å)	$\sum\angle$(P–M–P) (°)
Fe	**B**[c]	(P_3^B)Fe(Br)	(15 e^-)	–	–	3/2	2.458(5)	–	2.41	343
		$[(P_3^B)Fe]^+$	(13 e^-)	–	–	3/2	2.217(2)	–	2.38	359
		(P_3^B)Fe(N_2)	(16 e^-)	2011	–	1	–	–	–	–
		$[(P_3^B)Fe(N_2)]^-$	(17 e^-)	1905	−2.10	1/2	2.293(3)	1.781(2)	2.25	353
	C[d]	$[(P_3^C)Fe(N_2)]^+$	(16 e^-)	2128	–	1	2.081(3)	1.864(7)	2.36	358
		(P_3^C)Fe(N_2)	(17 e^-)	1992	−1.20	1/2	2.152(3)	1.797(2)	2.25	354
		$[(P_3^C)Fe(N_2)]^-$	(18 e^-)	1905	−2.55	0	2.165(2)	–	2.20[h]	357[h]
	Si[e]	$[(P_3^{Si})Fe(N_2)]^+$	(16 e^-)	2143	–	1	2.298(7)	1.914(2)	2.39	352
		(P_3^{Si})Fe(N_2)	(17 e^-)	2003	−1.00	1/2	2.2713(6)	1.8191(1)	2.29	354
		$[(P_3^{Si})Fe(N_2)]^-$	(18 e^-)	1920	−2.20	0	2.236(1)	1.795(3)	2.20	354
Co	**B**	(P_3^B)Co(Br)[f]	(16 e^-)	–	–	1	2.4629(8)	–	2.34	338
		$[(P_3^B)Co]^+$	(14 e^-)	–	–	1	2.256(2)	–	2.33	359
		(P_3^B)Co(N_2)	(17 e^-)	2089	−0.20	1/2	2.319(1)	1.865(1)	2.28	349
		$[(P_3^B)Co(N_2)]^-$	(18 e^-)	1978	−2.00	0	2.300(3)	1.792(2)	2.19	353
	C	$[(P_3^C)Co(N_2)]^+$	(17 e^-)	2182	–	1/2	2.054(2)	1.886(3)	2.29	358
		(P_3^C)Co(N_2)	(18 e^-)	2057	–	0	2.135(4)	1.814(5)	2.23	355
	Si[g]	(P_3^{Si})Co(N_2)	(18 e^-)	2063	–	0	2.2327(7)	1.814(2)	2.23	355

Unless noted otherwise, data for cationic species are referenced from the $[BAr^F{}_4]^-$ salts and data for anionic species are referenced from the 12-c-4 encapsulated Na^+ or K^+ salts. Valence electron counts are provided for bookkeeping purposes. [a]IR data were collected in the solid state (KBr pellet or thin film). [b]All potentials referenced to $Fc^{+/0}$ in THF electrolyte. [c]Data taken from [26, 28]. [d]Data taken from [22]. [e]Data taken from [34, 35]. [f]Data taken from [27]. [g]Data taken from [29]. [h]Metrics calculated from the non-encapsulated K^+ salt.

$HBAr^F_4$ followed by excess KC_8 under an atmosphere of N_2 leads to the formation of 2.4 ± 0.3 equiv of NH_3 (240% per Co; Table 2.2, A). Yields of NH_3 were determined by the indophenol method;[32] no hydrazine was detected by a standard UV–vis quantification method.[33] While we acknowledge that the NH_3 yields are close to stoichiometric, we underscore that the yields are reproducibly above 2.1 equiv. While such yields are merely suggestive of bona fide catalysis, they are consistently greater than 200% yield of NH_3 normalized to the Co in $[(P_3{}^B)Co(N_2)]^-$ and represent an order of magnitude improvement over what was, at the time of publication, the only previous report of N_2-to-NH_3 conversion mediated by well-defined cobalt complexes (NH_3 yield ≤ 0.21 equiv per Co,[2] *vide supra*).

Notably, no NH_3 is formed when either $[(P_3{}^B)Co(N_2)]^-$, $HBAr^F_4$, or KC_8 is omitted from the standard conditions, indicating that all three components are necessary for NH_3 production. In an effort to study the fate of $[(P_3{}^B)Co(N_2)]^-$ under the reaction conditions, we treated $[(P_3{}^B)Co(N_2)]^-$ with 10 equiv of $HBAr^F_4$ and 12 equiv of KC_8 and observed signs of ligand decomposition by ^{31}P NMR. If the observed reactivity indeed represents modest catalysis, ligand decomposition under the reaction conditions provides a plausible rationale for the limited turnover number. As a control, free ligand ($P_3{}^B$) was subjected to the standard conditions as a precatalyst, leading to no detectable NH_3 production.

Interestingly, although $[(P_3{}^B)Co(N_2)]^-$ and $[(P_3{}^B)Co]^+$ both generated substantial NH_3 under the standard conditions, submitting the charge neutral complex $(P_3{}^B)Co(N_2)$ to these conditions provided attenuated yields of NH_3, comparable to the yields obtained with $(P_3{}^B)Co(Br)$ (Table 2.2, B–D). Furthermore, complexes $(P_3{}^{Si})Co(N_2)$ and $(P_3{}^C)Co(N_2)$, which are isoelectronic to $[(P_3{}^B)Co(N_2)]^-$, are not competent for the reduction of N_2 with protons and electrons, producing ≤ 0.1 equiv of NH_3 and no detectable hydrazine under identical conditions (Table 2.2, E and F). This result appears to underscore the importance of the nature of the M–E interaction in facilitating N_2 fixation by $(P_3{}^E)M$ complexes.

To further explore the generality of N_2 conversion activity for Co complexes under these

Table 2.2: NH_3 Generation from N_2 Mediated by Cobalt Precursors[a]

$$N_2 + HBAr^F{}_4 + KC_8 \xrightarrow[-78\,^\circ C,\ Et_2O]{\text{Co complex}} NH_3$$

Entry	Cobalt complex	NH_3 equiv per Co
A	$[Na(12\text{-c-}4)_2][(P_3{}^B)Co(N_2)]$	2.4 ± 0.3[b]
B	$(P_3{}^B)Co(N_2)$	0.8 ± 0.3
C	$[(P_3{}^B)Co(N_2)][BAr^F{}_4]$	1.6 ± 0.2
D	$(P_3{}^B)Co(Br)$	0.7 ± 0.4
E	$(P_3{}^{Si})Co(N_2)$	< 0.1
F	$(P_3{}^C)Co(N_2)$	0.1 ± 0.1
G	$[(NArP_3)Co(Cl)][BPh_4]$	< 0.1
H	$(PBP)Co(N_2)$	0.4 ± 0.2
I	$Co(PPh_3)_2I_2$	0.4 ± 0.1
J	$CoCp_2$	0.1 ± 0.1
K	$Co_2(CO)_8$	< 0.1

[a]Cobalt precursors at −78 °C under an N_2 atmosphere treated with an Et_2O solution containing 47 equiv of $HBAr^F{}_4$, followed by an Et_2O suspension containing 60 equiv of KC_8. Yields are reported as an average of three runs.
[b]Average of six runs.

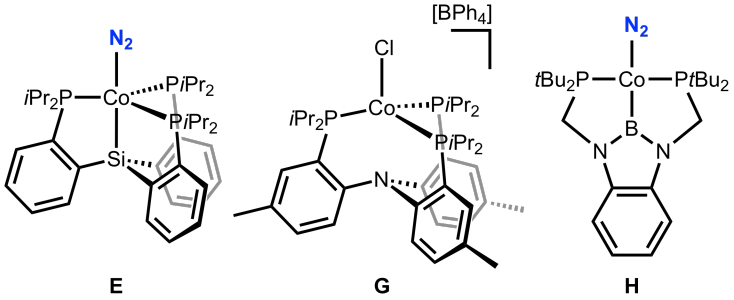

conditions, we screened a number of additional Co species. We targeted, for instance, a Co complex of the ligand tris(2-diisopropylphosphino-4-methylphenyl)amine ($NArP_3$).[36] The synthesis of a $(NArP_3)Co$ complex completes a family of tris(phosphino)cobalt complexes featuring *L*-, *X*-, and *Z*-type axial donors. The chloro complex $[(NArP_3)Co(Cl)][BPh_4]$ (Table 2.2, G) was isolated as purple crystals in 90% yield from the reaction of the $NArP_3$ ligand with $CoCl_2$ and $NaBPh_4$. An X-ray diffraction study revealed a pseudo-tetrahedral geometry at the Co center, with minimum interaction with the apical N atom of the ligand (d = 2.64 Å). As expected for tetrahedral Co(II), $[(NArP_3)Co(Cl)][BPh_4]$ is high-spin ($S = 3/2$), with a solution magnetic moment of 3.97 β_e in CD_2Cl_2 at 23 °C. We also tested

a known bis(phosphino)boryl Co(N_2) complex (Table 2.2, H),[37] as well as various other common Co complexes (Table 2.2, I–K). Of all of the cobalt precursors subjected to the standard conditions, only $P_3{}^B$-ligated Co complexes generated > 0.5 equiv of NH_3 per metal center.

2.2.3 Factors Correlated to N_2 fixation Activity

At this point, we can begin to delineate the structural and electronic factors correlated to NH_3 production by ($P_3{}^E$)M complexes. Among ($P_3{}^E$)Fe complexes, NH_3 production appears to be correlated both with the flexibility of the M–E interaction and with the degree of N_2 activation, with more flexible and more activating platforms providing greater yields of NH_3. Moving from Fe to Co, the degree of N_2 activation is systematically lower, which is expected because of the decreased spatial extent of the Co 3d orbitals (due to increased Z_{eff}).[38] Nevertheless, NH_3 production is still correlated among these ($P_3{}^E$)Co complexes with N_2 activation. However, comparing the Fe and Co complexes demonstrates that, in an absolute sense, the degree of N_2 activation is not predictive of the yield of NH_3 (Figure 2.7). For example, [Na(12-c-4)$_2$][($P_3{}^{Si}$)Fe(N_2)] shows a higher degree of N_2 activation than [($P_3{}^B$)Co(N_2)]$^-$, yet [($P_3{}^B$)Co(N_2)]$^-$ demonstrates higher N_2-to-NH_3 conversion activity. The relative activity of these two complexes is predicted, on the other hand, by the flexibility of the M–E interactions *trans* to bound N_2. Indeed, among the factors considered here, only M–E interaction flexibility appears to predict the comparatively high N_2 conversion activity of [($P_3{}^B$)Co(N_2)]$^-$.

The potentials at which the anionic states of the complexes depicted in Figure 2.7 are achieved do not follow a clear trend regarding their relative N^2 conversion activity. However, a comparison of the Fe and Co systems does demonstrate that the accessibility of highly reduced, anionic [($P_3{}^E$)M(N^2)]$^-$ complexes is favorably correlated to NH_3 production. It may be the case that the relative basicity of the β-N atom (N_β) plays an important role in N_2 conversion activity, with anionic species being appreciably more basic. The

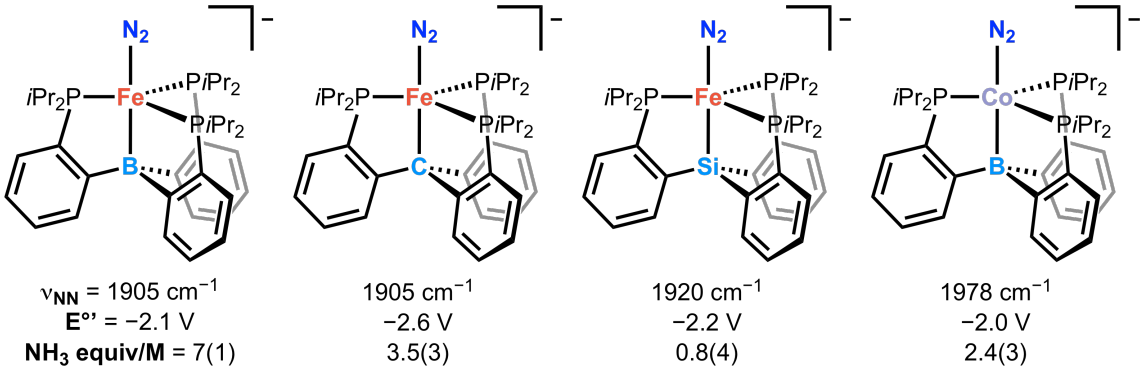

Figure 2.7: Vibrational spectroscopy, electrochemistry, and catalytic competence data for select $[(P_3{}^E)M(N_2)]^-$ complexes. Data for M = Fe and E = B are from [21, 26], data for M = Fe and E = C, Si are from [22, 35]. Note: NH_3 yields based on the addition of 50 equiv of $HBAr^F{}_4$ and 60 equiv of KC_8.

enhanced basicity of N_β in the anion would, in turn, favor protonation to produce a diazenido complex, $Co(N_2H)$, the first intermediate along a Chatt-type nitrogen fixation pathway. Considering the complexes $[(P_3{}^B)Co(N_2)]^-$ and $(P_3{}^C)Co(N_2)$, neutral $(P_3{}^C)Co(N_2)$ affords $< 5\%$ NH_3 per Co under the standard reaction conditions, whereas the isoelectronic and isostructural, yet anionic, species $[(P_3{}^B)Co(N_2)]^-$ produces $> 200\%$ NH_3 (Table 2.2). We have performed quantum-chemical calculations to compare molecular electrostatic potentials of $[(P_3{}^B)Co(N_2)]^-$ and $(P_3{}^C)Co(N_2)$. As shown in Figure 2.8, in accordance with expectations, N_β of the anionic complex $[(P_3{}^B)Co(N_2)]^-$ shows a far greater degree of negative charge accumulation relative to the same atom in the neutral complex $(P_3{}^C)Co(N_2)$. Corroborating this analysis, monitoring mixtures of $(P_3{}^C)Co(N_2)$ with 1 equiv of MeOTf or TMSOTf reveals no reaction over the course of hours at room temperature, i.e., N_β is not sufficiently basic to undergo attack by electrophiles.

2.2.4 Reactivity of $(P_3{}^C)Co(N_2)$ with H_2

Given that the N_2 ligand of $(P_3{}^C)Co(N_2)$ does not appear to be sufficiently activated to undergo protonation at N_β, we hypothesized that, instead, protonation at Co to produce a hydrido species may occur under catalytic conditions. This reactivity has been proposed to occur for $(P_3{}^E)Fe$ complexes,[21,22] and may contribute to catalyst deactivation (however,

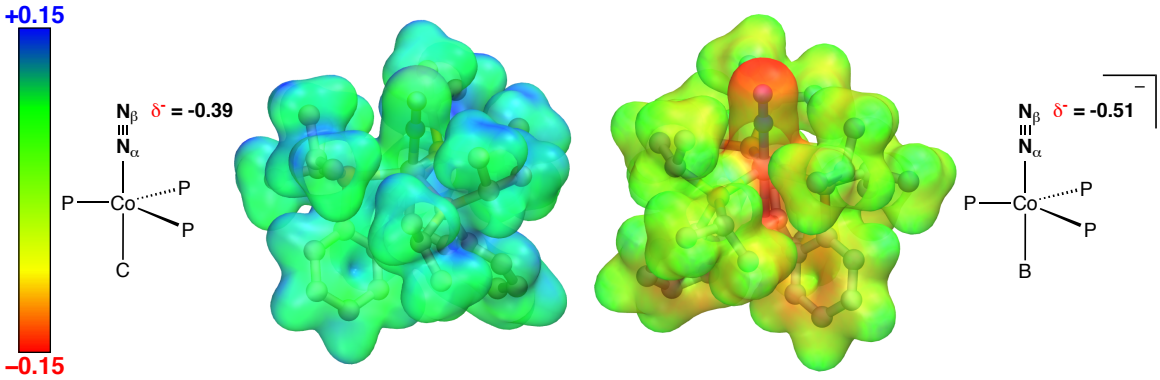

Figure 2.8: Electrostatic potential maps of $(P_3{}^C)Co(N_2)$ and $[(P_3{}^B)Co(N_2)]^-$(isovalue = 0.015 a.u., color map in hartrees) and Mulliken charges for N_β.

see Chapter 3). To explore this possibility, we investigated the reactivity of $(P_3{}^C)Co(N_2)$ towards H_2.

Exposure of $(P_3{}^C)Co(N_2)$ to 1 atm of H_2 results in an immediate color change along with the quantitative formation of a new diamagnetic species. The ^{31}P NMR spectrum of this species exhibits a single broad resonance at 80.0 ppm, and the ^{1}H NMR spectrum exhibits a resonance at −16.0 ppm, which at room temperature is coupled to three equivalent P atoms ($^2J_{HP}$ = 33 Hz) and integrates to 2 H per molecule. Two limiting structural assignments are consistent with these data, a nonclassical Co(I) H_2 adduct or a classical Co(III) dihydride. In either case, rapid exchange of the H atoms produces a C_3 symmetric structure on the NMR time scale from 213 to 298 K. Temperature dependent spin–lattice relaxation (T_1) studies show that $T_{1,\,\mathrm{min}}$ = 90 ms (233 K, 500 MHz). The expected range of $T_{1,\,\mathrm{min}}$ for a nonclassical hydride is ≤ 160 ms, and that for a classical dihydride is ≥ 300 ms (at 500 MHz). However, these values hold only if the dominant relaxation mechanism is due to dipolar coupling between the metal-bound H atoms. When other relaxation mechanisms exist, for example dipolar coupling to a metal with a high gyromagnetic ratio (e.g., Co, $\gamma \approx 10$ MHz T^{-1}), these ranges are no longer accurate.[39] In these cases, a measurement of $^1J_{HD}$ can be more conclusive, with values ≥ 10 Hz typically taken as strong evidence of a nonclassical structure.[40]

Exposing $(P_3{}^C)Co(N_2)$ to one atmosphere of 1:1 H_2:D_2 rapidly leads to H/D scrambling, as evidenced by the observation of HD gas ($^1J_{HD}$ = 43 Hz) by ^{1}H NMR. Moreover, an additional resonance is observable 0.04 ppm upfield of the hydride resonance of "$(P_3{}^C)Co(H_2)$", which is assigned to the hydride resonance for "$(P_3{}^C)Co(HD)$". Although this resonance is coupled to three equivalent P nuclei ($^2J_{HP}$ = 33 Hz), no H–D coupling is observed (Figure 2.9, A). Given the approximate FWHM of 17 Hz for this resonance, any unresolved H–D coupling must be quite small, $\lesssim$ 10 Hz.

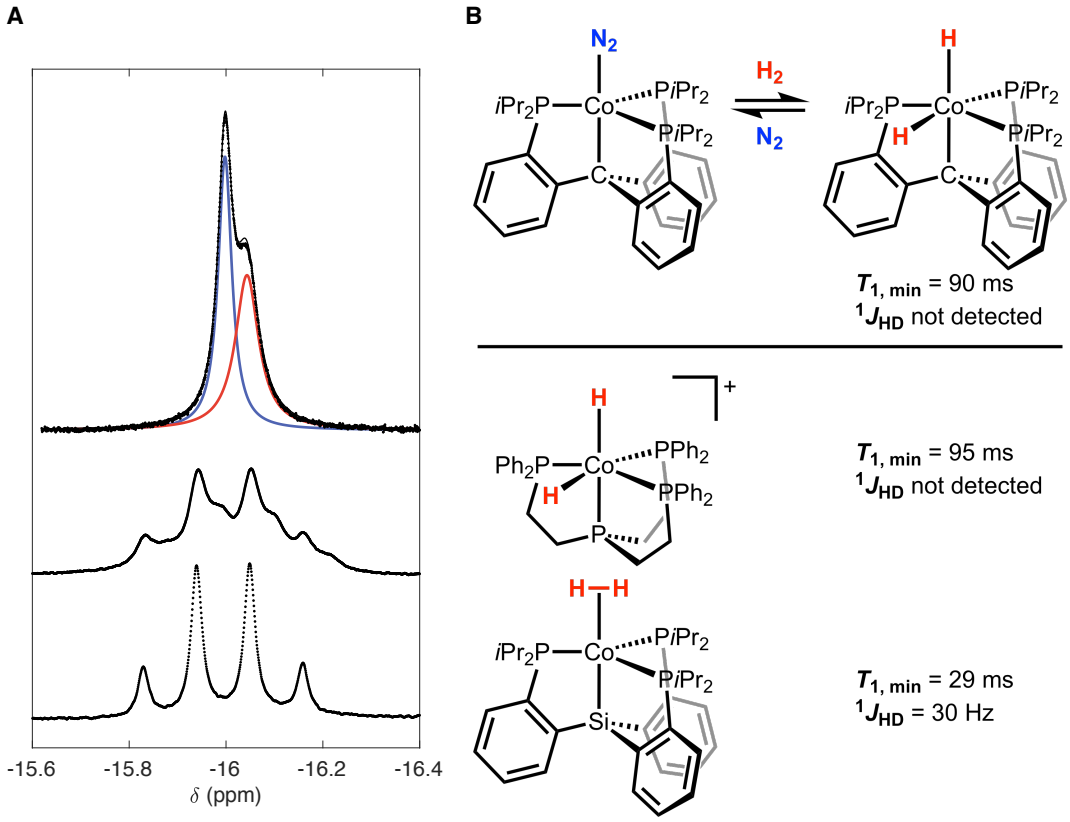

Figure 2.9: (A) The hydridic ^{1}H NMR resonances of $(P_3{}^C)Co(H)_2$ (bottom) and a mixture of $(P_3{}^C)Co(H)_2$ and $(P_3{}^C)Co(H)(D)$ (middle and top). The top spectrum is the $^1H\{^{31}P\}$ spectrum corresponding to that in the middle, and shows a spectral deconvolution. (B) Summary of the Co–H_2 chemistry described in the text.

We can compare these results with isoelectronic Co complexes featuring tetrapodal C_3 symmetric ligand scaffolds. Heinekey and co-workers have performed a detailed investigation of the structural dynamics of $[(PP_3)Co(H)_2]^+$ (PP_3 = tris(2-diphenylphosphinoethyl)-

phosphine).[40] For this complex, $T_{1,\,\mathrm{min}}$ = 95 ms (226 K, 500 MHz), and no H–D coupling is observed for the monodeuterated isotopologue. These data were used to argue that $[(PP_3)Co(H)_2]^+$ is properly formulated as a classical dihydride, with the moderate value of $T_{1,\,\mathrm{min}}$ due to dipolar coupling to the Co nucleus. In contrast, we have previously characterized $(P_3{}^{Si})Co(H_2)$ as a nonclassical H_2 adduct on the basis of the low $T_{1,\,\mathrm{min}}$ (29 ms, 243 K, 500 MHz) and large $^1J_{HD}$ coupling constant of the monodeuterated isotopologue (30 Hz).[27] The similarity between "$(P_3{}^{C})Co(H_2)$" and the PP_3 complex leads us to conclude that the former is best described as a classical Co(III) dihydride—$(P_3{}^{C})Co(H)_2$ (Figure 2.9, B). In support of this formulation, the IR spectrum of $(P_3{}^{C})Co(H)_2$ exhibits a broad resonance at 1827 cm^{-1}, with a shoulder at 1801 cm^{-1}, attributed to the two Co–H stretching modes expected for a dihydride complex.

Although $(P_3{}^{C})Co(H)_2$ is stable to vacuum, exposure of solutions of $(P_3{}^{C})Co(H)_2$ to N_2 results in the formation of $(P_3{}^{C})Co(N_2)$, presumably via an associative mechanism. This behavior is identical to that of the isoelectronic $(P_3{}^{Si})Co$ complexes.[27] Nevertheless, these results serve as an instructive demonstration of the difference in donor properties conferred by E = C vs Si in $(P_3{}^{E})M$ complexes. If the values of ν_{NN} can be taken as an indicator of the electron density at the metal center, then even the modest reduction of 6 cm^{-1} observed for $(P_3{}^{C})Co(N_2)$ relative to $(P_3{}^{Si})Co(N_2)$ (Table 2.1) is sufficient to promote the cleavage of H_2 at the Co(I) center of the former, as opposed to adduct formation at the latter. This reinforces the idea that the $P_3{}^{Si}$ ligand is more electronically-similar to $P_3{}^{B}$ than it is to $P_3{}^{C}$—that is, a $[R_3Si]^+$ disconnection is appropriate for E = Si, whereas the $[R_3C{:}]^-$ resonance dominates when E = C (*vide supra*, Figure 2.6).

2.3 Conclusion

We have demonstrated the ability of a molecular $Co(N_2)$ complex to facilitate the conversion of N_2 to NH_3 at −78 °C in the presence of proton and electron sources (2.4 equiv of NH_3 generated per Co center on average). Prior to this report, the only well-

defined molecular systems (including nitrogenase enzymes) capable of directly mediating the catalytic conversion of N_2 to NH_3 contained either Mo or Fe. While the measured NH_3 production by the featured Co complex is very modest with respect to *bona fide* catalysis, this result highlights non-biological Group IX metals as targets for the development of synthetic N_2 fixation catalysts. Indeed, subsequent to this work, the group of Nishibayashi has reported a (PNP)Co complex that catalyzes the reduction of N_2 to NH_3 under the same reaction conditions as $(P_3{}^B)Co$.[41]

The propensity of the $(P_3{}^E)M$ complexes that we have studied to perform productive N_2 fixation does not appear to depend solely on the ability of the precursor complex to activate N_2. The observations collected herein indicate that the anionic charge and hence the basicity of the bound N_2 ligand, in addition to flexibility of the M–E interaction *trans* to the bound N_2 ligand, correlate with more favorable NH_3 production. Of course, correlation does not presume causation, and the factors that lead to different NH_3 yields may be numerous. While some of the design features important to consider in catalysts of the $(P_3{}^E)M(N_2)$ type have been highlighted here, other factors, including the comparative rates of H_2 evolution and catalyst degradation/poisoning rates, warrant further studies.

2.4 Experimental Section

2.4.1 General Considerations

All manipulations were carried out using standard Schlenk or glovebox techniques under an N_2 atmosphere. Solvents were deoxygenated and dried by thoroughly sparging with N_2, followed by passage through an activated alumina column in a solvent purification system by SG Water, USA LLC. Nonhalogenated solvents were tested with sodium benzophenone ketyl in tetrahydrofuran (THF) in order to confirm the absence of oxygen and water. Deuterated solvents were purchased from Cambridge Isotope Laboratories, Inc., degassed, and dried over activated 3-Å molecular sieves prior to use. $HBAr^F{}_4$,[42] KC_8,[43] $(P_3{}^B)Co(N_2)$,[27] $(P_3{}^B)Co(Br)$,[27] $(P_3{}^{Si})Co(N_2)$,[29] $NArP_3$,[36] $(PBP)Co(N_2)$,[37] $(P_3{}^C)H$,[22] and

$Co(PPh_3)_2I_2$[44] were prepared according to literature procedures. All other reagents were purchased from commercial vendors and used without further purification unless otherwise stated. Et_2O for NH_3 generation reactions was stirred over Na/K alloy ($\geq$ 2 h) and filtered before use.

2.4.2 Physical Methods

Elemental analyses were performed by Midwest Microlab, LLC (Indianapolis, IN). ^1H and ^{13}C chemical shifts are reported in ppm relative to tetramethylsilane, using ^1H and ^{13}C resonances from a residual solvent as internal standards. ^{31}P chemical shifts are reported in ppm relative to 85% aqueous H_3PO_4. Solution-phase magnetic measurements were performed by the method of Evans.[45] IR measurements were obtained as solutions or thin films formed by the evaporation of solutions using a Bruker Alpha Platinum ATR spectrometer with OPUS software. Optical spectroscopy measurements were collected with a Cary 50 UV–vis spectrophotometer using a 1 cm two-window quartz cell. Electrochemical measurements were carried out in a glovebox under an N_2 atmosphere in a one-compartment cell using a CH Instruments 600B electrochemical analyzer. A glassy carbon electrode was used as the working electrode, and platinum wire was used as the auxiliary electrode. The reference electrode was $Ag/AgNO_3$ in THF. The $Fc^{+/0}$ couple was used as an internal reference. THF solutions of the electrolyte (0.1 M [TBA][PF_6]) and analyte were also prepared under an inert atmosphere. X-band EPR spectra were obtained on a Bruker EMX spectrometer.

X-ray diffraction (XRD) studies were carried out at the Caltech Division of Chemistry and Chemical Engineering X-ray Crystallography Facility on a Bruker three-circle SMART diffractometer with a SMART 1K CCD detector. Data were collected at 100 K using Mo K_α radiation (λ = 0.71073 Å). Structures were solved by direct or Patterson methods using SHELXS and refined against F^2 on all data by full-matrix least squares with SHELXL-97. All non-H atoms were refined anisotropically. All H atoms were placed at geometrically

calculated positions and refined using a riding model. The isotropic displacement parameters of all H atoms were fixed at 1.2 (1.5 for methyl groups) times U_{eq} of the atoms to which they are bonded.

2.4.3 Synthesis

2.4.3.1 [Na(12-c-4)$_2$][(P_3^B)Co(N_2)]

To a −78 °C solution of (P_3^B)Co(Br) (70.5 mg, 0.0967 mmol) in THF (2 mL) was added a freshly prepared solution of $NaC_{10}H_8$ (23.5 mg of $C_{10}H_8$, 0.222 mmol) in THF (3 mL). The solution was brought to room temperature and allowed to stir for 6 h. The addition of 12-c-4 (51.1 mg, 0.290 mmol) and removal of solvent in vacuo provided a dark-red solid. Et_2O was added and subsequently removed in vacuo. The residue was suspended in C_6H_6 and filtered, and the solids were washed with C_6H_6 (2 × 2 mL) and pentane (2 × 2 mL) to furnish a red solid (68.8 mg, 0.0660 mmol, 68%). Single crystals were grown by vapor diffusion of pentane onto a THF solution of the title compound that had been layered with Et_2O. ^{1}H NMR (400 MHz, THF-d_8): δ 7.41 (3H), 6.94 (3H), 6.66 (3H), 6.44 (3H), 3.64 (32H), 2.29 (br), 1.37 (6H), 1.20 (6H), 0.93 (6H), −0.26 (6H). ^{11}B NMR (128 MHz, THF-d_8): δ 9.32. ^{31}P NMR (162 MHz, THF-d_8): δ 62.03. IR (thin film, cm^{-1}): 1978 (N_2). Anal. Calcd for $C_{52}H_{86}BCoN_2NaO_8P_3$: C, 59.32; H, 8.23; N, 2.66. Found: C, 59.05; H, 7.99; N, 2.47.

2.4.3.2 [(P_3^B)Co][$BAr^F{}_4$]

To a −78 °C solution of (P_3^B)Co(N_2) (91.5 mg, 0.135 mmol) in Et_2O (2 mL) was added solid $HBAr^F{}_4$ (134.0 mg, 0.132 mmol). The reaction was brought to room temperature and vented to allow for the escape of H_2. The purple-brown solution was stirred for 1 h. The solution was layered with pentane (5 mL) and stored at −35 °C to furnish red-purple single crystals of the title compound (162.9 mg, 0.0952 mmol, 82%), which were washed with pentane (3 × 2 mL). ^{1}H NMR (400 MHz, C_6D_6): δ 26.25, 23.80, 8.64, 8.44 ([$BAr^F{}_4$]$^-$), 7.88 ([$BAr^F{}_4$]$^-$), 6.33, −2.16, −3.68. UV-vis [Et_2O; l, nm (ϵ, L cm^{-1} mol^{-1})]: 585 (1500),

760 (532). Anal. Calcd for $C_{68}H_{66}B_2CoF_{24}P_3$: C, 53.99; H, 4.40. Found: C, 53.94; H, 4.51.

2.4.3.3 $(P_3{}^C)Co(N_2)$

$(P_3{}^C)H$ (100 mg, 0.169 mmol) and $CoCl_2 \cdot 1.5THF$ (40 mg, 0.169 mmol) were mixed at room temperature in THF (10 mL). This mixture was allowed to stir for 1 h, yielding a homogeneous cyan solution. This solution was chilled to −78 °C, and a solution of MeMgCl in THF (0.5 M, 0.560 mmol) was added in three 370 μL portions over 3 h. The mixture was allowed to warm slowly to room temperature and then was concentrated to ca. 1 mL. 1,4-Dioxane (2 mL) was added, and the resultant suspension was stirred vigorously for at least 2 h before filtration. The filtrate was concentrated to a tacky red-brown solid, which was extracted with 1:1 C_6H_6:pentane (10 mL), filtered over Celite, and lyophilized to yield the product as a red powder (96 mg, 0.141 mmol, 83%). Crystals suitable for XRD were grown via the slow evaporation of a pentane solution. ^{1}H NMR (300 MHz, C_6D_6): δ 7.28 (br, 3H), 6.82 (m, 9H), 2.82 (oct, -C*H*, 3H), 2.09 (sept, -C*H*, 3H), 1.49 (m, 18H), 1.06 (dd, -CHC*H*$_3$, 9H), 0.30 (dd, -CHC*H*$_3$, 9H). ^{31}P{^{1}H} NMR (121 MHz, C_6D_6): δ 47.39. IR (thin film, cm^{-1}): 2057 (ν_{NN}). Anal. Calcd for $C_{37}H_{54}CoN_2P_3$: C, 65.48; H, 8.02; N, 4.13. Found: C, 64.14; H, 8.36; N, 4.03.

2.4.3.4 $(P_3{}^C)Co(N_2)][BAr^F{}_4]$

$(P_3{}^C)Co(N_2)$ (75 mg, 0.11 mmol) and $[Fc][BAr^F{}_4]$ (122 mg, 0.12 mmol) were dissolved separately in Et_2O (ca. 3 mL each), and the ethereal solutions were cooled to −78 °C. The chilled solution of $[Fc][BAr^F{}_4]$ was added dropwise to the solution of $(P_3{}^C)Co(N_2)$, and the resultant mixture was allowed to stir at low temperature for 1 h. At this point, the mixture was allowed to warm to room temperature before filtration over Celite and concentration to ca. 2 mL. The concentrated filtrate was layered with pentane and placed in a freezer at −35 °C to induce crystallization. Decanting the mother liquor off crystalline solids

and washing thoroughly with pentane yields [(P_3^C)Co(N_2)][BAr^F_4] as dark green-brown crystals (147 mg, 0.095 mmol, 86%). Crystals suitable for XRD were grown by the slow diffusion of pentane vapors into an ethereal solution of [(P_3^C)Co(N_2)][BAr^F_4] at −35 °C. μ_{eff} (5:1 toluene-d_8-THF:d_8, Evans method, 23 °C): 3.49 β_e. ^{1}H NMR (300 MHz, C_6D_6): δ 17.22, 9.94, 8.24 ([BAr^F_4]$^-$), 7.72 ([BAr^F_4]$^-$), 3.13, 2.57, +1.5 to −2 (br, m), −3.68. IR (cm^{-1}): 2182 (ν_{NN}, thin film), 2180 (ν_{NN}, solution). Elemental analysis shows low values for N consistent with a labile N_2 ligand. Anal. Calcd for $C_{69}H_{66}BCoF_{24}N_2P_3$: C, 53.75; H, 4.31; N, 1.82. Found: C, 53.86; H, 4.31; N, 0.27. Note: The magnetic moment for [(P_3^C)Co(N_2)][BAr^F_4] in solution may be complicated by some degree of solvent exchange for N_2 at the Co center, as described in the text.

2.4.3.5 [(NArP$_3$)Co(Cl)][BPh$_4$]

THF (5 mL) was added to a solid mixture of $NArP_3$ (58 mg, 91.2 mmol), $CoCl_2$ (12 mg, 92.4 mmol), and $NaBPh_4$ (31 mg, 90.6 mmol). The reaction was stirred for 4 h at room temperature, during which the color evolved from yellow to green to purple. The solvent was removed in vacuo, and the residue was taken up in dichloromethane. The suspension was filtered over a plug of Celite, and the filtrate was dried, yielding a purple powder (86 mg, 82.1 mmol, 90%). Single crystals were grown by the slow evaporation of a saturated solution of [(NArP$_3$)Co(Cl)][BPh$_4$] in diethyl ether:dichloromethane (1:2, v/v). ^{1}H NMR (CD_2Cl_2, 300 MHz): δ 177.77, 37.50, 23.78, 13.48, 12.96, 7.37, 7.08, 6.92, 4.41, 1.50, −3.60, −9.81. UV-vis [THF; l, nm (d, L cm^{-1} mol^{-1})]: 564 (452), 760 (532). μ_{eff} (CD_2Cl_2, Evans method, 23 °C): 3.97 β_e. Anal. Calcd for $C_{63}H_{80}BClCoNP_3$: C, 72.10; H, 7.68; N, 1.33. Found: C, 71.97; H, 7.76; N, 1.30.

2.4.3.6 (P_3^C)Co(H)$_2$

In an NMR tube equipped with a J-Young valve, (P_3^C)Co(N_2) (13 mg, 0.019 mmol) was dissolved in C_6D_6 and degassed via a single freeze-pump-thaw cycle. The solution was

then frozen, placed under an atmosphere of H_2, and thawed. The reaction is quantitative by ^{1}H and ^{31}P NMR spectroscopy. Isolating a brown solid is possible by lyophilization of this solution, but accurate yields could not be obtained due to reversion to the starting material upon exposure to an atmosphere of N_2; for this reason, elemental analysis was not conducted. ^{1}H NMR (300 MHz, C_6D_6) δ 7.35 (d, 3H), 7.09 (d, 3H), 6.98 (t, 3H), 6.90 (t, 3H), 2.10 (m, -C*H*, 3H), 1.96 (m, -C*H*, 3H), 1.49 (m, 18H), 0.90 (dd, -CHCH_3, 9H), 0.63 (br, -CHCH_3, 9H), −16.0 (q, Co*H*, 2H, $^2J_{HP}$ = 33 Hz). ^{31}P{^{1}H} (121 MHz, C_6D_6): δ 80.0. IR (thin film, cm^{-1}): 1827, 1801 (shoulder) (ν_{CoH}).

2.4.4 Standard NH_3 Generation Reaction Procedure

[Na(12-c-4)$_2$][(P_3^B)Co(N_2)] (2.2 mg, 0.002 mmol) was suspended in Et_2O (0.5 mL) in a 20 mL scintillation vial equipped with a stir bar. This suspension was cooled to −78 °C in a cold well inside of an N_2 glovebox. A solution of $HBAr^F_4$ (95 mg, 0.094 mmol) in Et_2O (1.5 mL) similarly cooled to −78 °C was added to this suspension in one portion with stirring. Residual acid was dissolved in cold Et_2O (0.25 mL) and added subsequently. This mixture was allowed to stir for 5 min at −78 °C, before being transferred to a precooled Schlenk tube equipped with a stir bar. The original reaction vial was washed with cold Et_2O (0.25 mL), which was added subsequently to the Schlenk tube. KC_8 (16 mg, 0.119 mmol) was suspended in cold Et_2O (0.75 mL) and added to the reaction mixture over the course of 1 min. The Schlenk tube was then sealed, and the reaction was allowed to stir for 40 min at −78 °C before being warmed to room temperature and stirred for 15 min.

2.4.5 NH_3 Quantification

A Schlenk tube was charged with HCl (3 mL of a 2.0 M solution in Et_2O, 6 mmol). Reaction mixtures were vacuum transferred into this collection flask. Residual solid in the reaction vessel was treated with a solution of NaO*t*Bu (40 mg, 0.4 mmol) in 1,2-dimethoxyethane (1 mL) and sealed. The resulting suspension was allowed to stir for 10 min before all volatiles were again vacuum-transferred into the collection flask. After completion

of the vacuum transfer, the flask was sealed and warmed to room temperature. The solvent was removed in vacuo, and the remaining residue was dissolved in H_2O (1 mL). An aliquot of this solution (20 μL) was then analyzed for the presence of NH_3 (present as NH_4Cl) by the indophenol method.[32] Quantification was performed with UV-vis spectroscopy by analyzing the absorbance at 635 nm.

References

(1) Hidai, M.; Takahashi, T.; Yokotake, I.; Uchida, Y. *Chem. Lett.* **1980**, *9*, 645–646.

(2) Yamamoto, A.; Miura, Y.; Ito, T.; Chen, H. L.; Iri, K.; Ozawa, F.; Miki, K.; Sei, T.; Tanaka, N.; Kasai, N. *Organometallics* **1983**, *2*, 1429–1436.

(3) Chatt, J.; Dilworth, J. R.; Richards, R. L. *Chem. Rev.* **1978**, *78*, 589–625.

(4) Peters, J. C.; Mehn, M. P. In *Activation of Small Molecules*; Wiley-Blackwell: 2006; Chapter 3, pp 81–119.

(5) Chirik, P. J. *Dalton Trans.* **2007**, 16–25.

(6) Schrock, R. R. *Angew. Chem. Int. Ed.* **2008**, *47*, 5512–5522.

(7) Fryzuk, M. D. *Acc. Chem. Res.* **2009**, *42*, 127–133.

(8) Crossland, J. L.; Tyler, D. R. *Coord. Chem. Rev.* **2010**, *254*, 1883–1894.

(9) Siedschlag, R. B.; Bernales, V.; Vogiatzis, K. D.; Planas, N.; Clouston, L. J.; Bill, E.; Gagliardi, L.; Lu, C. C. *J. Am. Chem. Soc.* **2015**, *137*, 4638–4641.

(10) Laplaza, C. E.; Cummins, C. C. *Science* **1995**, *268*, 861–863.

(11) Zanotti-Gerosa, A.; Solari, E.; Giannini, L.; Floriani, C.; Chiesi-Villa, A.; Rizzoli, C. *J. Am. Chem. Soc.* **1998**, *120*, 437–438.

(12) Clentsmith, G. K. B.; Bates, V. M. E.; Hitchcock, P. B.; Cloke, F. G. N. *J. Am. Chem. Soc.* **1999**, *121*, 10444–10445.

(13) Fryzuk, M. D.; Kozak, C. M.; Bowdridge, M. R.; Patrick, B. O.; Rettig, S. J. *J. Am. Chem. Soc.* **2002**, *124*, 8389–8397.

(14) Vidyaratne, I.; Crewdson, P.; Lefebvre, E.; Gambarotta, S. *Inorg. Chem.* **2007**, *46*, 8836–8842.

(15) Curley, J. J.; Cook, T. R.; Reece, S. Y.; Müller, P.; Cummins, C. C. *J. Am. Chem. Soc.* **2008**, *130*, 9394–9405.

(16) Nikiforov, G. B.; Vidyaratne, I.; Gambarotta, S.; Korobkov, I. *Angew. Chem. Int. Ed.* **2009**, *48*, 7415–7419.

(17) Rodriguez, M. M.; Bill, E.; Brennessel, W. W.; Holland, P. L. *Science* **2011**, *334*, 780–783.

(18) Hebden, T. J.; Schrock, R. R.; Takase, M. K.; Muller, P. *Chem. Commun.* **2012**, *48*, 1851–1853.

(19) Yandulov, D. V.; Schrock, R. R. *Science* **2003**, *301*, 76–78.

(20) Arashiba, K.; Miyake, Y.; Nishibayashi, Y. *Nat. Chem.* **2010**, *3*, 120–125.

(21) Anderson, J. S.; Rittle, J.; Peters, J. C. *Nature* **2013**, *501*, 84–87.

(22) Creutz, S. E.; Peters, J. C. *J. Am. Chem. Soc.* **2014**, *136*, 1105–1115.

(23) Kuriyama, S.; Arashiba, K.; Nakajima, K.; Tanaka, H.; Kamaru, N.; Yoshizawa, K.; Nishibayashi, Y. *J. Am. Chem. Soc.* **2014**, *136*, 9719–9731.

(24) Ung, G.; Peters, J. C. *Angew. Chem. Int. Ed.* **2015**, *54*, 532–535.

(25) Moret, M.-E.; Peters, J. C. *J. Am. Chem. Soc.* **2011**, *133*, 18118–18121.

(26) Moret, M.; Peters, J. C. *Angew. Chem. Int. Ed.* **2011**, *50*, 2063–2067.

(27) Suess, D. L. M.; Tsay, C.; Peters, J. C. *J. Am. Chem. Soc.* **2012**, *134*, 14158–14164.

(28) Anderson, J. S.; Moret, M.-E.; Peters, J. C. *J. Am. Chem. Soc.* **2013**, *135*, 534–537.

(29) Whited, M. T.; Mankad, N. P.; Lee, Y.; Oblad, P. F.; Peters, J. C. *Inorg. Chem.* **2009**, *48*, 2507–2517.

(30) Vela, J.; Cirera, J.; Smith, J. M.; Lachicotte, R. J.; Flaschenriem, C. J.; Alvarez, S.; Holland, P. L. *Inorg. Chem.* **2007**, *46*, 60–71.

(31) Moret, M.; Peters, J. C. *Angew. Chem. Int. Ed.* **2011**, *50*, 2063–2067.

(32) Weatherburn, M. W. *Anal. Chem.* **1967**, *39*, 971–974.

(33) Watt, G. W.; Chrisp, J. D. *Anal. Chem.* **1952**, *24*, 2006–2008.

(34) Mankad, N. P.; Whited, M. T.; Peters, J. C. *Angew. Chem. Int. Ed.* **2007**, *46*, 5768–5771.

(35) Lee, Y.; Mankad, N. P.; Peters, J. C. *Nat. Chem.* **2010**, *2*, 558–565.

(36) MacBeth, C. E.; Harkins, S. B.; Peters, J. C. *Can. J. Chem.* **2005**, *83*, 332–340.

(37) Lin, T.-P.; Peters, J. C. *J. Am. Chem. Soc.* **2013**, *135*, 15310–15313.

(38) Miessler, G. L.; Tarr, D. A., *Inorganic Chemistry*, 4th ed.; Pearson Prentice Hall: New Jersey, 2011, pp 37–43.

(39) Desrosiers, P. J.; Cai, L.; Lin, Z.; Richards, R.; Halpern, J. *J. Am. Chem. Soc.* **1991**, *113*, 4173–4184.

(40) Heinekey, D. M.; van Roon, M. *J. Am. Chem. Soc.* **1996**, *118*, 12134–12140.

(41) Kuriyama, S.; Arashiba, K.; Tanaka, H.; Matsuo, Y.; Nakajima, K.; Yoshizawa, K.; Nishibayashi, Y. *Angew. Chem. Int. Ed.* **2016**, *55*, 14291–14295.

(42) Brookhart, M.; Grant, B.; Volpe, A. F. *Organometallics* **1992**, *11*, 3920–3922.

(43) Weitz, I. S.; Rabinovitz, M. *J. Chem. Soc., Perkin Trans.* **1993**, 117–120.

(44) Cotton, F. A.; Faut, O. D.; Goodgame, D. M. L.; Holm, R. H. *J. Am. Chem. Soc.* **1961**, *83*, 1780–1785.

(45) Evans, D. F. *J. Chem. Soc.* **1959**, 2003–2005.

Chapter 3

A SYNTHETIC SINGLE-SITE FE NITROGENASE: HIGH TURNOVER, FREEZE-QUENCH ^{57}FE MÖSSBAUER DATA, AND A HYDRIDE RESTING STATE

3.1 Introduction

The fixation of molecular nitrogen into ammonia is a transformation of fundamental importance to both biology and industry,[1] a fact which has prompted mechanistic study of the few known systems capable of catalyzing this reaction. The industrial Haber–Bosch process has been the subject of exhaustive investigation, resulting in a detailed mechanistic understanding in large part supported by surface spectroscopic studies on model systems.[2,3] The nitrogenase family of enzymes provides an example of catalytic N_2 conversion under ambient conditions and has also been studied extensively. While many questions remain unanswered regarding the mechanism of nitrogenase, a great deal of kinetic and reactivity information has been collected.[4] Additionally, important insights have been provided by protein crystallography, X-ray emission spectroscopy, and site-directed mutagenesis studies, as well as in situ freeze-quench ENDOR and EPR spectroscopy.[5–9]

Hypotheses underpinning the mechanisms of both of these systems are bolstered by synthetic model chemistry and efforts to develop molecular N_2 conversion catalysts.[10,11] This search has yielded systems capable of the catalytic reduction of N_2 to hydrazine (N_2H_4),[12,13] tris(trimethylsilyl)amine,[14–22] and a few examples of the direct catalytic fixation of N_2 to NH_3 (Figure 3.1).[19,23–42] While a wealth of mechanistic information for the original Mo catalyst system developed by Schrock has been derived from stoichiometric studies and theory,[43–45] in situ spectroscopic studies during catalysis have not been reported. These synthetic catalysts operate under heterogeneous conditions and are likely to generate

Reproduced in part with permission from Del Castillo, T. J.;† Thompson, N. B.;† Peters, J. C. *J. Am. Chem. Soc.* **2016**, *138*, 5341–5350. © 2016 American Chemical Society. †Denotes equal contribution.

mixtures of intermediate species that are both diamagnetic and paramagnetic, making it challenging to reliably determine speciation under turnover. This latter limitation is also true of biological nitrogenases. While continuous-wave and pulsed EPR techniques can and have been elegantly applied,[8] such studies are subject to quantum-mechanical selection rules and practical limitations that restrict the range of observable species under turnover conditions.

Iron is the only transition metal that is essential in the cofactor for nitrogenase function, and this fact has motivated a great deal of recent interest in Fe(N_2) model chemistry.[46–49] In recent years we have focused on a family of tetradentate ligands, (P_3^E), in which three phosphine donors are bonded to a central atom through an *o*-phenylene linker (E = B, Si, C). We have shown that (P_3^E)M (M = Fe, Co) complexes promote the binding and activation of N_2, as well as the functionalization of bound N_2 with various electrophiles.[50–55] Moreover, we discovered that (P_3^B)Fe and (P_3^C)Fe complexes mediate the catalytic reduction of N_2 to NH_3 at low temperature using a strong acid, $HBAr^F_4$, and a strong reductant, KC_8 (Figure 3.1, K).[26,27] One unique aspect of these Fe-based systems is their suitability for in situ spectroscopic study by freeze-quench ^{57}Fe Mössbauer spectroscopy. In principle, this technique enables observation of the total Fe speciation as frozen snapshots during turnover.[56,57] For single-site Fe nitrogenase mimics of the type we have developed, analysis of such data is far simpler than in a biological nitrogenase where many Fe centers are present.[58,59]

For the most active (P_3^B)Fe catalyst system, many (P_3^B)Fe(N_xH_y) model complexes that may be mechanistically relevant (e.g., $[(P_3^B)Fe]^+$, $[(P_3^B)Fe(N_2)]^-$, $[(P_3^B)Fe(NNH_2)]^+$, $[(P_3^B)Fe(NH_3)]^+$) have now been independently generated and characterized, including by ^{57}Fe Mössbauer spectroscopy, and these data facilitate interpretation of the freeze-quench Mössbauer data reported here. In combination with chemical quenching methods that we present to study the dynamics of product formation, it becomes possible to attempt to correlate the species observed spectroscopically with the N_2 fixing activity to gain a better

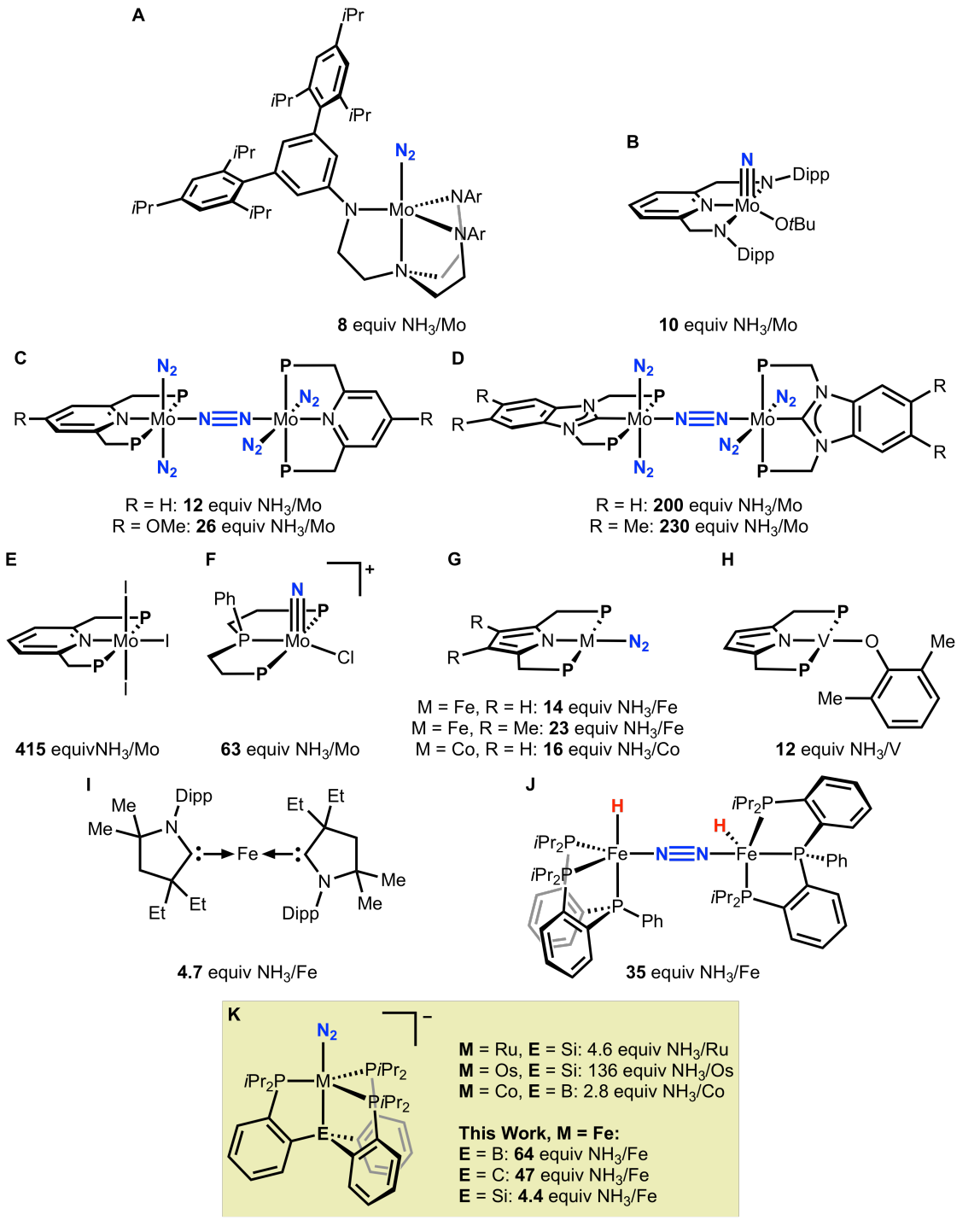

Figure 3.1: Synthetic catalysts for N_2 fixation to NH_3, along with the maximum observed TON for each catalyst system. **P** = P*t*Bu$_2$. (A) See [23]. (B) See [38]. (C) See [25, 28–30]. (D) See [37]. (E) See [36]. (F) See [32]. (G) See [33–35, 41]. (H) See [42]. (I) See [19]. (J) See [39]. (K) See [26, 27, 31, 40]

understanding of the overall catalytic system. Such a strategy complements the studies of model complexes and stoichiometric reactions steps that we have previously undertaken and offers a fuller mechanistic picture. While many questions remain, this approach to studying N_2-to-NH_3 conversion mediated by synthetic Fe catalysts is a mechanistically powerful one.

Here we undertake tandem spectroscopy/activity studies using the $P_3{}^E$ (E = B, C, Si) Fe catalyst systems and report the following: (i) two of these Fe-based catalysts (E = B, C) are unexpectedly robust under the reaction conditions, demonstrating comparatively high yields of NH_3 that are nearly an order of magnitude larger than in initial reports at lower acid/reductant loadings; (ii) based on electrochemical measurements the dominant catalysis by the $(P_3{}^B)$Fe system likely occurs at the $[(P_3{}^B)Fe(N_2)]^{0/-}$ couple, corroborated by demonstrating catalysis with Na/Hg and electrolytic N_2-to-NH_3 conversion in a controlled-potential bulk electrolysis; (iii) the $(P_3{}^B)$Fe system shows first order rate dependence on Fe catalyst concentration and zero order dependence on acid concentration; (iv) kinetic competition between rates of N_2 versus H^+ reduction are a key factor in determining whether productive N_2-to-NH_3 conversion is observed; and (v) a metal hydrido-borohydrido species is an off-path resting state of the $(P_3{}^B)$Fe catalysis system.

3.2 Results and Discussion

3.2.1 Increased Turnover of Fe-Catalyzed N_2 Fixation and Evidence for Catalysis at the $[(P_3{}^B)Fe(N_2)]^{0/-}$ Couple

Following our initial discovery that the addition of excess $HBAr^F{}_4$ and KC_8 to the anionic dinitrogen complex $[Na(12\text{-c-}4)_2][(P_3{}^B)Fe(N_2)]$ at low temperature in Et_2O under an atmosphere of N_2 furnishes catalytic yields of NH_3, we pursued the optimization of this system for NH_3 yield (Equation 3.1).

$$N_2 + HBAr^F{}_4 + KC_8 \xrightarrow[Et_2O,\ -78\ °C]{\text{cat. } [(P_3{}^B)Fe(N_2)]^-} NH_3 \tag{3.1}$$

Under our initially reported conditions (in Et_2O at −78 °C with 48 equiv of $HBAr^F{}_4$ and 58 equiv of KC_8) the catalysis furnishes 7.0 ± 1.0 equiv of NH_3 per Fe-atom, corresponding to

44% of added protons being delivered to N_2 to make NH_3. Initial attempts at optimization showed that neither the overall concentration of the reactants nor the slow addition of the acid and/or reductant substantially altered the yield of NH_3 with respect to proton equivalents.

We have since examined whether the post-reaction material retained any catalytic competence when more substrate was delivered. We found that if, after stirring at −78 °C for 1 hr the reaction mixture was frozen (at −196 °C), delivered additional substrate, and then thawed to −78 °C, significantly more NH_3 was formed. Iterating this reloading process several times resulted in a steady increase in the total yield of NH_3 per Fe-atom (Figure 3.2), demonstrating that some active catalyst remains at −78 °C, even after numerous turnovers. This result implies that the yield of NH_3 is limited by competitive consumption of substrate in a hydrogen-evolving reaction (HER).

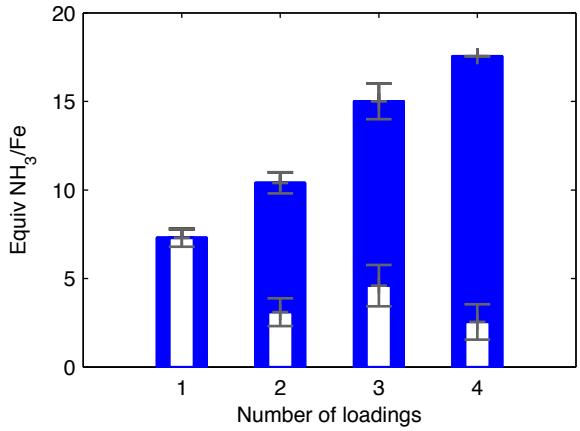

Figure 3.2: Yields of NH_3 obtained using $[(P_3{}^B)Fe(N_2)]^-$ from successive reloading of $HBAr^F{}_4$ and KC_8 to reactions maintained at ≤ −70 °C in Et_2O. Blue bars denote total observed yields and white inset bars denote the average increase in total yield from the final loading of substrate. Each loading corresponds to 48 equiv of $HBAr^F{}_4$ and 58 equiv of KC_8 relative to Fe. Data presented are averages of two experiments.

The apparent stability of at least some of the catalyst at low temperature suggested that it may be possible to observe higher turnover numbers if the catalyst is delivered more substrate at the beginning of the reaction. Indeed, as shown in Table 3.1, addition of increasing equivalents of $HBAr^F{}_4$ and KC_8 to $[(P_3{}^B)Fe(N_2)]^-$ at low temperature furnished steadily increasing yields of NH_3 relative to catalyst, with a maximal observed yield of

64 equiv of NH_3 per Fe-atom (average of 59 ± 6 over 9 iterations, Table 3.1, entries 1–5) at an acid loading of 1500 equiv with respect to Fe. This yield is nearly an order of magnitude larger than that reported at the original acid loading of 48 equiv. We note that the yields of NH_3 under these conditions are highly sensitive to the purity of the acid source, unsurprising given the high acid substrate loading relative to catalyst. To obtain reproducible yields, we have developed a tailored protocol for the synthesis of sufficiently pure $NaBAr^F{}_4/HBAr^F{}_4$, which is detailed in the Supporting Information. It is also important to ensure good mixing and a high gas-liquid interfacial surface area to enable proper mass transfer in the heterogeneous reaction mixture. We also note that efficient catalysis requires the lowering of the catalyst concentration relative to substrate, rather than *vice versa*.

Having discovered that $[(P_3{}^B)Fe(N_2)]^-$ is a significantly more robust catalyst than originally appreciated, we investigated the activity of the alkyl N_2 anion $[(Et_2O)_{0.5}K][(P_3{}^C)Fe(N_2)]$ toward N_2 fixation at higher substrate loading. Significantly higher yields of NH_3 per Fe are also attainable using this catalyst, albeit with roughly 2/3 the activity of $[(P_3{}^B)Fe(N_2)]^-$ (Table 3.1, entries 6–10). As a point of comparison, we also submitted the silyl congener $[Na(12\text{-c-}4)_2][(P_3{}^{Si})Fe(N_2)]$ to these conditions and observed dramatically lower yields of NH_3, consistent with earlier reports (Table 3.1, entries 11 and 12). Although the $[(P_3{}^{Si})Fe(N_2)]^-$ system displays worse selectivity for NH_3 formation vs HER than $[(P_3{}^B)Fe(N_2)]^-$ (*vide infra*), $[(P_3{}^{Si})Fe(N_2)]^-$ still demonstrates catalytic yields of NH_3 under sufficiently high substrate loading (up to 4 equiv of NH_3 per Fe, Table 3.1, entry 12).

Table 1 also contains data for catalytic trials with the borohydrido-hydrido complex $(P_3{}^B)(\mu\text{-H})Fe(H)(N_2)$ as a catalyst in mixed Et_2O/toluene solvent. In the presence of admixed toluene $(P_3{}^B)(\mu\text{-H})Fe(H)(N_2)$ is observed to be partially soluble and demonstrates competence as a catalyst (Table 3.1, entry 14); in the absence of toluene $(P_3{}^B)(\mu\text{-H})Fe(H)(N_2)$ shows poor solubility and lower than catalytic yields of NH_3 were observed under the originally reported catalytic conditions (0.50 ± 0.1 equiv of NH_3 per Fe).[26] The significance of these observations is discussed below (Section 3.2.4).

Table 3.1: NH_3 Generation from N_2 Mediated by Synthetic Fe Catalysts[a]

$$N_2 + HBAr^F{}_4 + KC_8 \xrightarrow[Et_2O,\ -78\ ^\circ C]{\text{Catalyst}} NH_3$$

Entry	Catalyst	[Fe] (mM)	$HBAr^F{}_4$ (equiv)	KC_8 (equiv)	Variation	NH_3/Fe (equiv)	yield NH_3/H^+ (%)
1	$[(P_3{}^B)Fe(N_2)]^-$	1.3	48	58	–	7.3 ± 0.5	45 ± 3
2	$[(P_3{}^B)Fe(N_2)]^-$	0.64	96	120	–	12 ± 1	38 ± 3
3	$[(P_3{}^B)Fe(N_2)]^-$	0.43	150	185	–	17.4 ± 0.2	35.6 ± 0.4
4	$[(P_3{}^B)Fe(N_2)]^-$	0.08	720	860	–	43 ± 4	18 ± 2
5	$[(P_3{}^B)Fe(N_2)]^-$	0.04	1500	1800	–	59 ± 6	12 ± 1
6[b]	$[(P_3{}^C)Fe(N_2)]^-$	1.0	37	40	$[HBAr^F{}_4]$ = 31 mM	4.6 ± 0.8	36 ± 6
7	$[(P_3{}^C)Fe(N_2)]^-$	0.56	110	120	–	11.3 ± 0.9	31 ± 2
8	$[(P_3{}^C)Fe(N_2)]^-$	0.28	220	230	–	14 ± 3	19 ± 4
9	$[(P_3{}^C)Fe(N_2)]^-$	0.08	750	810	–	19 ± 4	7 ± 2
10	$[(P_3{}^C)Fe(N_2)]^-$	0.04	1500	1600	–	36 ± 7	7 ± 1
11[c]	$[(P_3{}^{Si})Fe(N_2)]^-$	0.58	48	58	$[HBAr^F{}_4]$ = 31 mM	0.8 ± 0.5	5 ± 3
12	$[(P_3{}^{Si})Fe(N_2)]^-$	0.04	1500	1800	–	3.8 ± 0.8	0.8 ± 0.2
13	$(P_3{}^B)(\mu\text{-H})Fe(H)(N_2)$[d]	–	150	185	3% toluene	1.1 ± 0.1	2.4 ± 0.3
14	$(P_3{}^B)(\mu\text{-H})Fe(H)(N_2)$	0.44	150	185	25% toluene	5.6 ± 0.9	12 ± 2
15	$[(P_3{}^B)Fe(N_2)]^-$	0.41	150	185	25 equiv NH_3 added	6.4 ± 0.1	13.2 ± 0.2
16	$[(P_3{}^B)Fe(N_2)]^-$	0.41	150	0	1900 equiv 10 wt% Na/Hg	5.0 ± 0.2	10.3 ± 0.5

[a]Fe precursor, $HBAr^F{}_4$, KC_8, and Et_2O sealed in a vessel at −196 °C under an N_2 atmosphere followed by warming to −78 °C and stirring at −78 °C. Unless noted otherwise, $[HBAr^F{}_4]$ = 63 mM. Yields are reported as an average of at least 2 iterations.
[b]Data taken from [27].
[c]Data taken from [26].
[d]Not fully soluble under reaction conditions.

The efficiency of NH_3 production with respect to acid substrate decreases under increasingly high turnover conditions for these Fe systems. Our understanding of the HER kinetics (*vide infra*) rationalizes this phenomenon in that under comparatively low catalyst concentration (which engenders higher turnover) the background HER should be increasingly competitive, thereby reducing the N_2 fixation efficiency. The product of the reaction (NH_3) may also act as an inhibitor of catalysis. To test this latter possibility, catalytic runs with 150 equiv of $HBAr^F{}_4$ and 185 equiv of KC_8 in the presence of $[(P_3{}^B)Fe(N_2)]^-$ were conducted with the inclusion of 25 equiv of NH_3 (Table 3.1, entry 15). The fixed N_2 yield of this reaction is substantially lower than that of the comparable experiment without added NH_3 (Table 3.1, entry 3). One contributing cause for NH_3 inhibition is that it sequesters $HBAr^F{}_4$ as $[NH_4][BAr^F{}_4]$; however, the yield of NH_3 observed in entry 15 is suppressed compared to an experiment with only 100 equiv of $HBAr^F{}_4$. This observation indicates that NH_3 inhibits the catalytic reaction, and that the degree of inhibition is more substantial than a stoichiometric leveling of the acid strength.

We also sought to establish the minimum reducing potential required to drive catalysis with $[(P_3{}^B)Fe(N_2)]^-$. We have shown in previous work that $[(P_3{}^B)Fe(N_2)]^-$ reacts favorably with $HBAr^F{}_4$ in Et_2O at −78 °C along a productive N_2 fixation pathway.[55] Specifically, $[(P_3{}^B)Fe(N_2)]^-$ can be doubly protonated in Et_2O at −78 °C to generate $[(P_3{}^B)Fe(NNH_2)]^+$ (Equation 3.2). If only stoichiometric acid is present, $[(P_3{}^B)Fe(N_2)]^-$ is instead unproductively oxidized to $(P_3{}^B)Fe(N_2)$ (Equation 3.3). We have only observed net oxidation in the reaction of the neutral $(P_3{}^B)Fe(N_2)$ state with $HBAr^F{}_4$ in Et_2O to produce $[(P_3{}^B)Fe]^+$ (Equation 3.4).

$$[(P_3{}^B)Fe(N_2)]^- + \text{xs } HBAr^F{}_4 \rightarrow [(P_3{}^B)Fe(NNH_2)]^+ \tag{3.2}$$

$$[(P_3{}^B)Fe(N_2)]^- + HBAr^F{}_4 \rightarrow (P_3{}^B)Fe(N_2) + 0.5\,H_2 \tag{3.3}$$

$$(P_3{}^B)Fe(N_2) + HBAr^F{}_4 \rightarrow [(P_3{}^B)Fe(N_2)]^+ + 0.5\,H_2 \tag{3.4}$$

These observations suggest that N_2-fixing catalysis likely occurs at the $[(P_3^B)Fe(N_2)]^{0/-}$ redox couple (−2.1 V vs $Fc^{+/0}$), but not at the $[(P_3^B)Fe]^+/(P_3^B)Fe(N_2)$ potential (−1.5 V vs $Fc^{+/0}$). We have explored this hypothesis via cyclic voltammetry (CV) experiments. Figure 3.3 shows electrochemical data for $[(P_3^B)Fe]^+$ dissolved in Et_2O at −45 °C under 1 atm N_2 in the presence of 0.1 M $NaBAr^F_4$ as a soluble electrolyte to create a modestly conductive ethereal solution; data were not collected at −78 °C due to lower solubility of $NaBAr^F_4$ at that temperature. The blue trace shows the expected irreversible $[(P_3^B)Fe]^+/(P_3^B)Fe(N_2)$ feature centered around −1.5 V and the $[(P_3^B)Fe(N_2)]^{0/-}$ couple at −2.1 V, as previously reported.[52] The red trace shows the electrochemical behavior of $[(P_3^B)Fe]^+$ in the presence of 5 equiv of $HBAr^F_4$. The data reveal a sharp plateaued increase in current coincident with the $[(P_3^B)Fe(N_2)]^{0/-}$ redox couple, and very little increase in current at the $[(P_3^B)Fe]^+/(P_3^B)Fe(N_2)$ feature. The onset of the rise in current at the $[(P_3^B)Fe(N_2)]^{0/-}$ couple intimates that electrocatalysis may be feasible, and that chemical reductants with weaker reduction potentials than KC_8 may also be competent for N_2-to-NH_3 conversion catalyzed by $[(P_3^B)Fe(N_2)]^-$. Also, the onset potential of the pseudo-catalytic wave does not shift from the $[(P_3^B)Fe(N_2)]^{0/-}$ couple, indicating that this reduction precedes the first protonation event.

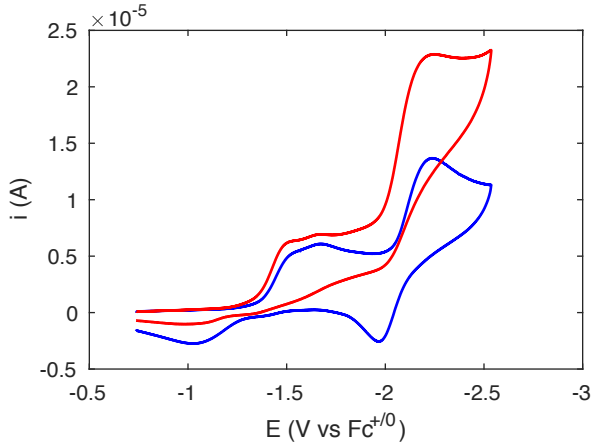

Figure 3.3: Cyclic voltammetry of $[(P_3^B)Fe][BAr^F_4]$ in the presence of 0 (blue) and 5 (red) equiv of $HBAr^F_4$, collected in Et_2O with 0.1 M $NaBAr^F_4$ electrolyte at −45 °C using a glassy carbon electrode and referenced to the $Fc^{+/0}$ couple. Scan rate is 100 mV s^{-1}.

To determine whether electrolytic N_2-to-NH_3 conversion contributes to the feature observed in the CV data,[60] a controlled-potential bulk electrolysis of $[(P_3{}^B)Fe]^+$ and 10 equiv of $HBAr^F{}_4$ in Et_2O at −45 °C under 1 atm N_2 in the presence of 0.1 M $NaBAr^F{}_4$ electrolyte with a reticulated vitreous carbon working electrode was performed. The electrolysis was held at −2.6 V (vs $Fc^{+/0}$) for 4.6 h, after which time 5.85 C of charge had been passed. Product analysis revealed the formation of NH_3 (18% faradaic efficiency) as well as H_2 (58% faradaic efficiency). The amount of NH_3 generated in this experiment corresponds to 0.5 equiv with respect to Fe and 14% yield with respect to acid. When the experiment was performed at higher acid loading (50 equiv), the NH_3 yield increased substantially (2.2 equiv per Fe; 25% faradaic efficiency; electrolysis held at −2.3 V in this instance with 8.39 C charge passed over 16.5 h). This electrolysis also produced 21.7 μmol of H_2 corresponding to 48% faradaic efficiency. While these yields of NH_3 with respect to Fe do not demonstrate formal turnover, they do suggest that electrocatalytic N_2-to-NH_3 conversion by this Fe system may be feasible. That the NH_3 yield increases with increased acid correlates well with our chemical activity results. Studies to more thoroughly explore the electrocatalytic N_2-to-NH_3 conversion behavior of $(P_3{}^B)Fe$ species are underway.

The electrochemical data presented in Figure 3.3 also suggest that chemical reductants with weaker reduction potentials than KC_8 may be competent for N_2-to-NH_3 conversion catalysis by $[(P_3{}^B)Fe(N_2)]^-$. Consistent with this notion, we find that catalytic yields of NH_3 (5 equiv per Fe) are obtainable using $[(P_3{}^B)Fe(N_2)]^-$ in the presence of 150 equiv of $HBAr^F{}_4$ and 1900 equiv of 10 wt% Na/Hg amalgam under ca. 1 atm N_2 at −78 °C in Et_2O (Table 3.1, entry 16; a larger excess of 10 wt% Na/Hg amalgam was employed to compensate for the lower surface area of the reagent). This result demonstrates that the catalysis is not unique to the presence of either potassium or graphite. KC_8 is a stronger reductant than is needed for N_2-to-NH_3 conversion, but shows more favorable selectivity for N_2 reduction relative to H_2 generation than other reductants we have thus far canvassed.

3.2.2 Kinetics of Ammonia and Hydrogen Formation

To better understand the competing NH_3- and H_2-forming reactions that occur during catalysis, we measured the time profiles of product formation using the most active catalyst, $[(P_3{}^B)Fe(N_2)]^-$. Our method for quenching catalytic NH_3 production uses rapid freeze-quenching of reactions to −196 °C, followed by addition of *t*BuLi, and subsequent annealing to −78 °C. Employing this method allows for the measurement of NH_3 production as a function of time. The time courses of NH_3 formation obtained for the previously reported substrate loading (blue trace)[26] as well as a higher substrate loading (red trace) are shown in Figure 3.4.

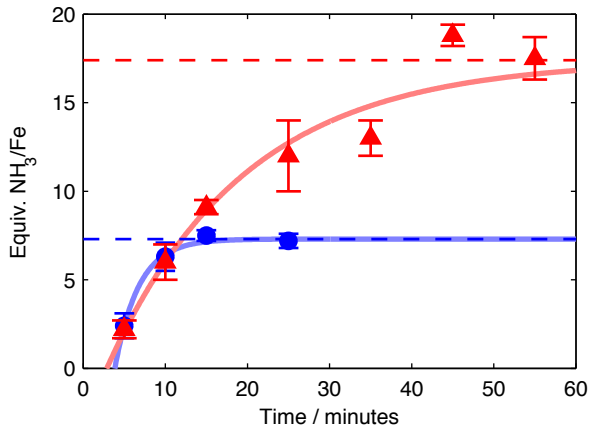

Figure 3.4: Time profiles of the formation of NH_3 from N_2 using $[(P_3{}^B)Fe(N_2)]^-$ as a catalyst at −78 °C under previously reported reaction conditions (blue circles, 0.64 mM Fe, 48 equiv of $HBAr^F{}_4$, 58 equiv of KC_8) and higher-turnover conditions (red triangles, 0.43 mM Fe, 150 equiv of $HBAr^F{}_4$, 185 equiv of KC_8). Dashed lines show expected final yields from the corresponding entries in Table 3.1 (entries 1 and 3). Each point represents an average of two experiments. Solid lines are provided as guides for the eye only.

Under both substrate loadings shown in Figure 3.4, the reaction proceeds to completion at −78 °C. Furthermore, under the higher-turnover conditions (with 150 equiv of $HBAr^F{}_4$ and 185 equiv of KC_8, Figure 3, red triangles) the reaction proceeds to completion over ca. 45 min, a time scale that enables us to measure the dependence of $d[NH_3]/dt$ on the concentrations of the soluble reagents—$[(P_3{}^B)Fe(N_2)]^-$ and $HBAr^F{}_4$—via the method of initial rates. As shown in Figure 3.5 (left), an initial rates analysis demonstrates that the

reaction is first order in [Fe], showing that a mononuclear (P_3^B)Fe species is involved in the turnover-limiting step for NH_3 formation. Comparing conditions ranging from 15 to 250 mM [$HBAr^F_4$] revealed no significant correlation between initial [$HBAr^F_4$] and initial NH_3 production rate; for instance, there is no measurable difference in the amount of NH_3 produced after 5 min. This observation suggests zero-order rate dependence on acid concentration, which is borne out by the initial rates analysis (Figure 3.5, right).

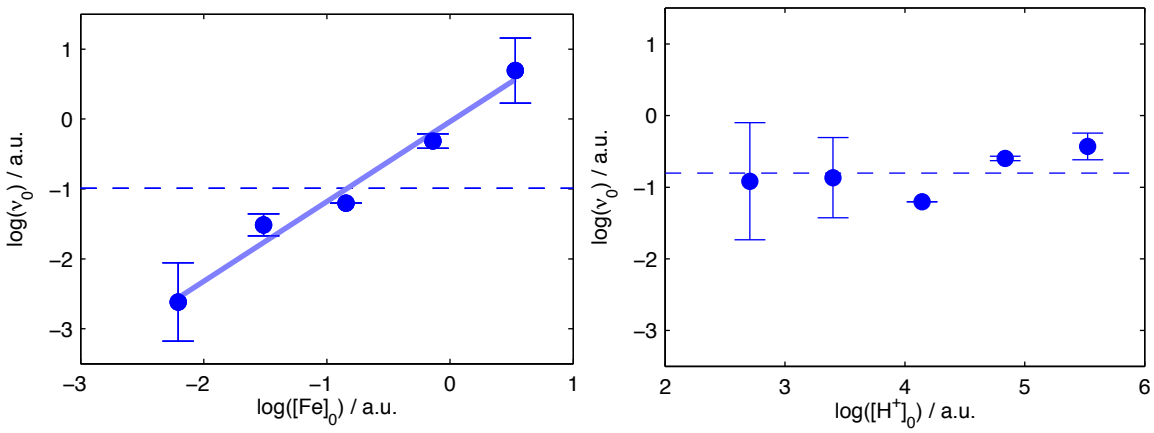

Figure 3.5: Log–log plots of the initial rate of NH_3 formation (v_0) versus initial concentrations of soluble reagents. (Left) v_0 versus $[Fe]_0$ for a range of [Fe] from 0.11 to 1.7 mM. The dashed line shows a constant function fit to the mean of the data, while the solid trend line shows the result of least-squares linear regression ($\log v_0 = (-0.04 \pm 0.1) + (1.1 \pm 0.1) \cdot \log([Fe]_0)$, $r^2 = 0.98$). (Right) v_0 versus $[HBAr^F_4]_0$ for a range of [$HBAr^F_4$] from 15 to 250 mM. The dashed line shows a constant function fit to the mean of the data (RMSE = 0.3), which is not statistically different from the result of a least-squares linear regression (RMSE = 0.3).

These data provide an estimate of the initial TOF (determined as moles of NH_3 produced per minute per Fe-atom) of this catalyst system of 1.2 ± 0.1 min^{-1}. While the TOF of this catalyst is not directly comparable to other N_2-to-NH_3 conversion catalysts due to differences in conditions and substrate, it is notable that [(P_3^B)Fe(N_2)]$^-$ under the conditions used here furnishes a substantially higher TOF than the other synthetic systems in Figure 3.1 for which data is available (Table 3.2) while operating over 100 °C lower in temperature (albeit with the benefit of a stronger reductant). MoFe nitrogenase purified from *Klebsiella pneumoniae* exhibits a TOF of approximately 80 min^{-1},[61] nearly 2 orders

of magnitude faster than that of the present synthetic Fe system, while operating at room temperature.

Table 3.2: Comparison of NH_3-Generating Reactions

Catalyst	Temp (°C)	Maximum yield[a]	TOF (min^{-1})	Efficiency (%)
Figure 3.1, C (R = H)[b]	25	12	0.14	31
Figure 3.1, F[c]	25	63	0.26	35
$[(P_3{}^B)Fe(N_2)]^-$	−78	64	1.2	12

[a]Expressed in NH_3 equivalents.
[b]Conditions: 2,6-lutidinium trifluoromethanesulfonate and cobaltocene in toluene. Data from [32].
[c]Conditions: 2,4,6-trimethylpyridinium trifluoromethanesulfonate and decamethylcobaltocene in toluene. Data from [32].

To determine potential HER activity of $[(P_3{}^B)Fe(N_2)]^-$, we measured the time course of $H_{2(g)}$ formation from $HBAr^F{}_4$ and KC_8 in the absence and presence of $[(P_3{}^B)Fe(N_2)]^-$, under catalytic conditions. As shown in Figure 3.6, the initial rate of $H_{2(g)}$ evolution at −78 °C is enhanced by the presence of $[(P_3{}^B)Fe(N_2)]^-$. The Fe-catalyzed HER is > 85% complete within the first hour with a final yield of ca. 40% (blue trace). Quantifying the NH_3 produced in this reaction (34% yield based on $HBAr^F{}_4$) accounts for 74% of the acid added. We also confirm that there is significant background HER from $HBAr^F{}_4$ and KC_8 (black trace), as expected. We conclude that both catalyzed and background HER are competing with NH_3 formation in the catalyst system.

As a point of comparison, we also measured the rate of $H_{2(g)}$ evolution in the presence of $[(P_3{}^{Si})Fe(N_2)]^-$. As shown in Figure 3.6, $[(P_3{}^{Si})Fe(N_2)]^-$ also catalyzes HER, with an initial rate that is comparable to $[(P_3{}^B)Fe(N_2)]^-$. However, in this case, $H_{2(g)}$ evolution approaches completion over 2 hr, resulting in a final measured yield of 88%. This is consistent with the low N_2-fixing activity of $[(P_3{}^{Si})Fe(N_2)]^-$; in the absence of a competitive NH_3-producing reaction, $[(P_3{}^{Si})Fe(N_2)]^-$ catalyzes the reduction of protons to H_2. Understanding the fundamental differences that give rise to the divergent selectivity of these Fe catalysts is an important goal in the context of designing selective N_2 reduction catalysts.

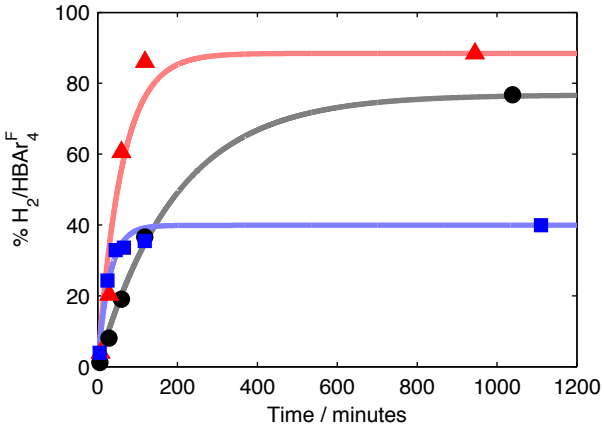

Figure 3.6: Time profiles of the formation of H_2 from $HBAr^F{}_4$ and KC_8 in Et_2O at −78 °C. Data is presented for the reaction of these reagents alone (black circles) as well as in the presence of $[(P_3{}^B)Fe(N_2)]^-$ (blue squares) and $[(P_3{}^{Si})Fe(N_2)]^-$ (red triangles). Each time course was collected continuously from a single experiment. Solid lines are provided as guides for the eye only.

3.2.3 Spectroscopic Characterization of Fe Speciation under Turnover

Considering the relatively slow rate of NH_3 formation ascertained from low temperature quenching experiments, we sought to determine the Fe speciation under turnover using the $[(P_3{}^B)Fe(N_2)]^-$ catalyst. By rapidly freeze-quenching reaction mixtures using ^{57}Fe-enriched $[(P_3{}^B)Fe(N_2)]^-$ as a catalyst, time-resolved Mössbauer spectra can be obtained that are reflective of catalysis.[62,63]

The Mössbauer parameters of some independently synthesized $(P_3{}^B)Fe$ species that may be relevant to the present catalysis have been measured and are collected in Table 3.3. Mössbauer isomer shifts (δ) can often be used to assign the relative oxidation state of structurally related compounds,[51,64] yet in this series of $(P_3{}^B)Fe$ compounds there is a poor correlation between δ and formal oxidation state assignments (e.g., $[(P_3{}^B)Fe(N_2)]^-$ and $[(P_3{}^B)Fe(NNH_2)]^+$ have nearly identical isomer shifts). This fact reflects the high degree of covalency present in these $(P_3{}^B)Fe(N_xH_y)$ complexes, skewing classical interpretations of the Mössbauer data. That is, the degree of true oxidation/reduction at the Fe centers in $(P_3{}^B)Fe$ species is buffered by covalency with the surrounding ligand field.[65,66] We do, however, find a useful linear correlation ($r^2 = 0.90$) between the measured ground

spin states (S) of $(P_3{}^B)Fe(N_xH_y)$ compounds and δ (Figure 3.7),[i] providing an empirical relationship that guides analysis of Mössbauer spectra obtained from catalytic reactions (Table 3.4). Ground spin states can be reliably correlated with the type of N_xH_y ligand, and possibly the presence of hydride ligands, coordinated to a $(P_3{}^E)Fe$ center. This knowledge, combined with freeze-quench Mössbauer data, enables us to predict with some confidence the type(s) of Fe species that are present in a spectrum obtained after freeze-quenching during turnover.

Table 3.3: Mössbauer Parameters for $(P_3{}^B)Fe$ Complexes[a]

Compound	S	Conditions	δ (mm s^{-1})	$\lvert\Delta E_Q\rvert$ (mm s^{-1})
$[(P_3{}^B)Fe]^+$ [b]	3/2	frozen solution, 50 mT	0.75	2.55
$[(P_3{}^B)Fe(N_2H_4)]^+$	3/2	frozen solution, 50 mT	0.70	2.30
$[(P_3{}^B)Fe(NH_3)]^+$	3/2	frozen solution, zero field	0.68	1.94
$(P_3{}^B)Fe(NH_2)$	3/2	frozen solution, zero field	0.60	1.47
$(P_3{}^B)Fe(N_2)$ [b]	1	frozen solution, 50 mT	0.56	3.34
$[(P_3{}^B)Fe(N_2)]^-$ [b]	1/2	frozen solution, 50 mT	0.40	0.99
$[(P_3{}^B)Fe(NNH_2)]^+$[b]	1/2	frozen solution, 50 mT	0.35	1.02
$[(P_3{}^B)Fe(NAd)]^+$	1/2	powder, 50 mT	0.15	1.31
$(P_3{}^B)(\mu\text{-H})Fe(H)(N_2)$	0	frozen solution, zero field	0.21	1.44
$(P_3{}^B)(\mu\text{-H})Fe(H)(H_2)$	0	frozen solution, zero field	0.19	1.55
$(P_3{}^B)Fe(NAd)$	0	powder, zero field	0.04	1.40

[a] All data were collected at 80 K under the conditions noted; external magnetic fields applied in parallel mode.
[b] Data taken from [55].

Table 3.4: Mössbauer Isomer Shift vs. Spin State Correlation for $(P_3{}^B)Fe$ Complexes[a]

S	$\delta_{predicted}$ (mm s^{-1})
0	0.1 ± 0.1
1/2	0.3 ± 0.1
1	0.5 ± 0.2
3/2	0.7 ± 0.2

[a] The expectation values for δ based on S computed from the linear fit shown in Figure 3.7 (ranges reported as 95% confidence interval).

[i] Indeed, if the alkylimido species $[(P_3{}^B)Fe(NAd)]^{+/0}$ are excluded from the series of data collected in Figure 3.7, the correlation improves significantly ($r^2 = 0.96$). The isomer shifts of these imides appear to be systematically reduced by ca. 0.1 to 0.2 mm s^{-1} from the trend exhibited by the rest of the compounds in Table 3.3.

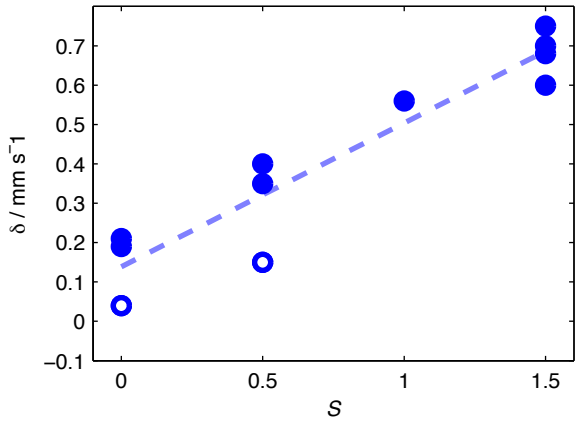

Figure 3.7: Plot of δ versus ground spin state S for the compounds listed in Table 3.3 (blue circles), along with a linear least-squares fit to the data (dotted line, $r^2 = 0.90$). The isomer shifts of $[(P_3{}^B)Fe(NAd)]^{0/+}$ are highlighted by open circles (See i, page 57).

Figure 3.8 shows time-resolved Mössbauer spectra of freeze-quenched catalytic reaction mixtures of $[(P_3{}^B)Fe(N_2)]^-$ with 48 equiv of $HBAr^F{}_4$ and 58 equiv of KC_8. Figure 3.8, A shows the spectrum of ^{57}Fe-enriched $[(P_3{}^B)Fe(N_2)]^-$ as a 0.64 mM solution in THF, which features a sharp, asymmetric quadrupole doublet at 80 K in the presence of a 50 mT external magnetic field. Figure 3.8, B shows the spectrum of a catalytic reaction mixture freeze-quenched after 5 min of stirring, revealing the major Fe species (blue, representing ca. 60% of all Fe) present during active turnover to have parameters $\delta = 0.16 \pm 0.2$ mm s^{-1} and $|\Delta E_Q| = 1.63 \pm 0.03$ mm s^{-1}, which, within the error of the simulation, is consistent with the diamagnetic borohydrido-hydrido species $(P_3{}^B)(\mu\text{-H})Fe(H)(L)$ (L = N_2 or H_2).[67] This observation correlates well with the previously reported result that $(P_3{}^B)(\mu\text{-H})Fe(H)(N_2)$ is produced from the reaction of $[(P_3{}^B)Fe(N_2)]^-$ with smaller excesses of $HBAr^F{}_4$ and KC_8.[26] Further corroborating this assignment, data collected at liquid He temperature with a small applied magnetic field suggest that this species is a non-Kramers spin system,[68] and should be $S = 0$ given the observed correlation between δ and S (*vide supra*). Also present in Figure 3.8, B is a minor component (ca. 8%, shown in white) with parameters $\delta = 0.02 \pm 0.2$ mm s^{-1} and $|\Delta E_Q| = 0.97 \pm 0.2$ mm s^{-1}, and a broad residual absorbance centered at $\delta \approx 0.9$ mm s^{-1} encompassing a width of ca. 2 mm s^{-1} (representing ca. 20 to 30% of all Fe in

the sample, shown in gray). Due to the broadness of the latter resonance ($\Gamma \approx 1$ mm s^{-1}), this feature could not be accurately modeled. Nevertheless, the signal is consistent with several known $S = 3/2$ ($P_3{}^B$)Fe species. For example, the vacant cation, [($P_3{}^E$)Fe]$^+$, and the cationic species [($P_3{}^B$)Fe(N_2H_4)]$^+$ and [($P_3{}^B$)Fe(NH_3)]$^+$, are $S = 3/2$ species and give rise to quadrupole doublets that lie within the envelope of this broad signal (Tables 3.3 and 3.4).[ii]

Figure 3.8, C shows that the primary Fe species present after 25 min of reaction time is the starting catalyst [($P_3{}^B$)Fe(N_2)]$^-$ (shown in red, representing ca. 70% of all Fe in the sample). Also present is ca. 20% of the species we assign as ($P_3{}^B$)(μ-H)Fe(H)(L) ($\delta = 0.22 \pm 0.2$ mm s^{-1} and $|\Delta E_Q| = 1.62 \pm 0.03$ mm s^{-1}, shown in blue), < 5% of the neutral dinitrogen complex, ($P_3{}^B$)Fe(N_2) (green), and ca. 7% of an as-yet unknown species with parameters $\delta = 0.00 \pm 0.02$ mm s^{-1} and $|\Delta E_Q| = 2.97 \pm 0.06$ mm s^{-1} (white). Thus, as acid substrate is consumed in the reaction to produce NH_3 and H_2, the mixture of Fe species shown in Figure 3.8, B at an early time point evolves back to the starting material [($P_3{}^B$)Fe(N_2)]$^-$. A slight residual excess of KC_8 is needed to ensure recovery of the active catalyst. These data help rationalize the results of the substrate reloading experiments (*vide supra*). The utility of freeze-quench ^{57}Fe Mössbauer spectroscopy is evident: in a single spectral snapshot the presence of ($P_3{}^B$)Fe components with varied spin states including $S = 0$, $1/2$, 1, and $3/2$ are observed.

The increasingly low Fe concentrations used to achieve the highest yields of NH_3 reported here make the collection of well-resolved Mössbauer spectra under such conditions challenging. Nonetheless, we repeated freeze-quench experiments for one set of higher-turnover conditions (Figure 3.9). Although in this case the Fe speciation at intermediate times is more complex, these data exhibit the same gross behavior shown in Figure 3.8; under active turnover the major Fe species present is consistent with hydride ($P_3{}^B$)(μ-H)Fe(H)(L)

[ii] Although the low isomer shift of the minor component present in Figure 3.8, B is suggestive of a diamagnetic ground state, its identity is presently unknown.

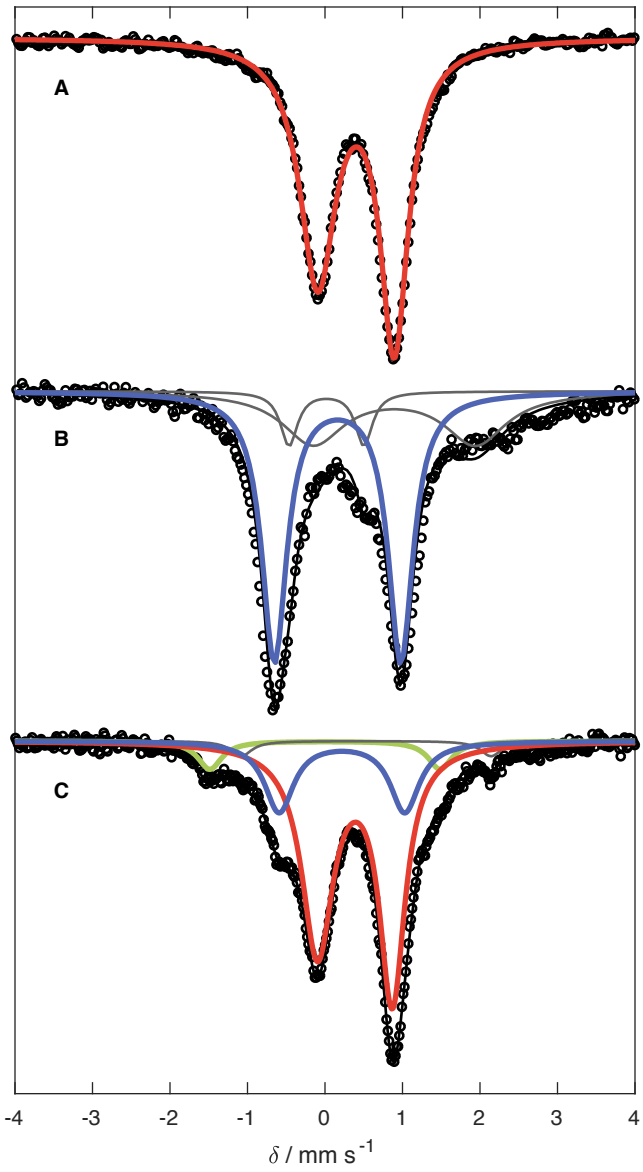

Figure 3.8: Frozen solution Mössbauer spectra collected at 80 K in the presence of a 50 mT parallel magnetic field. (A) Spectrum of $[(P_3{}^B)Fe(N_2)]^-$ (0.64 mM in THF). (B) A catalytic mixture (Et_2O, [Fe] = 0.64 mM, 48 equiv of $HBAr^F{}_4$, 58 equiv of KC_8) freeze-quenched after 5 min of stirring at −78 °C. (C) A catalytic mixture (Et_2O, [Fe] = 0.64 mM, 48 equiv of $HBAr^F{}_4$, 58 equiv of KC_8) freeze-quenched after 25 min of stirring at −78 °C. Data are presented as black circles and simulations as solid black lines with components plotted in red, blue, green, and gray.

($\geq$ 50%, average parameters δ = 0.20 ± 0.2 mm s^{-1} and $|\Delta E_Q|$ = 1.49 ± 0.09 mm s^{-1}; Figure 3.9 A and B, blue),[iii] and as the extent of reaction increases significant amounts of $[(P_3{}^B)Fe(N_2)]^-$ reform (ca. 50%; Figure 3.9 C, red).[iv]

3.2.4 Precatalyst Activity of $(P_3{}^B)(\mu\text{-H})Fe(H)(N_2)$ and Identification of a Catalyst Resting State

The observations presented in Section 3.2.3 suggest that hydride $(P_3{}^B)(\mu\text{-H})Fe(H)(L)$ builds up as the major Fe-containing species during active turnover and appears to be converted back to the active catalyst $[(P_3{}^B)Fe(N_2)]^-$ when catalysis is complete. We previously observed that this species can form under conditions that model the catalytic conditions (10 equiv of acid/12 equiv of reductant) and our initial thinking that $(P_3{}^B)(\mu\text{-H})Fe(H)(N_2)$ may be a catalyst deactivation product was guided by the poor activity of isolated $(P_3{}^B)(\mu\text{-H})Fe(H)(N_2)$ as a precatalyst under the standard conditions (generating only 0.5 ± 0.1 equiv of NH_3 per Fe at 50 equiv of acid/60 equiv of reductant).[26] However, in that initial report we also noted that isolated $(P_3{}^B)(\mu\text{-H})Fe(H)(N_2)$ is not solubilized under the catalytic conditions. Therefore, in light of the current in situ spectroscopy, and the observation that $(P_3{}^B)(\mu\text{-H})Fe(H)(N_2)$ liberated some NH_3 under the original conditions, we wondered whether its insolubility may be responsible for its comparatively low activity as an isolated precursor. If $(P_3{}^B)(\mu\text{-H})Fe(H)(N_2)$ is brought into solution, or formed in solution during turnover, it may exhibit activity. To test this hypothesis we explored the activity of $(P_3{}^B)(\mu\text{-H})Fe(H)(N_2)$ under modified catalytic conditions where a toluene/Et_2O mixture (which improves the solubility of $(P_3{}^B)(\mu\text{-H})Fe(H)(N_2)$) was employed as the solvent. In this case we find that $P_3{}^B)(\mu\text{-H})Fe(H)(N_2)$ serves as a viable precatalyst (Table

[iii] Also present in Figure 3.9, A: ca. 20% of the species with parameters δ = −0.03 ± 0.04 mm s^{-1} and $|\Delta E_Q|$ = 2.88 ± 0.09 mm s^{-1} that is present in Figure 3.8, C, and ca. 20% of a broad residual signal consistent with an unresolved quartet species. Also present in Figure 3.9, B: ca. 20% of neutral $(P_3{}^B)Fe(N_2)$ (green); ca. 15% of a sharply resolved species with parameters δ = 0.68 mm s^{-1} and $|\Delta E_Q|$ = 1.40 mm s^{-1} that is consistent with a quartet species such as $(P_3{}^B)Fe(NH_2)$; and ca. 20% of a broad residual signal consistent with an unresolved quartet species.

[iv] Also present in Figure 3.9 C: ca. 10% of the species with parameters δ = −0.03 ± 0.04 mm s^{-1} and $|\Delta E_Q|$ = 2.88 ± 0.09 mm s^{-1} that is present in Figures 3.8, C and 3.9, A, and ca. 15% of a broad residual signal consistent with an unresolved quartet species.

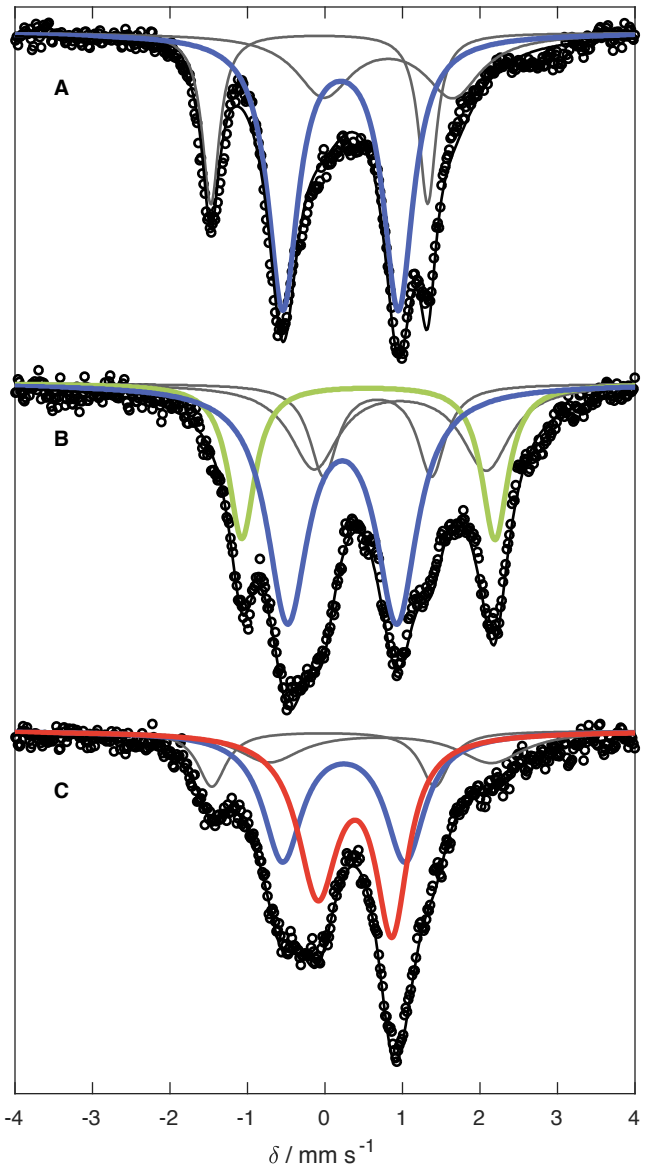

Figure 3.9: Frozen solution Mössbauer spectra collected at 80 K in the presence of a 50 mT parallel magnetic field. (A) A catalytic mixture (Et_2O, [Fe] = 0.43 mM, 150 equiv of $HBAr^F{}_4$, 185 equiv of KC_8) freeze-quenched after 5 min of stirring at −78 °C. (B) A catalytic mixture (Et_2O, [Fe] = 0.43 mM, 150 equiv of $HBAr^F{}_4$, 185 equiv of KC_8) freeze-quenched after 10 min of stirring at −78 °C. (C) A catalytic mixture (Et_2O, [Fe] = 0.43 mM, 150 equiv of $HBAr^F{}_4$, 185 equiv of KC_8) freeze-quenched after 25 min of stirring at −78 °C. Data presented as black points, simulations as solid black lines with components plotted in red, blue, green, and gray.

3.1, entries 13 and 14). We suppose then that under the standard conditions (in pure Et_2O), if $(P_3{}^B)(\mu\text{-H})Fe(H)(L)$ is generated in solution during catalysis, it should be able to react productively so long as it does not precipitate, which may be slow at −78 °C. Accordingly, we have observed that the Mössbauer spectrum of a sample taken from a standard catalytic mixture as described in Section 3.2.3 can be filtered at low temperature and still displays substantial $(P_3{}^B)(\mu\text{-H})Fe(H)(L)$.

These results suggest the feasibility of the stoichiometric transformation of hydride $(P_3{}^B)(\mu\text{-H})Fe(H)(L)$ into $[(P_3{}^B)Fe(N_2)]^-$ under catalytically relevant conditions. In a previous report, we showed that $(P_3{}^B)(\mu\text{-H})Fe(H)(N_2)$ is stable for short periods to either $HBAr^F{}_4$ or KC_8 in Et_2O at room temperature, again noting its insolubility under these conditions.[26] Given the results above, we have reinvestigated this reactivity in Et_2O/toluene mixtures. Thus, the reaction of $(P_3{}^B)(\mu\text{-H})Fe(H)(N_2)$ with 1 equiv of $HBAr^F{}_4$ in 6:1 d_8-toluene:Et_2O results in consumption of the starting material along with the appearance of several new, paramagnetically shifted ^{1}H NMR resonances. We hypothesize that protonolysis of either the terminal or bridging hydride moieties in $(P_3{}^B)(\mu\text{-H})Fe(H)(N_2)$ produces a cationic "$[(P_3{}^B)Fe(H)]^+$" species, which may then be reduced to liberate 0.5 equiv of H_2 and re-enter the catalytic manifold of $[(P_3{}^B)Fe(N_2)]^n$ species under an N_2 atmosphere. Indeed, the sequential addition of 1.5 equiv of $HBAr^F{}_4$ followed by 6 equiv of KC_8 to $(P_3{}^B)(\mu\text{-H})Fe(H)(N_2)$ at −78 °C in 3:1 Et_2O:toluene produces substantial amounts of $[(P_3{}^B)Fe(N_2)]^-$ (32% yield, unoptimized; Figure 3.10). This stoichiometric reactivity provides support for the idea that as $(P_3{}^B)(\mu\text{-H})Fe(H)(L)$ is formed under the standard reaction conditions it can react with acid and reductant to produce the starting catalyst $[(P_3{}^B)Fe(N_2)]^-$, consistent with the observations provided in Section 3.2.3.

Given that (i) $(P_3{}^B)(\mu\text{-H})Fe(H)(L)$ appears to be the predominant Fe-containing species observed by freeze-quench Mössbauer spectroscopy under turnover conditions at early time points, (ii) this species serves as a competent precatalyst when solubilized, and (iii) $(P_3{}^B)(\mu\text{-H})Fe(H)(N_2)$ can be synthetically converted to $[(P_3{}^B)Fe(N_2)]^-$ by $HBAr^F{}_4$ and KC_8, we

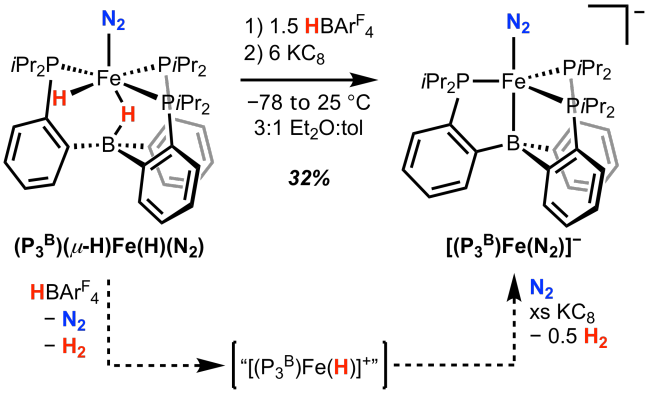

Figure 3.10: Stoichiometric conversion of $(P_3{}^B)(\mu\text{-H})Fe(H)(N_2)$ into $[(P_3{}^B)Fe(N_2)]^-$, under catalytically relevant conditions. A proposed reaction pathway is shown along the dashed arrows. "$[(P_3{}^B)Fe(H)]^+$" is a plausible intermediate of this conversion but has not been thoroughly characterized.

conclude that $(P_3{}^B)(\mu\text{-H})Fe(H)(L)$ is a major resting state of the catalysis. This conclusion does not require $(P_3{}^B)(\mu\text{-H})Fe(H)(L)$ to be an "on-path" intermediate; we instead think $(P_3{}^B)(\mu\text{-H})Fe(H)(L)$ is more likely a resting state that ties up the catalyst, but one that reversibly leaks into the on-path catalytic cycle in which $[(P_3{}^B)Fe(N_2)]^-$ is ultimately protonated.

The observation of a hydride resting state for this synthetic Fe catalyst may have additional relevance in the context of biological nitrogen fixation, where the intermediacy of metal hydride species has been proposed on the basis of spectroscopic data obtained during turnover.[8] It has further been proposed that the reductive elimination of hydrides as H_2 may be a prerequisite for N_2 binding to the nitrogenase active-site cofactor,[61,69–72] giving rise to obligate H_2 evolution in the limiting stoichiometry of N_2 conversion to NH_3.[73,74] The results described here directly implicate the relevance of a synthetic Fe hydride species to a system capable of catalytic N_2-to-NH_3 conversion. This in turn motivates complementary model reactivity studies on Fe hydride species such as $(P_3{}^B)(\mu\text{-H})Fe(H)(L)$, targets whose relevance might otherwise be overlooked.

3.2.5 Summary of Mechanistically Relevant Observations

To help collect the information presented here and in related studies of the (P_3^B)Fe catalyst system, Figure 3.11 provides a mechanistic outline for the key Fe species and plausible transformations we think are most relevant to the catalytic N_2-to-NH_3 conversion cycle. The complexes shown in blue, along with their respective spin states S, have been thoroughly characterized. Also, the net conversions between complexes that are indicated by solid blue arrows have been experimentally demonstrated. Those complexes depicted in black have not (as yet) been experimentally detected (however, see Chapter 4).

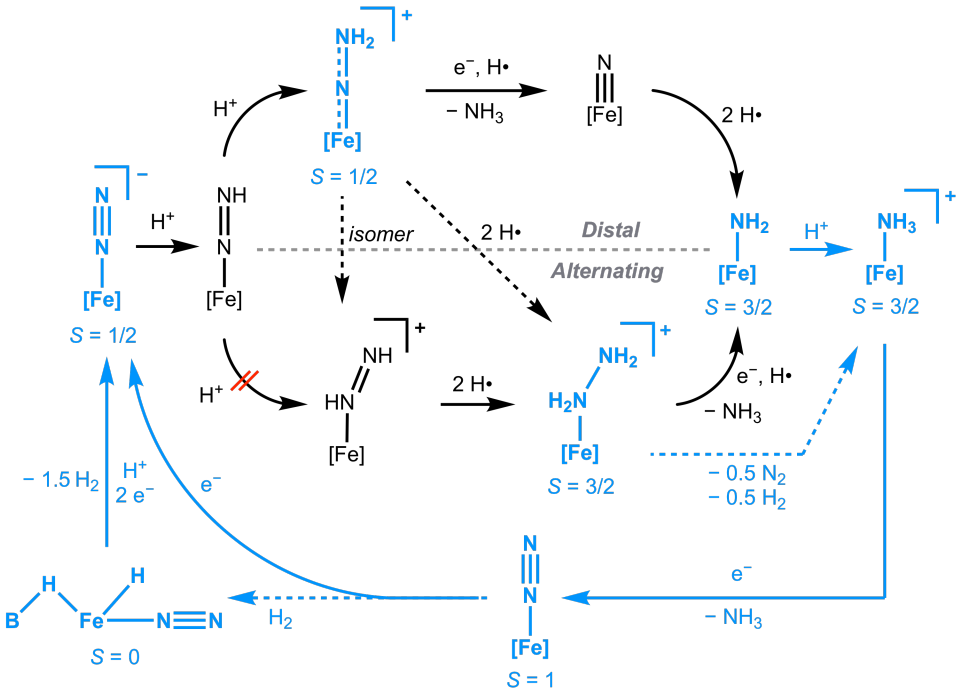

Figure 3.11: Possible Catalytic Scenarios for N_2-to-NH_3 Conversion by $[(P_3^B)Fe(N_2)]^-$. [Fe] = (P_3^B)Fe. Thoroughly characterized species and their respective ground spin states S are shown in blue, while as-yet undetected species are shown in black. Blue arrows indicate known pathways that are likely kinetically competent (solid) at −78 °C. Dashed blue arrows are likely incompetent pathways at −78 °C.

Several results are worth underscoring: (i) we have characterized the $S = 3/2$, substrate-free state $[(P_3^B)Fe]^+$, and shown that it binds N_2 upon electron loading, generating $S = 1$ $(P_3^B)Fe(N_2)$ or $S = 1/2$ $[(P_3^B)Fe(N_2)]^-$ depending on reducing equivalents provided;[52–54] (ii) $[(P_3^B)Fe]^+$ is competent for catalytic N_2-to-NH_3 conversion,[26] and fa-

cilitates this conversion electrolytically as established herein; (iii) in its most reduced state, $[(P_3{}^B)Fe(N_2)]^-$, the catalyst can be doubly protonated at low temperature to generate $[(P_3{}^B)Fe(NNH_2)]^+$,[55] a distal pathway intermediate (the diamagnetic relative of this compound, $[(P_3{}^{Si})Fe(NNH_2)]^+$, has very recently been structurally characterized);[75] (iv) the $[(P_3{}^B)Fe(NNH_2)]^+$ intermediate anneals (in the absence of reductant) to generate significant amounts of $[(P_3{}^B)Fe(NH_3)]^+$;[26,55] and (v) $[(P_3{}^B)Fe(NH_3)]^+$ can also be generated by protonation of $(P_3{}^B)Fe(NH_2)$, and reductive displacement of NH_3 from $[(P_3{}^B)Fe(NH_3)]^+$ under N_2 regenerates $[(P_3{}^B)Fe(N_2)]^-$.[54]

Also worth emphasizing is that diamagnetic $[(P_3{}^{Si})Fe(NNH_2)]^+$ can be reduced at low temperature to $S = 1/2$ $(P_3{}^{Si})Fe(NNH_2)$, and this species (in the presence of acid/reductant equivalents) decays to a mixture of $[(P_3{}^{Si})Fe(N_2H_4)]^+$ and $[(P_3{}^{Si})Fe(NH_3)]^+$.[75] Notably, $[(P_3{}^{Si})Fe(N_2H_4)]^+$, and also $[(P_3{}^B)Fe(N_2H_4)]^+$, readily disproportionate the bound N_2H_4 to generate the corresponding NH_3 adducts $[(P_3{}^{Si})Fe(NH_3)]^+$ and $[(P_3{}^B)Fe(NH_3)]^+$,[51,54] each of which evolves NH_3 upon reduction to regenerate (under N_2) $[(P_3{}^{Si})Fe(N_2)]^-$ and $[(P_3{}^B)Fe(N_2)]^-$, respectively. The reaction pathway observed for $[(P_3{}^{Si})Fe(NNH_2)]^+$, more readily studied than for $[(P_3{}^B)Fe(NNH_2)]^+$ because the former can be isolated in pure form, highlights the possibility of a hybrid crossover mechanistic pathway wherein a distal intermediate—$Fe(NNH_2)$—traverses to an alternating intermediate—$Fe(N_2H_4)$—that may then be converted to NH_3, possibly via disproportionation.[55,75]

By demonstrating first-order rate dependence on the concentration of $[(P_3{}^B)Fe(N_2)]^-$, the present study remains consistent with our hypothesis that a single-site mechanism is likely operative during N_2-to-NH_3 conversion catalysis. The direct observation of both $[(P_3{}^B)Fe(N_2)]^-$ and its neutral form $(P_3{}^B)Fe(N_2)$ in catalytic mixtures by freeze-quench Mössbauer spectroscopy lends further credence to this idea.

A plausible pathway for the formation of the putative resting state species $(P_3{}^B)(\mu$-$H)Fe(H)(L)$ would be hydrogenation of $(P_3{}^B)Fe(N_2)$ by H_2 evolved as a side product during

catalysis. This process has been demonstrated independently at room temperature in benzene.[67] Follow-up control experiments in Et_2O, however, suggest that this reaction is not kinetically competent at −78 °C. We are therefore at present unsure of the dominant pathway by which $(P_3{}^B)(\mu\text{-H})Fe(H)(L)$ is formed during catalysis. Alternative pathways might include bimolecular H-atom transfers from as-yet unobserved intermediates with reactive N–H bonds, such as $(P_3{}^B)Fe(N_2H)$ and/or $(P_3{}^B)Fe(NNH_2)$.

3.3 Conclusion

In the present study we have shown that N_2-fixing catalyst systems with $(P_3{}^E)Fe$ (E = B, C, Si) species give rise to high yields of NH_3 if supplied with sufficient acid and reductant. These yields (for E = B and C) compare very favorably against those of known Mo catalysts and are almost an order of magnitude greater than the yields presented in our previous reports. While we do not rule out some degree of catalyst degradation at −78 °C, these Fe catalysts are unexpectedly robust and it is possible that the lower efficiency of catalysis at higher turnover is in part due to buildup of NH_3 product, which is an inhibitor. We have also provided new mechanistic insights for reactions with catalyst $[(P_3{}^B)Fe(N_2)]^-$, such as the observation that catalysis proceeds at −78 °C, the demonstration of first-order rate dependence on catalyst concentration, the demonstration of zeroth-order rate dependence on $HBAr^F{}_4$ concentration, and the observation that $[(P_3{}^B)Fe(N_2)]^-$ catalyzes HER as well as NH_3 formation. Preliminary electrochemistry data suggests that reductive chemistry mediated by the $(P_3{}^B)Fe$ system can be driven at the formal $[(P_3{}^B)Fe(N_2)]^{0/-}$ couple around −2.1 V vs $Fc^{+/0}$, consistent with Na/Hg also serving as a viable reductant for catalytic turnover. Cyclic voltammetry and controlled potential electrolysis of $[(P_3{}^B)Fe]^+$ at −45 °C demonstrate that electrolytic N_2 reduction is possible.

The present study has also demonstrated the utility of coupling in situ freeze-quench ^{57}Fe Mössbauer spectroscopy with kinetic analysis of product formation as a powerful tool for the mechanistic study of Fe-catalyzed N_2 fixation. Prior to this work, no synthetic

molecular N_2-to-NH_3 conversion catalyst system had been studied spectroscopically under active turnover conditions. Our freeze-quench Mössbauer results suggest that $(P_3{}^B)(\mu$-H)Fe(H)(L) is an off-path resting state of the overall catalysis; this hydride species, which we previously posited to be primarily a catalyst sink, can instead reenter the catalytic pathway via its conversion to catalytically active $[(P_3{}^B)Fe(N_2)]^-$. This observation underscores the importance of understanding metal hydride reactivity in the context of Fe-mediated nitrogen fixation. It may be that HER activity provides a viable strategy for recovering catalytically active states from the unavoidable generation of iron hydride intermediates.

3.4 Experimental Section

3.4.1 Experimental Details

3.4.1.1 General considerations

All manipulations were carried out using standard Schlenk or glovebox techniques under an N_2 atmosphere. Solvents were deoxygenated and dried by thoroughly sparging with N_2 followed by passage through an activated alumina column in a solvent purification system by SG Water, USA LLC. Nonhalogenated solvents were tested with sodium benzophenone ketyl in THF in order to confirm the absence of oxygen and water. Deuterated solvents were purchased from Cambridge Isotope Laboratories, Inc., degassed, and dried over activated 3 Å molecular sieves prior to use. KC_8,[76] $[Na(12\text{-c-}4)_2][(P_3{}^B)Fe(N_2)]$,[52] $[K(Et_2O)_{0.5}][(P_3{}^C)Fe(N_2)]$,[27] $[Na(12\text{-c-}4)_2][(P_3{}^{Si})Fe(N_2)]$,[50] $(P_3{}^B)(\mu$-H)Fe(H)(N_2),[67] $(P_3{}^B)(\mu$-H)Fe(H)(H_2),[67] $[(P_3{}^B)Fe(NH_3)][BAr^F{}_4]$,[54] $[(P_3{}^B)Fe(N_2H_4)][BAr^F{}_4]$,[54] $(P_3{}^B)Fe(NH_2)$,[54] $[(P_3{}^B)Fe][BAr^F{}_4]$,[54] $(P_3{}^B)Fe(NAd)$,[55] and $[(P_3{}^B)Fe(NAd)][BAr^F{}_4]$[55] were prepared according to literature procedures. $NaBAr^F{}_4$ and $HBAr^F{}_4$ were prepared and purified according to a procedure modified from the literature as described below. All other reagents were purchased from commercial vendors and used without further purification unless otherwise stated. Et_2O and THF used in NH_3 generation experiments were stirred over Na/K ($\geq$ 2 hr) and filtered before use.

3.4.1.2 Physical Methods

^{1}H chemical shifts are reported in ppm relative to tetramethylsilane, using ^{1}H resonances from residual solvent as internal standards. IR measurements were obtained as solutions or thin films formed by evaporation of solutions using a Bruker Alpha Platinum ATR spectrometer with OPUS software (solution IR collected in a cell with KBr windows and a 1 mm pathlength). Optical spectroscopy measurements were collected with a Cary 50 UV-vis spectrophotometer using a 1-cm two-window quartz cell. H_2 was quantified on an Agilent 7890A gas chromatograph (HP-PLOT U, 30 m, 0.32 mm ID; 30 °C isothermal; nitrogen carrier gas) using a thermal conductivity detector. Cyclic voltammetry measurements were carried out in a glovebox under an N_2 atmosphere in a one-compartment cell using a CH Instruments 600B electrochemical analyzer. A glassy carbon electrode was used as the working electrode and platinum wire was used as the auxiliary electrode. The reference electrode was Ag/AgOTf in Et_2O isolated by a CoralPor frit (obtained from BASi). The ferrocene couple ($Fc^{+/0}$) was used as an external reference. Et_2O solutions of electrolyte (0.1 M $NaBAr^F{}_4$) and analyte were also prepared under an inert atmosphere.

3.4.1.3 Mössbauer Spectroscopy

Mössbauer spectra were recorded on a spectrometer from SEE Co. (Edina, MN) operating in the constant acceleration mode in a transmission geometry. The sample was kept in an SVT-400 cryostat form Janis (Wilmington, MA). The quoted isomer shifts are relative to the centroid of the spectrum of a metallic foil of α-Fe at room temperature. Solid samples were prepared by grinding solid material into a fine powder and then mounted in to a Delrin cup fitted with a screw-cap as a boron nitride pellet. Solution samples were transferred to a sample cup and chilled to 77 K inside of the glovebox, and unless noted otherwise, quickly removed from the glovebox and immersed in liquid N_2 until mounted in the cryostat. Data analysis was performed using version 4 of the program WMOSS[77] and quadrupole doublets were fit to Lorentzian lineshapes. See discussion below for detailed notes on the fitting

procedure.

3.4.1.4 Ammonia Quantification

Reaction mixtures were cooled to 77 K and allowed to freeze. The reaction vessel was then opened to atmosphere and to the frozen solution was slowly added a fourfold excess (with respect to acid) solution of a NaO*t*Bu solution in MeOH (0.25 mM) over 1 to 2 minutes. This solution was allowed to freeze, then the headspace of the tube was evacuated and the tube was sealed. The tube was then allowed to warm to RT and stirred at room temperature for 10 minutes. An additional Schlenk tube was charged with HCl (3 mL of a 2.0 M solution in Et_2O, 6 mmol) to serve as a collection flask. The volatiles of the reaction mixture were vacuum transferred into this collection flask. After completion of the vacuum transfer, the collection flask was sealed and warmed to room temperature. Solvent was removed in vacuo, and the remaining residue was dissolved in H_2O (1 mL). An aliquot of this solution (20–100 μL) was then analyzed for the presence of NH_3 (present as NH_4Cl) by the indophenol method.[78] Quantification was performed with UV-vis spectroscopy by analyzing absorbance at 635 nm.

3.4.2 Synthetic Details

3.4.2.1 Synthesis and Purification of $NaBAr^F{}_4$ and $HBAr^F{}_4$

Crude $NaBAr^F{}_4$ was prepared according to a literature procedure.[79] The crude material, possessing a yellow-tan hue, was purified by a modification to the procedure published by Bergman,[80] as follows. The crude $NaBAr^F{}_4$ was ground into a fine powder and partially hydrated by exposure to air for at least 24 hours ($NaBAr^F{}_4$ is a hygroscopic solid and crystallizes as a hydrate containing between 0.5 to 3.0 equivalents of H_2O when isolated under air). This material was first washed with dichloromethane (ca. 3 mL g^{-1}, in three portions), washing liberally with pentane between each portion of dichloromethane. The remaining solids were washed with boiling fluorobenzene (ca. 1 mL g^{-1}, in three portions),

to yield a bright white powder. Anhydrous $NaBAr^F{}_4$ was obtained by drying this material under vacuum at 100 °C over P_2O_5 for at least 18 hours. Note that additional $NaBAr^F{}_4$ may be recrystallized from the fluorobenzene washings via slow diffusion of pentane vapors at room temperature, and further purified if necessary.

Crude $HBAr^F{}_4$ was prepared according to a literature procedure, using $NaBAr^F{}_4$ purified as described above.[81] The crude material was purified by iterative recrystallization from 4 mL g^{-1} Et_2O layered with an equivalent volume of pentane at −30 °C. The purity of the recrystallized $HBAr^F{}_4$ was assayed by collecting a UV-vis spectrum of a 10 mM solution in Et_2O, where the presence of yellow-brown impurities appear as a broad absorbance centered at ca. 330 nm. Typically 2 to 3 recrystallizations were required to obtain material of suitable purity for catalytic reactions.

3.4.2.2 Preparation of 10 wt% Na/Hg shot

In a three-neck round bottom flask equipped with a mechanical stirrer, reflux condenser, and a dropping funnel was added Na (0.5 g) and a sufficient volume of toluene to completely submerse the Na. The dropping funnel was charged with 5 grams of Hg. The toluene was brought to reflux and the molten Na was finely dispersed by rapid agitation with the mechanical stirrer, at which point the Hg was added in one shot. *Caution: upon contact with Na, the Hg boils and there is a brief but intense exotherm.* The pelleted 10 wt% Na/Hg immediately formed, at which point the toluene was decanted, and the shot was washed with Et_2O and pentane before being dried in vacuo. After breaking up coagulated pieces, this procedure yields somewhat uniform shot ranging 1 to 3 mm in diameter

3.4.3 Ammonia production and quantification studies

3.4.3.1 Standard Ammonia Generation Reaction Procedure with $[Na(12\text{-}c\text{-}4)_2][(P_3{}^B)Fe(N_2)]$

All solvents were stirred with Na/K for ≥ 2 hours and filtered prior to use. In a nitrogen-filled glovebox, a stock solution of $[Na(12\text{-}c\text{-}4)_2][(P_3{}^B)Fe(N_2)]$ in THF (9.5 mM) was prepared. Note that a fresh stock solution was prepared for each experiment and used immediately. An aliquot of this stock solution (50 to 200 μL, 0.47 to 1.9 μmol) was added to a Schlenk tube and evaporated to dryness under vacuum, depositing a film of $[Na(12\text{-}c\text{-}4)_2][(P_3{}^B)Fe(N_2)]$. The tube was then charged with a stir bar and cooled to 77 K in a cold well. To the cold tube was added a solution of $HBAr^F{}_4$ in Et_2O. This solution was allowed to cool and freeze for 5 minutes. Then a suspension of KC_8 in Et_2O (1.2 equiv relative to $HBAr^F{}_4$) was added to the cold tube. The temperature of the system was allowed to equilibrate for 5 minutes and then the tube was sealed with a Teflon screw-valve. This tube was passed out of the box into a liquid N_2 bath and transported to a fume hood. The tube was then transferred to a dry ice acetone bath where it thawed and was allowed to stir at −78 °C for the desired length of time. At this point the tube was allowed to warm to room temperature with stirring, and stirred at room temperature for 5 minutes. To ensure reproducibility, all experiments were conducted in 200 mL Schlenk tubes (51 mm OD) using 25 mm stir bars, and stirring was conducted at ca. 900 rpm.

3.4.3.2 Standard Ammonia Generation Reaction Procedure with $[K(Et_2O)_{0.5}][(P_3{}^C)Fe(N_2)]$

The procedure was identical to that of the standard NH_3 generation reaction protocol with the changes noted. The precursor used was $[K(Et_2O)_{0.5}][(P_3{}^C)Fe(N_2)]$.

3.4.3.3 Standard Ammonia Generation Reaction Procedure with $[Na(12\text{-}c\text{-}4)_2][(P_3^{Si})Fe(N_2)]$

The procedure was identical to that of the standard NH_3 generation reaction protocol with the changes noted. The precursor used was $[Na(12\text{-}c\text{-}4)_2][(P_3^{Si})Fe(N_2)]$.

3.4.3.4 Standard Ammonia Generation Reaction Procedure with $(P_3^{B})(\mu\text{-}H)Fe(H)(N_2)$

The procedure was identical to that of the standard NH_3 generation reaction protocol with the changes noted. The precursor used was $(P_3^{B})(\mu\text{-}H)Fe(H)(N_2)$. Note that $(P_3^{B})(\mu\text{-}H)Fe(H)(N_2)$ is not indefinitely stable in the solid state, even at −30 °C; accordingly $(P_3^{B})(\mu\text{-}H)Fe(H)(N_2)$ was used within 24 hours after isolation as a solid. The addition of toluene was necessary to load the precatalyst volumetrically.

3.4.3.5 NH_3 Generation Reaction Procedure with $[Na(12\text{-}c\text{-}4)_2][(P_3^{B})Fe(N_2)]$ with the inclusion of NH_3

A standard catalytic reaction was prepared according to the procedure detailed in Section 3.4.3.1. After the frozen Schlenk tube was removed from the glovebox, it was brought to a Schlenk line and attached to the line via a 0.31 mL calibrated volume (corresponding to 12.7 μmol gas when filled at 21 °C and 1 atm). The gas manifold of the line was first filled with N_2 by three pump-refill cycles, and subsequently sparged (through a mineral oil bubbler) with $NH_{3(g)}$ for 30 minutes, passing the $NH_{3(g)}$ through a −30 °C trap to remove adventitious water. At this point the calibrated volume was filled with $NH_{3(g)}$ via 5 pump-refill cycles, and then sealed from the gas manifold. The frozen Schlenk tube was opened and allowed to equilibrate with the calibrated volume for 1 hour before it was resealed, and the reaction carried out in the usual manner. As a control, several trials were conducted with only an 2.0 M ethereal solution of HCl frozen in the tube, and it assumed that the average amount of NH_3 recovered in those trials was added to the catalytic reactions.

3.4.3.6 Standard NH_3 Generation Reaction Procedure with $[Na(12\text{-}c\text{-}4)_2][(P_3{}^B)Fe(N_2)]$ using Na/Hg as the reductant

The procedure was identical to that of the standard NH_3 generation reaction protocol with the changes noted. The precursor used was $[Na(12\text{-}c\text{-}4)_2][(P_3{}^B)Fe(N_2)]$ and 10 wt% Na/Hg shot of approximately 1 to 3 mm diameter was employed as the reductant (1900 Na atom equiv relative to catalyst).

3.4.4 NH_3 Generation Reaction with Periodic Substrate Reloading

All solvents were stirred with Na/K for $\geq$ 2 hours and filtered prior to use. In a nitrogen-filled glovebox, a stock solution of $[Na(12\text{-}c\text{-}4)_2][(P_3{}^B)Fe(N_2)]$ in THF (9.5 mM) was prepared. Note that a fresh stock solution was prepared for each experiment and used immediately. An aliquot of this stock solution (50 to 200 μL, 0.47 to 1.9 μmol) was added to a Schlenk tube. This aliquot was evaporated to dryness under vacuum, depositing a film of $[Na(12\text{-}c\text{-}4)_2][(P_3{}^B)Fe(N_2)]$. The tube was then charged with a stir bar and cooled to 77 K in a cold well. To the cold tube was added a solution of $HBAr^F{}_4$ (48 equiv with respect to $[Na(12\text{-}c\text{-}4)_2][(P_3{}^B)Fe(N_2)]$) in Et_2O. This solution was allowed to cool and freeze for 5 minutes. Then a suspension of KC_8 (1.3 equiv with respect to $HBAr^F{}_4$) in Et_2O was added to the cold tube. The temperature of the system was allowed to equilibrate for 5 minutes and then the tube was sealed. The cold well cooling bath was switched from a $N_{2(l)}$ bath to a dry ice/acetone bath. In the cold well the mixture in the sealed tube thawed with stirring and was allowed to stir at -78 °C for 40 minutes. Then, without allowing the tube to warm above -78 °C , the cold well bath was switched from dry ice/acetone to $N_{2(l)}$. After ten minutes the reaction mixture was observed to have frozen, at this time the tube was opened. To the cold tube was added a solution of $HBAr^F{}_4$ (48 equiv with respect to $[Na(12\text{-}c\text{-}4)_2][(P_3{}^B)Fe(N_2)]$) in Et_2O. This solution was allowed to cool and freeze for 5 minutes. Then a suspension of KC_8 (1.3 equiv with respect to $HBAr^F{}_4$) in Et_2O was added to the cold tube. The temperature of the system was allowed to equilibrate for 5 minutes and

then the tube was sealed. The cold well cooling bath was switched from a $N_{2(l)}$ bath to a dry ice/acetone bath. In the cold well the mixture in the sealed tube thawed with stirring and was allowed to stir at −78 °C for 40 minutes. These last steps are repeated for the desired number of loadings. Then the tube was allowed to warm to RT with stirring, and stirred at RT for 5 minutes.

3.4.5 General Procedure for Time-resolved NH_3 Quantification via Low-temperature Quenching:

A typical catalytic reaction was prepared according to the procedure described above. The timer was set to zero as soon as the frozen reaction mixture was transferred to the dry ice/acetone bath; note that the average thaw time was 2.0 ± 0.3 minutes (measured for a 1.1 mL solution of Et_2O over 8 trials). At the desired reaction time, the Schlenk tube was rapidly transferred to a liquid N_2 bath and the reaction mixture was allowed to freeze. Under N_2 counterflow, a solution of *t*BuLi (1.6 M in hexanes, 4 equiv with respect to $HBAr^F{}_4$) was added to the frozen reaction mixture. The Schlenk tube was then sealed, thawed to −78 °C, and stirred rapidly for 10 minutes. The Schlenk tube was transferred to a liquid N_2 bath and the reaction mixture was re-frozen. The reaction vessel was opened to atmosphere and to the frozen solution was slowly added a fivefold excess (with respect to $HBAr^F{}_4$) solution of a NaO*t*Bu solution in MeOH (0.25 mM) over 1 to 2 minutes. This solution was allowed to freeze, then the headspace of the tube was evacuated and the tube was sealed. The tube was then allowed to warm to RT and stirred at room temperature for 10 minutes. At this point the reaction was quantified for the presence of NH_3 (*vide supra*).

As a control to determine that the action of *t*BuLi is sufficiently fast to enable rapid quenching of catalytic reactions at low temperature, we added *t*BuLi to reaction mixtures prepared as described above before allowing them to thaw to −78 °C for the first time (effectively at time 0) and no detectable NH_3 formation was observed .

3.4.5.1 Kinetic Study of NH_3 Generation by $[Na(12\text{-}c\text{-}4)_2][(P_3{}^B)Fe(N_2)]$ via the Method of Initial Rates

Typical catalytic reactions were prepared at various concentrations of $[Na(12\text{-}c\text{-}4)_2][(P_3{}^B)Fe(N_2)]$ and $HBAr^F{}_4$ (1.1 mL Et_2O total for each reaction). For each given concentration of $[Na(12\text{-}c\text{-}4)_2][(P_3{}^B)Fe(N_2)]$ and $HBAr^F{}_4$, the time profile of NH_3 generation was measured over the first 15 minutes by quenching reactions at 5, 10, and 15 minutes, as described above. The initial rate of NH_3 formation, $\nu_0 = \frac{d[NH_3]}{dt}(0)$, was measured as the slope of a least-squares linear regression for these data. For the cases where the timescale of the reaction was too fast to obtain pseudo-first-order behavior over the first 15 minutes, ν_0 was approximated as the slope of the line between the yield of NH_3 at 5 minutes and a zero point at 2 minutes (the average thaw time for the reaction, *vide supra*). The reaction order in $[Na(12\text{-}c\text{-}4)_2][(P_3{}^B)Fe(N_2)]$ and $HBAr^F{}_4$ was determined by applying a least-squares linear analysis to the initial rates determined for 5 different concentrations in each reagent, ranging over a factor of 16.

3.4.6 General Procedure for Time-resolved H_2 Quantification

Inside of a nitrogen filled glovebox, the Fe precursor ($[Na(12\text{-}c\text{-}4)_2][(P_3{}^B)Fe(N_2)]$ or $[Na(12\text{-}c\text{-}4)_2][(P_3{}^{Si})Fe(N_2)]$, 3.0 μmol) was added to a 500 mL round bottom flask as a solution in THF, and subsequently deposited as a thin film by removing the solvent in vacuo. To this flask was added solid $HBAr^F{}_4$ (0.44 mmol), KC_8 (0.56 mmol), and a stir bar. The flask was sealed with a septum at room temperature and subsequently chilled to −196 °C in the cold well of a nitrogen filled glovebox. Et_2O (7 mL) was added via syringe into the flask and completely frozen; the total volume of Et_2O was 7 mL, corresponding to a [Fe] = 0.43 mM and $[HBAr^F{}_4]$ = 63 mM. The flask was passed out of the glovebox into a liquid N_2 bath, and subsequently thawed in a dry ice acetone bath. The timer was set to zero as soon as the flask was transferred to the dry ice/acetone bath. The headspace of the reaction vessel was periodically sampled with a sealable gas sampling syringe (10

mL), which was immediately loaded into the GC, and analyzed for the presence of $H_{2(g)}$. From these data, the percent H_2 evolved (relative to $HBAr^F{}_4$) was calculated, correcting for the vapor pressure of Et_2O and the removed H_2 from previous samplings. Each time course was measured from a single reaction maintained at −78 °C. For the reaction using $[Na(12\text{-c-}4)_2][(P_3{}^B)Fe(N_2)]$ as a precursor, the post-reaction material was analyzed for the presence of NH_3 via the methodology described above.

3.4.7 Solution IR calibration of $[Na(12\text{-c-}4)_2][(P_3{}^B)Fe(N_2)]$

A series of dilutions of $[Na(12\text{-c-}4)_2][(P_3{}^B)Fe(N_2)]$ in THF were prepared, their solution IR spectra collected, and the absorbance at 1918 cm^{-1} (ν_{NN}) recorded. A least-squares linear regression provides a calibration curve relating [Fe] (mM) to the absorbance of the N–N stretching mode.

3.4.8 Stoichiometric reaction of $(P_3{}^B)(\mu\text{-H})Fe(H)(N_2)$ with $HBAr^F{}_4$ and KC_8

Note that $(P_3{}^B)(\mu\text{-H})Fe(H)(N_2)$ is not indefinitely stable in the solid state, even at −30 °C; accordingly $(P_3{}^B)(\mu\text{-H})Fe(H)(N_2)$ was used within 24 hours after isolation as a solid.

Reaction with $HBAr^F{}_4$ alone. To a solution of $(P_3{}^B)(\mu\text{-H})Fe(H)(N_2)$ (8 mg, 0.012 mmol) in 600 μL d_8-toluene was added a solution of $HBAr^F{}_4$ (12 mg, 0.012 mmol) in 100 μL Et_2O. This mixture was loaded into an NMR tube equipped with a J-Young valve and sealed. The tube was mixed over the course of 1.5 hrs with periodic monitoring by ^1H NMR. Over the course of this time the signals attributable to $(P_3{}^B)(\mu\text{-H})Fe(H)(N_2)$ slowly disappeared concomitant with the appearance of several new, paramagnetically-shifted resonances. An IR spectrum of the reaction material shows no characteristic resonances in the region from 1700 to 2500 cm^{-1} (except for a trace of residual $(P_3{}^B)(\mu\text{-H})Fe(H)(N_2)$ at 2070 cm^{-1}), suggesting the absence of terminally-coordinated N_2.

Sequential reaction with $HBAr^F{}_4$ and KC_8. A 20 mL scintillation vial was charged with a magnetic stir bar, $(P_3{}^B)(\mu\text{-H})Fe(H)(N_2)$ (5.0 mg, 0.0074 mmol), 0.75 mL of toluene

and chilled to −78 °C in the cold well of a N_2 filled glove box. A solution of $HBAr^F{}_4$ (1.5 equiv, 11 mg, 0.011 mmol) was dissolved in 2.25 mL of Et_2O and similarly chilled. Subsequently, the ethereal $HBAr^F{}_4$ solution was added to the toluene solution of $(P_3{}^B)(\mu$-H)Fe(H)(N_2), and the resultant mixture was stirred at low temperature for 1 hour, at which point it was pipetted into a pre-chilled vial containing solid KC_8 (6 equiv, 6.0 mg, 0.044 mmol). After stirring a low temperature for 30 minutes, this mixture was allowed to warm to room temperature for 15 minutes before all volatiles were removed in vacuo. The remaining solids were extracted with THF (2 × 1 mL) and filtered into a vial containing 6 μL of 12-c-4. A sample of this filtrate was loaded into a solution IR cell and its spectrum was collected. The sharp resonance characteristic of $[Na(12\text{-c-}4)_2][(P_3{}^B)Fe(N_2)]$ was observed at 1918 cm^{-1} (ν_{NN}), with an absorbance of 0.23, corresponding to [Fe] = 1.2 mM (0.0024 mmol, 32% yield). In addition to this resonance, a sharp resonance at 2070 cm^{-1} was observed, characteristic of $(P_3{}^B)(\mu$-H)Fe(H)(N_2) (ν_{NN}).

3.4.9 Rapid Freeze-quench Mössbauer Spectroscopy

3.4.9.1 General Procedure for Preparation of Rapid-freeze-quench Mössbauer Samples of Catalytic Reaction Mixtures using $[Na(12\text{-c-}4)_2][(P_3{}^B)Fe(N_2)]$

All manipulations are carried out inside of a nitrogen filled glovebox. Into a 150 mL Schlenk tube (51 mm OD) is deposited a film of $[Na(12\text{-c-}4)_2][(P_3{}^B)^{57}Fe(N_2)]$ from a freshly prepared stock solution in THF. The tube is charged with a 25 mm stir bar and chilled to −196 °C in dewar filled with liquid N_2. A solution of $HBAr^F{}_4$ in Et_2O is added to the chilled tube and allowed to freeze; subsequently a suspension of KC_8 in Et_2O is added and also allowed to freeze. The tube is sealed, and transferred to a pre-chilled cold well at −78 °C (the cold well temperature is monitored directly with a thermocouple). The timer is set to zero as soon as the stir bar is freed from the thawing solvent. At the desired time, the tube is opened, and ca. 1 mL of the well-stirred suspension is transferred to a delrin cup pre-chilled to −78 °C using a similarly pre-chilled pipette. The sample in the delrin cup is

then rapidly frozen in liquid N_2. At this point the sample, immersed in liquid N_2, is taken outside of the glovebox and mounted in the cryostat.

3.4.9.2 General Procedure for Fitting of Rapid-freeze-quench Mössbauer Samples

Data analysis was performed using version 4 of the program WMOSS and quadrupole doublets were fit to Lorentzian lineshapes. Simulations were constructed from the minimum number of quadrupole doublets required to attain a quality fit to the data (convergence of the reduced χ^2). Quadrupole doublets were constrained to be symmetric, unless $[(P_3{}^B)Fe(N_2)]^-$ was included in the model (the presence of $[(P_3{}^B)Fe(N_2)]^-$ in samples was confirmed by comparison of zero-field spectra with spectra collected in an external 50 mT magnetic field, which dramatically sharpens the resonances attributable to $[(P_3{}^B)Fe(N_2)]^-$[55]). Using the nonlinear error analysis algorithm provided by WMOSS, the errors in the computed parameters are estimated to be 0.02 mm s^{-1} for δ and 2% for $|\Delta E_Q|$.

3.4.10 Controlled Potential Electrolysis of $[(P_3{}^B)Fe][BAr^F{}_4]$ and $HBAr^F{}_4$

General considerations. All manipulations were carried out in an N_2 filled glove box. A sealable H-cell consisting of two compartments separated by a fine porosity sintered glass frit was charged with 15 mL (working chamber) and 7 mL (auxiliary chamber) of 0.1 M $NaBAr^F{}_4$ solution in Et_2O. The working chamber was outfitted with a reticulated vitreous carbon working electrode (100 pores per inch (ppi) grade obtained from K.R. Reynolds Company, prepared by holding the electrode at −3.0 V vs $Fc^{+/0}$ in a separate 0.1 M $NaBAr^F{}_4$ solution for 30 minutes and rinsing with Et_2O), the working electrode was rectangular prismatic in shape with dimensions of 10 mm × 6 mm and was submerged in the working chamber solution to a depth of ca. 2 to 3 mm. The working chamber also featured a $Ag/AgPF_6$ in Et_2O reference electrode isolated by a CoralPor frit (obtained from BASi) and referenced externally to $Fc^{+/0}$. The auxiliary chamber was outfitted with a Zn foil electrode of dimensions 21.5 cm × 1.5 cm. The cell was cooled to −45 °C in a

cold well and then sealed before electrolysis. The cell was connected to a CH Instruments 600B electrochemical analyzer and controlled potential bulk electrolysis experiments were performed at −45 °C with stirring.

Electrolysis with 10 equiv $HBAr^F{}_4$ at −2.6 V vs $Fc^{+/0}$. To the working chamber was added 11.3 mg of [($P_3{}^B$)Fe][$BAr^F{}_4$] (7.5 μmol), 76 mg of $HBAr^F{}_4$ (75 μmol), and a magnetic stir bar. The cell passed 5.85 C of charge over the course of 4.6 hours. After that time the potential bias was removed, and the headspace of the cell was sampled with a sealable gas syringe (10 mL), which was immediately analyzed by GC for the presence of $H_{2(g)}$. Then $HBAr^F{}_4$ solutions in Et_2O were injected through rubber septa into both chambers to sequester NH_3 as [NH_4][$BAr^F{}_4$] (25 mg, 25 μmol for the working chamber and 10 mg, 10 μmol for the auxiliary chamber). The cell was allowed to stir at −45 °C for 10 minutes and then warmed to room temperature and stirred an additional 15 minutes. The contents of both chambers were then transferred to a Schlenk tube (cell washed with additional Et_2O) and this material was analyzed for NH_3 by base digestion, vacuum transfer of volatiles, and the indophenol method (*vide supra*). The results of the two product analyses were that 3.5 μmol of NH_3 and 17.5 μmol of H_2 had been produced.

Electrolysis with 50 equiv $HBAr^F{}_4$ at −2.3 V vs $Fc^{+/0}$. To the working chamber was added 5.0 mg of [($P_3{}^B$)Fe][$BAr^F{}_4$] (3.3 μmol), 170 mg of HBArF4 (168 μmol), and a magnetic stir bar. The cell passed 8.39 C of charge over the course of 16.5 hours. After that time the potential bias was removed, and the headspace of the cell was sampled with a sealable gas syringe (10 mL), which was immediately analyzed by GC for the presence of $H_{2(g)}$, and $HBAr^F{}_4$ solutions in Et_2O were injected through rubber septa into both chambers to sequester NH_3 as [NH_4][$BAr^F{}_4$] (40 mg, 40 μmol for the working chamber and 20 mg, 20 μmol for the auxiliary chamber). The cell was allowed to stir at −45 °C for 10 minutes and then warmed to room temperature and stirred an additional 15 minutes. The contents of both chambers were then transferred to a Schlenk tube (cell washed with additional Et_2O) and this material was analyzed for NH_3 by base digestion, vacuum transfer of volatiles, and

the indophenol method (*vide supra*). The results of the two product analyses were that 7.3 μmol of NH_3 and 21.7 μmol of H_2 had been produced.

References

(1) Smil, V., *Enriching the Earth: Fritz Haber, Carl Bosch, and the Transformation of World Food Production*; MIT Press: Cambridge, 2001.

(2) Ertl, G. *J. Vac. Sci. Technol., A* **1983**, *1*, 1247–1253.

(3) Ertl, G. *Angew. Chem. Int. Ed.* **2008**, *47*, 3524–3535.

(4) Burgess, B. K.; Lowe, D. J. *Chem. Rev.* **1996**, *96*, 2983–3012.

(5) Howard, J. B.; Rees, D. C. *Chem. Rev.* **1996**, *96*, 2965–2982.

(6) Einsle, O.; Tezcan, F. A.; Andrade, S. L. A.; Schmid, B.; Yoshida, M.; Howard, J. B.; Rees, D. C. *Science* **2002**, *297*, 1696–1700.

(7) Spatzal, T.; Aksoyoglu, M.; Zhang, L.; Andrade, S. L. A.; Schleicher, E.; Weber, S.; Rees, D. C.; Einsle, O. *Science* **2011**, *334*, 940–940.

(8) Hoffman, B. M.; Lukoyanov, D.; Yang, Z.-Y.; Dean, D. R.; Seefeldt, L. C. *Chem. Rev.* **2014**, *114*, 4041–4062.

(9) Kowalska, J.; DeBeer, S. *Biochim. Biophys. Acta, Mol. Cell Res.* **2015**, *1853*, 1406–1415.

(10) Chatt, J.; Heath, G. A.; Richards, R. L. *J. Chem. Soc., Chem. Commun.* **1972**, 1010–1011.

(11) Khoenkhoen, N.; de Bruin, B.; Reek, J. N. H.; Dzik, W. I. *Eur. J. Inorg. Chem. 2015*, 567–598.

(12) Bazhenova, T.; Shilov, A. *Coord. Chem. Rev.* **1995**, *144*, 69–145.

(13) Hill, P. J.; Doyle, L. R.; Crawford, A. D.; Myers, W. K.; Ashley, A. E. *J. Am. Chem. Soc.* **2016**, *138*, 13521–13524.

(14) Shiina, K. *J. Am. Chem. Soc.* **1972**, *94*, 9266–9267.

(15) Komori, K.; Oshita, H.; Mizobe, Y.; Hidai, M. *J. Am. Chem. Soc.* **1989**, *111*, 1939–1940.

(16) Tanaka, H.; Sasada, A.; Kouno, T.; Yuki, M.; Miyake, Y.; Nakanishi, H.; Nishibayashi, Y.; Yoshizawa, K. *J. Am. Chem. Soc.* **2011**, *133*, 3498–3506.

(17) Ogawa, T.; Kajita, Y.; Wasada-Tsutsui, Y.; Wasada, H.; Masuda, H. *Inorg. Chem.* **2013**, *52*, 182–195.

(18) Liao, Q.; Saffon-Merceron, N.; Mézailles, N. *Angew. Chem. Int. Ed.* **2014**, *53*, 14206–14210.

(19) Ung, G.; Peters, J. C. *Angew. Chem. Int. Ed.* **2015**, *54*, 532–535.

(20) Siedschlag, R. B.; Bernales, V.; Vogiatzis, K. D.; Planas, N.; Clouston, L. J.; Bill, E.; Gagliardi, L.; Lu, C. C. *J. Am. Chem. Soc.* **2015**, *137*, 4638–4641.

(21) Prokopchuk, D. E.; Wiedner, E. S.; Walter, E. D.; Popescu, C. V.; Piro, N. A.; Kassel, W. S.; Bullock, R. M.; Mock, M. T. *J. Am. Chem. Soc.* **2017**, *139*, 9291–9301.

(22) Kendall, A. J.; Johnson, S. I.; Bullock, R. M.; Mock, M. T. *J. Am. Chem. Soc.* **2018**, *140*, 2528–2536.

(23) Yandulov, D. V.; Schrock, R. R. *Science* **2003**, *301*, 76–78.

(24) Ritleng, V.; Yandulov, D. V.; Weare, W. W.; Schrock, R. R.; Hock, A. S.; Davis, W. M. *J. Am. Chem. Soc.* **2004**, *126*, 6150–6163.

(25) Arashiba, K.; Miyake, Y.; Nishibayashi, Y. *Nat. Chem.* **2011**, *3*, 120–125.

(26) Anderson, J. S.; Rittle, J.; Peters, J. C. *Nature* **2013**, *501*, 84–87.

(27) Creutz, S. E.; Peters, J. C. *J. Am. Chem. Soc.* **2014**, *136*, 1105–1115.

(28) Tanaka, H.; Arashiba, K.; Kuriyama, S.; Sasada, A.; Nakajima, K.; Yoshizawa, K.; Nishibayashi, Y. *Nat. Commun.* **2014**, *5*, 3737.

(29) Kuriyama, S.; Arashiba, K.; Nakajima, K.; Tanaka, H.; Kamaru, N.; Yoshizawa, K.; Nishibayashi, Y. *J. Am. Chem. Soc.* **2014**, *136*, 9719–9731.

(30) Kuriyama, S.; Arashiba, K.; Nakajima, K.; Tanaka, H.; Yoshizawa, K.; Nishibayashi, Y. *Chem. Sci.* **2015**, *6*, 3940–3951.

(31) Del Castillo, T. J.; Thompson, N. B.; Suess, D. L. M.; Ung, G.; Peters, J. C. *Inorg. Chem.* **2015**, *54*, 9256–9262.

(32) Arashiba, K.; Kinoshita, E.; Kuriyama, S.; Eizawa, A.; Nakajima, K.; Tanaka, H.; Yoshizawa, K.; Nishibayashi, Y. *J. Am. Chem. Soc.* **2015**, *137*, 5666–5669.

(33) Kuriyama, S.; Arashiba, K.; Nakajima, K.; Matsuo, Y.; Tanaka, H.; Ishii, K.; Yoshizawa, K.; Nishibayashi, Y. *Nat. Commun.* **2016**, *7*, 12181.

(34) Kuriyama, S.; Arashiba, K.; Tanaka, H.; Matsuo, Y.; Nakajima, K.; Yoshizawa, K.; Nishibayashi, Y. *Angew. Chem. Int. Ed.* **2016**, *55*, 14291–14295.

(35) Sekiguchi, Y.; Kuriyama, S.; Eizawa, A.; Arashiba, K.; Nakajima, K.; Nishibayashi, Y. *Chem. Commun.* **2017**, *53*, 12040–12043.

(36) Arashiba, K.; Eizawa, A.; Tanaka, H.; Nakajima, K.; Yoshizawa, K.; Nishibayashi, Y. *B. Chem. Soc. Jpn.* **2017**, *90*, 1111–1118.

(37) Eizawa, A.; Arashiba, K.; Tanaka, H.; Kuriyama, S.; Matsuo, Y.; Nakajima, K.; Yoshizawa, K.; Nishibayashi, Y. *Nat. Commun.* **2017**, *8*, 14874.

(38) Wickramasinghe, L. A.; Ogawa, T.; Schrock, R. R.; Müller, P. *J. Am. Chem. Soc.* **2017**, *139*, 9132–9135.

(39) Buscagan, T. M.; Oyala, P. H.; Peters, J. C. *Angew. Chem. Int. Ed.* **2017**, *56*, 6921–6926.

(40) Fajardo, J.; Peters, J. C. *J. Am. Chem. Soc.* **2017**, *139*, 16105–16108.

(41) Higuchi, J.; Kuriyama, S.; Eizawa, A.; Arashiba, K.; Nakajima, K.; Nishibayashi, Y. *Dalton Trans.* **2018**, *47*, 1117–1121.

(42) Nishibayashi, Y.; Sekiguchi, Y.; Arashiba, K.; Tanaka, H.; Eizawa, A.; Nakajima, K.; Yoshizawa, K. *Angew. Chem. Int. Ed.* **2018**, DOI: 10.1002/anie.201802310.

(43) Schrock, R. R. *Angew. Chem. Int. Ed.* **2008**, *47*, 5512–5522.

(44) Tian, Y.-H.; Pierpont, A. W.; Batista, E. R. *Inorg. Chem.* **2014**, *53*, 4177–4183.

(45) Tanaka, H.; Nishibayashi, Y.; Yoshizawa, K. *Acc. Chem. Res.* **2016**, *49*, 987–995.

(46) Peters, J. C.; Mehn, M. P. In *Activation of Small Molecules*; Wiley-Blackwell: 2006; Chapter 3, pp 81–119.

(47) Crossland, J. L.; Tyler, D. R. *Coord. Chem. Rev.* **2010**, *254*, 1883–1894.

(48) Hazari, N. *Chem. Soc. Rev.* **2010**, *39*, 4044–4056.

(49) McWilliams, S. F.; Holland, P. L. *Acc. Chem. Res.* **2015**, *48*, 2059–2065.

(50) Mankad, N. P.; Whited, M. T.; Peters, J. C. *Angew. Chem. Int. Ed.* **2007**, *46*, 5768–5771.

(51) Lee, Y.; Mankad, N. P.; Peters, J. C. *Nat. Chem.* **2010**, *2*, 558–565.

(52) Moret, M.; Peters, J. C. *Angew. Chem. Int. Ed.* **2011**, *50*, 2063–2067.

(53) Moret, M.-E.; Peters, J. C. *J. Am. Chem. Soc.* **2011**, *133*, 18118–18121.

(54) Anderson, J. S.; Moret, M.-E.; Peters, J. C. *J. Am. Chem. Soc.* **2013**, *135*, 534–537.

(55) Anderson, J. S.; Cutsail, G. E.; Rittle, J.; Connor, B. A.; Gunderson, W. A.; Zhang, L.; Hoffman, B. M.; Peters, J. C. *J. Am. Chem. Soc.* **2015**, *137*, 7803–7809.

(56) Krebs, C.; Price, J. C.; Baldwin, J.; Saleh, L.; Green, M. T.; Bollinger, J. M. *Inorg. Chem.* **2005**, *44*, 742–757.

(57) Krebs, C.; Martin Bollinger, J. *Photosynth. Res.* **2009**, *102*, 295.

(58) McLean, P. A.; Papaefthymiou, V.; Orme-Johnson, W. H.; Münck, E. *J. Biol. Chem.* **1987**, *262*, 12900–12903.

(59) Yoo, S. J.; Angove, H. C.; Papaefthymiou, V.; Burgess, B. K.; Münck, E. *J. Am. Chem. Soc.* **2000**, *122*, 4926–4936.

(60) Pickett, C. J.; Talarmin, J. *Nature* **1985**, *317*, 652–653.

(61) Lowe, D. J.; Thorneley, R. N. *Biochem. J.* **1984**, *224*, 877–886.

(62) Daifuku, S. L.; Al-Afyouni, M. H.; Snyder, B. E. R.; Kneebone, J. L.; Neidig, M. L. *J. Am. Chem. Soc.* **2014**, *136*, 9132–9143.

(63) Daifuku, S. L.; Kneebone, J. L.; Snyder, B. E. R.; Neidig, M. L. *J. Am. Chem. Soc.* **2015**, *137*, 11432–11444.

(64) Berry, J. F.; Bill, E.; Bothe, E.; George, S. D.; Mienert, B.; Neese, F.; Wieghardt, K. *Science* **2006**, *312*, 1937–1941.

(65) Lee, Y.; Peters, J. C. *J. Am. Chem. Soc.* **2011**, *133*, 4438–4446.

(66) Ye, S.; Bill, E.; Neese, F. *Inorg. Chem.* **2016**, *55*, 3468–3474.

(67) Fong, H.; Moret, M.-E.; Lee, Y.; Peters, J. C. *Organometallics* **2013**, *32*, 3053–3062.

(68) Münck, E. *Method. Enzymol.* **1978**, *54*, 346–379.

(69) Thorneley, R. N. F.; Lowe, D. J. *Biochem. J.* **1984**, *224*, 887–894.

(70) Lowe, D. J.; Thorneley, R. N. F. *Biochem. J.* **1984**, *224*, 895–901.

(71) Thorneley, R. N. F.; Lowe, D. J. *Biochem. J.* **1984**, *224*, 903–909.

(72) Lukoyanov, D.; Yang, Z.-Y.; Khadka, N.; Dean, D. R.; Seefeldt, L. C.; Hoffman, B. M. *J. Am. Chem. Soc.* **2015**, *137*, 3610–3615.

(73) Rivera-Ortiz, J. M.; Burris, R. H. *J. Bacteriol.* **1975**, *123*, 537–545.

(74) Simpson, F.; Burris, R. *Science* **1984**, *224*, 1095–1097.

(75) Rittle, J.; Peters, J. C. *J. Am. Chem. Soc.* **2016**, *138*, 4243–4248.

(76) Weitz, I. S.; Rabinovitz, M. *J. Chem. Soc., Perkin Trans.* **1993**, 117–120.

(77) Prisecaru, I. "WMOSS4 Mössbauer Spectral Analysis Software", www.wmoss.org, 2009–2016.

(78) Weatherburn, M. W. *Anal. Chem.* **1967**, *39*, 971–974.

(79) Lesley, M. J. G. et al. In *Inorganic Syntheses*, Shapley, J. R., Ed.; Wiley-Blackwell: 2004; Chapter 1, pp 1–48.

(80) Yakelis, N. A.; Bergman, R. G. *Organometallics* **2005**, *24*, 3579–3581.

(81) Brookhart, M.; Grant, B.; Volpe, A. F. *Organometallics* **1992**, *11*, 3920–3922.

Chapter 4

NITROGEN FIXATION VIA A TERMINAL IRON(IV) NITRIDE

4.1 Introduction

A key step in any scheme for the catalytic fixation of dinitrogen to ammonia is the cleavage of the strong N≡N triple bond. While mechanisms for this step can be classified as *early* or *late*, depending on the number of H^+/e^- equivalents transferred to the N–N moiety prior to bond scission,[i] they may also be categorized in terms of *homolytic* versus *heterolytic* activation. In a homolytic mechanism, the two N-atom containing fragments produced after bond cleavage are found in the same valence state.[ii] A now classic example of this mechanism is the homolytic clevage of N_2 by triamido Mo(III), producing two equivalents of the Mo(VI) nitrido shown in Figure 4.1, A (both N atoms have VN = −3).[1] This mechanism can be extended to larger clusters of transition metal ions (e.g., Figure 4.1, B),[2,3] and, conceptually, represents the rate-limiting step of the Haber–Bosch process.[4] A homolytic N–N bond cleavage mechanism need not produce nitrido (N^{3-}) ions, but can operate at a later stage in N_2 reduction, for example, at the N_2H_4 state to produce two amido (NH_2^-) fragments.[5]

The heterolytic activation of N_2 can also be mediated by polynuclear transition metal species. For example, the binuclear Ta complex shown in Figure 4.1, C, which binds N_2 asymmetrically in an end-on, side-on fashion, can be treated with 9-borabicyclo[3.3.1]-nonane (9-BBN) to produce a cluster containing N^{3-} (VN = −3) and NR^{2-} fragments (VN = −1).[6] However, perhaps the most well-known example of a heterolytic mechanism for N–N bond cleavage is that described by the Chatt cycles for mononuclear transition metal

Reproduced in part with permission from Thompson, N. B.; Green, M. T.; Peters, J. C. *J. Am. Chem. Soc.* **2017**, *139*, 15312–15315.

[i] And, hence, the degree of reduction of the N–N multiple bonding.

[ii] Defined by the valence number (VN) of the closed-shell fragment.

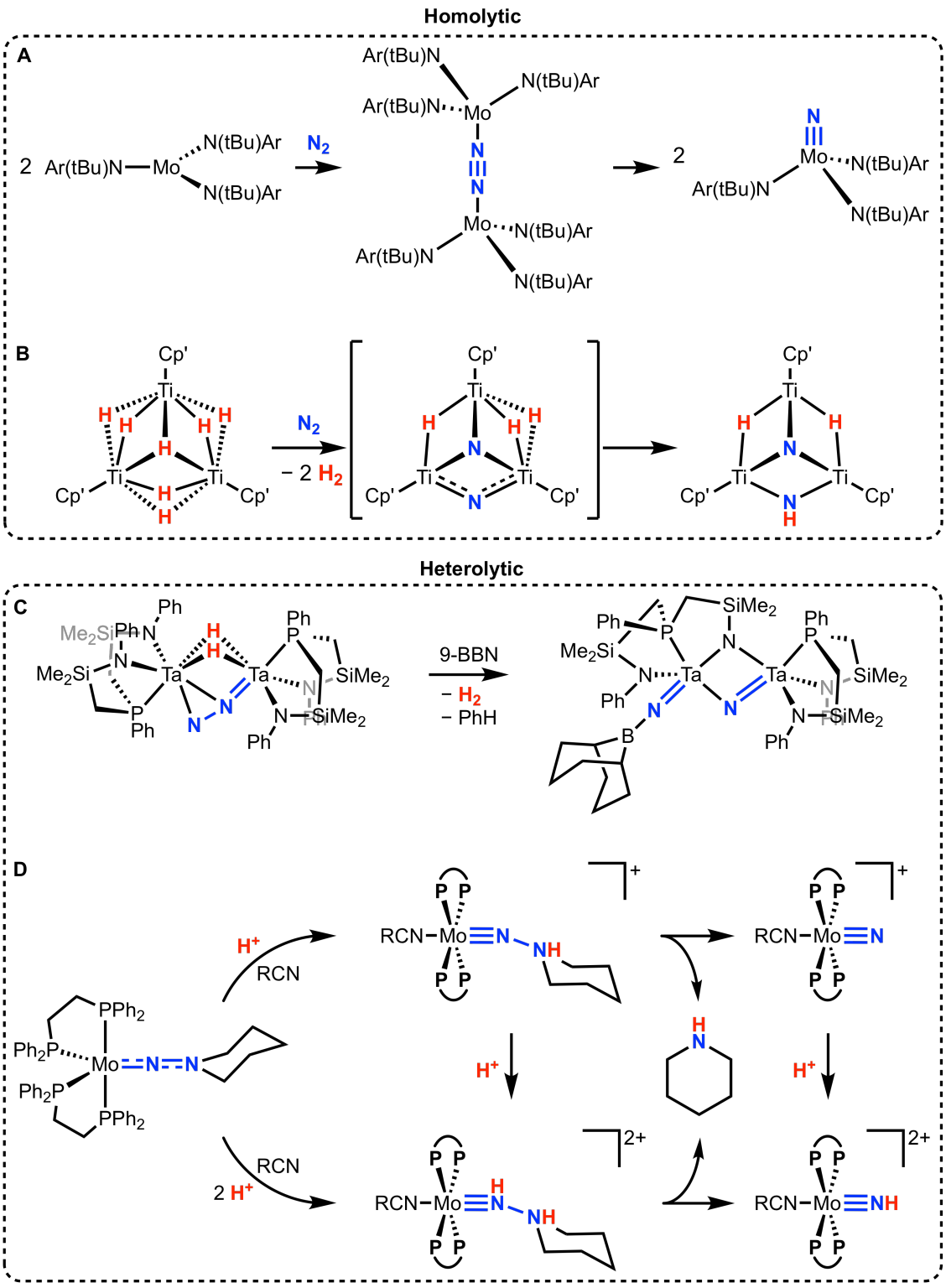

Figure 4.1: Examples of homolytic (A and B) and heterolytic (C and D) N–N bond cleavage reactions. (A) See [1]. (B) See [3]. (C) See [6]. (D) See [7, 8].

complexes,[9] and is thought to be operative in the catalytic cycles of known Mo species for this reaction.[10–12] A mechanistically well-defined example of this reactivity is shown in Figure 4.1, D.[7,8]

The chemistry of high valent Fe plays a central role in many challenging chemical transformations.[13] For example, the heme oxygenases, as in the cytochrome P450 superfamily, hydroxylate unactivated C–H bonds via oxoferryl (Fe^{IV}=O) intermediates derived from the *heterolytic* reduction of dioxygen (Equation 4.1; Figure 4.2, A).[13–15]

$$Fe^{II} + O_2 + 2\,H^+ + 2\,e^- \rightarrow Fe^{IV}{=}O + H_2O \tag{4.1}$$

The nitrido ion is isolobal to the oxo ion (O^{2-}), and, by analogy to Fe-mediated catalytic O_2 reduction, we have proposed that Fe-mediated (bio)catalytic nitrogen fixation might proceed heterolytically at a single Fe site (Equation 4.2; Figure 4.2, B).[16,17]

$$Fe^{I} + N_2 + 3\,H^+ + 3\,e^- \rightarrow Fe^{IV}{\equiv}N + NH_3 \tag{4.2}$$

Such a scenario would be similar to that originally proposed by Chatt for N_2-to-NH_3 conversion mediated by Group VI complexes.[9] While the reaction described by Equation 4.2 has not been realized to-date, prior work from our group has demonstrated that the microscopic reverse of the reaction shown in Figure 4.1, A (i.e., the *homolytic* cleavage of N_2) is feasible for Fe (Equation 4.3).[16]

$$2\,Fe^{IV}{\equiv}N \rightarrow Fe^{I}{-}N{\equiv}N{-}Fe^{I} \tag{4.3}$$

Whereas terminal Fe≡N complexes have been shown to liberate NH_3 via reductive protonation,[16,18] such Fe≡N species have to-date been generated by N atom transfer reactions from azide (N_3^-) or alternative reagents, but not from N_2.[16,18–26] Therefore, their potential role in synthetic or biological N_2-to-NH_3 conversion catalysis has remained unclear.

Our recent discovery that the anionic N_2 complex $[(P_3{}^B)Fe(N_2)]^-$ catalyzes N_2-to-NH_3 conversion has positioned us to probe the mechanism(s) by which the key N–N cleavage

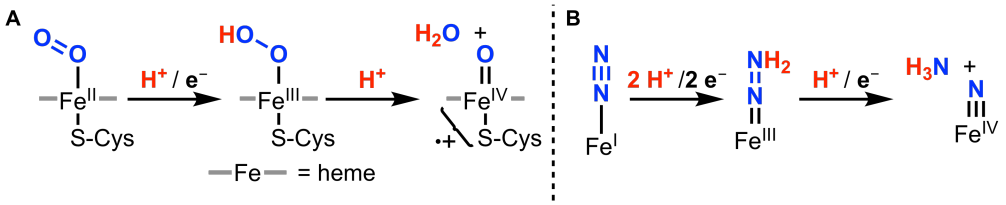

Figure 4.2: (A) Heterolytic activation of O_2 by heme. (B) Schematic depiction of heterolytic activation of N_2 by a single Fe site.

step occurs in a catalytically functional Fe system.[27–29] Of particular interest has been to distinguish between an early Chatt-type cleavage pathway (a distal mechanism via an Fe≡N intermediate) and a late-stage cleavage pathway (an alternating mechanism via an Fe(N_2H_4) intermediate).[30] While we have considered the possibility that both scenarios might be viable,[31] a key feature of the tri(phosphine)borane Fe system is its structurally and electronically flexible Fe–B interaction, which allows access to both reduced trigonal bipyramidal Fe(N_2) species as well as, in principle, pseudo-tetrahedral, terminal Fe≡N.[32] Here we detail the stepwise reduction and protonation of this Fe-based N_2 fixation catalyst to yield a terminal Fe(IV) nitride and NH_3, derived from N_2. This result provides a plausible mechanism for the N–N bond cleavage step under catalytic turnover and highlights a terminally bound Fe^{IV}≡N as a viable intermediate of catalytic N_2 fixation.

4.2 Results and Discussion

4.2.1 Results

The Fe borane complex [(P_3^B)Fe(N_2)]$^-$, or its oxidized congener [(P_3^B)Fe]$^+$, catalyze the reduction of N_2 to NH_3 at low temperature in Et_2O using various acid/reductant combinations, including $HBAr^F{}_4$/KC_8 and [Ph_2NH_2][OTf]/$CoCp^*{}_2$.[27–29] In a separate synthetic study, it was shown that [(P_3^B)Fe(N_2)]$^-$ reacts rapidly with excess $HBAr^F{}_4$ at very low temperatures to form the cationic hydrazido(2−) complex [(P_3^B)Fe(NNH_2)]$^+$ (Figure 4.3; here and elsewhere, potentials shown are in THF vs $Fc^{+/0}$).[33] To probe further steps in the catalytic N_2 fixation mechanism, we therefore sought access to the one-electron reduced hydrazido complex (P_3^B)Fe(NNH_2) to evaluate the viability of N–N bond cleavage via

subsequent protonation.

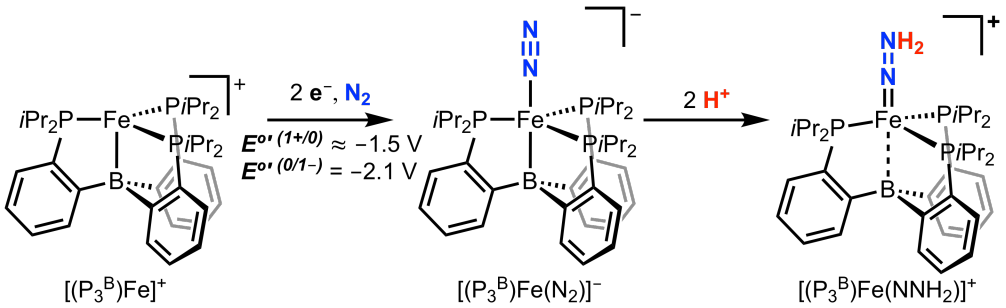

Figure 4.3: Stepwise reduction and protonation of $[(P_3^B)Fe]^+$ to form the cationic hydrazido(2−) complex $[(P_3^B)Fe(NNH_2)]^+$, as detailed in [33].

Preparations of $[(P_3^B)Fe(NNH_2)]^+$ typically contain several Fe-based impurities,[33] so rather than direct reduction of this species, we determined that protonation of the 18 e^- dianionic complex $[(P_3^B)Fe(N_2)]^{2-}$ produces $(P_3^B)Fe(NNH_2)$ most cleanly. Reduction of the $[Na(12\text{-c-}4)_2]^+$ salt of $[(P_3^B)Fe(N_2)]^-$ with KC_8 in dimethoxyethane (DME) followed by crystallization enables the isolation of $[Na(12\text{-c-}4)_2][K(DME)_x][(P_3^B)Fe(N_2)]$ as a black solid, featuring an N–N stretching vibration at 1836 cm^{-1}. Given the highly sensitive nature of this species ($E^{\circ\prime} = -3.2$ V), for all subsequent studies $[(P_3^B)Fe(N_2)]^{2-}$ was produced in situ and used immediately. The ^{57}Fe Mössbauer spectrum of $[(P_3^B)Fe(N_2)]^{2-}$ produced from the reduction of ^{57}Fe-enriched $[Na(12\text{-c-}4)_2][(P_3^B)Fe(N_2)]$ (Figure 4.4, A) reveals parameters consistent with its diamagnetic ground state (Table 4.1),[28] and which are nearly identical with those of the isoelectronic and isostructural silyl complex $[(P_3^{Si})Fe(N_2)]^-$.[34]

An in situ prepared sample of ^{57}Fe-enriched $[(P_3^B)Fe(N_2)]^{2-}$ was combined with an excess of either TfOH or $HBAr^F_4$ in supercooled[iii] 2-MeTHF, and the products were analyzed by Mössbauer spectroscopy. The dianion $[(P_3^B)Fe(N_2)]^{2-}$ reacts cleanly with both acids to form a new species in ca. 90% yield with $\delta = 0.14$ and $|\Delta E_Q| = 1.63$ mm s^{-1} (Figure 4.4, C) over the course of ca. 15 min. These parameters are similar to those of the diamagnetic hydrazido complex $[(P_3^{Si})Fe(NNH_2)]^+$ ($\delta = 0.13$ and $|\Delta E_Q| = 1.48$ mm s^{-1}),[31] and we therefore assign this species as the isoelectronic, isostructural,

[iii] I.e., between the glass transition at 91 K and the freezing point at 137 K.

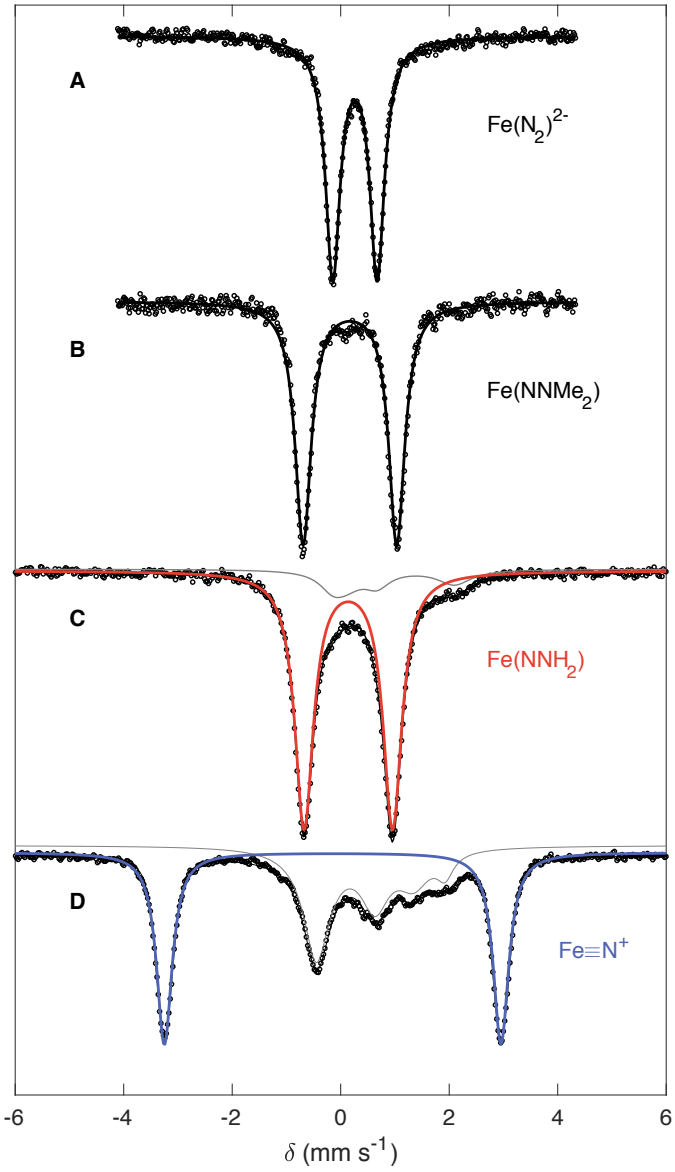

Figure 4.4: Collected Mössbauer data; raw data are shown as circles, and the simulated data as a solid black line with individual subspectra plotted in gray, red, and blue. (A) Spectrum of $[(P_3^B)Fe(N_2)]^{2-}$ prepared in situ from $[(P_3^B)Fe(N_2)]^{-}$. (B) Spectrum of $(P_3^B)Fe(NNMe_2)$. (C, D) Freeze-quench Mössbauer spectra from the reaction of $[(P_3^B)Fe(N_2)]^{2-}$ with excess TfOH, showing conversion to $(P_3^B)Fe(NNH_2)$ (red subspectrum, ca. 90%) after mixing for 15 min (C), and subsequent formation of $[(P_3^B)Fe{\equiv}N]^{+}$ (blue subspectrum, ca. 60%) after mixing for 120 min (D).

neutral hydrazido (P_3^B)Fe(NNH_2) in an $S = 0$ ground state. Unlike its silyl analog, (P_3^B)Fe(NNH_2) is very thermally sensitive, decomposing in acid solution within 15 min upon warming to 195 K. To further cement our assignment, we prepared the isoelectronic, but more stable, alkylhydrazido(2−) complex (P_3^B)Fe($NNMe_2$) as a spectroscopic model. The alkylhydrazido (P_3^B)Fe($NNMe_2$) has been structurally characterized, and its Mössbauer spectrum reveals parameters very similar to those observed for (P_3^B)Fe(NNH_2) (Figure 4.4, B; Table 4.1). We note that although the ground state of (P_3^B)Fe($NNMe_2$) has $S = 0$, this alkylhydrazido possesses a low-energy triplet ($S = 1$) excited state, which is also expected for (P_3^B)Fe(NNH_2) on the basis of computational studies.

Mixing $[(P_3^B)Fe(N_2)]^{2-}$ with either acid in excess for longer times produces a new species in the Mössbauer spectrum as the major Fe-containing product (≥ 50 % yield with TfOH; Figure 4.4, D), suggesting a product resulting from the decay of (P_3^B)Fe(NNH_2). This new species ($\delta = -0.15$ and $|\Delta E_Q| = 6.20$ mm s^{-1}) has parameters that are diagnostic for Fe(IV) nitrides under C_3 symmetry[17,18,23] and is therefore assigned as the $S = 0$ nitrido cation $[(P_3^B)Fe{\equiv}N]^+$. Negative isomer shifts are observed for Fe species featuring short, covalent interactions, such as those made with terminal N^{3-} and O^{2-} ligands, which drive Fe s-electron density toward the nucleus (see Appendix E).[35] The observation of quadrupole splittings > 5 mm s^{-1} is limited to C_3-symmetric Fe complexes featuring Fe≡L triple bonds, which results in an axial polarization of the electric field gradient due to localization of the Fe 3d electrons to a δ-symmetry e orbital set.[17,18,23,36] Thus, the simultaneous observation of a negative δ and $|\Delta E_Q| > 6$ mm s^{-1} argues strongly in favor of our assignment of $[(P_3^B)Fe{\equiv}N]^+$, which is also corroborated by XAS studies (*vide infra*). The absence of magnetic hyperfine splitting in spectra of (P_3^B)Fe(NNH_2) and $[(P_3^B)Fe{\equiv}N]^+$ collected at 5 K in the presence of a 50 mT field is consistent with our assignment of non-Kramers spin states.[35] Computational studies reveal a diamagnetic ground state in both cases, and only the $S = 0$ states accurately reproduce the observed Mössbauer spectroscopic parameters (Table 4.1). As with hydrazido (P_3^B)Fe(NNH_2), nitrido $[(P_3^B)Fe{\equiv}N]^+$ is thermally unstable

in solution and degrades upon warming to temperatures ≥ 195 K for longer than 30 min to a mixture of $(P_3{}^B)$Fe(OTf) and unknown species with parameters consistent with high-spin Fe(II).

Table 4.1: Collected Mössbauer Parameters

Species		δ (mm s^{-1})	$\lvert\Delta E_Q\rvert$ (mm s^{-1})
$[(P_3{}^B)Fe(N_2)]^{2-}$	Expt.	0.26	0.82
	DFT	0.36(4)	0.8(3)
$(P_3{}^B)Fe(NNMe_2)$		0.17	1.73
$(P_3{}^B)Fe(NNH_2)$	Expt.	0.14	1.63
	DFT	0.19(4)	1.7(3)
$[(P_3{}^B)Fe{\equiv}N]^+$	Expt.	−0.15	6.20
	DFT	−0.21(4)	5.6(3)

To gain additional structural characterization of the thermally unstable complexes $(P_3{}^B)Fe(NNH_2)$ and $[(P_3{}^B)Fe{\equiv}N]^+$, we turned to Fe *K*-edge X-ray absorption spectroscopy. The XANES spectrum of $(P_3{}^B)Fe(NNH_2)$ features two moderate intensity resonances in the pre-edge region separated by 4.3 eV (Figure 4.5, A). The XANES spectrum of $(P_3{}^B)Fe(NNMe_2)$ displays two resonances of similar intensity separated by 4.1 eV, but red-shifted by ca. 0.3 eV, consistent with replacement of the N–H substituents with more electron-rich N–Me (Figure 4.5, A; Table 4.2). As observed previously for the C_3-symmetric Fe(IV) nitrides $(PhBP^R{}_3)Fe{\equiv}N$ (R = *i*Pr, CH_2Cy),[37] the pre-edge XANES spectrum of $[(P_3{}^B)Fe{\equiv}N]^+$ is dominated by an intense resonance at 7112.1 eV integrating to 87 units (Figure 4.5, A). Based on the purity of the XAS sample, this integration represents a lower limit of the true intensity of the resonance, and is therefore, to our knowledge, the most intense Fe *K*-edge XANES feature ever observed,[37] except perhaps that of ferrate ($[FeO_4]^{2-}$).[38] This resonance is attributable to a transition from the 1s to an a_1-symmetry orbital with significant Fe 4p and ligand 2p admixture (*vide infra*). This imparts dipole-allowed character to the transition and is a hallmark of M-to-N/O multiple bonding.[37,39] Furthermore, the pre-edge spectra of $(P_3{}^B)Fe(NNH_2)$ and $[(P_3{}^B)Fe{\equiv}N]^+$ predicted by TD-DFT are in excellent agreement with those observed experimentally (Figure 4.5, B).

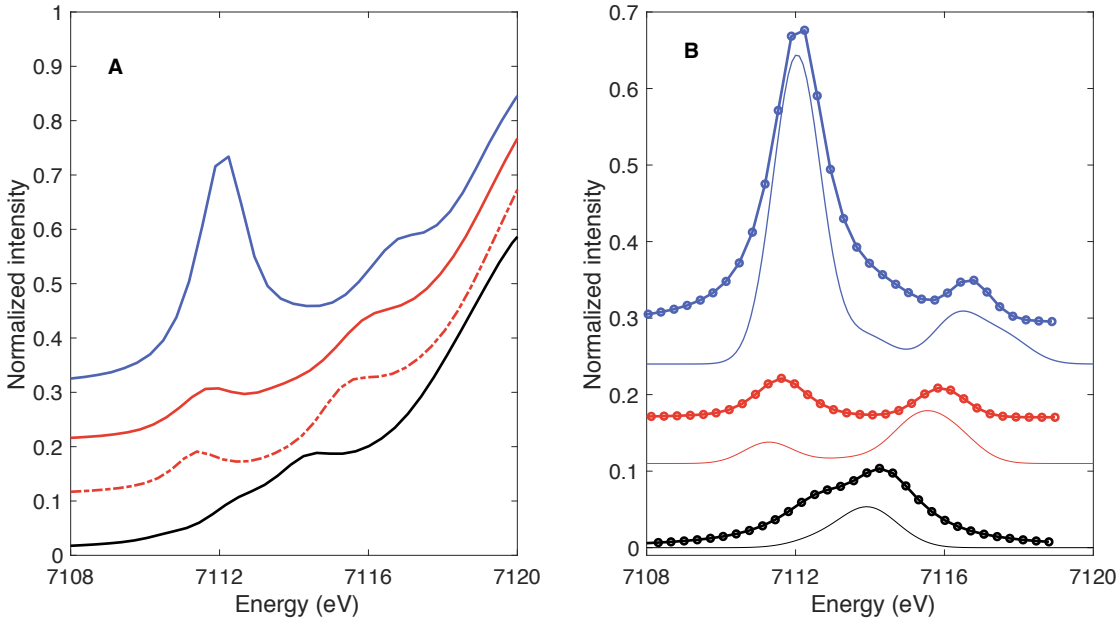

Figure 4.5: Collected XANES data. (A) XANES spectra of $[(P_3^B)Fe(N_2)]^{2-}$ (black), $(P_3^B)Fe(NNMe_2)$ (red, dash-dotted), $(P_3^B)Fe(NNH_2)$ (red), and $[(P_3^B)Fe{\equiv}N]^+$ (blue). (B) Comparison of experimental XANES spectra (dotted lines), after subtraction of the rising edge, and TD-DFT-predicted spectra (solid lines) of $[(P_3^B)Fe(N_2)]^{2-}$ (black), $(P_3^B)Fe(NNH_2)$ (red), and $[(P_3^B)Fe{\equiv}N]^+$ (blue).

The EXAFS region reveals a short Fe–N bond of 1.65(2) Å in $(P_3^B)Fe(NNH_2)$ (Figure 4.6, C), which compares favorably with that predicted by DFT and observed experimentally for the model complex $(P_3^B)Fe(NNMe_2)$ (Figure 4.6, B; Table 4.2). Upon cleavage of the N–N bond in $(P_3^B)Fe(NNH_2)$ to form $[(P_3^B)Fe{\equiv}N]^+$, the Fe–N bond contracts to 1.54(2) Å (Figure 4.6, D; Table 1F), which is within the range observed in previously characterized C_3-symmetric Fe(IV) nitrides (1.51 to 1.55 Å),[23,24,37] and shorter than those observed in C_4-symmetric, octahedral Fe(V/VI) nitrides (1.57 to 1.64 Å).[21,22,25] A peak at $R + \Delta \approx 2.5$ Å in the Fourier transformed EXAFS of $[(P_3^B)Fe(N_2)]^{2-}$, $(P_3^B)Fe(NNH_2)$, and $(P_3^B)Fe(NNMe_2)$, due to an Fe–N–N multiple scattering path, is notably absent in the transform of $[(P_3^B)Fe{\equiv}N]^+$ (Figure 4.6), consistent with complete rupture of the N–N bond.

Figure 4.7, A shows the calculated frontier (Kohn-Sham) orbitals of $[(P_3^B)Fe{\equiv}N]^+$,

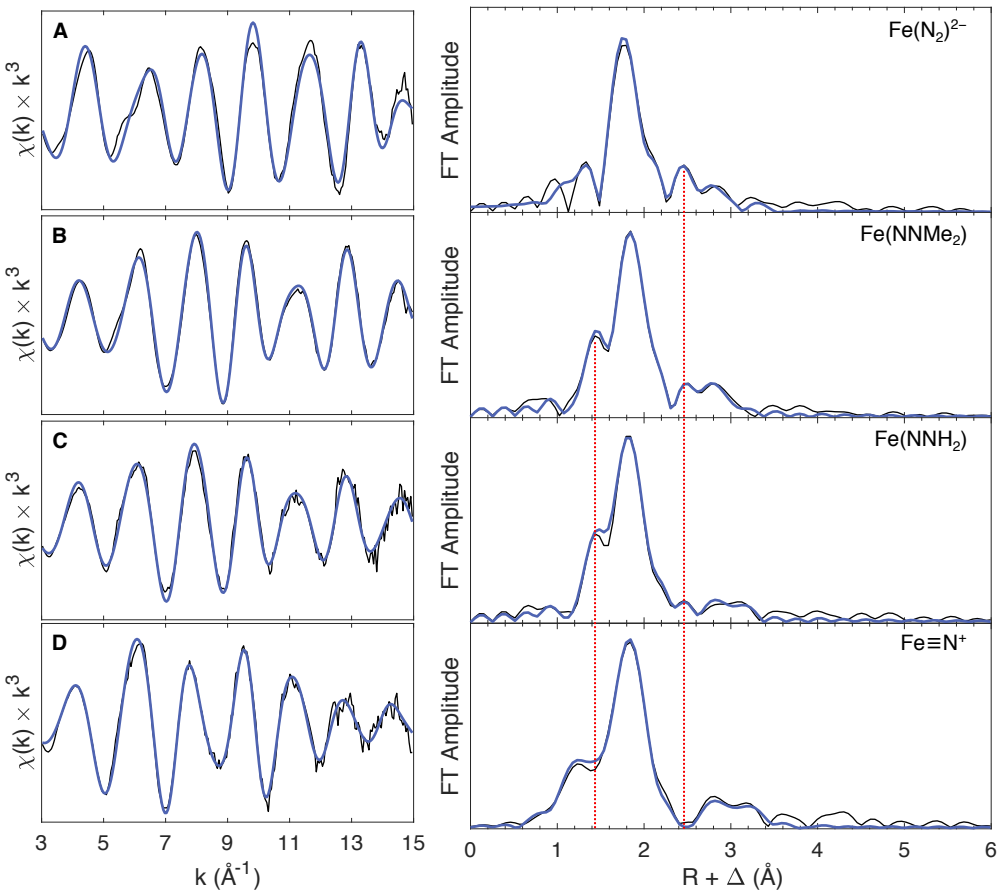

Figure 4.6: Collected EXAFS data. On the left are shown the raw k^3-weighted EXAFS oscillations, and on the right are shown the corresponding phase-uncorrected Fourier-transformed data for (A) $[(P_3{}^B)Fe(N_2)]^{2-}$, (B) $(P_3{}^B)Fe(NNMe_2)$, (C) $(P_3{}^B)Fe(NNH_2)$, and (D) $[(P_3{}^B)Fe{\equiv}N]^+$. The data are plotted in black, with simulations in blue. Note that the phase-shift, Δ, is typically on the order of 0.4 Å. The dashed red line at $R + \Delta \approx 1.4$ Å indicates the position of a peak due to an Fe–N scatterer in $(P_3{}^B)Fe(NNMe_2)$, while that at $R + \Delta \approx 2.5$ Å indicates the position of a peak due to an Fe–N–N multiple scatterer in both $[(P_3{}^B)Fe(N_2)]^{2-}$ and $(P_3{}^B)Fe(NNMe_2)$.

which has the expected,

$$|1e(3d_{xy}, 3d_{x^2-y^2})^4 1a_1(3d_{z^2})^0 2e(3d_{xz}, 3d_{yz})^0\rangle$$

configuration for a C_3 symmetric, formally Fe(IV) nitride.[16,24] The low energy of the virtual $1a_1$ orbital has been explained in terms of (i) an axial distortion which reduces the σ^* character of the orbital with respect to the equatorial ligands and (ii) by 3d–4p mixing. In $[(P_3{}^B)Fe{\equiv}N]^+$, the $1a_1$ orbital is additionally stabilized by a bonding interaction with the vacant B $2p_z$ orbital (Figure 4.7, B). A Löwdin population analysis of this orbital reveals

Table 4.2: Collected XAS Data

Species		Fe–N (Å)	N–N (Å)[a]	Pre-edge (eV [area])
$[(P_3{}^B)Fe(N_2)]^{2-}$	Expt.	1.77	1.16(2)	7112.6 [14]
	DFT	1.771	1.158	7114.4 [29] 7113.5 [7] 7114.1 [5]
$(P_3{}^B)Fe(NNMe_2)$	Expt.	1.65(2)	1.34(3)	7111.4 [15] 7115.5 [29]
	XRD	1.680	1.293	
$(P_3{}^B)Fe(NNH_2)$	Expt.	1.65(2)	1.34(3)	7111.5 [11]
	DFT	1.653	1.326	7115.9 [6] 7111.4 [5] 7115.6 [16]
$[(P_3{}^B)Fe{\equiv}N]^+$	Expt.	1.54(2)		7112.1 [87]
	DFT	1.514		7114.3 [5] 7116.7 [14] 7112.0 [65] 7113.9 [5] 7116.7 [17]

[a]These distances were calculated by subtracting the Fe–N scattering distance from an Fe–N–N multiple scattering path, and are thus associated with greater uncertainty.

nearly equal distribution among the Fe, N, and B atoms, with identical Fe 3d (9.5%) and 4p (9.1%) character. The significant amount of predicted ligand 2p character of this orbital (43%) is consistent with the intensity of the first pre-edge transition observed in the Fe *K*-edge XAS of $[(P_3{}^B)Fe{\equiv}N]^+$, which is not expected on the basis of the 3d–4p mixing alone.[37,39,40]

Based on these collective data, we propose the sequence of reactions shown in Figure 4.8. Rapid protonation of $[(P_3{}^B)Fe(N_2)]^{2-}$ at low temperature results in the formation of the hydrazido complex $(P_3{}^B)Fe(NNH_2)$.[iv] In the rate-limiting step, $(P_3{}^B)Fe(NNH_2)$ is protonated to form an unobserved transient (or transition state) hydrazidium cation $[(P_3{}^B)Fe(NNH_3)]^+$, which decays via heterolytic rupture of the N–N bond to yield NH_3 and $[(P_3{}^B)Fe{\equiv}N]^+$. In a larger-scale experiment, protonation of $[(P_3{}^B)Fe(N_2)]^{2-}$ with TfOH

[iv]Via a presumed anionic diazenido complex, $[(P_3{}^B)Fe(N_2H)]^-$.

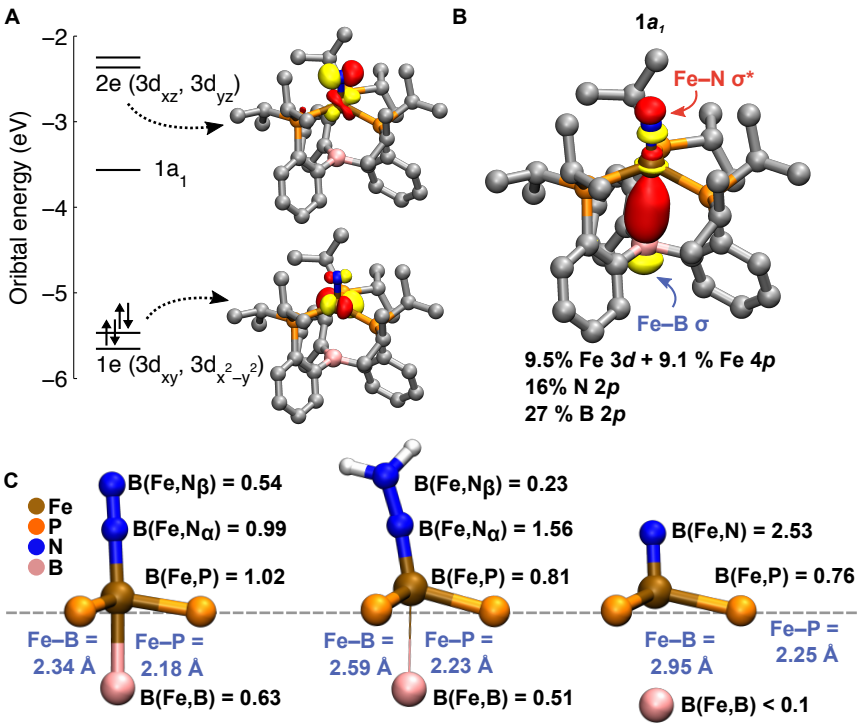

Figure 4.7: (A) Frontier Kohn–Sham orbitals computed for $[(P_3{}^B)Fe{\equiv}N]^+$. (B) Löwdin population analysis of the empty $1a_1$ frontier orbital of $[(P_3{}^B)Fe{\equiv}N]^+$. (C) Geometric analysis of the bonding in $[(P_3{}^B)Fe(N_2)]^{2-}$, $(P_3{}^B)Fe(NNH_2)$, and $[(P_3{}^B)Fe{\equiv}N]^+$. The Fe–B distances from DFT models are given, along with the average Fe–P bond length from the EXAFS data. Shown in black are the Mayer bond orders (the average in the case of Fe–P).

in supercooled 2-MeTHF produced NH_3 in 36.0(5)% isolated yield, comparable to the observed yield of $[(P_3{}^B)Fe{\equiv}N]^+$ under identical conditions (ca. 50%). Under catalytic conditions (i.e., with a reductant present), we propose that $[(P_3{}^B)Fe{\equiv}N]^+$ can be reduced by 3 H^+/3 e^- to form a second equivalent of NH_3 and $[(P_3{}^B)Fe]^+$ (or $[(P_3{}^B)Fe(NH_3)]^+$),[16,18] from which $[(P_3{}^B)Fe(N_2)]^-$ can be regenerated in turn upon reduction (see Section 4.2.2).[41] Indeed, sequential reaction of $[(P_3{}^B)Fe(N_2)]^{2-}$ with TfOH and $CoCp^*_2$ in supercooled 2-MeTHF doubles the isolated yield of NH_3 to 73(17)%.

We have shown that two reductants, KC_8 and $CoCp^*_2$, can drive catalytic N_2 fixation in this system, yet only KC_8 is sufficiently reducing to access the dianion $[(P_3{}^B)Fe(N_2)]^{2-}$ under catalytic turnover. The most reduced state of the catalyst accessible with Cp^*_2Co is the anion $[(P_3{}^B)Fe(N_2)]^-$,[29] and this state appears to be catalytically relevant under all con-

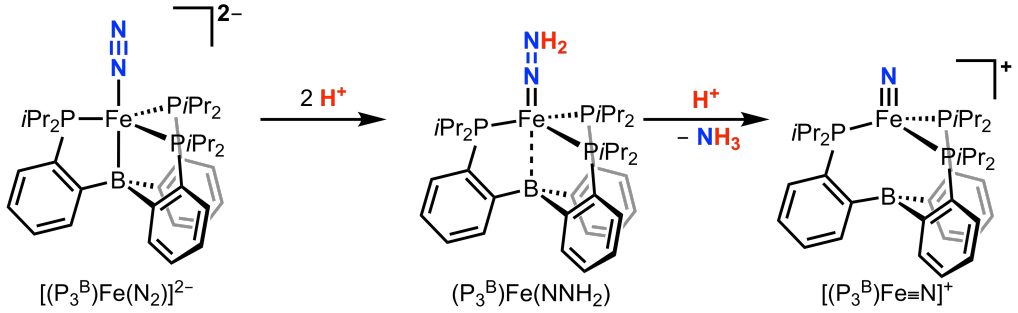

Figure 4.8: Stepwise protonation of $[(P_3{}^B)Fe(N_2)]^{2-}$ to form the cationic nitrido complex $[(P_3{}^B)Fe{\equiv}N]^+$.

ditions canvassed,[28] including with TfOH and $CoCp^*_2$ as the acid/reductant combination. An alternative pathway to form $[(P_3{}^B)Fe{\equiv}N]^+$ under these milder conditions is via reduction of the known cationic hydrazido $[(P_3{}^B)Fe(NNH_2)]^+$ (Figure 4.3), followed by protonation.[33] We estimate the reduction potential of this species to be $E^{\circ\prime} \geq -1.2$ V based on the alkyl congener, and thus $[(P_3{}^B)Fe(N_2)]^-$ (or its oxidized congener $(P_3{}^B)Fe(N_2)$) is a sufficiently strong reductant to produce $(P_3{}^B)Fe(NNH_2)$ from $[(P_3{}^B)Fe(NNH_2)]^+$. The viability of this pathway is demonstrated by a low temperature protonation experiment of $[(P_3{}^B)Fe(N_2)]^-$ with excess TfOH (i.e., without exogenous reductant), which produced appreciable quantities of $[(P_3{}^B)Fe{\equiv}N]^+$ (ca. 20%) and NH_3 (34(3)%) along with competitive oxidation to $(P_3{}^B)Fe(OTf)$. The same reaction sequence is thermodynamically accessible under turnover conditions using $CoCp^*_2$ as the terminal source of reducing equivalents. Under catalytic conditions, other routes to $[(P_3{}^B)Fe{\equiv}N]^+$ via metallocene-mediated proton-coupled electron

transfer (PCET) reactions are also conceivable.[29] [v]

In the transformation from $[(P_3{}^B)Fe(N_2)]^{2-}$ to $[(P_3{}^B)Fe{\equiv}N]^+$, the Fe center spans six formal oxidation states, from d^{10} Fe(−II) to d^4 Fe(IV). However, these formal assignments do not account for *Z*-type Fe-to-B σ-backbonding,[42] in addition to π-backbonding with the phosphines. Indeed, the presence of pre-edge transitions in the XANES spectrum of $[(P_3{}^B)Fe(N_2)]^{2-}$, which is reproduced by TD-DFT, requires a physical oxidation state d^n with $n < 10$ (Figure 4.5)—for example d^8 Fe(0) as a result of electron transfer to the B atom.

The physical oxidation state range of Fe is buffered by these soft electron-accepting interactions, which allow e^- to be stored in covalent Fe–B/P backbonding interactions until transferred to the N–N unit upon protonation. The three sequential H^+ transfers to the distal N atom of $[(P_3{}^B)Fe(N_2)]^{2-}$ to form $[(P_3{}^B)Fe{\equiv}N]^+$ and NH_3 result in a lengthening of the Fe–B distance by 0.61 Å (distances from DFT) and a lengthening of the average Fe–P distance by 0.07 Å (distances from EXAFS), reflecting loss of Fe–B/P covalency (Figure 4.7, C). Owing to the highly flexible Fe–borane interaction, which increases from 2.34 Å ($[(P_3{}^B)Fe(N_2)]^{2-}$) to 2.59 Å ($(P_3{}^B)Fe(NNH_2)$) to 2.95 Å ($[(P_3{}^B)Fe{\equiv}N]^+$), the valency of Fe is largely conserved, as it distorts out of the P_3 plane to form π bonds with the $NNH_2{}^{2-}$ and N^{3-} ions (see Chapter 5 for a detailed analysis). This is reflected in the nearly constant

[v] Even the protonation of $[(P_3{}^B)Fe(N_2)]^-$ to produce $[(P_3{}^B)Fe{\equiv}N]^+$ in the absence of $CoCp^*_2$ may proceed via a more complex mechanism involving PCET. For example, an autocatalytic disproportionation can be envisioned, e.g.,

$$[Fe(N_2)]^- + 2\,H^+ \rightarrow [Fe(NNH_2)]^+ \tag{4.4}$$

$$2\,[Fe(NNH_2)]^+ \rightarrow [Fe(N_2H)]^+ + [Fe{\equiv}N]^+ + NH_3 \tag{4.5}$$

$$[Fe(N_2H)]^+ + [Fe(N_2)]^- \rightarrow Fe(N_2H) + Fe(N_2) \tag{4.6}$$

$$Fe(N_2H) + H^+ \rightarrow [Fe(NNH_2)]^+ \tag{4.7}$$

$$2\,[Fe(N_2)]^- + 3\,H^+ \rightarrow Fe(N_2) + [Fe{\equiv}N]^+ + NH_3 \tag{4.8}$$

and similar mechanisms using $(P_3{}^B)Fe(N_2)$ as the reductant to ultimately produce $(P_3{}^B)Fe(OTf)$. A priori, the disproportionative step is reasonable on thermodyamic grounds, given the weak N–H bonds of $[(P_3{}^B)Fe(NNH_2)]^+$.[29] However, the simpler ET-PT mechanism is more consistent with the experimental result that nitride formation is not observed when $[(P_3{}^B)Fe(N_2)]^-$ is protonated with $HBAr^F{}_4$, where high yields of $[(P_3{}^B)Fe(NNH_2)]^+$ are obtained.[33]

sum of the Mayer bond orders about Fe for $[(P_3{}^B)Fe(N_2)]^{2-}$ (5.2), $(P_3{}^B)Fe(NNH_2)$ (4.7), and $[(P_3{}^B)Fe{\equiv}N]^+$ (4.8), a notion supported by the fact that the change in isomer shift ($\Delta\delta$) is only 0.38 mm s^{-1} (0.06 mm s^{-1}/e^-). For comparison, $\Delta\delta$ is nearly 1 mm s^{-1} for a series of isostructural Fe complexes supported by a hard ligand field of N/O donors ranging over only five formal oxidation states (ca. 0.2 mm s^{-1}/e^-) .[22]

4.2.2 Discussion

At this stage, we are in a position to propose a complete catalytic cycle for nitrogen fixation by the $(P_3{}^B)Fe$ system that is fully consistent with experiment (Figure 4.9, A).[27–29] Starting with the "vacant" species $[(P_3{}^B)Fe]^+$, two electron reduction under N_2, at the limiting potential of catalysis (−2.1 V; see Chapter 3),[28] produces the anionic dinitrogen adduct $[(P_3{}^B)Fe(N_2)]^-$. Protonation of this anion at low temperature produces the cationic hydrazido complex $[(P_3{}^B)Fe(NNH_2)]^+$,[33] which, following one electron reduction to its charge neutral congener $(P_3{}^B)Fe(NNH_2)$ ($E^{\circ\prime} \geq -1.2$ V), undergoes protolytic cleavage of the N–N bond to produce the first equivalent of NH_3 and the cationic Fe(IV) nitrido $[(P_3{}^B)Fe{\equiv}N]^+$. The 3 H^+/3 e^- reduction of this nitride yields the known cationic NH_3 adduct $[(P_3{}^B)Fe(NH_3)]^+$, which is then reduced in the presence of N_2 to close the catalytic cycle.[41]

While there is precedent for the reductive protonation of terminal Fe nitrides to yield NH_3,[16,18] a closer examination of this step is warranted. Figure 4.9, B shows all of the conceivable pathways for the reduction of $[(P_3{}^B)Fe{\equiv}N]^+$ involving single electron steps, ultimately producing the known charge neutral amido $(P_3{}^B)Fe(NH_2)$, which can be protonated to yield $[(P_3{}^B)Fe(NH_3)]^+$.[41] Given that $[(P_3{}^B)Fe{\equiv}N]^+$ appears stable to protonation at low temperature, the next key step in the catalytic cycle is either one electron reduction to produce the formally Fe(III) nitrido $(P_3{}^B)Fe{\equiv}N$, or direct N–H bond formation via PCET to produce the terminal imido $[(P_3{}^B)Fe{=}NH]^+$. Naïvely, it might be assumed either pathway should be challenging under catalytic conditions, given that the formation of a strong Fe≡N

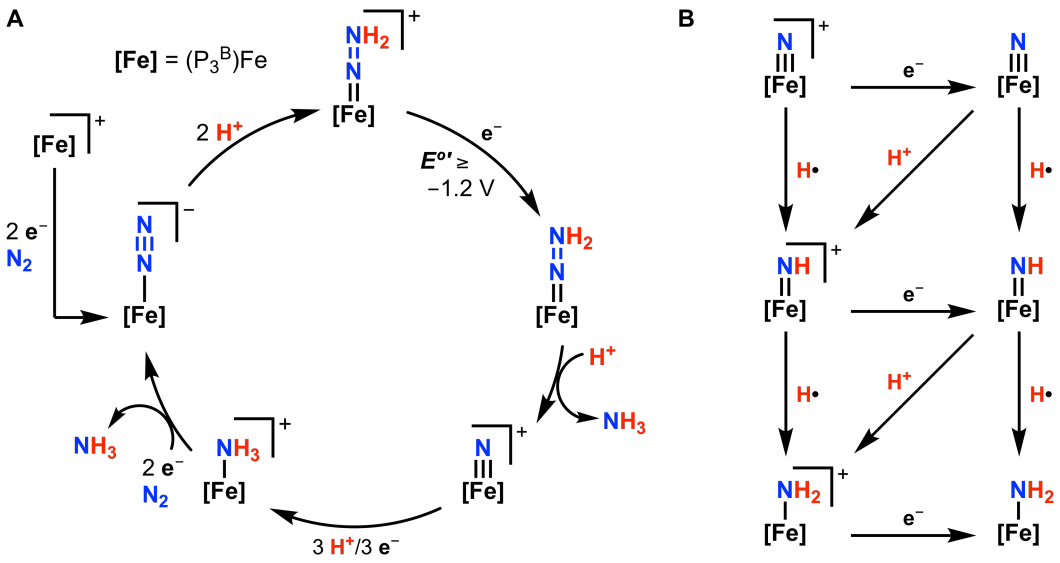

Figure 4.9: Proposed mechanism for nitrogen fixation by $(P_3{}^B)Fe$. (A) Proposed catalytic cycle. (B) Possible mechanisms for the 3 H^+/3 e^- reduction of $[(P_3{}^B)Fe{\equiv}N]^+$.

triple bond would be expected to result in a large ligand field splitting, and, hence, large barriers to reduction. However, the detailed electronic structure of $[(P_3{}^B)Fe{\equiv}N]^+$ revealed by XAS and DFT shows that the a_1 symmetry LUMO is stabilized by mixing with the vacant B $2p_z$ orbital. Indeed, this virtual orbital is predicted to possess greater ligand character than Fe character (*vide supra*). We can recognize this as a manifestation of the classic 3-center σ bonding found in, for example, the linear XeF_2 molecule,[43] although in this case only two electrons occupy the bonding combination, and the LUMO (the SOMO for $(P_3{}^B)Fe{\equiv}N$) is the effectively non-bonding orbital (Figure 4.10, A).

DFT calculations on the charge neutral nitrido $(P_3{}^B)Fe{\equiv}N$ (assuming a doublet ground state), corroborate this conjecture. Upon reduction from $[(P_3{}^B)Fe{\equiv}N]^+$ to $(P_3{}^B)Fe{\equiv}N$, the Fe–N and Fe–P bond distances change by ≤ 0.05 Å, while the Fe–B distance shortens from 2.95 to 2.70 Å as a result of the Fe–B σ character of the SOMO. A Löwdin spin population analysis reveals that the B and N atoms bear the majority of the unpaired spin density, which is consistent with a formulation of this species as a low-spin Fe(IV) ion ($S = 0$) coupled to a ligand-centered radical—i.e., $[(P_3{}^B)^{\frac{1}{2}\bullet}]Fe^{IV}[(N)^{\frac{1}{2}\bullet}]$ (Figure 4.10, B). It is then reasonable to estimate a lower bound for reduction potential of $[(P_3{}^B)Fe{\equiv}N]^+$ by that of,

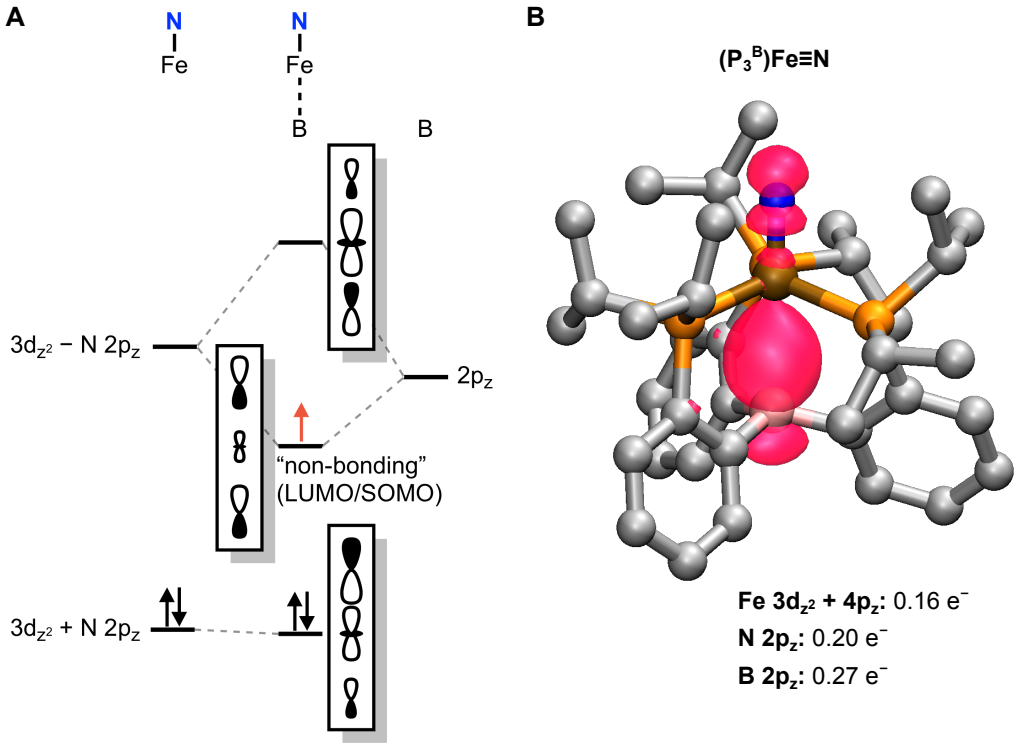

Figure 4.10: (A) Qualitative MO diagram describing the 3-center σ bonding of $[(P_3^B)Fe{\equiv}N]^{0/+}$. (B) Spin density isosurface (isovalue = 0.005 a.u.) calculated for $(P_3^B)Fe{\equiv}N$ in the doublet state, along with Löwdin spin populations.

for example, Ph_3B (−2.2 V vs. $Fc^{+/0}$ in THF),[44,45] although the actual potential will be shifted anodically given the positive charge. On these grounds, we predict this potential to be positive of the $[(P_3^B)Fe(N_2)]^{0/-}$ couple, and therefore the reduction of $[(P_3^B)Fe{\equiv}N]^+$ should accessible under catalytic conditions, be it by direct ET or PCET, which is consistent with experiment (*vide supra*). Indeed, the predicted nitridyl ($N^{\bullet 2-}$) character of the N atom of $(P_3^B)Fe{\equiv}N$ may even facilitate N–H bond formation via PCET.[46] While we have preliminary, indirect evidence for the formation of $(P_3^B)Fe{\equiv}N$ upon photoreduction of XAS samples of $[(P_3^B)Fe{\equiv}N]^+$ (See Appendix C),[47] evaluation of these predictions awaits the detailed experimental characterization of this no-doubt highly reactive species.

4.3 Conclusion

To conclude, we have demonstrated that the sequential reduction and low-temperature protonation of the N_2 fixation catalyst $[(P_3^B)Fe(N_2)]^-$ yields NH_3 and a terminal Fe(IV)

nitride. $[(P_3{}^B)Fe{\equiv}N]^+$ is the first example of a terminal Fe nitride synthesized from N_2, and thus confirms the long-standing hypothesis that a single Fe center can support a distal Chatt-type N_2 fixation mechanism in which the N–N bond is cleaved heterolytically. While the results described herein do not preclude alternative, late-stage N–N bond cleavage mechanisms under catalytic turnover,[31] they do complete a comprehensive mechanistic proposal that is fully consistent with experiment.[27–29]

These results also provide insight into how this mechanism evolves from the electronic structure of the $(P_3{}^B)Fe$ unit. In the multi-step, multi-electron process,

$$[(P_3{}^B)Fe^I]^+ + N_2 + 3\,H^+ + 3\,e^- \rightarrow [(P_3{}^B)Fe^{IV}{\equiv}N]^+ + NH_3 \tag{4.9}$$

the reducing equivalents are distributed over the Fe center and the ligand. In this way, the redox behavior of the $(P_3{}^B)Fe$ unit crudely models that of a metallocluster, in which the potential range of multi-electron processes is compressed by delocalization of electrons/holes among many metals.[48] Analogy may also be made to the reduction of O_2 to ferryl and H_2O mediated by heme cofactors, in which the last reducing equivalent necessary to cleave the O–O bond is derived from the porphyrin and/or thiolate ligand (Figure 4.2, A).[14] In a similar fashion, the challenging multi-electron transformation described by Equation 4.9 is facilitated by covalency with the ligand atoms, which buffers the physical oxidation state range of Fe in this system. This is a feature of potential relevance to biological N_2 fixation, where the multimetallic [FeS] assembly may serve the same function.[30]

4.4 Experimental Section

4.4.1 Experimental Details

4.4.1.1 General Considerations

Unless noted otherwise, all manipulations were carried out using standard Schlenk or glovebox techniques under an N_2 atmosphere. Solvents were deoxygenated and dried by thoroughly sparging with N_2 followed by passage through an activated alumina col-

umn in a solvent purification system by SG Water, USA LLC. Deoxygenated, anhydrous 2-MeTHF was purified by stirring over Na/K alloy and filtering through a short column of activated alumina prior to use. Nonhalogenated solvents were tested with sodium benzophenone ketyl in THF in order to confirm the absence of oxygen and water. Deuterated solvents were purchased from Cambridge Isotope Laboratories, Inc., degassed, and dried over activated 3 Å molecular sieves prior to use. The compounds $P_3{}^B$,[49] $(P_3{}^B)Fe(Br)$,[32] $(P_3{}^B)Fe(Me)$,[41] $[Na(Et_2O)_2][(P_3{}^B)Fe(N_2)]$,[32] $[Na(12\text{-c-}4)_2][(P_3{}^B)Fe(N_2)]$,[32] $HBAr^F{}_4$,[28] and $^{57}FeCl_2$,[50] were prepared according to literature procedures. ^{57}Fe-labelled $[Na(12\text{-c-}4)_2][(P_3{}^B)Fe(N_2)]$ was prepared as usual, but using $(P_3{}^B)^{57}Fe(Cl)$ as the precursor. $(P_3{}^B)^{57}Fe(Cl)$ was prepared by a synthesis analogous to that of the bromide analog, but replacing $FeBr_2$ with $^{57}FeCl_2$ as the Fe precursor. All other reagents were purchased from commercial vendors and used without further purification unless otherwise stated.

4.4.1.2 NMR Spectroscopy

Chemical shifts for ^{1}H and ^{13}C are reported in ppm relative to tetramethylsilane, using resonances from residual solvent as internal standards; ^{31}P and ^{11}B resonances are reported in ppm, referenced to the signal of the deuterated solvent used to lock the instrument.

4.4.1.3 IR Spectroscopy

IR measurements were obtained as powders or thin films formed by evaporation of solutions using a Bruker Alpha Platinum ATR spectrometer with OPUS software.

4.4.1.4 UV-vis Spectroscopy

Optical spectroscopy measurements were collected with a Cary 50 UV-vis spectrophotometer using a 1-cm two-window quartz cell.

4.4.1.5 Electrochemistry

Cyclic voltammetry measurements were carried out in a glovebox under an N_2 atmosphere in a one-compartment cell using a CH Instruments 600B electrochemical analyzer. A glassy carbon electrode was used as the working electrode and a carbon rod was used as the auxiliary electrode. The reference electrode was AgOTf/Ag in THF isolated by a CoralPor frit (obtained from BASi). The $Fc^{+/0}$ was used as an external reference. THF solutions of electrolyte (0.1 M [TBA][PF_6]) and analyte were also prepared under an inert atmosphere.

4.4.1.6 X-ray Crystallography

X-ray diffraction studies were carried out at the Caltech Division of Chemistry and Chemical Engineering X-ray Crystallography Facility using a dual source Bruker D8 Venture, four-circle diffractometer with a PHOTON CMOS detector. Data was collected at 100 K using Mo K_α radiation ($\lambda = 0.71073$ Å). The crystals were mounted on a glass fiber under Paratone N oil. Structures were solved using SHELXT and refined against F^2 on all data by full-matrix least squares with SHELXL.[51,52] All non-hydrogen atoms were refined anisotropically. All hydrogen atoms were placed at geometrically calculated positions and refined using a riding model. The isotropic displacement parameters of all hydrogen atoms were fixed at 1.2 (1.5 for methyl groups) times the U_{eq} of the atoms to which they are bonded.

4.4.1.7 Mössbauer Spectroscopy

Mössbauer spectra were recorded on a spectrometer from SEE Co. (Edina, MN) operating in the constant acceleration mode in a transmission geometry. The sample was kept in an SVT-400 cryostat form Janis (Wilmington, MA), using liquid He as a cryogen for temperatures below 80 K, and liquid N_2 as a cryogen for 80 K measurements. The quoted isomer shifts are relative to the centroid of the spectrum of a metallic foil of α-Fe at room temperature. Solid samples were prepared by grinding solid material into a fine powder and then mounted in to a Delrin cup fitted with a screw-cap as a boron nitride pellet. Solution samples were

transferred to a sample cup and chilled to 77 K inside of the glovebox, and quickly removed from the glovebox and immersed in liquid N_2 until mounted in the cryostat. Data analysis was performed using version 4 of the program WMOSS (www.wmoss.org) and quadrupole doublets were fit to Lorentzian lineshapes.[53]

4.4.1.8 X-ray Absorption Spectroscopy

Samples for XAS measurements were prepared in modified Mössbauer sample cups in which the bottom of the Delrin cup was removed and sealed with Kapton tape. All samples thus prepared were analyzed by Mössbauer spectroscopy at 80 K prior to collection of XAS data. Samples were maintained at temperatures of 80 K and below at all times.

XAS data collection was conducted at the Stanford Synchrotron Radiation Laboratory (SSRL) with the SPEAR 3 storage ring containing 500 mA at 3.0 GeV. Fe *K*-edge data were collected on the beamline 9-3 operating with a wiggler field of 2 T and employing a Si(220) double-crystal monochromator. Beamline 9-3 is equipped with a rhodium-coated vertical collimating mirror upstream of the monochromator and a bentcylindrical focusing mirror (also rhodium-coated) downstream of the monochromator. Harmonic rejection was accomplished by setting the energy cutoff angle of the mirrors to 10 keV. The incident and transmitted X-ray intensities were monitored using nitrogen filled ionization chambers, and for dilute samples X-ray absorption was monitored by measuring the Fe K_α fluorescence intensity using an array of 100 Canberra germanium detectors. For concentrated samples ($\geq$ 10 mM), fluorescence was measured using a single-channel PIPS detector. During data collection, samples were maintained at a temperature of approximately 10 K using an Oxford instruments liquid helium flow cryostat. The energy was calibrated by reference to the absorption of a standard iron metal foil measured simultaneously with each scan, assuming a lowest energy inflection point of the iron foil to be 7111.3 eV. Samples were monitored for photodamage by comparing the pre-edge region between consecutive scans. In cases where photodamage was detected, the sample was moved to a previously unexposed

region and single scans were collected; in this fashion, six first scans could be collected and integrated for each sample.

The raw XAS data were analyzed using the EXAFSPAK suite of programs.[54] Data were calibrated to the first inflection of the iron foil reference and averaged over all first scans for each sample. The edge region was background corrected by fitting a Gaussian function through the pre-edge region and subtracting this from the entire spectrum. A four-segment fourth-order spline was fit to the EXAFS region, and the spectrum was normalized to the edge jump. In most cases, a monochromator glitch at $k \approx 12$ Å^{-1} was removed by fitting a cubic polynomial to the raw data. For dilute samples, a step at the Co K-edge (7709 eV) due to a small Co impurity detected in the incident X-rays was observed; note that since the step was present in the incident channel, the impurity was due to Co on the slits which focus the X-rays on the sample, not in the sample itself. This impurity was corrected by fitting a fourth-order polynomial through the step in the raw data to determine a constant offset, which was subsequently subtracted from the data after the step. Interatomic distances obtained from simulation of the raw, uncorrected EXAFS data were found to be identical to those obtained from simulation of the data deglitched in this manner. No smoothing, filtering, or related operations were performed on the data. The pre-edge region was fit between 7108 and 7119 eV using the `EDG_FIT` utility. Resonances were fit with pseudo-Voigt lineshapes, where the weight of the Lorentzian and Gaussian components were allowed to refine freely. The EXAFS oscillations $\chi(k)$ were quantitatively analyzed by non-linear least square curve-fitting. The k^3-weighted data were fit from $k = 3$ to 15 Å^{-1}. Ab initio theoretical phase and amplitude functions were calculated using the program FEFF version 7.[55]

4.4.2 Synthetic Details

4.4.2.1 Synthesis of $[(P_3^B)Fe(N_2)]^{2-}$

From [Na(Et$_2$O)$_2$][(P_3^B)Fe(N$_2$)]. A solution of [Na(Et$_2$O)$_2$][(P_3^B)Fe(N$_2$)] in THF (7 mM) was passed iteratively 3 times through a short column of KC_8 (ca. 0.7×0.7 mm) packed on top of a glass microfiber filter. An aliquot of this solution was dried to a thin film on the sample plate of an ATR-IR spectrometer. The resultant IR spectrum displays an intense vibration at 1803 cm^{-1} attributable to the N–N vibration of $[(P_3^B)Fe(N_2)]^{2-}$. The difference in N_2 stretching frequencies between $[(P_3^B)Fe(N_2)]^{2-}$ produced from reduction of [Na(Et$_2$O)$_2$][(P_3^B)Fe(N$_2$)] and $[(P_3^B)Fe(N_2)]^{2-}$ produced from reduction of [Na(12-c-4)$_2$][(P_3^B)Fe(N$_2$)] ($\Delta\nu_{NN}$ = 31 cm^{-1}) is nearly identical to that observed for [Na(12-c-4)$_2$][(P_3^B)Fe(N$_2$)] versus [Na(Et$_2$O)$_2$][(P_3^B)Fe(N$_2$)] ($\Delta\nu_{NN}$ = 29 cm^{-1}), suggesting coordination of Na^+ to the N_2 ligand of $[(P_3^B)Fe(N_2)]^{2-}$ produced in situ from [Na(Et$_2$O)$_2$][(P_3^B)Fe(N$_2$)].

From [Na(12-c-4)$_2$][(P_3^B)Fe(N$_2$)]. A solution of [Na(12-c-4)$_2$][(P_3^B)Fe(N$_2$)] in DME (1 to 10 mM) was similarly reduced via iterative passage through a column of KC_8. The filtered supernatant was layered with an equal volume of Et_2O and placed in a freezer at −35 °C. After ca. 24 hrs, the mother liquor was decanted off of black crystalline solids, which were liberally washed with Et_2O before drying in vacuo. The solid state IR spectrum shows an intense resonance at 1836 cm^{-1} attributable to the N–N vibration of [Na(12-c-4)$_2$][K(DME)$_x$][(P_3^B)Fe(N$_2$)]. For NMR analysis, deuterated THF was employed as the solvent, and the filtered black solution was sealed in an NMR tube fitted with a J-Young adapter containing a spatula tip of KC_8. Based on the NMR data, $[(P_3^B)Fe(N_2)]^{2-}$ maintains C_3 symmetry in solution, with a single set of aromatic resonances in the ^{1}H spectrum, and one singlet in the ^{31}P spectrum. As $[(P_3^B)Fe(N_2)]^{2-}$ (−3.2 V vs $Fc^{+/0}$) is more reducing than its alkali metal counterions (e.g., −3.04 V vs $Fc^{+/0}$ for $Na^{+/0}$) in ethereal solvents, it is subject to disproportionation in solution, and such preparations invariably contain

$[K(DME)_x][(P_3{}^B)Fe(N_2)]$ as a contaminant (ν_{NN} = 1893 cm^{-1}). Thus elemental analysis was not collected. For Mössbauer studies, ^{57}Fe-enriched $[Na(12\text{-c-}4)_2][K(Solv)_x][(P_3{}^B)Fe(N_2)]$ was prepared in situ from 100% ^{57}Fe-enriched $[Na(12\text{-c-}4)_2][(P_3{}^B)Fe(N_2)]$ using the same method with THF or 2-MeTHF as the solvent, and the filtered solution was immediately frozen into a Delrin sample holder.

^{1}H NMR (400 MHz, d_8-THF, 293 K, ppm): δ 7.14 (d, J = 5 Hz, Ar-C*H*, 3H) , 6.84 (d, J = 5 Hz, Ar-C*H*, 3H), 6.45 (t, J = 6.5 Hz, Ar-C*H*, 3H), 6.29 (t, J = 6.5 Hz, Ar-C*H*, 3H), 3.61 (br, 12-c-4), 3.59 (br, THF), 2.35 (br, -C*H*$(CH_3)_2$, 6H), 1.78 (br, -CH(C*H*$_3$)), 1.73 (br, THF); N.B., accurate integrations for the isopropyl methyl protons of the ligand and the methylene protons of the $[Na(12\text{-c-}4)_2]^+$ ion could not be obtained due to overlap with the residual THF resonances appearing at 1.73 and 3.59 ppm. $^{31}P\{^1H\}$ (162 MHz, d_8-THF, 293 K, ppm): δ 79.65.

4.4.2.2 Synthesis of $(P_3{}^B)Fe(NNMe_2)$

To a suspension of $(P_3{}^B)Fe(Br)$ (200 mg, 0.275 mmol) in 5.5 mL Et_2O was added MeOTf (65 μL, 0.578 mmol), and the mixture was subsequently cooled to −78 °C with stirring in the cold well of an N_2-filled glove box. A scintillation vial containing KC_8 (123 mg, 0.909 mmol) suspended in 2.5 mL Et_2O was similarly chilled, and then transferred to the stirring $(P_3{}^B)Fe(Br)$/MeOTf mixture via pipette; this vial was additionally washed with 1 mL of pre-chilled Et_2O, which was subsequently added to the reaction mixture. The mixture was allowed to stir at −78 °C for 1 hr, and then allowed to warm to room temperature and stirred an additional 3 hrs. The solvent was removed in vacuo, and the remaining solids extracted with pentane and filtered over a pad of celite until the filtrate, containing crude product, was colorless (ca. 50 mL). The filtrate was concentrated to dryness, and THF (ca. 5 mL) and 0.7 wt% Na/Hg (1.375 mmol Na^0) were added. This mixture was stirred rapidly overnight (ca. 12 hrs), at which point the dark solution was decanted from the excess Na/Hg, the solvent removed in vacuo, and the remaining solids extracted with pentane and filtered through a

celite pad until the filtrate runs colorless. The pentane extract was concentrated to ca. 5 mL and then cooled to −35 °C. After 2 days, the mother liquor was decanted, the remaining solids washed with cold pentane (5 × 1 mL), and dried in vacuo to yield ($P_3{}^B$)Fe($NNMe_2$) as dark brown crystals (24 mg, 13%). Crystals suitable for XRD were obtained by slow evaporation of a pentane solution of ($P_3{}^B$)Fe($NNMe_2$) at room temperature.

^{1}H NMR (400 MHz, C_6D_6, 293 K, ppm): δ 9.73 (d, J = 7 Hz, Ar-C*H*, 3H) , 8.19 (t, J = 7 Hz, Ar-C*H*, 3H), 6.97 (d, J = 7 Hz, Ar-C*H*, 3H), 5.40 (t, J = 7 Hz, Ar-C*H*, 3H), 5.29 (br, -C*H*(CH_3)$_2$, 3H), 4.06 (br, -C*H*(CH_3)$_2$, 3H), 1.11 (d, J = 6 Hz, -CH(C*H*$_3$), 9H), 0.95 (d, J = 6Hz, -CH(C*H*$_3$), 9H), 0.64 (d, J = 6 Hz, -CH(C*H*$_3$), 9H), 0.06 (d, J = 6 Hz, -CH(C*H*$_3$), 9H), −18.66 (br, -N(C*H*$_3$), 6H). ^{13}C{^{1}H} NMR (101 MHz, C_6D_6, 293 K, ppm): δ 241.88 (Ar-*C*), 137.78 (Ar-*C*H), 120.34 (Ar-*C*H), 119.28 (Ar-*C*H), 75.39 (Ar-*C*), 62.24 (Ar-*C*H), 45.38 (-*C*H(CH_3)$_2$), 33.56 (-CH(*C*H$_3$)), 22.62 (-CH(*C*H$_3$)), 17.67 (-CH(*C*H$_3$)), 16.92 (-CH(*C*H$_3$)), −10.74 (-*C*H(CH_3)$_2$); N.B., a resonance for the *N*-methyl carbon atom could not be located in the chemical shift range from 1000 to −500 ppm, even by ^{1}H-detected HSQC/HMQC. The resonance is likely too broad at 293 K by exchange with the paramagnetic excited state to be observed. ^{31}P{^{1}H} (162 MHz, C_6D_6, 293 K, ppm): δ 806.61 (br, FWHM = 2741 Hz). ^{11}B (128 MHz, C_6D_6, 293 K, ppm) δ −396.23 (br, FWHM = 909 Hz). UV-vis (toluene, 293 K, nm {ϵ, cm^{-1} M^{-1}}): 551 {636}, 774 {139}. Anal. Calc. for $C_{38}H_{60}BFeN_2P_3$: C, 64.79; H, 8.58; N, 3.98. Found: C, 65.06; H, 8.56; N, 3.70.

4.4.2.3 Synthesis of ($P_3{}^B$)Fe(OTf)

A suspension of ($P_3{}^B$)Fe(Me) (25 mg, 0.038 mmol) in 1 mL of Et_2O was chilled to −78 °C in the cold well of an N_2 filled glove box. A similarly chilled solution of TfOH (3.5 mL, 0.040 mmol) in 1 mL of Et_2O was added dropwise to the suspension of ($P_3{}^B$)Fe(Me), and the resultant mixture was removed from the cold well and allowed to warm to room temperature with stirring over the course of 1 hour. The solvent was removed in vacuo, and the remaining brown-green solids were extracted with pentane (3 × 15 mL) and filtered through a pad of

celite. The filtrate was dried in vacuo to yield analytically pure ($P_3{}^B$)Fe(OTf) as a yellow-green powder (25 mg, 83%). Crystals suitable for XRD were grown by slow evaporation of a pentane solution of ($P_3{}^B$)Fe(OTf) at room temperature.

^{1}H NMR (400 MHz, C_6D_6, 293 K, ppm): δ 57.27, 35.29, 26.52, 24.70, 5.32, 4.38, 2.93, 0.86, −3.15, −26.04. μ_{eff} (C_6D_6, Evans method, 293 K): 4.1 β_e. UV-vis (2-MeTHF, 293 K, nm {ϵ, cm^{-1} M^{-1}}): 562 {126}, 749 {124}. Anal. Calc. for $C_{37}H_{54}BF_3FeO_3P_3S$: C, 55.87; H, 6.84. Found: C, 55.78; H, 6.76.

4.4.3 Low-Temperature Protonation Studies

4.4.3.1 Protonation studies of [($P_3{}^B$)Fe(N_2)]$^{2-}$

Using TfOH. As described above, a solution of [($P_3{}^B$)Fe(N_2)]$^{2-}$ (0.0028 mmol) in 500 μL 2-MeTHF was prepared in situ from ^{57}Fe-labelled [Na(12-crown4)$_2$][($P_3{}^B$)Fe(N_2)], and immediately transferred to a Mössbauer or XAS sample holder and glassed (91 K) in the cold well of an N_2 filled glove box chilled to 77 K. A solution of TfOH in 2-MeTHF (200 μL 80 mM, 0.016 mmol, 6 equiv) was layered on top and allowed to form a glass (final [Fe] = 4 mM, final [TfOH] = 24 mM). Using pre-chilled stainless steel forceps, the sample cup was lifted off of the bottom of the cold well, and the mixture was allowed to de-glass. A pre-chilled stainless steel stir rod was used to mix the viscous, supercooled 2-MeTHF briefly before replacing the cup on the bottom of the well and allowing the solvent to re-glass. This procedure was repeated until the desired mixing time was reached, at which point the sample was allowed to re-glass on the bottom of the cold well before it was transferred quickly out of the glovebox and stored at 77 K prior to analysis.

N.B., at early reaction times (<15 min. of mixing) it is critical that the temperature be maintained low enough that the 2-MeTHF appears as a very viscous gel. However, with enough reaction time, the mixture occasionally flash-freezes (typically after about 20 min. of mixing), at which point the frozen mixture must be carefully thawed to 137 K before re-glassing and repeating the above procedure.

Using HBAr$^F{}_4$. The procedure is identical to that using TfOH, but HBAr$^F{}_4$ was used as the proton source (58 mg, 0.057 mmol, 20 equiv).

4.4.3.2 Protonation of [Na(12-c-4)$_2$][(P$_3{}^B$)Fe(N$_2$)]

The procedure use was identical to that described above for protonation of [(P$_3{}^B$)Fe(N$_2$)]$^{2-}$, with the following changes: [(P$_3{}^B$)Fe(N$_2$)]$^{2-}$ was replaced with ^{57}Fe-labelled [Na(12-c-4)$_2$][(P$_3{}^B$)Fe(N$_2$)] (2.0 mg, 0.0019 mmol); 15 equiv of TfOH was used (2.5 μL, 0.028 mmol); and the total reaction volume was 500 μL (final [Fe] = 4 mM). This mixture was stirred for 15 min. before re-glassing and collecting Mössbauer spectra.

4.4.3.3 Studies with NH$_3$/N$_2$H$_4$ quantification:

Protonation of [(P$_3{}^B$)Fe(N$_2$)]$^{2-}$ or [Na(12-c-4)$_2$][(P$_3{}^B$)Fe(N$_2$)] with TfOH was carried out as described above, but in a 20 mL scintillation vial, on larger scale (0.0095 mmol Fe, [Fe] = 4 mM), and with a higher concentration of TfOH (80 mM, 20 equiv). The reaction was mixed for 30 min. at T $\leq$ 137 K. (Mössbauer experiments under identical conditions shows that the yield of [(P$_3{}^B$)Fe$\equiv$N]$^+$ is typically ca. 50%.) At this point, a stir bar was added to the mixture, which was allowed to warm to room temperature with stirring over the course of 15 min. The warmed solution was then transferred to Schlenk tube and refrozen in the liq. N$_2$ chilled cold well before a solution of NaO*t*Bu (37 mg, 0.38 mmol) in 1 mL THF was added and frozen on top of the reaction mixture. The Schlenk tube was sealed and thawed to room temperature with stirring over the course of 15 min. At this point, the Schlenk tube was removed from the N$_2$-filled glove box, and the volatiles vacuum-transferred onto an excess of 2.0 M HCl in Et$_2$O and analyzed for [NH$_4$][Cl] and [N$_2$H$_6$][Cl]$_2$ as described previously.[28]

For experiments in which reductant was added after initial protonation of [(P$_3{}^B$)Fe(N$_2$)]$^{2-}$, an identical procedure was used, with the following modification. After mixing [(P$_3{}^B$)Fe(N$_2$)]$^{2-}$ and TfOH in supercooled 2-MeTHF for 30 min., the solution was re-

glassed, and a solution of $CoCp^*_2$ in 2-MeTHF (31 mg, 0.095 mmol, 10 equiv) was layered on top and allowed to glass. The mixture was mechanically stirred at T $\leq$ 137 K for an additional 30 min. At this point, a stir bar was added to the mixture, which was allowed to warm to room temperature with stirring over the course of 15 min. The reaction was subsequently worked up as described above.

The following procedure was employed for a catalytic reaction: In a nitrogen filled glovebox, a stock solution of $[(P_3{}^B)Fe][BAr^F{}_4]$ in Et_2O was prepared. An aliquot of this stock solution (2.3 μmol) was added to a Schlenk tube and evaporated to dryness under vacuum, depositing a film of $[(P_3{}^B)Fe][BAr^F{}_4]$. The tube was then charged with a stir bar and cooled to 77 K in a cold well. To the cold tube was added solid Cp^*_2Co (0.124 mmol, 54 equiv) and a solution of TfOH in Et_2O (0.247 mmol, 107 equiv). The final volume of solvent was 1 mL. This solution was allowed to cool and freeze for 5 minutes. The temperature of the system was allowed to equilibrate for 5 minutes and then the tube was sealed with a Teflon screw-valve. This tube was passed out of the box into a liquid N_2 bath and transported to a fume hood. The tube was then transferred to a dry ice/acetone bath where was thawed and allowed to stir at 195 K for 3 hrs. At this point the tube was warmed to room temperature with stirring, and stirred at room temperature for 5 min. The reaction was subsequently worked up and quantified for the presence of NH_3/N_2H_4 as described above.

N.B., during vacuum transfer the temperature of the system was maintained at 298 K and below to prevent decomposition of N_2H_4.

4.4.4 Computational Methods

All calculations were carried out using version 3.0.3 of the ORCA package.[56] Given the experimentally measured structure and ground state/excited state energy splitting for $(P_3{}^B)Fe(NNMe_2)$, this was used as a model for testing the pure exchange-correlation functionals BP86,[57,58] M06-L,[59] and TPSS.[60] For the purposes of testing, gas-phase geome-

try optimizations were carried out using the def2-SVP(C,H)/def2-TZVP basis set (with atomic coordinates from XRD as inputs),[61] followed by a frequency calculation at the same level of theory to ensure a true minimum. Calculations employed a fine integration grid (ORCA Grid5) during geometry optimization, as well as during the final single-point calculation (Grid6). The importance of relativistic effects were tested by inclusion of the zeroth order regular approximation (ZORA) with the BP86 functional,[62] using the scalar relativistically-recontracted def2- ZORA-SVP(C,H)/def2-ZORA-TZVP basis sets and def2-SVP(C,H)/def2-TZVP auxiliary basis sets.[63] From these calculations, it was determined that the ZORA-BP86 method produces the most accurate geometry, as well as a singlet-triplet ΔH that agrees well with the experimental value, although the TPSS functional performed nearly as well. All subsequent geometry optimizations and single-point energy calculations employed the ZORA-BP86 method. All optimized structures are available online free of charge: DOI:10.1021/jacs.7b09364.

For the calculation of Mössbauer parameters, the hybrid functional TPSSh[64] was used with the def2-SVP(C,H)/def2-TZVP basis set on all non-Fe atoms and the "core properties" CP(PPP) basis set for Fe.[65] The angular integration grid was set to Grid4 (NoFinalGrid), with increased radial accuracy for the Fe atom (IntAcc 7). To simulate solid state effects, a continuum solvation model was included (COSMO) with a solvent of intermediate dielectric (methanol). To calibrate the isomer shift scale and estimate the error in the calculated quadrupole splitting using this method, the Mössbauer parameters of 8 ($P_3{}^B$)Fe complexes were computed from crystallographically- or computationally-determined structures; in addition, the parameters of the previously-characterized nitrido complex ($PhBP_3{}^{iPr}$)Fe≡N were computed using coordinates from the ZORA-BP86 method.[17] Given the accuracy of the predicted spectroscopic parameters, all orbital analysis presented in the main text utilized the wavefunctions computed using this method.

For the calculation of XAS spectra, the TPSSh functional was used in conjunction with the def2-TZVP basis set on all non-Fe atoms and the CP(PPP) basis set for Fe. The

angular integration grid was set to Grid4 (NoFinalGrid), with increased radial accuracy for the Fe atom (IntAcc 7). To simulate solid state effects, a continuum solvation model was included (COSMO) with an infinite dielectric. TD-DFT transitions were calculated using the Tamm-Dancoff approximation with excitations restricted from the Fe 1s orbital. The first 50 lowest-energy transitions were calculated, and the total intensity was computed including both dipole and quadrupole transition intensities. To calibrate the energy scale of the computed spectra, the XAS spectrum of ($PhBP_3^{iPr}$)Fe≡N was calculated from BP86-ZORA optimized coordinates, and compared with the experimentally-reported spectrum.[37] A constant shift of 154.25 eV was determined to align the intense pre-edge transitions of the experimental and calculated spectra; subsequently, this same shift was applied to all calculated spectra. A line broadening of 1.5 eV was applied to the calculated spectra to approximate the experimentally-observed linewidth. Spectra were normalized by setting the area of the ($PhBP_3^{iPr}$)Fe≡N spectrum to 0.92, which is the estimated area normalized to the edge-jump (based on the related ($PhBP_3^{CH_2Cy}$)Fe≡N variant).[37] To compare with the experimental pre-edge spectra, the line-broadened TD-DFT spectrum was fit to 2 or 3 Gaussian functions, from which predicted pre-edge areas were calculated.

References

(1) Laplaza, C. E.; Cummins, C. C. *Science* **1995**, *268*, 861–863.

(2) Rodriguez, M. M.; Bill, E.; Brennessel, W. W.; Holland, P. L. *Science* **2011**, *334*, 780–783.

(3) Shima, T.; Hu, S.; Luo, G.; Kang, X.; Luo, Y.; Hou, Z. *Science* **2013**, *340*, 1549–1552.

(4) Ertl, G. *Angew. Chem. Int. Ed.* **2008**, *47*, 3524–3535.

(5) Kiernicki, J. J.; Zeller, M.; Szymczak, N. K. *J. Am. Chem. Soc.* **2017**, *139*, 18194–18197.

(6) Fryzuk, M. D. *Acc. Chem. Res.* **2009**, *42*, 127–133.

(7) Henderson, R. A.; Leigh, G. J.; Pickett, C. J. *J. Chem. Soc., Dalton Trans.* **1989**, 425–430.

(8) Dreher, A.; Mersmann, K.; Näther, C.; Ivanovic-Burmazovic, I.; van Eldik, R.; Tuczek, F. *Inorg. Chem.* **2009**, *48*, 2078–2093.

(9) Chatt, J.; Dilworth, J. R.; Richards, R. L. *Chem. Rev.* **1978**, *78*, 589–625.

(10) Yandulov, D. V.; Schrock, R. R. *J. Am. Chem. Soc.* **2002**, *124*, 6252–6253.

(11) Yandulov, D. V.; Schrock, R. R. *Science* **2003**, *301*, 76–78.

(12) Tanaka, H.; Arashiba, K.; Kuriyama, S.; Sasada, A.; Nakajima, K.; Yoshizawa, K.; Nishibayashi, Y. *Nat. Commun.* **2014**, *5*, 3737.

(13) Hohenberger, J.; Ray, K.; Meyer, K. *Nat. Commun.* **2012**, *3*, 720.

(14) Poulos, T. L. *Chem. Rev.* **2014**, *114*, 3919–3962.

(15) Que, L. *Acc. Chem. Res.* **2007**, *40*, 493–500.

(16) Betley, T. A.; Peters, J. C. *J. Am. Chem. Soc.* **2004**, *126*, 6252–6254.

(17) Hendrich, M. P.; Gunderson, W.; Behan, R. K.; Green, M. T.; Mehn, M. P.; Betley, T. A.; Lu, C. C.; Peters, J. C. *Proc. Natl. Acad. Sci.* **2006**, *103*, 17107–17112.

(18) Scepaniak, J. J.; Vogel, C. S.; Khusniyarov, M. M.; Heinemann, F. W.; Meyer, K.; Smith, J. M. *Science* **2011**, *331*, 1049–1052.

(19) Wagner, W. D.; Nakamoto, K. *J. Am. Chem. Soc.* **1988**, *110*, 4044–4045.

(20) Meyer, K.; Bill, E.; Mienert, B.; Weyhermüller, T.; Wieghardt, K. *J. Am. Chem. Soc.* **1999**, *121*, 4859–4876.

(21) Aliaga-Alcalde, N.; George, S. D.; Mienert, B.; Bill, E.; Wieghardt, K.; Neese, F. *Angew. Chem. Int. Ed.* **2005**, *44*, 2908–2912.

(22) Berry, J. F.; Bill, E.; Bothe, E.; George, S. D.; Mienert, B.; Neese, F.; Wieghardt, K. *Science* **2006**, *312*, 1937–1941.

(23) Vogel, C.; Heinemann, F. W.; Sutter, J.; Anthon, C.; Meyer, K. *Angew. Chem. Int. Ed.* **2008**, *47*, 2681–2684.

(24) Scepaniak, J. J.; Fulton, M. D.; Bontchev, R. P.; Duesler, E. N.; Kirk, M. L.; Smith, J. M. *J. Am. Chem. Soc.* **2008**, *130*, 10515–10517.

(25) Sabenya, G.; Lázaro, L.; Gamba, I.; Martin-Diaconescu, V.; Andris, E.; Weyhermüller, T.; Neese, F.; Roithova, J.; Bill, E.; Lloret-Fillol, J.; Costas, M. *J. Am. Chem. Soc.* **2017**, *139*, 9168–9177.

(26) Maity, A. K.; Murillo, J.; Metta-Magaña, A. J.; Pinter, B.; Fortier, S. *J. Am. Chem. Soc.* **2017**, *139*, 15691–15700.

(27) Anderson, J. S.; Rittle, J.; Peters, J. C. *Nature* **2013**, *501*, 84–87.

(28) Del Castillo, T. J.; Thompson, N. B.; Peters, J. C. *J. Am. Chem. Soc.* **2016**, *138*, 5341–5350.

(29) Chalkley, M. J.; Del Castillo, T. J.; Matson, B. D.; Roddy, J. P.; Peters, J. C. *ACS Cent. Sci.* **2017**, *3*, 217–223.

(30) Seefeldt, L. C.; Hoffman, B. M.; Dean, D. R. *Annu. Rev. Biochem.* **2009**, *78*, 701–722.

(31) Rittle, J.; Peters, J. C. *J. Am. Chem. Soc.* **2016**, *138*, 4243–4248.

(32) Moret, M.; Peters, J. C. *Angew. Chem. Int. Ed.* **2011**, *50*, 2063–2067.

(33) Anderson, J. S.; Cutsail, G. E.; Rittle, J.; Connor, B. A.; Gunderson, W. A.; Zhang, L.; Hoffman, B. M.; Peters, J. C. *J. Am. Chem. Soc.* **2015**, *137*, 7803–7809.

(34) Lee, Y.; Mankad, N. P.; Peters, J. C. *Nat. Chem.* **2010**, *2*, 558–565.

(35) Gütlich, P.; Bill, E.; Trautwein, A. X., *Mössbauer Spectroscopy and Transition Metal Chemistry: Fundamentals and Applications*; Springer: New York, 2011.

(36) Rudd, P. A.; Liu, S.; Planas, N.; Bill, E.; Gagliardi, L.; Lu, C. C. *Angew. Chem. Int. Ed.* **2013**, *52*, 4449–4452.

(37) Rohde, J.-U.; Betley, T. A.; Jackson, T. A.; Saouma, C. T.; Peters, J. C.; Que, L. *Inorg. Chem.* **2007**, *46*, 5720–5726.

(38) Kemner, K. M.; Kelly, S. D.; Orlandini, K. A.; Tsapin, A. I.; Goldfeld, M. G.; Perfiliev, Y. D.; Nealson, K. H. *J. Synchrotron Rad.* **2001**, *8*, 949–951.

(39) Weng, T.-C.; Hsieh, W.-Y.; Uffelman, E. S.; Gordon-Wylie, S. W.; Collins, T. J.; Pecoraro, V. L.; Penner-Hahn, J. E. *J. Am. Chem. Soc.* **2004**, *126*, 8070–8071.

(40) Westre, T. E.; Kennepohl, P.; DeWitt, J. G.; Hedman, B.; Hodgson, K. O.; Solomon, E. I. *J. Am. Chem. Soc.* **1997**, *119*, 6297–6314.

(41) Anderson, J. S.; Moret, M.-E.; Peters, J. C. *J. Am. Chem. Soc.* **2013**, *135*, 534–537.

(42) Bouhadir, G.; Bourissou, D. *Chem. Soc. Rev.* **2016**, *45*, 1065–1079.

(43) DeKock, R. L.; Bosma, W. B. *J. Chem. Ed.* **1988**, *65*, 194.

(44) DuPont, T. J.; Mills, J. L. *J. Am. Chem. Soc.* **1975**, *97*, 6375–6382.

(45) Connelly, N. G.; Geiger, W. E. *Chem. Rev.* **1996**, *96*, 877–910.

(46) Cutsail III, G. E.; Stein, B. W.; Subedi, D.; Smith, J. M.; Kirk, M. L.; Hoffman, B. M. *J. Am. Chem. Soc.* **2014**, *136*, 12323–12336.

(47) George, S. J.; Fu, J.; Guo, Y.; Drury, O. B.; Friedrich, S.; Rauchfuss, T.; Volkers, P. I.; Peters, J. C.; Scott, V.; Brown, S. D.; Thomas, C. M.; Cramer, S. P. *Inorg. Chim. Acta* **2008**, *361*, 1157–1165.

(48) Hernández Sánchez, R.; Zheng, S.-L.; Betley, T. A. *J. Am. Chem. Soc.* **2015**, *137*, 11126–11143.

(49) Bontemps, S.; Bouhadir, G.; Dyer, P. W.; Miqueu, K.; Bourissou, D. *Inorg. Chem.* **2007**, *46*, 5149–5151.

(50) Berto, T. C.; Hoffman, M. B.; Murata, Y.; Landenberger, K. B.; Alp, E. E.; Zhao, J.; Lehnert, N. *J. Am. Chem. Soc.* **2011**, *133*, 16714–16717.

(51) Sheldrick, G. M. *Acta Crystallogr. A* **2015**, *71*, 3–8.

(52) Sheldrick, G. M. *Acta Crystallogr. C* **2015**, *71*, 3–8.

(53) Prisecaru, I. "WMOSS4 Mössbauer Spectral Analysis Software", www.wmoss.org, 2009–2016.

(54) G. N. George, I. J. Pickering, EXAFSPAK: A suite of computer programs for analysis of X-ray absorption spectra. SSRL, Stanford. (1995).

(55) Rehr, J. J.; Kas, J. J.; Vila, F. D.; Prange, M. P.; Jorissen, K. *Phys. Chem. Chem. Phys.* **2010**, *12*, 5503–5513.

(56) Neese, F. *WIRES Comput. Mol. Sci.* **2011**, *2*, 73–78.

(57) Becke, A. D. *Phys. Rev. A* **1988**, *38*, 3098–3100.

(58) Perdew, J. P. *Phys. Rev B* **1986**, *33*, 8822–8824.

(59) Zhao, Y.; Truhlar, D. G. *J. Chem. Phys.* **2006**, *125*, 194101.

(60) Tao, J.; Perdew, J. P.; Staroverov, V. N.; Scuseria, G. E. *Phys. Rev. Lett.* **2003**, *91*, 146401.

(61) Weigend, F.; Ahlrichs, R. *Phys. Chem. Chem. Phys.* **2005**, *7*, 3297–3305.

(62) Van Wüllen, C. *J. Chem. Phys.* **1998**, *109*, 392–399.

(63) Pantazis, D. A.; Chen, X.-Y.; Landis, C. R.; Neese, F. *J. Chem. Theory Comput.* **2008**, *4*, 908–919.

(64) Staroverov, V. N.; Scuseria, G. E.; Tao, J.; Perdew, J. P. *J. Chem. Phys.* **2003**, *119*, 12129–12137.

(65) Neese, F. *Inorg. Chim. Acta* **2002**, *337*, 181–192.

Chapter 5

THE ELECTRONIC STRUCTURES OF AN [IRON–(NNR_2)]$^{+/0/-}$ REDOX SERIES: LIGAND NON-INNOCENCE AND IMPLICATIONS FOR CATALYTIC NITROGEN FIXATION

5.1 Introduction

Since the pioneering studies of Chatt and co-workers,[1–3] the synthesis and reaction chemistry of transition metal complexes featuring terminal hydrazido(2−) ligands ($[NNR_2]^{2-}$) has been pursued due the proposed intermediacy of M(NNH_2) species in the fixation of dinitrogen to ammonia.[4,5] In this context, the closed-shell hydrazido(2−) configuration of the "NNR_2" fragment is typically invoked to explain the susceptibility of the distal N atom (N_β) toward attack by electrophiles to produce metal hydrazidium complexes, M(NNR_3), en route to N–N bond cleavage.[6–10] At the same time, many M(NNR_2) complexes, especially those of the late transition metals, are characterized as adducts of the charge-neutral isodiazene (NNR_2) oxidation state.[5] For example, the porphyrin complexes (TPP)Fe(NNC_9H_{18}) (TPP = *meso*-tetraphenyl-, *meso*-tetra-*p*-tolyl-, or *meso*-tetra-*p*-chlorophenyl porphyrin; NC_9H_{18} = 2,2,6,6-tetramethylpiperidyl) feature structural and Mössbauer properties more consistent with a dominant Fe^{II}–N=NR_2 resonance as opposed to an Fe^{IV}=N–NR_2 alternative.[11,12] Valence tautomerization between these two closed-shell configurations—hydrazido(2−) and isodiazene—has also been proposed to explain the reactivity of an Ir(NNC_9H_{18}) complex.[13]

Despite the prominence of Fe in the catalytic fixation of N_2,[14] the corresponding chemistry of Fe(NNR_2) complexes is comparatively underdeveloped.[5,11,12,15] Recently, we have characterized [(P_3^B)Fe(NNH_2)]$^+$ as a plausible intermediate in the catalytic fixation of N_2 by [(P_3^B)Fe(N_2)]$^-$ (Figure 5.1).[16] Upon one-electron reduction to form the charge-neutral complex (P_3^B)Fe(NNH_2), this species can be further protonated at N_α to yield

NH_3 and a terminal Fe(IV) nitride, $[(P_3^B)Fe{\equiv}N]^+$,[17] consistent with hydrazido(2−)-like reactivity. At the same time, the isoelectronic and isostructural complex $[(P_3^{Si})Fe(NNH_2)]^+$ appears stable toward protonation at low temperature.[18] Instead, this species can be further reduced to form the formally 19 e^- complex $(P_3^{Si})Fe(NNH_2)$, which is unstable toward disproportionation to produce complex mixtures that notably include the hydrazine adduct $[(P_3^{Si})Fe(N_2H_4)]^+$. When $[(P_3^{Si})Fe(NNH_2)]^+$ is formed in situ and subsequently treated with substoichiometric $CoCp^*_2$, high yields of both $[(P_3^{Si})Fe(N_2H_4)]^+$ and $(P_3^{Si})Fe(N_2)$ are produced (Figure 5.1), representing, on balance, the exchange of two H-atom equivalents between the $[(P_3^{Si})Fe(NNH_2)]^{+/0}$ redox pair to effect functionalization of the proximal N atom (N_α).[18]

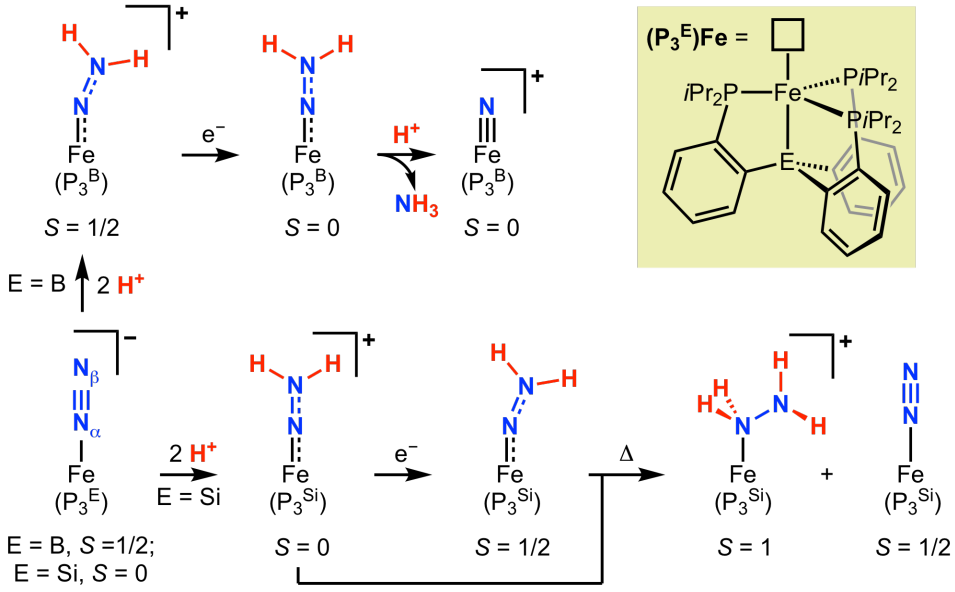

Figure 5.1: Observed reactivity of $(P_3^E)Fe(NNH_2)$ complexes.

While the precise mechanism(s) of these processes are currently under investigation, the latter reactivity is consistent with N–H bond formation via concerted proton-electron transfer (CPET) steps at N_α.[i] Preliminary EPR data on $(P_3^{Si})Fe(NNH_2)$ and its alkylated analogue $(P_3^{Si})Fe(NNMe_2)$ reveal significant spin density on at least a single N atom

[i] A CPET mechanism involves the transfer of a H^+/e^- in a single kinetic step, although the orbital transfering the e^- need not be localized on the H^+. This is a generalization of a hydrogen atom transfer (HAT) mechanism, where the H^+/e^- are transfered together in the same σ symmetry orbital interaction (i.e., as an H atom).[19]

(presumably N_α) which may serve a functional role in promoting CPET chemistry at this center.[20,21] Although $[(P_3^{Si})Fe(N_2)]^-$ is an inefficient catalyst for N_2 fixation,[22] we have recently proposed that similar PCET processes (not necessarily concerted[ii]) may play a role in increasing the efficiency of N_2 fixation by $[(P_3^{B})Fe(N_2)]^-$ when using metallocene-based reductants.[23,24]

Although commonly considered non-innocent in the two-electron sense described above, to our knowledge there are no reported $M(NNR_2)$ complexes in which the NNR_2 fragment has been characterized in the intermediate, open-shell hydrazyl radical anion configuration ($[NNR_2]^{\bullet-}$).[25,26] By contrast, many transition metal complexes coordinating the isomeric diazene radical anion ($[RNNR]^{\bullet-}$) are known.[27] This discrepancy may be due, in part, to the dearth of paramagnetic $M(NNR_2)$ species amenable to a detailed characterization of the spin density distribution on the "NNR_2" ligand via EPR-based methods.[5,10,28–33] Given the apparently large N-centered spin density and the potential radical-type reactivity of $(P_3^{Si})Fe(NNH_2)$, as well as the proposed role of PCET in catalytic N_2 fixation by $[(P_3^{B})Fe(N_2)]^-$, we were curious to determine whether the electronic structures of $[(P_3^{E})Fe(NNR_2)]^n$ complexes feature a significant weight of a $[NNR_2]^{\bullet-}$ configuration of this redox-active ligand. For $(P_3^{Si})Fe(NNH_2)$, for example, this might correspond to an intermediate-spin ($S = 1$) Fe(II) center antiferromagnetically-coupled to a $[NNR_2]^{\bullet-}$ ($S = 1/2$) ligand to produce the observed $S_{tot} = 1/2$ ground state, an electronic structure similar to that proposed for metal imidyl ($[NR]^{\bullet-}$) and aminyl ($[NR_2]^{\bullet}$) complexes that promote PCET reactivity.[21] A priori, this electronic structure seems reasonable given the low-energy π^* orbital of both parent and *N*,*N*-dialkylisodiazenes,[34–36] which thus bear resemblance to the classically redox non-innocent ligand, NO.[27] Indeed, both neutral and cationic hydrazyl radicals ($[HNNR_2]^{\bullet}$/ $[H_2NNR_2]^{\bullet+}$; R = H, alkyl) have been characterized in their free forms.[37–39]

[ii]We use the term PCET to encompass all reactions involving the net transfer of H^+ and e^- equivalents, which thus includes CPET/HAT reactions, but also step-wise electron transfer and proton transfer.

To probe this question, and potentially explain the reactivity patterns of $(P_3{}^B)Fe(NNH_2)$ and $[(P_3{}^{Si})Fe(NNH_2)]^+$, in this chapter we characterize the electronic structures of the $[(P_3{}^B)Fe(NNMe_2)]^{+/0/-}$ redox series. While we have reported preliminary characterization of $[(P_3{}^B)Fe(NNH_2)]^+$ by ENDOR spectroscopy,[16] we were unable to determine the complete anisotropic hyperfine coupling (HFC) tensors for the N atoms of the "NNH_2" ligand. Complementary solution-phase studies of $[(P_3{}^B)Fe(NNH_2)]^{+/0}$ are hampered by the instability of these species.[16,17] However, previous work has shown that the *N*,*N*-dialkylated complexes $[(P_3{}^{Si})Fe(NNMe_2)]^{+/0}$ and $(P_3{}^B)Fe(NNMe_2)$ are excellent spectroscopic models for their protonated congeners, while exhibiting greater stability.[17,18] Herein, we have exploited this stability to characterize the nature of the Fe–$NNMe_2$ interaction over three oxidation states. This rich redox chemistry allows us to study complexes in $S_{tot} = 1/2$ ground states that are isoelectronic to both $[(P_3{}^B)Fe(NNH_2)]^+$ and $(P_3{}^{Si})Fe(NNH_2)$. Using CW and pulsed EPR, ^{57}Fe Mössbauer, NMR, UV-vis, and X-ray absorption spectroscopies, in combination with DFT and correlated ab initio calculations, herein we demonstrate that these "hydrazido" complexes possess multiconfigurational ground and low-lying excited states that are characterized by antiferromagnetic interactions between Fe and the "$NNMe_2$" ligand. A discussion of the relevance of these complex electronic structures to catalytic nitrogen fixation by $(P_3{}^E)Fe$ species is presented.

5.2 Results and Discussion

5.2.1 Preliminary Bonding Considerations

While the molecular orbital (MO) picture of the bonding between a transition metal center and isodiazene has been reviewed in the context of four-fold symmetry,[25,26] we will present a brief MO analysis under pseudo-three-fold symmetry, which applies the complexes under consideration here. As a free molecule, NNH_2 exhibits a planar, C_{2v} geometry.[36] The important orbitals for interaction with a transition metal center consist of an a_1-symmetry N_α lone pair (σ_N), a b_1-symmetry N_α lone pair (π_N), and the orthogonal b_2-symmetry π^*

orbital (π^*_{NN}); the low-lying, b_2-symmetry π-bonding orbital is not expected to interact strongly with a metal center in an end-on geometry, owing both to the energy- and overlap-mismatch.[25,26] The ground-state electron configuration is thus,

$$|(\sigma_N)^2(\pi_N)^2(\pi^*_{NN})^0\rangle$$

and sequential reduction to $[NNH_2]^{\bullet-}$ and $[NNH_2]^{2-}$ involves occupation of the π^*_{NN} orbital, reducing the formal N–N bond order from 2, to 1.5, and, finally, to 1, and increasing the pyramidalization at N_β from $\sum(\angle N_\beta) = 360°$, to 342°, and, finally, to 314°.[25] Both parent and *N*,*N*-dialkylisodiazenes are characterized by small π_N–π^*_{NN} energy gaps, giving rise to low-lying singlet and triplet states with the configuration[34–36]

$$|(\sigma_N)^2(\pi_N)^1(\pi^*_{NN})^1\rangle$$

The qualitative MO picture for a charge-neutral R'_3B–Fe–NNR_2 fragment under pseudo-C_{2v} symmetry is shown in Figure 5.2, A. Due to its low energy, σ_N should interact with the Fe center in an ionic, dative fashion.[25] The closely-spaced π_N and π^*_{NN} orbitals are expected to be closer in energy to the Fe 3d orbitals (low ionicity).[40] In the limit of large orbital overlap, this should result in the formation of two π-bonding interactions, one "in-plane" (b_1-symmetry) and one "out-of-plane" (b_2-symmetry). This simple imide-like bonding situation could be represented by a Fe≡N–$\ddot{N}H_2$ valence bond picture;[41] however, if N_β donates its lone pair into the b_2-symmetry π bond, this will lift the degeneracy of the two orthogonal π interactions (denoted $\Delta\epsilon_\pi$ in Figure 5.2, A) and produce a frontier π-orbital system isolobal to ketene ($O{=}C{=}CH_2$),[40,42] i.e., a Fe=N=NH_2 valence bond picture (Figure 5.2, B, top). In the limit of small orbital overlap, the Fe–NNR_2 bonding may be better described in terms of an exchange coupling interaction involving pairwise antiferromagnetic ordering of the π-symmetry electrons (Figure 5.2, B, bottom). In this limit, the bonding interactions within the Fe–NNR_2 moiety take on diradical character, which, in a configuration interaction (CI) *ansatz*, manifests in significant weights of the singly- and doubly-excited determinants shown schematically in Figure 5.2, C.[43–46]

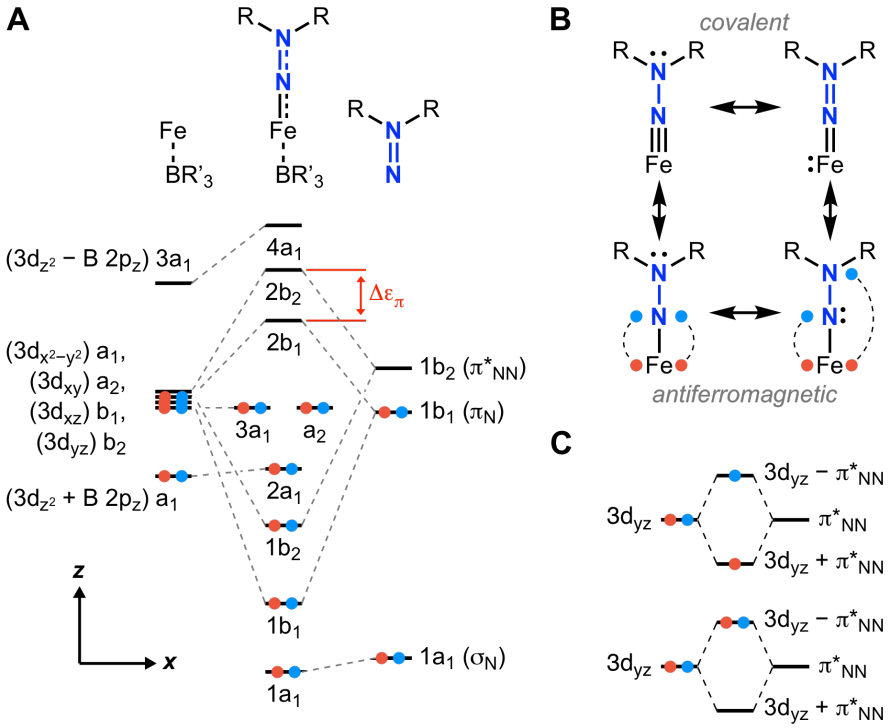

Figure 5.2: (A) Qualitative MO diagram for R'$_3$B–Fe–NNH$_2$ under pseudo-C_{2v} symmetry. (B) Valence bond diagrams describing possible resonance structures of the Fe–NNR$_2$ moiety, including covalent (top) and antiferromagnetic (bottom) extremes. Red dots indicate α spin electrons while blue dots indicate β spin electrons, with dotted lines indicating an antiferromagnetic exchange-coupling interaction. (C) Examples of electron configurations responsible for diradical bonding character, which can be interpreted in terms of antiferromagnetic coupling.

Introduction of an equatorial field of phosphine donors (i.e., the full $P_3{}^B$ ligand) reduces the molecular symmetry and changes the symmetry labels from b_1 to ($3d_{xz} \pm \pi_N$) and from b_2 to ($3d_{yz} \pm \pi^*_{NN}$). However, as the phosphine group orbitals are expected to mix most strongly with the $3d_{xy}$ and $3d_{x^2-y^2}$ orbitals, which are of δ symmetry with respect to the B–Fe–N$_\alpha$ axis, this will not alter the qualitative picture developed above, nor will in-plane distortions in the P–Fe–P angles. On the other hand, the degree of π-overlap will depend upon the Fe–N$_\alpha$–N$_\beta$ angle (*vide infra*).

5.2.2 Synthesis and Structural Analysis of [($P_3{}^B$)Fe(NNMe$_2$)]$^{+/0/-}$

The CV of ($P_3{}^B$)Fe(NNMe$_2$) reveals a reversible oxidation centered at −1.16 V vs. $Fc^{+/0}$ in THF.[17] Accordingly, one-electron oxidation by [FeCp*$_2$][BAr$^F{}_4$] yields

$[(P_3^B)Fe(NNMe_2)][BAr^F{}_4]$ in a $S_{tot} = 1/2$ ground state (Figure 5.3). $[(P_3^B)Fe(NNMe_2)]^+$ is moderately stable in the solid state and in solution, but decomposes to an intractable mixture upon prolonged heating at 70 °C. The CV of $(P_3^B)Fe(NNMe_2)$ also shows a quasi-reversible reduction centered around −2.65 V. This couple becomes increasingly reversible at higher scan rates, prompting us to see if the reduction product could be characterized in situ at low temperature. Indeed, reduction of $(P_3^B)Fe(NNMe_2)$ in 2-MeTHF with stoichiometric KC_8 at −78 °C produces a species which, on the basis of its distinctive Mössbauer and EPR properties (*vide infra*), we assign as $[(P_3^B)Fe(NNMe_2)]^-$ (Figure 5.3). $[(P_3^B)Fe(NNMe_2)]^-$ is unstable in solution and in the solid state, decomposing within minutes upon warming to ambient temperatures. Nevertheless, we were able to obtain a single crystal of the $[K(benzo\text{-}15\text{-}c\text{-}5)_2]$ salt of $[(P_3^B)Fe(NNMe_2)]^-$ suitable for X-ray diffraction, confirming the structural assignment made on the basis of spectroscopy.

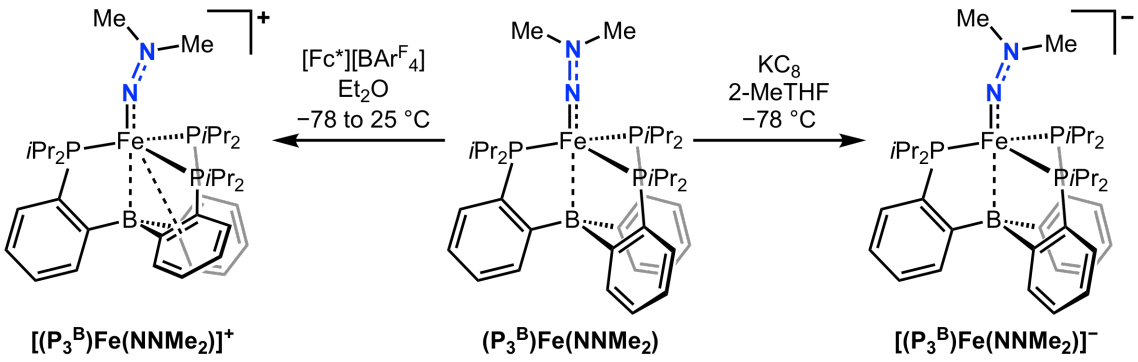

Figure 5.3: Synthesis of $[(P_3^B)Fe(NNMe_2)]^{+/-}$.

The solid-state structures of $[(P_3^B)Fe(NNMe_2)]^{+/0/-}$ determined by X-ray diffraction are shown in Figure 5.4. The "$NNMe_2$" ligand of $(P_3^B)Fe(NNMe_2)$ is planar ($\sum(\angle N_\beta)$ = 359.8°), and the molecular symmetry is pseudo-C_s, with an approximate mirror plane defined by P1, Fe, and N_α. The equatorial phosphine substituents adopt a slightly distorted trigonal arrangement about the Fe center, which approaches a tetrahedral geometry (τ = 0.34[47]). The Fe–N_α–N_β and B–Fe–N_α angles are close to linear (176.1° and 168.9°, respectively), and thus the solid-state geometry is consistent with the C_3 symmetry observed in solution, where rotation about the Fe–N_α or N_α–N_β bond is fast on the NMR time-scale,

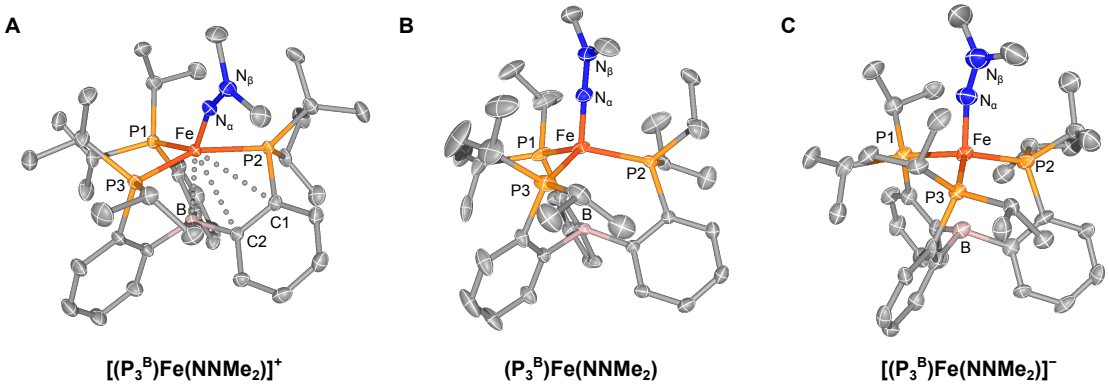

Figure 5.4: Solid-state structures of the $[(P_3{}^B)Fe(NNMe_2)]^{+/0/-}$ redox series. Ellipsoids are shown at 50% probability, with H-atoms and counterions omitted for clarity. Selected distances (Å) and angles (°): (A) d(Fe–B) = 2.315(3), d(Fe–P1) = 2.2816(9), d(Fe–P2) = 2.3168(9), d(Fe–P3) = 2.2626(9), d(Fe–C1) = 2.727(3), d(Fe–C2) = 2.683(3), ∠(P1–Fe–P2) = 100.31(3), ∠(P1–Fe–P3) = 96.10(3), ∠(P2–Fe–P3) = 154.93(4), ∠(B–Fe–N_α) = 157.36(1); (B) d(Fe–B) = 2.534(3), d(Fe–P1) = 2.2390(8), d(Fe–P2) = 2.2670(8), d(Fe–P3) = 2.2469(9), ∠(P1–Fe–P2) = 104.28(3), ∠(P1–Fe–P3) = 109.88(4), ∠(P2–Fe–P3) = 125.03(3), ∠(B–Fe–N_α) = 168.91(1); (C) d(Fe–B) = 2.472(9), d(Fe–P1) = 2.280(2), d(Fe–P2) = 2.243(2), d(Fe–P3) = 2.233(2), ∠(P1–Fe–P2) = 115.00(9), ∠(P1–Fe–P3) = 112.22(9), ∠(P2–Fe–P3) = 118.13(9), ∠(B–Fe–N_α) = 177.9(3).

even at −80 °C.[17] Upon oxidation to $[(P_3{}^B)Fe(NNMe_2)]^+$, the P2–Fe–P3 angle widens as an η^3-B, C, C interaction forms between the Fe center and the phenylene linker of one of the phosphine substituents. This distortion can be understood in terms of the MO diagram presented in Figure 5.2, A; oxidation should remove an electron from the quasi-degenerate ($3d_{xy}$, $3d_{x^2-y^2}$) pair, introducing a hole with which the phenylene π electrons can interact in a dative fashion. However, the approximate C_s symmetry is retained, as N_β remains planar ($\sum(\angle N_\beta)$ = 359.9°). In the oxidized complex, the Fe–N_α–N_β angle becomes significantly bent (159.6°), which is also observed for the isoelectronic complex $[(P_3{}^B)Fe(NNH_2)]^+$ (ca. 150°),[16] suggesting that the alkylated complex is a faithful structural model of this protonated species. In the reduced complex, $[(P_3{}^B)Fe(NNMe_2)]^-$, the planarity of N_β is preserved ($\sum(\angle N_\beta)$ = 359.9°), as is the pseudo-C_s symmetry, while the Fe–N_α–N_β angle bends to 161.7°, similar to that observed in the isoelectronic species, $(P_3{}^{Si})Fe(NNR_2)$ (R = H, 150.6° by DFT; R = Me, 158.6° by XRD).[18] The phosphine substituents are in a

nearly perfect trigonal arrangement about the Fe center, which adopts a geometry that is intermediate between trigonal bipyramidal and tetrahedral (τ = 0.53).

In this redox series, the Fe–N_α/N_α–N_β distances change in a non-linear fashion, from 1.738(3)/1.252(4) in $[(P_3{}^B)Fe(NNMe_2)]^+$, to 1.680(2)/1.293(3) in $(P_3{}^B)Fe(NNMe_2)$, to 1.771(7)/1.27(1) Å in $[(P_3{}^B)Fe(NNMe_2)]^-$. This range of N_α–N_β distances is longer than that calculated for free NNR_2 (1.20 to 1.22 Å[36,48]), but significantly shorter than that observed for free hydrazine (1.47 Å[49]) or $M(NNR_3)$ complexes (1.40 to 1.43 Å; R = H, alkyl, aryl[10,50–55]), suggesting some degree of N_α–N_β π bonding, and a formal bond order between a single and a double bond. This conclusion is supported by vibrational spectroscopy, which reveals N_α–N_β stretching vibrations for $[(P_3{}^B)Fe(NNMe_2)]^{+/0}$ (1495 and ~1337[iii] cm^{-1}) that span the range observed for $M(NNR_2)$ and $M(NNR_3)$ complexes (~1341 to 1420 cm^{-1}).[7,56,57] The greater range of variability in the Fe–N_α bond distances, relative to that observed for the N_α–N_β bond distances, is consistent with largely Fe-centered redox events. The Fe–N_α distance of $(P_3{}^B)Fe(NNMe_2)$ falls within the range observed for terminal Fe imido complexes (1.61 to 1.72 Å[58]), but is longer than those observed for C_3-symmetric terminal Fe nitrides (1.51 to 1.55 Å[17,59–61]), suggesting a formal bond order between a double and a triple bond. The Fe–N_α distances of $[(P_3{}^B)Fe(NNMe_2)]^{+/-}$ are longer than those typically observed for Fe imides, but are similar to those observed for the four-coordinate Fe(III) imidyl species reported by Betley and co-workers (1.77 Å).[62,63] Collectively, these data indicate that neither of the limiting closed-shell resonance structures shown in Figure 5.2, B dominate the valence-bond picture of these complexes.

5.2.3 ^{57}Fe Mössbauer Spectroscopy

The Mössbauer spectrum of $(P_3{}^B)Fe(NNMe_2)$ has been reported in a preliminary communication,[17] and its parameters are collected in Table 5.1, along with those of related $(P_3{}^E)Fe$ complexes. While $(P_3{}^B)Fe(NNMe_2)$ has very similar parameters to those

[iii]For $(P_3{}^B)Fe(NNMe_2)$, the N_α–N_β stretching vibration is mixed with N_β–C modes, and therefore the precise assignment of this resonance is dubious.

of $(P_3{}^B)Fe(NNH_2)$ and the isostructural, silylated complex $(P_3{}^B)Fe(NN[Si_2])$ (N[Si_2] = 2,2,5,5-tetramethyl-1-aza-2,5-disilacyclopentyl), the isomer shift of the isoelectronic terminal imido complex $(P_3{}^B)Fe(NAd)$ is significantly smaller than those of the $(P_3{}^B)Fe(NNR_2)$ complexes. This difference can be attributed to increased covalency in the Fe–N interaction of the genuine imido complex (see Appendix E),[17,22,64] which is consistent with the structural evidence for a significant contribution from the ketene-like valence-bond resonance structure shown in Figure 5.2, B for the "amino-imido" complex $(P_3{}^B)Fe(NNMe_2)$, and, by inference, $(P_3{}^B)Fe(NNH_2)$ and $(P_3{}^B)Fe(NN[Si_2])$.

The isomer shift of the oxidized complex increases by 0.14 mm s^{-1} relative to its charge-neutral congener, while that of the reduced complex increases by 0.22 mm s^{-1}, reflecting the increased Fe–N_α and Fe–P distances observed crystallographically (see Appendix E). The Mössbauer parameters of $[(P_3{}^B)Fe(NNMe_2)]^+$ are close to those reported for its protonated analogue,[16] further illustrating the utility of the alkylated complexes as spectroscopic models. Interestingly, even at temperatures as high as 80 K the ground state Kramer's doublet of $[(P_3{}^B)Fe(NNMe_2)]^+$ is in the limit of slow electronic relaxation, which has allowed us to estimate the ^{57}Fe HFC tensor from the field dependence of the spectrum (Figure 5.5, A).

$[(P_3{}^B)Fe(NNMe_2)]^-$ also exhibits slow electronic relaxation at 80 K (Figure 5.5, B), which was observed for the isoelectronic silyl complexes $(P_3{}^{Si})Fe(NNR_2)$ (R = H, Me).[18] A comparison of their ^{57}Fe hyperfine coupling constants shows that all of these formally 19 e^- species exhibit similar electronic structures (Table 5.1). Notably, the isotropic ^{57}Fe HFC constant ($a_{iso}(^{57}Fe)$) of $[(P_3{}^B)Fe(NNMe_2)]^-$ is more than two times larger than that of $[(P_3{}^B)Fe(NNMe_2)]^+$; indeed, a similar trend in a_{iso} is observed for nearly every magnetic nucleus in the coordination sphere of Fe (*vide infra*).

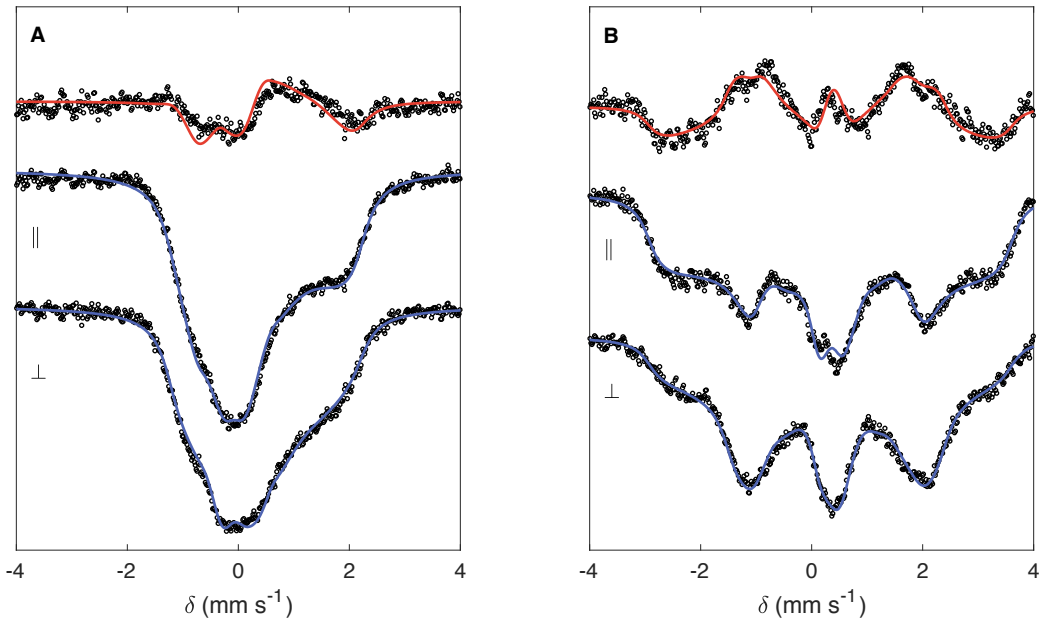

Figure 5.5: Frozen-solution Mössbauer spectra collected at 80 K in the presence of a 50 mT external vield, oriented parallel or perpendicular to the γ-rays, as indicated. Data are shown as open circles, with simulations in blue; the field orientation difference spectra are shown at the top, with the simulated difference spectrum in red. For clarity, quadrupole doublet impurities have been subtracted from the spectra. (A) Spectra of $[(P_3{}^B)Fe(NNMe_2)]^+$. (B) Spectra of $[(P_3{}^B)Fe(NNMe_2)]^-$.

Table 5.1: Collected ^{57}Fe Mössbauer Parameters

Complex	S (vec^a)	δ (mm s^{-1})	$\lvert\Delta E_Q\rvert$ (mm s^{-1})	A_1 (MHz)^b	A_2 (MHz)^b	A_3 (MHz)^b	a_{iso} (MHz)
$(P_3{}^B)Fe(NNMe_2)$	0 (18)	0.17	1.73	–	–	–	–
$(P_3{}^B)Fe(NNH_2)$[c]	0 (18)	0.14	1.63	–	–	–	–
$(P_3{}^B)Fe(NN[Si_2])$	0 (18)	0.19	1.85	–	–	–	–
$[(P_3{}^{Si})Fe(NNH_2)]^+$ [d]	0 (18)	0.13	1.48	–	–	–	–
$[(P_3{}^{Si})Fe(NNMe_2)]^+$ [d]	0 (18)	0.14	1.49	–	–	–	–
$(P_3{}^B)Fe(NAd)$ [e]	0 (18)	0.04	1.40	–	–	–	–
$[(P_3{}^B)Fe(NNMe_2)]^+$	1/2 (17)	0.31	1.16	24.0	9.0	0.1	11.0
$[(P_3{}^B)Fe(NNH_2)]^+$ [f]	1/2 (17)	0.35	1.02	n.d.	n.d.	n.d.	n.d.
$[(P_3{}^B)Fe(NNMe_2)]^-$	1/2 (19)	0.39	1.20	18.1	15.3	53.9	29.1
$(P_3{}^{Si})Fe(NNH_2)$[d]	1/2 (19)	0.31	0.86	20.1	10.2	45.7	25.4
$(P_3{}^{Si})Fe(NNMe_2)$[d]	1/2 (19)	0.36	0.90	17.7	12.2	49.6	26.5

[a] *vec* is the valence electron count assuming the NNR_2 ligand is a 4 e^- donor.

[b] The orientation of the HFC tensor is $g_1 = g_{min}$, $g_2 = g_{mid}$, $g_3 = g_{max}$. The g-tensors were determined from EPR spectroscopy. The orientation of the HFC tensor should be taken as approximate, given that only two magnetically-split spectra were used to constrain the simulation. However, as a_{iso} is invariant to rotations, this value is determined more accurately.

[c] Data from [17].

[d] Data from [18].

[e] Data from [22].

[f] Data from [16].

5.2.4 Electronic Structure and Excited State Chemistry of (P_3^B)Fe($NNMe_2$)

5.2.4.1 Excited states from UV-vis and VT NMR

The optical spectra of (P_3^B)Fe($NNMe_2$), [(P_3^{Si})Fe(NNH_2)]$^+$, and [(P_3^{Si})Fe($NNMe_2$)]$^+$ all exhibit resonances in the range from 12,500 to 13,500 and from 18,000 to 19,000 cm^{-1}, which we hypothesize are due to transitions involving the common Fe–NNR_2 core (*vide infra*). To investigate this in greater detail we have collected UV-vis spectra of (P_3^B)Fe(NAd), (P_3^B)Fe(NN[SiH_2]), and (P_3^B)Fe($NNMe_2$), which are shown in Figure 5.6, A through C, with a Gaussian spectral deconvolution. (P_3^B)Fe(NAd) features just a single resolved optical resonance (Figure 5.6, A), which we assign as the transition from the filled, quasi-degenerate e orbital set (of $3d_{xy}$ and $3d_{x^2-y^2}$ parentage) into the empty, quasi-degenerate e orbital set of π*-symmetry (of $3d_{xz}$ and $3d_{yz}$ parentage) expected for a pseudo-tetrahedral, terminal Fe imide under C_3 symmetry.[41] This assignment is corroborated by TD-DFT calculations.

In the optical spectrum of (P_3^B)Fe(NN[SiH_2]) (Figure 5.6, B), these transitions are preserved, but the degeneracy of the excited states is lifted slightly, presumably due to donation of the N_β lone pair into the "in-plane" π*-symmetry interaction ($3d_{yz} - \pi$). Using the UV-vis transitions as a proxy for a one-particle spectrum based on the MO diagram of Figure 5.2, A, we can estimate $\Delta\epsilon_\pi \approx 1,740$ cm^{-1}. Moving to the alkylated complex (P_3^B)Fe($NNMe_2$), the splitting in these transitions is even more dramatic (Figure 5.6, C); in fact, three resonances are now required to adequately fit the experimental spectrum. From this spectrum, we estimate $\Delta\epsilon_\pi \approx 5,570$ cm^{-1}, indicating a significant N_α–N_β π interaction, in agreement with the crystallographic analysis. We note that the Fe *K*-edge XANES spectrum of (P_3^B)Fe($NNMe_2$) also exhibits two resolved resonances, which likely arise from similar acceptor states to those observed optically;[65] moreover, the XANES spectrum of the protonated analogue, (P_3^B)Fe(NNH_2), is nearly identical to that of (P_3^B)Fe($NNMe_2$).[17]

Although (P_3^B)Fe($NNMe_2$) is a diamagnet in its ground state, preliminary VT NMR and DFT studies have evidenced the presence of a low-lying, $S_{tot} = 1$ paramagnetic excited

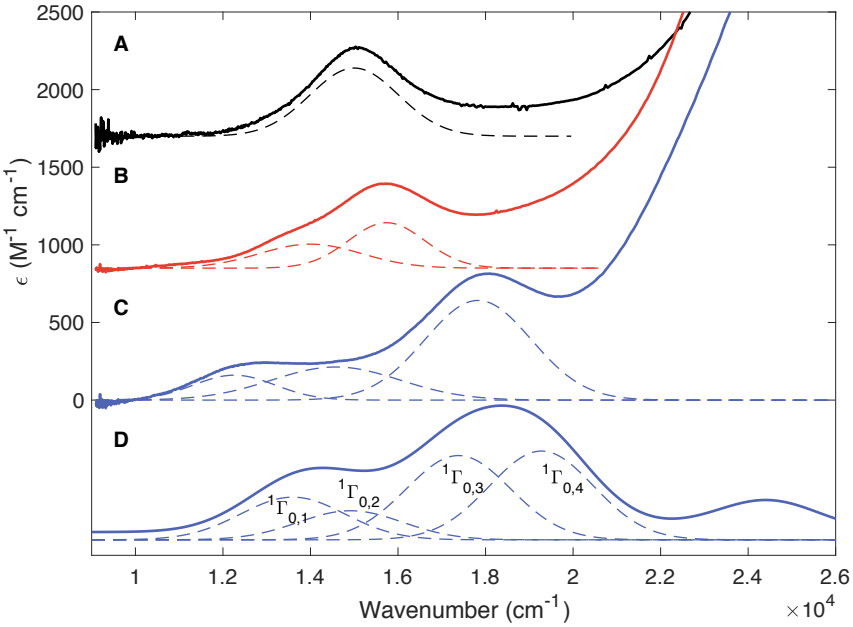

Figure 5.6: (A) UV-vis spectrum of $(P_3{}^B)$Fe(NAd) (THF, 298 K). (B) UV-vis spectrum of $(P_3{}^B)$Fe(NN[Si_2]) (2-MeTHF, 153 K). (C) UV-vis spectrum of $(P_3{}^B)$Fe($NNMe_2$) (2-MeTHF, 153 K). For A through C, raw data are plotted as a solid line, with a Gaussian spectral deconvolution shown in dotted lines. (D) Ab initio electronic spectrum of $(P_3{}^B)$Fe($NNMe_2$) computed from an NEVPT2 calculation on top of a SA-CASSCF(10,10) reference including 10 singlet roots. Contributions from individual states are shown in dotted lines.

state.[17] Similar behavior was observed for the isoelectronic complex $[(P_3{}^{Si})Fe(NNMe_2)]^+$.[18] In both of these cases, fitting the VT NMR data to a simple two-state, Boltzmann-weighted magnetization function showed that these triplet states lie only 3.7 ± 0.1 and 6.7 ± 0.3 kcal mol^{-1} (1300 ± 30 and 2300 ± 100 cm^{-1}) above the diamagnetic ground states, respectively.[17,18] It is noteworthy that the entropic contributions to these energy differences appear to be small, and we have obtained a more precise estimate of the adiabatic singlet–triplet gap of $(P_3{}^B)$Fe($NNMe_2$) of 1266 ± 7 cm^{-1} assuming $\Delta G \approx \Delta H$.

While the atoms directly coordinated to the Fe center of $(P_3{}^B)$Fe($NNMe_2$) are expected to experience large magnetization in this excited state, VT ^{15}N NMR studies of $(P_3{}^B)$Fe($^{15}N^{15}NMe_2$) reveal that both N_α and N_β accumulate significant spin density in the excited state (Figure 5.7, A). Moreover, an examination of the VT ^1H NMR data shows

that the magnetization experienced by the N_β-CH_3 protons is roughly an order of magnitude greater than that of any of the protons on the $P_3{}^B$ ligand (Figure 5.7, B). This is most consistent with significant spin delocalization onto the entire "$NNMe_2$" moiety in the excited state, as opposed to only spin polarization by Fe-centered electrons. For example, if one assumes that the N_β-CH_3 protons can be treated as point-dipoles, which would be reasonable for a largely Fe-centered spin given that these protons are, on average, > 4 Å from the Fe ion based on the DFT-optimzed triplet geometry, one would estimate that $|a_{iso}| \approx 50$ MHz. Given that $a_{iso}(^1H_\gamma) = 19.4$ and 39.8 MHz for the *N*,*N*-dimethylhydrazyl radical and the *N*,*N*-dimethylhydrazyl radical cation,[37,39] respectively, this value appears to be unreasonably large. These data belie a more complex electronic structure, in which the both the Fermi- and pseudo-contact contributions to the paramagnetic ^1H NMR shift are large.

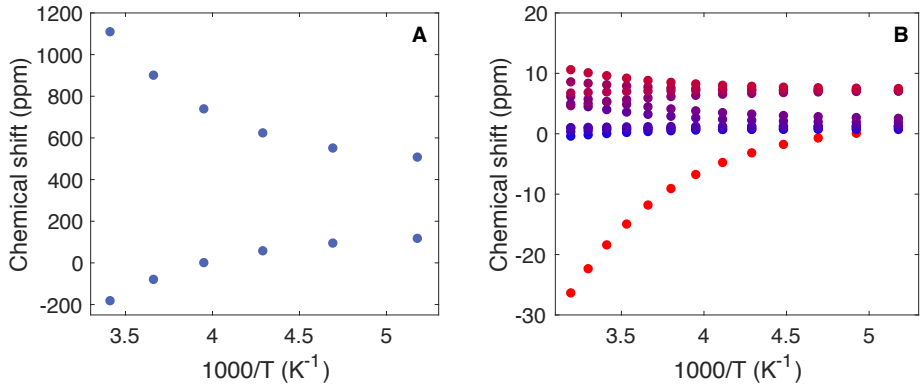

Figure 5.7: (A) Variable temperature ^{15}N NMR for $(P_3{}^B)Fe(^{15}N^{15}NMe_2)$. (B) Variable temperature ^1H NMR for $(P_3{}^B)Fe(NNMe_2)$. The resonance due to the N_β-CH_3 protons is plotted in red.

Under a point-dipole approximation, this would require large *g*-anisotropy in the excited state,[66] and, hence, manifold low-lying $S_{tot} = 1$ states, which is unusual for Fe centers in non-Kramer's spin states.[67–70] Alternatively, significant spin delocaliztion onto the entire "$NNMe_2$" moiety would invalidate the point-dipole approximation altogether. This latter interpretation is more consistent with the VT ^{15}N NMR data, and points to an electronic structure of the "$NNMe_2$" moiety with open-shell character in the excited state. This

could be explained, for example, in terms of a S= 1/2 $[NNMe_2]^{\bullet-}$ ligand either coupled ferromagnetically to an $S = 1/2$ or antiferromagnetically to an $S = 3/2$ Fe center. In turn, this suggests that the $S_{tot} = 0$ ground state of $(P_3{}^B)Fe(NNMe_2)$ may possesses open-shell singlet character.

5.2.4.2 Multireference Character from Broken-symmetry DFT and CASSCF

Open-shell singlets, and more general cases of exchange coupling, cannot be properly represented in a single-reference DFT *ansatz*, but can be approximated using the broken-symmetry (BS) method.[71] However, DFT spin-state energetics are highly dependent on the fraction of exact Hartree-Fock (HF) exchange included in the functional, so we undertook a series of DFT calculations using the same parent functional and basis set, but incorporating either 0% (TPSS), 10% (TPSSh), or 25% (TPSS0) HF exchange. These calculations were performed on the geometry of either the singlet or the triplet state of $(P_3{}^B)Fe(NNMe_2)$ optimized using 0% HF, which accurately reproduced the experimental ground-state structures of $[(P_3{}^B)Fe(NNMe_2)]^{+/0/-}$ determined by XRD.

Hereafter, we will refer to individual electronic states according to the nomenclature ${}^{2S+1}\Gamma_{n,m}$, where n is the charge of $[(P_3{}^B)Fe(NNMe_2)]^n$ and m numbers the state, with $m = 0$ corresponding to the ground state. In the singlet geometry of $(P_3{}^B)Fe(NNMe_2)$, attempts to find a BS, $S = 0$ solution (${}^1\Gamma_{0,0}^{BS}$) with 0% or 10% HF invariably collapsed to the spin-restricted solution (${}^1\Gamma_{0,0}^{RKS}$). However, such a solution was found in the 25% HF calculation, by first computing a high-spin ($S = 2$) solution, and then flipping the spins on the "$NNMe_2$" ligand and re-converging along the singlet surface. With every functional, the $S = 1$ solution exhibited BS character in either the singlet or the triplet geometry, as determined from performing the corresponding orbital transformation on the set of optimized Kohn-Sham orbitals.[72] These solutions could also be constructed explicitly using the BS method.

As expected, increasing the HF character decreases the energy differences between

the singlet, triplet, and quintet states (Table 5.2). It should be noted that the energies of the BS solutions are not corrected for spin contamination, and these calculations do not include thermal or environmental corrections. In light of this, the small absolute adiabatic singlet-triplet gaps predicted by the 0% and 10% HF calculations appear to provide the best accordance with experiment, although in the 10% case the ground state is incorrectly predicted to be $^{3}\Gamma_{0,0}$.

Table 5.2: Relative Electronic Energies (cm^{-1}) for ($P_3{}^B$)Fe($NNMe_2$) from VT NMR, DFT, and NEVPT2

State	VT NMR	0% HF	10% HF	25% HF	NEVPT2
		Singlet geometry			
$^{1}\Gamma_{0,0}^{RKS}$	–	0	0	693	–
$^{1}\Gamma_{0,0}$	0	–	–	0[a]	0
$^{3}\Gamma_{0,0}$	–	5526[b]	3137[b]	−577[b]	6324[c]
$^{5}\Gamma_{0,0}$	–	20050	16063	10117	23816[c]
		Triplet geometry			
$^{3}\Gamma_{0,0}$	1266 ± 7	1330[b]	−1415[b]	−6003[b]	6074[d]
$^{5}\Gamma_{0,0}$	–	14386	9931	3067	18819[d]

[a] Approximating $E(^{1}\Gamma) \approx E(^{1}\Gamma^{BS})$.
[b] Approximating $E(^{3}\Gamma) \approx E(^{3}\Gamma^{BS})$.
[c] An NEVPT2 calculation was performed using a SA-CASSCF(10,10) reference including three roots corresponding to the lowest energy singlet, triplet, and quintet states.
[d] An NEVPT2 calculation was performed using a SA-CASSCF(10,10) reference including two roots corresponding to the lowest energy triplet and quintet states.

To understand the nature of the spin-coupling in this system, the magnetic orbitals from the 10% HF $^{3}\Gamma_{0,0}^{BS}$ solution in the triplet geometry are shown in Figure 5.8, A. In both the singlet and triplet geometries, two pairs of magnetic orbitals can be identified that clearly correspond to strong antiferromagnetic coupling between the Fe $3d_{z^2}$ and B $2p_z$ orbitals, and the Fe $3d_{yz}$ and π^*_{NN} orbitals. In the singlet geometry, the SOMOs are largely Fe-centered and consist of the $3d_{x^2-y^2}$ and ($3d_{xz} - \pi_N$) orbitals. Upon relaxation to the triplet geometry, the antiferromagnetic couplings weaken, as judged by the overlap

between the corresponding α and β spin orbitals ($\langle\alpha|\beta\rangle$), concomitant with a bending of the Fe–N–N angle from 174° to 164°. This angular distortion is quite similar to that observed crystallographically in the reduction of $(P_3{}^B)Fe(NNMe_2)$ to $[(P_3{}^B)Fe(NNMe_2)]^-$, and is accompanied by decreased overlap between the $3d_{xz}$ and π_N orbitals, as judged by a Löwdin population analysis. Indeed, upon geometric relaxation, the Fe character of the $3d_{xz}$-derived SOMO increases from 69% to 78%, which can be understood in terms of a partial re-hybridization of the N_α π_N lone-pair to avoid unfavorable π^* interactions with the Fe ion.

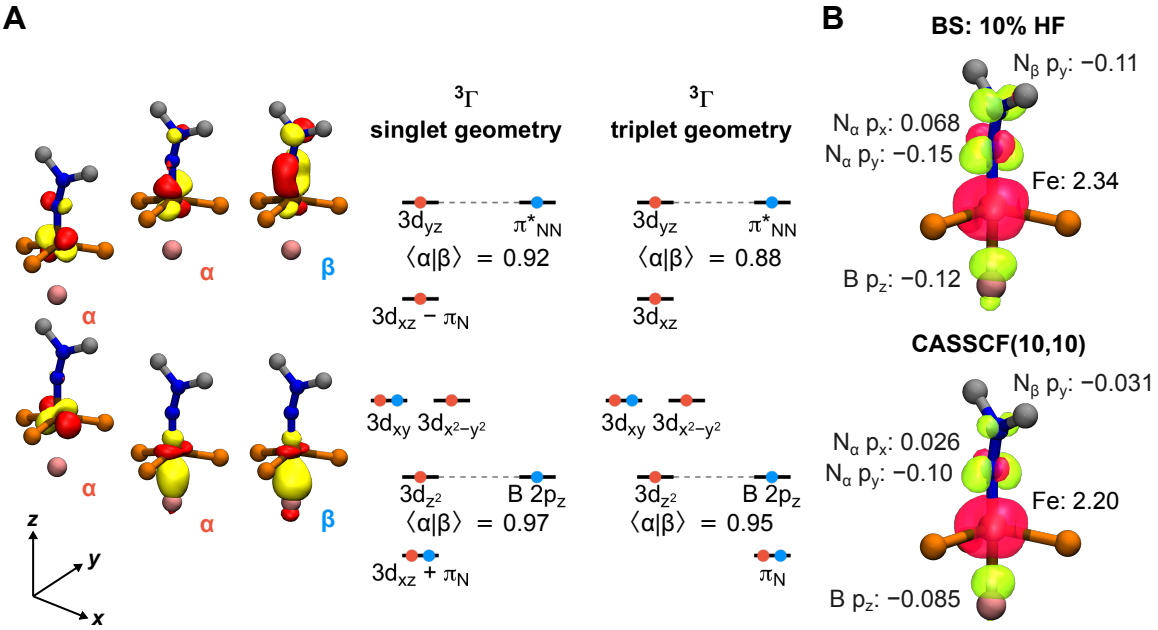

Figure 5.8: (A) Magnetic orbitals from the ${}^3\Gamma_{0,0}^{BS}$ state of $(P_3{}^B)Fe(NNMe_2)$ computed with 10% HF in the triplet geometry (isovalue = 0.075 a.u.), along with qualitative MO diagrams. α spins are shown in red, while β spins are shown in blue. (B) Spin density isosurfaces of the ${}^3\Gamma_{0,0}$ state of $(P_3{}^B)Fe(NNMe_2)$ in the triplet geometry (isovalue = 0.005 a.u.), from a 10% HF BS DFT calculation (top), and from a ground state specific CASSCF(10,10) wavefunction (bottom). α density is shown in red, while β density is shown in green. Selected Löwdin spin populations are shown.

These BS solutions can be understood in terms of the modified MO diagram of Figure 5.8, A, where the reduced overlap of the $3d_{yz}/\pi^*_{NN}$ and $3d_{z^2}/B\ 2p_z$ interactions produces an electronic structure most concisely described as a high-spin, $S = 2$, Fe(II) center antiferromagnetically coupled to both a $S = 1/2$ borane radical anion ($[R_3B]^{\bullet-}$)

and a $S = 1/2$ $[NNMe_2]^{\bullet-}$ ligand in the $^3\Gamma_{0,0}$ state. This electronic structure rationalizes the VT NMR data presented above, as it results in negative π-symmetry spin density at both N atoms due to population of the π^*_{NN} orbital. In addition, N_α is predicted to bear orthogonal, positive π-symmetry spin density due to delocalization via the $3d_{xz}$-based SOMO, producing an unusual, rhombic spin distribution about this atom (Figure 5.8, B).

According to this analysis, the $^1\Gamma_{0,0}$ state should correspond to the pairing of the two largely Fe-centered spins. However, the DFT calculations are ambiguous with respect to the open-shell singlet character of this state. To address this, we performed calculations based on the CASSCF *ansatz* using a CAS(10,10) reference with an active space composed of the five 3d, B $2p_z$, π_N, and π^*_{NN} orbitals, with an additional two second-shell 3d' orbitals to provide greater flexibility for the occupied $3d_{xy}$ and $3d_{x^2-y^2}$ orbitals.[73] From a ground-state-specific calculation, the $^1\Gamma_{0,0}$ state does indeed exhibit multireference character, with the closed-shell configuration,

$$|(3d_{xy})^2(3d_{x^2-y^2})^2(3d_{xz}+\pi_N)^2(3d_{z^2}+2p_z)^2(3d_{yz}+\pi^*_{NN})^2\rangle$$

composing only 79.8% of the zeroth order wavefunction. The next three most important configurations (comprising 8.7% of the wavefunction) involve single and double excitations from the bonding $(3d_{xz}+\pi_N)$, $(3d_{z^2}+2p_z)$, and $(3d_{yz}+\pi^*_{NN})$ orbitals into their antibonding counterparts, which indicates antiferromagnetic character. The antiferromagnetic nature of these interactions is hinted at from localization of the active space orbitals, which results in strong spatial separation of the Fe 3d and π_N[iv]/π^*_{NN} orbitals;[45] the B $2p_z$ orbital becomes largely B-centered, although the degree of localization is less, consistent with greater relative covalency (Figure 5.9). Unfortunately, in the localized basis, the CI expansion of the wavefunction becomes very diffuse, but an examination of the occupation numbers of the active space orbitals suggests a dominant configuration,

$$|(3d)^6(2p_z)^1(\pi_N)^2(\pi^*_{NN})^1\rangle$$

[iv]The π_N orbital is admixed with a σ-type phosphorous group orbital.

While an analysis of such localized orbitals has been used to argue for the presence of metal-ligand antiferromagnetic coupling,[45,46] this can be misleading because configurations corresponding to a normal covalent bond and an antiferromagnetic exchange coupling interaction cannot be distinguished.[44]

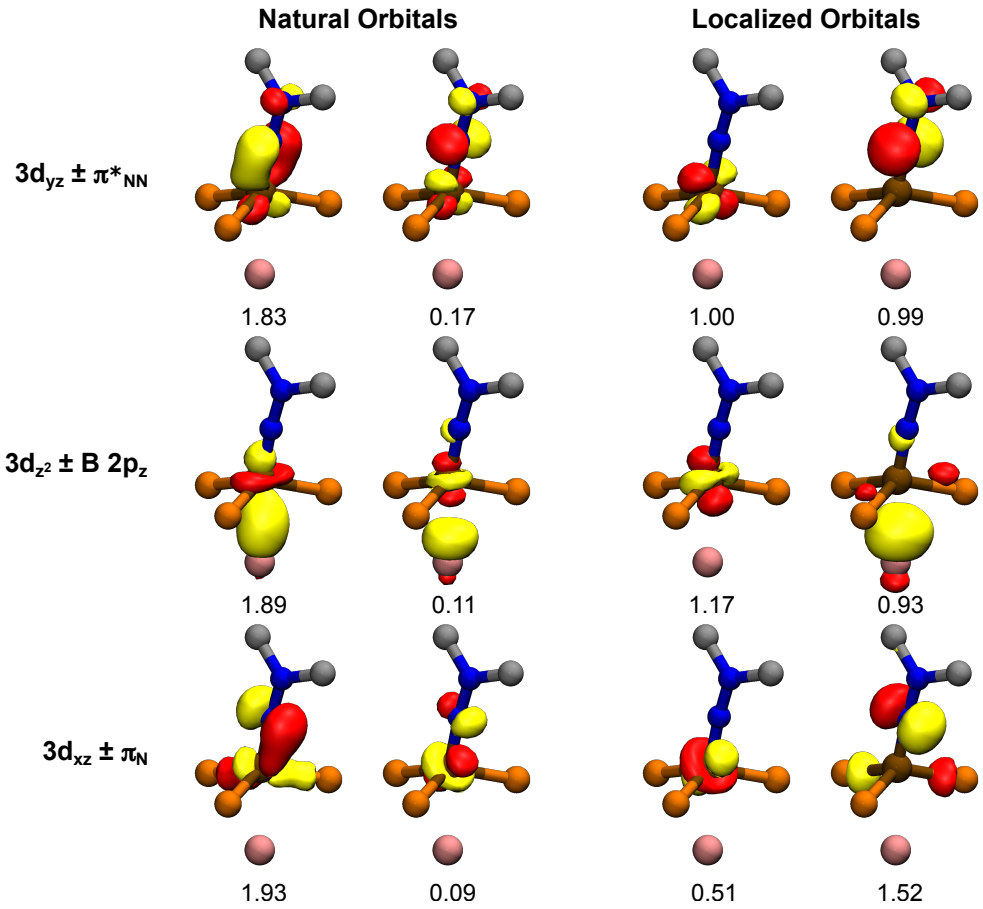

Figure 5.9: Active space orbitals (isovalue = 0.075) corresponding to the Fe–NNMe$_2$ π and Fe–B σ interactions from a ground state specific CASSCF(10,10) calculation of the $^1\Gamma_{0,0}$ state. Both the natural and localized orbital bases are presented. Occupations numbers are given below each orbital.

An unbiased, quantitative measure of antiferromagnetic character of the $^1\Gamma_{0,0}$ state can be obtained from the natural orbital occupation numbers (NOONs) of the bonding/antibonding NOs ($n_\pm$) describing the Fe–NNMe$_2$ π and Fe–B σ bonding. A measure of the diradical character (Y) of these interactions can be defined from their effective bond order ($b_{\text{eff}} = (n_+ - n_-)/2$), as a covalent bond has $b_{\text{eff}} = 1$ and a pure diradical

has $b_{\text{eff}} = 0$.[43,44] Using the NOONs from the entire active space, we can also ascertain the open-shell singlet character from the number of "effectively unpaired" electrons (using the Davidson–Yamaguchi definition, $N_D = \sum_i n_i(2 - n_i)$, or the Head-Gordon definition $N_U = \sum_i 1 - |1 - n_i|$, where i runs over the active space orbitals).[74–76] Using these indices, we have tabulated the diradical character of the Fe–$NNMe_2$ π and Fe–B σ bonding and the number of effectively unpaired electrons for the $^1\Gamma_{0,0}$ state in Table 5.3. Although there are only about 1 to 2 effectively unpaired electrons, which would seemingly correspond to a singlet diradical, the combined (unnormalized) polyradical character of 28% has significant contributions from both the π and the σ bonding.

Table 5.3: NOON-based Chemical Bonding Indices for ($P_3{}^B$)Fe($NNMe_2$) from CASSCF Calculations

NOs	$^1\Gamma_{0,0}$					$^3\Gamma_{0,0}{}^b$				
	n_+	n_-	Y^a	N_D	N_U	n_+	n_-	Y^a	N_D	N_U
$3d_{z^2} \pm$ B $2p_z$	1.89	0.11	0.11	0.42	0.22	1.79	0.21	0.21	0.75	0.42
$3d_{yz} \pm \pi^*_{NN}$	1.83	0.17	0.17	0.62	0.34	1.72	0.28	0.28	0.96	0.56
CAS	–	–	–	1.76	0.93	–	–	–	3.94	3.08

[a] $Y = 1 - \frac{n_+ - n_-}{2}$. Note that for a spatially-matched bond/antibond pair, $Y = n_-$.
[b] Computed in the triplet geometry.

Repeating these calculations for the $^3\Gamma_{0,0}$ state in the triplet geometry shows that, consistent with the BS DFT calculations, the antiferromagnetic character of the zeroth order wavefunction increases significantly, which is reflected in the increased polyradical character of the wavefunction (49%, Table 5.3), although the number of effectively unpaired electrons remains approximately 1 to 2 in excess of those expected for a triplet. Also consistent with the BS calculations, the overlap between the Fe $3d_{xz}$ and π_N orbitals decreases in the triplet state such that their antibonding combination is essentially a pure 3d orbital (87% Fe). The weakened antiferromagnetic couplings increase the multireference character of the wavefunction, with the configuration,

$$|(\pi_N)^2(3d_{xy})^2(3d_{z^2} + 2p_z)^2(3d_{yz} + \pi^*_{NN})^2(3d_{x^2-y^2})^1(3d_{xz})^1\rangle$$

comprising only 69.6% of the ground state wavefunction, with the next two most important configurations,

$$|(\pi_N)^2(3d_{xy})^2(3d_{z^2}+2p_z)^2(3d_{yz}+\pi^*_{NN})^0(3d_{x^2-y^2})^1(3d_{xz})^1(3d_{yz}-\pi^*_{NN})^2\rangle$$
$$|(\pi_N)^2(3d_{xy})^2(3d_{z^2}+2p_z)^2(3d_{yz}+\pi^*_{NN})^1(3d_{x^2-y^2})^1(3d_{xz})^1(3d_{yz}-\pi^*_{NN})^1\rangle$$

having a weight of 13%. These configurations are responsible, in part, for the antiferromagnetic character of the π bonding, and produce a spin density distribution that is, qualitatively, in agreement with the BS DFT results. Comparing the 10% HF-calculated spin density with that predicted by the CASSCF(10,10) wavefunction (Figure 5.8, B), it can be seen that these methods predict the same spin topology, but differ quantitatively. This can be attributed to the spin-contamination of the BS DFT solution ($\langle\hat{S}^2\rangle = 2.34$ for the 10% HF calculation).[77]

To determine whether these multireference calculations provide an accurate basis for the static correlation effects in the bonding in ($P_3{}^B$)Fe($NNMe_2$), we have performed second-order N-electron valence perturbation theory (NEVPT2) calculations on top of state-averaged (SA) CASSCF(10,10) reference wavefunctions to predict the energetic ordering of low-lying excited states. As can be seen in Table 5.2, these NEVPT2 calculations correctly predict the ground state multiplicity, although the adiabatic singlet-triplet gap is overestimated. However, as shown in Figure 5.6, D, the NEVPT2-calculated electronic spectrum is in nearly quantitative agreement with experiment. The overestimated singlet-triplet gap can thus be attributed, in part, to inaccuracy in the DFT-predicted geometry of the triplet state, rather than deficiencies in the zeroth order CASSCF reference or the perturbative treatment of dynamic correlation.

On the basis of these calculations, we can assign the optical transitions of ($P_3{}^B$)Fe($NNMe_2$) as being due principally to transitions from the filled $3d_{xy}$ and $3d_{x^2-y^2}$ orbitals into the ($3d_{xz} - \pi_N$) and ($3d_{yz} - \pi^*_{NN}$) orbitals, as postulated. One-electron excitations from these orbitals into the ($3d_{xz} - \pi_N$) orbital compose 60 to 70% of the wavefunctions of

the first two excited singlet states, $^1\Gamma_{0,1}$ and $^1\Gamma_{0,2}$. The next two states, $^1\Gamma_{0,3}$ and $^1\Gamma_{0,4}$, are of more mixed character, containing contributions from one-electron excitations from the $3d_{xy}$, $3d_{x^2-y^2}$, and $(3d_{z^2} + 2p_z)$ orbitals into both the $(3d_{xz} - \pi_N)$ and $(3d_{yz} - \pi^*_{NN})$ orbitals, although the latter is the dominant acceptor orbital.

These calculations validate the schematic MO description of the $^3\Gamma_{0,0}$ excited state proposed in Figure 5.8, A, and reveal the open-shell character of the singlet ground state, $^1\Gamma_{0,0}$. While the electronic structure of the ground state is clearly multiconfigurational, the dominant antiferromagnetic terms involve the $3d_{yz}/\pi^*_{NN}$ and $3d_{z^2}$/B $2p_z$ interactions, leading to a succinct description of the $^1\Gamma_{0,0}$ state as an intermediate-spin, $S = 1$ Fe(II) center coupled antiferromagnetically to $S = 1/2$ $[NNMe_2]^{\bullet-}$ and $S = 1/2$ $[R_3B]^{\bullet-}$ ligands.

5.2.5 Electronic Structures of $[(P_3{}^B)Fe(NNMe_2)]^{+/-}$ from Pulsed EPR Studies

With an understanding of the electronic structures of the charge-neutral states of $(P_3{}^B)Fe(NNMe_2)$, we now turn to the one-electron oxidized and reduced forms. As these redox states both exhibit slowly-relaxing $S_{tot} = 1/2$ ground states, we have applied CW and pulsed EPR techniques to completely determine the HFC tensors of the "$NNMe_2$" ligand and the other atoms in the primary coordination sphere of Fe. The experimental determination of the spin density distribution allows for validation of the electronic structures of these redox states predicted theoretically.

5.2.5.1 Experimental Spin Density Distribution

The ground state doublet of $[(P_3{}^B)Fe(NNMe_2)]^-$ ($^2\Gamma_{-,0}$) possesses low g-anisotropy, with a g-tensor that is quite similar to those of the isoelectronic silyl complexes, $(P_3{}^{Si})Fe(NNR_2)$ (R = H, Me; Table 5.4). Figure 5.10, A and B, shows the second-derivative CW X-band EPR spectra of $[(P_3{}^B)Fe(^{14}N^{14}NMe_2)]^-$ and $[(P_3{}^B)Fe(^{15}N^{15}NMe_2)]^-$, along with simulations. The simulation parameters are collected in Table 5.5. Although these simulations contain six independent HFC tensors, those of $^{14/15}N_\alpha$, $^{14/15}N_\beta$, ^{11}B, and the $^{31}P_\gamma$ nucleus were

determined independently via Q-band ENDOR and HYSCORE spectroscopy (Figure 5.11 and Appendix D). The HFC tensors of the remaining two, more strongly-coupled, ^{31}P atoms were determined through simultaneous fitting of X-band CW and ENDOR data. As can be seen from the ^{14}N–^{15}N difference spectrum shown in Figure 5.10, C, the final simulation is of high quality.

Table 5.4: Collected g-tensors from Experiment and Theory

Complex	g_1	g_2	g_3	g_{iso}	Δg^a
$[(P_3{}^B)Fe(NNMe_2)]^-$					
Expt.	2.006	2.041	2.068	2.038	0.062
10% HF	2.033	2.043	2.056	2.044	0.023
CASCI[b]	2.001	2.038	2.056	2.032	0.055
$(P_3{}^{Si})Fe(NNH_2)$	2.004	2.027	2.070	2.034	0.066
$(P_3{}^{Si})Fe(NNMe_2)$	2.000	2.030	2.080	2.037	0.080
$[(P_3{}^B)Fe(NNMe_2)]^+$					
Expt.	2.005	2.089	2.192	2.095	0.187
10% HF	2.009	2.055	2.078	2.047	0.069
CASCI[c]	2.004	2.115	2.248	2.122	0.244
$[(P_3{}^B)Fe(NNH_2)]^+$	2.006	2.091	2.222	2.106	0.216
$[(P_3{}^B)Fe(NAd)]^+$	1.970	2.058	2.419	2.149	0.449

[a] $\Delta g = g_3 - g_1$.
[b] Performed on top of a SA-CASSCF(11,10) reference averaged over the first 10 doublet states.
[c] Performed on top of a SA-CASSCF(9,10) reference averaged over the first 10 doublet states.

As compiled in Table 5.6, the HFC tensors of N_α/N_β are both dominated by their anisotropic parts (t). While N_β is well-simulated by an axial anisotropic HFC tensor, consistent with π-symmetry spin density on this center, N_α requires an extremely rhombic tensor ($\delta_{\text{HFC}}(N_\alpha) = 0.7$). This accords well with the theoretical description of N_α in the $^3\Gamma_{0,0}$ state of $(P_3{}^B)Fe(NNMe_2)$ (*vide supra*), a result that can be rationalized by examination of the qualitative MO diagram shown in Figure 5.8, A. One-electron reduction of the $^3\Gamma_{0,0}$ state would occupy the $3d_{x^2-y^2}$ orbital, which has little overlap with the "$NNMe_2$" ligand orbitals and would thus correspond to a primarily metal-centered reduction. In this framework, the electronic structure of $[(P_3{}^B)Fe(NNMe_2)]^-$ would be best described as an $S = 3/2$ Fe(I)

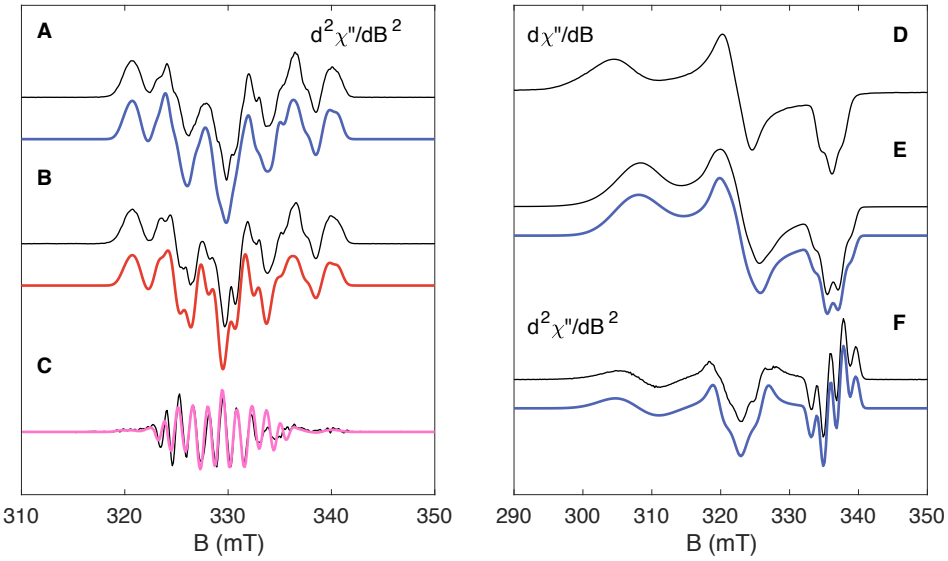

Figure 5.10: (A) CW X-band EPR spectrum of $[(P_3{}^B)Fe(^{14}N^{14}NMe_2)]^-$; data are plotted in black with a simuation in blue. (B) CW X-band EPR spectrum of $[(P_3{}^B)Fe(^{15}N^{15}NMe_2)]^-$; data are plotted in black with a simulation in red. (C) Difference spectrum for the data shown in (A) and (B); data are plotted in black with a simulation in pink. (D) CW X-band EPR spectrum of $[(P_3{}^B)Fe(NNH_2)]^+$. (E) CW X-band EPR spectrum of $[(P_3{}^B)Fe(NNMe_2)]^+$; data are plotted in black with a simulation in blue. (F) Second-derivative spectra of those presented in (E). All data were collected at 77 K.

center coupled antiferromagnetically to $S = 1/2$ $[NNMe_2]^{\bullet-}$ and $S = 1/2$ $[R_3B]^{\bullet-}$ ligands. This description is consistent with the relatively large isotropic ^{11}B HFC constant (15.3 MHz), which can be compared to those of planar $[Ph_3B]^{\bullet-}$ ($a_{iso}(^{11}B) = 22$ MHz) and the pyramidalized B atom of $(P_3{}^B)Cu$ ($a_{iso}(^{11}B) = 64$ MHz),[78,79] the latter of which has been characterized as containing a one-electron Cu–B σ bond.

To evaluate this electronic structure in more detail, we synthesized $[(P_3{}^B)Fe(NN(^{13}CH_3)_2)]^-$, incorporating a ^{13}C spin-probe distal to the Fe center (> 3.8 Å). Q-band ENDOR spectroscopy resolves a single ^{13}C HFC tensor for this isotopologue (Table 5.5). As with the VT ^1H NMR data of presented in Section 5.2.4.1, the large isotropic ^{13}C HFC of 19.6 MHz demonstrates that the "$NNMe_2$" ligand harbors significant spin density. The magnitude of this HFC constant is on par with that expected for a sp^3-hybridized carbon atom bonded directly to a π-radical center. For example, $a_{iso}(^{13}C) = 38$ MHz for the sp^3 carbon of the ethyl radical.[80] While the ^{13}C HFC constants of known *N*,*N*-dimethylhydrazyl

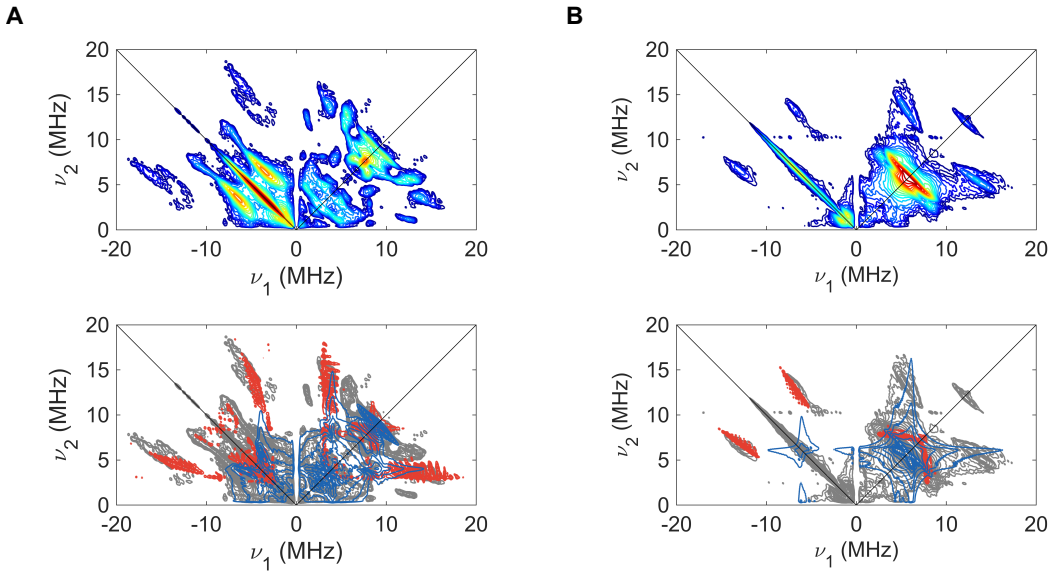

Figure 5.11: Selected HYSCORE spectra of (A) $[(P_3^B)Fe(^{14}N^{14}NMe_2)]^-$ and (B) $[(P_3^B)Fe(^{15}N^{15}NMe_2)]^-$, exhibiting HFC to two distinct N atoms. The top panels show the experimental spectrum, with intensities indicated by the color map. The bottom panels reproduce the experimental spectra in grey, and overlay simulations from a relatively strongly coupled N atom (red, assigned as N_α), and a relatively weakly coupled N atom (blue, assigned as N_β). Spectra were collected at 15 K at 1214 mT (g = 2.001).

radicals have not been determined, we can compare this to $a_{iso}(^{13}C)$ = 37 MHz calculated by DFT methods for $[NNMe_2]^{\bullet-}$ in its equilibrium geometry and $a_{iso}(^{13}C) = -22$ MHz in a planar geometry resembling that observed crystallographically for the "$NNMe_2$" ligand of $[(P_3^B)Fe(NNMe_2)]^-$.

The g-tensor of the ground state doublet of $[(P_3^B)Fe(NNMe_2)]^+$ ($^2\Gamma_{+,0}$) is significantly more anisotropic than that of its two-electron reduced congener, indicating of the presence of low-lying excited doublet states (*vide infra*), at least relative to the excited-state chemistry of $[(P_3^B)Fe(NNMe_2)]^-$. The overall rhombicity and anisotropy of the g-tensor of $[(P_3^B)Fe(NNMe_2)]^+$ closely matches that of the protonated complex $[(P_3^B)Fe(NNH_2)]^+$,[16] validating the use of the former as a spectroscopic model (Figure 5.10, D and E). This is in contrast to the g-tensor of the isoelectronic imido species, $[(P_3^B)Fe(NAd)]^+$, previously suggested to model $[(P_3^B)Fe(NNH_2)]^+$,[16] which is significantly more anisotropic (Table 5.4).

As above, we have determined the complete set of heteronuclear HFC tensors for $[(P_3{}^B)Fe(NNMe_2)]^+$ using a combination of X-band CW and Q-band ENDOR/HYSCORE experiments on ^{14}N, ^{15}N, and ^{13}C isotopologues. An examination of Table 5.5 shows that the magnitude of the isotropic couplings almost uniformly decrease upon two-electron oxidation of $[(P_3{}^B)Fe(NNMe_2)]^-$ to form $[(P_3{}^B)Fe(NNMe_2)]^+$. The only exceptions are a single ^{31}P nucleus, which remains essentially unchanged, and N_β, which has an increased isotropic component. However, both N atoms have notably decreased anisotropic hyperfine couplings in the oxidized complex (Table 5.6), indicating a uniform reduction in the π-symmetry spin density on these nuclei, although we note that N_α retains its rhombicity.

This trend can be simply rationalized in terms of an exchange-coupling model of the bonding in $[(P_3{}^B)Fe(NNMe_2)]^{+/-}$ in which oxidation produces stronger antiferromagnetic coupling between the Fe and its ligands, thereby reducing the overall degree of spin delocalization and core spin polarization. In an unrestricted *ansatz*, this occurs because the overlap between the α and β spin manifolds increases with greater coupling; in a CI *ansatz*, it is because the weight of configurations with antibonding character decreases. In either framework, there are, in a sense, fewer "effectively unpaired" spins.[v] Such an interpretation would be in agreement with the results of Section 5.2.4.2, where the transition from the $^1\Gamma_{0,0}$ to the $^3\Gamma_{0,0}$ state of $(P_3{}^B)Fe(NNMe_2)$ populates the repulsive $3d_{xz}$ orbital and weakens the Fe–$NNMe_2$ (and Fe–B) coupling. Conversely, oxidation of $[(P_3{}^B)Fe(NNMe_2)]^-$ should depopulate this orbital and strengthen the spin-coupling interactions in $[(P_3{}^B)Fe(NNMe_2)]^+$.

5.2.5.2 Computational Description of $^2\Gamma_{\pm,0}$

To validate this interpretation of the electronic structures of $[(P_3{}^B)Fe(NNMe_2)]^{+/-}$, we turn to quantum-chemical calculations. As with the $^3\Gamma_{0,0}$ state of $(P_3{}^B)Fe(NNMe_2)$, calculations of the ground states of $[(P_3{}^B)Fe(NNMe_2)]^{+/-}$ produce solutions with BS character regardless

[v] This is not to say that there is "more" than one unpaired electron in the weakly-coupled state, but rather that the distribution of the (real) spin density becomes less diffuse in the more strongly-coupled state.[75]

Table 5.5: Collected HFC Constants of $[(P_3{}^B)Fe(NNMe_2)]^n$ from Experiment and Theory

n	Nucleus	A_1 (MHz)[a]	A_2 (MHz)[a]	A_3 (MHz)[a]	a_{iso} (MHz)[b]			
					Expt.	0% HF	10% HF	25% HF
–	$^{14}N_\alpha$	−3.9	−29.2	11.8	−7.1	11.6	5.2	−5.2
–	$^{14}N_\beta$	1.6	−5.7	1.6	−0.9	2.8	−1.2	−5.2
–	*N*-Me ^{13}C	20.0	20.9	18.0	19.6	21.8/24.2	21.8/23.7	24.0/24.7
–	$^{31}P_\alpha$	134.6	124.6	116.6	125.3[c]	159.5	133.1	86.4
–	$^{31}P_\beta$	82.9	82.6	79.3	81.6[d]	−34.3	−53.9	−104.1
–	$^{31}P_\gamma$	28.1	30.0	27.6	28.6[e]	48.0	28.6	−2.6
–	^{11}B	15.9	15.2	14.7	15.3	−14.3	−32.7	−79.4
–	^{57}Fe	18.1	15.3	53.9	29.1	−14.2	−20.7	−31.9
+	$^{14}N_\alpha$	−10.7	−5.7	−0.1	−5.7	1.1	−0.5	−0.9
+	$^{14}N_\beta$	−1.5	−7.3	−1.5	−3.4	−3.8	−5.6	−10.0
+	*N*-Me $^{13}C_\alpha$	9.7	8.5	11.0	9.7	13.0	12.6	14.8
+	*N*-Me $^{13}C_\beta$	8.4	6.7	8.8	8.0	11.3	10.7	11.8
+	$^{31}P_\alpha$	48.5	73.0	51.7	57.7[e]	−71.5	−92.4	−120.0
+	$^{31}P_\beta$	55.2	49.0	36.5	46.9[f]	−65.9	−89.0	−130.4
+	$^{31}P_\gamma$	40.0	30.0	36.5	35.5[g]	−50.2	−72.9	−112.9
+	^{11}B	10.3	9.6	7.6	9.2	−7.3	−11.1	−22.1
+	^{57}Fe	24.0	9.0	0.1	11.0	13.5	7.4	−4.3

[a]The orientation of the HFC tensor is $g_1 = g_{min}$, $g_2 = g_{mid}$, $g_3 = g_{max}$.
[b]The absolute signs of a_{iso} have not been determined experimentally.
[c]P_α is taken to be P1.
[d]P_β is taken to be P2.
[e]P_γ is taken to be P3.
[f]P_α is taken to be P3.
[g]P_β is taken to be P1.
[h]P_γ is taken to be P2

Table 5.6: Collected Anisotropic HFC Constants of $[(P_3{}^B)Fe(NNMe_2)]^n$ from Experiment and Theory

n	Nucleus	T_1 (MHz)	T_2 (MHz)	T_3 (MHz)	t (MHz)[a]			δ_{HFC}		
					Expt.	10% HF	CASCI[b]	Expt.	10% HF	CASCI[b]
−	$^{14}N_\alpha$	3.3	−22.1	18.9	−11.1	−16.1	−8.0	0.7	0.6	0.6
−	$^{14}N_\beta$	2.4	−4.8	2.4	−2.4	−7.9	−1.8	~0	0.1	0.2
+	$^{14}N_\alpha$	−5.0	~0	5.0	−2.5	−5.5	−1.4	~1	0.5	0.5
+	$^{14}N_\beta$	1.9	−3.8	1.9	−1.9	−5	−0.6	~0	0.1	0.6

[a]The absolute signs of t have not been determined experimentally, but are assigned as negative to be consistent with DFT and CASCI calculations.

[b]Using a SA-CASSCF(11,10) reference for $n = -$, and a SA-CASSCF(9,10) reference for $n = +$. In both cases the first 10 doublet states were included.

of the degree of HF exchange included in the exchange-correlation functional. This character is, however, systematically larger with increased HF character.

As seen in Table 5.5, at 10% HF, the prediction of the isotropic parts of the metal and ligand HFC tensors is in good agreement for $[(P_3{}^B)Fe(NNMe_2)]^-$, with the exception of $a_{iso}(^{11}B)$, which is overestimated. This is likely due to contamination of the BS spin density by determinants of higher multiplicity (for ${}^2\Gamma^{BS}_{-,0}$, $\langle \hat{S}^2 \rangle = 1.02$), and suggests an empirical spin projection factor of roughly 2. The same effects can be seen for the anisotropic HFC tensors of N_α/N_β (Table 5.6), where the 10% HF calculation reproduces the experimental δ_{HFC}, but overestimates t by the same factor of ~2, on average. The zeroth order wavefunction from CASSCF is a proper eigenfunction of spin, so to estimate the effects of spin contamination, we have also calculated the anisotropic N HFC tensors using a CASCI calculation on top of a CASSCF(11,10) reference, utilizing the same active space composition as before. Including the lowest 10 doublet roots in this calculation, we obtain anisotropic tensors that are in excellent agreement with experiment (Table 5.6). Given that we have neglected dynamic correlation in these calculations, our results indicate that static correlation effects (i.e., antiferromagnetic interactions) dominate the valence electronic structure of $[(P_3{}^B)Fe(NNMe_2)]^-$.

For $[(P_3{}^B)Fe(NNMe_2)]^+$, the DFT calculations give poorer agreement with experiment at each level of HF inclusion (Table 5.5). This is particularly true of $a_{iso}(^{31}P)$, which are consistently overestimated, and $a_{iso}(^{14}N_\alpha)$, which is underestimated. However, at 10% HF, the DFT method appears to give a good description of the isotropic ^{57}Fe, ^{13}C, and ^{11}B couplings. Examining the anisotropic parts of N_α/N_β, we again see that the magnitudes are overestimated at 10% HF, but that the symmetries are in good agreement with experiment. As before, the agreement in t is improved from a CASCI calculation on top of a 10 root CASSCF(9,10) reference. It is noteworthy that the CASCI calculation produces an anisotropic HFC tensor for N_β that is too rhombic, suggesting that neglecting dynamic

correlation in this redox state is a poorer approximation.

Collectively, these calculations give a consistent, qualitative interpretation of the $^2\Gamma_{\pm,0}$ states. In $^2\Gamma_{-,0}$, the population of the $3d_{xz}$ orbital weakens the metal-ligand coupling interactions (cf. Figure 5.8 A), producing net negative spin densities at B and N_β, and a rhombic spin density about N_α. The same phenomenon was calculated above for the $^3\Gamma_{0,0}$ state (Figure 5.8, B), and is confirmed experimentally for $^2\Gamma_{-,0}$ (Table 5.6). Upon oxidation, stronger antiferromagnetic couplings partially quench the ligand-centered spins, producing an electronic structure that is more approximately a "simple" metalloradical. These effects are visualized in Figure 5.12, where it can be seen that, as expected, the DFT calculations tend to exaggerate the magnitude of the ligand-centered spin densities.[77]

This interpretation is made quantitative by a calculation of the polyradical character of ground-state specific CASSCF wavefunctions for the $^2\Gamma_{\pm,0}$ states. As seen in Table 5.7, the $^2\Gamma_{-,0}$ state has a similar degree of polyradical character as the $^3\Gamma_{0,0}$ state, and a number of effectively unpaired electrons significantly in excess of 1. Thus, as posited above, $[(P_3{}^B)Fe(NNMe_2)]^-$ is best viewed as an $S = 3/2$, Fe(I) center antiferromagnetically coupled to $S = 1/2$ $[NNMe_2]^{\bullet-}$ and $[R_3B]^{\bullet-}$ ligands. The polyradical character decreases by 50% upon two-electron oxidation to $^2\Gamma_{+,0}$, indicating much stronger antiferromagnetic coupling in the ground state of $[(P_3{}^B)Fe(NNMe_2)]^+$. The enhanced coupling is reflected by the reduced multireference character of the $^2\Gamma_{+,0}$ state (the least of the redox series, about 85% single-determinantal), although the symmetry of the antiferromagnetic interactions persists, and N_D/N_U remain larger than that expected for an orbitally-pure $S = 1/2$ state. This leads to a description of $[(P_3{}^B)Fe(NNMe_2)]^+$ in its ground state as an intermediate-spin, $S = 3/2$ Fe(III) ion strongly antiferromagnetically coupled to $[NNMe_2]^{\bullet-}$ and $[R_3B]^{\bullet-}$ ligands.

We have also examined the g-tensors of $^2\Gamma_{\pm,0}$ theoretically. As shown in Table 5.4, even for the relatively isotropic tensor of $^2\Gamma_{-,0}$, DFT methods fail to capture the correct levels

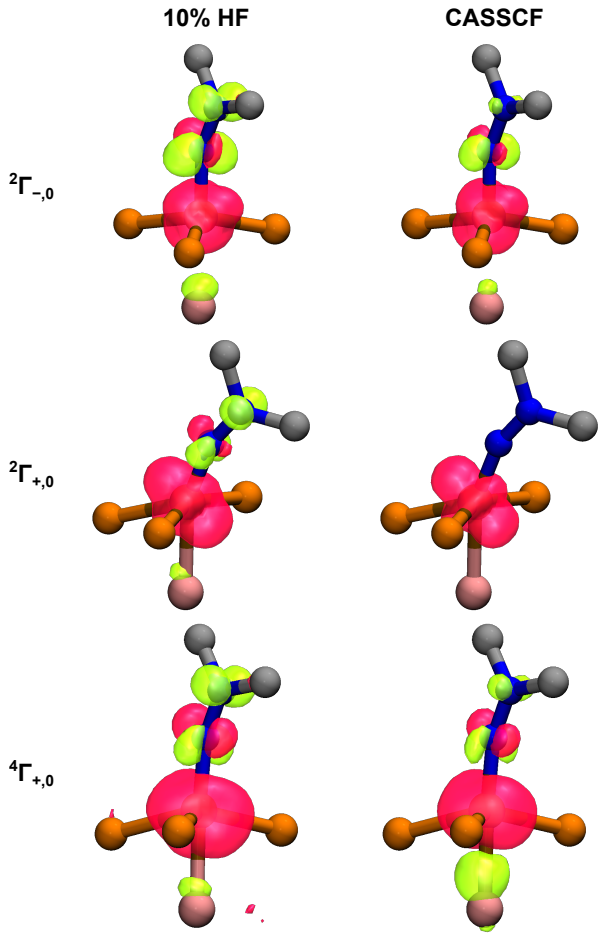

Figure 5.12: Spin density isosurfaces (isovalue = 0.005 a.u.) for the $^2\Gamma_{\pm,0}$ and $^4\Gamma_{+,0}$ states from BS DFT and CASSCF calculations. α density is shown in red, while β density is shown in green. For $^2\Gamma_{\pm,0}$, the DFT spin densities were calculated using the basis sets used for the prediction of EPR properties, while that of the $^4\Gamma_{+,0}$ state used the "valence" basis set described in the Experimental Section.

of g-anisotropy, an effect that has been attributed to the tendency of DFT to overestimate metal-ligand covalency.[81] An explicit treatment of the manifold of doublet excited states using CASCI produces g-tensors in much better agreement with experiment, even neglecting dynamic correlation. For $^2\Gamma_{-,0}$, NEVPT2 predicts the lowest-lying doublet excited state, $^2\Gamma_{-,1}$, to be ca. 11,000 cm^{-1} above $^2\Gamma_{-,0}$, which explains the low g-anisotropy. On the other hand, $^2\Gamma_{+,1}$ is predicted to be only ca. 7,000 cm^{-1} above $^2\Gamma_{+,0}$, and this state is almost completely responsible for the shift of g_3 above the free-electron value.

Table 5.7: NOON-based Chemical Bonding Indices for $[(P_3{}^B)Fe(NNMe_2)]^{+/-}$ from CASSCF calculations

NOs	$^2\Gamma_{-,0}$					$^2\Gamma_{+,0}$				
	n_+	n_-	Y^a	N_D	N_U	n_+	n_-	Y^a	N_D	N_U
$3d_{z^2} \pm B\ 2p_z$	1.85	0.15	0.15	0.56	0.30	1.90	0.10	0.10	0.39	0.20
$3d_{yz} \pm \pi^*_{NN}$	1.75	0.25	0.25	0.87	0.50	1.91	0.09	0.09	0.35	0.18
CAS	–	–	–	3.14	2.16	–	–	–	2.20	1.61
						$^4\Gamma_{+,0}{}^b$				
$3d_{z^2} \pm B\ 2p_z$						1.80	0.20	0.20	0.73	0.40
$3d_{yz} \pm \pi^*_{NN}$						1.86	0.14	0.14	0.53	0.29
CAS						–	–	–	4.33	3.71

$^aY = 1 - \frac{n_+ - n_-}{2}$. Note that for a spatially-matched bond/antibond pair, $Y = n_-$.
^{b}Computed in the quartet geometry.

5.2.6 Excited State Chemistry of $[(P_3{}^B)Fe(NNMe_2)]^+$

To gain insight into the ligand field and relative oxidation state of $[(P_3{}^B)Fe(NNMe_2)]^+$, we have collected its Fe *K*-edge XAS spectrum. A comparison of the XANES spectrum of $[(P_3{}^B)Fe(NNMe_2)]^+$ with that previously reported for its reduced congener, $(P_3{}^B)Fe(NNMe_2)$, is consistent with a largely metal-centered oxidation (Figure 5.13, A and B). While two resonances are observed in the spectrum of $(P_3{}^B)Fe(NNMe_2)$, three resonances are resolved for $[(P_3{}^B)Fe(NNMe_2)]^+$, which can be attributed to an additional metal-centered hole at the valence level. In addition, the remaining transitions are systematically shifted to higher energies (by ca. 1.3 eV) when compared with those of $(P_3{}^B)Fe(NNMe_2)$. Thus, if a Fe(II) oxidation state is assigned for $(P_3{}^B)Fe(NNMe_2)$, $[(P_3{}^B)Fe(NNMe_2)]^+$ should be formally assigned a Fe(III) oxidation state (*vide supra*).

This interpretation is supported by a TD-DFT calculation of the XANES region (Figure 5.13, C). The three lowest-energy TD-DFT core-hole states, which can be assigned to the resonance at 7111.8 eV, arise from excitations from the Fe 1s to the Fe-centered SOMO and an empty 3d orbital, both of which contain admixed $3d_{x^2-y^2}$ and $3d_{xz}$ character, likely due to the reduced symmetry of the $^2\Gamma_{+,0}$ state. Similar d–d mixing is predicted by a ground-state specific CASSCF calculation, which lends credence to the TD-DFT assignments. These assignments are also consistent with the qualitative MO diagram of Figure 5.8, A, where

a metal-centered oxidation to produce a low spin configuration predicts the SOMO to be $3d_{x^2-y^2}$.

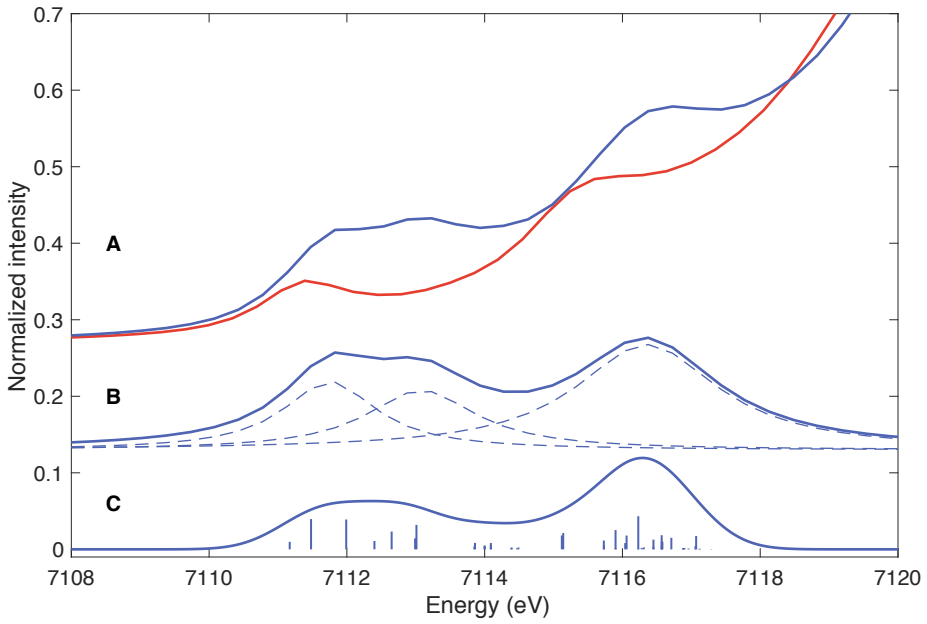

Figure 5.13: (A) Overlaid XANES spectra of $(P_3{}^B)Fe(NNMe_2)$ (red) and $[(P_3{}^B)Fe(NNMe_2)]^+$ (blue). (B) Pre-edge resonances of $[(P_3{}^B)Fe(NNMe_2)]^+$ after subtraction of the rising edge. (C) TD-DFT predicted XANES spectrum of $[(P_3{}^B)Fe(NNMe_2)]^+$.

Giving the d–d mixing, *g*-anisotropy, and similar distribution of core-hole excited states of $(P_3{}^B)Fe(NNMe_2)$ and $[(P_3{}^B)Fe(NNMe_2)]^+$, we were curious whether the latter also populates an excited state of higher multiplicity at low temperatures, corresponding to a shell-opening d $\rightarrow$ d transition. Variable temperature magnetic susceptibility measurements confirm this hypothesis, revealing an increase of almost 1 β_e as the temperature is raised over a 140 °C range. While it is not possible to determine the excited state multiplicity from these data alone, DFT calculations indicate that the first sextet state is significantly higher in energy than the first quartet state. From the susceptibility measurements, we estimate that the quartet state lies only ca. 5 kcal mol^{-1} above the doublet ground state of $[(P_3{}^B)Fe(NNMe_2)]^+$, which is quite similar to the adiabatic singlet-triplet gap measured for the $(P_3{}^B)Fe(NNMe_2)$ redox state.

In its DFT-predicted geometry, the quartet state of $[(P_3{}^B)Fe(NNMe_2)]^+$ ($^4\Gamma_{+,0}$) distorts toward trigonal symmetry, as the η^3-*B*, *C*, *C* interaction weakens (d(Fe–C1/C2) > 3 Å). The Fe–N_α distance also elongates by 0.05 Å, suggesting weakened antiferromagnetic coupling. This is corroborated by a state-specific CASSCF calculation, which predicts an increase in the polyradical character of both the Fe–B σ and Fe-$NNMe_2$ π bonding (Table 5.7). The multireference character of this state is also increased relative to the ground state, with the configuration

$$|(\pi_N)^2(3d_{yz} + \pi^*_{NN})^2(3d_{z^2} + 2p_z)^2(3d_{xy})^1(3d_{x^2-y^2})^1(3d_{xz})^1\rangle$$

accounting for only 77.5% of the ground-state wavefunction. This electronic state can be neatly interpreted in terms of the schematic MO diagram for the $^3\Gamma_{0,0}$ state shown in Figure 5.8, A. One-electron oxidation to produce a high spin state de-populates the $3d_{xy}$ orbital, producing an electronic structure that can be described as a high-spin Fe(III) ion ($S = 5/2$) antiferromagnetically coupled to $S = 1/2$ $[NNMe2]^{\bullet-}$ and $[R_3B]^{\bullet-}$ ligands, producing a $S_{tot} = 3/2$ state. This interpretation is in good agreement with the calculated ligand-centered spin density (Figure 5.12), which bears qualitative resemblance to those of the $^3\Gamma_{0,0}$ and $^2\Gamma_{-,0}$ states.

5.2.7 Summary and Implications for Catalytic Nitrogen Fixation

To summarize our results, we have leveraged a variety of spectrocopic and quantum-chemical techniques to characterize the electronic structures of the $[(P_3{}^B)Fe(NNMe_2)]^{+/0/-}$ redox series. While these studies reveal the complex, multiconfigurational nature of these species, a simple, qualitative, model that captures their essential features is that of intermediate spin Fe centers coupled antiferromagnetically to $[NNMe_2]^{\bullet-}$ and $[R_3B]^{\bullet-}$ ligands (Figure 5.14). As the Fe center is reduced from formally Fe(III) in $[(P_3{}^B)Fe(NNMe_2)]^+$, to Fe(II) in $(P_3{}^B)Fe(NNMe_2)$, and finally to Fe(I) in $[(P_3{}^B)Fe(NNMe_2)]^-$, this produces ground states with $S_{tot} = 1/2$, $S_{tot} = 0$, and $S_{tot} = 1/2$. For $(P_3{}^B)Fe(NNMe_2)$ and $[(P_3{}^B)Fe(NNMe_2)]^+$, additional evidence for these intermediate spin configurations comes from the presence of

low-lying ($\Delta E \leq 5$ kcal mol^{-1}) excited states with $S_{tot} = 1$ and $S_{tot} = 3/2$ respectively, corresponding to the high-spin configuration of the Fe(III) and Fe(II) centers. Given its Fe(I) configuration, [(P_3^B)Fe(NNMe$_2$)]$^-$ does not possess low-lying excited multiplets with $S_{tot} = 1/2$, which is reflected by its low g-anisotropy. As revealed by magnetic resonance spectroscopies and correlated ab initio calculations, the strength of the magnetic coupling between the Fe and its ligands decreases monotonically upon reduction, and also in the thermally-populated excited states of (P_3^B)Fe(NNMe$_2$) and [(P_3^B)Fe(NNMe$_2$)]$^+$ (Figure 5.15).

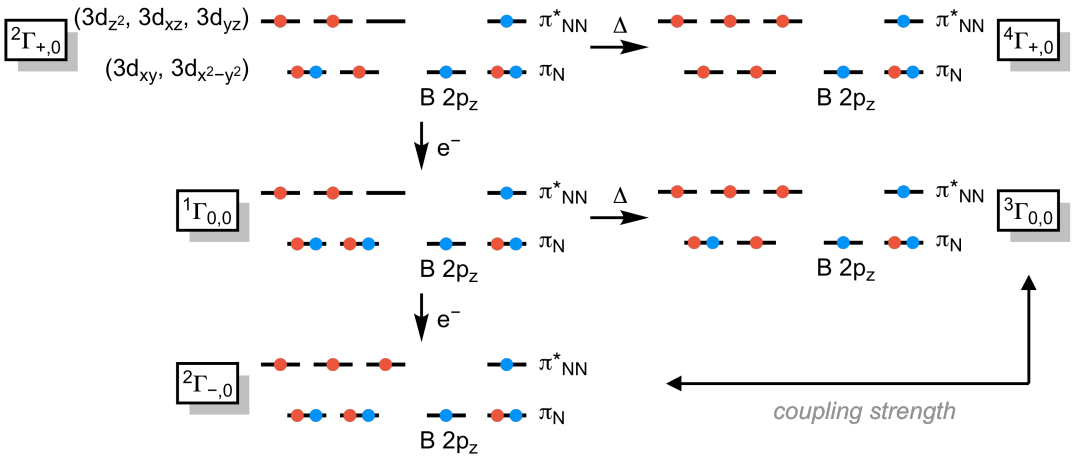

Figure 5.14: Simple model of the electronic structures of [(P_3^B)Fe(NNMe$_2$)]$^{+/0/-}$. Here, we assume an approximately T_d ligand field splitting (with the principle axis along the Fe–N$_\alpha$ bond), and ignore covalency, which determines the actual metal-ligand coupling strength. The arrows in the lower-left indicate the trends in coupling strength (See Figure 5.15 for a quantitative measure).

Combined with our previous work,[17,18] the studies presented here demonstrate that the *N*-alkylated complexes [(P_3^E)Fe(NNMe$_2$)]^n serve as faithful electronic models of their *N*-protonated congeners, as judged by EPR, Mössbauer, NMR, UV-vis, and X-ray absorption spectroscopies. Moreover, when making isoelectronic comparisons, the (P_3^B)Fe complexes do not appear to differ meaningfully from those supported by the P_3^{Si} ligand, leading us to propose analogous electronic structures. So, the question naturally arises: Do the electronic structures of title compounds rationalize the differential reactivity of the isoelectronic complexes (P_3^B)Fe(NNH$_2$) and [(P_3^{Si})Fe(NNH$_2$)]$^+$ in the context of nitrogen fixation?

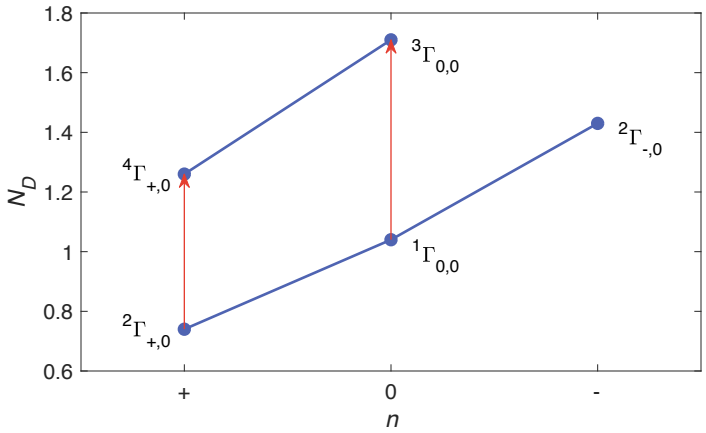

Figure 5.15: Number of effectively unpaired electrons (measured by N_D) within the $3d_{z^2}$ ± B $2p_z$ and $3d_{yz}$ ± π^*_{NN} interactions as a function of charge state (n) and multiplicity ($2S+1$), which can be taken as a measure of the antiferromagnetic coupling strength. Qualitatively similar plots are obtained using N_U or Y, and by extending this analysis over the complete active space and subtracting $2S$.

Assigning an $[NNH_2]^{\bullet-}$ oxidation state to the "NNH_2" ligand of $(P_3{}^B)Fe(NNH_2)$ may seem at odds with its apparent susceptibilty toward protonation at N_β to yield NH_3 and $[(P_3{}^B)Fe{\equiv}N]^+$,[17] although it should be noted that the dominant resonance structure of $[NNH_2]^{\bullet-}$ results in lone-pair character on N_β. Moreover, in $(P_3{}^B)Fe(NNH_2)$, additional reducing equivalents are harbored in the redox-active Fe–B interaction. Thus, as N_β becomes protonated, the $[R_3B]^{\bullet-}$ ligand can facilitate N–H bond formation by simultaneously reducing the $[NNH_2]^{\bullet-}$ ligand. From this perspective, the protonation reaction could be viewed as a form of "intramolecular" CPET. This flow of electrons is consistent with the XAS/TD-DFT characterization of $[(P_3{}^B)Fe{\equiv}N]^+$, which shows that the LUMO of the system is an a_1-symmetry orbital of dominant ($3d_{z^2}$ + B $2p_z$) character, i.e., the B atom becomes oxidized in the transformation shown in Figure 5.16, A. Our proposal here is consistent with previous observations made by us,[17] and a similar conclusion was reached in a recent computational study.[82]

This behavior helps to explain why a similar N–N bond cleavage reaction is not observed for $[(P_3{}^{Si})Fe(NNH_2)]^+$. From a coarse-grained perspective, the stability of this

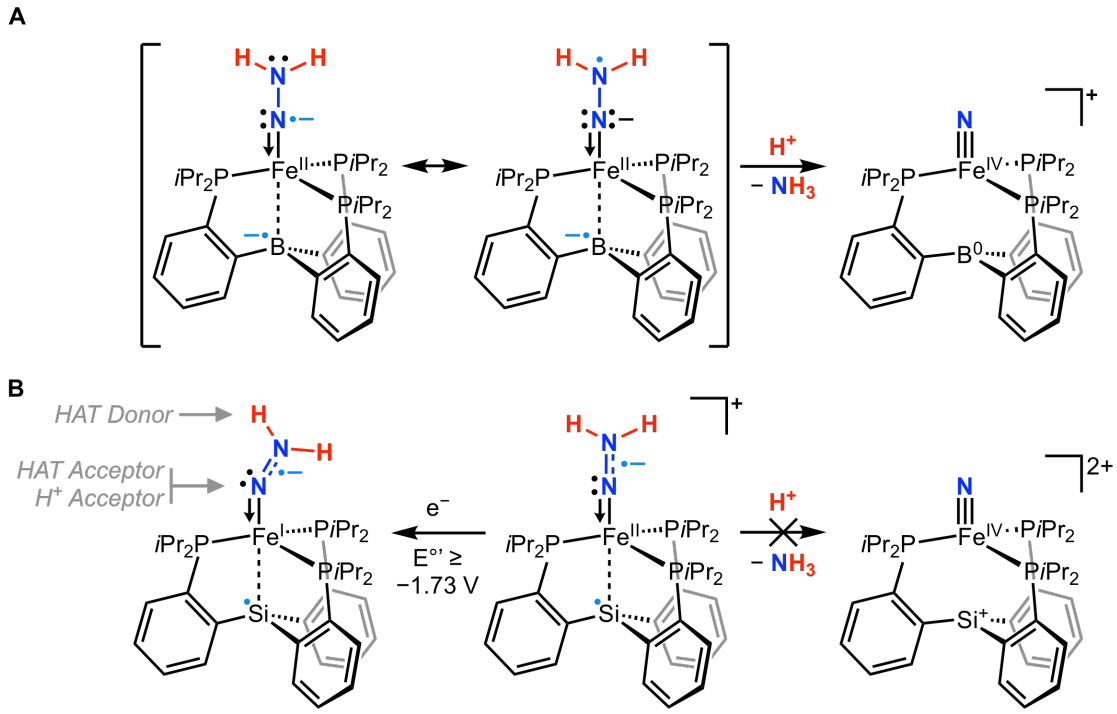

Figure 5.16: (A) Proposed role of ligand radical character in the N–N bond cleavage reaction of $(P_3^B)Fe(NNH_2)$. (B) Proposed role of ligand radical character in the N–H bond forming reactivity of $(P_3^{Si})Fe(NNH_2)$.

species toward protonation can be rationalized in terms of electrostatic effects. That is, owing to its cationic nature, one would expect the N_β atom of $[(P_3^{Si})Fe(NNH_2)]^+$ to be less basic than that of $(P_3^B)Fe(NNH_2)$.[83] With an understanding of the electronic structure of $[(P_3^{Si})Fe(NNH_2)]^+$, we can reformulate this statement in terms of the reducing power of the silyl ligand. That is, protonation at N_β and N–N bond cleavage would produce an Fe(IV) nitrido in which the silyl ligand becomes oxidized to $[R_3Si]^+$ (Figure 5.16, B). As the $[R_3Si]^\bullet \overset{-e^-}{\rightleftharpoons} [R_3Si]^+$ couple should occur at much higher potentials than the corresponding $[R_3B]^{\bullet-} \overset{-e^-}{\rightleftharpoons} [R_3B]$ couple, one would expect this transformation to be more challenging for the P_3^{Si} ligand when compared with the P_3^B ligand. If the Fe–Si bonding is substantially more covalent than the Fe–B bonding, then the Fe center would have to provide the reducing equivalents necessary for N–N bond cleavage, producing a Fe(V) or Fe(VI) oxidation state, which should occur at similarly high potentials.

Although $[(P_3^{Si})Fe(NNH_2)]^+$ is thus stable to protonation, it can be reduced in the

presence of $CoCp^*_2$ (Figure 5.16, B). In the Fe(I) (or Fe(II) in the case of covalent Fe–Si bonding) state, we expect the antiferromagnetic coupling between the Fe center and the $[NNH_2]^{\bullet-}$ ligand to weaken substantially, resulting in significant spin density delocalization onto both N atoms. Based on EPR studies of $[(P_3{}^B)Fe(NNMe_2)]^-$, the distribution of ligand-centered spin should be weighted in favor of N_α ($|t(N_\alpha)/t(N_\beta)| \approx 5$), which would explain preferential N_α functionalization if N–H bond formation occurs via HAT. Either $[(P_3{}^{Si})Fe(NNH_2)]^+$ or $(P_3{}^{Si})Fe(NNH_2)$ could serve as suitable HAT donors, given the extremely weak N–H bonds of these species (BDEs estimated to be 49 and 37 kcal mol^{-1}, respectively).[84] It should also be noted that the bending of the Fe–N_α–N_β is accompanied by greater lone-pair character at N_α (*vide supra*), and N–H bond formation via a proton transfer or CPET mechanism is thus also conceivable.

Given the low potential of the $[(P_3{}^B)Fe(NNMe_2)]^{0/-}$ couple (ca. −2.7 V), we do not expect $[(P_3{}^B)Fe(NNH_2)]^-$ to be a relevant oxidation state in catalytic nitrogen fixation by $[(P_3{}^B)Fe(N_2)]^-$ using our most efficient conditions in which $CoCp^*_2$ is the reductant ($E^{\circ\prime}$ = −2.1 V).[23] However, based on the results above, the $[(P_3{}^B)Fe(NNH_2)]^+$ and $(P_3{}^B)Fe(NNH_2)$ redox states should possess low-lying excited multiplets that are characterized by weakened antiferromagnetic metal-ligand coupling. Indeed, the similarity between these excited states and the reduced Fe(I) state, at least from the perspective of the $[NNH_2]^{\bullet-}$ ligand, suggests that population of these states under catalytic conditions could engender "$(P_3{}^{Si})$Fe-like" reactivity—that is, a preference for a distal-to-hybrid mechanism producing N_2H_4,[18] rather than a purely distal mechanism producing NH_3.[17] While direct thermal population of these states seems unlikely at the low temperatures relevant to catalysis (−78 °C), it may be possible to access similar electronic structures photochemically (cf. Figure 5.6, C and D). Studies evaluating this hypothesis are currently underway.

5.3 Conclusion

Herein, we have provided experimental and theoretical evidence supporting the formulation of $[(P_3{}^E)Fe(NNR_2)]^n$ complexes as containing a $[NNR_2]^{\bullet-}$ ligand coupled antiferromagnetically to the Fe center. This characterization completes the set of "NNR_2" redox states commonly considered in $M(NNR_2)$ complexes—isodiazene, hydrazido(2−), and, now, hydrazyl radical anion. In many ways, this mirrors the redox-activity of the nitrosyl ligand, which can be present in $[NO]^+$, $NO^{\bullet}$, or $[NO]^-$ oxidation states. The analogy with nitrosyliron complexes is an apt one. For example, Wieghardt, Bill, and coworkers have characterized *trans*-$[(cyclam)Fe(NO)(Cl)]^+$ as an intermediate-spin Fe(III) ion ($S = 3/2$) antiferromagnetically-coupled to an $[NO]^-$ ligand ($S = 1$), producing the observed $S_{tot} = 1/2$ ground state,[85] which is similar to the proposed electronic structure of $[(P_3{}^B)Fe(NNMe_2)]^+$. In fact, we note that the magnetically-perturbed Mössbauer spectrum of this nitroysl complex in the limit of slow electronic relaxation is almost superimposable with that of $[(P_3{}^B)Fe(NNMe_2)]^+$, reflecting the similar ^{57}Fe HFC constants of these apparently distinct complexes ($|a_{iso}(^{57}Fe)| = 11.6$ and 11.0 MHz, respectively).[85]

The one electron redox noninnocence of the "NNR_2" ligand may manifest itself in other examples of transition metal mediated nitrogen fixation. For example, a key intermediate proposed in the catalytic cycle of Schrock's triamidoamine-supported Mo catalyst is a cationic, formally Mo(VI) $[Mo(NNH_2)]^+$ complex; upon reduction to the proposed Mo(V) redox state, this species undergoes a complex series of disproportionation reactions, yielding mixtures of Mo(NNH), Mo≡N, and $[Mo(NH_3)]^{+/0}$.[33] This chemistry is formally similar to that which occurs upon the reduction of $[(P_3{}^{Si})Fe(NNH_2)]^+$,[18] and may have a common physical basis. Although the Mo(V) "hydrazido" complex has not been observed experimentally, DFT studies suggest that the Mo-based SOMO is the repulsive $4d_{xz}$ orbital,[86] causing a bending of the Mo–N_α–N_β angle, quite analogous to the reduction of $(P_3{}^B)Fe(NNMe_2)$ to $[(P_3{}^B)Fe(NNMe_2)]^-$ (or the reduction of $[(P_3{}^{Si})Fe(NNH_2)]^+$ to $(P_3{}^{Si})Fe(NNH_2)$). While it has not been considered explicitly in the literature, our results suggest that an electronic

structure consisting of a high-spin Mo(IV) ion ($S = 1$) antiferromagnetically-coupled to a $[NNH_2]^{\bullet-}$ ligand should be considered for this complex. More broadly, given the central role of $M(NNR_2)$ complexes in the catalytic fixation of N_2, potentially including even biological nitrogen fixation,[87] the elucidation of their electronic structures remains an important goal.

5.4 Experimental Section

5.4.1 Experimental Details

5.4.1.1 General Considerations

Unless noted otherwise, all manipulations were carried out using standard Schlenk or glovebox techniques under an N_2 atmosphere. Solvents were deoxygenated and dried by thoroughly sparging with N_2 followed by passage through an activated alumina column in a solvent purification system by SG Water, USA LLC. Deoxygenated, anhydrous 2-MeTHF was purified by stirring over sodium-potassium alloy and filtering through a short column of activated alumina prior to use. Nonhalogenated solvents were tested with sodium benzophenone ketyl in THF in order to confirm the absence of oxygen and water. Deuterated solvents were purchased from Cambridge Isotope Laboratories, Inc., degassed, and dried over activated 3 Å molecular sieves prior to use.

The compounds $(P_3{}^B)^{57}Fe(Cl)$,[17] $(P_3{}^B)Fe(NNMe_2)$,[17] $(P_3{}^B)Fe(NN[Si_2])$,[15] $(P_3{}^B)Fe(NAd)$,[16] and $[(P_3{}^B)Fe(NAd)][BAr^F{}_4]$[16] were prepared according to literature procedures. All other reagents were purchased from commercial vendors and used without further purification unless otherwise stated.

5.4.1.2 NMR Spectroscopy

Chemical shifts for ^1H are reported in ppm relative to tetramethylsilane, using resonances from residual solvent as internal standards; ^{15}N resonances are reported in ppm relative to the chemical shift of $^{15}NH_{3,(liq)}$, referenced to the signal of the deuterated solvent used to lock the instrument.

5.4.1.3 IR Spectroscopy

IR measurements were obtained as powders or thin films formed by evaporation of solutions using a Bruker Alpha Platinum ATR spectrometer with OPUS software.

5.4.1.4 UV-vis Spectroscopy

Optical spectroscopy measurements were collected with a Cary 50 UV-vis spectrophotometer using a 1 cm two-window quartz cell. Variable temperature measurements were collected with a Unisoku CoolSpek cryostat mounted within the Cary spectrophotometer.

5.4.1.5 Electrochemistry

Cyclic voltammetry measurements were carried out in a glovebox under an N_2 atmosphere in a one-compartment cell using a CH Instruments 600B electrochemical analyzer. A glassy carbon electrode was used as the working electrode and a carbon rod was used as the auxiliary electrode. The reference electrode was AgOTf/Ag in THF isolated by a CoralPor frit (obtained from BASi). The $Fc^{+/0}$ couple was used as an external reference. THF solutions of electrolyte (0.1 M [TBA][PF_6]) and analyte were also prepared under an inert atmosphere.

5.4.1.6 X-ray Crystallography

X-ray diffraction studies were carried out at the Caltech Division of Chemistry and Chemical Engineering X-ray Crystallography Facility using a dual source Bruker D8 Venture, four-circle diffractometer with a PHOTON CMOS or a PHOTON II CPAD detector. Data was collected at 100K using Mo K_α (λ = 0.71073 Å) or Cu K_α (λ = 1.54178 Å) radiation. The crystals were mounted on a glass fiber under Paratone N oil. Structures were solved using SHELXT[88] and refined against F^2 on all data by full-matrix least squares with SHELXL.[89] All non-hydrogen atoms were refined anisotropically. All hydrogen atoms were placed at geometrically calculated positions and refined using a riding model. The isotropic

displacement parameters of all hydrogen atoms were fixed at 1.2 (1.5 for methyl groups) times the U_{eq} of the atoms to which they are bonded.

5.4.1.7 ^{57}Fe Mössbauer Spectroscopy

Mössbauer spectra were recorded on a spectrometer from SEE Co. (Edina, MN) operating in the constant acceleration mode in a transmission geometry. The sample was kept in an SVT-400 cryostat form Janis (Wilmington, MA), using liquid N_2 as a cryogen for 80 K measurements. Magnetically-perturbed spectra were recorded in the presence of a 50 mT permanent magnet, aligned either parallel or perpendicular to the direction of γ-ray propagation. The quoted isomer shifts are relative to the centroid of the spectrum of a metallic foil of α-Fe at room temperature. Solution samples were transferred to a sample cup and chilled to 77 K inside of the glovebox, and quickly removed from the glovebox and immersed in liquid N_2 until mounted in the cryostat. Data analysis was performed using version 4 of the program WMOSS (www.wmoss.org) and all resonances were fit to Lorentzian lineshapes.[90] Magnetically-perturbed spectra collected on samples in $S = 1/2$ ground states were simulated using the following spin Hamiltonian,[64]

$$\hat{H}_{SH} = \beta_e \hat{S} \cdot \boldsymbol{g} \cdot \vec{B} + \hat{I} \cdot \boldsymbol{A} \cdot \hat{S} - g_N \beta_N \hat{I} \cdot \vec{B} + \hat{I} \cdot \boldsymbol{Q} \cdot \hat{I} \tag{5.1}$$

where β_e is the Bohr magneton, $\hat{S}$ is the electronic spin operator, $\boldsymbol{g}$ is the electronic g-tensor, $\vec{B}$ is the applied magnetic field, $\hat{I}$ is the nuclear spin operator, $\boldsymbol{A}$ is the hyperfine coupling tensor, g_N and β_N are the nuclear g-factor and magneton, and $\boldsymbol{Q}$ is the electric field gradient tensor. In the presence of even a weak external field, the electronic Zeeman interaction dominates this Hamiltonian, and the nuclear terms can be solved in a basis of the eigenstates of the electronic Zeeman operator.[64,90] In this case, the nuclear terms are separable for every such eigenstate, $|i\rangle$,

$$\hat{H}_{\mathrm{nuc},i} = \hat{I} \cdot \boldsymbol{A} \cdot \langle \hat{S} \rangle_i - g_N \beta_N \hat{I} \cdot \vec{B} + \hat{I} \cdot \boldsymbol{Q} \cdot \hat{I} \tag{5.2}$$

$$= -g_N \beta_N \hat{I} \cdot \left(\frac{-\boldsymbol{A} \langle \hat{S} \rangle_i}{g_N \beta_N} + \vec{B} \right) + \frac{eQV_{zz}}{4I(2I-1)} \left[3\hat{I}_z^2 - I(I+1) + \frac{\eta}{2}(\hat{I}_+^2 + \hat{I}_-^2) \right] \tag{5.3}$$

where eQV_{zz} is the nuclear quadrupole coupling constant, η is the asymmetry parameter, and $\hat{S}$ has been replaced by its expectation value for state $|i\rangle$. Conventionally, $\eta = \frac{V_{yy}-V_{xx}}{V_{zz}}$, where V_{kk} are the principle components of $\boldsymbol{Q}$ with $V_{zz} \geq V_{yy} \geq V_{xx}$. In the limit of slow electronic relaxation, separate Mössbauer spectra are computed for each state $|i\rangle$, and the experimental spectrum is reproduced as their Boltzmann-weighted sum. During simulation, the g-tensor was fixed as determined from EPR studies. Note that $\boldsymbol{A}$ in the model above is expressed in units of the "internal" field about the ^{57}Fe nucleus. This can be converted into the HFC tensor in units of MHz for the nuclear ground state of ^{57}Fe by application of,[64]

$$\boldsymbol{A}(\text{MHZ}) = 1.38152 \times \boldsymbol{A}(\text{T}) \tag{5.4}$$

5.4.1.8 EPR Spectroscopy

CW EPR spectroscopy: X-band (9.4 GHz) CW EPR spectra were acquired using a Bruker EMX spectrometer equipped with a Super High-Q (SHQE) resonator using Bruker WinEPR software (ver. 3.0). Spectra were acquired at 77 K using a vacuum-insulated quartz liquid nitrogen immersion dewar inserted into the EPR resonator. Spectra were simulated using the EasySpin[91] simulation toolbox (release 5.2.15) with Matlab R2016b.

Pulse EPR spectroscopy: All pulse X-band (9.7 GHz) and Q-band (34 GHz) EPR, hyperfine sublevel correlation (HYSCORE) and electron nuclear double resonance (ENDOR) spectra were acquired using a Bruker ELEXSYS E580 pulse EPR spectrometer equipped with a Bruker MD4 (X-band) or D2 (Q-band) resonator. Temperature control was achieved using an ER 4118HV-CF5-L Flexline Cryogen-Free VT cryostat manufactured by ColdEdge equipped with an Oxford Instruments Mercury ITC temperature controller. Spectra were simulated using the EasySpin[91] simulation toolbox (release 5.2.15) with Matlab R2016b.

Pulse X- and Q-band electron spin-echo detected EPR (ESE-EPR) field-swept spectra were acquired using the 2-pulse "Hahn-echo" sequence ($\pi/2$–τ–π–τ–echo) where τ was held constant. Subsequently, each field swept echo-detected EPR absorption spectrum was

modified using a pseudo-modulation function to approximate the effect of field modulation and produce the CW-like 1st derivative spectrum.[92] Spin-spin relaxation times (T_2) were measured at Q-band using the same "Hahn-echo" pulse sequence ($\pi/2$–τ–π–τ–echo) where τ was incremented to produce a time-domain spectrum of the decay of the spin-echo intensity as a function of time.

Pulse Q-band HYSCORE spectra were acquired using the 4-pulse sequence ($\pi/2$–τ–$\pi/2$–T_1–π–T_2–$\pi/2$–τ–echo), where τ is a fixed delay, and T_1 and T_2 are variable delays independently incremented by ΔT_1 and ΔT_2, respectively. The microwave power of the $\pi/2$ pulses were reduced such that the lengths of these pulses were equal to the π pulse to ensure that each pulse provided the same excitation bandwidth. Sixteen step phase cycling was utilized. The time domain spectra were baseline-corrected (third-order polynomial), apodized with a Hamming window function, zero-filled to eight-fold points, and fast Fourier-transformed to yield the frequency domain. Acquisition parameters for all spectra included the following: T = 15 K; microwave frequency = 34.096 GHz ($[(P_3{}^B)Fe(NNMe_2)]^-$), 34.04 GHz ($[(P_3{}^B)Fe(NNMe_2)]^+$) ; $\pi/2 = \pi = 24$ ns; $\tau = 100$ ns; $T_1 = T_2 = 100$ ns; $\Delta T_1 = \Delta T_2 = 16$ ns; srt = 1 ms.

Pulse X- and Q-band ENDOR spectra were acquired using the Davies pulse sequence (π–T_{RF}–π_{RF}–T_{RF}–$\pi/2$–τ–π–echo), where T_{RF} is the delay between MW pulses and RF pulses, π_{RF} is the length of the RF pulse. The RF frequency was randomly sampled during each pulse sequence.

In general, the ENDOR spectrum for a given nucleus with spin $I = 1/2$ (e.g., ^{1}H) coupled to the $S = 1/2$ electron spin exhibits a doublet at frequencies,

$$\nu_{\pm} = \left| \frac{A}{2} \pm \nu_N \right| \tag{5.5}$$

where ν_N is the nuclear Larmor frequency and A is the hyperfine coupling. For nuclei with $I \geq 1$ (e.g., ^{14}N), an additional splitting of the $\nu_{\pm}$ manifolds is produced by the nuclear

quadrupole interaction (P),

$$\nu_{\pm,m_I} = \left| \nu_N \pm \frac{3P(2m_I - 1)}{2} \right| \tag{5.6}$$

In HYSCORE spectra, these signals manifest as cross-peaks or ridges in the 2-D frequency spectrum which are generally symmetric about the diagonal of a given quadrant. This technique allows hyperfine levels corresponding to the same electron-nuclear submanifold to be differentiated, as well as separating features from hyperfine couplings in the weak-coupling regime ($|A| < 2|\nu_I|$) in the $(+,-)$ quadrant from those in the strong coupling regime ($|A| > 2|\nu_I|$) in the $(-,-)$ quadrant. The $(-,-)$ and $(+,-)$ quadrants of these frequency spectra are symmetric to the $(+,+)$ and $(-,+)$ quadrants, thus typically only two of the quadrants are typically displayed in literature. For systems with appreciable hyperfine anisotropy in frozen solutions or solids, HYSCORE spectra typically do not exhibit sharp cross peaks, but show ridges that represent the sum of cross peaks from selected orientations at the magnetic field position at which the spectrum is collected. The length and curvature of these correlation ridges allow for the separation and estimation of the magnitude of the isotropic and dipolar components of the hyperfine tensor.

For systems exhibiting significant rhombic symmetry in the hyperfine tensor, as is the case for the N_α for $[(P_3{}^B)Fe(NNMe_2)]^{+/-}$, such simple analysis of these correlation ridges is less facile, and even cursory analysis requires spectral simulations. For systems coupled to nuclei with $I = 1$, such as ^{14}N, the double-quantum peaks are often the most intense feature. These cross-peaks are defined by the following equations:

$$\nu_\alpha = \pm 2\sqrt{(\nu_I + A/2)^2 + K^2(3 + \eta^2)} \tag{5.7}$$

$$\nu_\beta = \pm 2\sqrt{(\nu_I - A/2)^2 + K^2(3 + \eta^2)} \tag{5.8}$$

where $K = e^2qQ/4\hbar$. For weakly coupled nuclei ($|A| < 2|\nu_I|$), ν_α and ν_β are both positive, appearing in the $(+,+)$ quadrant, while for strongly coupled nuclei they will show up in the $(-,+)$ quadrant. In the intermediate coupling regime where $|A| \approx |2\nu_I|$, peaks will often appear in both the $(+,+)$ and $(-,+)$ quadrants of the HYSCORE spectrum.

The HFC tensor, $\boldsymbol{A}$, can be decomposed into its isotropic, a_{iso}, and anisotropic, $\boldsymbol{T}$, parts,[93]

$$\boldsymbol{A} = a_{\mathrm{iso}}\mathbf{1} + \boldsymbol{T} \tag{5.9}$$

where the anisotropic HFC tensor, $\boldsymbol{T}$, is the traceless matrix formed by,

$$\boldsymbol{T} = \boldsymbol{A} - \frac{1}{3}\operatorname{Tr}\boldsymbol{A} \tag{5.10}$$

Thus, $a_{\mathrm{iso}} = \frac{1}{3}\operatorname{Tr}\boldsymbol{A}$. $\boldsymbol{T}$ can be further decomposed into scalar components: t (in units of energy), describing the magnitude of the anisotropic HFC coupling, and a dimensionless term δ_{HFC} ($0 \leq \delta_{\mathrm{HFC}} \leq 1$), describing the rhombicity of the tensor,

$$\boldsymbol{T} = \begin{pmatrix} 2t & & \\ & -t(1-\delta_{\mathrm{HFC}}) & \\ & & -t(1+\delta_{\mathrm{HFC}}) \end{pmatrix} \tag{5.11}$$

5.4.1.9 X-ray Absorption Spectroscopy

Samples for XAS measurements were prepared in modified Mössbauer sample cups in which the bottom of the Delrin cup was removed and sealed with Kapton tape. All samples thus prepared were analyzed by Mössbauer spectroscopy at 80 K prior to collection of XAS data. Samples were maintained at temperatures of 80 K and below at all times.

XAS data collection was conducted at the Stanford Synchrotron Radiation Laboratory (SSRL) with the SPEAR 3 storage ring containing 500 mA at 3.0 GeV. Fe *K*-edge data were collected on the beamline 9-3 operating with a wiggler field of 2 T and employing a Si(220) double-crystal monochromator. Beamline 9-3 is equipped with a rhodium-coated vertical collimating mirror upstream of the monochromator and a bent cylindrical focusing mirror (also rhodium-coated) downstream of the monochromator. Harmonic rejection was accomplished by setting the energy cutoff angle of the mirrors to 10 keV. The incident and transmitted X-ray intensities were monitored using nitrogen filled ionization chambers, and fluorescence was measured using a single-channel PIPS detector. During

data collection, samples were maintained at a temperature of approximately 10 K using an Oxford instruments liquid helium flow cryostat. The energy was calibrated by reference to the absorption of a standard iron metal foil measured simultaneously with each scan, assuming a lowest energy inflection point of the iron foil to be 7111.3 eV. Samples were monitored for photodamage by comparing the pre-edge region between consecutive scans. In cases where photodamage was detected, the sample was moved to a previously unexposed region and single scans were collected; in this fashion, six first scans could be collected and integrated for each sample.

The raw XAS data were analyzed using the EXAFSPAK suite of programs.[94] Data were calibrated to the first inflection of the iron foil reference and averaged over all first scans for each sample. The edge region was background corrected by fitting a Gaussian function through the pre-edge region and subtracting this from the entire spectrum. A four-segment fourth-order spline was fit to the EXAFS region, and the spectrum was normalized to the edge jump. A monochromator glitch at $k \approx 12$ Å^{-1} was removed by fitting a cubic polynomial to the raw data. The pre-edge region was fit between 7108 and 7119 eV using the `EDG_FIT` utility. Resonances were fit with pseudo-Voigt lineshapes, where the weight of the Lorentzian and Gaussian components was allowed to refine freely.

5.4.2 Synthetic Details

5.4.2.1 Synthesis of $(P_3{}^B)Fe(^{15}N^{15}NMe_2)$

The synthesis of $(P_3{}^B)Fe(^{15}N^{15}NMe_2)$ followed the reported procedure,[17] but replacing the atmosphere of $^{14}N_2$ gas with $^{15}N_2$ gas.

5.4.2.2 Synthesis of $(P_3{}^B)Fe(NN(^{13}CH_3)_2)$

The synthesis of $(P_3{}^B)Fe(NN(^{13}CH_3)_2)$ followed the reported procedure,[17] but replacing MeOTf with $(^{13}CH_3)OTf$.

5.4.2.3 Synthesis of $(P_3{}^B)^{57}Fe(NNMe_2)$

The synthesis of $(P_3{}^B)^{57}Fe(NNMe_2)$ followed the reported procedure,[17] but replacing $(P_3{}^B)Fe(Br)$ as the iron precursor with $(P_3{}^B)^{57}Fe(Cl)$.

5.4.2.4 Synthesis of $[(P_3{}^B)Fe(NNMe_2)][BAr^F{}_4]$

$(P_3{}^B)Fe(NNMe_2)$ (25 mg, 0.036 mmol) was suspended in 1 mL Et_2O in a 20 mL scintillation vial, which was subsequently charged with a magnetic stir bar and chilled to −78 °C in the cold well of a N_2-filled glovebox. A solution of $[FeCp^*_2][BAr^F{}_4]$ (43 mg, 0.036 mmol) in 4 mL Et_2O was similarly chilled, and then added dropwise to the stirring solution of $(P_3{}^B)Fe(NNMe_2)$. After stirring 30 minutes in the cold well, the resultant solution was allowed to warm to room temperature with stirring over 1 hour, during which time a deep orange-brown color developed. The solvent was then removed in vacuo, the remaining solids washed with C_6H_6 (3 × 1 mL), and then extracted with Et_2O (3 × 1 mL) and filtered. The filtrate was concentrated to ca. 1 mL, layered with pentane, and cooled to −35 °C. After 24 hours, the mother liquor was decanted, and the remaining orange-red crystals were washed liberally with pentane and dried in vacuo to afford 49 mg of $[(P_3{}^B)Fe(NNMe_2)][BAr^F{}_4]$. Recrystallization from 4:1 toluene:Et_2O at −35 °C yields material that is analytically pure except for the presence of co-crystallized toluene, which is not removed even under prolonged evacuation. NMR and elemental analysis indicate a $[(P_3{}^B)Fe(NNMe_2)][BAr^F{}_4]$:toluene stoichiometry of 1:1. Crystals suitable for X-ray diffraction were obtained by layering an Et_2O solution of $[(P_3{}^B)Fe(NNMe_2)][BAr^F{}_4]$ with pentane and cooling to −35 °C.

^{1}H NMR (400 MHz, d_8-THF, 293 K): δ 10.89 (v. br.), 7.79 (s, $BAr^F{}_4$ *o*-Ar-C*H*, 8H), 7.57 (s, $BAr^F{}_4$, *p*-Ar-C*H*, 4H), 2.22 (v. br.), −0.14 (v. br.). μ_{eff} (d_8-THF, Evans method, 293 K): 2.4 β_e (see discussion of variable temperature magnetization data in Appendix D). UV-vis (THF, 293 K, nm (ϵ, cm^{-1} M^{-1})): ~270 (20720), 309 (12100), 407 (3024), 499 (734), 698 (106). Anal. Calc. for $C_{64}H_{58}B_2F_{24}FeN_2P_3 + C_7H_6$: C, 55.72; H, 4.86; N, 1.69.

Found: C, 55.98; H, 4.67; N, 1.26.

5.4.2.5 Synthesis of [(P_3^B)Fe($NNMe_2$)][BAr^F_4] Isotopologues

The synthesis of isotopologues of [(P_3^B)Fe($NNMe_2$)][BAr^F_4] including ^{57}Fe, ^{15}N, and ^{13}C were prepared as described above, but using the corresponding isotopologue of (P_3^B)Fe($NNMe_2$) as the starting material.

5.4.2.6 Synthesis of [(P_3^B)Fe($NNMe_2$)]$^-$

A solution of (P_3^B)Fe($NNMe_2$) in 2-MeTHF (5 to 10 mM) was chilled to −78 °C in the cold well of a N_2-filled glovebox. A vial containing 1.2 equiv of KC_8 and a magnetic stir bar was similarly chilled in the cold well. Using a pre-chilled glass pipette, the solution of (P_3^B)Fe($NNMe_2$) was added to the vial containing solid KC_8 in a single shot, and this mixture was allowed to stir at −78 °C for 30 minutes. At this point, the procedure diverged, depending on the analysis. For X-band EPR measurements, this suspension was passed through a pre-chilled glass microfiber filter into a pre-chilled quartz X-band sample tube. A similar procedure was used for the preparation of Q-band samples, but, in order to prevent warming of the sample during transfer into the narrow Q-band sample tube, the suspension was filtered into a pre-chilled syringe equipped with a 22-gauge steel needle inserted into the tube. After the filtered solution had passed through the needle into the quartz tube, the syringe assembly was removed. For Mössbauer analysis, the suspension was transferred into a pre-chilled delrin sample holder without filtration. At this point, in each of these cases, the cold well bath was replaced with liquid N_2, and the sample of [(P_3^B)Fe($NNMe_2$)]$^-$ was frozen before being passed out of the glovebox and stored at 77 K prior to analysis.

Solutions of [(P_3^B)Fe($NNMe_2$)]$^-$ are unstable upon warming, which has prevented its isolation in a pure form. The decomposition kinetics are consistent with a unimolecular process, with a half-life at room temperature of approximately 4 min. Mössbauer analysis suggests that fresh preparations of [(P_3^B)Fe($NNMe_2$)]$^-$ kept at T ≤ −78 °C are typically ca.

75% pure. Owing to this purity, and the slow electronic relaxation of $[(P_3{}^B)Fe(NNMe_2)]^-$, NMR analysis was not conducted.

To obtain a crystal of $[(P_3{}^B)Fe(NNMe_2)]^-$ suitable for X-ray diffraction, a 5 mM 2-MeTHF solution of $(P_3{}^B)Fe(NNMe_2)$ was reduced to $[(P_3{}^B)Fe(NNMe_2)]^-$ as described above, and subsequently filtered into a vial containing 2.1 equiv of solid benzo-15-c-5. The resultant solution was layered with *n*-pentane chilled to −78 °C (2:1 *n*-pentane:2-MeTHF), and this mixture was placed in a freezer at −35 °C. After ca. 24 hours, a crop of dark crystals formed on the bottom of the vial; this sample was transferred to the X-ray diffractometer on dry ice, where the crystals were quickly removed from their mother liquor and suspended in Paratone N oil. A suitable crystal was selected and mounted on the diffractometer, which was pre-chilled to 100 K under a stream of dry N_2. Under a microscope, the crystals begin to visually decompose as soon as they are removed from their chilled mother liquor, requiring this procedure to be performed in a matter of minutes; multiple attempts were required before a strongly diffracting crystal was obtained. To confirm that the coordination of benzo-15-c-5 to the K^+ counterion of $[(P_3{}^B)Fe(NNMe_2)]^-$ does not affect its spectroscopic properties, we repeated this experiment, but transferred the 2-MeTHF solution containing $[(P_3{}^B)Fe(NNMe_2)]^-$ to a pre-chilled quartz X-band sample tube, which was subsequently frozen and analyzed by CW EPR spectroscopy. The spectra of $[(P_3{}^B)Fe(NNMe_2)]^-$ prepared in this fashion with or without added benzo-15-c-5 are identical.

5.4.2.7 Synthesis of $[(P_3{}^B)Fe(NNMe_2)]^-$ Isotopologues

The synthesis of isotopologues of $[(P_3{}^B)Fe(NNMe_2)]^-$ including ^{57}Fe, ^{15}N, and ^{13}C were prepared as described above, but using the corresponding isotopologue of $(P_3{}^B)Fe(NNMe_2)$ as the starting material.

5.4.3 Computational Methods

All calculations were carried out using version 4.0.1.2 of the ORCA package.[95] Based on previous work,[17,24] DFT calculations utilized the TPSS family of meta-GGA exchange-correlation functionals, incorporating either 0% (TPSS),[96] 10% (TPSSh),[97] or 25% (TPSS0) Hartree-Fock exchange,[98,99] in combination with the zeroth order regular approximation (ZORA) to account for relativistic effects.[100] Gas-phase geometry optimizations were carried out using the TPSS functional in combination with the scalar relativistically recontracted versions of the def2-SVP (ZORA-def2-SVP) basis sets on C and H, and the scalar relativistically recontracted versions of the def2-TZVP (ZORA-def2-TZVP) basis sets on Fe, B, P, and N atoms and the C and H atoms of the "$NNMe_2$" ligand.[101] For all atoms, the general-purpose segmented all-electron relativistically contracted auxiliary Coulomb-fitting basis (SARC/J) was employed, which is a decontraction of the def2/J basis developed by Weigend.[102] Optimizations were followed by a frequency calculation to ensure a true minimum. For the computation of state energies and valence electronic structures, single point calculations were carried out on these optimized geometries using an enlarged basis set, ZORA-def2-TZVPP, on Fe, B, P and the "$NNMe_2$" ligand.[101] These calculations employed a fine integration grid (ORCA Grid5) during geometry optimization, as well as during the final single-point calculation (Grid6). Calculations employing the hybrid meta-GGA functionals TPSSh/TPSS0 were accelerated using the RIJCOSX approximation with a fine auxiliary integration grid (ORCA GridX5).[103] Broken-symmetry (BS) DFT calculations employed the `FlipSpin` method implemented in ORCA. In this approach, a high-spin solution is converged self-consistently, the spins on a selected group of atoms are "flipped" by exchanging the α and β spin density matrix elements on these centers, and then a solution of the desired multiplicity is converged. The BS character of the resultant solution can be determined following the corresponding orbital transformation of the converged Kohn-Sham orbitals,[72] where pairs of spin-coupled orbitals have spatial overlap less than 1. The degree of orbital overlap can be interpreted as a measure of the strength of the

magnetic coupling.[104] In all cases, however, the BS solutions obtained explicitly via this method could also be arrived at by simply performing spin-unrestricted DFT calculations on the state of interest.

For DFT calculations of EPR properties (g-tensors and HFC constants), the def2-TZVP basis was employed on all C and H atoms not involving the $NNMe_2$ ligand,[105] while the CP(PPP) basis was employed for Fe,[106] and the IGLO-III basis employed for the B, P, and "$NNMe_2$" atoms.[107] Given the lack of recontracted versions of these bases, scalar relativistic effects were ignored. The general purpose def2/J Coulomb fitting basis was employed on atoms using the def2-TZVP basis,[102] while the AutoAux feature of ORCA was used to generate auxiliary bases for the other atoms on-the-fly;[108] all auxiliary bases were fully decontracted. To capture core polarization effects, the radial integration accuracy was increased around the Fe, B, P, and "$NNMe_2$" atoms (`IntAcc 7`). The calculation of g-tensors and HFC constants employed the `eprnmr` module of ORCA. Calculation of the g-tensors and the spin-orbit coupling (SOC) contributions to the Fe HFC constant used the `SOMF(1X)` mean-field SOC operator,[109] which is employed in a coupled-perturbed Kohn-Sham framework.[81,110] DFT calculation of the EPR properties of free *N*,*N*-dimethylhydrazyl radicals used the same methods for geometry optimization and property prediction described above, as this was found to almost quantitatively reproduce the experimental spectra of the known radicals $[HNNMe_2]^{\bullet}$ and $[H_2NNMe_2]^{\bullet+}$.[37,39,111] When calculating the EPR properties of $[NNMe_2]^{\bullet-}$, we considered both the ground-state geometry as well as a theoretical planar geometry more closely matching that of the "$NNMe_2$" ligands of $[(P_3{}^B)Fe(NNMe_2)]^{+/0/-}$ observed crystallographically. The planar structure was obtained using a constrained geometry optimization under C_{2v} symmetry.

The TD-DFT calculation of the optical spectrum of $(P_3{}^B)Fe(NAd)$ utilized the TPSSh functional, the def2-SVP basis set on C and H, and the def2-TZVPP basis set on the remaining atoms, along with the def2/J auxiliary basis. The first 25 roots were included in the calculation, which was performed using the Tamm-Dancoff approximation. The

TD-DFT calculation of the XANES spectrum of [(P_3^B)Fe($NNMe_2$)][BAr^F_4] utilized the same calibrated methods reported earlier.[17] It should be noted that the COSMO continuum solvation model was removed from version 4 of ORCA, so solid-state effects were instead approximated using the conductor-like polarizable continuum model (CPCM) using an infinite dielectric.

Multireference calculations employed the scalar relativistically recontracted versions of Dunning's correlation-consistent basis sets tailored for use with the Douglas-Kroll-Hess (DKH) Hamiltonian to account for relativistic effects. The basis sets were of double-ζ quality on the C and H atoms (cc-pVDZ-DK),[112] and triple-ζ quality on the Fe, B, P, and "$NNMe_2$" atoms, the latter being augmented with additional diffuse functions for greater flexibility (aug-cc-pVTZ-DK).[113] In all calculations, the second order DKH Hamiltonian (DKH2) was used.[114] To accelerate these calculations, the RIJK approximation was used in combination with the aug-cc-pVTZ/JK auxiliary Coulomb/exchange fitting basis for the C, H, B, P, and N atoms;[115] the AutoAux feature was used to generate an auxiliary basis set for Fe,[108] and all auxiliary bases were decontracted. Input orbitals were taken from the quasi-restricted orbitals[116] of a DFT calculation employing the BP86 exchange-correlation functional.[117,118] State-averaged CASSCF calculations employed equal weights for all roots. After convergence of the CASSCF reference was achieved, a second-order N-electron perturbation theory (NEVPT2) calculation was performed to account for dynamic correlation effects.[119] For efficiency, NEVPT2 calculations employed the strongly-contracted variant of NEVPT2 parameterized in ORCA (SC-NEVPT2).[120] The calculation of g-tensors and the anisotropic parts of the HFC tensors was performed using the multireference CI (`mrci`) module. CAS-CI calculations were performed using a converged SA-CASSCF reference. The MRCI module computes g-tensors and HFC tensors using a sum-over-states formalism, as described elsewhere.[121] In all cases, the first 10 roots of the same multiplicity as the ground state were considered in these calculations. Localization of the active space orbitals used the algorithm of Foster and Boys.[122]

References

(1) Chatt, J.; Heath, G. A.; Richards, R. L. *J. Chem. Soc., Chem. Commun.* **1972**, 1010–1011.

(2) Chatt, J.; Heath, G. A.; Richards, R. L. *J. Chem. Soc., Dalton Trans.* **1974**, 2074–2082.

(3) Chatt, J.; Hussain, W.; Leigh, G. J.; Neukomm, H.; Pickett, C. J.; Rankin, D. A. *J. Chem. Soc., Chem. Commun.* **1980**, 1024–1025.

(4) Chatt, J.; Dilworth, J. R.; Richards, R. L. *Chem. Rev.* **1978**, *78*, 589–625.

(5) Dilworth, J. R. *Coord. Chem. Rev.* **2017**, *330*, 53–94.

(6) Hussain, W.; Leigh, G. J.; Pickett, C. J. *J. Chem. Soc., Chem. Commun.* **1982**, 747–748.

(7) Horn, K. H.; Böres, N.; Lehnert, N.; Mersmann, K.; Näther, C.; Peters, G.; Tuczek, F. *Inorg. Chem.* **2005**, *44*, 3016–3030.

(8) Dreher, A.; Mersmann, K.; Näther, C.; Ivanovic-Burmazovic, I.; van Eldik, R.; Tuczek, F. *Inorg. Chem.* **2009**, *48*, 2078–2093.

(9) Patel, S.; Li, Y.; Odom, A. L. *Inorg. Chem.* **2007**, *46*, 6373–6381.

(10) Keane, A. J.; Zavalij, P. Y.; Sita, L. R. *J. Am. Chem. Soc.* **2013**, *135*, 9580–9583.

(11) Mansuy, D.; Battioni, P.; Mahy, J. P. *J. Am. Chem. Soc.* **1982**, *104*, 4487–4489.

(12) Mahy, J. P.; Battioni, P.; Mansuy, D.; Fisher, J.; Weiss, R.; Mispelter, J.; Morgenstern-Badarau, I.; Gans, P. *J. Am. Chem. Soc.* **1984**, *106*, 1699–1706.

(13) Pearce, A. J.; Cassabaum, A. A.; Gast, G. E.; Frontiera, R. R.; Tonks, I. A. *Angew. Chem. Int. Ed.* **2016**, *55*, 13169–13173.

(14) Stucke, N.; Flöser, B. M.; Weyrich, T.; Tuczek, F. *Eur. J. Inorg. Chem.* **2018**, 1337–1355.

(15) Moret, M.-E.; Peters, J. C. *J. Am. Chem. Soc.* **2011**, *133*, 18118–18121.

(16) Anderson, J. S.; Cutsail, G. E.; Rittle, J.; Connor, B. A.; Gunderson, W. A.; Zhang, L.; Hoffman, B. M.; Peters, J. C. *J. Am. Chem. Soc.* **2015**, *137*, 7803–7809.

(17) Thompson, N. B.; Green, M. T.; Peters, J. C. *J. Am. Chem. Soc.* **2017**, *139*, 15312–15315.

(18) Rittle, J.; Peters, J. C. *J. Am. Chem. Soc.* **2016**, *138*, 4243–4248.

(19) Hammes-Schiffer, S.; Soudackov, A. V. *J. Phys. Chem. B* **2008**, *112*, 14108–14123.

(20) Dietl, N.; Schlangen, M.; Schwarz, H. *Angew. Chem. Int. Ed.* **2012**, *51*, 5544–5555.

(21) Suarez Alma, I. O.; Lyaskovskyy, V.; Reek Joost, N. H.; van der Vlugt Jarl, I.; de Bruin, B. *Angew. Chem. Int. Ed.* **2013**, *52*, 12510–12529.

(22) Del Castillo, T. J.; Thompson, N. B.; Peters, J. C. *J. Am. Chem. Soc.* **2016**, *138*, 5341–5350.

(23) Chalkley, M. J.; Del Castillo, T. J.; Matson, B. D.; Roddy, J. P.; Peters, J. C. *ACS Cent. Sci.* **2017**, *3*, 217–223.

(24) Matson, B. D.; Peters, J. C. *ACS Catal.* **2018**, *8*, 1448–1455.

(25) Kahlal, S.; Saillard, J.-Y.; Hamon, J.-R.; Manzur, C.; Carrillo, D. *J. Chem. Soc., Dalton Trans.* **1998**, 1229–1240.

(26) Kahlal, S.; Saillard, J.-Y.; Hamon, J.-R.; Manzur, C.; Carrillo, D. *New J. Chem.* **2001**, *25*, 231–242.

(27) Kaim, W. *Inorg. Chem.* **2011**, *50*, 9752–9765.

(28) Wiberg, N.; Häring, H. W.; Schieda, O. *Angew. Chem. Int. Ed.* **1976**, *15*, 386–387.

(29) Veith, M. *Angew. Chem. Int. Ed.* **1976**, *15*, 387–388.

(30) Crichton, B. A. L.; Dilworth, J. R.; Pickett, C. J.; Chatt, J. *J. Chem. Soc., Dalton Trans.* **1981**, 419–424.

(31) Huynh, M. H. V.; El-Samanody, E.-S.; Demadis, K. D.; White, P. S.; Meyer, T. J. *Inorg. Chem.* **2000**, *39*, 3075–3085.

(32) Nicholson, T.; Kramer, D. J.; Davison, A.; Jones, A. G. *Inorg. Chim. Acta* **2003**, *353*, 269–275.

(33) Yandulov, D. V.; Schrock, R. R. *Inorganic Chemistry* **2005**, *44*, 1103–1117.

(34) Hinsberg, W. D.; Dervan, P. B. *J. Am. Chem. Soc.* **1978**, *100*, 1608–1610.

(35) Sylwester, A. P.; Dervan, P. B. *J. Am. Chem. Soc.* **1984**, *106*, 4648–4650.

(36) Stepanić, V.; Baranović, G. *Chem. Phys.* **2000**, *254*, 151–168.

(37) Malatesta, V.; Ingold, K. U. *J. Am. Chem. Soc.* **1973**, *95*, 6110–6113.

(38) Malatesta, V.; Lindsay, D.; Horswill, E. C.; Ingold, K. U. *Can. J. Chem.* **1974**, *52*, 864–866.

(39) Smith, P.; Stevens, R. D.; Kaba, R. A. *J. Phys. Chem.* **1971**, *75*, 2048–2055.

(40) Tonks, I. A.; Durrell, A. C.; Gray, H. B.; Bercaw, J. E. *J. Am. Chem. Soc.* **2012**, *134*, 7301–7304.

(41) Moret, M.; Peters, J. C. *Angew. Chem. Int. Ed.* **2011**, *50*, 2063–2067.

(42) Dykstra, C. E.; Schaefer, H. F. *J. Am. Chem. Soc.* **1976**, *98*, 2689–2695.

(43) Shoji, M.; Nishiyama, Y.; Maruno, Y.; Koizumi, K.; Kitagawa, Y.; Yamanaka, S.; Kawakami, T.; Okumura, M.; Yamaguchi, K. *Int. J. Quantum Chem.* **2004**, *100*, 887–906.

(44) Pierloot, K.; Zhao, H.; Vancoillie, S. *Inorg. Chem.* **2010**, *49*, 10316–10329.

(45) Radoń, M.; Broclawik, E.; Pierloot, K. *J. Phys. Chem. B* **2010**, *114*, 1518–1528.

(46) Tomson, N. C.; Crimmin, M. R.; Petrenko, T.; Rosebrugh, L. E.; Sproules, S.; Boyd, W. C.; Bergman, R. G.; DeBeer, S.; Toste, F. D.; Wieghardt, K. *J. Am. Chem. Soc.* **2011**, *133*, 18785–18801.

(47) Vela, J.; Cirera, J.; Smith, J. M.; Lachicotte, R. J.; Flaschenriem, C. J.; Alvarez, S.; Holland, P. L. *Inorg. Chem.* **2007**, *46*, 60–71.

(48) Pasinszki, T.; Krebsz, M.; Tarczay, G.; Wentrup, C. *J. Org. Chem.* **2013**, *78*, 11985–11991.

(49) Cotton, F. A.; Wilkinson, G., *Advanced Inorganic Chemistry*, 5th ed.; Wiley: New York, 1988.

(50) Galindo, A.; Hills, A.; Hughes, D. L.; Richards, R. L. *J. Chem. Soc., Chem. Commun.* **1987**, 1815–1816.

(51) Galindo, A.; Hills, A.; Hughes, D. L.; Richards, R. L.; Hughes, M.; Mason, J. *J. Chem. Soc., Dalton Trans.* **1990**, 283–288.

(52) Vale, M. G.; Schrock, R. R. *Inorg. Chem.* **1993**, *32*, 2767–2772.

(53) Li, Y.; Shi, Y.; Odom, A. L. *J. Am. Chem. Soc.* **2004**, *126*, 1794–1803.

(54) Clulow, A. J.; Selby, J. D.; Cushion, M. G.; Schwarz, A. D.; Mountford, P. *Inorg. Chem.* **2008**, *47*, 12049–12062.

(55) Tiong, P. J.; Nova, A.; Schwarz, A. D.; Selby, J. D.; Clot, E.; Mountford, P. *Dalton Trans.* **2012**, *41*, 2277–2288.

(56) Lehnert, N.; Tuczek, F. *Inorg. Chem.* **1999**, *38*, 1659–1670.

(57) Horn, K. H.; Lehnert, N.; Tuczek, F. *Inorg. Chem.* **2003**, *42*, 1076–1086.

(58) Groom, C. R.; Bruno, I. J.; Lightfoot, M. P.; Ward, S. C. *Acta Crystallogr. B* **2016**, *72*, 171–179.

(59) Vogel, C.; Heinemann, F. W.; Sutter, J.; Anthon, C.; Meyer, K. *Angew. Chem. Int. Ed.* **2008**, *47*, 2681–2684.

(60) Scepaniak, J. J.; Fulton, M. D.; Bontchev, R. P.; Duesler, E. N.; Kirk, M. L.; Smith, J. M. *J. Am. Chem. Soc.* **2008**, *130*, 10515–10517.

(61) Rohde, J.-U.; Betley, T. A.; Jackson, T. A.; Saouma, C. T.; Peters, J. C.; Que, L. *Inorg. Chem.* **2007**, *46*, 5720–5726.

(62) King, E. R.; Hennessy, E. T.; Betley, T. A. *J. Am. Chem. Soc.* **2011**, *133*, 4917–4923.

(63) Iovan, D. A.; Betley, T. A. *J. Am. Chem. Soc.* **2016**, *138*, 1983–1993.

(64) Gütlich, P.; Bill, E.; Trautwein, A. X., *Mössbauer Spectroscopy and Transition Metal Chemistry: Fundamentals and Applications*; Springer: New York, 2011.

(65) Westre, T. E.; Kennepohl, P.; DeWitt, J. G.; Hedman, B.; Hodgson, K. O.; Solomon, E. I. *J. Am. Chem. Soc.* **1997**, *119*, 6297–6314.

(66) Komorovsky, S.; Repisky, M.; Ruud, K.; Malkina, O. L.; Malkin, V. G. *J. Phys. Chem. A* **2013**, *117*, 14209–14219.

(67) Jensen, M. P.; Costas, M.; Ho, R. Y. N.; Kaizer, J.; Mairata i Payeras, A.; Münck, E.; Que, L.; Rohde, J.-U.; Stubna, A. *J. Am. Chem. Soc.* **2005**, *127*, 10512–10525.

(68) Krzystek, J.; England, J.; Ray, K.; Ozarowski, A.; Smirnov, D.; Que, L.; Telser, J. *Inorg. Chem.* **2008**, *47*, 3483–3485.

(69) Lacy, D. C.; Gupta, R.; Stone, K. L.; Greaves, J.; Ziller, J. W.; Hendrich, M. P.; Borovik, A. S. *J. Am. Chem. Soc.* **2010**, *132*, 12188–12190.

(70) Bucinsky, L. et al. *Inorg. Chem.* **2017**, *56*, 4751–4768.

(71) Neese, F. *Coord. Chem. Rev.* **2009**, *253*, 526–563.

(72) Neese, F. *J. Phys. Chem. Solids.* **2004**, *65*, 781–785.

(73) Pierloot, K. *Mol. Phys.* **2003**, *101*, 2083–2094.

(74) Takatsuka, K.; Fueno, T.; Yamaguchi, K. *Theor. Chim. Acta* **1978**, *48*, 175–183.

(75) Staroverov, V. N.; Davidson, E. R. *Chem. Phys. Lett.* **2000**, *330*, 161–168.

(76) Head-Gordon, M. *Chem. Phys. Lett.* **2003**, *372*, 508–511.

(77) Boguslawski, K.; Jacob, C. R.; Reiher, M. *J. Chem. Theory Comput.* **2011**, *7*, 2740–2752.

(78) Leffler, J. E.; Watts, G. B.; Tanigaki, T.; Dolan, E.; Miller, D. S. *J. Am. Chem. Soc.* **1970**, *92*, 6825–6830.

(79) Moret, M.-E.; Zhang, L.; Peters, J. C. *J. Am. Chem. Soc.* **2013**, *135*, 3792–3795.

(80) Fessenden, R. W. *J. Phys. Chem.* **1967**, *71*, 74–83.

(81) Neese, F. *J. Chem. Phys.* **2001**, *115*, 11080–11096.

(82) Lu, J.-B.; Ma, X.-L.; Wang, J.-Q.; Liu, J.-C.; Xiao, H.; Li, J. *J. Phys. Chem. A* **2018**, DOI: 10.1021/acs.jpca.8b02089.

(83) Del Castillo, T. J.; Thompson, N. B.; Suess, D. L. M.; Ung, G.; Peters, J. C. *Inorg. Chem.* **2015**, *54*, 9256–9262.

(84) Rittle, J.; Peters, J. C. *J. Am. Chem. Soc.* **2017**, *139*, 3161–3170.

(85) Hauser, C.; Glaser, T.; Bill, E.; Weyhermüller, T.; Wieghardt, K. *J. Am. Chem. Soc.* **2000**, *122*, 4352–4365.

(86) Mersmann, K.; Horn, K. H.; Böres, N.; Lehnert, N.; Studt, F.; Paulat, F.; Peters, G.; Ivanovic-Burmazovic, I.; van Eldik, R.; Tuczek, F. *Inorg. Chem.* **2005**, *44*, 3031–3045.

(87) Sippel, D.; Rohde, M.; Netzer, J.; Trncik, C.; Gies, J.; Grunau, K.; Djurdjevic, I.; Decamps, L.; Andrade, S. L. A.; Einsle, O. *Science* **2018**, *359*, 1484–1489.

(88) Sheldrick, G. M. *Acta Crystallogr. A* **2015**, *71*, 3–8.

(89) Sheldrick, G. M. *Acta Crystallogr. C* **2015**, *71*, 3–8.

(90) Prisecaru, I. "WMOSS4 Mössbauer Spectral Analysis Software", www.wmoss.org, 2009–2016.

(91) Stoll, S.; Schweiger, A. *J. Magn. Reson.* **2006**, *178*, 42–55.

(92) Hyde, J. S.; Pasenkiewicz-Gierula, M.; Jesmanowicz, A.; Antholine, W. E. *Appl. Magn. Reson.* **1990**, *1*, 483.

(93) Oyala, P. H.; Stich, T. A.; Britt, R. D. *Photosynth. Res.* **2015**, *124*, 7–18.

(94) G. N. George, I. J. Pickering, EXAFSPAK: A suite of computer programs for analysis of X-ray absorption spectra. SSRL, Stanford. (1995).

(95) Neese, F. *WIRES Comput. Mol. Sci.* **2011**, *2*, 73–78.

(96) Tao, J.; Perdew, J. P.; Staroverov, V. N.; Scuseria, G. E. *Phys. Rev. Lett.* **2003**, *91*, 146401.

(97) Staroverov, V. N.; Scuseria, G. E.; Tao, J.; Perdew, J. P. *J. Chem. Phys.* **2003**, *119*, 12129–12137.

(98) Grimme, S. *J. Phys. Chem. A* **2005**, *109*, 3067–3077.

(99) Quintal, M. M.; Karton, A.; Iron, M. A.; Boese, A. D.; Martin, J. M. L. *J. Phys. Chem. A* **2006**, *110*, 709–716.

(100) Van Wüllen, C. *J. Chem. Phys.* **1998**, *109*, 392–399.

(101) Pantazis, D. A.; Chen, X.-Y.; Landis, C. R.; Neese, F. *J. Chem. Theory Comput.* **2008**, *4*, 908–919.

(102) Weigend, F. *Phys. Chem. Chem. Phys.* **2006**, *8*, 1057–1065.

(103) Neese, F.; Wennmohs, F.; Hansen, A.; Becker, U. *Chem. Phys.* **2009**, *356*, 98–109.

(104) Ye, S.; Geng, C.-Y.; Shaik, S.; Neese, F. *Phys. Chem. Chem. Phys.* **2013**, *15*, 8017–8030.

(105) Weigend, F.; Ahlrichs, R. *Phys. Chem. Chem. Phys.* **2005**, *7*, 3297–3305.

(106) Neese, F. *Inorg. Chim. Acta* **2002**, *337*, 181–192.

(107) Huzinaga, S. *J. Chem. Phys.* **1965**, *42*, 1293–1302.

(108) Stoychev, G. L.; Auer, A. A.; Neese, F. *J. Chem. Theory Comput.* **2017**, *13*, 554–562.

(109) Neese, F. *J. Chem. Phys.* **2005**, *122*, 034107.

(110) Neese, F. *J. Chem. Phys.* **2003**, *118*, 3939–3948.

(111) Hermosilla, L.; Calle, P.; García de la Vega, J. M.; Sieiro, C. *J. Phys. Chem. A* **2006**, *110*, 13600–13608.

(112) De Jong, W. A.; Harrison, R. J.; Dixon, D. A. *J. Chem. Phys.* **2001**, *114*, 48–53.

(113) Balabanov, N. B.; Peterson, K. A. *J. Chem. Phys.* **2005**, *123*, 064107.

(114) Reiher, M. *WIRES Comput. Mol. Sci.* **2012**, *2*, 139–149.

(115) Furche, F.; Ahlrichs, R.; Hättig, C.; Klopper, W.; Sierka, M.; Weigend, F. *WIRES Comput. Mol. Sci.* **2014**, *4*, 91–100.

(116) Neese, F. *J. Am. Chem. Soc.* **2006**, *128*, 10213–10222.

(117) Becke, A. D. *Phys. Rev. A* **1988**, *38*, 3098–3100.

(118) Perdew, J. P. *Phys. Rev B* **1986**, *33*, 8822–8824.

(119) Angeli, C.; Cimiraglia, R.; Evangelisti, S.; Leininger, T.; Malrieu, J. P. *J. Chem. Phys.* **2001**, *114*, 10252–10264.

(120) Angeli, C.; Cimiraglia, R.; Malrieu, J.-P. *Chem. Phys. Lett.* **2001**, *350*, 297–305.

(121) Neese, F. *Magn. Reson. Chem.* **2004**, *42*, S187–S198.

(122) Foster, J. M.; Boys, S. F. *Rev. Mod. Phys.* **1960**, *32*, 300–302.

Appendix A

SUPPLEMENTARY INFORMATION FOR CHAPTER 2

A.1 XRD Refinement Details

A.1.1 [Na(12-c-4)$_2$][(P_3^B)Co(N_2)]

The 12-c-4 fragments are disordered for [Na(12-c-4)$_2$][(P_3^B)Co(N_2)]. One 12-c-4 is fully disordered over two unique positions. The other 12-c-4 shows a disorder in the methyl carbons but not the oxygen atoms. In all cases, the positions of the carbons could be located in the difference map and refined anisotropically and the hydrogen atoms were placed at geometrically calculated positions as usual. The oxygen atom in one of the solvent THF molecules is disordered over two positions. The other THF molecule shows large thermal ellipsoids, potentially indicating an unresolved disorder of this moiety. A Et_2O molecule was located on an inversion center and is therefore disordered about this symmetry element. The occupancies of all disordered fragments were freely refined and the bond lengths and angles were restrained to be the same for the disordered fragments. Hydrogen atoms were not included on any of the solvent molecules for these reasons. Several fluorine atoms of the -CF_3 substituents of the [$BAr^F{}_4$]$^-$ anion are disordered by rotation about the C_{Ar}–C bonds to varying extents and were refined as two-part positional disorders in each case. The occupancies of the disordered fragments were freely refined and the bond lengths and angles were restrained to be the same for the disordered fragments.

A.1.2 (P_3^C)Co(N_2)

One phosphorous isopropyl group is disordered for (P_3^C)Co(N_2); one methyl group is disordered over two positions. Each position was located in the difference map and refined anisotropically with hydrogen atoms calculated in the usual manner. The occupancies of the two fragments were refined freely. In addition, after refinement, the model displays large

positive residual electron density located within 0.06 Å of the Co atom. This is likely due to unresolved disorder; attempts to include this as disorder with respect to the Co atom do not improve the model upon refinement. The residual electron density may also be due to poor data at high angles, as imposing a high-angle cutoff (using `SHEL 100.0 0.84`) during refinement reduces the residual density significantly. Importantly, the bond distances about the Co atom do not change significantly when this restraint is imposed.

A.1.3 $[(P_3{}^C)Co(N_2)][BAr^F{}_4]$

The isopropyl substituents on on phosphorous atom are disordered for $[(P_3{}^C)Co(N_2)][BAr^F{}_4]$. The disorder reflects simultaneous rotation of the methyl substituents about the methine carbon for each isopropyl group, which was modeled as a two-part positional disorder. All carbons in the disordered fragments were located in the difference map and refined anisotropically, with hydrogen atoms geometrically calculated in the usual manner. In addition, two -CF_3 groups of the $[BAr^F{}_4]^-$ anion are disordered between two positions, reflecting rotation of the -CF_3 group with simultaneous rotation of the aryl fragment attached to B. Both -CF_3 groups were refined as two-part positional disorders. In all cases, the occupancies of disordered fragments were freely refined and the bond lengths and angles were restrained to be the same for disordered fragments of the same type.

A.2 Computational Methods

All computations were carried out using version 3.0.2 of the ORCA program system.[1] DFT calculations employed the BP86 exchange correlation functional. The 6-31+G* basis set[2–8] was used for all geometry optimizations, while single point calculations were performed at the 6-311+G** level of theory.[9] The atomic coordinates of $[(P_3{}^B)Co(N_2)]^-$ and $(P_3{}^C)Co(N_2)$ obtained from XRD studies were used as inputs for geometry optimizations at the lower level of theory, and the optimized geometries obtained in this way were used as inputs for single point calculations of the electron densities at the higher level of theory. Molecular electrostatic potentials were computed from the calculated electron densities us-

ing the `orca_vpot` subroutine. Atomic charges were computed using the CHELPG method developed by Breneman and Wiberg.[10]

A.3 Treatment of [Na(12-c-4)$_2$][(P_3^B)Co(N_2)] with 10 equiv $HBAr^F_4$ and 12 equiv KC_8

[Na(12-c-4)$_2$][(P_3^B)Co(N_2)] (10 mg, 0.01 mmol) was suspended in Et_2O (0.5 mL) in a 20 mL scintillation vial equipped with a stir bar. This suspension was cooled to −78 °C in a cold well inside of a N_2 glovebox. A solution of $HBAr^F_4$ (95 mg, 0.094 mmol) in Et_2O (1.5 mL) similarly cooled to −78 °C was added to this suspension in one portion with stirring. Residual acid was dissolved in cold Et_2O (0.25 mL) and added subsequently. This mixture was allowed to stir for 5 minutes. Then KC_8 (16 mg, 0.119 mmol) was suspended in cold Et_2O (0.75 mL) and added to the reaction mixture over the course of 1 minute. The vial was then sealed, and the reaction was allowed to stir for 40 min at −78 °C before being warmed to room temperature and stirred for 15 min. The reaction mixture was then filtered and evaporated to dryness under vacuum. The resulting residue was extracted with C_6D_6 and submitted to ^{31}P NMR spectroscopy, revealing a signal consistent with uncoordinated phosphine at 10.8 ppm.

A.4 Variable Temperature T_1 measurements for (P_3^C)Co(H_2):

A sample of (P_3^C)Co(H_2) was prepared in an NMR tube equipped with a J-Young valve as described. T_1 measurements were performed via a standard pulse–inversion–recovery method using a 180°–τ–90° pulse sequence. The 90° pulse was recalibrated periodically at low temperature. Raw magnetization data were fit according to,

$$M_z = M_o\left(1 - 2\exp(-\frac{\tau}{T_1})\right) \tag{A.1}$$

to extract values of T_1 at each temperature (Figure A.1).

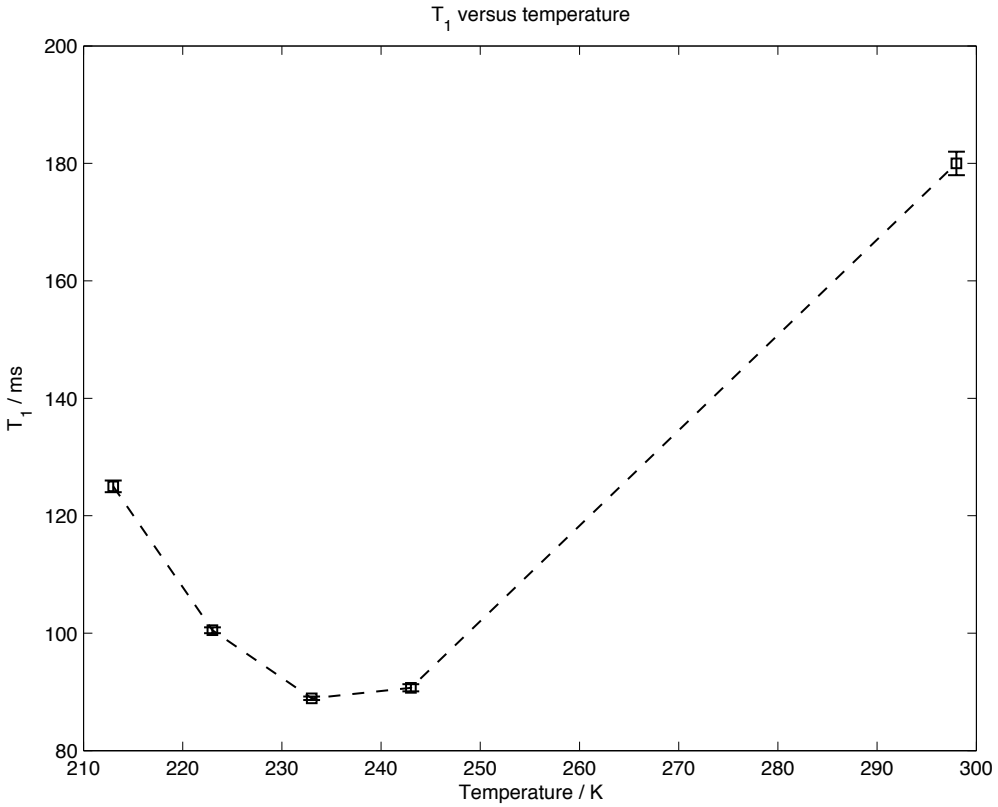

Figure A.1: Variable temperature T_1 measurements for the hydride resonance of $(P_3{}^C)Co(H)_2$.

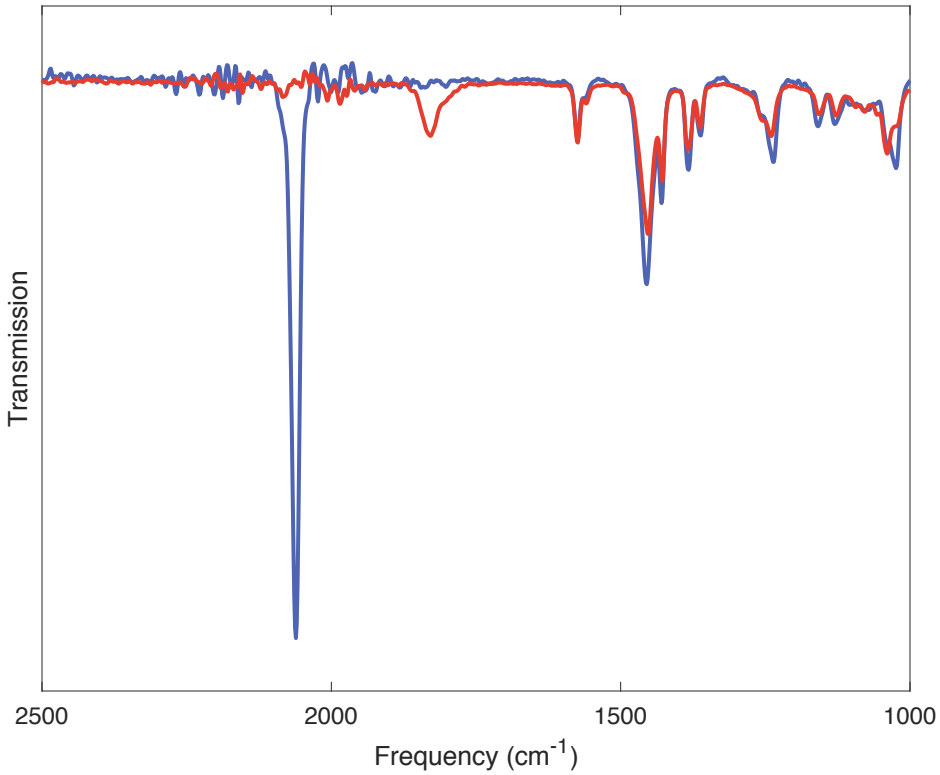

Figure A.2: IR spectra of $(P_3{}^C)Co(N_2)$ (blue) and $(P_3{}^C)Co(H)_2$ (red), collected on thin films deposited from C_6D_6 solutions. The sample of $(P_3{}^C)Co(H)_2$ was dried under a stream of H_2 to prevent reversion to $(P_3{}^C)Co(N_2)$.

A.5 NH_3 Generation Results

A.5.1 Standard NH_3 Generation Reaction Procedure with $[Na(12\text{-}c\text{-}4)_2][(P_3{}^BCo(N_2)]$

Table A.1: UV-vis quantification results for standard NH_3 generation experiments with $[Na(12\text{-}c\text{-}4)_2][(P_3{}^BCo(N_2)]$

Iteration	Absorbance (635 nm)	Equiv NH_3/Co	% Yield Based on H^+
A	0.225	2.3	16
B	0.187	2.1	14
C	0.199	2.2	14
D	0.240	2.5	18
E	0.255	2.8	19
F	0.197	2.2	14
Average	0.217 ± 0.027	2.4 ± 0.3	16 ± 2

Hydrazine was not detected in the catalytic runs using a standard UV-vis quantification method [11].

A.5.2 Standard NH_3 Generation Reaction Procedure with $(P_3{}^B)Co(N_2)$

The procedure was identical to that of the standard NH_3 generation reaction protocol with the changes noted. The precursor used was $(P_3{}^B)Co(N_2)$ (1.3 mg, 0.002 mmol).

Table A.2: UV-vis quantification results for standard NH_3 generation experiments with $(P_3{}^B)Co(N_2)$

Iteration	Absorbance (635 nm)	Equiv NH_3/Co	% Yield Based on H^+
A	0.064	0.7	4
B	0.058	0.6	4
C	0.107	1.2	8
Average	0.076 ± 0.027	0.8 ± 0.3	5 ± 2

A.5.3 Standard NH_3 Generation Reaction Procedure with $[(P_3{}^B)Co(N_2)][BAr^F{}_4]$

The procedure was identical to that of the standard NH_3 generation reaction protocol with the changes noted. The precursor used was $[(P_3{}^B)Co(N_2)][BAr^F{}_4]$ (2.3 mg, 0.002 mmol).

Table A.3: UV-vis quantification results for standard NH_3 generation experiments with $[(P_3{}^B)Co(N_2)][BAr^F{}_4]$

Iteration	Absorbance (635 nm)	Equiv NH_3/Co	% Yield Based on H^+
A	0.092	1.4	6
B	0.122	1.8	9
C[a]	0.091	1.5	6
Average	0.107 ± 0.021	1.6 ± 0.2	7 ± 1

[a]Used 2.0 mg (0.001 mmol) of catalyst; omitted from average absorbance.

A.5.4 Standard NH_3 Generation Reaction Procedure with $(P_3{}^B)Co(Br)$

The procedure was identical to that of the standard NH_3 generation reaction protocol with the changes noted. The precursor used was $(P_3{}^B)Co(Br)$ (1.6 mg, 0.002 mmol).

Table A.4: UV-vis quantification results for standard NH_3 generation experiments with $(P_3{}^B)Co(Br)$

Iteration	Absorbance (635 nm)	Equiv NH_3/Co	% Yield Based on H^+
A	0.035	0.3	2
B	0.101	1.0	7
C[a]	0.088	0.7	6
Average	0.068 ± 0.047	0.7 ± 0.4	5 ± 3

[a]Used 2.0 mg (0.003 mmol) of catalyst; omitted from average absorbance.

A.5.5 Standard NH_3 Generation Reaction Procedure with $(P_3{}^{Si})Co(N_2)$

The procedure was identical to that of the standard NH_3 generation reaction protocol with the changes noted. The precursor used was $(P_3{}^{Si})Co(N_2)$ (1.5 mg, 0.002 mmol).

Table A.5: UV-vis quantification results for standard NH_3 generation experiments with $(P_3{}^{Si})Co(N_2)$

Iteration	Absorbance (635 nm)	Equiv NH_3/Co	% Yield Based on H^+
A	< 0.005	< 0.1	–
B	< 0.005	< 0.1	–
C	< 0.005	< 0.1	–
Average	-	< 0.1	–

A.5.6 Standard NH_3 Generation Reaction Procedure with $(P_3{}^C)Co(N_2)$

The procedure was identical to that of the standard NH_3 generation reaction protocol with the changes noted. The precursor used was $(P_3{}^C)Co(N_2)$ (1.4 mg, 0.002 mmol).

Table A.6: UV-vis quantification results for standard NH_3 generation experiments with $(P_3{}^C)Co(N_2)$

Iteration	Absorbance (635 nm)	Equiv NH_3/Co	% Yield Based on H^+
A	0.044	0.21	1.5
B	< 0.005	< 0.1	–
C	< 0.005	< 0.1	–
Average	0.02 ± 0.02	0.1 ± 0.1	–

A.5.7 Standard NH_3 Generation Reaction Procedure with $[(NArP_3)Co(Cl)][BPh_4]$

The procedure was identical to that of the standard NH_3 generation reaction protocol with the changes noted. The precursor used was $[(NArP_3)Co(Cl)][BPh_4]$ (1.9 mg, 0.002 mmol).

Table A.7: UV-vis quantification results for standard NH_3 generation experiments with $[(NArP_3)Co(Cl)][BPh_4]$

Iteration	Absorbance (635 nm)	Equiv NH_3/Co	% Yield Based on H^+
A	< 0.005	< 0.1	–
B	< 0.005	< 0.1	–
C	< 0.005	< 0.1	–
Average	-	< 0.1	–

A.5.8 Standard NH_3 Generation Reaction Procedure with (PBP)Co(N_2)

The procedure was identical to that of the standard NH_3 generation reaction protocol with the changes noted. The precursor used was (PBP)Co(N_2) (1.1 mg, 0.002 mmol).

Table A.8: UV-vis quantification results for standard NH_3 generation experiments with (PBP)Co(N_2)

Iteration	Absorbance (635 nm)	Equiv NH_3/Co	% Yield Based on H^+
A	0.021	0.15	1
B	0.03	0.29	2
C	0.057	0.62	4
Average	0.036 ± 0.019	0.4 ± 0.2	2 ± 1

A.5.9 Standard NH_3 Generation Reaction Procedure with $Co(PPh_3)_2I_2$

The procedure was identical to that of the standard NH_3 generation reaction protocol with the changes noted. The precursor used was $Co(PPh_3)_2I_2$ (1.8 mg, 0.002 mmol).

Table A.9: UV-vis quantification results for standard NH_3 generation experiments with $Co(PPh_3)_2I_2$

Iteration	Absorbance (635 nm)	Equiv NH_3/Co	% Yield Based on H^+
A[a]	0.036	0.3	2
B	0.036	0.3	2
C	0.046	0.4	3
Average	0.041 ± 0.007	0.4 ± 0.1	2 ± 0.4

[a]Used 2.0 mg (0.0024 mmol) of catalyst; omitted from average absorbance.

A.5.10 Standard NH_3 Generation Reaction Procedure with $CoCp_2$

The procedure was identical to that of the standard NH_3 generation reaction protocol with the changes noted. The precursor used was $CoCp_2$ (0.6 mg, 0.003 mmol).

Table A.10: UV-vis quantification results for standard NH_3 generation experiments with $CoCp_2$

Iteration	Absorbance (635 nm)	Equiv NH_3/Co	% Yield Based on H^+
A	0.020	0.09	1
B	0.008	0.02	0
C	0.033	0.20	2
Average	0.020 ± 0.013	0.1 ± 0.1	1 ± 1

A.5.11 Standard NH_3 Generation Reaction Procedure with $Co_2(CO)_8$

The procedure was identical to that of the standard NH_3 generation reaction protocol with the changes noted. The precursor used was $Co_2(CO)_8$ (0.4 mg, 0.001 mmol, 0.002 mmol Co) sampled as a 100 μL aliquot of a stock solution (2.0 mg $Co_2(CO)_8$ in 0.5 mL Et2O).

Table A.11: UV-vis quantification results for standard NH_3 generation experiments with $Co_2(CO)_8$

Iteration	Absorbance (635 nm)	Equiv NH_3/Co	% Yield Based on H^+
A	< 0.005	< 0.1	–
B	< 0.005	< 0.1	–
C	< 0.005	< 0.1	–
Average	-	< 0.1	–

A.5.12 NH_3 Generation Reaction of $[(P_3^B)Co(N_2)]^-$ with Reductant Added First Followed by Acid

N.B., the following experiment was conducted to study the effect of the order of addition of reagents in the NH_3 generation reaction with $[(P_3^B)Co(N_2)]^-$.

$[Na(12\text{-}c\text{-}4)_2][(P_3^B)Co(N_2)]$ (2.2 mg, 0.002 mmol) was suspended in Et_2O (0.5 mL) in a 20 mL scintillation vial. This suspension was cooled to −78 °C in a cold well inside of a N_2 glovebox. This suspension was transferred to a precooled Schlenk tube equipped with a stir bar. Residual solid was suspended in additional cold Et_2O (2×0.25 mL) and transferred subsequently. To this mixture was added a precooled suspension of KC_8 (16 mg, 0.119 mmol) in 0.5 mL Et_2O. Residual solid was suspended in additional cold Et_2O (2×0.25 mL) and transferred subsequently. This mixture was allowed to stir for 5 minutes at −78 °C. To this mixture was then added a similarly cooled to −78 °C solution of $HBAr^F_4$ (95 mg, 0.094 mmol) in Et_2O (1.5 mL) in one portion with stirring. Residual acid was dissolved in cold Et_2O (0.25 mL) and added subsequently. The Schlenk tube was then sealed, and the reaction was allowed to stir for 40 min at −78 °C before being warmed to room temperature and stirred for 15 min.

Table A.12: UV-vis quantification results for NH3 generation experiments with $[Na(12\text{-}c\text{-}4)_2][(P_3^B)Co(N_2)]$ and reductant being added first

Iteration	Absorbance (635 nm)	Equiv NH_3/Co	% Yield Based on H^+
A[a]	0.175	2.2	13
B	0.153	1.7	11
Average	–	1.9 ± 0.4	12 ± 1

[a]Used 1.9 mg (0.0018 mmol) of catalyst; omitted from average absorbance.

A.6 Calibration Curves for NH_3 and N_2H_4 Quantification

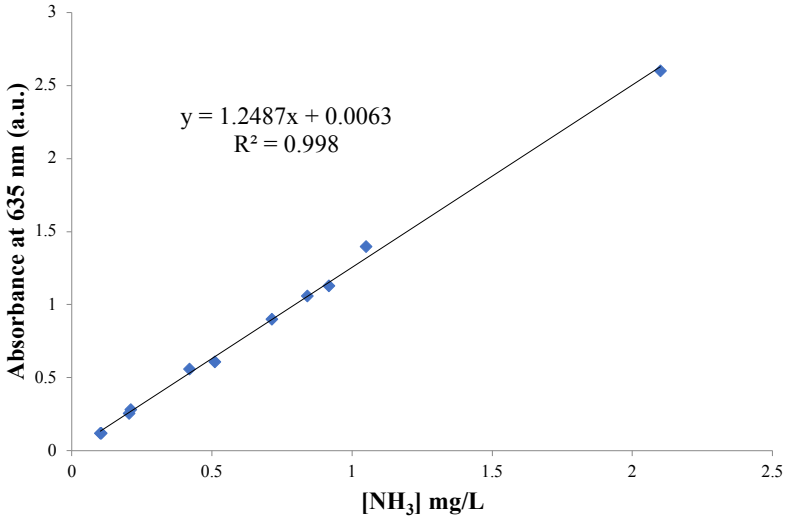

Figure A.3: Calibration curve for NH_3 quantification by indophenol method.

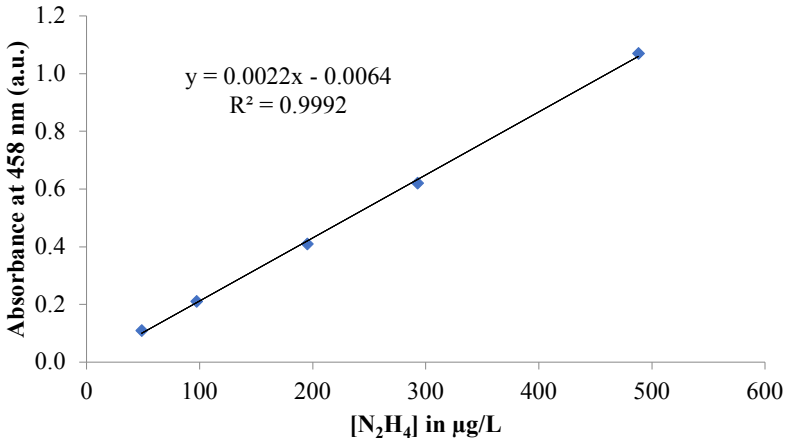

Figure A.4: Calibration curve for UV-vis quantification of N_2H_4.

A.7 XRD Tables

Table A.13: Crystal data and structure refinement for [Na(12-c-4)$_2$][($P_3{}^B$)Co(N_2)]

Empirical formula	$C_{62}H_{86}BCoN_2NaO_{10.5}P_3$
Formula weight	1212.97
Temperature (K)	100(2)
Crystal system	monoclinic
Space group	$P2_1/n$
a (Å)	10.8142(5)
b (Å)	27.5046(13)
c (Å)	22.3660(10)
α (°)	90
β (°)	91.141(2)
γ (°)	90
Volume (Å^3)	6651.2(5)
Z	4
ρ_{calc} (g cm^{-3})	1.211
μ (mm^{-1})	0.391
F(000)	2576
Crystal size (mm^3)	$0.38 \times 0.30 \times 0.25$
Radiation	Mo K_α (λ = 0.71073 Å)
2θ range for data collection (°)	3.94 to 86.26
Index ranges	$-20 \leq h \leq 20, -52 \leq k \leq 52, -43 \leq l \leq 43$
Reflections collected	451328
Independent reflections	49547 (R_{int} = 0.0632, R_σ = 0.1797)
Data/restraints/parameters	49547/1385/952
Goodness-of-fit on F^2	1.091
Final R indexes (I $\geq 2\sigma$(I))	R_1 = 0.0629, wR_2 = 0.1600
Final R indexes (all data)	R_1 = 0.0999, wR_2 = 0.1797
Largest diff. peak/hole (e Å^{-3})	1.78/−0.83

Table A.14: Crystal data and structure refinement for $[(P_3{}^B)Co(N_2)][BAr^F{}_4]$

Empirical formula	$C_{68}H_{66}B_2CoF_{24}P_3$
Formula weight	1512.67
Temperature (K)	100(2)
Crystal system	orthorhombic
Space group	Pbca
a (Å)	126.3920(15)
b (Å)	19.7049(13)
c (Å)	26.4995(19)
α (°)	90
β (°)	90
γ (°)	90
Volume (Å^3)	13781.1(16)
Z	8
ρ_{calc} (g cm^{-3})	1.458
μ (mm^{-1})	0.424
F(000)	6176
Crystal size (mm^3)	$0.35 \times 0.32 \times 0.24$
Radiation	Mo K_α (λ = 0.71073 Å)
2θ range for data collection (°)	3.72 to 64.06
Index ranges	$-39 \leq h \leq 39, -23 \leq k \leq 29, -39 \leq l \leq 39$
Reflections collected	377520
Independent reflections	23962 (Ri_{nt} = 0.0539, R_σ = 0.0255)
Data/restraints/parameters	23962/1174/1007
Goodness-of-fit on F^2	1.052
Final R indexes (I $\geq 2\sigma$(I))	R_1 = 0.0459, wR_2 = 0.1084
Final R indexes (all data)	R_1 = 0.0720, wR_2 = 0.124
Largest diff. peak/hole (e Å^{-3})	1.27/−1.34

Table A.15: Crystal data and structure refinement for $(P_3{}^C)Co(N_2)$

Empirical formula	$C_{37}H_{54}CoN_2P_3$
Formula weight	678.66
Temperature (K)	100(2)
Crystal system	trigonal
Space group	R-3
a (Å)	19.3720(4)
b (Å)	19.3720(4)
c (Å)	48.1269(14)
α (°)	90
β (°)	90
γ (°)	120
Volume (Å^3)	15641.1(8)
Z	18
ρ_{calc} (g cm^{-3})	1.297
μ (mm^{-1})	0.660
F(000)	6516
Crystal size (mm^3)	$0.380 \times 0.330 \times 0.210$
Radiation	Mo K_α (λ = 0.71073 Å)
2θ range for data collection (°)	2.57 to 49.982
Index ranges	$-20 \leq h \leq 22, -23 \leq k \leq 23, -57 \leq l \leq 57$
Reflections collected	56089
Independent reflections	6124 (R_{int} = 0.0480)
Data/restraints/parameters	6124/0/412
Goodness-of-fit on F^2	1.088
Final R indexes (I $\geq 2\sigma$(I))	R_1 = 0.0738, wR_2 = 0.1910
Final R indexes (all data)	R_1 = 0.0825, wR_2 = 0.2046
Largest diff. peak/hole (e Å^{-3})	3.13/−0.82

Table A.16: Crystal data and structure refinement for $[(P_3{}^C)Co(N_2)][BAr^F{}_4]$

Empirical formula	$C_{50}H_{60}BN_2F_{24}P_3Co$
Formula weight	1541.89
Temperature (K)	100(2)
Crystal system	orthorhombic
Space group	Pbca
a (Å)	19.7869(17)
b (Å)	25.670(2)
c (Å)	26.680(3)
α (°)	90
β (°)	90
γ (°)	90
Volume (Å^3)	13552(2)
Z	8
ρ_{calc} (g cm^{-3})	1.511
μ (mm^{-1})	0.421
F(000)	6296
Crystal size (mm^3)	$0.5 \times 0.3 \times 0.2$
Radiation	Mo K_α (λ = 0.71073 Å)
2θ range for data collection (°)	3.014 to 69.836
Index ranges	$-31 \leq h \leq 30, -40 \leq k \leq 40, -42 \leq l \leq 22$
Reflections collected	259812
Independent reflections	28701 (R_{int} = 0.0932)
Data/restraints/parameters	28701/138/1046
Goodness-of-fit on F^2	1.027
Final R indexes (I $\geq 2\sigma$(I))	R_1 = 0.0747, wR_2 = 0.1811
Final R indexes (all data)	R_1 = 0.1609, wR_2 = 0.2254
Largest diff. peak/hole (e Å^{-3})	1.42/−0.99

Table A.17: Crystal data and structure refinement for $[(NArP_3)Co(Cl)][BPh_4]$

Empirical formula	$C_{63}H_{80}BClCoNP_3$
Formula weight	1049.38
Temperature (K)	100(2)
Crystal system	triclinic
Space group	P-1
a (Å)	10.9491(7)
b (Å)	14.9096(10)
c (Å)	17.8512(11)
α (°)	83.935(3)
β (°)	79.063(3)
γ (°)	89.303(3)
Volume (Å^3)	2845.1(3)
Z	2
ρ_{calc} (g cm^{-3})	1.225
μ (mm^{-1})	0.472
F(000)	1118
Crystal size (mm^3)	$0.06 \times 0.04 \times 0.02$
Radiation	Mo K_α (λ = 0.71073 Å)
2θ range for data collection (°)	2.746 to 59.26
Index ranges	$-15 \leq h \leq 15, -20 \leq k \leq 20, -24 \leq l \leq 24$
Reflections collected	103727
Independent reflections	15990 (R_{int} = 0.0972, R_σ = 0.0851)
Data/restraints/parameters	15990/0/646
Goodness-of-fit on F^2	1
Final R indexes (I $\geq 2\sigma$(I))	R_1 = 0.0457, wR_2 = 0.0837
Final R indexes (all data)	R_1 = 0.0986, wR_2 = 0.0978
Largest diff. peak/hole (e Å^{-3})	0.53/−0.53

A.8 Optimized Coordinates from DFT Calculations

Table A.18: Optimized coordinates for $[(P_3{}^B)Co(N_2)]^-$

Atom	x (Å)	y (Å)	z (Å)
Co	5.278117	27.030827	17.095131
P	6.125307	28.046072	18.886124
P	3.060970	26.876003	16.921108
P	6.470673	27.144088	15.217970
N	5.627731	25.347668	17.547636
B	4.817109	29.224289	16.525303
C	5.694135	28.434162	14.141827
C	6.659431	29.741719	18.371700
C	8.356512	27.596015	15.041523
H	8.852351	26.898761	15.744263
C	2.349616	28.554979	17.254355
C	5.919014	30.203287	17.243942
C	4.249169	30.366935	14.143766
H	3.613935	31.089718	14.672539
C	3.298031	29.589854	17.025977
C	2.039333	26.364325	15.342342
H	2.508052	25.411985	15.027534
C	8.632318	29.033776	15.509744
H	9.724234	29.225133	15.517654
H	8.240887	29.232546	16.516177
H	8.165162	29.763658	14.825147
C	5.776139	28.504122	12.734994
H	6.347344	27.754542	12.173135
C	4.916069	29.360531	14.888824
C	7.654097	30.537197	18.977000
H	8.234583	30.154477	19.825542
C	7.696175	27.281935	19.678655
H	8.113875	28.047126	20.361713
C	6.505175	25.578416	14.108638
H	6.911463	25.889319	13.126608
C	5.097816	25.012789	13.875878
H	5.149571	24.119288	13.221278
H	4.435311	25.751866	13.395731
H	4.640644	24.714059	14.833576

Atom	x (Å)	y (Å)	z (Å)
C	8.769269	26.956916	18.629434
H	9.662297	26.521936	19.121695
H	9.088697	27.858071	18.080500
H	8.389141	26.224844	17.897330
C	5.086680	29.504431	12.026363
H	5.132996	29.537479	10.930024
C	6.213374	31.510860	16.783934
H	5.686654	31.896838	15.901416
C	7.428237	24.484391	14.686274
H	7.051899	24.114548	15.653220
H	8.463576	24.833229	14.841144
H	7.469612	23.621753	13.990762
C	8.994765	27.410878	13.648312
H	8.510202	28.063279	12.900483
H	8.967805	26.373773	13.274978
H	10.061346	27.711202	13.698303
C	2.863843	30.916667	17.272552
H	3.572857	31.743962	17.141225
C	7.207457	32.308686	17.379210
H	7.426705	33.305361	16.974755
C	5.200391	28.462003	20.552587
H	4.768821	27.487389	20.853188
C	4.046442	29.450732	20.325145
H	3.455086	29.562047	21.256355
H	3.367768	29.136369	19.521294
H	4.435636	30.447730	20.053591
N	5.856363	24.255842	17.849517
C	2.156451	25.748101	18.179342
H	1.079237	25.995091	18.113992
C	2.219078	27.389988	14.211139
H	1.747463	27.013325	13.281694
H	3.274732	27.607010	13.999641
H	1.735394	28.347886	14.470504
C	4.325635	30.444635	12.741090
H	3.772521	31.226887	12.204249
C	7.366421	26.022881	20.507880
H	6.952413	25.222948	19.873021
H	6.643132	26.219178	21.317461

Atom	*x* (Å)	*y* (Å)	*z* (Å)
H	8.291398	25.631095	20.977402
C	7.941743	31.818806	18.473149
H	8.737444	32.423937	18.925743
C	2.330158	24.252065	17.843386
H	3.384122	23.944599	17.933429
H	1.991543	23.999396	16.823928
H	1.738459	23.637376	18.550680
C	1.569705	31.207822	17.738468
H	1.280539	32.247270	17.943962
C	1.047615	28.839125	17.714406
H	0.337713	28.028272	17.918176
C	0.527783	26.123393	15.537653
H	0.020513	27.043374	15.878152
H	0.291949	25.313607	16.248614
H	0.074957	25.846405	14.563890
C	0.654345	30.165915	17.966300
H	-0.349915	30.380368	18.352394
C	2.613088	26.022466	19.619329
H	2.062411	25.370398	20.325778
H	2.433085	27.070631	19.910027
H	3.692725	25.819015	19.729581
C	6.065299	28.994192	21.714186
H	6.545033	29.952417	21.444344
H	6.851377	28.295209	22.046501
H	5.415134	29.194200	22.590266

Table A.19: Optimized coordinates for $(P_3{}^C)Co(N_2)$

Atom	*x* (Å)	*y* (Å)	*z* (Å)
Co	-6.493886	11.262439	3.205589
N	-6.498954	11.321632	1.436042
N	-6.509619	11.38545	0.291428
P	-8.326503	12.522417	3.530507
P	-4.468119	12.255409	3.466626
P	-6.717203	9.021548	3.482688

Atom	*x* (Å)	*y* (Å)	*z* (Å)
C	-6.448223	11.249419	5.315842
C	-7.421986	10.199514	5.854976
C	-6.831755	12.659131	5.809506
C	-3.940694	11.432267	5.038929
C	-7.788337	13.400564	5.064772
C	-5.023737	10.903746	5.778111
C	-7.568622	8.990937	5.132867
C	-7.603117	15.26563	6.637577
H	-7.887795	16.279035	6.939901
C	-4.742746	10.136998	6.931716
H	-5.568096	9.715601	7.513927
C	-8.127028	10.359559	7.068594
H	-8.021476	11.293607	7.630781
C	-2.350013	10.456601	6.62353
H	-1.315073	10.282269	6.938001
C	-3.418954	9.90469	7.345217
H	-3.227213	9.293903	8.23474
C	-8.171005	14.68813	5.486194
H	-8.895772	15.267989	4.902966
C	-6.290306	13.242663	6.974586
H	-5.546257	12.689483	7.558133
C	-6.663915	14.53763	7.381966
H	-6.211178	14.975618	8.278356
C	-2.618218	11.224609	5.475974
H	-1.778935	11.644663	4.91062
C	-8.973486	9.348391	7.556041
H	-9.520264	9.499953	8.49335
C	-9.117028	8.151983	6.83815
H	-9.780016	7.359107	7.201788
C	-8.41086	7.978161	5.633634
H	-8.543338	7.044435	5.079921
C	-8.870946	13.927902	2.377234
H	-9.579139	14.549161	2.960254
C	-7.900856	7.939713	2.420048
H	-8.881225	8.224247	2.846787
C	-2.97498	11.978914	2.30612
H	-2.138575	12.558042	2.749566
C	-11.07349	0 12.80331	5 4.510635

Atom	*x* (Å)	*y* (Å)	*z* (Å)
H	-11.46051	5 13.35393	0 3.634190
H	-10.70149	9 13.53724	2 5.246478
H	-11.93394	6 12.28073	7 4.970473
C	-3.155907	14.432185	4.93614
H	-2.159615	14.205199	4.51304
H	-3.26317	13.874622	5.878956
H	-3.168058	15.512103	5.177167
C	-4.285126	14.122349	3.935571
H	-5.248225	14.315181	4.440866
C	-9.996182	11.77797	4.114182
H	-9.6746	11.254092	5.032798
C	-5.136224	6.885483	4.794468
H	-5.782644	6.041163	4.502203
H	-5.478636	7.259548	5.772591
H	-4.112307	6.486414	4.928211
C	-5.111683	8.001046	3.732927
H	-4.43667	8.792666	4.106835
C	-4.174136	15.079503	2.733239
H	-4.366117	16.114986	3.072409
H	-4.893794	14.855473	1.930931
H	-3.157001	15.06498	2.302688
C	-9.609634	13.412697	1.125076
H	-9.843467	14.26527	0.459541
H	-10.56174	4 12.91838	3 1.372599
H	-8.98997	12.703071	0.551246
C	-10.55826	4 10.71399	3 3.153910
H	-11.27541	9 10.06519	7 3.690750
H	-9.7562	10.075649	2.751813
H	-11.09531	5 11.16058	2 2.300029
C	-7.678939	14.805649	1.96715
H	-6.977841	14.237435	1.333723
H	-7.125591	15.188887	2.840252
H	-8.036167	15.674064	1.381632
C	-4.537403	7.491093	2.393519
H	-3.4544	7.295446	2.497673
H	-4.667629	8.21641	1.571018
H	-5.01133	6.545616	2.083009
C	-7.792465	6.401362	2.524942

Atom	*x* (Å)	*y* (Å)	*z* (Å)
H	-8.705875	5.949101	2.092706
H	-7.694497	6.03041	3.555785
H	-6.938697	6.01039	1.948296
C	-7.904811	8.352731	0.936507
H	-6.9203	8.196505	0.460825
H	-8.178301	9.409648	0.801834
H	-8.640228	7.738209	0.384056
C	-3.216013	12.48365	0.865156
H	-3.500306	13.543308	0.80754
H	-4.003415	11.894901	0.368387
H	-2.285833	12.356421	0.279678
C	-2.570856	10.495897	2.228057
H	-3.389036	9.905335	1.785547
H	-2.324313	10.056729	3.20709
H	-1.685878	10.388535	1.571978

References

(1) Neese, F. *WIRES Comput. Mol. Sci.* **2011**, *2*, 73–78.

(2) Hehre, W. J.; Ditchfield, R.; Pople, J. A. *J. Chem. Phys.* **1972**, *56*, 2257–2261.

(3) Dill, J. D.; Pople, J. A. *J. Chem. Phys.* **1975**, *62*, 2921–2923.

(4) Krishnan, R.; Binkley, J. S.; Seeger, R.; Pople, J. A. *J. Chem. Phys.* **1980**, *72*, 650–654.

(5) McLean, A. D.; Chandler, G. S. *J. Chem. Phys.* **1980**, *72*, 5639–5648.

(6) Francl, M. M.; Pietro, W. J.; Hehre, W. J.; Binkley, J. S.; Gordon, M. S.; DeFrees, D. J.; Pople, J. A. *J. Chem. Phys.* **1982**, *77*, 3654–3665.

(7) Clark, T.; Chandrasekhar, J.; Spitznagel, G. W.; Schleyer, P. V. R. *J. Comput. Chem.* **1983**, *4*, 294–301.

(8) Rassolov, V. A.; Pople, J. A.; Ratner, M. A.; Windus, T. L. *J. Chem. Phys.* **1998**, *109*, 1223–1229.

(9) Schäfer, A.; Horn, H.; Ahlrichs, R. *J. Chem. Phys.* **1992**, *97*, 2571–2577.

(10) Breneman, C. M.; Wiberg, K. B. *J. Comput. Chem.* **1990**, *11*, 361–373.

(11) Watt, G. W.; Chrisp, J. D. *Anal. Chem.* **1952**, *24*, 2006–2008.

Appendix B

SUPPLEMENTARY INFORMATION FOR CHAPTER 3

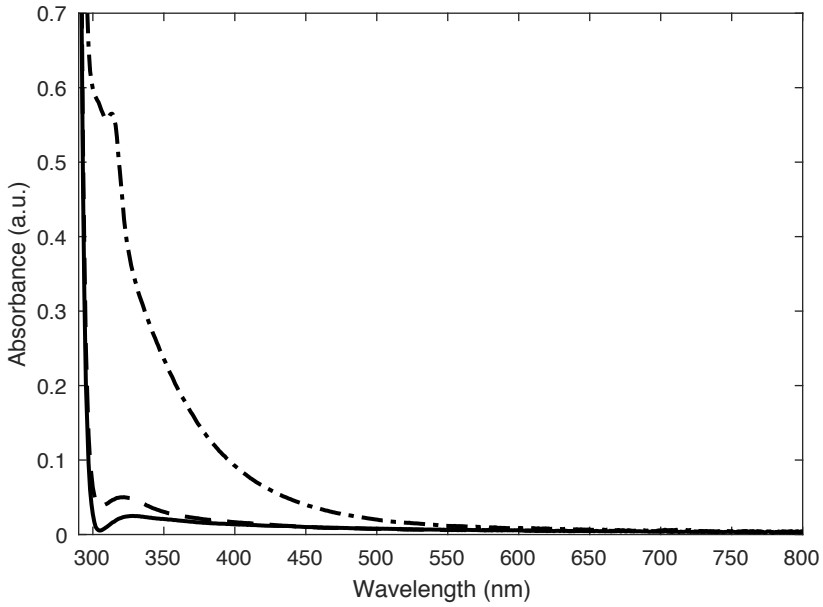

Figure B.1: UV-vis traces of 10 mM solutions of $HBAr^F{}_4$ in Et_2O at various stages of purity. (Dash-dotted trace) $HBAr^F{}_4$ prepared from crude $NaBAr^F{}_4$without additional purification; (Dotted trace) $HBAr^F{}_4$ prepared from $NaBAr^F{}_4$ purified according to the procedure described in the main text, and recrystallized once; (Solid trace) $HBAr^F{}_4$ prepared from $NaBAr^F{}_4$ purified according to the procedure described in the main text, and recrystallized twice.

B.1 NH_3 Quantification Results

Table B.1: UV-vis quantification results for standard NH_3 generation experiments with $[Na(12\text{-}c\text{-}4)_2][(P_3{}^B)Fe(N_2)]$

Entry	Total volume of Et_2O (mL)	Fe μmol (mM)	$HBAr^F{}_4$ equiv (mM)	NH_4Cl (μmol)	Equiv NH_3/Fe	% Yield Based on H^+
A	1.5	1.9 (1.3)	48 (63)	13.2	7.0	43.2
B	1.5	1.9 (1.3)	48 (63)	14.5	7.6	47.2
Avg.	–	–	–	–	7.3 ± 0.5	45 ± 3
C	3.0	1.9 (0.64)	97 (63)	22.1	11.6	35.9
D	3.0	1.9 (0.64)	97 (63)	25.1	13.2	40.8
Avg.	–	–	–	–	12 ± 1	38 ± 3
E	1.1	0.48 (0.43)	150 (63)	8.34	17.5	36.1
F	1.1	0.48 (0.43)	150 (63)	8.19	17.2	35.5
Avg.	–	–	–	–	17.4 ± 0.2	35.8 ± 0.4
G	5.5	0.48 (0.087)	730 (63)	23.3	48.9	20.2
H	5.5	0.48 (0.087)	730 (63)	20.3	42.5	17.6
I	5.5	0.48 (0.087)	730 (63)	19.1	40.2	16.6
J	1.4	0.12 (0.087)	730 (63)	4.82	40.5	16.7
Avg.	–	–	–	–	43 ± 4	18 ± 2
K	11.0	0.48 (0.043)	1500 (63)	28.4	59.5	12.3
L	11.0	0.48 (0.043)	1500 (63)	27.1	56.8	11.7
M	11.0	0.48 (0.043)	1500 (63)	22.9	48.1	9.9
N	11.0	0.48 (0.043)	1500 (63)	25.4	53.4	11.0
O	11.0	0.48 (0.043)	1500 (63)	30.2	63.5	13.1
P	2.8	0.12 (0.043)	1500 (63)	7.67	64.4	13.3
Q	2.8	0.12 (0.043)	1500 (63)	7.53	63.3	13.0
R	2.8	0.12 (0.043)	1500 (63)	7.67	64.4	13.3
S	2.8	0.12 (0.043)	1500 (63)	6.85	57.5	11.9
Avg.	–	–	–	–	59 ± 6	12 ± 1

Hydrazine was not detected in the catalytic runs using a standard UV-vis quantification method.[1]

Table B.2: UV-vis quantification results for standard NH_3 generation experiments with $[K(Et_2O)_{0.5}][(P_3{}^C)Fe(N_2)]$

Entry	Total volume of Et_2O (mL)	Fe μmol (mM)	$HBAr^F{}_4$ equiv (mM)	NH_4Cl (μmol)	Equiv NH_3/Fe	% Yield Based on H^+
A*	2.5	2.5 (1.0)	37 (37)	–	4.6 ± 0.8	36 ± 6
B	1.1	0.63 (0.56)	110 (60)	6.66	10.7	29.7
C	1.1	0.63 (0.56)	110 (60)	7.41	11.9	33.0
Avg.	–	–	–	–	11.3 ± 0.9	31 ± 2
D	2.3	0.63 (0.28)	220 (60)	7.41	11.9	16.4
E	2.3	0.63 (0.28)	220 (60)	9.89	15.8	21.9
Avg.	–	–	–	–	14 ± 3	19 ± 4
F	2.0	0.16 (0.080)	750 (60)	2.49	15.6	6.2
G	2.0	0.16 (0.080)	750 (60)	3.50	21.9	8.8
Avg.	–	–	–	–	19 ± 4	7 ± 2
H	4.0	0.16 (0.040)	1500 (60)	7.46	46.8	9.3
I	4.0	0.16 (0.040)	1500 (60)	4.63	29.0	5.8
J	4.0	0.16 (0.040)	1500 (60)	5.82	36.5	7.3
K	4.0	0.16 (0.040)	1500 (60)	5.56	34.8	6.9
L	4.0	0.16 (0.040)	1500 (60)	5.13	32.1	6.4
Avg.	–	–	–	–	36 ± 7	7 ± 1

Hydrazine was not detected in the catalytic runs using a standard UV-vis quantification method.[1]
*Data is an average of experiments described in [2].

Table B.3: UV-vis quantification results for standard NH_3 generation experiments with $[Na(12\text{-}c\text{-}4)_2][(P_3{}^{Si})Fe(N_2)]$

Entry	Total volume of Et_2O (mL)	Fe μmol (mM)	$HBAr^F{}_4$ equiv (mM)	NH_4Cl (μmol)	Equiv NH_3/Fe	% Yield Based on H^+
A*	3.25	1.9 (0.58)	49 (28)	–	0.8 ± 0.5	5 ± 3
B	3.0	0.12 (0.039)	1500 (60)	0.516	4.4	0.9
C	3.0	0.12 (0.039)	1500 (60)	0.380	3.2	0.6
Avg.	–	–	–	–	3.8 ± 0.8	0.8 ± 0.2

Hydrazine was not detected in the catalytic runs using a standard UV-vis quantification method.[1]
*Data is an average of experiments described in [3].

Table B.4: UV-vis quantification results for standard NH_3 generation experiments with $(P_3{}^B)(\mu\text{-H})Fe(H)(N_2)$

Entry	Total volume of Et_2O (mL)	Fe μmol (mM)	$HBAr^F{}_4$ equiv (mM)	NH_4Cl (μmol)	Equiv NH_3/Fe	% Yield Based on H^+
A	1.1*	0.48	150 (63)	0.582	1.19	2.56
B	1.1*	0.48	150 (63)	0.490	1.00	2.15
Avg.	–	–	–	–	1.1 ± 0.1	2.4 ± 0.3
C	1.7**	0.74 (0.44)	150 (63)	3.66	4.95	10.3
D	1.7**	0.74 (0.44)	150 (63)	4.63	6.26	13.0
Avg.	–	–	–	–	5.6 ± 0.9	12 ± 2

Hydrazine was not detected in the catalytic runs using a standard UV-vis quantification method.[1]
*Not fully soluble under these conditions. Final solvent composition was 3% toluene in Et_2O.
**Final solvent composition was 25% toluene in Et_2O.

Table B.5: UV-vis quantification results for NH_3 generation experiments with $[Na(12\text{-}c\text{-}4)_2][(P_3{}^BFe(N_2)]$ with the inclusion of NH_3

Entry	Total volume of Et_2O (mL)	Fe μmol (mM)	$HBAr^F{}_4$ equiv (mM)	NH_4Cl (μmol)	NH_4Cl due to Fe (μmol)	Equiv NH_3/Fe
A	3.0	0	0	12.5	N/A	N/A
B	3.0	0	0	11.8	N/A	N/A
C	3.0	0	0	12.1	N/A	N/A
D	3.0	0	0	12.0	N/A	N/A
E	3.0	0	0	12.2	N/A	N/A
Avg.	–	–	–	12.1		
C	1.1	0.48 (0.43)	150 (63)	15.1	3.0	6.3
D	1.1	0.48 (0.43)	150 (63)	15.2	3.1	6.5
Avg.	–	–	–	–	–	6.4 ± 0.1

Hydrazine was not detected in the catalytic runs using a standard UV-vis quantification method.[1]

Table B.6: UV-vis quantification results for standard NH_3 generation experiments with $[Na(12\text{-}c\text{-}4)_2][(P_3{}^BFe(N_2)]$ using Na/Hg as the reductant

Entry	Total volume of Et_2O (mL)	Fe μmol (mM)	$HBAr^F{}_4$ equiv (mM)	NH_4Cl (μmol)	Equiv NH_3/Fe	% Yield Based on H^+
A	1.1	0.48 (0.43)	150 (63)	2.45	5.15	10.6
B	1.1	0.48 (0.43)	150 (63)	2.30	4.84	9.97
Avg.	–	–	–	–	5.0 ± 0.2	10.3 ± 0.5

Hydrazine was not detected in the catalytic runs using a standard UV-vis quantification method.[1]

Table B.7: UV-vis quantification results for NH_3 generation experiments with [Na(12-c-4)$_2$][($P_3{}^B$)Fe(N_2)], with reloading

Entry	Number of loadings	Fe (μmol)	$HBAr^F{}_4$ (equiv)	NH_4Cl (μmol)	Equiv NH_3/Fe	% Yield Based on H^+
A	1	1.9	48	13.3	6.96	43.2
B	1	1.9	48	14.5	7.60	47.2
Avg.	–	–	–	–	7.3 ± 0.5	45 ± 3
C	2	0.95	96	9.56	10.0	31.5
D	2	0.95	96	10.3	10.9	34.0
Avg.	–	–	–	–	10.4 ± 0.6	33 ± 2
E	2	0.95	150	13.4	14.1	32.7
F	2	0.95	150	14.9	15.6	29.4
Avg.	–	–	–	–	15 ± 1	31 ± 2
G	2	1.0	190	18.4	17.6	29.0
H	2	1.0	190	18.4	17.6	29.0
Avg.	–	–	–	–	17.6	29

Hydrazine was not detected in the catalytic runs using a standard UV-vis quantification method.[1]

Table B.8: Time profiles for NH_3 generation by $[Na(12\text{-c-}4)_2][(P_3{}^B)Fe(N_2)]$

Entry	Total volume of Et_2O (mL)	Fe μmol (mM)	$HBAr^F{}_4$ equiv (mM)	Quench time (min)	$[NH_3]$ (mM)	Equiv NH_3/Fe
A	3.0	1.9 (0.64)	48 (31)	0	0	0
B	3.0	1.9 (0.64)	48 (31)	5	1.21	1.91
C	3.0	1.9 (0.64)	48 (31)	5	1.87	2.94
Avg.	–	–	–	5	1.5 ± 0.5	2.4 ± 0.2
D	3.0	1.9 (0.64)	48 (31)	10	4.36	6.86
E	3.0	1.9 (0.64)	48 (31)	10	3.66	5.76
Avg.	–	–	–	10	4.0 ± 0.5	6.3 ± 0.8
F	3.0	1.9 (0.64)	48 (31)	15	4.87	7.68
G	3.0	1.9 (0.64)	48 (31)	15	4.63	7.29
Avg.	–	–	–	15	4.8 ± 0.2	7.5 ± 0.3
H	3.0	1.9 (0.64)	48 (31)	25	4.40	6.93
I	3.0	1.9 (0.64)	48 (31)	25	4.79	7.54
Avg.	–	–	–	25	4.6 ± 0.3	7.2 ± 0.4
J	1.1	0.48 (0.43)	150 (63)	5	0.806	1.86
K	1.1	0.48 (0.43)	150 (63)	5	1.09	2.51
Avg.	–	–	–	5	0.9 ± 0.2	2.2 ± 0.5
L	1.1	0.48 (0.43)	150 (63)	10	2.08	4.81
M	1.1	0.48 (0.43)	150 (63)	10	2.74	6.33
Avg.	–	–	–	10	2.4 ± 0.5	6 ± 1
N	1.1	0.48 (0.43)	150 (63)	15	3.79	8.75
O	1.1	0.48 (0.43)	150 (63)	15	4.06	9.39
Avg.	–	–	–	15	3.9 ± 0.2	9.1 ± 0.4
P	1.1	0.48 (0.43)	150 (63)	25	5.73	13.2
Q	1.1	0.48 (0.43)	150 (63)	25	4.68	10.8
Avg.	–	–	–	25	5.2 ± 0.7	12 ± 2
R	1.1	0.48 (0.43)	150 (63)	35	6.11	14.1
S	1.1	0.48 (0.43)	150 (63)	35	5.51	12.7

Entry	Total volume of Et_2O (mL)	Fe μmol (mM)	$HBAr^F{}_4$ equiv (mM)	Quench time (min)	[NH_3] (mM)	Equiv NH_3/Fe
Avg.	–	–	–	35	5.8 ± 0.4	13 ± 1
T	1.1	0.48 (0.43)	150 (63)	45	7.99	18.5
U	1.1	0.48 (0.43)	150 (63)	45	8.37	19.3
Avg.	–	–	–	45	8.2 ± 0.3	18.9 ± 0.6
V	1.1	0.48 (0.43)	150 (63)	55	7.18	16.6
W	1.1	0.48 (0.43)	150 (63)	55	7.94	18.3
Avg.	–	–	–	55	7.6 ± 0.5	17 ± 1

Table B.9: Time resolved NH_3 quantification data used in initial rates analysis for NH_3 generation by by $[Na(12\text{-c-}4)_2][(P_3{}^B)Fe(N_2)]$

Entry	Total volume of Et_2O (mL)	Fe μmol (mM)	$HBAr^F{}_4$ equiv (mM)	Quench time (min)	$[NH_3]$ (mM)
A	1.1	0.12 (0.11)	560 (63)	5	0.268
B	1.1	0.12 (0.11)	560 (63)	5	0.273
Avg.	–	–	–	5	0.270 ± 0.004
C	1.1	0.12 (0.11)	560 (63)	10	0.225
D	1.1	0.12 (0.11)	560 (63)	10	0.338
Avg.	–	–	–	10	0.28 ± 0.08
E	1.1	0.12 (0.11)	560 (63)	15	0.747
F	1.1	0.12 (0.11)	560 (63)	15	1.27
Avg.	–	–	–	15	1.0 ± 0.4
G	1.1	0.24 (0.22)	290 (63)	5	0.538
H	1.1	0.24 (0.22)	290 (63)	5	0.763
Avg.	–	–	–	5	0.7 ± 0.2
I	1.1	0.24 (0.22)	290 (63)	10	1.81
J	1.1	0.24 (0.22)	290 (63)	10	1.29
Avg.	–	–	–	10	1.5 ± 0.4
K	1.1	0.24 (0.22)	290 (63)	15	3.47
L	1.1	0.24 (0.22)	290 (63)	15	2.23
Avg.	–	–	–	15	2.9 ± 0.9
M	1.1	0.95 (0.87)	73 (63)	5	1.98
N	1.1	0.95 (0.87)	73 (63)	5	1.64
Avg.	–	–	–	5	1.8 ± 0.2
O	1.1	0.95 (0.87)	73 (63)	10	5.36
P	1.1	0.95 (0.87)	73 (63)	10	4.20
Avg.	–	–	–	10	4.8 ± 0.8
Q	1.1	0.95 (0.87)	73 (63)	15	9.27
R	1.1	0.95 (0.87)	73 (63)	15	8.84
Avg.	–	–	–	15	9.1 ± 0.3

Entry	Total volume of Et_2O (mL)	Fe μmol (mM)	$HBAr^F{}_4$ equiv (mM)	Quench time (min)	$[NH_3]$ (mM)
S	1.1	1.9 (1.7)	36 (63)	5	4.53
T	1.1	1.9 (1.7)	36 (63)	5	7.24
Avg.	–	–	–	5	6 ± 2
U	1.1	1.9 (1.7)	36 (63)	10	10.8
V	1.1	1.9 (1.7)	36 (63)	10	10.3
Avg.	–	–	–	10	10.5 ± 0.3
W	1.1	1.9 (1.7)	36 (63)	15	10.4
X	1.1	1.9 (1.7)	36 (63)	15	10.4
Avg.	–	–	–	15	10.44 ± 0.02
Y	1.1	0.48 (0.43)	35 (15)	5	1.06
Z	1.1	0.48 (0.43)	35 (15)	5	1.27
Avg.	–	–	–	5	1.2 ± 0.2
AA	1.1	0.48 (0.43)	35 (15)	10	1.33
BB	1.1	0.48 (0.43)	35 (15)	10	1.43
Avg.	–	–	–	10	1.38 ± 0.07
CC	1.1	0.48 (0.43)	35 (15)	15	1.26
DD	1.1	0.48 (0.43)	35 (15)	15	1.53
Avg.	–	–	–	15	1.4 ± 0.2
EE	1.1	0.48 (0.43)	68 (30)	5	1.23
FF	1.1	0.48 (0.43)	68 (30)	5	1.29
Avg.	–	–	–	5	1.26 ± 0.04
GG	1.1	0.48 (0.43)	68 (30)	10	3.22
HH	1.1	0.48 (0.43)	68 (30)	10	2.76
Avg.	–	–	–	10	3.0 ± 0.3
II	1.1	0.48 (0.43)	68 (30)	15	3.42
JJ	1.1	0.48 (0.43)	68 (30)	15	3.50
Avg.	–	–	–	15	3.46 ± 0.05
KK	1.1	0.48 (0.43)	290 (130)	5	0.736
LL	1.1	0.48 (0.43)	290 (130)	5	1.04

Entry	Total volume of Et_2O (mL)	Fe μmol (mM)	$HBAr^F{}_4$ equiv (mM)	Quench time (min)	$[NH_3]$ (mM)
Avg.	–	–	–	5	0.9 ± 0.2
MM	1.1	0.48 (0.43)	290 (130)	10	4.11
NN	1.1	0.48 (0.43)	290 (130)	10	3.47
Avg.	–	–	–	10	3.8 ± 0.4
OO	1.1	0.48 (0.43)	290 (130)	15	6.24
PP	1.1	0.48 (0.43)	290 (130)	15	6.64
Avg.	–	–	–	15	6.4 ± 0.3
QQ	1.1	0.48 (0.43)	580 (250)	5	0.495
RR	1.1	0.48 (0.43)	580 (250)	5	1.13
Avg.	–	–	–	5	0.8 ± 0.5
SS	1.1	0.48 (0.43)	580 (250)	10	3.56
TT	1.1	0.48 (0.43)	580 (250)	10	2.50
Avg.	–	–	–	10	3.0 ± 0.8
UU	1.1	0.48 (0.43)	580 (250)	15	7.13
VV	1.1	0.48 (0.43)	580 (250)	15	7.40
Avg.	–	–	–	15	7.3 ± 0.2

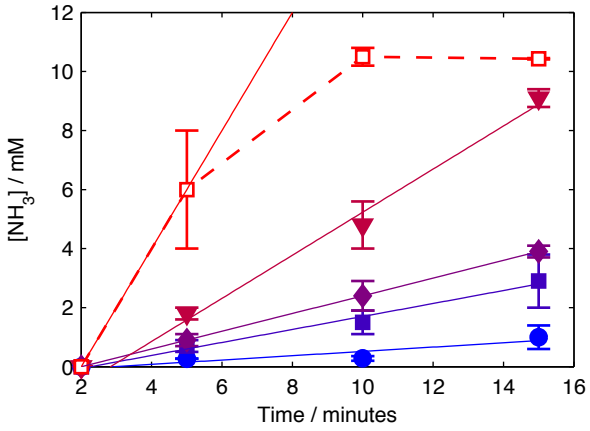

Figure B.2: Time courses for NH_3 generation by $[Na(12\text{-}c\text{-}4)_2][(P_3{}^B)Fe(N_2)]$ at varying concentrations of $[Na(12\text{-}c\text{-}4)_2][(P_3{}^B)Fe(N_2)]$. All reactions conducted in 63 mM $HBAr^F{}_4$ with 1.2 equiv KC_8 with respect to $HBAr^F{}_4$. (Blue circles) [Fe] = 0.11 mM; (Indigo squares) [Fe] = 0.22 mM; (purple diamonds) [Fe] = 0.43 mM; (maroon triangles) [Fe] = 0.87 mM; (red squares) [Fe] = 1.7 mM. Solid lines show the least-squares linear regression fit to the 5, 10, and 15 minute data, except for the [Fe] = 1.7 mM trace (red squares), which deviates from pseudo-first-order behavior; in this case, the line is fit from the data at 5 minutes to a zero point at t = 2 minutes.

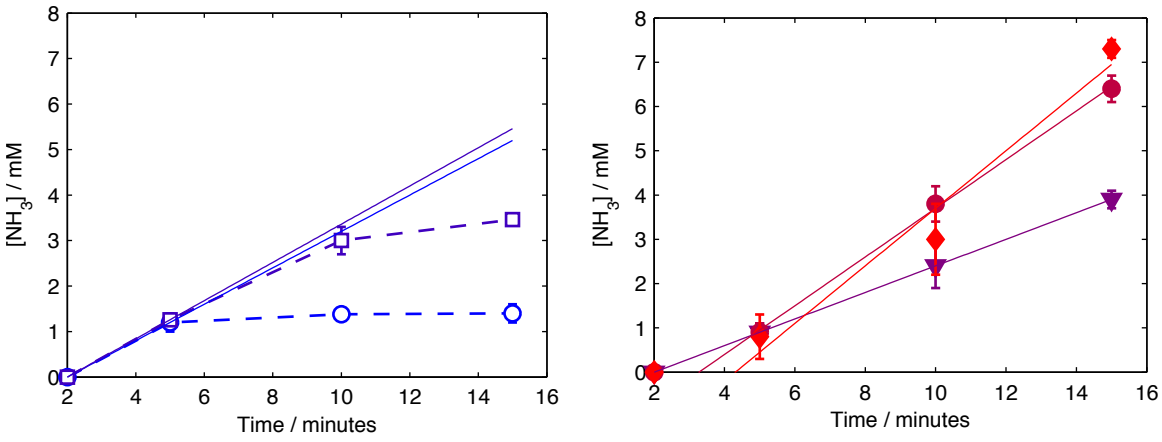

Figure B.3: Time courses for NH_3 generation by $[Na(12\text{-}c\text{-}4)_2][(P_3{}^B)Fe(N_2)]$ at varying concentrations of $HBAr^F{}_4$. All reactions conducted in 0.43 mM $[Na(12\text{-}c\text{-}4)_2][(P_3{}^B)Fe(N_2)]$ with 185 equiv KC_8 with respect to $[Na(12\text{-}c\text{-}4)_2][(P_3{}^B)Fe(N_2)]$. Left: (Blue circles) $[HBAr^F{}_4]$ = 15 mM; (Indigo squares) $[HBAr^F{}_4]$ = 30 mM. Right: (purple triangles) $[HBAr^F{}_4]$ = 63 mM; (maroon circles) $[HBAr^F{}_4]$ = 130 mM; (red diamonds) $[HBAr^F{}_4]$ = 250 mM. Left: Solid lines show the line connecting the 5 minute data with a zero point at t = 2 minutes. Right: solid lines show the least-squares linear regression fit to the 5, 10, and 15 minute data.

Table B.10: Results of initial rates determination for NH_3 generation by $[Na(12\text{-c-}4)_2][(P_3{}^B)Fe(N_2)]$

Entry	$[Fe]_0$ (mM)	$[HBAr^F{}_4]_0$ (mM)	v_0 (mM min^{-1})	r^2*
A	0.11	63	0.07 ± 0.04	0.76
B	0.22	63	0.22 ± 0.03	0.98
C	0.43	63	0.30	1.0
D	0.87	63	0.73 ± 0.08	0.99
E	1.7	63	2.0 ± 0.9	N/A
F	0.43	15	0.4 ± 0.3	N/A
G	0.43	30	0.4 ± 0.2	N/A
H	0.43	130	0.55 ± 0.02	0.99
I	0.43	250	0.65 ± 0.1	0.97

*Coefficient of correlation for least-squares fits shown in Figures B.2 and B.3, where applicable.

Table B.11: Least-squares analysis of log-transformed initial rates data from Table B.10

Entry	Data fit (from Table B.10)	Optimal model	r^2
A	A–E	$\log v_0 = (-0.04 \pm 0.1) + (1.1 \pm 0.1) \cdot \log [Fe]_0$	0.98
B	C, F–I	$\log v_0 = (-1.5 \pm 0.5) + (0.17 \pm 0.12) \cdot \log [H^+]_0$	0.42

Table B.12: Time profiles for the generation of H_2 in the presence of Fe precursors

Entry	Fe precursor	Time (min)	$H_{2(g)}$ (μmol)	% H_2 Based on H^+	% NH_3 Based on H^+
A	–	0	0	0	–
B	–	6	2.50	1.14	–
C	–	28	17.8	8.09	–
D	–	60	42.0	19.1	–
E	–	118	80.7	36.6	–
F	–	1039	169	76.7	–
G	$[(P_3{}^B)Fe(N_2)]^-$	0	0	0	–
H		5	8.63	3.92	–
I		25	53.5	24.3	–
J		45	72.4	32.9	–
K		66	74.0	33.6	–
L		118	78.2	35.5	–
M		1110	87.9	39.9	34
N	$[(P_3{}^{Si})Fe(N_2)]^-$	0	0	0	–
O		7.5	8.63	3.92	–
P		29	44.8	20.3	–
Q		60	133	60.6	–
R		119	190	86.0	–
S		945	195	88.4	–

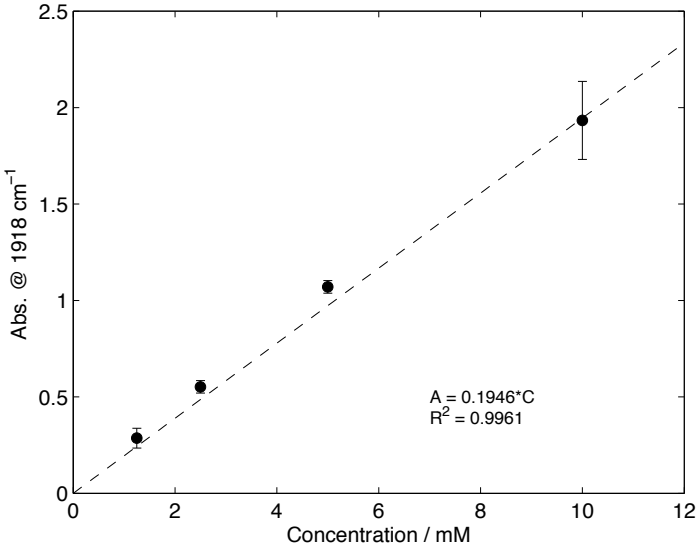

Figure B.4: Solution IR calibration curve for $[(P_3{}^B)Fe(N_2)]^-$. Data for individual points are presented in Table B.13

Table B.13: Results of solution IR calibration of $[(P_3{}^B)Fe(N_2)]^-$

Entry	[Fe] (mM)	Absorbance at 1918 cm^{-1} (a.u.)
A	1.25	0.3225
B	1.25	0.2495
Avg.	–	0.29 ± 0.05
C	2.5	0.5748
D	2.5	0.5295
Avg.	–	0.55 ± 0.03
E	5	1.0937
F	5	1.0471
Avg.	–	1.07 ± 0.03
G	10	1.7906
H	10	2.0769
Avg.	–	1.9 ± 0.2

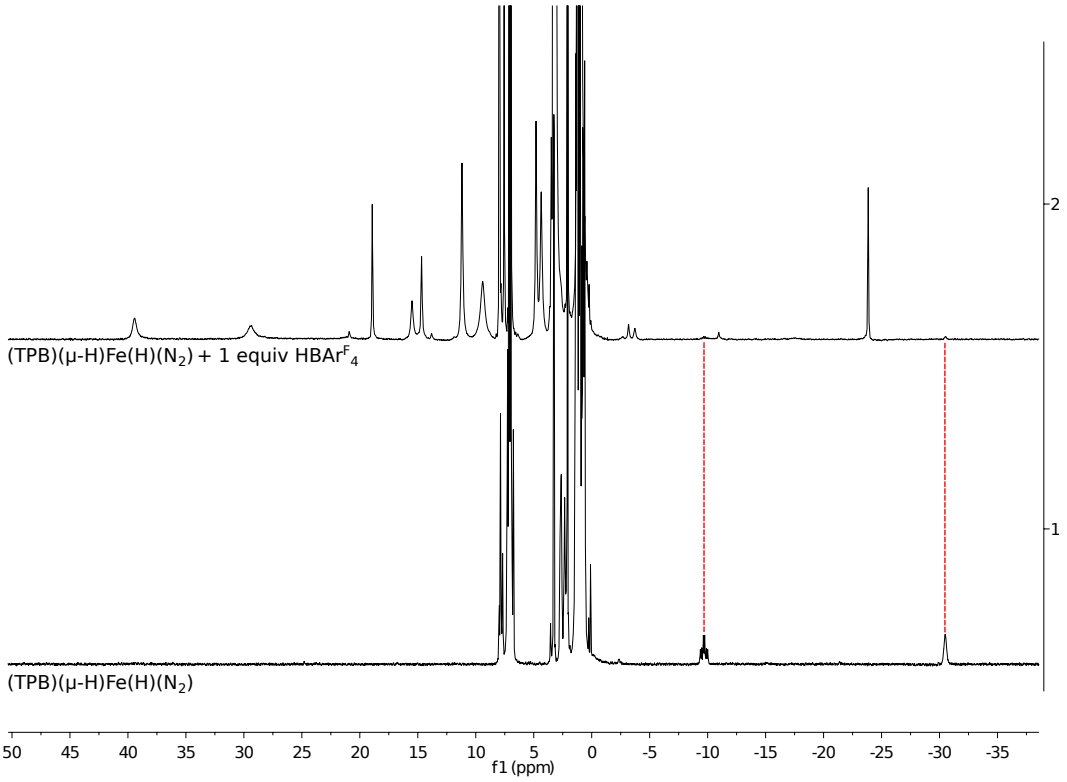

Figure B.5: (Bottom) ^{1}H NMR spectrum of $(P_3{}^{B})(\mu\text{-H})Fe(H)(N_2)$, highlighting the characteristic hydride resonances appearing at ca. -10 and -30 ppm. (Top) Spectrum of the reaction between $(P_3{}^{B})(\mu\text{-H})Fe(H)(N_2)$ and $HBAr^{F}{}_4$ in 6:1 d_8-toluene:Et_2O after 1.5 hr of mixing at room temperature.

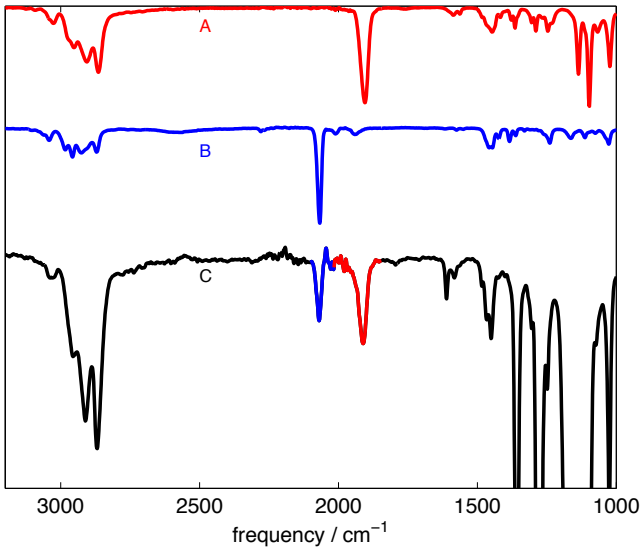

Figure B.6: (A) Solid state IR spectrum of $[(P_3{}^B)Fe(N_2)]^-$ deposited as a thin film from THF. (B) Solid state IR spectrum of $(P_3{}^B)(\mu\text{-H})Fe(H)(N_2)$ deposited as a thin film from C_6D_6. (C) Solid state IR spectrum of the reaction mixture obtained from the sequential reaction of $(P_3{}^B)(\mu\text{-H})Fe(H)(N_2)$ with $HBAr^F{}_4$ and KC_8, deposited as a thin film from THF.

B.2 Mössbauer Spectra

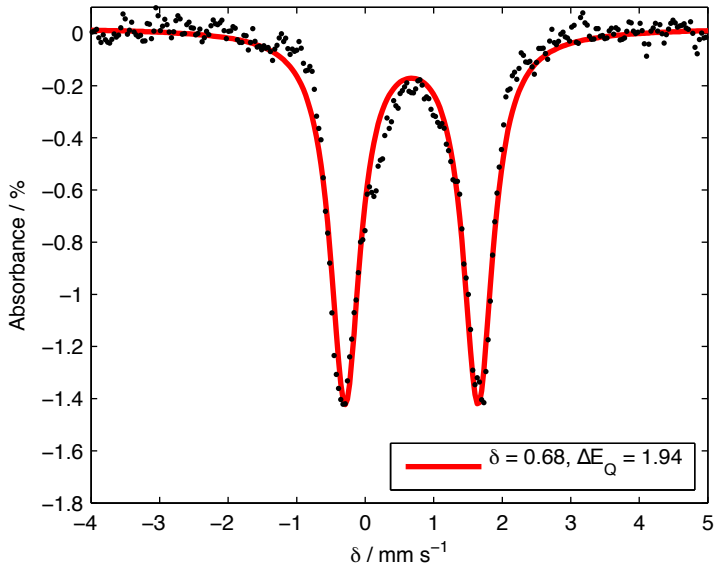

Figure B.7: Zero field Mössbauer spectrum of $[(P_3{}^B)Fe(NH_3)][BAr^F{}_4]$, prepared by the addition of an atmosphere of $NH_{3(g)}$ to a solution of $[(P_3{}^B)Fe][BAr^F{}_4]$ in 6:1 C_6D_6:THF. Raw data presented as black points, simulated data shown as a solid red line. Data collected on a frozen solution sample at 80 K.

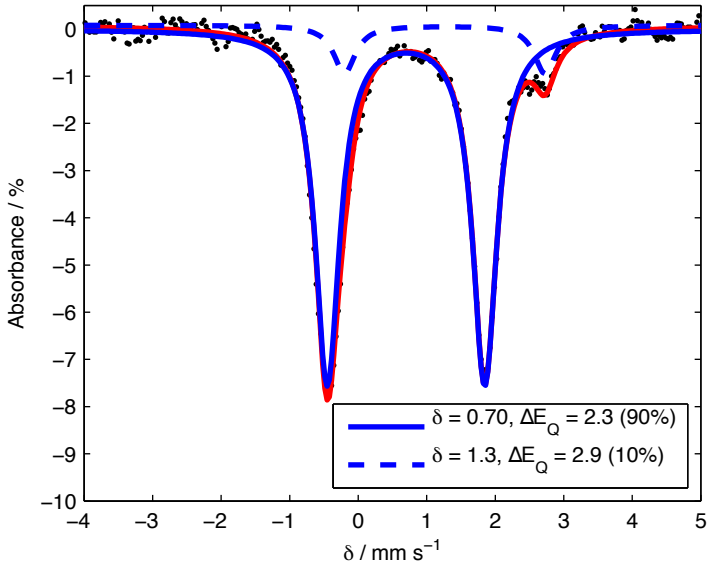

Figure B.8: Zero field Mössbauer spectrum of $[(P_3{}^B)Fe(N_2H_4)][BAr^F{}_4]$, prepared by the addition of N_2H_4 to a solution of $[(P_3{}^B)Fe][BAr^F{}_4]$ in 6:1 C_6D_6:THF. Raw data presented as black points, simulated data shown as a solid red line. The simulation is fit to two quadrupole doublets, that of $[(P_3{}^B)Fe(N_2H_4)][BAr^F{}_4]$ (solid blue line) and that of an unknown impurity (dashed blue line, < 10%). Data collected on a frozen solution sample at 80 K.

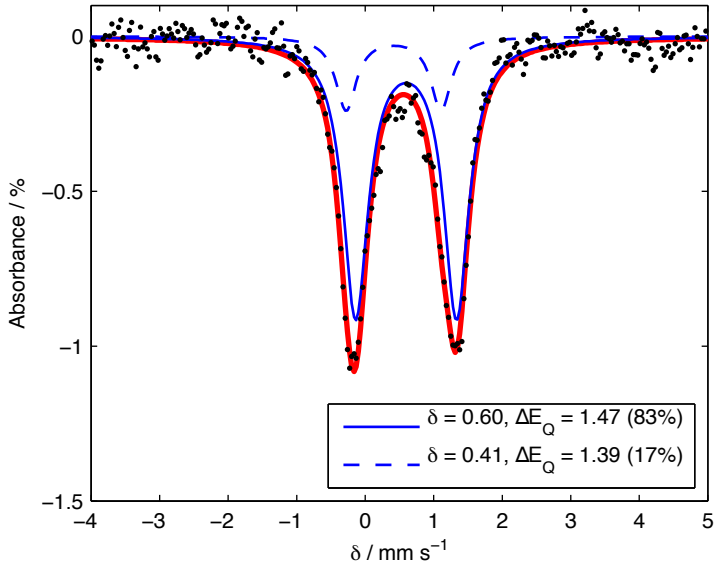

Figure B.9: Zero field Mössbauer spectrum of $(P_3{}^B)Fe(NH_2)$, prepared by the addition $NaNH_2$ to a solution of $[(P_3{}^B)Fe][BAr^F{}_4]$ in Et_2O. Raw data presented as black points, simulated data shown as a solid red line. The simulation is fit to two quadrupole doublets, that of $(P_3{}^B)Fe(NH_2)$ (solid blue line) and that of $(P_3{}^B)Fe(OH)$ (dashed blue line), resulting from NaOH contamination in $NaNH_2$. Data collected on a frozen solution sample at 80 K.

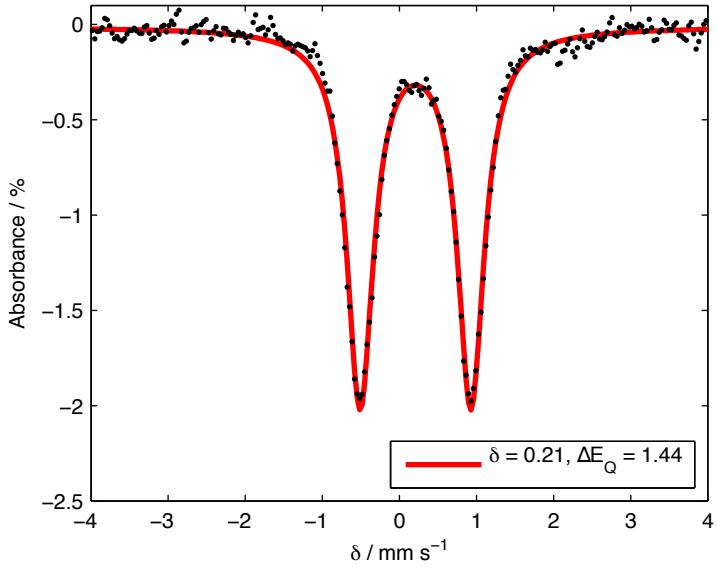

Figure B.10: Zero field Mössbauer spectrum of $(P_3{}^B)(\mu\text{-H})Fe(H)(N_2)$, prepared by the addition of an H_2 atmosphere to a degassed solution of $(P_3{}^B)Fe(N_2)$ in C_6D_6, followed by removal of excess H_2 and mixing under an N_2 atmosphere overnight. Raw data presented as black points, simulated data shown as a solid red line. Data collected on a frozen solution sample at 80 K.

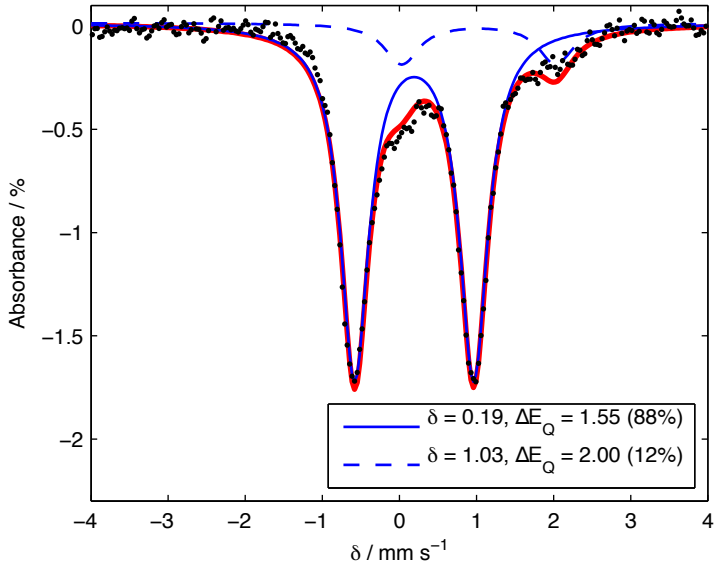

Figure B.11: Zero field Mössbauer spectrum of $(P_3{}^B)(\mu\text{-H})Fe(H)(H_2)$, prepared by the addition of an H_2 atmosphere to a degassed solution of $(P_3{}^B)Fe(N_2)$ in C_6D_6. Raw data presented as black points, simulated data shown as a solid red line. The simulation is fit to two quadrupole doublets, that of $(P_3{}^B)(\mu\text{-H})Fe(H)(H_2)$ (solid blue line) and that of unknown decomposition product(s) (dashed blue line), likely resulting from B–C bond cleavage under excess H_2. Data collected on a frozen solution sample at 80 K.

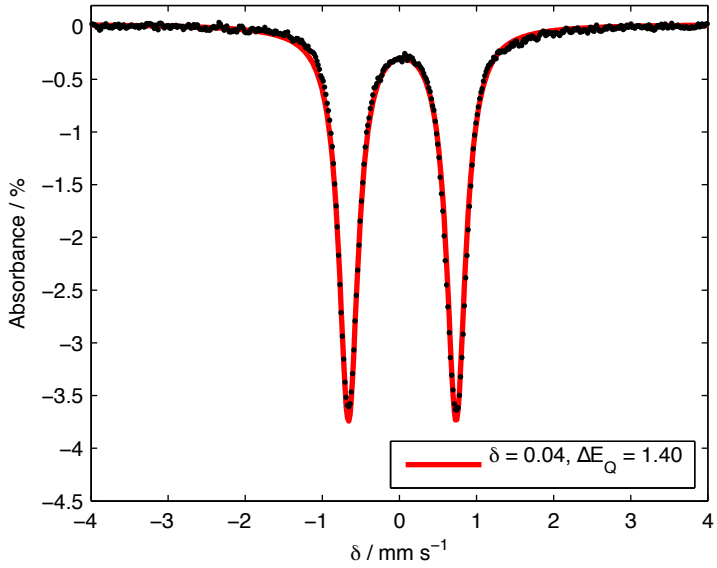

Figure B.12: Zero field Mössbauer spectrum of $(P_3{}^B)$Fe(NAd). Raw data presented as black points, simulated data shown as a solid red line. Data collected on a powder sample at 80 K.

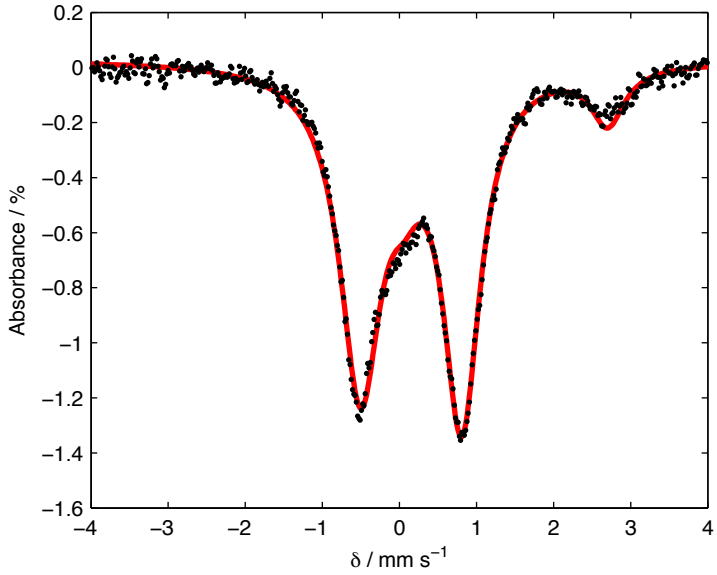

Figure B.13: Zero field Mössbauer spectrum of [(P_3^B)Fe(NAd)][BAr^F_4]. Raw data presented as black points, simulated data shown as a solid red line. The simulation is fit to two quadrupole doublets, that of [(P_3^B)Fe(NAd)][BAr^F_4] (90%) and that of unknown high spin decomposition product (ca. 10%). Data collected on a powder sample at 80 K in the presence of a 50 mT external magnetic field (parallel mode).

B.2.1 Freeze-quench Mössbauer Spectra

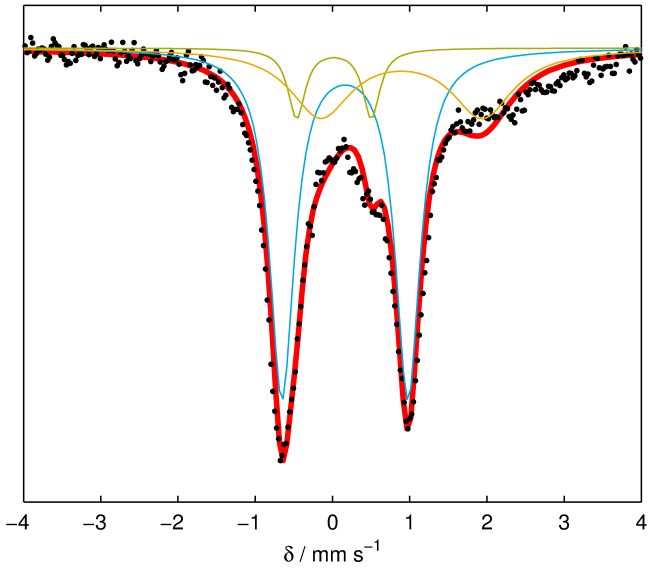

Figure B.14: Mössbauer spectrum collected from a catalytic reaction quenched after 5 minutes. Conditions: [[Na(12-c-4)$_2$][(P_3^B)^{57}Fe(N_2)]] = 0.64 mM, [HBar$^F{}_4$] = 31 mM (48 equiv), 1.2 equiv KC_8 relative to HBar$^F{}_4$. Raw data shown as black points, simulation as a solid red line, with components in blue, green, orange (see Table B.14 for parameters). Collected at 80 K with a parallel applied magnetic field of 50 mT.

Table B.14: Simulation parameters for Mössbauer spectrum in Figure B.14

Component	δ (mm s^{-1})	$\lvert\Delta E_Q\rvert$ (mm s^{-1})	Linewidths, Γ_L/Γ_R (mm s^{-1})	Relative area
A (blue)	0.16 ± 0.02	1.63 ± 0.03	0.39/0.39	0.61
B (green)	0.02 ± 0.02	0.97 ± 0.02	0.27/0.27	0.085
C (orange)	0.89 ± 0.02	2.10 ± 0.04	0.96/0.96	0.28

Fitting details for Figure B.14: Three pairs of quadrupole doublets were found to be necessary to obtain an adequate simulation of these data. The simulation parameters are given in Table B.14. The major component (shown in blue in Figure B.14) is the only species with resolved lineshapes, while the remaining components (shown in green and orange) were fit to the broad residual signal by least-squares refinement. While this fitting procedure is necessary to get an accurate integration of the major species, the Mössbauer parameters for the minor components should not be considered reliable. It is possible that the broad residual signal arises from multiple minor components whose resonances are not well-resolved.

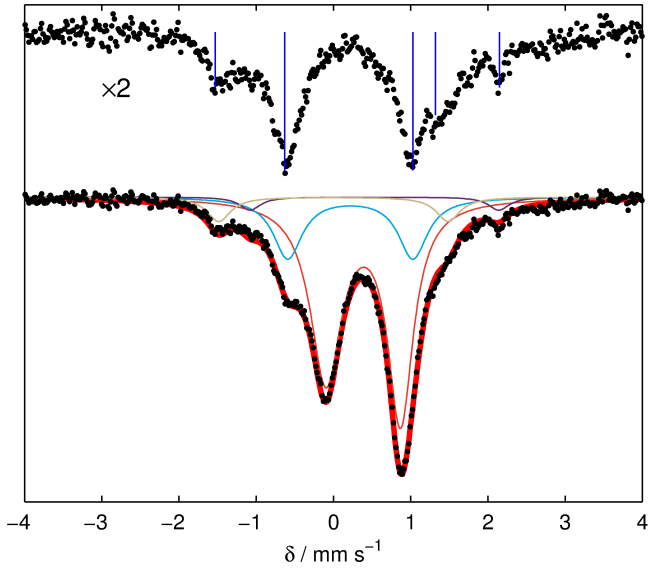

Figure B.15: Mössbauer spectrum collected from a catalytic reaction quenched after 25 minutes. Conditions: [[Na(12-c-4)$_2$][(P_3^B)^{57}Fe(N_2)]] = 0.64 mM, [HBar$^F{}_4$] = 31 mM (48 equiv), 1.2 equiv KC_8 relative to HBar$^F{}_4$. (Bottom) Raw data shown as black points, simulation as a solid red line, with components in blue, red, tan, and purple (see Table B.15 for parameters). (Top) Raw data after subtraction of major component, shown at twice the scale of the bottom spectrum for clarity. Collected at 80 K with a parallel applied magnetic field of 50 mT.

Table B.15: Simulation parameters for Mössbauer spectrum in Figure B.15

Component	δ (mm s^{-1})	$\lvert\Delta E_Q\rvert$ (mm s^{-1})	Linewidths, Γ_L/Γ_R (mm s^{-1})	Relative area
A (blue)	0.22 ± 0.02	1.62 ± 0.03	0.46/0.46	0.22
B (red)	0.39 ± 0.02	0.97 ± 0.02	0.49/0.40	0.70
C (tan)	0.00 ± 0.02	2.97 ± 0.06	0.37/0.37	0.072
D (purple)	0.53 ± 0.02	3.22 ± 0.06	0.33/0.33	0.034

Fitting details for Figure B.15: Four quadrupole doublets were found to be necessary to obtain an adequate simulation. The simulation parameters are given in Table B.15. The major species present in this spectrum is well-simulated by the parameters of [Na(12-c-4)$_2$][(P_3^B)Fe(N_2)]. After subtraction of this component, the residual signal exhibits five resolved lines, indicating the presence of at least three quadrupole doublets (Figure B.15, Top). The most intense of these has parameters nearly identical to species A in Table B.14. The remaining signal is well-simulated by two sharp quadrupole doublets, one with

parameters nearly identical to those of $(P_3{}^B)Fe(N_2)$ (D, purple), and one novel species with an unusually low isomer shift (C, tan).

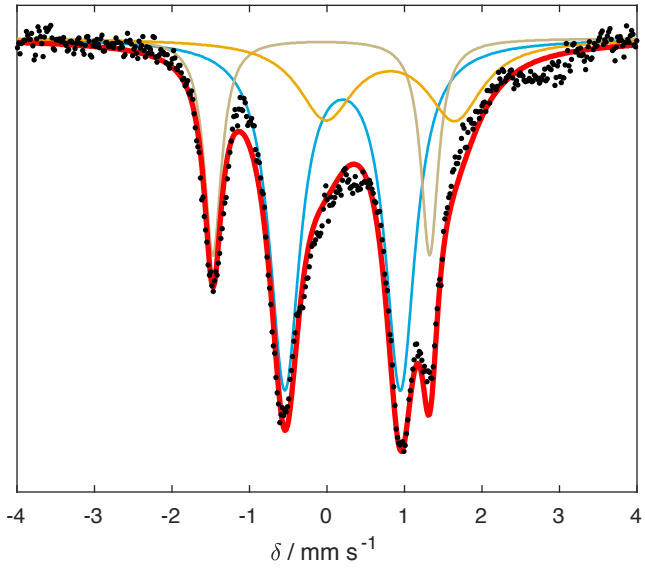

Figure B.16: Mössbauer spectrum collected from a catalytic reaction quenched after 5 minutes. Conditions: [[Na(12-c-4)$_2$][(P_3^B)^{57}Fe(N_2)]] = 0.43 mM, [HBar$^F_4$] = 63 mM (150 equiv), 1.2 equiv KC_8 relative to HBar$^F_4$. Raw data shown as black points, simulation as a solid red line, with components in blue, tan, and orange (see Table B.16 for parameters). Collected at 80 K with a parallel applied magnetic field of 50 mT.

Table B.16: Simulation parameters for Mössbauer spectrum in Figure B.16

Component	δ (mm s^{-1})	$\lvert\Delta E_Q\rvert$ (mm s^{-1})	Linewidths, Γ_L/Γ_R (mm s^{-1})	Relative area
A (blue)	0.20 ± 0.02	1.49 ± 0.03	0.47/0.47	0.61
B (tan)	−0.07 ± 0.02	2.80 ± 0.06	0.27/0.27	0.23
C (orange)	0.82 ± 0.02	1.67 ± 0.03	0.87/0.87	0.25

Fitting details for Figure B.16: Four quadrupole doublets were found to be necessary to obtain an adequate simulation. The simulation parameters are given in Table B.16. The major species present in this spectrum has parameters very similar to those of the major component in the spectrum in Figure B.14 (Table B.16, A); indeed, in both cases this species comprises approximately 60% of the signal. This spectrum also features a second well-resolved quadrupole doublet, which has parameters nearly identical to those of the novel minor component shown in tan in Figure B.15 (Table B.15, C). As with the spectrum in Figure B.14, after fitting these two resolved doublets there is a broad residual signal centered around 0.8 mm s^{-1}. Due to the broadness of this signal, the parameters for this

component should not be considered reliable, but its inclusion in the simulation is required for accurate integration.

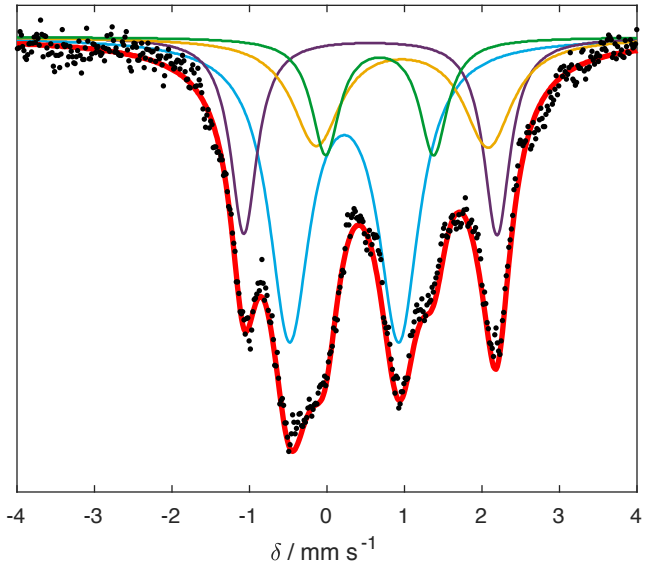

Figure B.17: Mössbauer spectrum collected from a catalytic reaction quenched after 10 minutes. Conditions: [[Na(12-c-4)$_2$][(P_3^B)^{57}Fe(N_2)]] = 0.43 mM, [$HBar^F_4$] = 63 mM (150 equiv), 1.2 equiv KC_8 relative to $HBar^F_4$. Raw data shown as black points, simulation as a solid red line, with components in blue, tan, and orange (see Table B.17 for parameters). Collected at 80 K with a parallel applied magnetic field of 50 mT.

Table B.17: Simulation parameters for Mössbauer spectrum in Figure B.17

Component	δ (mm s^{-1})	$\lvert\Delta E_Q\rvert$ (mm s^{-1})	Linewidths, Γ_L/Γ_R (mm s^{-1})	Relative area
A (blue)	0.22 ± 0.02	1.41 ± 0.03	0.64/0.64	0.50
B (purple)	0.56 ± 0.02	3.27 ± 0.07	0.41/0.41	0.22
C (green)	0.68 ± 0.02	1.40 ± 0.03	0.44/0.44	0.14
D (orange)	0.97 ± 0.02	2.22 ± 0.04	0.76/0.76	0.21

Fitting details for Figure B.17: Four quadrupole doublets were found to be necessary to obtain an adequate simulation. The simulation parameters are given in Table B.17. The spectrum shown in Figure B.17 exhibits six clearly resolved features, indicating at least three pairs of quadrupole doublets. The two most extreme resonances are well-modeled by the parameters for (P_3^B)Fe(N_2). After fitting this component (purple), the residual signal shows a pair of nearly overlapping quadrupole doublets, as well as an additional broad baseline component centered around 1 mm s^{-1}. The resolved features fit to two species, one with parameters nearly identical to those of the major species show in Figure B.16 (Table B.16, A), and another with parameters quite similar to those of (P_3^B)Fe(NH_2) (green). As

with previous spectra, a final component (orange) was included to model the broad residual baseline signal.

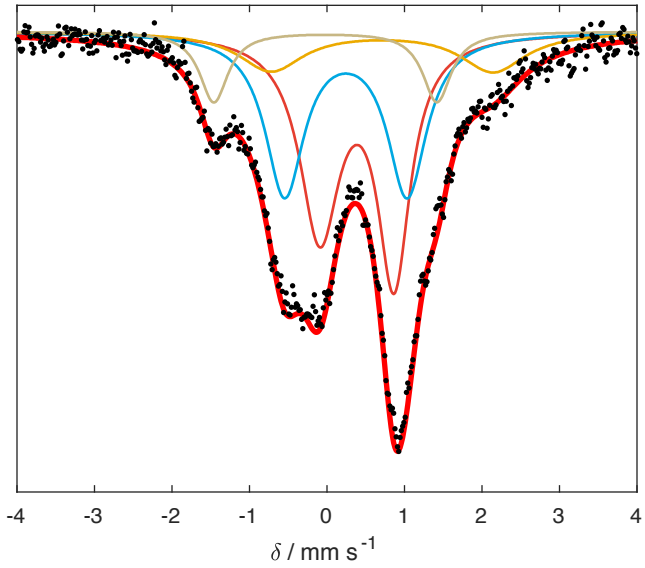

Figure B.18: Mössbauer spectrum collected from a catalytic reaction quenched after 25 minutes. Conditions: [[Na(12-c-4)$_2$][(P_3^B)^{57}Fe(N_2)]] = 0.43 mM, [$HBar^F_4$] = 63 mM (150 equiv), 1.2 equiv KC_8 relative to $HBar^F_4$. Raw data shown as black points, simulation as a solid red line, with components in blue, tan, and orange (see Table B.18 for parameters). Collected at 80 K with a parallel applied magnetic field of 50 mT.

Table B.18: Simulation parameters for Mössbauer spectrum in Figure B.18

Component	δ (mm s^{-1})	$\lvert\Delta E_Q\rvert$ (mm s^{-1})	Linewidths, Γ_L/Γ_R (mm s^{-1})	Relative area
A (blue)	0.24 ± 0.02	1.58 ± 0.03	0.61/0.61	0.39
B (red)	0.39 ± 0.02	0.96 ± 0.02	0.63/0.51	0.49
C (tan)	−0.02 ± 0.02	2.88 ± 0.06	0.44/0.44	0.13
D (orange)	0.71 ± 0.02	2.87 ± 0.06	1.01/1.01	0.15

Fitting details for Figure B.18: Four quadrupole doublets were found to be necessary to obtain an adequate simulation. The simulation parameters are given in Table B.18. The spectrum shown in Figure B.18 exhibits four clearly resolved features, the intensities of which indicate at least three pairs of quadrupole doublets. The major component is well modeled by the parameters for [(P_3^B)Fe(N_2)]$^-$ (red). After subtraction of this component, the residual signal exhibits two resolved quadrupole doublets in addition to a broad baseline signal centered around 0.7 mm s^{-1}. The two resolved species fit well to the two major components shown in Figure B.16 (blue and tan), while the residual signal was fit to a broad quadrupole doublet for accurate integration.

N.B. Note that the simulations of each of the spectra above were allowed to refine freely by a least-squares optimization model. Given that each spectrum reflects a mixture of species, some uncertainty in the fitting parameters is expected. Operating under the assumption that the signal assigned to species A in Tables B.14–B.18 is due to the same Fe compound, then we can estimate the uncertainty in the spectral simulations by the standard deviation in the optimized fits for each spectrum. We thus assign the parameters of A as $\delta = 0.21 \pm 0.03$ mm s^{-1} and $|\Delta E_Q| = 1.55 \pm 0.09$ mm s^{-1}. Performing the same analysis for the tan components in Tables B.15, B.16, and B.18 yields parameters $\delta = -0.03 \pm 0.04$ mm s^{-1} and $|\Delta E_Q| = 2.88 \pm 0.09$ mm s^{-1}.

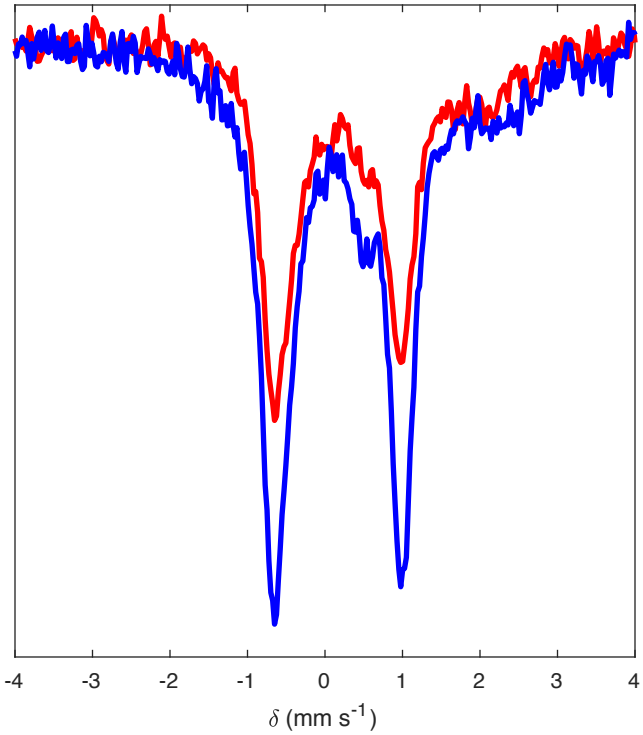

Figure B.19: Low temperature Mössbauer spectra of a freeze-quenched catalytic reaction mixture. The sample is identical to that presented in Figure B.14. Data collected in a 50 mT perpendicular magnetic field at 80 K (red trace) and 5 K (blue trace). The lack of magnetic hyperfine interactions in the 5 K spectrum of the major component strongly favors a non-Kramers spin system assignment.

References

(1) Watt, G. W.; Chrisp, J. D. *Anal. Chem.* **1952**, *24*, 2006–2008.

(2) Creutz, S. E.; Peters, J. C. *J. Am. Chem. Soc.* **2014**, *136*, 1105–1115.

(3) Anderson, J. S.; Rittle, J.; Peters, J. C. *Nature* **2013**, *501*, 84–87.

Appendix C

SUPPLEMENTARY INFORMATION FOR CHAPTER 4

C.1 Excited state paramagnetism of $(P_3{}^B)Fe(NNMe_2)$

The chemical shifts of the NMR resonances of complex $(P_3{}^B)Fe(NNMe_2)$ were found to be strongly temperature dependent, with significant deviations from linearity when plotted versus T^{-1}. This observation is consistent with the thermal occupation of a paramagnetic excited state, as has been observed for the isoelectronic hydrazido complex $[(P_3{}^{Si})Fe(NNMe_2)]^+$.[1] This temperature dependence can be modeled accurately as a low-spin/high-spin equilibrium by adopting a simple model assuming: (i) rapid interconversion of the spin states on the NMR timescale; (ii) temperature independence of the diamagnetic shift; (iii) Curie-behavior for the paramagnetic shift; and (iv) a Boltzmann distribution of states. Under these assumptions, the observed chemical shift will be the Boltzmann-weighted sum of those of the diamagnetic state and the paramagnetic state,

$$\begin{aligned}\delta_{\text{obs}} &= \delta_d \cdot \gamma_d + \delta_p \cdot \gamma_p \\ &= \delta_d \cdot (1-\gamma_p) + \left(\delta_d + \frac{C}{T}\right) \cdot \gamma_p \\ &= \delta_d + \frac{C}{T} \cdot \gamma_p \\ &= \delta_d + \frac{C}{T} \cdot \frac{g_p}{g_p + \exp\left(\frac{1}{R}\left(\frac{\Delta H}{T} - \Delta S\right)\right)}\end{aligned} \tag{C.1}$$

where δ_d is the diamagnetic shift, C is the Curie factor of the paramagnetic shift, and g_p is the electronic degeneracy of the excited state. Fitting this equation to both the temperature dependence of the N-CH_3 resonance from ^{1}H NMR (which has the largest Curie factor) and the ^{31}P chemical shift produces $\Delta H = 3.7(1)$ kcal mol^{-1} and $\Delta S = 2(3)$ cal mol^{-1} K^{-1} for $g_p = 3$ and $\Delta H = 3.7(1)$ and $\Delta S = 0(2)$ for $g_p = 5$. The fits are of equivalent quality, therefore, while ΔH is well-determined from the variable temperature NMR data, g_p is not. However, on the basis of computational studies (*vide infra*), we assign $g_p = 3$ (i.e. a triplet

excited state), given that a quintet state is predicted to be > 20 kcal mol^{-1} higher in energy than the diamagnetic ground state.

C.2 XRD refinement details for $(P_3{}^B)Fe(NNMe_2)$

The crystal structure of $(P_3{}^B)Fe(NNMe_2)$ suffered from two-part positional disorder of the two *N*-methyl carbons, coupled with two-part positional disorder of the isopropyl substituents on one P atom. This disorder reflects rotation about the N–N bond by ca. 30°, which forces the isopropyl substituents on the P atom to rotate to avoid unfavorable steric clashing. Each position of the two-part disorder was located in the difference map and refined anisotropically with hydrogen atoms calculated in the usual manner. To test the robustness of this model, the occupancies of both conformations of the $NNMe_2$ ligand and both conformations of the phosphine substituents were refined separately. The major conformations refined to 64% and 65% occupancy, respectively, confirming that the two conformational changes are coupled.

C.3 Mössbauer simulation details

All spectra were fit assuming symmetric quadrupole doublets with Lorentzian line shapes. This is the correct model for frozen solution spectra in the limit of fast electronic relaxation, which is typical at 80 K. However, the presence of small amounts of multiple (possibly paramagnetic and not necessarily in the fast relaxation limit) contaminants prevents accurate integration of spectra collected from protonation experiments of $[(P_3{}^B)Fe(N_2)]^{2-}$ and $[Na(12\text{-c-}4)_2][(P_3{}^B)Fe(N_2)]$ at long mixing times. However, given the well-separated spectral features of nitrido $[(P_3{}^B)Fe{\equiv}N]^+$, masking the spectra from $\delta = -2.2$ to 2.8 mm s^{-1} allowed for accurate integrations of $[(P_3{}^B)Fe{\equiv}N]^+$, when present. The results of simulations including the minimal number of quadrupole doublets necessary for a reasonable simulation (reduced $\chi^2 \approx 1$) are given in Tables C.3 to C.6, where the integrations of $[(P_3{}^B)Fe{\equiv}N]^+$ from masking the interior region of the spectra are also given. The latter integrations should be taken as more accurate.

C.4 EXAFS simulation details

The EXAFS spectrum of $(P_3{}^B)Fe(NNMe_2)$ was initially refined using phase and amplitude functions from the McHale curved wave theory tables included in EXAFSPAK, finding a prominent peak in the phase-uncorrected Fourier transform at $R + \Delta \approx 1.9$ Å due to three P-atom scatterers and a smaller peak at $R + \Delta \approx 1.5$ Å due to a single N-atom scatterer. Using coordinates from XRD, a model was constructed including the intact $NNMe_2$ ligand as well as a single iPr$_2$P moiety bonded to the B atom through a phenylene linker (i.e. all "symmetry-inequivalent" atoms of the pseudo-C_3 symmetric molecule). This model was used as input for the calculation of ab initio phase and amplitude functions using FEFF. In addition to single-scattering paths for the N_α atom of the $NNMe_2$ ligand and the P atom, two single-scattering paths due to carbon atoms were found to contribute significantly to the spectrum. One involves the C atom of the phenylene linker bonded directly to B (Fe–C = 3.38 Å from XRD), while the other involves a methyne C atom on the P iPr substitutent (Fe–C = 3.42 Å from XRD). Finally, a single multiple-scattering path was found involving the nearly linear Fe–N–N vector (Fe–N–N = 2.97 Å and ∠(Fe–N–N) = 176° from XRD); inclusion of this multiple-scattering path was necessary to completely simulate the Fourier-transformed EXAFS in the region from 0 to 3 Å. Inclusion of a path due to a B atom scatter improves the simulation marginally; however, with $Z = 5$, the B atom only weakly scatters the Fe photoelectron, which is reflected in the relatively high uncertainty in the simulated parameters. If the multiple-scattering path is omitted from the simulation, the data in the region $R + \Delta > 2$ Å is poorly fit.

For simulation of the EXAFS spectra of $(P_3{}^B)Fe(NNH_2)$ and $[(P_3{}^B)Fe{\equiv}N]^+$, the phase and amplitude functions computed from the XRD coordinates of $(P_3{}^B)Fe(NNMe_2)$ were employed. As expected, the EXAFS spectrum of $(P_3{}^B)Fe(NNH_2)$ was found be very similar to that found for $(P_3{}^B)Fe(NNMe_2)$. A single N-atom scatterer and 3 P-atom scatterers account for the majority of the spectrum below $R + \Delta = 2.5$ Å. Inclusion of two C-atom scatterers and the Fe–N–N multiple scattering path found above for $(P_3{}^B)Fe(NNMe_2)$ was

necessary to model the data above $R + \Delta = 2.5$ Å. The latter is consistent with a still-intact N–N bond in $(P_3{}^B)Fe(NNH_2)$. Inclusion of a B atom scatterer improves the simulation only marginally, and the fitted parameters for this path obtains a somewhat higher degree of uncertainty compared with the other shells. As before, if the multiple-scattering path is omitted from the simulation, the data in the region $R + \Delta > 2$ Å is poorly fit.

The EXAFS spectrum of $[(P_3{}^B)Fe{\equiv}N]^+$ is dominated by a single N-atom scatterer and 3 P-atom scatterers below $R + \Delta = 2.5$ Å. Beyond this, two prominent peaks in the Fourier transformed data at $R + \Delta = 2.8$ and 3.2 Å were simulated as ligand C atom scatterers. The slightly longer Fe–C distances found in $[(P_3{}^B)Fe{\equiv}N]^+$ are consistent with the observed elongation of the Fe–P bonds, which is also reproduced in the DFT calculated structure. (N.B., based on the DFT structure, we can assign the short C-atom scatterer as the phenylene C bonded P rather than that bonded to B, Fe–C = 3.40 Å.) To determine whether the phase and amplitude functions calculated from the crystal structure of $(P_3{}^B)Fe(NNMe_2)$ lead to any error in the measured bond lengths of $[(P_3{}^B)Fe{\equiv}N]^+$, we re-calculated single-scattering phase and amplitude functions using the refined N and P distances of $[(P_3{}^B)Fe{\equiv}N]^+$. However, using these new phase and amplitude functions did not alter the fitted Fe–N or Fe–P distances. Notably, no peak appears at ca. 2.5 Å (observed in $(P_3{}^B)Fe(NNH_2)$ and $(P_3{}^B)Fe(NNMe_2)$ from the Fe–N–N multiple scatterer), which suggests cleavage of the previously-intact N–N bond. Using the refined Fe–N–N distance of ca. 3 Å from $(P_3{}^B)Fe(NNH_2)$ and $(P_3{}^B)Fe(NNMe_2)$, the Fe–N bond length of 1.54(2) Å of $[(P_3{}^B)Fe{\equiv}N]^+$, $\Delta R = 0.1$ Å for $k_{max} = 16$ Å^{-1}, and assuming a quasi-linear Fe–N–N vector, the absence of such a peak implies an N–N bond length > 1.5 Å, if it were still present. This is significantly longer than the N–N single bond of N_2H_4, and thus the most consistent interpretation of the data is complete rupture of the N–N bond in $[(P_3{}^B)Fe{\equiv}N]^+$, in accordance with the Mössbauer data.

Comparing the set of second scans with the set of first scans of the sample of $[(P_3{}^B)Fe{\equiv}N]^+$, there is a noticeable reduction in the intensity of the pre-edge feature at

7112.1 eV (reduced by 20%), suggesting photodamage upon exposure to the high-energy X-rays. However, despite the changes in the pre-edge region, simulation of the EXAFS region on the set of second scans reveals no changes in the observed interatomic distances, within error. A plausible hypothesis is thus clean photoreduction of the Fe(IV) nitrido to its formally Fe(III) congener.[2] Given the relatively small amount of 3d character calculated for the a_1-symmetry LUMO of $[(P_3{}^B)Fe{\equiv}N]^+$, photoreduction would be expected to produce an $S = 1/2$ ground state with significant delocalization of the radical onto the N and B atoms. As a result, a resonance structure involving Fe(IV) and a ligand-centered radical would be a strong contributor, and little change in the Fe-ligand bond distances is expected. A comparison of the DFT calculated structures of $[(P_3{}^B)Fe{\equiv}N]^+$ ($S = 0$) and $(P_3{}^B)Fe{\equiv}N$ ($S = 1/2$) corroborates this prediction, revealing changes in the Fe–N and Fe–P interatomic distances that would not be resolved by EXAFS ($\ll 0.1$ Å). Furthermore, a comparison of the experimental XANES spectra of the sample of $[(P_3{}^B)Fe{\equiv}N]^+$ before and after exposure to X-rays reveals changes that are reproduced by TD-DFT calculations of the XANES spectra of $[(P_3{}^B)Fe{\equiv}N]^+$ and $(P_3{}^B)Fe{\equiv}N$, and is thus consistent with clean photoreduction (Figure C.35).

To test the robustness of the deglitching procedure used on the raw data, the EXAFS spectra of $(P_3{}^B)Fe(NNH_2)$ and $[(P_3{}^B)Fe{\equiv}N]^+$ were additionally simulated in the range $k = 2$ to 12 $Å^{-1}$, using the unaltered raw data. Within experimental error, the fitted parameters were identical to the simulations of the deglitched data, although inclusion of a B-atom scatterer and the second C-atom scatterer in the simulation of $(P_3{}^B)Fe(NNH_2)$ resulted in negative σ^2, and were thus excluded. We also note that although Fe impurities were present in the samples of $(P_3{}^B)Fe(NNH_2)$ and $[(P_3{}^B)Fe{\equiv}N]^+$ examined by XAS ($\geq$ 70% and 60% pure, respectively), attempts to include additional scattering shells (e.g., P or N/O atoms) from these impurities did not significantly improve the simulations. This is mostly like due to the fact that, in both cases, no single impurity is present in more than ca. 20% yield. However, the presence of impurities may be the cause of the moderately large σ^2 values

for the Fe–N scatterers in $(P_3{}^BFe(NNH_2)$ and $[(P_3{}^B)Fe{\equiv}N]^+$. For example, if N for the N-atom scatterer of $[(P_3{}^B)Fe{\equiv}N]^+$ is allowed to refine freely, the best-fit value changes from $N = 1$ to $N = 0.77$, which is accompanied by a 0.002 Å^2 reduction in σ^2. Setting $N = 0.7$ and including a second N-atom scatterer at 1.66 Å results in a very minor improvement to the simulation (< 1% in the reduced χ^2). Moreover, this has no effect on the best-fit value for the nitrido N-atom distance R (1.53(2) Å), within error. Given typical uncertainties of 20% in N, these were restricted to 1 for both N-atom scatterers of $(P_3{}^BFe(NNH_2)$ and $[(P_3{}^B)Fe{\equiv}N]^+$, for simplicity.

The EXAFS spectrum of $[(P_3{}^B)Fe(N_2)]^{2-}$ was simulated in the same fashion as that of $(P_3{}^BFe(NNMe_2)$, except ab initio phase and amplitude functions were computed from the DFT-optimized coordinates of $[(P_3{}^B)Fe(N_2)]^{2-}$. Again, in addition to N and P scatterers, two shells of ligand C-atom scatterers and a single Fe–N–N multiple-scatterer were included to simulate the EXAFS spectrum above $R + \Delta = 2.5$ Å. In this case, the degeneracy of one C scatterer was increased from 3 to 6 to include the phenylene C bonded to the P atom (Fe–C = 3.34 Å from DFT). Attempts to include a B atom scatterer resulted in unreasonably large uncertainties in σ^2, presumably due to the greater number and intensity of Fe–C paths, and this path was thus excluded.

N.B., for those simulations where inclusion of a Fe–N–N multiple scattering path was found to be necessary to fully simulate the data, an estimate of the N–N interatomic distance can be obtained by subtraction of the distance of the Fe–N single scattering path from that of the multiple scattering path.

C.5 NMR Spectra

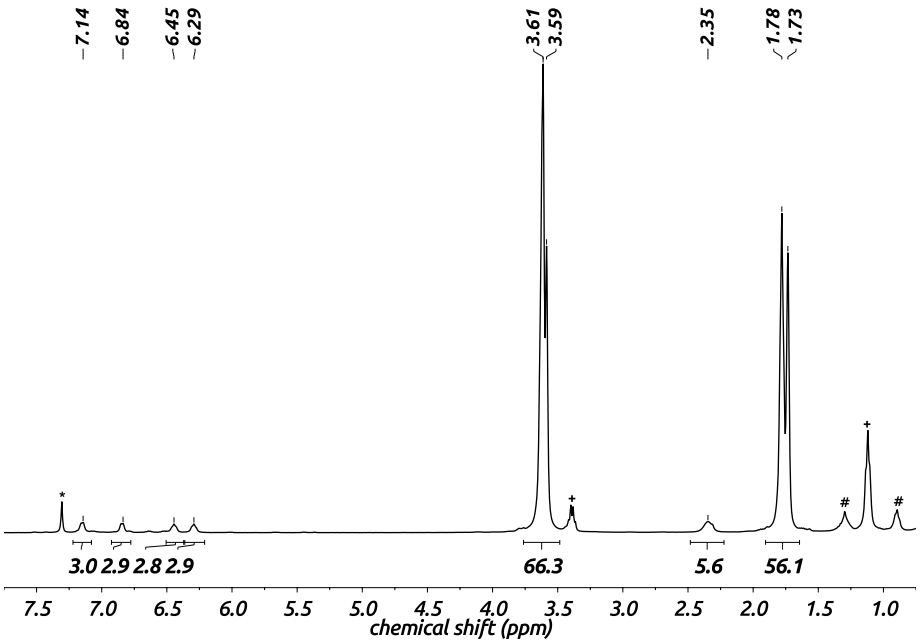

Figure C.1: ^{1}H NMR spectrum of $[(P_3{}^{B})Fe(N_2)]^{2-}$ (400 MHz, d_8-THF, 293 K) produced from in situ reduction of $[Na(12\text{-c-}4)_2][(P_3{}^{B})Fe(N_2)]$. Owing to the slight shift of the residual THF resonances due to interaction with Lewis acidic K^+ ions, the chemical shifts were referenced internally to a C_6H_6 standard at 7.31 ppm (denoted by *). Accurate integrations for the isopropyl methyl protons of the ligand and the methylene protons of the $[Nq(12\text{-c-}4)_2]^+$ ion could not be obtained due to overlap with the residual THF resonances appearing at 1.73 and 3.59 ppm. $^{+}$Denotes Et_2O impurity. $^{\#}$Denotes *n*-pentane impurity.

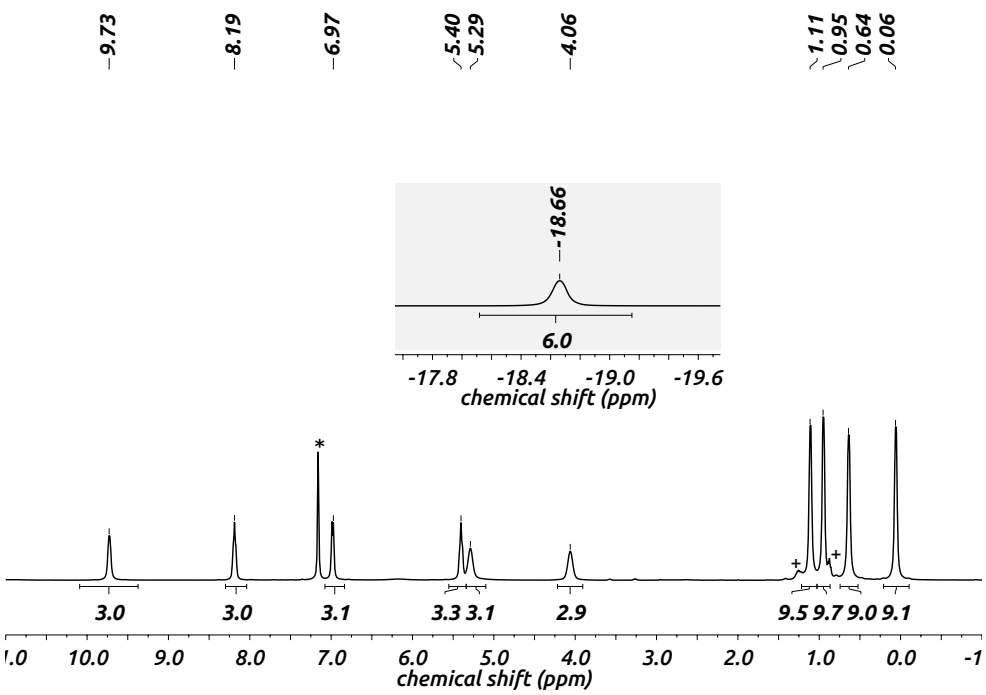

Figure C.2: ^{1}H NMR spectrum of ($P_3{}^{B}$)Fe($NNMe_2$) (400 MHz, C_6D_6, 293 K). Inset shows the resonance due to the *N*-methyl protons. *Denotes residual C_6H_6 signal. $^{+}$Denotes trace *n*-pentane impurity.

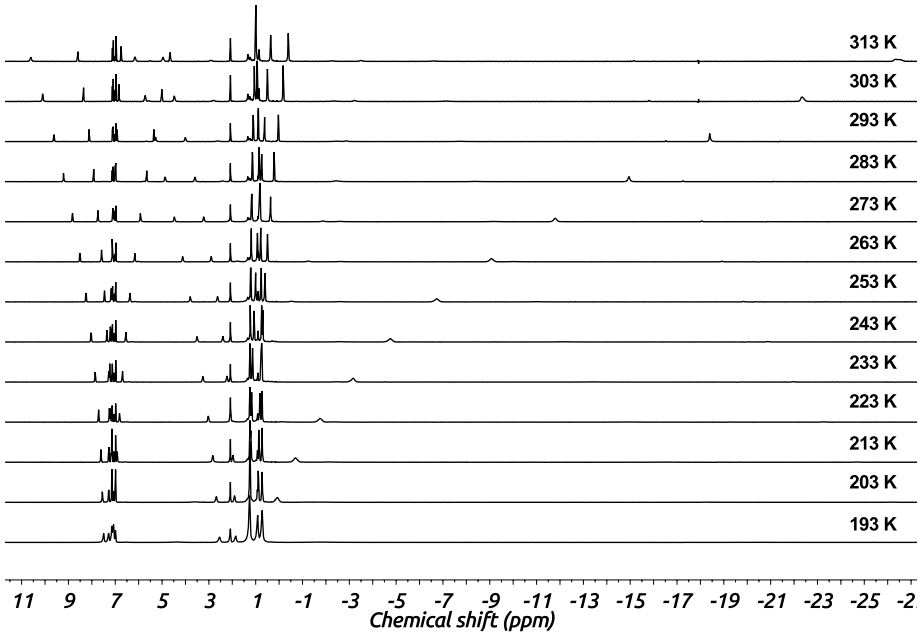

Figure C.3: Variable temperature ^{1}H NMR spectra of ($P_3{}^B$)Fe($NNMe_2$) (500 MHz, d_8-toluene). Temperatures of individual spectra are indicated on the right. The large magnitude of the Curie factor of the N-CH_3 resonance is evident by its highly temperature dependent position, relative to the $P_3{}^B$ ligand-based proton signals.

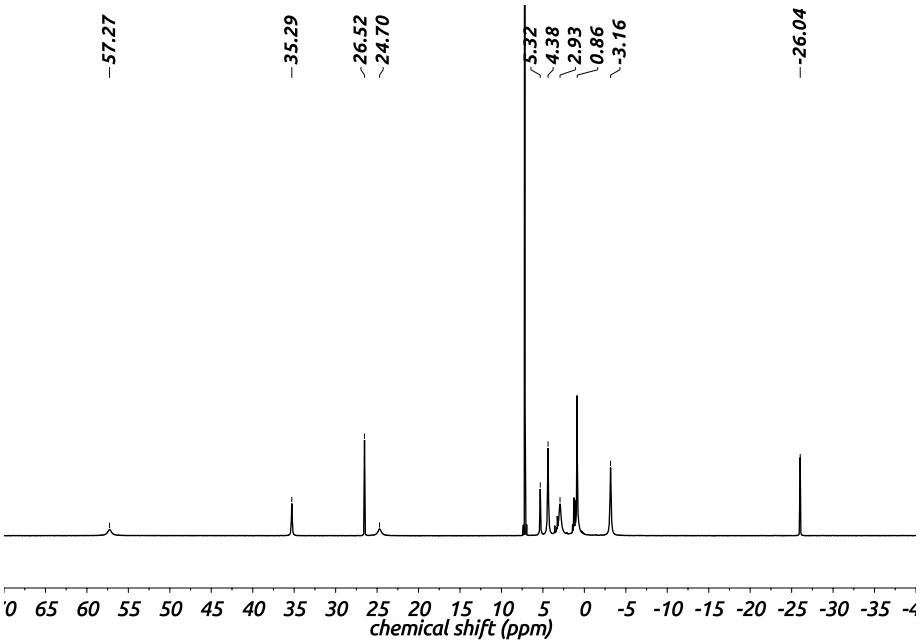

Figure C.4: ^{1}H NMR spectrum of (P_3^B)Fe(OTf) (400 MHz, C_6D_6, 293 K).

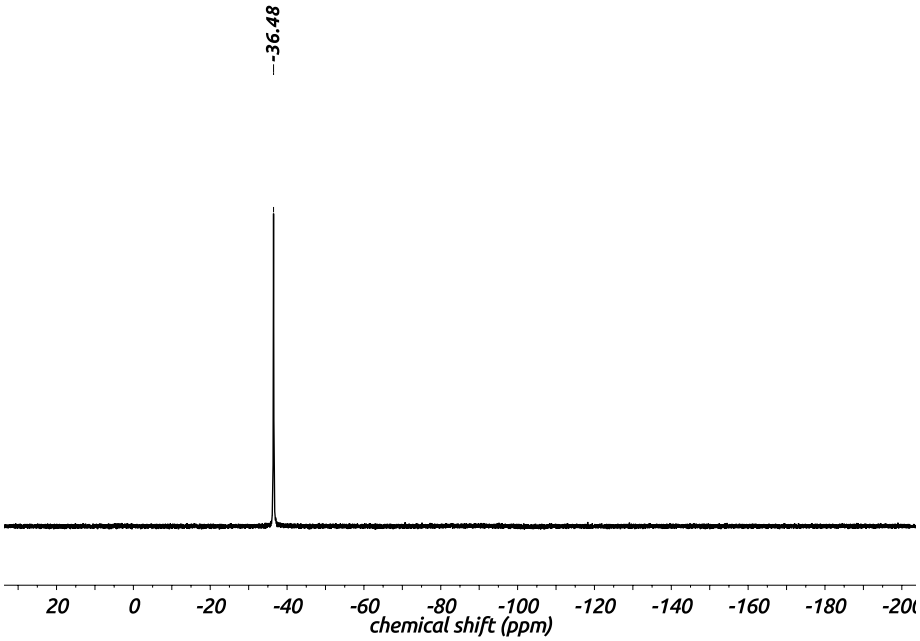

Figure C.5: ^{19}F NMR spectrum of $(P_3{}^B)Fe(OTf)$ (376 MHz, C_6D_6, 293 K).

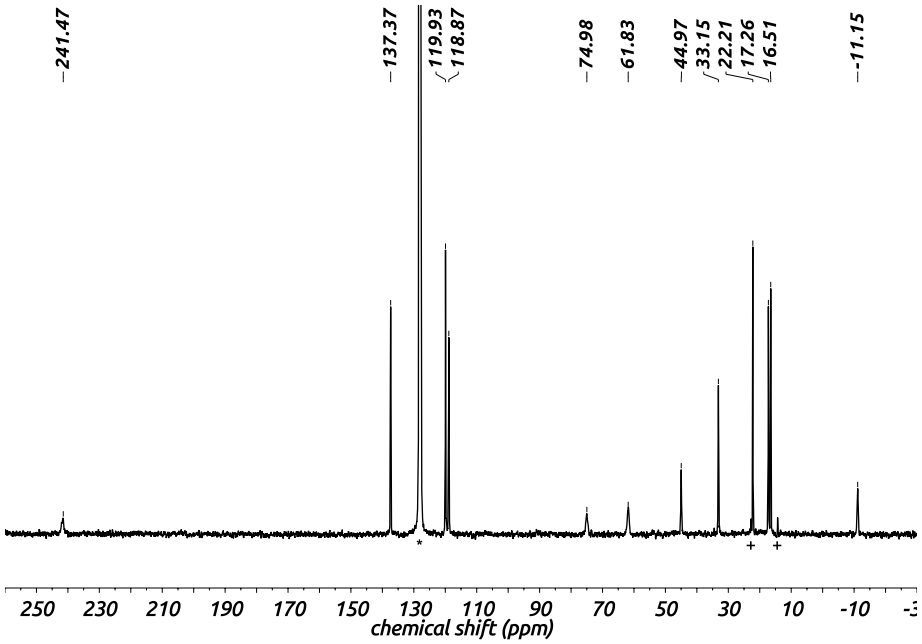

Figure C.6: ^{13}C NMR spectrum of $(P_3^B)Fe(NNMe_2)$ (101 MHz, C_6D_6, 293 K). *Denotes residual C_6H_6 signal. $^+$Denotes trace *n*-pentane impurity. Note that a resonance for the *N*-methyl carbon could not be observed at this temperature, even over a range of 1000 to −500 ppm.

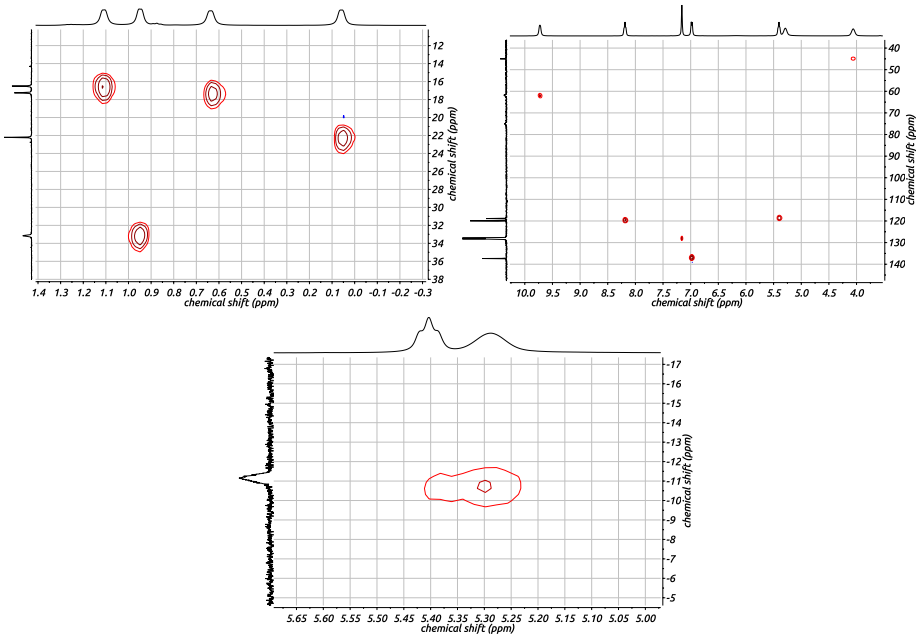

Figure C.7: ^{1}H–^{13}C HMQC spectra of (P_3^B)Fe(NNMe$_2$) (^{1}H 400 MHz, ^{13}C 101 MHz, C_6D_6, 293 K). Abscissa: ^{1}H chemical shifts; Ordinate: ^{13}C chemical shifts.

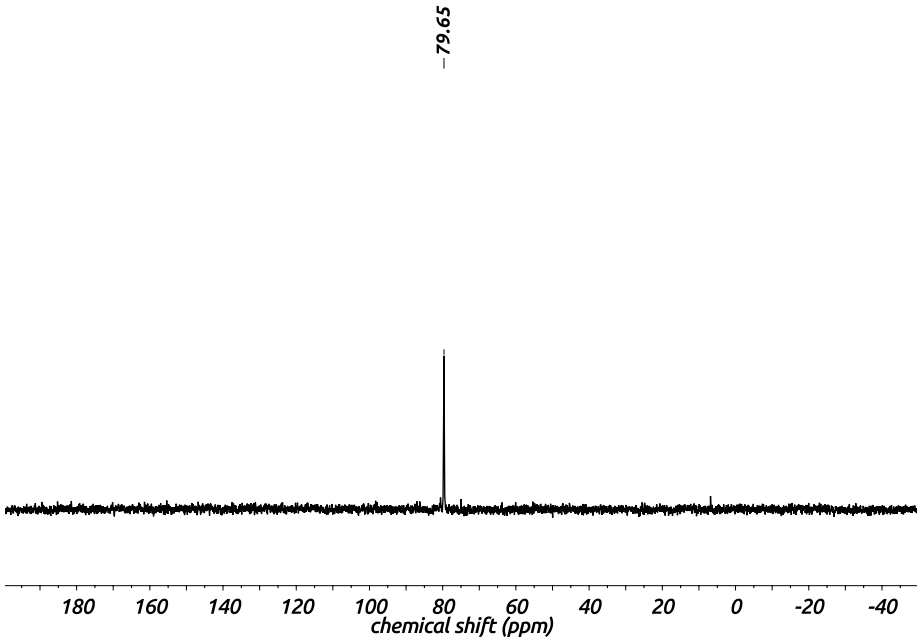

Figure C.8: ^{31}P NMR spectrum of $[(P_3{}^B)Fe(N_2)]^{2-}$ (162 MHz, d_8-THF, 293 K) produced from in situ reduction of $[Na(12\text{-c-}4)_2][(P_3{}^B)Fe(N_2)]$.

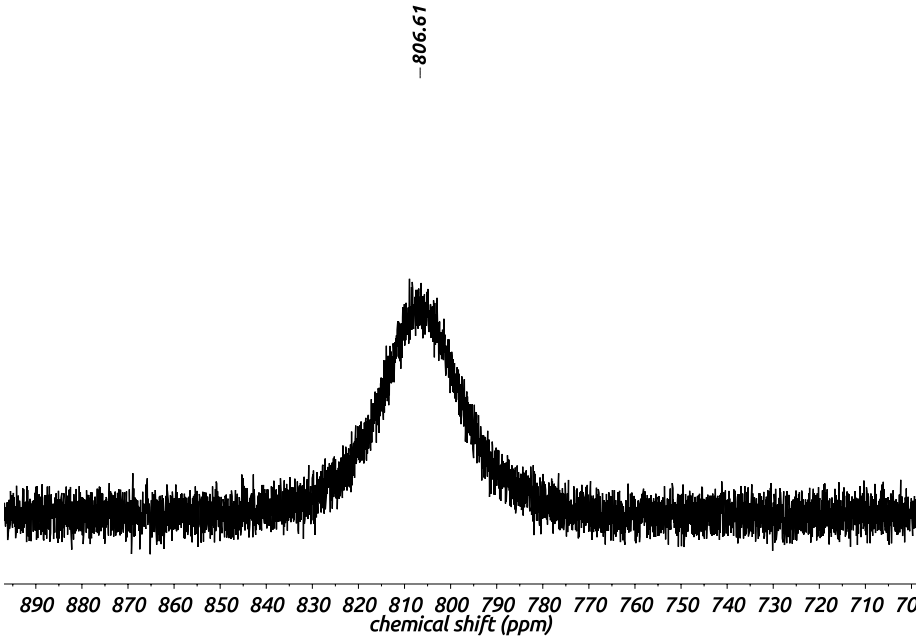

Figure C.9: ^{31}P NMR spectrum of $(P_3{}^B)Fe(NNMe_2)$ (162 MHz, C_6D_6, 293 K).

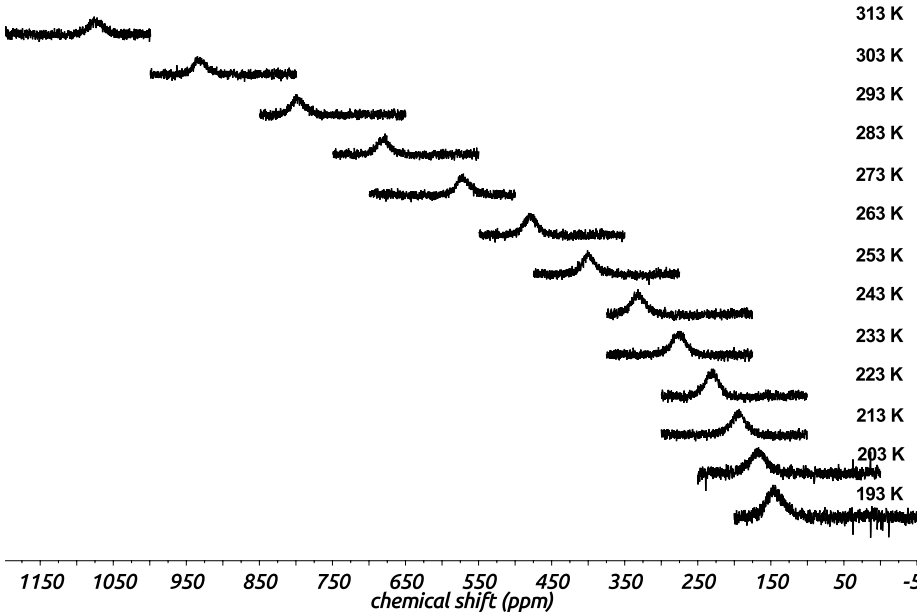

Figure C.10: Variable temperature ^{31}P NMR spectra of ($P_3{}^B$)Fe($NNMe_2$) (202 MHz, d_8-toluene). Temperatures of individual spectra are indicated on the right.

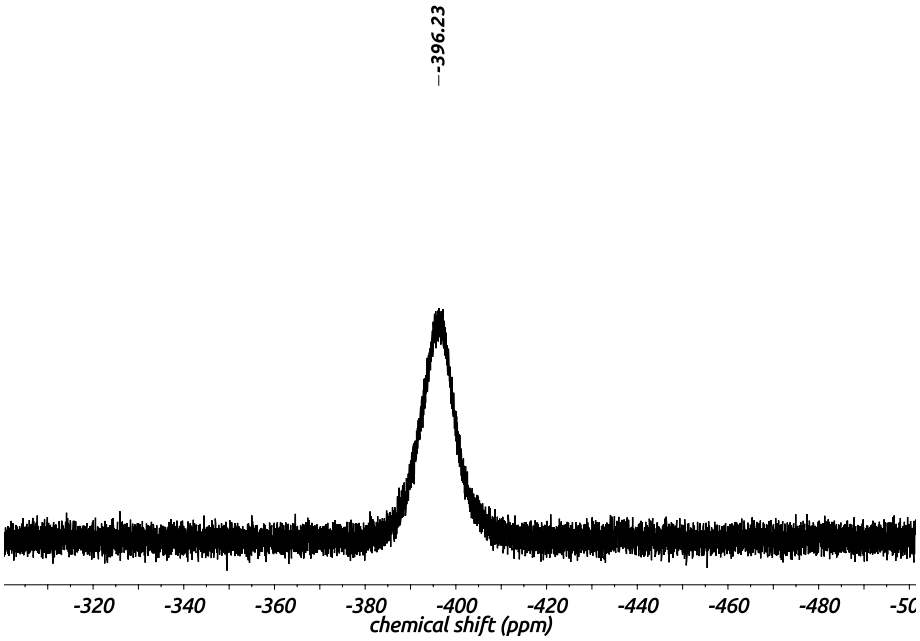

Figure C.11: ^{11}B NMR spectrum of ($P_3{}^B$)Fe($NNMe_2$) (128 MHz, C_6D_6, 293 K).

C.6 IR Spectra

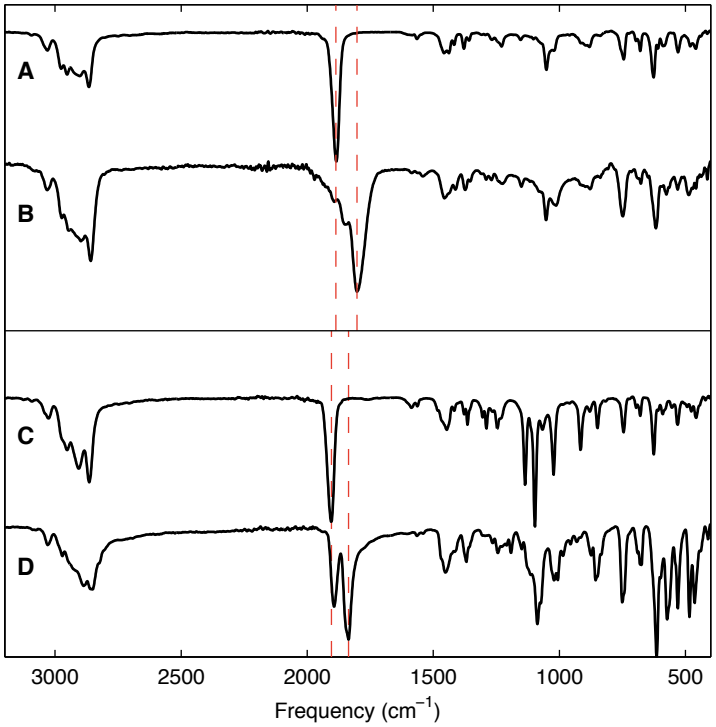

Figure C.12: (A) IR spectrum of $[Na(Et_2O)_2][(P_3{}^B)Fe(N_2)]$ deposited as a thin film from a THF solution. (B) IR spectrum of $[(P_3{}^B)Fe(N_2)]^{2-}$ generated in situ from a THF solution of $[Na(Et_2O)_2][(P_3{}^B)Fe(N_2)]$ by iterative passage through a column of KC_8, and depositing as a thin film. (C) IR spectrum of $[Na(12\text{-c-}4)_2][(P_3{}^B)Fe(N_2)]$ deposited as a thin film from a THF solution. (D) IR spectrum of $[(P_3{}^B)Fe(N_2)]^{2-}$ generated from a DME solution of $[Na(12\text{-c-}4)_2][(P_3{}^B)Fe(N_2)]$ by iterative passage through a column of KC_8, and subsequent recrystallization. The spectrum was collected on a powder generated from the recrystallized material and shows contamination with $[K(DME)_x][(P_3{}^B)Fe(N_2)]$ (ν_{NN} = 1893 cm^{-1}). The red dashed lines in the top panel are at energies 1886 and 1803 cm^{-1} while the red dashed lines in the bottom panel are at energies 1904 and 1836 cm^{-1}.

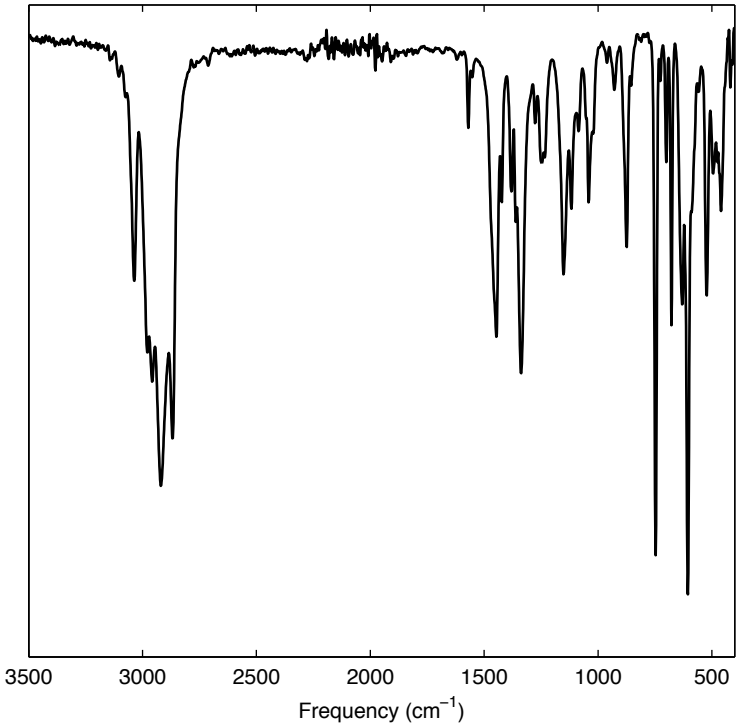

Figure C.13: IR spectrum of ($P_3{}^B$)Fe($NNMe_2$) deposited as a thin film from a C_6D_6 solution.

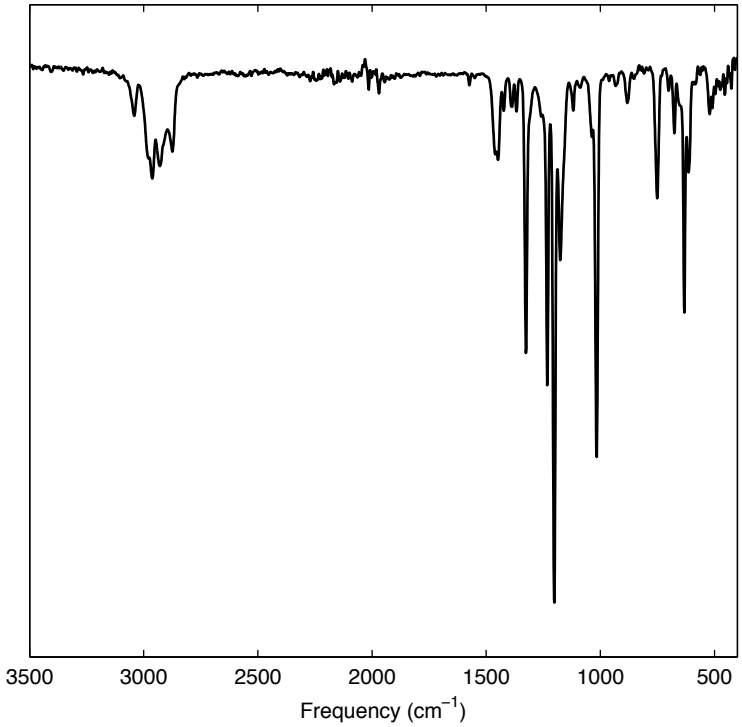

Figure C.14: IR spectrum of ($P_3{}^B$)Fe(OTf) deposited as a thin film from a C_6D_6 solution.

C.7 UV-vis Spectra

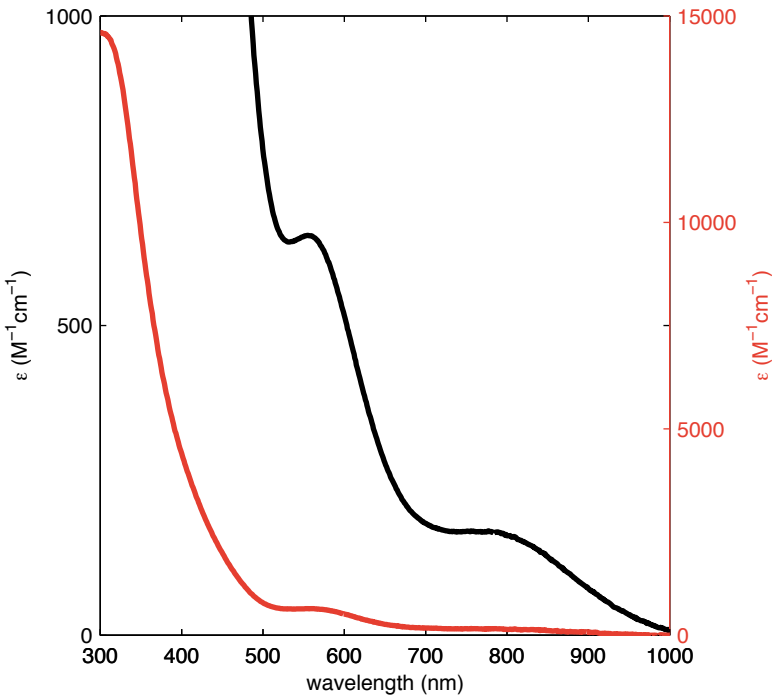

Figure C.15: UV-vis spectrum of $(P_3{}^B)Fe(NNMe_2)$ (toluene, 293 K). The black trace corresponds to the left axis scale, while the red trace corresponds to the right axis scale.

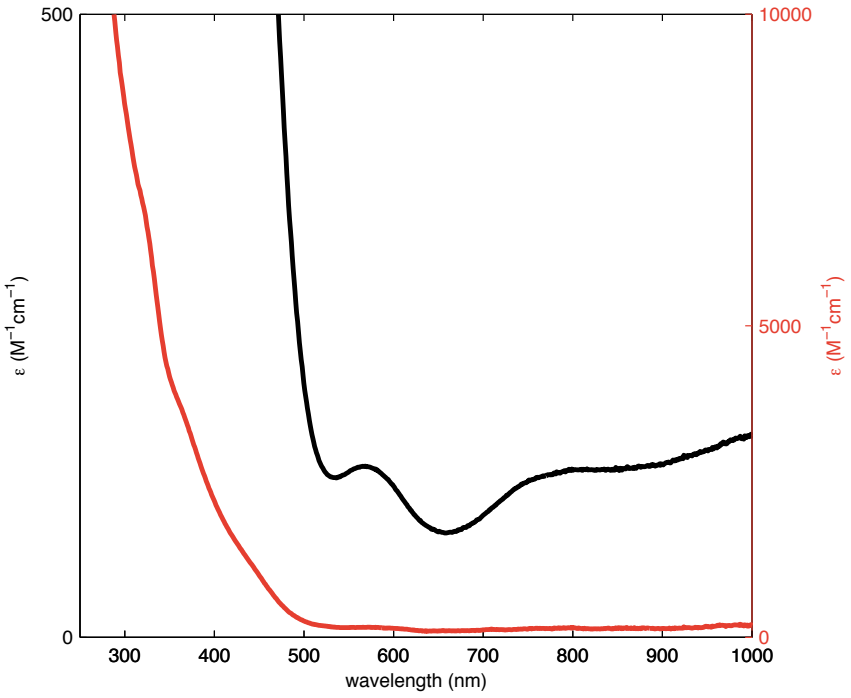

Figure C.16: UV-vis spectrum of ($P_3{}^B$)Fe(OTf) (2-MeTHF, 293 K). The black trace corresponds to the left axis scale, while the red trace corresponds to the right axis scale.

C.8 Mössbauer Spectra

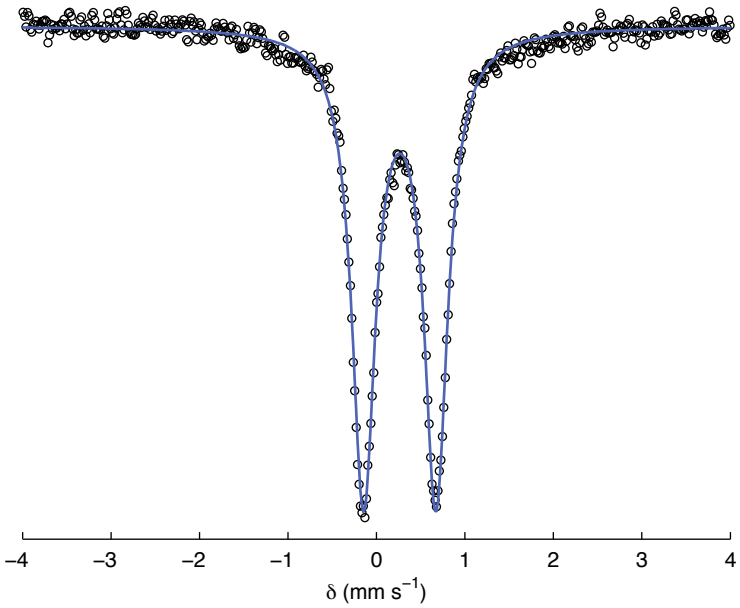

Figure C.17: Mössbauer spectrum of $[(P_3{}^B)Fe(N_2)]^{2-}$ generated from in situ reduction of ^{57}Fe labelled $[Na(12\text{-c-}4)_2][(P_3{}^B)Fe(N_2)]$ in THF (1.4 mM; sample was frozen as a suspension with excess KC_8). The spectrum was collected at 80 K in the presence of a 50 mT magnetic field oriented parallel to the γ-ray propagation. Raw data are shown as open circles, simulation as a solid line. Simulation parameters: $\delta = 0.26$ mm s^{-1}; $|\Delta E_Q| = 0.82$ mm s^{-1}; $\Gamma = 0.32$ mm s^{-1}.

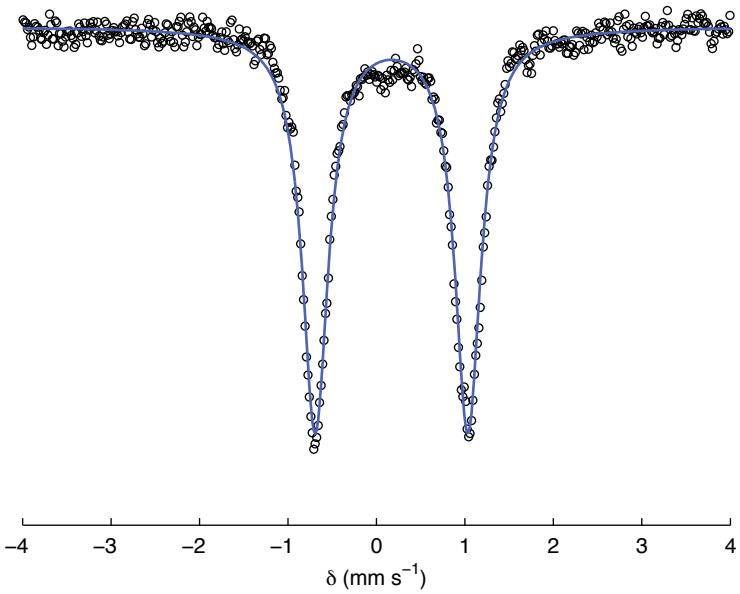

Figure C.18: Mössbauer spectrum of $(P_3{}^BFe(NNMe_2)$ as a frozen solution in 2-MeTHF (30 mM; natural abundance ^{57}Fe). The spectrum was collected at 80 K in the presence of a 50 mT magnetic field oriented parallel to the γ-ray propagation. Raw data are shown as open circles, simulation as a solid line. Simulation parameters: δ = 0.17 mm s^{-1}; $|\Delta E_Q|$ = 1.73 mm s^{-1}; Γ = 0.36 mm s^{-1}.

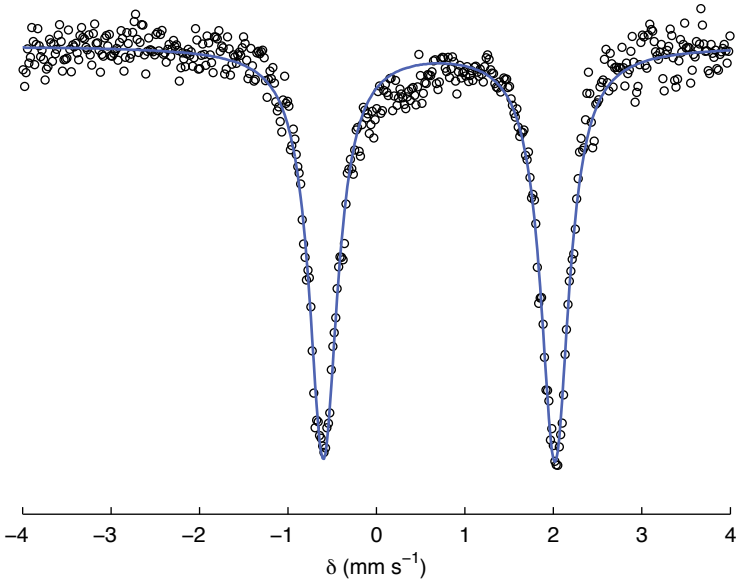

Figure C.19: Mössbauer spectrum of $(P_3{}^B)$Fe(OTf) as a powder suspended in boron nitride (natural abundance ^{57}Fe). The spectrum was collected at 80 K in the presence of a 50 mT magnetic field oriented parallel to the γ-ray propagation. Raw data are shown as open circles, simulation as a solid line. Simulation parameters: δ = 0.71 mm s^{-1}; $|\Delta E_Q|$ = 2.62 mm s^{-1}; Γ = 0.39 mm s^{-1}.

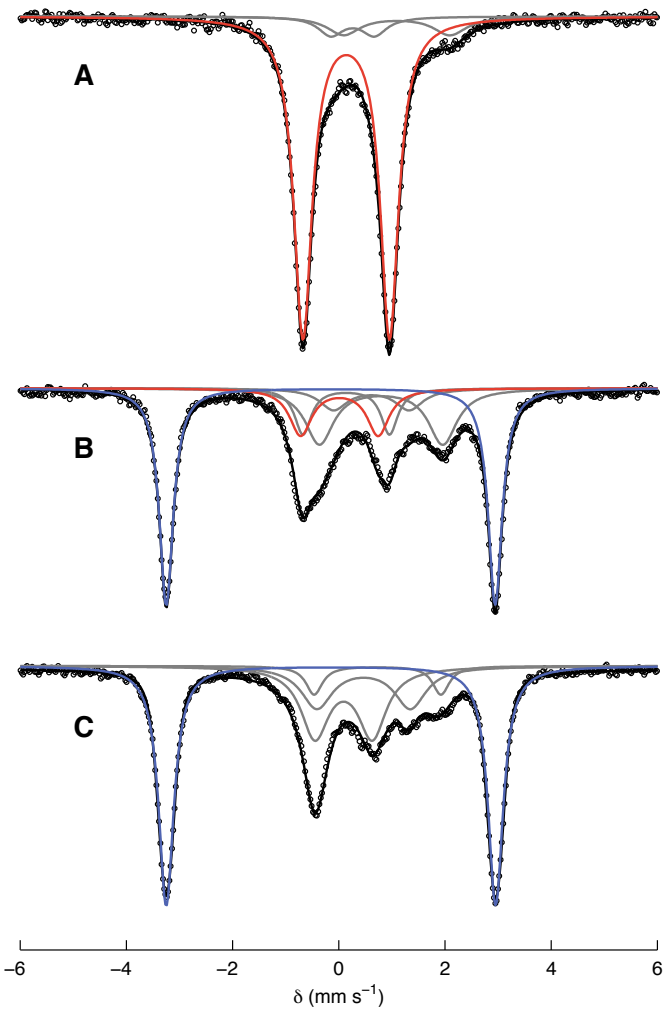

Figure C.20: Freeze-quenched Mössbauer spectra from protonation studies of ^{57}Fe labelled $[(P_3{}^B)Fe(N_2)]^{2-}$ using TfOH as the proton source. Spectra were collected as frozen 2-MeTHF solutions at 80 K in the presence of a 50 mT magnetic field oriented parallel to the γ-ray propagation. Raw data are shown as open circles, simulation as a solid black line, with individual sub-spectra plotted in grey, red, and blue. Full simulation parameters are given in Table C.3. (A) Reaction freeze-quenched after 15 min. of mechanical mixing, showing the major species to be $(P_3{}^B)Fe(NNH_2)$ (red sub-spectrum). (B) Reaction freeze-quenched after 60 min. of mechanical mixing, showing ca. 50% yield of $[(P_3{}^B)Fe{\equiv}N]^+$ (blue sub-spectrum) and ca. 10% yield of $(P_3{}^B)Fe(NNH_2)$ (red sub-spectrum). (C) Reaction freeze-quenched after 120 min. of mechanical mixing, showing ca. 60% yield of $[(P_3{}^B)Fe{\equiv}N]^+$ (blue sub-spectrum), and complete consumption of $(P_3{}^B)Fe(NNH_2)$.

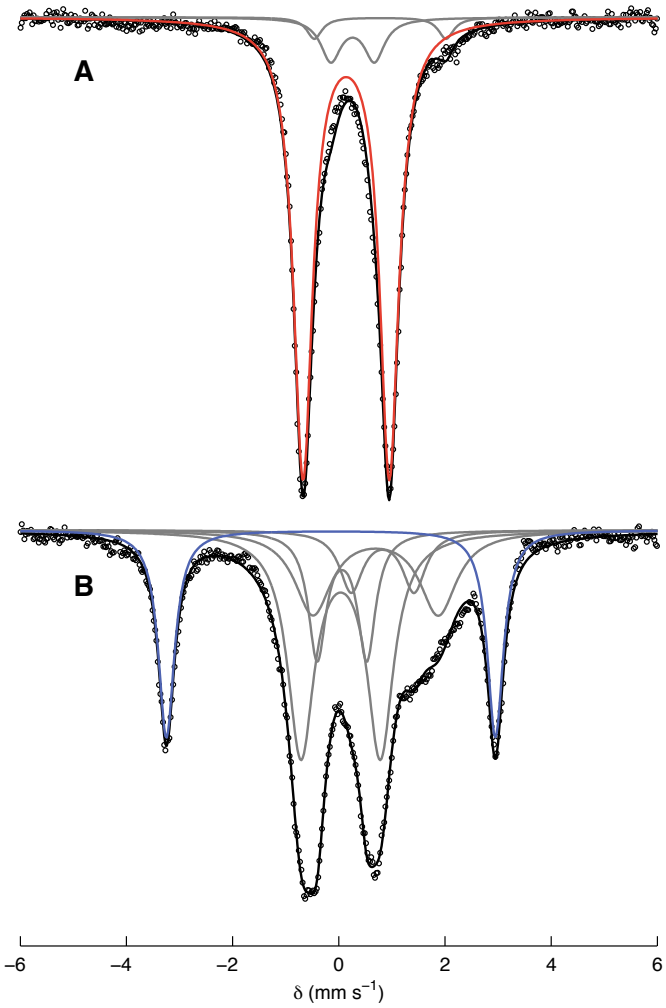

Figure C.21: Freeze-quenched Mössbauer spectra from protonation studies of ^{57}Fe labelled $[(P_3{}^B)Fe(N_2)]^{2-}$ using $HBAr^F{}_4$ as the proton source. Spectra were collected as frozen 2-MeTHF solutions at 80 K in the presence of a 50 mT magnetic field oriented parallel to the γ-ray propagation. Raw data are shown as open circles, simulation as a solid black line, with individual sub-spectra plotted in grey, red, and blue. Full simulation parameters are given in Table C.4. (A) Reaction freeze-quenched after 15 min. of mechanical mixing, showing the major species to be $(P_3{}^B)Fe(NNH_2)$ (red sub-spectrum). (B) Reaction freeze-quenched after 30 min. of mechanical mixing, showing ca. 20% yield of $[(P_3{}^B)Fe{\equiv}N]^+$ (blue sub-spectrum).

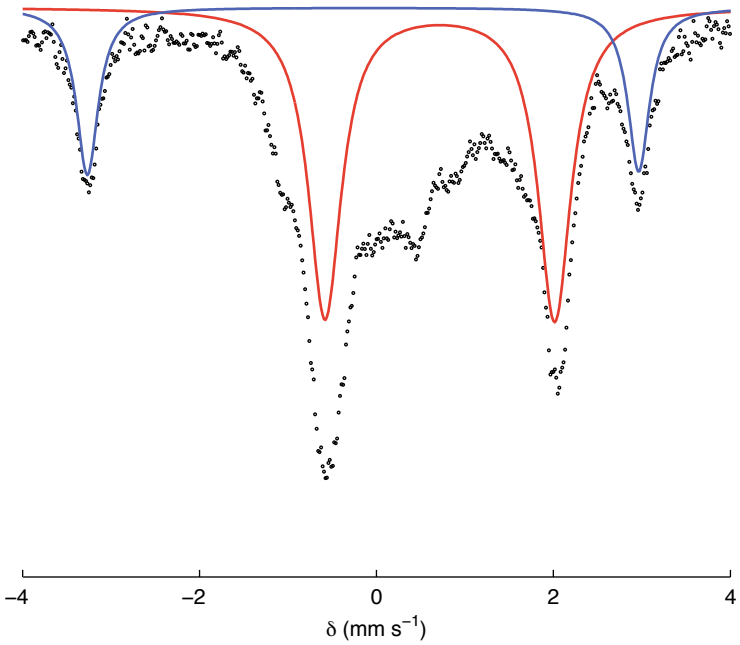

Figure C.22: Freeze-quenched Mössbauer spectra from protonation of ^{57}Fe labelled [Na(12-c-4)$_2$][(P_3^B)Fe(N_2)] using TfOH as the proton source, mixing for 15 min. in supercooled 2-MeTHF. The spectrum was collected as frozen 2-MeTHF solutions at 80 K in the presence of a 50 mT magnetic field oriented parallel to the γ-ray propagation. Raw data are shown as open circles, with a simulation containing [(P_3^B)Fe≡N]$^+$ (ca. 20%, blue subspectrum) and (P_3^B)Fe(OTf) (ca. 50%, red sub-spectrum) shown as solid lines.

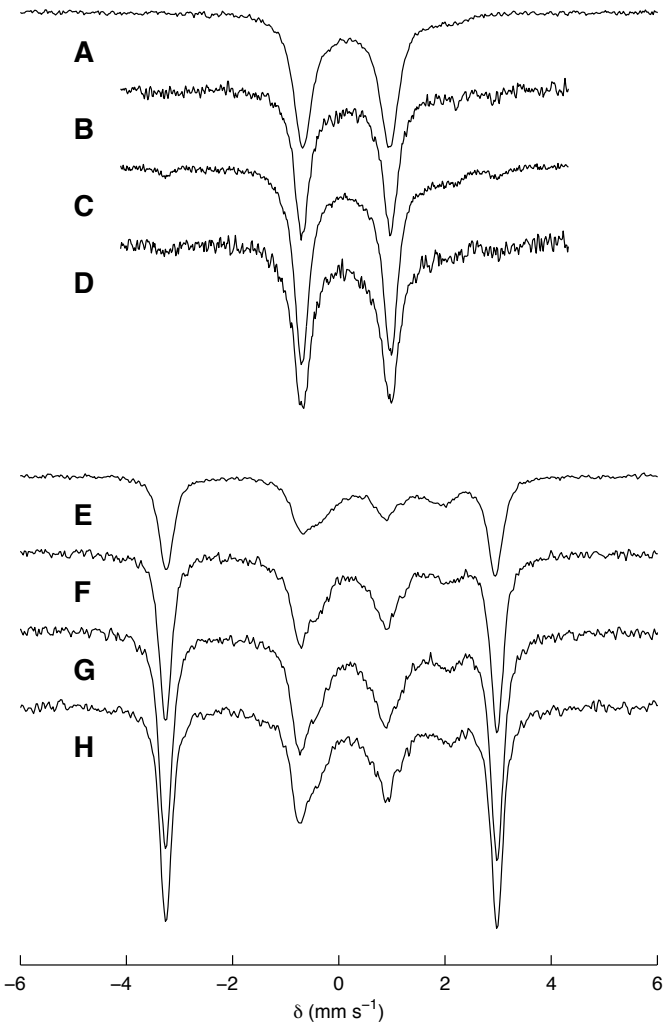

Figure C.23: Freeze-quenched Mössbauer spectra from protonation studies of ^{57}Fe labelled $[(P_3{}^B)Fe(N_2)]^{2-}$ using TfOH as the proton source. Spectra A through D were collected on the sample presented in Figure C.20 A, while spectra E through H were collected on the sample presented in Figure C.20 B. (A) Collected at 80 K with a parallel 50 mT magnetic field. (B) Collected at 5 K in zero applied field. (C) Collected at 5 K with a parallel 50 mT magnetic field. (D) Collected at 5 K with a perpendicular 50 mT magnetic field. (E) Collected at 80 K with a parallel 50 mT magnetic field. (F) Collected at 5 K in zero applied field. (G) Collected at 5 K with a parallel 50 mT magnetic field. (H) Collected at 5 K with a perpendicular 50 mT magnetic field.

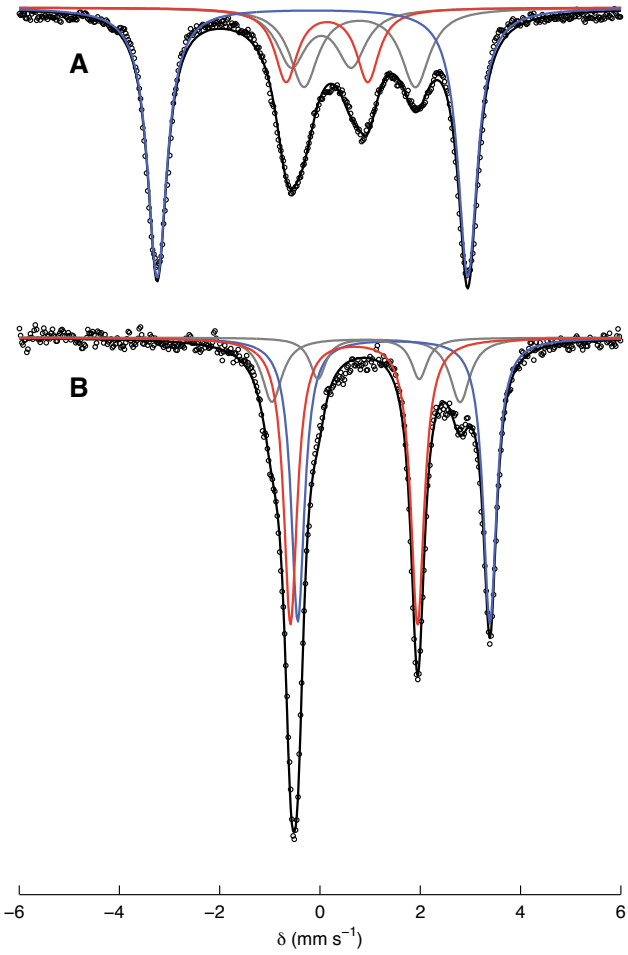

Figure C.24: Freeze-quenched Mössbauer spectra from protonation studies of ^{57}Fe labelled $[(P_3{}^B)Fe(N_2)]^{2-}$ using TfOH as the proton source ([Fe] = 4 mM; [TfOH] = 80 mM). Spectra were collected as frozen 2-MeTHF solutions at 80 K in the presence of a 50 mT magnetic field oriented parallel to the γ-ray propagation. Raw data are shown as open circles, simulation as a solid black line, with individual sub-spectra plotted in grey, red, and blue. Full simulation parameters are given in Table C.5. (A) Reaction freeze-quenched after 30 min. of mechanical mixing, showing ca. 50% yield of $[(P_3{}^B)Fe{\equiv}N]^+$ (blue sub-spectrum) and ca. 18% yield of $(P_3{}^B)Fe(NNH_2)$ (red sub-spectrum). (B) Spectrum resulting from annealing the sample to room temperature for 10 min, showing decomposition of $(P_3{}^B)Fe(NNH_2)$ and $[(P_3{}^B)Fe{\equiv}N]^+$ to a mixture of primarily composed of $(P_3{}^B)Fe(OTf)$ (42%, red sub-spectrum) and a high-spin Fe(II) species (42%, blue sub-spectrum). A qualitatively similar spectrum is obtained if an identically-prepared sample is annealed to 195 K for longer than 30 minutes.

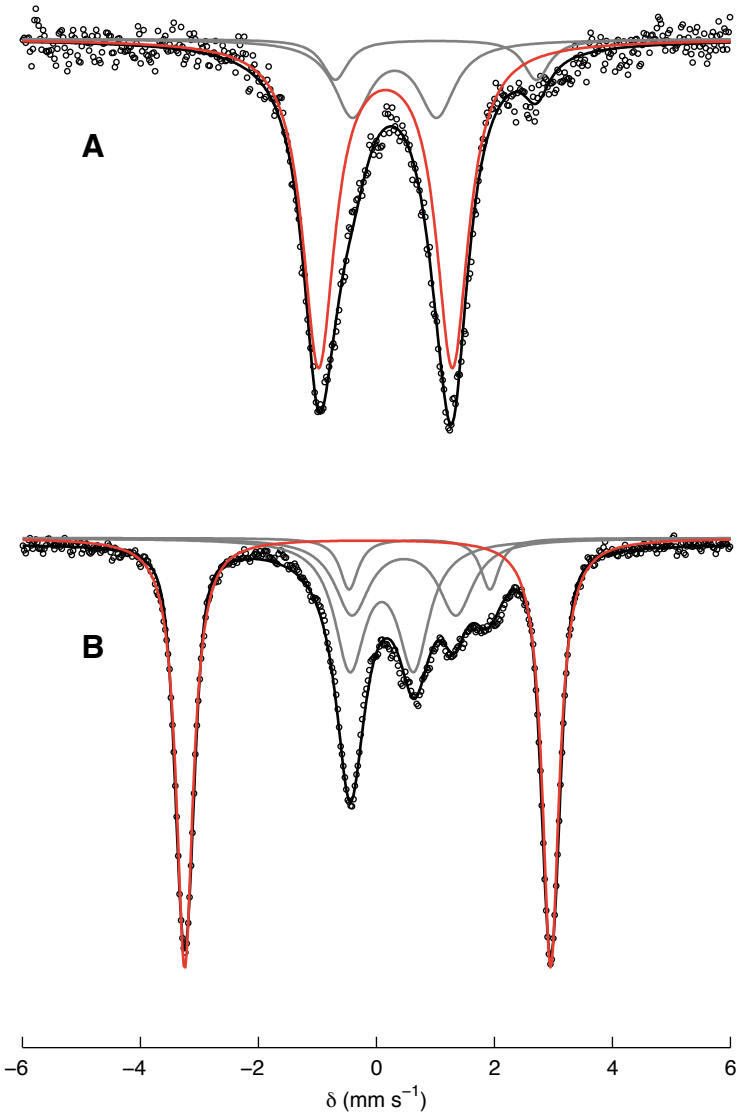

Figure C.25: Freeze-quenched Mössbauer spectra from protonation studies of ^{57}Fe labelled $[(P_3{}^B)Fe(N_2)]^{2-}$ using TfOH as the proton source, prepared for XAS studies. Spectra were collected as frozen 2-MeTHF solutions at 80 K in the presence of a 50 mT magnetic field oriented parallel to the γ-ray propagation. Raw data are shown as open circles, simulation as a solid black line, with individual sub-spectra plotted in grey, red, and blue. Full simulation parameters are given in Table C.6. (A) Reaction freeze-quenched after 15 minutes, showing $>$ 70% of $(P_3{}^B)Fe(NNH_2)$ (red sub-spectrum). (B) Reaction freeze-quenched after 30 min. of mechanical mixing, showing ca. 60% yield of $[(P_3{}^B)Fe{\equiv}N]^+$ (red sub-spectrum).

C.9 XAS Spectra

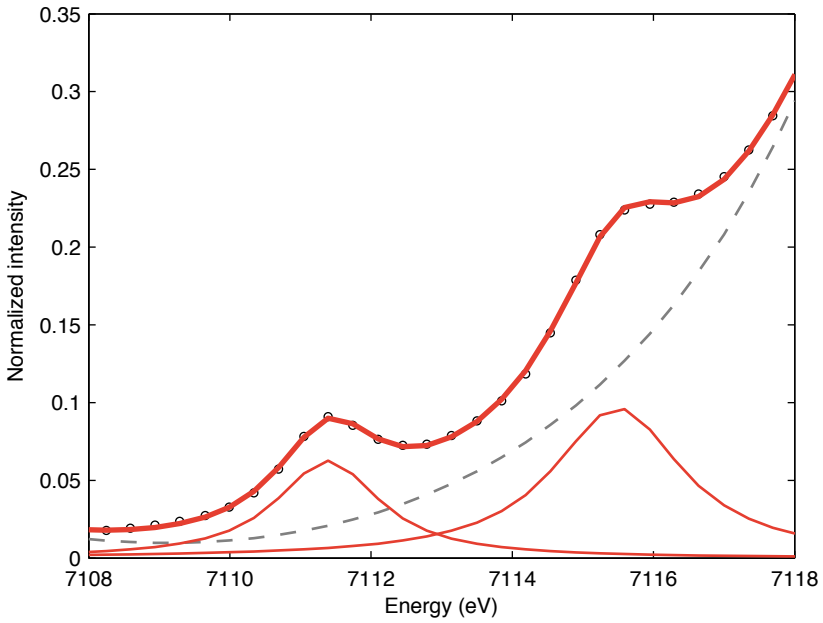

Figure C.26: Pre-edge XANES spectrum of $(P_3{}^B)Fe(NNMe_2)$. Raw data are shown as open circles, simulation as a bold red line, with individual components as thin red lines and the baseline as a dotted grey line. Full simulation parameters are given in Table C.7.

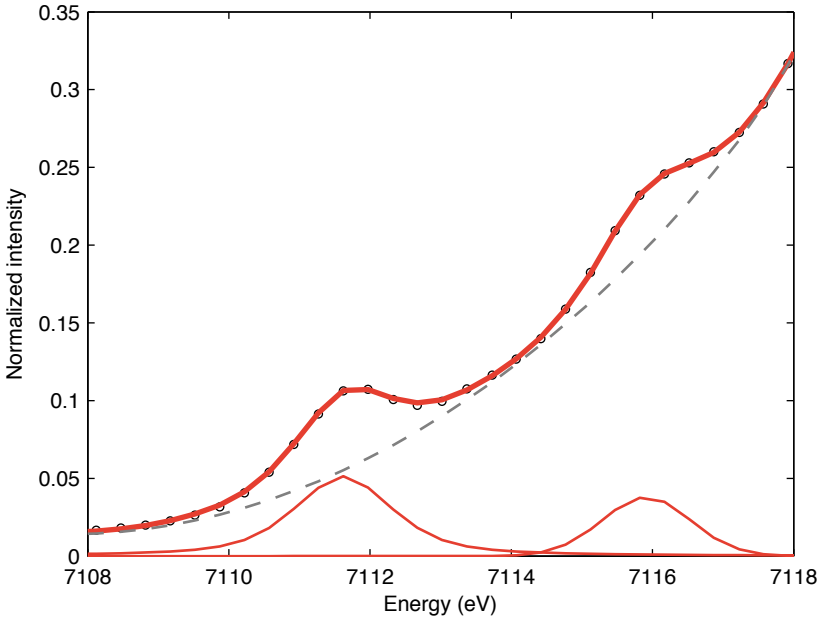

Figure C.27: Pre-edge XANES spectrum of an XAS sample containing predominantly ($P_3{}^B$)Fe(NNH_2) (> 70%, see Fig. S25A). Raw data are shown as open circles, simulation as a bold red line, with individual components as thin red lines and the baseline as a dotted grey line. Full simulation parameters are given in Table C.7.

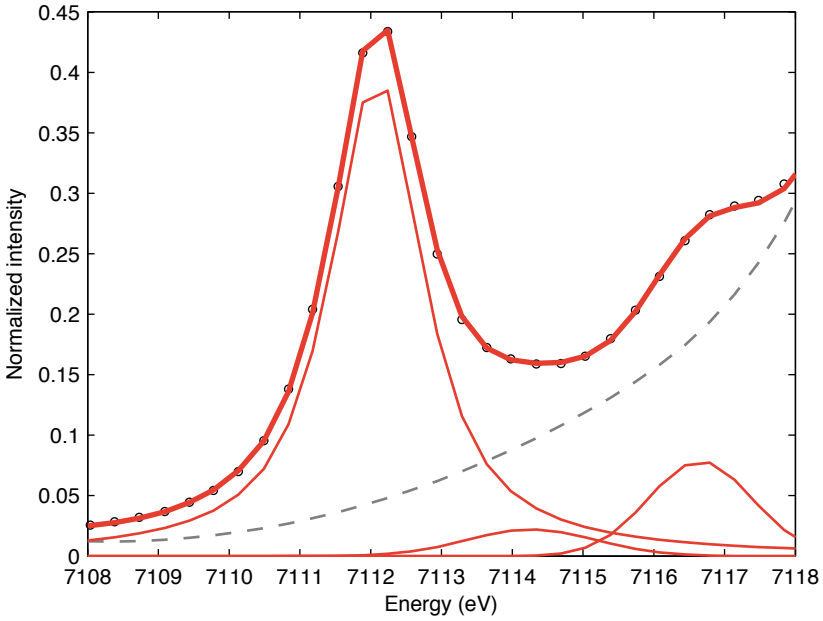

Figure C.28: Pre-edge XANES spectrum of an XAS sample containing predominantly $[(P_3{}^B)Fe{\equiv}N]^+$ (60%, see Fig. S25B). Raw data are shown as open circles, simulation as a bold red line, with individual components as thin red lines and the baseline as a dotted grey line. Full simulation parameters are given in Table C.7.

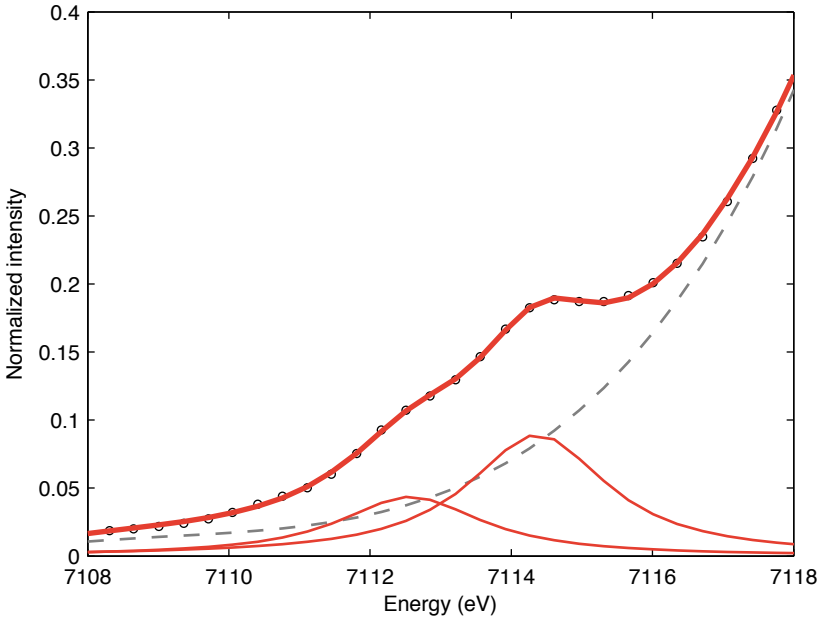

Figure C.29: Pre-edge XANES spectrum of $[(P_3{}^B)Fe(N_2)]^{2-}$. Raw data are shown as open circles, simulation as a bold red line, with individual components as thin red lines and the baseline as a dotted grey line. Full simulation parameters are given in Table C.7.

C.10 Cyclic voltammograms

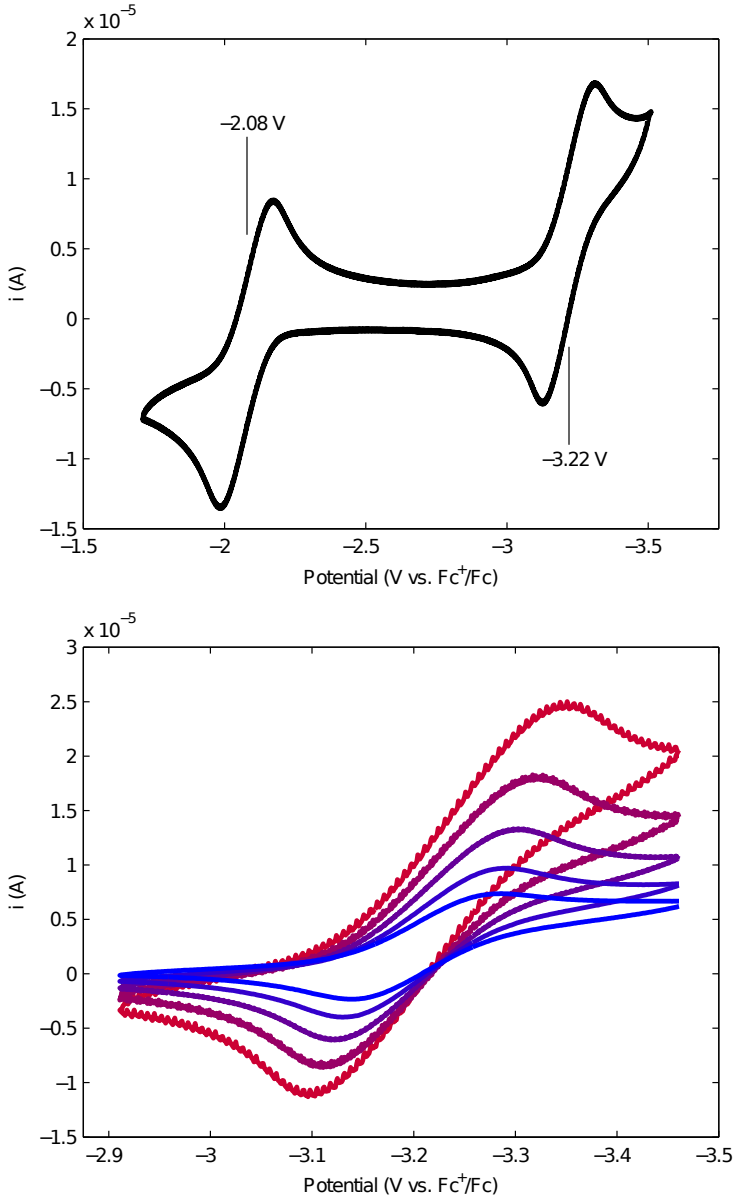

Figure C.30: (Top) Cyclic voltammogram of [Na(12-c-4)$_2$][(P_3^B)Fe(N_2)], scanning in the cathodic direction at a rate of 100 mV s^{-1}. (Bottom) Scan rate dependence of the wave observed at −3.2 V in the voltammogram of [Na(12-c-4)$_2$][(P_3^B)Fe(N_2)]. The scan rate was varied by factors of two from 400 (red) to 25 (blue) mV s^{-1}.

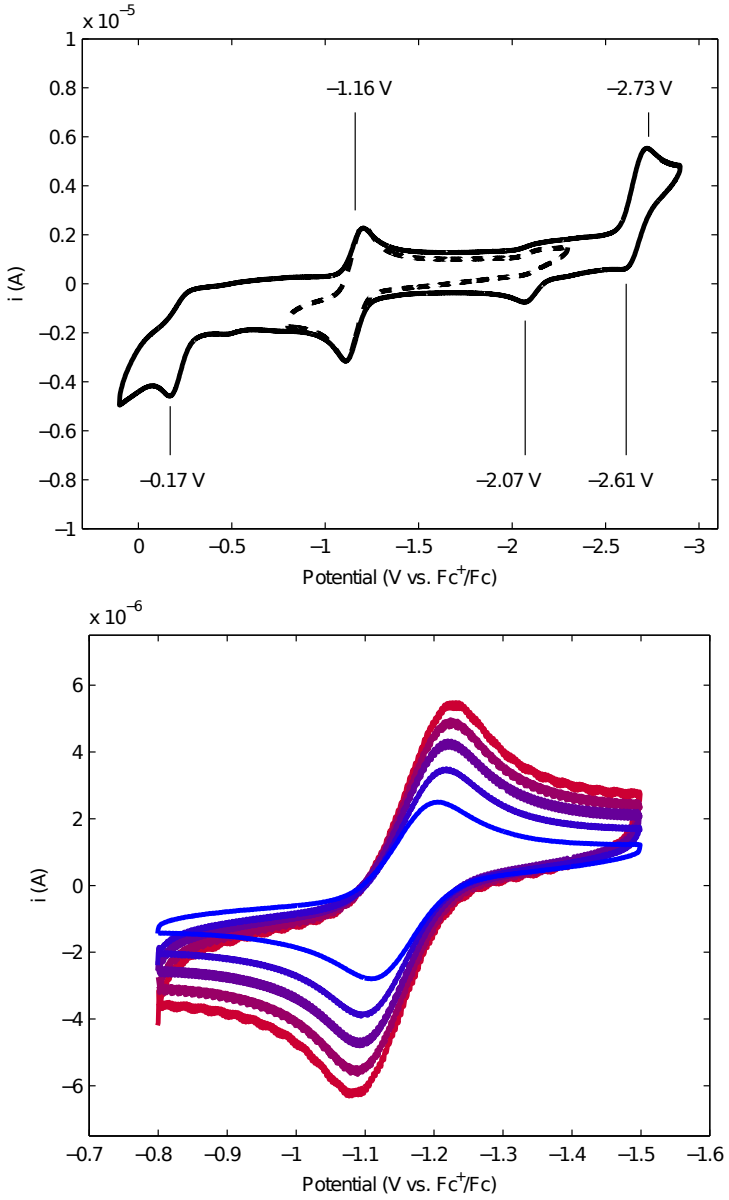

Figure C.31: (Top) Cyclic voltammogram of ($P_3{}^B$)Fe(NNMe$_2$), scanning in the cathodic direction at a rate of 50 mV s^{-1}. The dotted lines show a voltammogram scanning from −2.4 to −0.9 V, demonstrating that the feature at −2.07 V appearing in the wider scan results from a decomposition product formed upon one electron reduction. (Bottom) Scan rate dependence of the wave observed at −1.2 V in the voltammogram of ($P_3{}^B$)Fe(NNMe$_2$).The scan rate was varied in increments of 50 mV from 250 (red) to 50 (blue) mV s^{-1}.

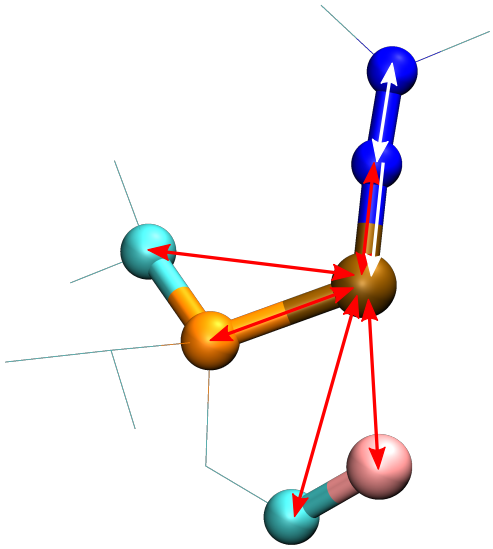

Figure C.32: Single (red arrows) and multiple (white arrows) scattering paths computed by FEFF for $(P_3{}^B)Fe(NNMe_2)$ from crystallographic coordinates. Fe is shown in brown, P in orange, N in blue, B in pink, and C in cyan.

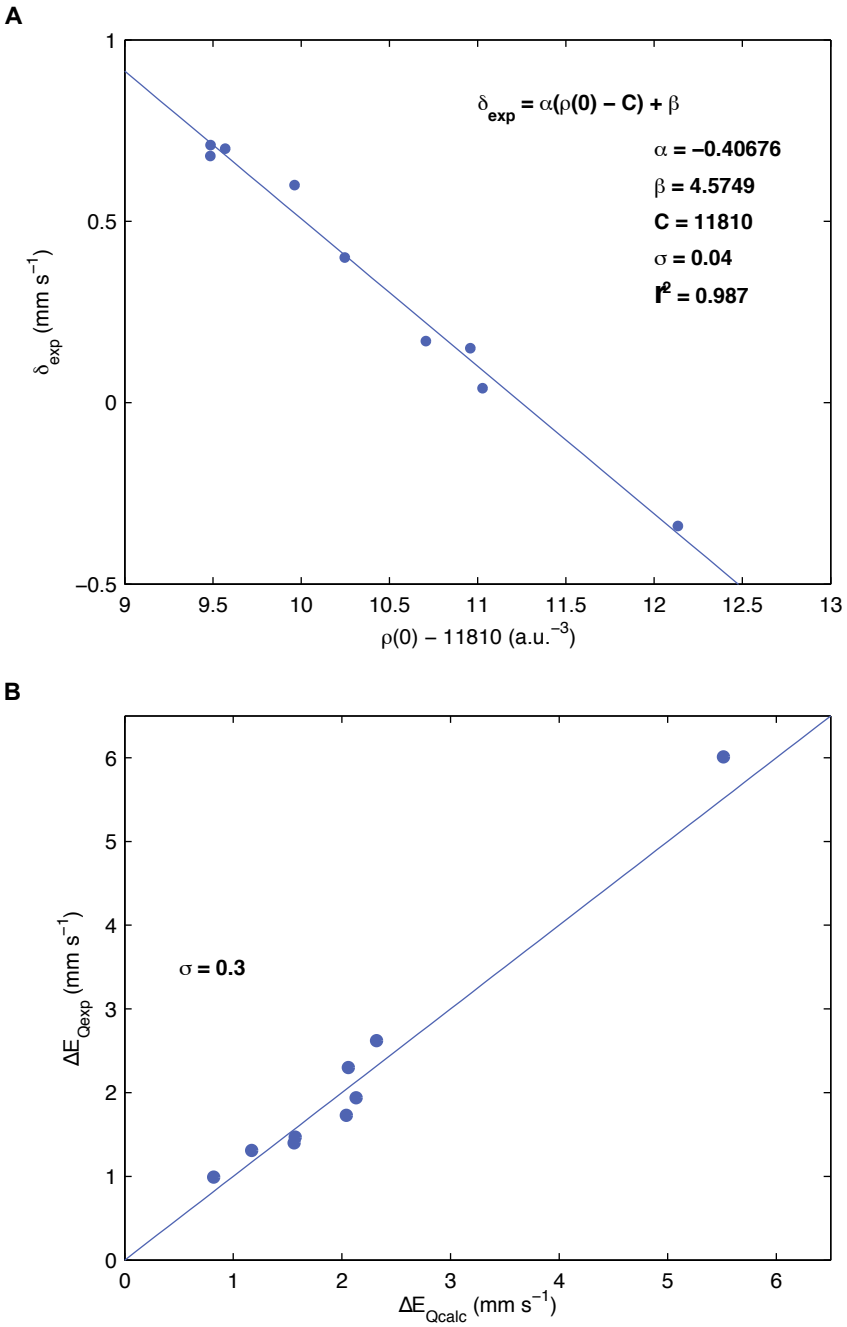

Figure C.33: (A) Plot of δ_{exp} versus $\rho(0) - 11810$ used to calibrate DFT-predicted isomer shifts. Data (Table C.16) are plotted as solid circles, with the least squares linear regression plotted as a solid line. (B) Plot of experimental versus calculated quadrupole splittings. Data (Table C.16) are plotted as solid circles, with the function $y = x$ plotted as a solid line.

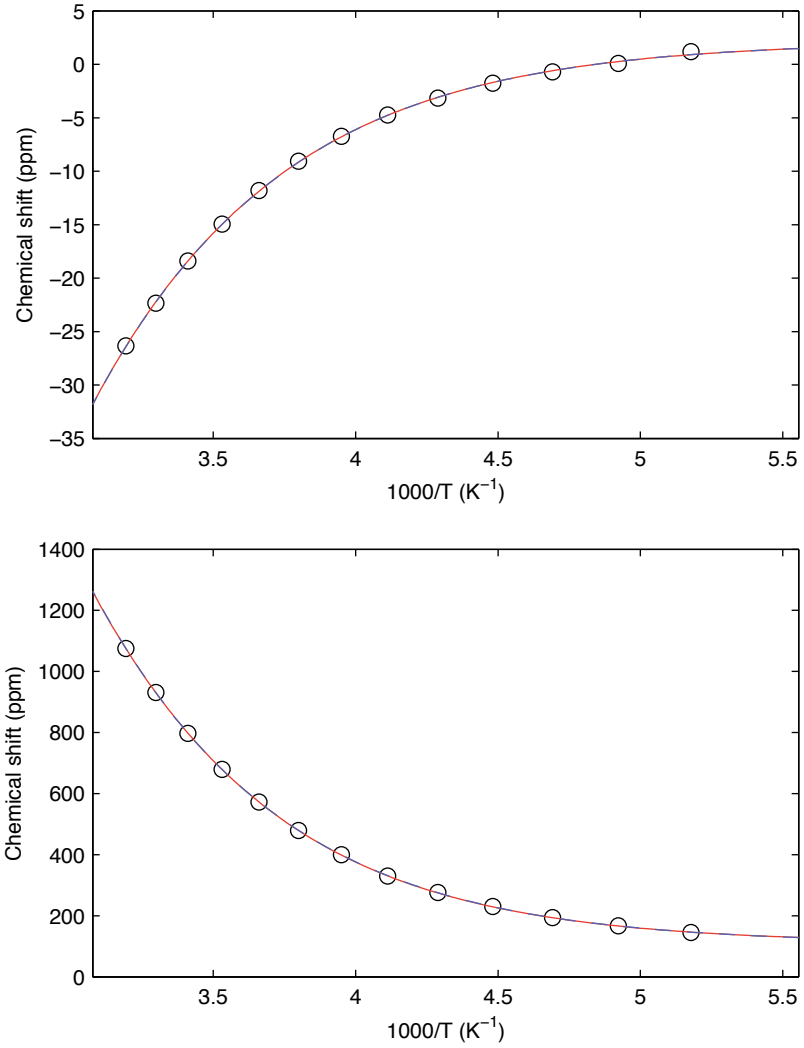

Figure C.34: Plots of chemical shift versus temperature for ($P_3{}^B$)Fe($NNMe_2$). Data are plotted as open circles, with fits to equation (1) assuming $g_p = 3$ (solid red) and $g_p = 5$ (dashed blue). The top plot shows the behavior of the N-CH_3 resonance from ^{1}H NMR, while the bottom plot shows the behavior of the ^{31}P resonance. The best fit parameters for each curve are given in Table C.13.

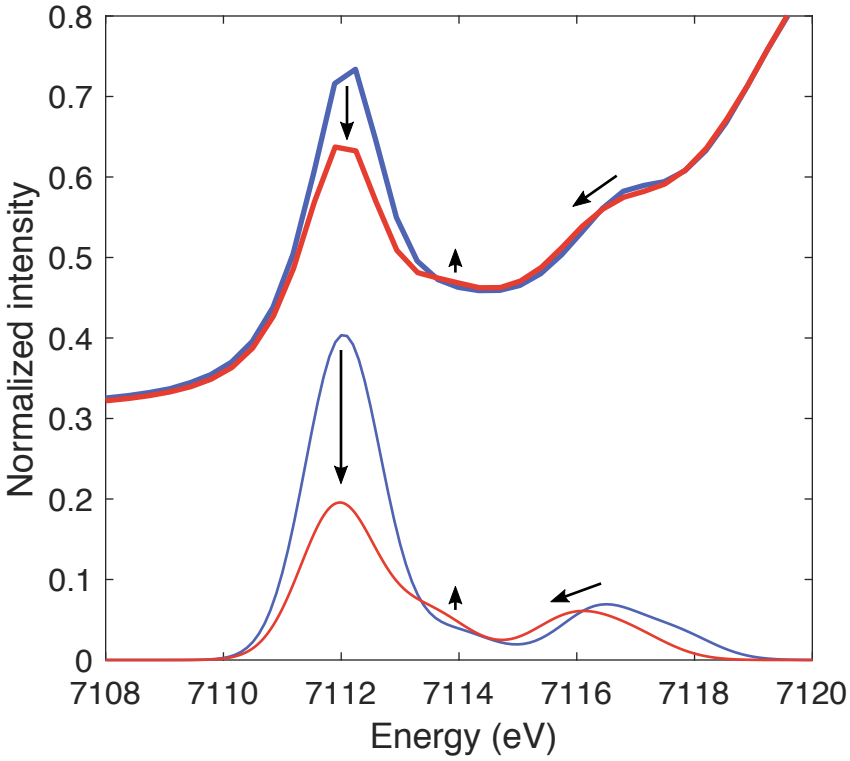

Figure C.35: Pre-edge region of the XANES spectrum of the sample of $[(P_3{}^B)Fe{\equiv}N]^+$ for the first set of scans (bold, blue) and the second set of scans (bold, red), showing evidence of photoreduction. The TD-DFT predicted spectra of $[(P_3{}^B)Fe{\equiv}N]^+$ (faint, blue) and $(P_3{}^B)Fe{\equiv}N$ (faint, red), are shown at the bottom. The arrows annotate the changes in the XANES spectra that occur upon reduction.

C.11 XRD Tables

Table C.1: Crystal data and structure refinement for $(P_3{}^B)Fe(NNMe_2)$

Empirical formula	$C_{38}H_{60}BFeN_2P_3$
Formula weight	704.45
Temperature (K)	100(2)
Crystal system	Triclinic
Space group	P-1
a (Å)	10.6719(10)
b (Å)	10.7538(9)
c (Å)	16.3248(16)
α (°)	91.269(3)
β (°)	91.242(4)
γ (°)	104.316(3)
Volume (Å^3)	1814.2(3)
Z	2
ρ_{calc} (g cm^{-3})	1.290
μ (mm^{-1})	0.578
F(000)	756
Crystal size (mm^3)	$0.120 \times 0.110 \times 0.060$
Radiation	Mo K_α (λ = 0.71073 Å)
2θ range for data collection (°)	2.712 to 28.282
Index ranges	$-14 \leq h \leq 14, -14 \leq k \leq 14, -21 \leq l \leq 21$
Reflections collected	69829
Independent reflections	9018 (R_{int} = 0.0429)
Data/restraints/parameters	9018 / 9 / 500
Goodness-of-fit on F^2	1.040
Final R indexes (I $\geq 2\sigma$(I))	R_1 = 0.0591, wR_2 = 0.1509
Final R indexes (all data)	R_1 = 0.0712, wR_2 = 0.1587
Largest diff. peak/hole (e Å^{-3})	2.463 and −1.309

Table C.2: Crystal data and structure refinement for $(P_3{}^B)Fe(OTf)$

Empirical formula	$C_{37}H_{54}BF_3FeO_3P_3S$
Formula weight	795.43
Temperature (K)	100(2)
Crystal system	Monoclinic
Space group	$P2_1/c$
a (Å)	10.8053(4)
b (Å)	14.9993(5)
c (Å)	24.4155(9)
α (°)	90
β (°)	92.4740(10)
γ (°)	90
Volume (Å^3)	3953.4(2)
Z	4
ρ_{calc} (g cm^{-3})	1.336
μ (mm^{-1})	0.604
F(000)	1676
Crystal size (mm^3)	$0.1 \times 0.1 \times 0.1$
Radiation	Mo K_α (λ = 0.71073 Å)
2θ range for data collection (°)	2.442 to 38.334
Index ranges	$-18 \leq h \leq 18, -26 \leq k \leq 26, -42 \leq l \leq 42$
Reflections collected	334561
Independent reflections	21954 (R_{int} = 0.0510)
Data/restraints/parameters	21954 / 0 / 454
Goodness-of-fit on F^2	1.042
Final R indexes (I $\geq 2\sigma$(I))	R_1 = 0.0354, wR_2 = 0.0790
Final R indexes (all data)	R_1 = 0.0503, wR_2 = 0.0844
Largest diff. peak/hole (e Å^{-3})	0.924 and −1.286

Table C.3: Mössbauer simulation parameters for the spectra shown in Figure C.20.

Component	δ (mm s^{-1})	$\lvert\Delta E_Q\rvert$ (mm s^{-1})	Γ (mm s^{-1})	Relative area
		Spectrum A		
1 (((P$_3$^{B})Fe(NNH$_2$))	0.14	1.63	0.41	0.89
2 ([(P$_3$^{B})Fe(N$_2$)]$^{2-}$)	0.26	0.82	0.57	0.07
3	1.09	2.01	0.76	0.09
		Spectrum B		
1 ([(P$_3$^{B})Fe≡N]$^+$)	−0.15	6.20	0.32	0.47
2 ((P$_3$^{B})Fe(NNH$_2$))	0.14	1.63	0.38	0.12
3	0.01	1.46	0.50	0.16
4	0.61	1.43	0.64	0.09
5	0.80	2.32	0.65	0.24
1 (Mask)	−0.15	6.20	0.32	0.48
		Spectrum C		
1 ([(P$_3$^{B})Fe≡N]$^+$)	−0.15	6.20	0.35	0.56
2	0.09	1.08	0.64	0.30
3	0.47	1.76	0.71	0.20
4	0.73	2.39	0.38	0.07
1 (Mask)	−0.15	6.20	0.35	0.57

Table C.4: Mössbauer simulation parameters for the spectra shown in Figure C.21.

Component	δ (mm s^{-1})	$\lvert\Delta E_Q\rvert$ (mm s^{-1})	Γ (mm s^{-1})	Relative area
Spectrum A				
1 (($P_3{}^B$)Fe(NNH_2))	0.14	1.63	0.43	0.91
2 ([($P_3{}^B$)Fe(N_2)]$^{2-}$)	0.26	0.82	0.46	0.09
3	0.78	2.48	0.35	0.03
Spectrum B				
1 ([($P_3{}^B$)Fe≡N]$^+$)	−0.15	6.20	0.37	0.22
2	0.03	1.49	0.61	0.39
3	0.06	0.93	0.41	0.15
4	0.83	1.19	0.53	0.09
5	0.70	2.36	0.84	0.20
1 (Mask)	−0.15	6.20	0.39	0.24

Table C.5: Mössbauer simulation parameters for the spectra shown in Figure C.24.

Component	δ (mm s^{-1})	$\lvert\Delta E_Q\rvert$ (mm s^{-1})	Γ (mm s^{-1})	Relative area
Spectrum A				
1 ([(P_3^B)Fe≡N]$^+$)	−0.15	6.20	0.47	0.58
2 ((P_3^B)Fe(NNH_2))	0.14	1.63	0.55	0.18
3	0.03	1.20	0.70	0.18
4	0.79	2.22	0.68	0.24
1 (Mask)	−0.15	6.20	−0.50[a]	0.49
Spectrum B				
1 ((P_3^B)Fe(OTf))[b]	0.68	2.53	0.32	0.42
2	1.47	3.83	0.32	0.42
3	0.92	3.75	0.49	0.14
4	0.97	2.02	0.39	0.07

[a]In this case, a pseudo-Voigt line shape was found to provide a superior fit to the masked data. The pseudo-Voigt is given by the convolution of a Gaussian function of linewidth 0.50 mm s^{-1} with a Lorentzian function of intrinsic Mössbauer linewidth (0.19 mm s^{-1}). This line shape reflects a distribution of quadrupole splittings in the sample arising from inhomogeneity, e.g. from partial crystallization of the 2-MeTHF.

[b]The best-fit parameters for this species are, within typical experimental error, identical to that of (P_3^B)Fe(OTf). However, the parameters are also quite similar to [(P_3^B)Fe]$^+$, so the slight deviation may be due to [(P_3^B)Fe][OTf], i.e. outer-sphere versus inner-sphere OTf^-.

Table C.6: Mössbauer simulation parameters for the spectra shown in Figure C.25.

Component	δ (mm s^{-1})	$\lvert\Delta E_Q\rvert$ (mm s^{-1})	Γ (mm s^{-1})	Relative area
		Spectrum A		
1 ((P_3^B)Fe(NNH_2))[a]	0.14 ± 0.03	1.54 ± 0.1	0.45	0.80
2 ([(P_3^B)Fe(N_2)]$^{2-}$)[a]	0.24 ± 0.03	0.97 ± 0.1	0.51	0.21
3	0.72	2.31	0.36	0.08
4	0.79	2.22	0.68	0.24
		Spectrum B		
1 ([(P_3^B)Fe≡N]$^+$)	−0.15	6.20	0.35	0.56
2	0.09	1.08	0.64	0.30
3	0.47	1.76	0.71	0.20
4	0.73	2.39	0.38	0.07
1 (Mask)	−0.15	6.20	0.35	0.57

[a]The additional broad component in the baseline (species 3) was simulated by a symmetric quadrupole doublet with Lorentzian line shape, but an examination of the residual shows that this only approximates the true sub-spectrum, possibly due to magnetic hyperfine splitting. Accordingly, the uncertainty in the simulated parameters for the first two components is increased, estimated to be $\sigma = \pm 0.03$ mm s^{-1} in δ and $\sigma = \pm 0.1$ mm s^{-1} in $\lvert\Delta E_Q\rvert$ from a Monte Carlo simulation of the error in counting statistics.

Table C.7: Pre-edge XANES fitting parameters

Figure C.26 (($P_3{}^B$)Fe($NNMe_2$))

Baseline

Amplitude	*Position (eV)*	*FWHM (eV)*	*Mixing*	*Offset*	*Slope*	*Twist*
8.98	7123.89	0.14	0	−0.29	−0.009	0.0008

Components

	Amplitude	*Position (eV)*	*FWHM (eV)*	*Mixing*	*LW-ratio*
1	0.06	7111.39	0.88	0	–
2	0.10	7115.49	1.11	0	–

Figure C.27 (($P_3{}^B$)Fe(NNH_2))

Baseline

Amplitude	*Position (eV)*	*FWHM (eV)*	*Mixing*	*Offset*	*Slope*	*Twist*
0.38	7118.73	0.66	0	−0.1	0.03	0.003

Components

	Amplitude	*Position (eV)*	*FWHM (eV)*	*Mixing*	*LW-ratio*
1	0.05	7111.62	0.82	0.43	0.94
2	0.04	7115.91	0.74	1	1

Figure C.28 ([($P_3{}^B$)Fe≡N]$^+$)

Baseline

Amplitude	*Position (eV)*	*FWHM (eV)*	*Mixing*	*Offset*	*Slope*	*Twist*
0.56	7118.97	1.46	0.68	0.06	0.02	0.002

Components

	Amplitude	*Position (eV)*	*FWHM (eV)*	*Mixing*	*LW-ratio*
1	0.40	7112.09	0.79	0.09	1.07
2	0.02	7114.27	1.07	1	0.80
3	0.08	7116.66	0.87	1	1.07

Figure C.29 ([($P_3{}^B$)Fe(N_2)]$^{2-}$)

Baseline

Amplitude	*Position (eV)*	*FWHM (eV)*	*Mixing*	*Offset*	*Slope*	*Twist*
10.16	7137.66	9.15	0	−11.79	−0.42	−0.01

Components

	Amplitude	*Position (eV)*	*FWHM (eV)*	*Mixing*	*LW-ratio*
1	0.04	7112.58	1.23	0	–
2	0.09	7114.37	1.19	0	–

Table C.8: EXAFS fitting parameters for $(P_3{}^B)Fe(NNMe_2)$. The final simulation is highlighted in grey.

Shell	N	R (Å)	σ^2 (Å^2)	E_0 (eV)	F[a]	Red. χ^2 [b]
Simulation 1						
N	1	1.652(4)	0.0024(4)			
P	3	2.233(2)	0.0025(1)	−11.4(6)	0.248	0.673
Simulation 2						
N	1	1.654(4)	0.0024(4)			
P	3	2.229(3)	0.0026(1)			
B	1	2.44(3)	0.005(4)	−12.6(8)	0.248	0.679
Simulation 3[c]						
N	1	1.655(4)	0.0025(3)			
P	3	2.231(2)	0.0026(1)			
B	1	2.43(3)	0.007(6)			
C	3	3.367(8)	0.0023(6)	−12.0(5)	0.229	0.584
Simulation 4						
N	1	1.654(2)	0.0022(2)			
P	3	2.232(1)	0.0027(1)			
B	1	2.49(2)	0.007(2)			
N–N	2	2.997(3)	0.0020(2)			
C1	3	3.31(2)	0.010(5)			
C2	3	3.38(1)	0.0030(7)	−11.7(5)	0.127	0.184

[a] $F = \left(\frac{\Sigma k^6(\chi_{expt}-\chi_{calc})^2}{\Sigma k^6 \chi^2_{expt}}\right)^{1/2}$

[b] Reduced $\chi^2 = \frac{F}{N-p}$ where N is the number of experimental data points and p is the number of parameters refined in the least-squares fitting.

[c] Attempting to include a second C-atom scatterer in this simulation produced an unphysically short distance of ca. 3.1 Å. Thus only a single C-scatterer was considered.

Table C.9: EXAFS fitting parameters for $(P_3{}^B)Fe(NNH_2)$. The final simulation is highlighted in grey.

Shell	N	R (Å)	σ^2 (Å^2)	E_0 (eV)	F[a]	Red. χ^2 [b]
Simulation 1						
N	1	1.653(4)	0.0042(4)			
P	3	2.229(2)	0.0042(1)	−13.8(6)	0.258	0.383
Simulation 2						
N	1	1.654(4)	0.0044(4)			
P	3	2.232(2)	0.0042(1)			
B	1	2.79(1)	0.002(1)	−13.2(6)	0.242	0.340
Simulation 3[c]						
N	1	1.655(4)	0.0044(4)			
P	3	2.234(2)	0.0042(1)			
B	1	2.787(8)	0.0014(8)			
C	3	3.349(6)	0.0030(6)	−12.4(6)	0.228	0.305
Simulation 4						
N	1	1.654(3)	0.0043(3)			
P	3	2.233(2)	0.0042(1)			
B	1	2.79(4)	0.006(4)			
N–N	2	2.99(1)	0.008(1)			
C1	3	3.350(6)	0.0031(5)			
C2	3	3.67(2)	0.011(3)	−12.8(6)	0.196	0.228
Simulation 5[d]						
N	1	1.656(4)	0.0058(5)			
P	3	2.239(1)	0.0044(1)			
N–N	2	2.995(7)	0.0070(7)			
C	3	3.343(8)	0.0044(8)	−11.5(5)	0.168	0.171

[a] $F = \left(\frac{\Sigma k^6(\chi_{\text{expt}}-\chi_{\text{calc}})^2}{\Sigma k^6 \chi^2_{\text{expt}}}\right)^{1/2}$

[b] Reduced $\chi^2 = \frac{F}{N-p}$ where N is the number of experimental data points and p is the number of parameters refined in the least-squares fitting.

[c] Attempting to include a second C-atom scatterer in this simulation produced an unphysically short distance of ca. 3.1 Å. Thus only a single C-scatterer was considered.

[d] The simulation was performed over k = 2 to 12 Å^{-1}.

Table C.10: EXAFS fitting parameters for $[(P_3{}^B)Fe{\equiv}N]^+$. The final simulation is highlighted in grey.

Shell	N	R (Å)	σ^2 (Å^2)	E_0 (eV)	F[a]	Red. χ^2 [b]
Simulation 1						
N	1	1.544(5)	0.0061(6)			
P	3	2.255(2)	0.0043(1)	−12.5(6)	0.255	0.381
Simulation 2						
N	1	1.545(5)	0.0061(5)			
P	3	2.256(2)	0.0042(1)			
B	1	2.77(1)	0.0015(9)	−12.1(6)	0.242	0.340
Simulation 3						
N	1	1.546(3)	0.0060(4)			
P	3	2.257(1)	0.0042(1)			
B	1	2.770(6)	0.0008(5)			
C1	3	3.352(5)	0.0029(4)			
C2	3	3.711(9)	0.0045(9)	−11.9(5)	0.174	0.183
Simulation 4[c]						
N	1	1.541(3)	0.0057(3)			
P	3	2.249(2)	0.0047(1)			
B	1	2.751(7)	0.0010(5)			
C1	3	3.322(5)	0.0028(4)			
C2	3	3.677(6)	0.0028(5)	−17.6(6)	0.170	0.174
Simulation 5[d]						
N	1	1.548(3)	0.0066(4)			
P	3	2.258(1)	0.0038(1)			
B	1	2.72(1)	0.003(1)			
C1	3	3.351(4)	0.0009(3)			
C2	3	3.73(1)	0.008(2)	−11.6(6)	0.130	0.119
Simulation 6[e]						
N	1	1.551(3)	0.0053(4)			
P	3	2.243(2)	0.0045(1)			
B	1	2.75(2)	0.005(2)			
C1	3	3.328(4)	0.0019(3)			
C2	3	3.653(6)	0.0023(5)	−18.1(6)	0.180	0.202

[a] $F = \left(\frac{\Sigma k^6(\chi_{\text{expt}}-\chi_{\text{calc}})^2}{\Sigma k^6 \chi^2_{\text{expt}}}\right)^{1/2}$

[b] Reduced $\chi^2 = \frac{F}{N-p}$ where N is the number of experimental data points and p is the number of parameters refined in the least-squares fitting.

[c] The ab initio single-scattering Fe–N and Fe–P phase and amplitude functions were re-calculated from the optimized distances obtained in Simulation 3.

[d] The simulation was performed over k = 2 to 12 Å^{-1}.

[e] Data from the set of second scans, showing evidence for photoreduction (Figure C.35), were simulated using the same model as Simulation 4.

Table C.11: EXAFS fitting parameters for $[(P_3{}^BP)Fe(N_2)]^{2-}$. The final simulation is highlighted in grey.

Shell	N	R (Å)	σ^2 (Å^2)	E_0 (eV)	F^a	Red. χ^2 ^{b}
			Simulation 1			
N	1	1.774(4)	0.0006(3)			
P	3	2.183(3)	0.0025(1)	−11.2(9)	0.344	1.389
			Simulation 2			
N	1 1.775(3)	0.0005(2)				
P	3	2.181(2)	0.0026(1)			
N–N	2	2.937(3)	0.0009(2)			
C1	6	3.221(8)	0.0064(9)			
C2	3	3.67(2)	0.006(2)	−11.7(5)	0.223	0.601

$^a F = \left(\frac{\Sigma k^6 (\chi_{\text{expt}} - \chi_{\text{calc}})^2}{\Sigma k^6 \chi^2_{\text{expt}}} \right)^{1/2}$

^{b}Reduced $\chi^2 = \frac{F}{N-p}$ where N is the number of experimental data points and p is the number of parameters refined in the least-squares fitting.

Table C.12: NH_3/N_2H_4 quantification results from low temperature protonation of $[(P_3{}^B)Fe(N_2)]^{2-}$ and $[Na(12\text{-c-}4)_2][(P_3{}^B)Fe(N_2)]$, as well as the result of a catalytic reaction using $[(P_3{}^B)Fe][BAr^F{}_4]$ as a precursor. Yields are with respect to Fe.

Run	Fe precursor	Equiv. TfOH	Equiv. $Cp^*{}_2Co$	% Yield NH_3	% Yield N_2H_4
1	$[(P_3{}^B)Fe(N_2)]^{2-}$	20	0	36	n.d.
2	$[(P_3{}^B)Fe(N_2)]^{2-}$	20	0	37	n.d.
Avg.				36.0(5)	–
1	$[(P_3{}^B)Fe(N_2)]^{2-}$	20	10	85	n.d.
2	$[(P_3{}^B)Fe(N_2)]^{2-}$	20	10	61	n.d.
Avg.				73(17)	–
1	$[(P_3{}^B)Fe(N_2)]^{-}$	20	0	36	9
2	$[(P_3{}^B)Fe(N_2)]^{-}$	20	0	32	10
Avg.				34(3)	9(1)
		Catalytic reaction			
1	$[(P_3{}^B)Fe][BAr^F{}_4]$	107	54	654	n.d

Table C.13: Best fit parameters of variable temperature NMR data of $(P_3{}^B)Fe(NNMe_2)$ to Equation C.1. The 95% confidence interval is given in brackets below each parameter.

g_p	Resonance	ΔH (kcal mol^{-1})	ΔS (cal mol^{-1} K^{-1})	δ_d (ppm)	C (K^{-1} $\times 10^6$)
3	N-CH_3	3.62	−0.457	2.16	−1.27
		[3.26, 3.98]	[−38.9, 38.0]	[1.65, 2.68]	[−25.0, 22.5]
3	P	3.80	3.50	110	8.11
		[3.72, 3.89]	[1.67, 5.32]	[106, 114]	[1.90, 14.3]
	Avg.	3.7(1)	2(3)		
5	N-CH_3	3.62	−1.37	2.16	−1.21
	[3.26, 3.98]	[−38.0, 35.3]	[1.64, 2.67]	[−22.8, 20.4]	
5	P	3.77	1.78	109	11.0
	[3.70, 3.84]	[−0.265, 3.82]	[106, 112]	[1.14, 20.8]	
	Avg.	3.7(1)	0(2)		

Table C.14: Gas-phase optimized core structures of the ground state of $(P_3{}^B)Fe(NNMe_2)$ ($S = 0$) using a variety of pure functionals

	XRD	BP86	ZORA-BP86	M06-L	TPSS
d(F–N_α) (Å)	1.680	1.673	1.671	1.664	1.675
d(Fe–B) (Å)	2.534	2.554	2.564	2.478	2.499
d(Fe–P1) (Å)	2.267	2.307	2.304	2.277	2.310
d(Fe–P2) (Å)	2.247	2.224	2.231	2.190	2.227
d(Fe–P3) (Å)	2.239	2.244	2.251	2.230	2.247
d(N_α–N_β) (Å)	1.293	1.303	1.309	1.300	1.302
∠(P2FeP3) (°)	109.9	108.6	108.9	108.5	108.4
∠(P1FeP3) (°)	104.3	104.4	104.7	109.0	103.0
∠(P1FeP2) (°)	125.8	127.0	126.5	124.6	129.1
∠(BFeN_α) (°)	168.9	166.9	167.9	169.9	165.7
Mean Error (‰)[a]	–	0.828	0.755	1.44	1.26

[a]The mean error is calculated as the mean value of $|p_{exp} - p_{calc}|/p_{exp}$ for each parameter p in the table, multiplied by 100.

Table C.15: Gas-phase energy differences (ΔH and ΔS) for $(P_3{}^B)Fe(NNMe_2)$ as a function of spin state using a variety of pure functionals.

	BP86	ZORA-BP86	M06-L	TPSS
$\Delta H(S = 0)$ (kcal mol^{-1})	0	0	0	0
$\Delta H(S = 1)$ (kcal mol^{-1})	4.05	3.13	−7.36	1.99
$\Delta H(S = 2))$ (kcal mol^{-1})	28.5	26.7	12.1	25.1
$\Delta S(S = 0))$ (cal mol^{-1} K^{-1})	0	0	0	0
$\Delta S(S = 1)$ (cal mol^{-1} K^{-1})	8.22	8.79	6.78	9.46
$\Delta S(S = 2)$ (cal mol^{-1} K^{-1})	15.0	10.7	10.7	16.0

Table C.16: Experimental and computed Mössbauer parameters used to calibrate the DFT method.

	δ_{exp} (mm s^{-1})	δ_{calc} [a] (mm s^{-1})	$\rho(0)$ (a.u.$^{-3}$)	$\lvert\Delta E_{Q,exp}\rvert$ (mm s^{-1})	$\lvert\Delta E_{Q,calc}\rvert$ (mm s^{-1})
$[(P_3{}^B)Fe(NH_3)]^+$ [b]	0.68	0.71	11819.48535	1.94	2.13
$[(P_3{}^B)Fe(N_2H_4)]^+$ [b]	0.70	0.68	11819.56915	2.30	2.06
$(P_3{}^B)Fe(NH_2)$ [b]	0.60	0.52	11819.96313	1.47	1.57
$(P_3{}^B)Fe(OTf)$	0.71	0.71	11819.48664	2.62	2.32
$[(P_3{}^B)Fe(N_2)]^-$ [b]	0.40	0.40	11820.24712	0.99	0.82
$[(P_3{}^B)Fe(NAd)]^+$ [b]	0.15	0.12	11820.95795	1.31	1.17
$(P_3{}^B)Fe(NNMe_2)$	0.17	0.22	11820.70707	1.73	2.04
$(P_3{}^B)Fe(NAd)$ [b]	0.04	0.09	11821.02742	1.40	1.56
$(PhBP_3{}^{iPr})Fe{\equiv}N$ [c]	−0.34	−0.36	11822.13478	6.01	5.51
RMSD		0.04			0.3

[a]Isomer shifts were calculated according to the equation $\delta_{calc} = \alpha(\rho(0) - C) + \beta$, with $\alpha = -0.407$ mm s^{-1} a.u.^{3}, $\beta = 4.575$ mm s^{-1}, and $C = 11810$ a.u.$^{-3}$. The constants were determined from a least squares linear regression of δ_{exp} versus $\rho(0) - C$ ($r^2 = 0.99$).
[b]Parameters from [3].
[c]Parameters from [4].

Table C.17: Calculated gas-phase energy differences (ΔH and ΔS) and spectroscopic parameters for $(P_3{}^B)Fe(NNH_2)$ and $[(P_3{}^B)Fe{\equiv}N]^+$ as a function of spin state.

	$S = 0$	$S = 1$	$S = 2$
$(P_3{}^B)Fe(NNH_2)$			
ΔH (kcal mol^{-1})	0	1.80	23.9
ΔS (cal mol^{-1} K^{-1})	0	3.79	1.17
δ_{calc} (mm s^{-1})	0.19(4)	0.46(4)	0.56(4)
$\lvert\Delta E_{Q,calc}\rvert$ (mm s^{-1})	1.7(3)	0.7(3)	1.1(3)
$[(P_3{}^B)Fe{\equiv}N]^+$			
ΔH (kcal mol^{-1})	0	7.58	34.2
ΔS (cal mol^{-1} K^{-1})	0	5.57	12.2
δ_{calc} (mm s^{-1})	−0.21(4)	−0.23(4)	0.01(4)
$\lvert\Delta E_{Q,calc}\rvert$ (mm s^{-1})	5.6(3)	1.4(3)	2.5(3)

Table C.18: Comparison of the gas-phase optimized core structures of $[(P_3{}^B)Fe{\equiv}N]^+$ ($S = 0$) and $(P_3{}^B)Fe{\equiv}N$ ($S = 1/2$)

	$[(P_3{}^B)Fe{\equiv}N]^+$	$(P_3{}^B)Fe{\equiv}N$
d(Fe–N) (Å)	1.514	1.549
d(Fe–B) (Å)	2.954	2.702
d(Fe–P1) (Å)	2.315	2.274
d(Fe–P2) (Å)	2.305	2.271
d(Fe–P3) (Å)	2.292	2.253
∠(P2FeP3) (°)	108.4	109.3
∠(P1FeP3) (°)	115.6	116.1
∠(P1FeP2) (°)	122.4	121.5
∠(BFeN) (°)	175.5	176.2

References

(1) Rittle, J.; Peters, J. C. *J. Am. Chem. Soc.* **2016**, *138*, 4243–4248.

(2) George, S. J.; Fu, J.; Guo, Y.; Drury, O. B.; Friedrich, S.; Rauchfuss, T.; Volkers, P. I.; Peters, J. C.; Scott, V.; Brown, S. D.; Thomas, C. M.; Cramer, S. P. *Inorg. Chim. Acta* **2008**, *361*, 1157–1165.

(3) Del Castillo, T. J.; Thompson, N. B.; Peters, J. C. *J. Am. Chem. Soc.* **2016**, *138*, 5341–5350.

(4) Hendrich, M. P.; Gunderson, W.; Behan, R. K.; Green, M. T.; Mehn, M. P.; Betley, T. A.; Lu, C. C.; Peters, J. C. *Proc. Natl. Acad. Sci.* **2006**, *103*, 17107–17112.

Appendix D

SUPPLEMENTARY INFORMATION FOR CHAPTER 5

D.1 XRD Refinement Details

D.1.1 Refinement details for [(P_3^B)Fe($NNMe_2$)][BAr^F_4]

The crystal structure of [(P_3^B)Fe($NNMe_2$)][BAr^F_4] suffers from positional disorder of one -CF_3 substituent of the [BAr^F_4]$^-$ counterion due to rotation, resulting in prolate thermal ellipsoid for one F atom. Attempts to model this positional disorder did not significantly improve the refinement.

D.1.2 Refinement details for [K(benzo-15-c-5][(P_3^B)Fe($NNMe_2$)]

Over prolonged data collection, the crystal of [K(benzo-15-c-5][(P_3^B)Fe($NNMe_2$)] appeared to suffer some decomposition, as R_{int} began to diverge for later runs. This resulted in a lack of complete high-angle data (dataset 91% complete to $\theta = 61.165°$), and a number of disagreeable reflections. Omitting the disagreeable reflections did not significantly affect refinement, and they were thus included in the final model. There was no indication of twinning, merohedral or otherwise (e.g., using the `TwinRotMat` subroutine of PLATON[1]).

During refinement, these issues appear to be manifest only in the presence of four disordered co-crystallized solvent molecules (2-MeTHF). Two of these solvent molecules suffer from two-part positional disorder; each part was located in the difference map and refined anisotropically. The remaining two solvent molecules are also disordered (as judged by the size of their thermal ellipsoids), but a clear multi-part positional disorder could not be identified. During refinement, the bond distances/angles of these disordered solvent molecules were constrained to be similar using SAME/SADI restraints, and a rigid-bond restraint (DELU) was applied individually to each. Despite these disordered solvent molecules, both [(P_3^B)Fe($NNMe_2$)]$^-$ and its counterion refined without issue. The presence of the solvent

molecules lowers the average C–C bond precision to 0.02 Å, which can be alleviated by using the SQUEEZE procedure implemented in PLATON to remove the electron density associated with these molecules; however, as this does not significantly alter the ESDs of the atoms of interest, we report the complete dataset, solvent molecules included.

D.2 Estimation of $a_{\text{iso}}(^1\text{H})$ from VT NMR Data

For an orbitally-nondegenerate electronic state where the isotropic paramagnetic NMR shift is dominated by the Fermi contact term, the Bloembergen-McConnell formula gives,[2–4]

$$\delta_{\text{iso}}(\text{ppm}) = 10^6 \cdot \frac{g_{\text{iso}}\beta_e S(S+1)}{3g_N\beta_N k_B T} \cdot a_{\text{iso}}(\text{J}) \tag{D.1}$$

where g_{iso} is the isotropic electronic g-factor, k_B is the Boltzmann constant, and $a_{\text{iso}}(\text{J})$ is the isotropic hyperfine coupling constant, in J. Noting that $a_{\text{iso}}(\text{J}) = 10^6 \cdot h a_{\text{iso}}(\text{MHz})$, we have,

$$\delta_{\text{iso}}(\text{ppm}) = \frac{C}{T} \tag{D.2}$$

$$C = 10^{12} \cdot \frac{h g_{\text{iso}}\beta_e S(S+1)}{3g_N\beta_N k_B T} \cdot a_{\text{iso}}(\text{MHz}) \tag{D.3}$$

In other words, the isotropic hyperfine coupling constant (in MHz) can be estimated from the apparent Curie factor (C) using,

$$a_{\text{iso}}(\text{MHz}) = 10^{-12} \cdot \frac{3C g_N\beta_N k_B}{h g_{\text{iso}}\beta_e S(S+1)} \tag{D.4}$$

$$\approx 10^{-12} \cdot \frac{3C g_N\beta_N k_B}{h g_e\beta_e S(S+1)} \tag{D.5}$$

where the approximation $g_{\text{iso}} \approx g_e$ is justified given the initial assumption that the Fermi contact term dominates the paramagnetic shift. Using the previously-published value for the Curie factor for the N-CH_3 protons of $(P_3{}^B)$Fe(NNMe$_2$) (-1.27×10^6 K^{-1}),[5] one would thus estimate $a_{\text{iso}} \approx -120$ MHz. However, we note that the previous simulation of the VT NMR data of $(P_3{}^B)$Fe(NNMe$_2$) produced a Curie constant for these protons with relatively high uncertainty. An examination of the data revealed that this is due to the small absolute entropic contribution to the energy difference between the ground and excited states. Performing

a global, simultaneous, least-squares fit of each ^{1}H nucleus to the magnetization function described in our previous work,[5] but approximating $\Delta G \approx \Delta H \approx \Delta E$, produces fits with much smaller relative errors (See Figure D.34 and Table D.3). Using the above definition of the Curie factor, we estimate $a_{\text{iso}} \approx -48 \pm 1$ MHz. This value is still unreasonably large, demonstrating that neglecting the pseudocontact contribution to the isotropic paramagnetic shift is not a good approximation.

D.3 Excited State Energetics of $[(P_3{}^B)Fe(NNMe_2)]^+$ from VT Magnetic Susceptibility

In order to determine if $[(P_3{}^B)Fe(NNMe_2)]^+$, like its reduced congener, possesses a low-lying excited state, we recorded its solution magnetic moment as a function of temperature (Figure D.2). Note that before calculating magnetic moments, the raw susceptibility data were corrected for the density changes of the solvent (d_8-THF); the correction used the known temperature dependence of density reported for THF,[6] and assumed a constant shift of 0.1 g mL^{-1} to account for the density difference of THF versus d_8-THF. Increasing the temperature from 183 to 323 K, we observed a concomitant increase in the observed magnetic moment of ca. 1 β_e, consistent with thermal population of a state with $S > 1/2$. To model this behavior, we assume that each pure paramagnetic state obeys a Curie law, so that $\chi_M = C/T$, and hence $\mu_{\text{eff}} = 2.828 \cdot (\chi_M T)^{1/2}$ is temperature-independent. Then we can write,[7]

$$\mu_{\text{obs}} = \mu_1 \cdot \gamma_1 + \mu_2 \cdot \gamma_2 \tag{D.6}$$

$$= \mu_1 \cdot (1 - \gamma_2) + \mu_2 \cdot \gamma_2 \tag{D.7}$$

$$= \mu_1 + (\mu_2 - \mu_1) \cdot \gamma_2 \tag{D.8}$$

$$= \mu_1 + (\mu_2 - \mu_1) \cdot \frac{g_2}{g_2 + g_1 \exp\left(\frac{1}{RT}(\Delta H - T\Delta S)\right)} \tag{D.9}$$

where μ_i is the magnetic moment of state i and g_i is the electronic degeneracy of state i. We have used this equation to fit the variable temperature magnetic data of $[(P_3{}^B)Fe(NNMe_2)]^+$ assuming $g_2 = 4$ and $\mu_2 = 3.87$ (i.e., a quartet excited state) and $g_2 = 6$ and $\mu_2 = 5.92$ (i.e.,

a sextet excited state). The final fits are of equal quality, and have final fitting parameters that are identical, within error, except for ΔS (Figure D.35 and Table D.4). Given the limited thermal stability over which magnetization data could be reliably collected, an unambiguous distinction between these two models cannot be made experimentally. However, preliminary DFT calculations indicate that the sextet state state of $[(P_3{}^B)Fe(NNMe_2)]^+$ is significantly higher in energy than the quartet state (Table D.13), and on this basis we assign the excited state multiplicity as $S = 3/2$, and estimate the adiabatic doublet–quartet gap to be $\Delta H \approx 4.8 \pm 0.4$ kcal mol^{-1}.

D.4 Fitting of UV-vis Data

Using an idealized Gaussian line shape, an absorption band can be written,[8]

$$\epsilon(\bar{\nu}) = \epsilon_0 \exp\left(-\frac{4\log 2(\bar{\nu}-\bar{\nu}_0)^2}{\sigma_{1/2}^2}\right) \tag{D.10}$$

where ϵ_0 is the molar extinction coefficient at the absorption maximum, $\bar{\nu}_0$ is the energy at the absorption maximum, and $\sigma_{1/2}$ is the peak FWHM. The oscillator strength is given by,[8]

$$f = 4.33 \cdot 10^{-9} \int \epsilon(\bar{\nu}) d\bar{\nu} = 4.33 \cdot 10^{-9} \cdot \epsilon_0 \sigma_{1/2} \left(\frac{\pi}{4\log 2}\right)^{1/2} \tag{D.11}$$

And thus, we can express ϵ_0 in terms of f,

$$\epsilon(\bar{\nu}) = \frac{f}{4.33 \cdot 10^{-9}} \frac{2}{\sigma_{1/2}} \left(\frac{\log 2}{\pi}\right)^{1/2} \exp\left(-\frac{4\log 2(\bar{\nu}-\bar{\nu}_0)^2}{\sigma_{1/2}^2}\right) \tag{D.12}$$

Both experimental and ab initio electronic spectra were simulated using this expression. A minimum number of Gaussians to capture both the resolved features and the rising UV absorption edge were included in the experimental fits. Before fitting, low-temperature data were first corrected for the change in solvent density.[9]

D.5 Mössbauer simulation details

All magnetically-unperturbed components were fit assuming symmetric quadrupole doublets with Lorentzian line shapes. This is the correct model for homogeneous frozen

solution spectra in the limit of fast electronic relaxation, which is typical at 80 K. However, spectra of [(P_3^B)Fe(NNMe$_2$)][BAr^F_4] displayed a broad, asymmetric signal at 80 K, which sharpened considerably upon application of a 50 mT external magnetic field, indicating that this species is in the limit of slow electronic relaxation at these temperatures. The effects of this are also manifest in the observation of an EPR signature at room temperature (Figure D.4). This is apparently a result of unusually slow spin-spin relaxation (T_2), as a Mössbauer spectrum collected on a polycrystalline sample of [(P_3^B)Fe(NNMe$_2$)][BAr^F_4] features an asymmetrically-broadened quadrupole doublet, indicating an intermediate relaxation regime. That these relaxation effects are dominated by a long T_2 was confirmed by direct measurement of the spin-spin relaxation times of [(P_3^B)Fe(NNMe$_2$)][BAr^F_4] and [(P_3^B)Fe(NAd)][BAr^F_4], demonstrating that the former has a significantly longer T_2 (Figure D.47 and Table D.10). While both of these complexes possess $S = 1/2$ ground states, the latter displays a symmetric quadrupole doublet in its solid state Mössbauer spectrum.[10]

To simulate the spectrum of [(P_3^B)Fe(NNMe$_2$)][BAr^F_4], we employed the spin Hamiltonian described in the main text to simultaneously fit dilute frozen solution spectra of ^{57}Fe-enriched [(P_3^B)Fe(NNMe$_2$)][BAr^F_4] with the external field oriented parallel and perpendicular to the applied γ-radiation. The g-tensor components were fixed from EPR spectroscopy, while δ and $|\Delta E_Q|$ were fixed initially based on the apparent values from the polycrystalline sample (note that the sign of ΔE_Q cannot be determined from these low-field simulations). Assuming that the EFG and HFC tensors were coincident with the electronic g-tensor, two equally-good solutions could be obtained that differed in the value of η and the relative orientation of the minor components of the HFC tensor (reduced $\chi^2 = 1.44$ and 1.32). These solutions could be rotated into one another by application of a ca. 90° Euler angle γ about g_{max} (= g_x, all rotations in the z–y–z convention) in either the EFG or HFC frame, indicating that the EFG/HFC tensors are not coincident with the g-tensor. Introduction of a single Euler angle β in the HFC frame produced the final solution to the data; we caution that without data collected at multiple field strengths, the final values of

η and the orientation of the HFC frame are under-determined. An additional quadrupole doublet component was required in the final simulation (reduced χ^2 = 1.05), arising from an unknown impurity consistent with high-spin Fe(II), present in ca. 10% abundance.

The magnetic field-dependence of the spectra of $[(P_3{}^B)Fe(NNMe_2)]^-$ indicate that this species is also in the limit of slow electronic relaxation in dilute frozen solution at 80 K. This behavior was expected based on the isoelectronic complexes $(P_3{}^{Si})Fe(NNH_2)$ and $(P_3{}^{Si})Fe(NNMe_2)$.[11] Indeed, the Mössbauer spectra reported for $(P_3{}^{Si})Fe(NNR_2)$ are nearly identical with that of $[(P_3{}^B)Fe(NNMe_2)]^-$. To simulate the latter, we again employed the spin-Hamiltonian described above to simultaneously fit dilute frozen solution spectra with the external field oriented parallel and perpendicular to the applied γ-radiation. Using the g-tensor components measured independently from EPR spectroscopy, and the reported parameters of $(P_3{}^{Si})Fe(NNMe_2)$ as an initial guess,[11] we obtained a unique spectral simulation (Figure D.31 and Table D.9). It was found that two additional quadrupole doublet impurities (totaling ca. 30% of the spectral area) were required to obtain a satisfactory simulation (reduced χ^2 = 0.77), which is consistent with the typical purity reported for $(P_3{}^{Si})Fe(NNH_2)$ and $(P_3{}^{Si})Fe(NNMe_2)$.[11]

D.6 NMR Spectra

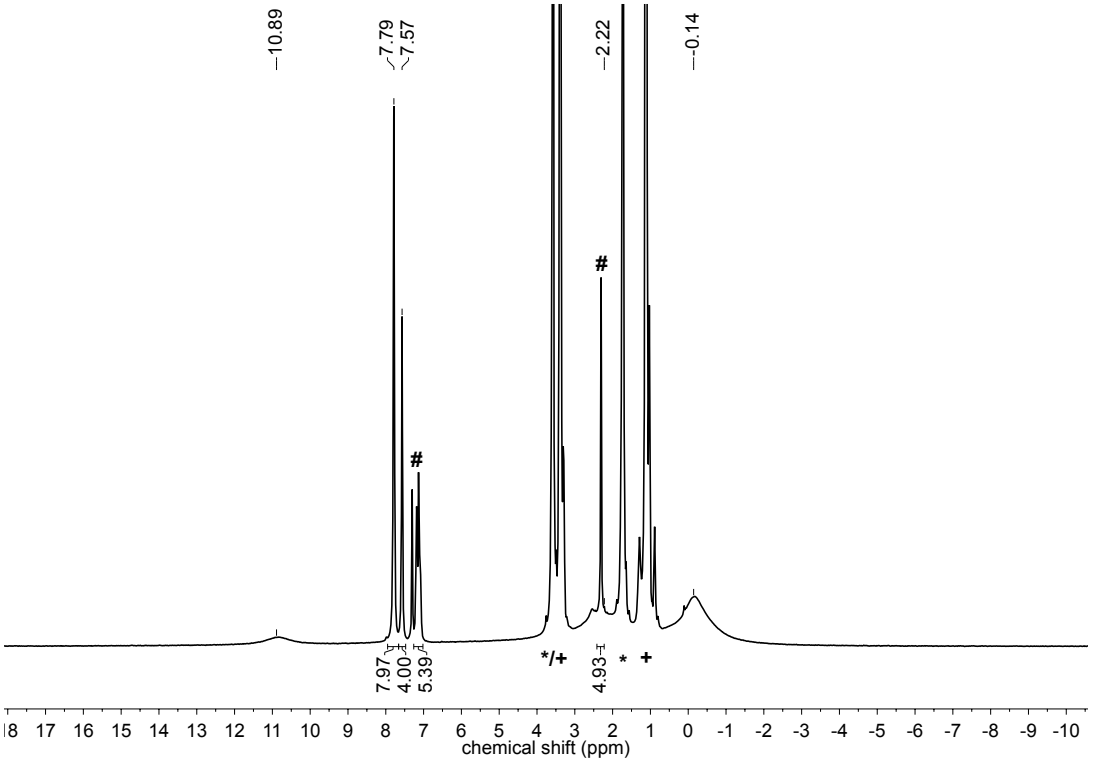

Figure D.1: ^{1}H NMR spectra of [($P_3{}^B$)Fe($NNMe_2$)][$BAr^F{}_4$] (500 MHz, d_8-THF, 293 K). $^{\#}$Denotes co-crystallized toluene. *Denotes signals from the lock solvent. $^{+}$Denotes signals from Et_2O added as a reference for the Evans method.

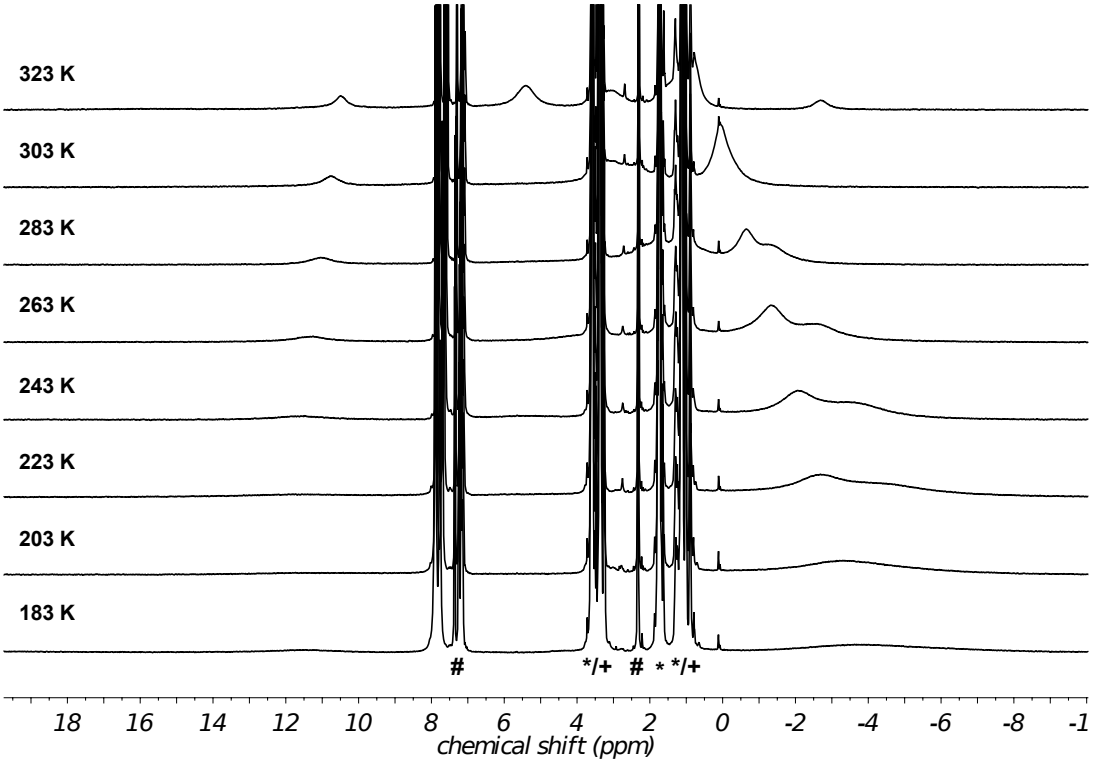

Figure D.2: Variable temperature ^{1}H NMR spectra of [(P_3^B)Fe(N$_2$Me$_2$)][BAr^F_4] (500 MHz, d_8-THF). $^{\#}$Denotes co-crystallized toluene. *Denotes signals from the lock solvent. $^{+}$Denotes signals from Et_2O added as a reference for the Evans method.

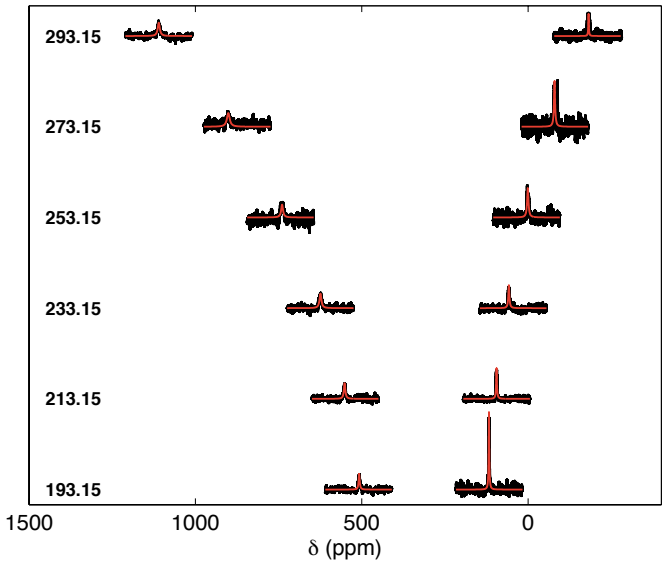

Figure D.3: Variable temperature ^{15}N NMR spectra of ($P_3{}^B$)Fe($^{15}N^{15}NMe_2$) (500 MHz, d_8-toluene). Temperatures (K) are shown to the left of each spectrum. The raw data are plotted in black, with least-squares fits to a Lorentzian peak shape shown in red.

D.7 EPR Spectra

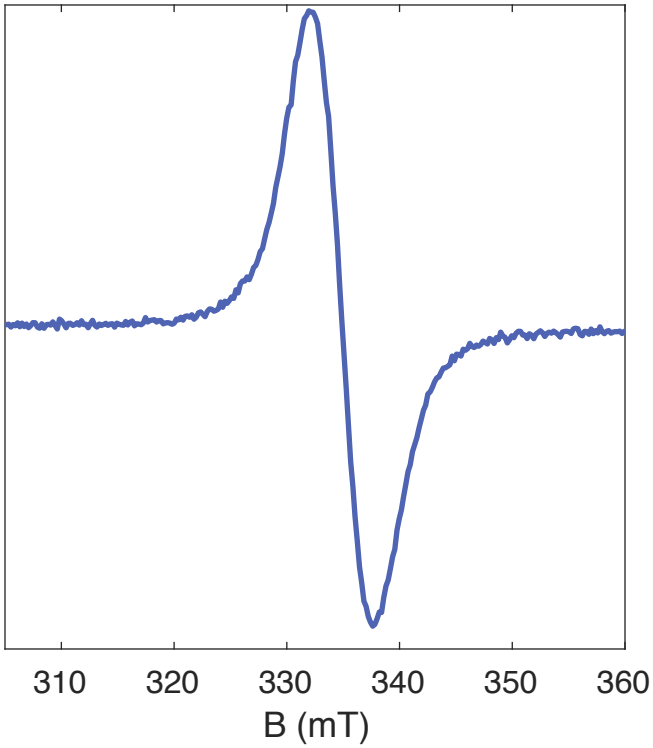

Figure D.4: Room-temperature X-band EPR spectrum of $[(P_3{}^B)Fe(NNMe_2)][BAr^F{}_4]$ (2 mM, 2-MeTHF).

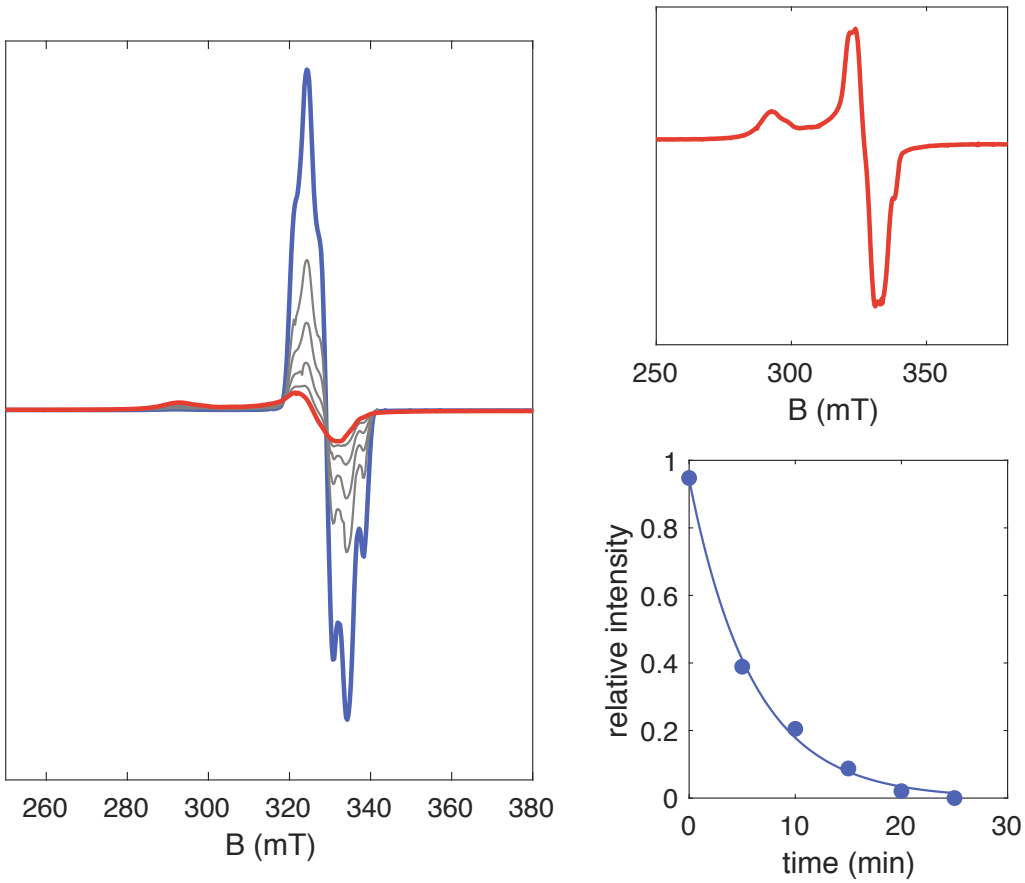

Figure D.5: The decay of $[(P_3{}^B)Fe(NNMe_2)]^-$, monitored by X-band EPR spectroscopy. The left panel shows a spectrum of $[(P_3{}^B)Fe(NNMe_2)]^-$ (10 mM, 2-MeTHF, 77 K) in blue. This sample was thawed to room temperature for five minutes, flash-frozen in liquid N_2, and its spectrum was recollected. Repeating this process several times lead to the monotonic decay of the signals attributed to $[(P_3{}^B)Fe(NNMe_2)]^-$ (gray spectra), producing a the final spectrum shown in red, which is also reproduced in the upper right panel. The approximate decay kinetics of the signal of $[(P_3{}^B)Fe(NNMe_2)]^-$ is shown in the lower right panel (closed circles), along with a mono-exponential fit (solid line).

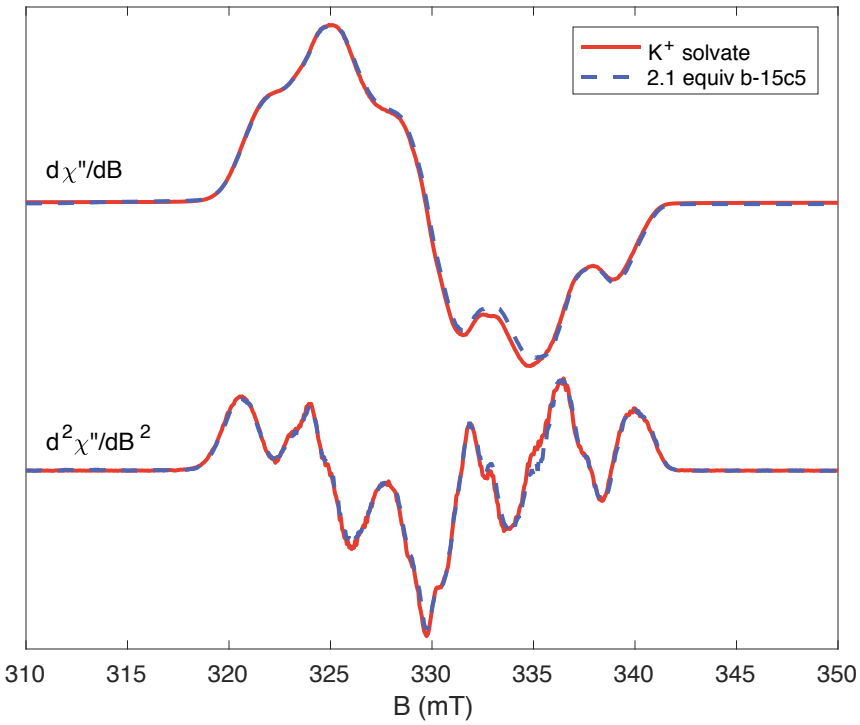

Figure D.6: Overlaid X-band EPR spectra of $[(P_3{}^B)Fe(NNMe_2)]^-$ with (dashed blue) and without (red) the addition of 2.1 equiv of benzo-15-c-5.

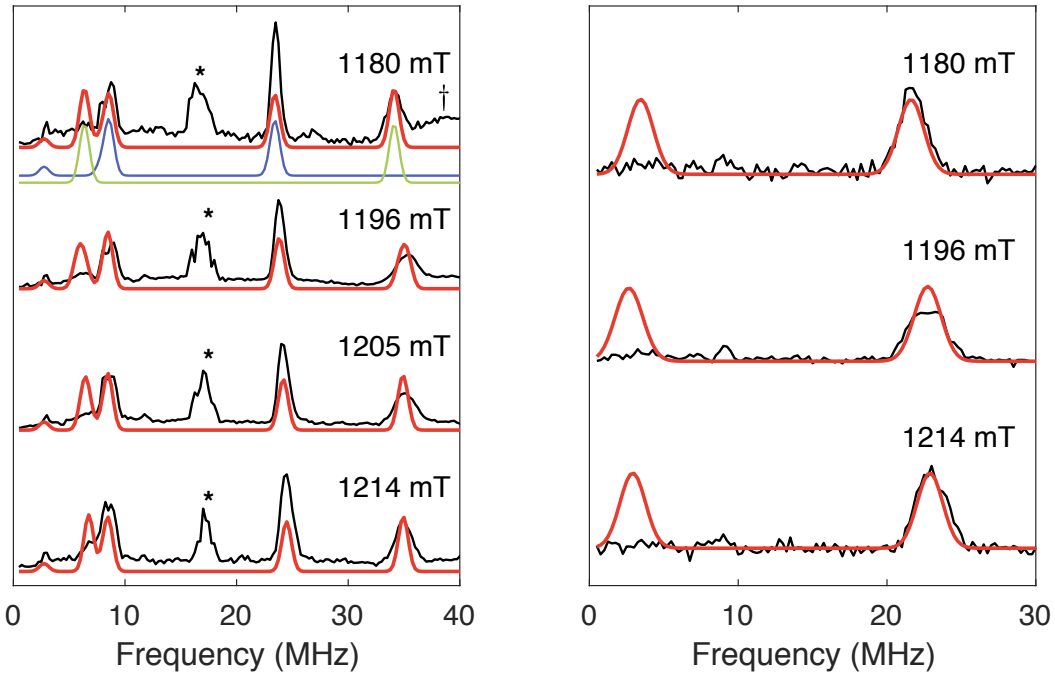

Figure D.7: Overlaid Q-band ENDOR spectra of $[(P_3{}^B)Fe(NNMe_2)]^-$; the field at which each spectrum was collected is indicated above each spectrum (*denotes a harmonic arising from weakly-coupled protons (ligand and/or solvent). (Left) Spectra collected on a natural abundance isotope (N.A.I.) sample. Raw data are shown in black, along with simulations in red. A deconvolution of the simulation in terms of the contributions from ^{11}B (blue) and $^{31}P_\gamma$ (green) is also shown for the spectrum collected at 1180 mT. See the main text for the full simulation parameters for these nuclei. (Right) Difference spectra between a sample of $[(P_3{}^B)Fe(NN(^{13}CH_3)_2)]^-$ and the N.A.I. sample, showing contributions from the N-^{13}C nuclei only. Raw data are shown in black, with simulations in red. See the main text for the full simulation parameters.

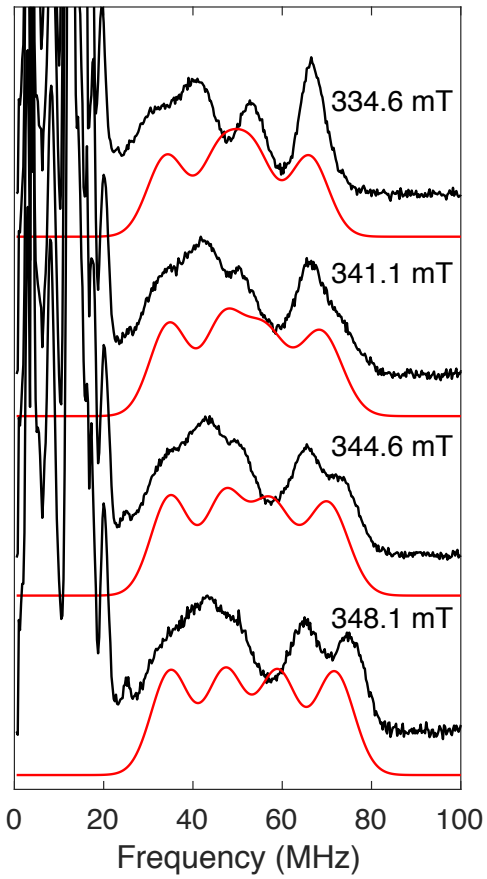

Figure D.8: Overlaid X-band ENDOR spectra of $[(P_3{}^B)Fe(NNMe_2)]^-$, showing resonances due to two strongly-coupled ^{31}P nuclei. The fields at which each spectrum was collected is indicated above each spectrum. Raw data are shown in black, with simulations shown in red. See the main text for the full simulation parameters for these nuclei.

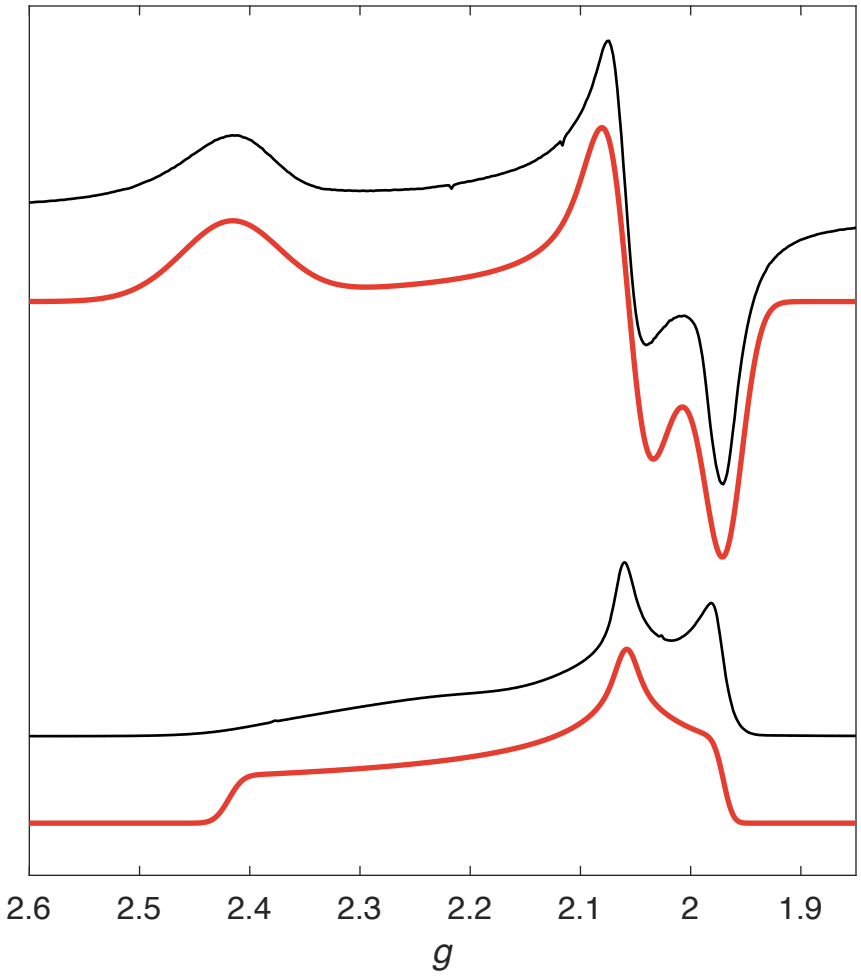

Figure D.9: (Top) CW X-band spectrum of [(P_3^B)Fe(NAd)][BAr^F_4] (5 mM, 2-MeTHF, 77 K). The experimental spectrum is shown in black, with a simulation in red. (Bottom) ESE-detected Q-band field-swept absorption spectrum of [(P_3^B)Fe(NAd)][BAr^F_4] (5 mM, 2-MeTHF, 10 K). The experimental spectrum is shown in black, with a simulation in red. Simulation parameters: g_{min} = 1.970, g_{mid} = 2.058, g_{max} = 2.419. To account for unresolved HFC, the CW spectrum was inhomogeneously-broadened using `HStrain = [187 190 400]`.

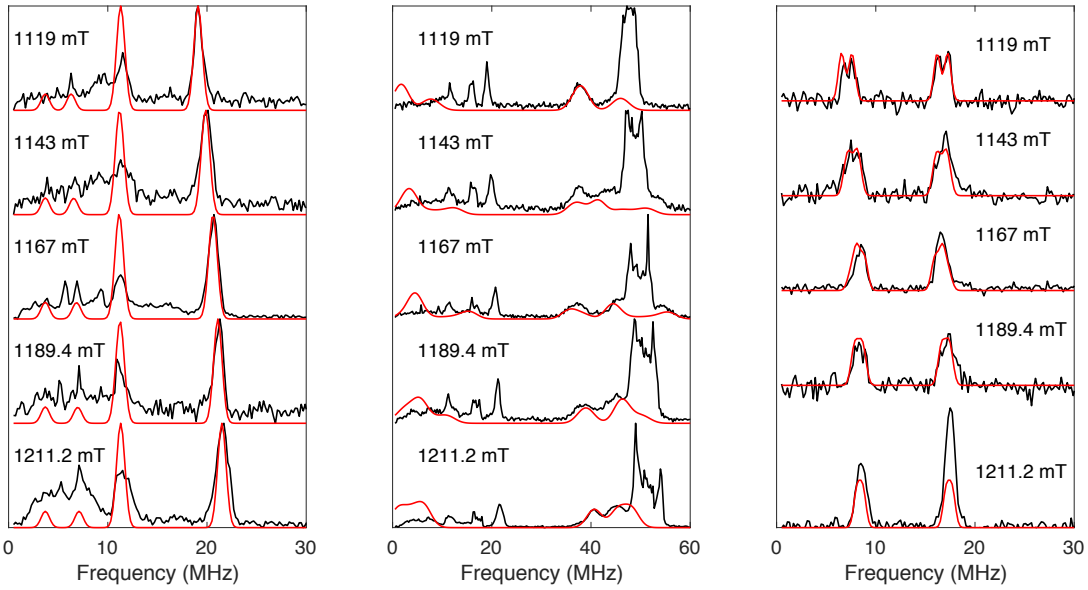

Figure D.10: Overlaid Q-band ENDOR spectra of $[(P_3{}^B)Fe(NNMe_2)]^+$; the field at which each spectrum was collected is indicated above each spectrum. (Left) Low frequency region of spectra collected on a natural abundance isotope (N.A.I.) sample. Raw data are shown in black, along with simulation of a single ^{11}B nucleus in red. (Middle) Wide frequency scans showing the contributions from three ^{31}P nuclei. Raw data are shown in black, with simulations in red. The features centered around 50 MHz are due to weakly-coupled ^1H nuclei (ligand and solvent). (Right) Difference spectra between a sample of $[(P_3{}^B)Fe(NN(^{13}CH_3)_2)]^+$ and the N.A.I. sample, showing contributions from the N-^{13}C nuclei only. Raw data are shown in black, with simulations in red. See the main text for the full simulation parameters.

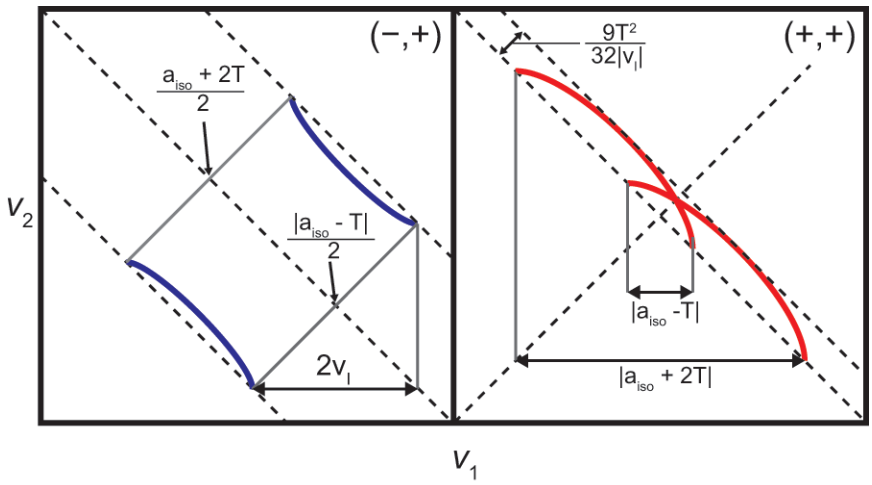

Figure D.11: Sample HYSCORE powder patterns for an $S = 1/2, I = 1/2$ spin system with an axial hyperfine tensor which contains isotropic (a_{iso}) and dipolar ($\boldsymbol{T}$) contributions. Blue correlation ridges represent the strong coupling case; red correlation ridges represent the weak coupling case.

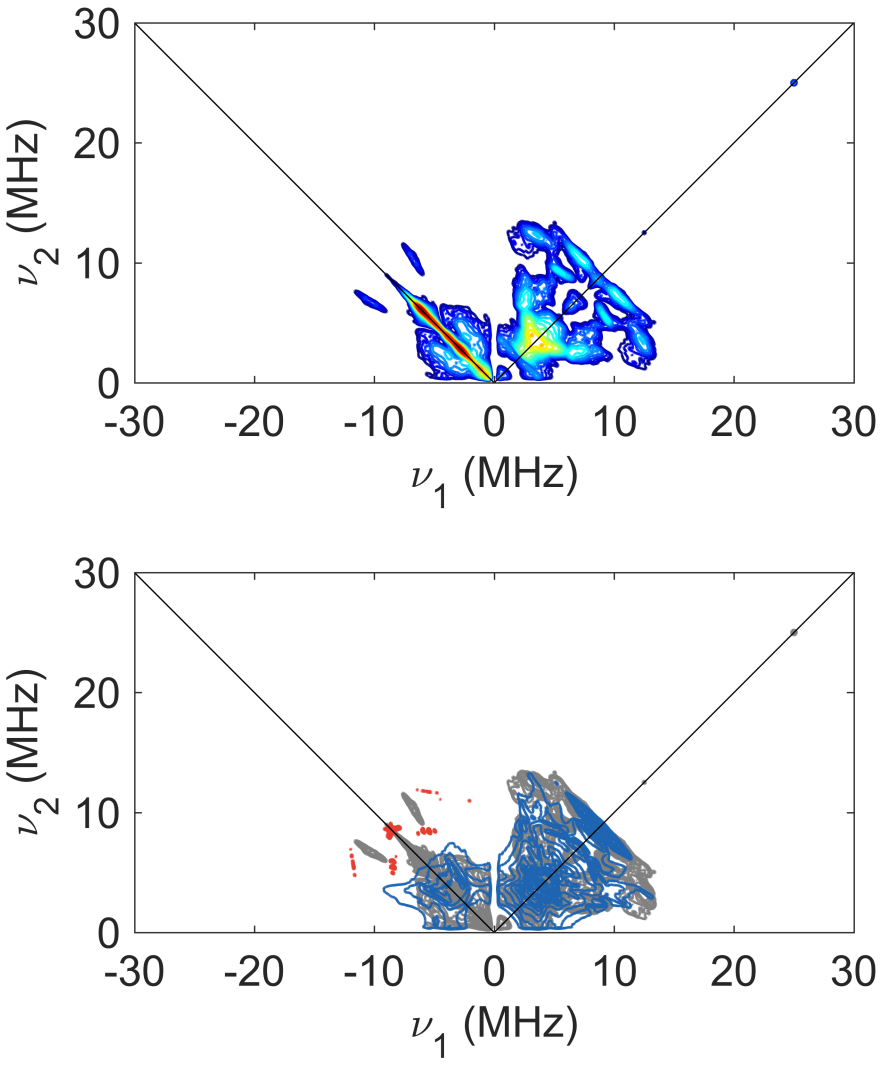

Figure D.12: Hyscore spectrum of $[(P_3{}^B)Fe(^{14}N^{14}NMe_2)]^-$ collected at a field of 1180 mT. The raw data are presented in the top panel, with intensities encoded by the color map. The bottom panel reproduces the experimental spectrum in grey, and overlays simulations due to N_α (red) and N_β (blue). Note that the simulations were calculated for each nucleus separately, and thus do not show effects due to multinuclear coherences. See Table D.25 for simulation details.

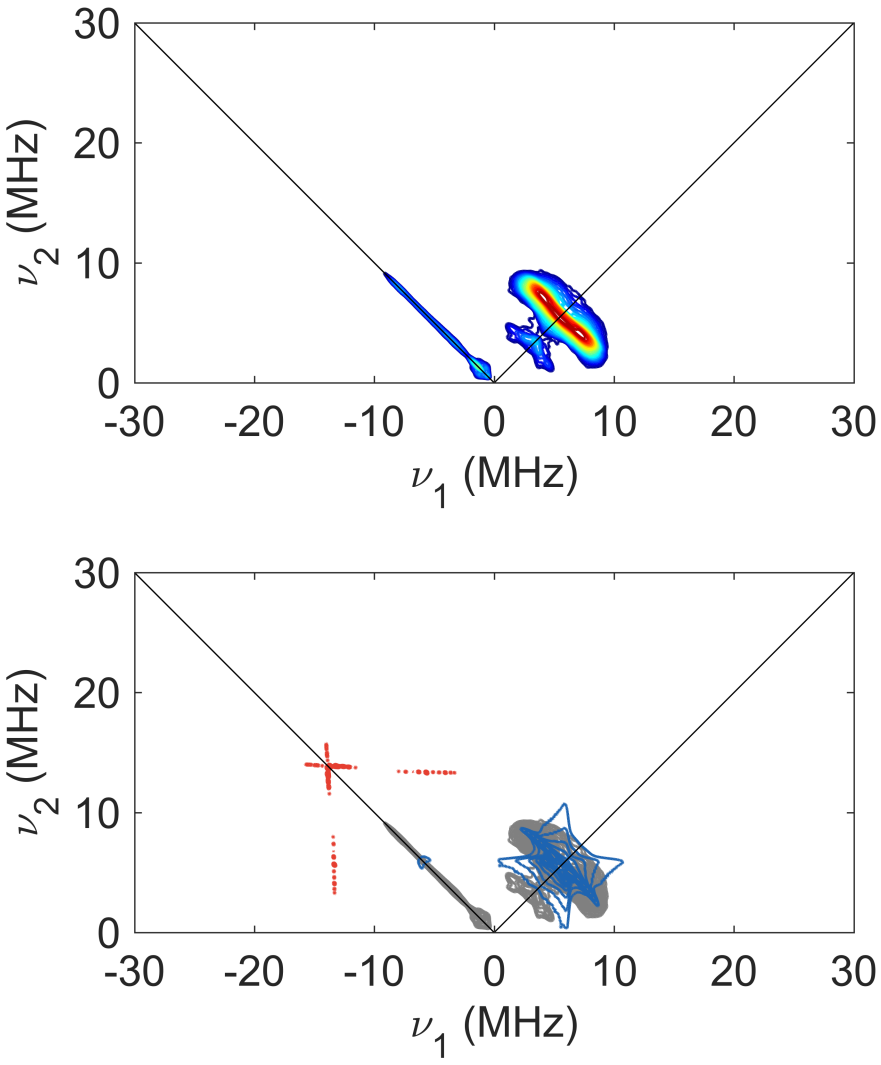

Figure D.13: Hyscore spectrum of $[(P_3{}^B)Fe(^{15}N^{15}NMe_2)]^-$ collected at a field of 1180 mT. The raw data are presented in the top panel, with intensities encoded by the color map. The bottom panel reproduces the experimental spectrum in grey, and overlays simulations due to N_α (red) and N_β (blue). Note that the simulations were calculated for each nucleus separately, and thus do not show effects due to multinuclear coherences. See Table D.25 for simulation details.

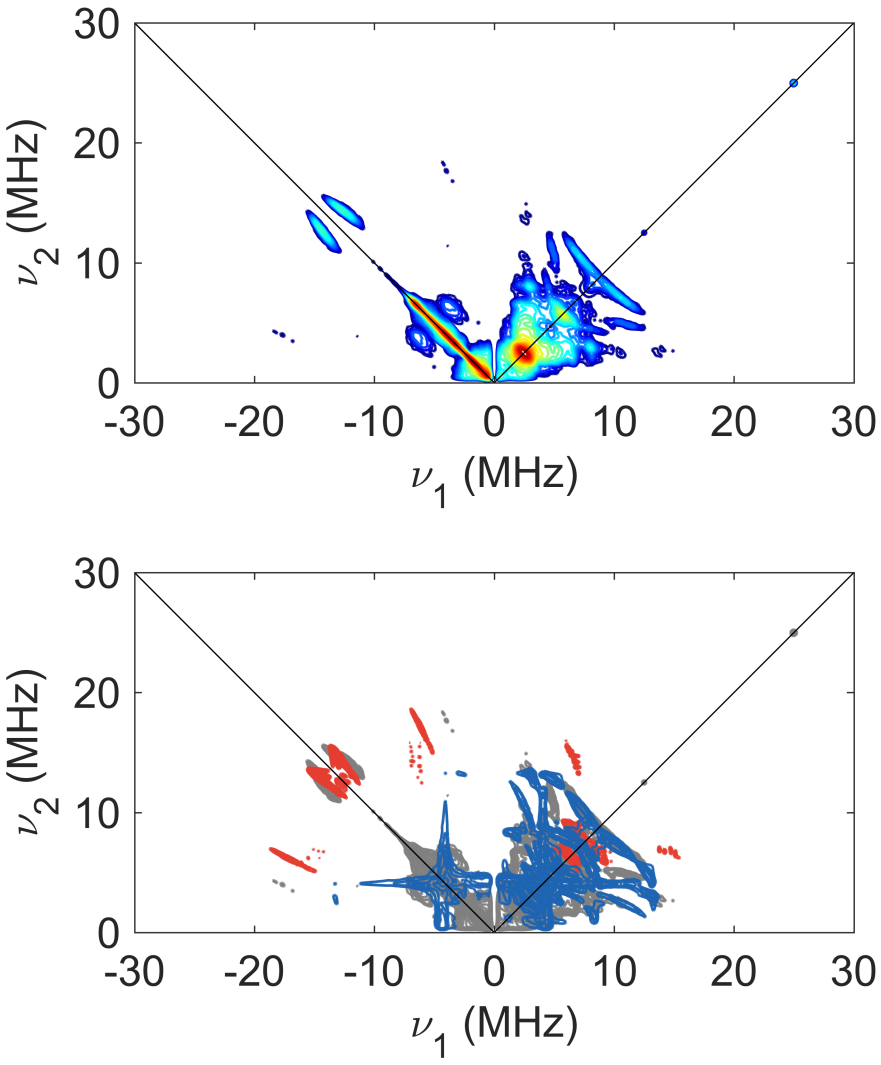

Figure D.14: Hyscore spectrum of $[(P_3{}^B)Fe(^{14}N^{14}NMe_2)]^-$ collected at a field of 1196 mT. The raw data are presented in the top panel, with intensities encoded by the color map. The bottom panel reproduces the experimental spectrum in grey, and overlays simulations due to N_α (red) and N_β (blue). Note that the simulations were calculated for each nucleus separately, and thus do not show effects due to multinuclear coherences. See Table D.25 for simulation details.

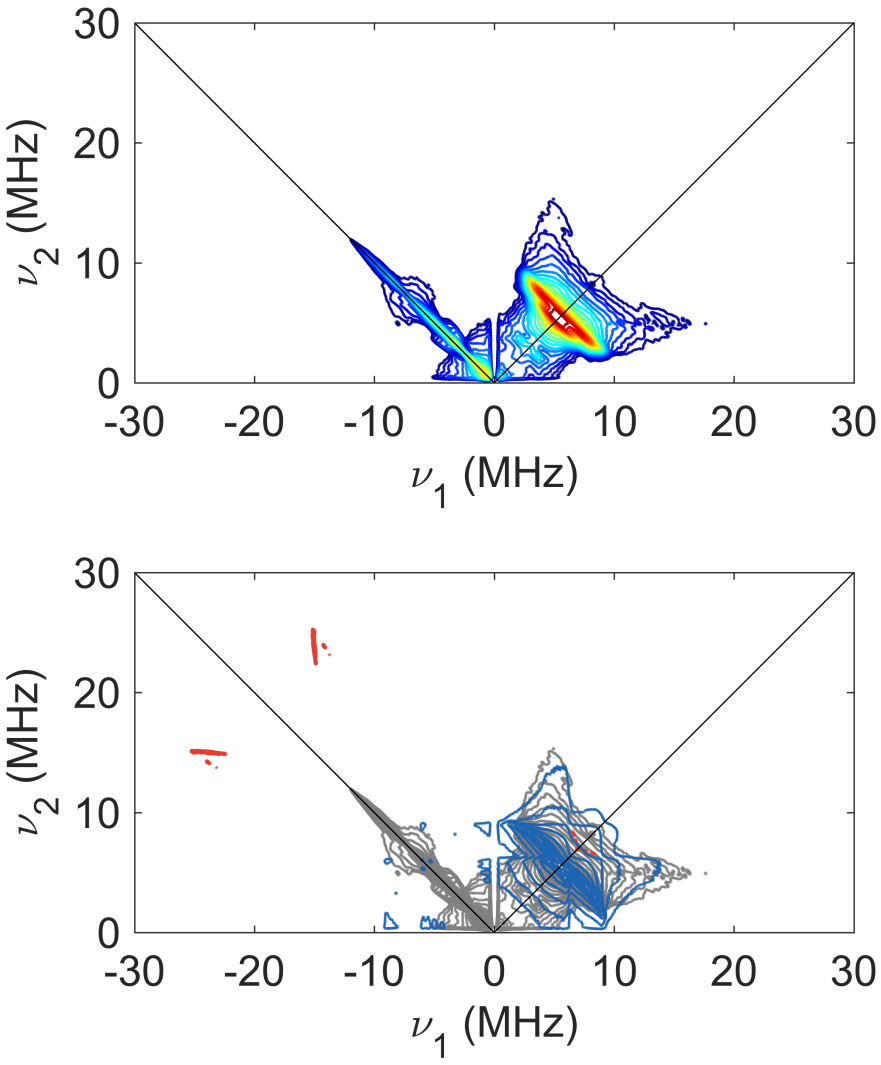

Figure D.15: Hyscore spectrum of $[(P_3{}^B)Fe(^{15}N^{15}NMe_2)]^-$ collected at a field of 1196 mT. The raw data are presented in the top panel, with intensities encoded by the color map. The bottom panel reproduces the experimental spectrum in grey, and overlays simulations due to N_α (red) and N_β (blue). Note that the simulations were calculated for each nucleus separately, and thus do not show effects due to multinuclear coherences. See Table D.25 for simulation details.

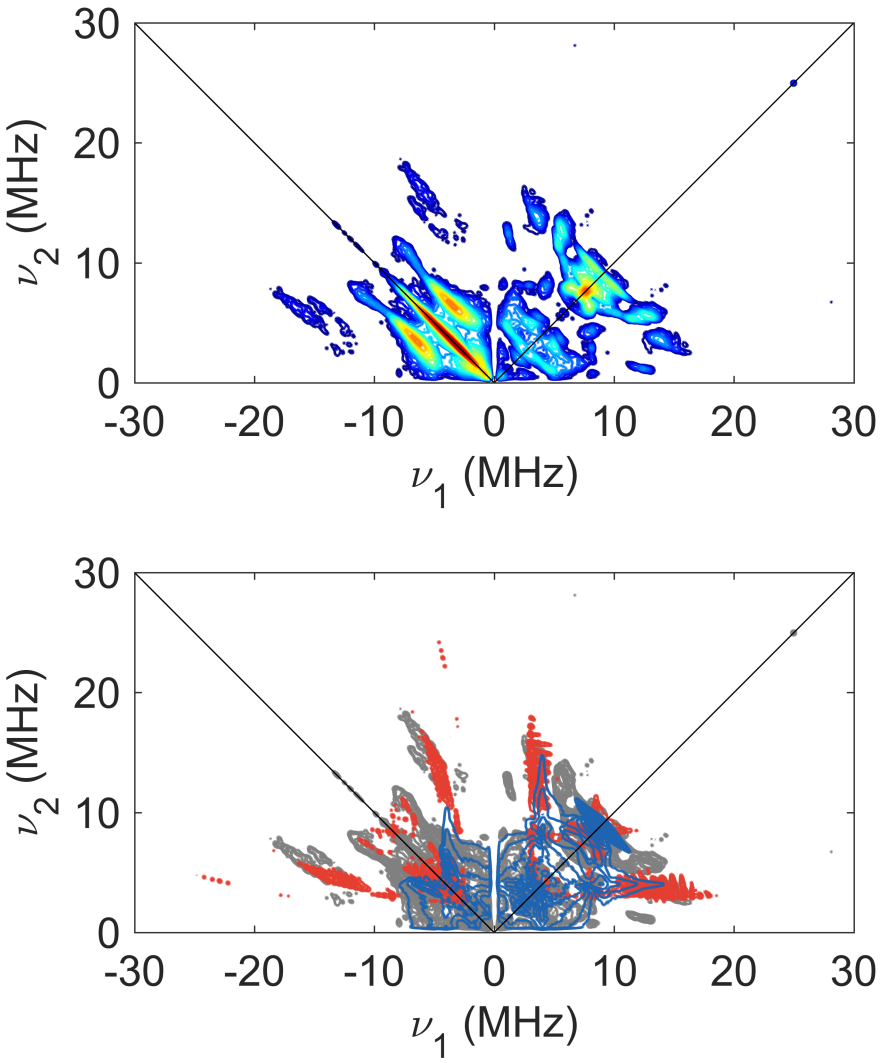

Figure D.16: Hyscore spectrum of $[(P_3{}^B)Fe(^{14}N^{14}NMe_2)]^-$ collected at a field of 1214 mT. The raw data are presented in the top panel, with intensities encoded by the color map. The bottom panel reproduces the experimental spectrum in grey, and overlays simulations due to N_α (red) and N_β (blue). Note that the simulations were calculated for each nucleus separately, and thus do not show effects due to multinuclear coherences. See Table D.25 for simulation details.

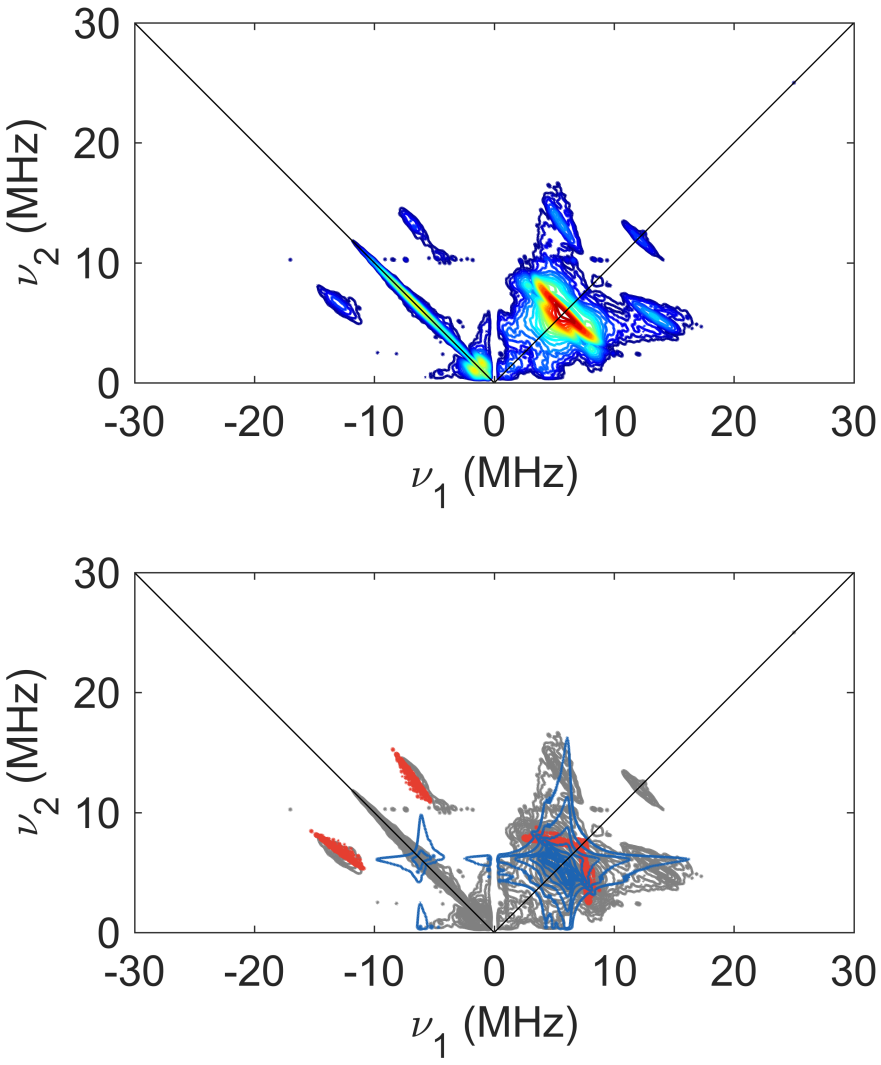

Figure D.17: Hyscore spectrum of $[(P_3{}^B)Fe(^{15}N^{15}NMe_2)]^-$ collected at a field of 1214 mT. The raw data are presented in the top panel, with intensities encoded by the color map. The bottom panel reproduces the experimental spectrum in grey, and overlays simulations due to N_α (red) and N_β (blue). Note that the simulations were calculated for each nucleus separately, and thus do not show effects due to multinuclear coherences. See Table D.25 for simulation details.

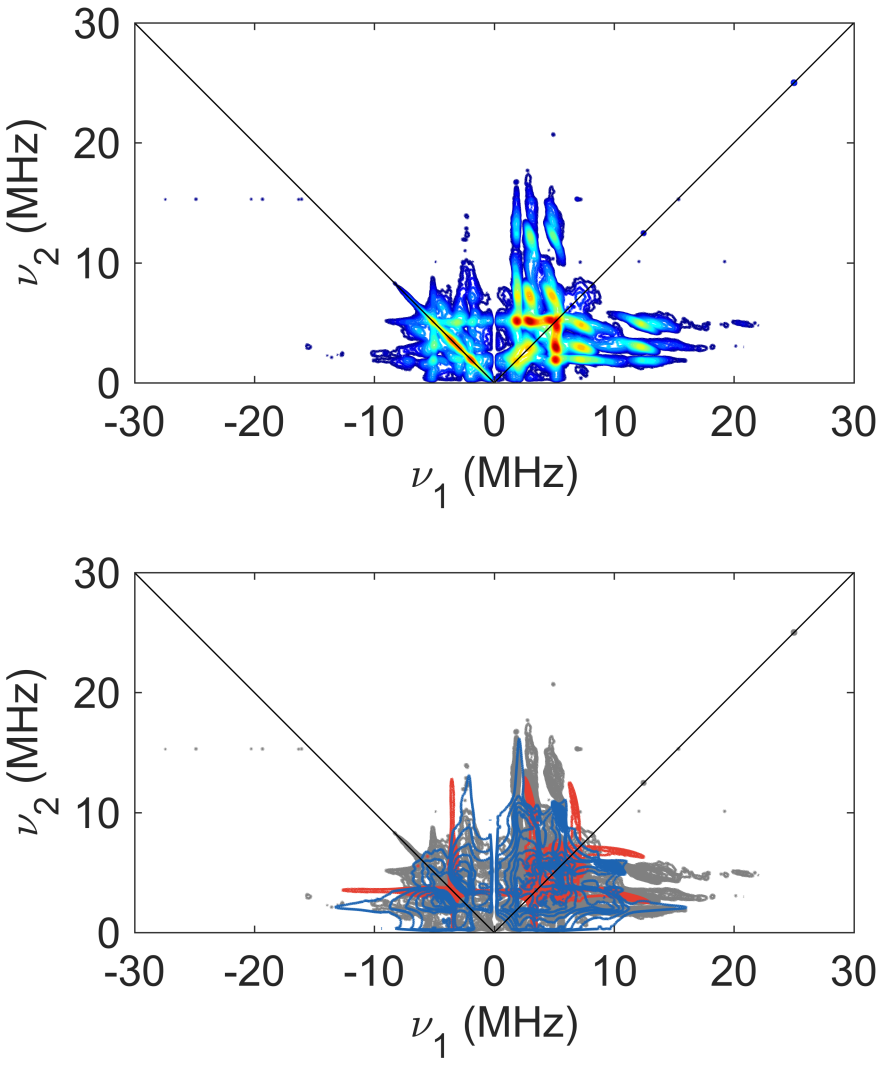

Figure D.18: Hyscore spectrum of $[(P_3{}^B)Fe(^{14}N^{14}NMe_2)]^+$ collected at a field of 1119 mT. The raw data are presented in the top panel, with intensities encoded by the color map. The bottom panel reproduces the experimental spectrum in grey, and overlays simulations due to N_α (red) and N_β (blue). Note that the simulations were calculated for each nucleus separately, and thus do not show effects due to multinuclear coherences. See Table D.25 for simulation details.

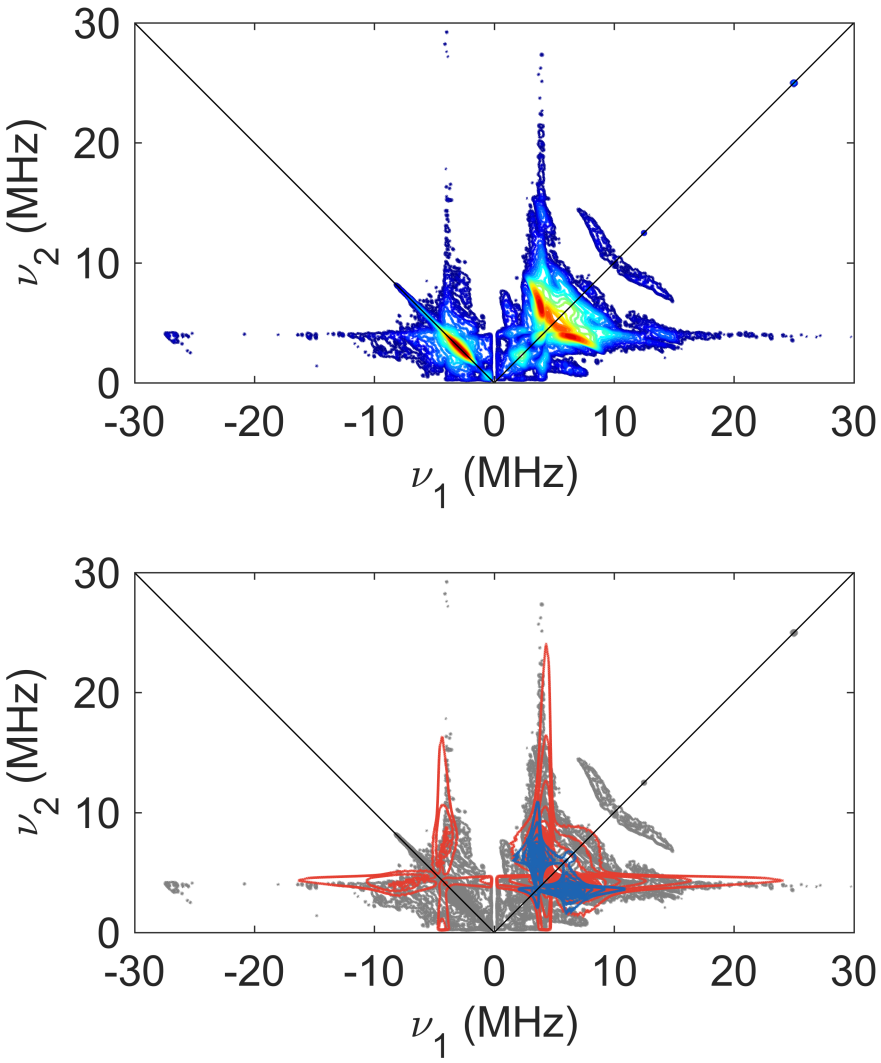

Figure D.19: Hyscore spectrum of $[(P_3{}^B)Fe(^{15}N^{15}NMe_2)]^+$ collected at a field of 1119 mT. The raw data are presented in the top panel, with intensities encoded by the color map. The bottom panel reproduces the experimental spectrum in grey, and overlays simulations due to N_α (red) and N_β (blue). Note that the simulations were calculated for each nucleus separately, and thus do not show effects due to multinuclear coherences. See Table D.25 for simulation details.

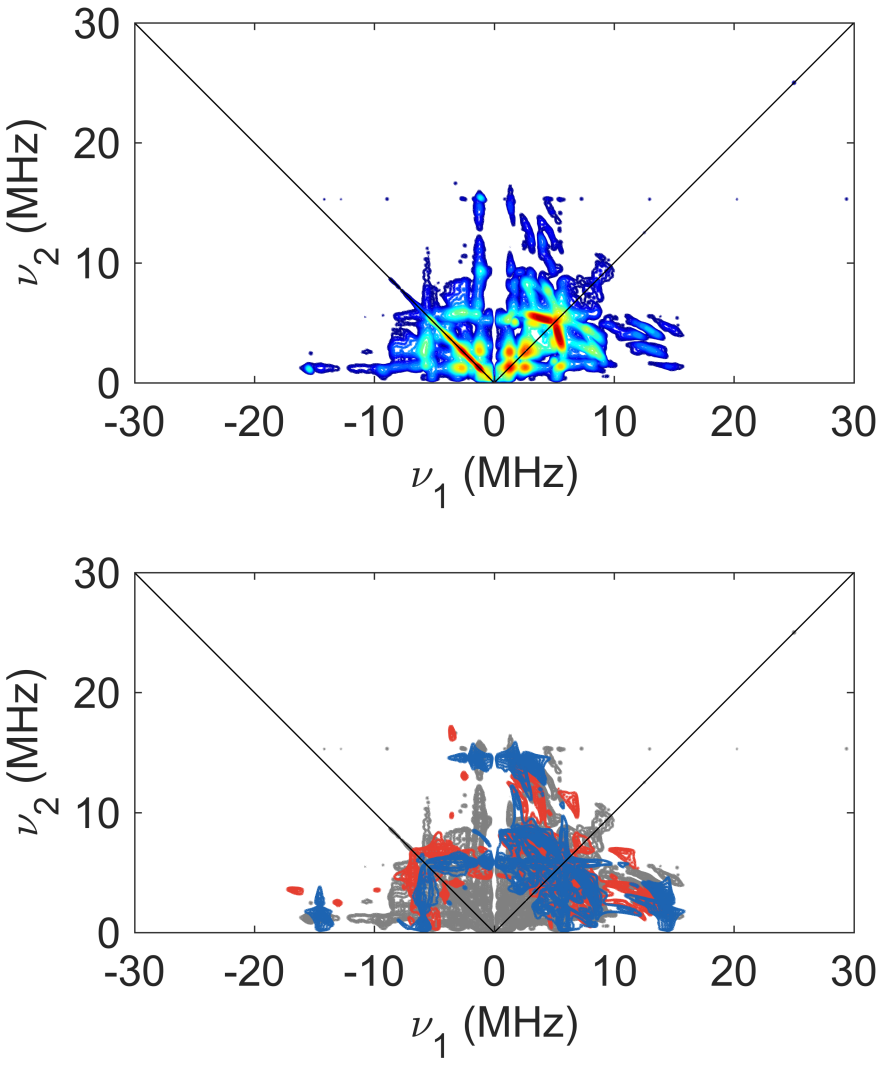

Figure D.20: Hyscore spectrum of $[(P_3{}^B)Fe(^{14}N^{14}NMe_2)]^+$ collected at a field of 1167 mT. The raw data are presented in the top panel, with intensities encoded by the color map. The bottom panel reproduces the experimental spectrum in grey, and overlays simulations due to N_α (red) and N_β (blue). Note that the simulations were calculated for each nucleus separately, and thus do not show effects due to multinuclear coherences. See Table D.25 for simulation details.

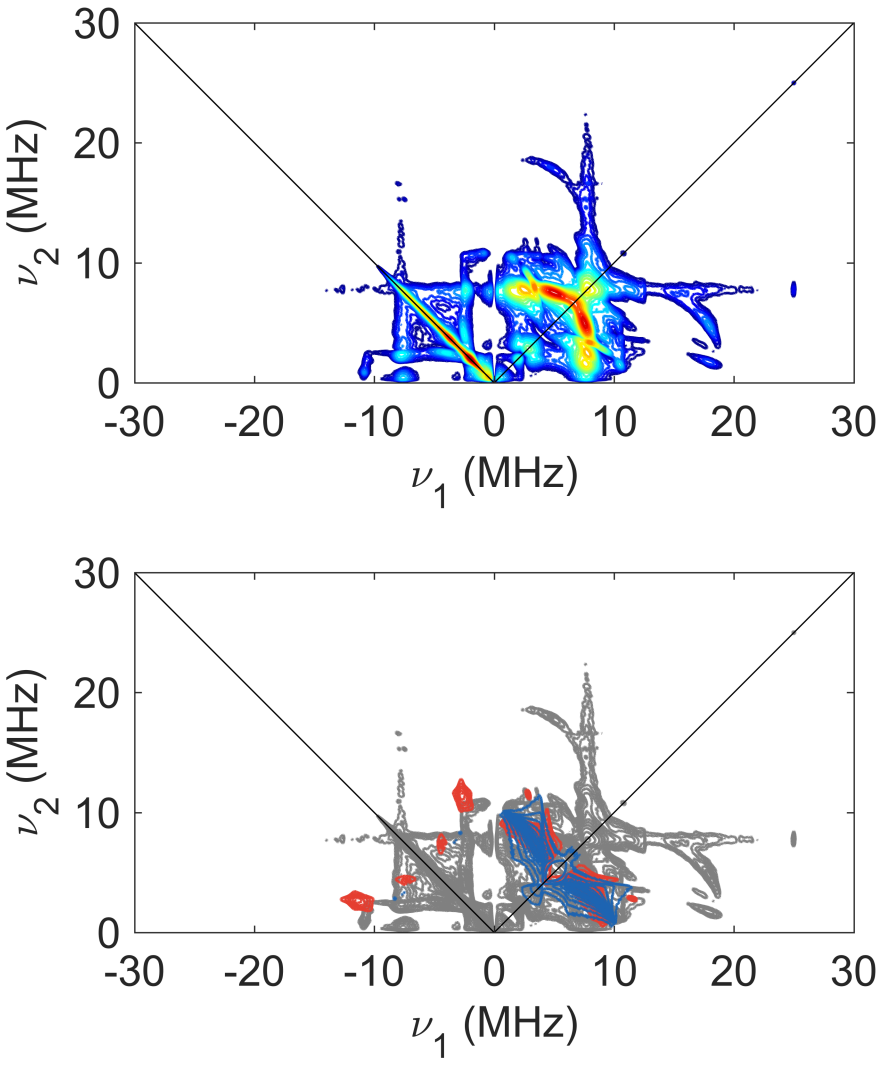

Figure D.21: Hyscore spectrum of $[(P_3{}^B)Fe(^{15}N^{15}NMe_2)]^+$ collected at a field of 1167 mT. The raw data are presented in the top panel, with intensities encoded by the color map. The bottom panel reproduces the experimental spectrum in grey, and overlays simulations due to N_α (red) and N_β (blue). Note that the simulations were calculated for each nucleus separately, and thus do not show effects due to multinuclear coherences. Such coherences can be observed in this spectrum in the $(+,+)$ quadrant in the region spanned by $(5, 20)$ to $(20, 5)$ MHz. See Table D.25 for simulation details.

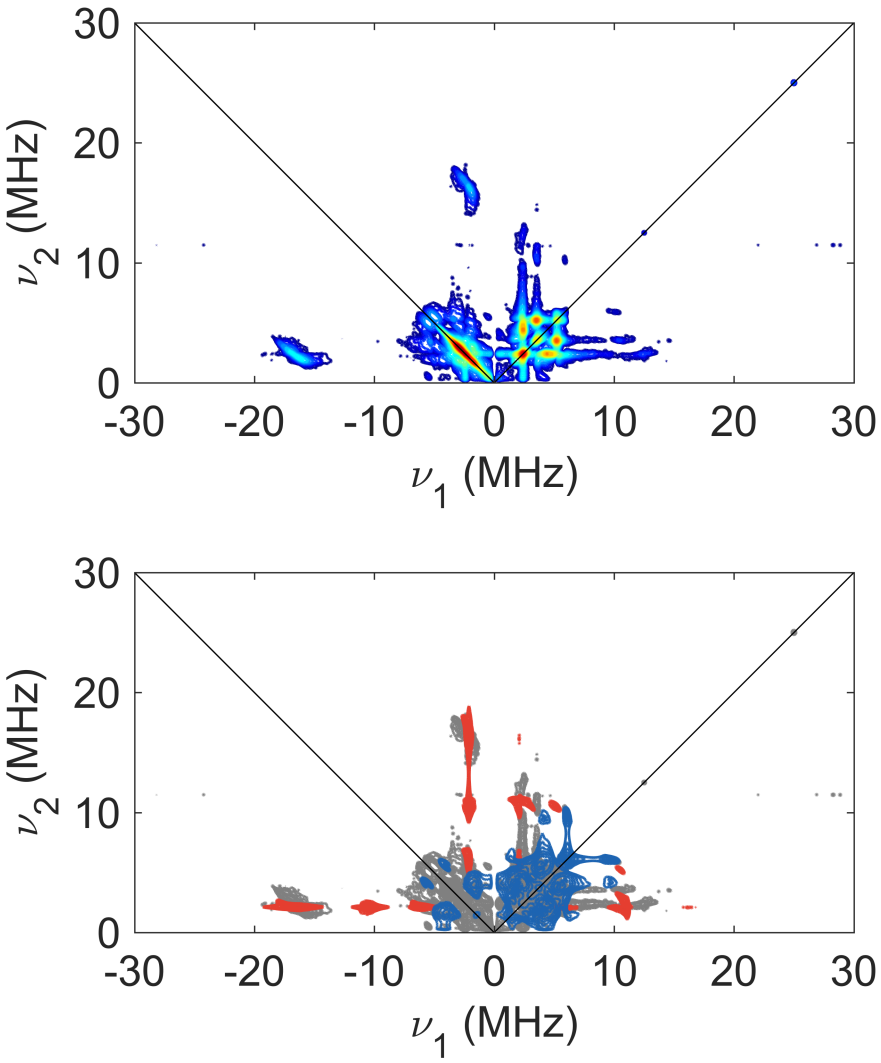

Figure D.22: Hyscore spectrum of $[(P_3{}^B)Fe(^{14}N^{14}NMe_2)]^+$ collected at a field of 1211 mT. The raw data are presented in the top panel, with intensities encoded by the color map. The bottom panel reproduces the experimental spectrum in grey, and overlays simulations due to N_α (red) and N_β (blue). Note that the simulations were calculated for each nucleus separately, and thus do not show effects due to multinuclear coherences. See Table D.25 for simulation details.

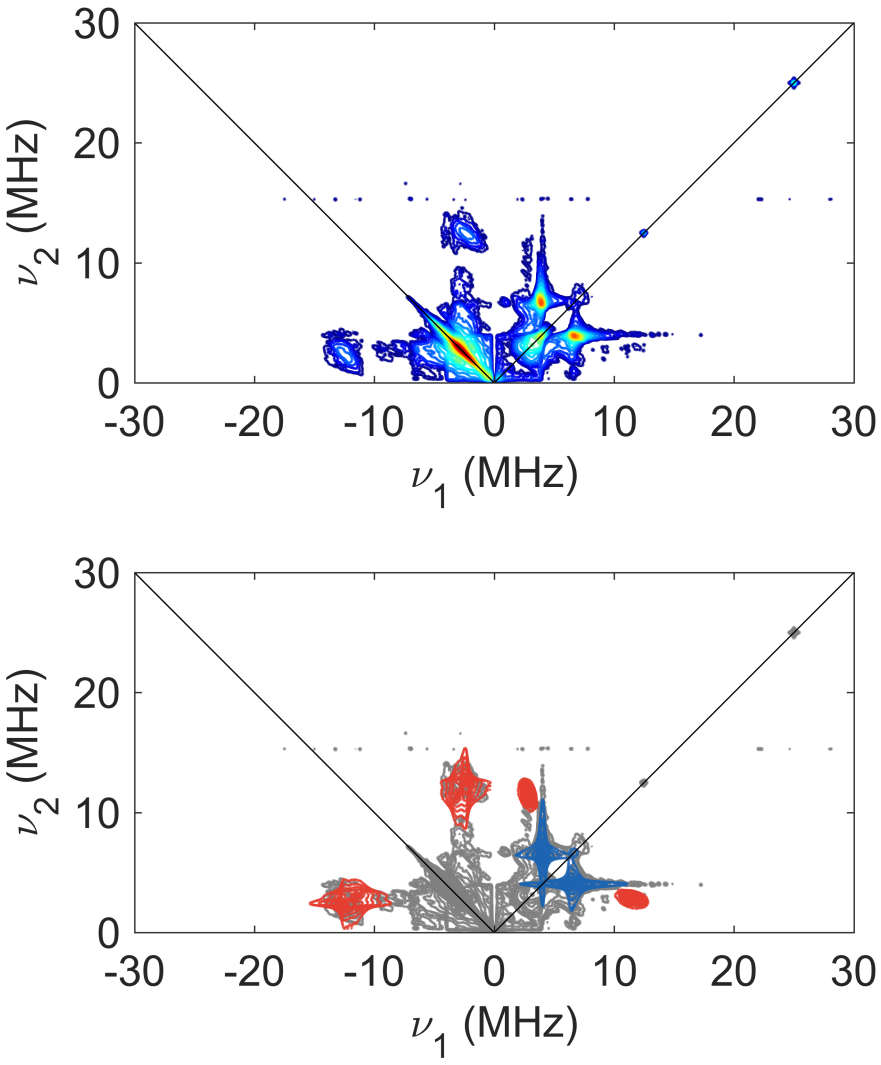

Figure D.23: Hyscore spectrum of $[(P_3{}^B)Fe(^{15}N^{15}NMe_2)]^+$ collected at a field of 1211 mT. The raw data are presented in the top panel, with intensities encoded by the color map. The bottom panel reproduces the experimental spectrum in grey, and overlays simulations due to N_α (red) and N_β (blue). Note that the simulations were calculated for each nucleus separately, and thus do not show effects due to multinuclear coherences. See Table D.25 for simulation details.

D.8 IR Spectra

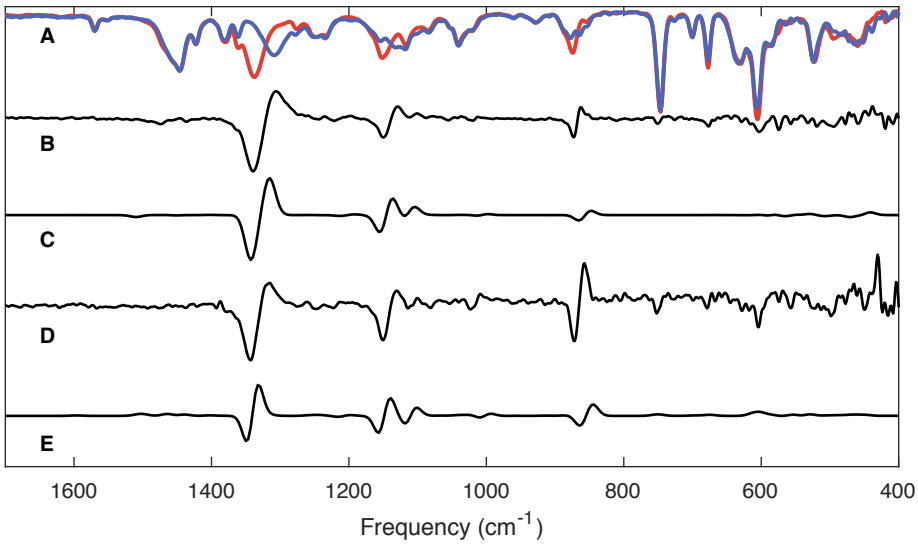

Figure D.24: IR spectra of (P_3^B)Fe($NNMe_2$) isotopologues. (A) Overlaid spectra of a natural abundance isotope (N.A.I.) sample (red), and that of (P_3^B)Fe($^{15}N^{15}NMe_2$) (blue). (B) Experimental N.A.I.–^{15}N difference spectrum. (C) DFT-calculated N.A.I.–^{15}N difference spectrum. (D) Experimental N.A.I–^{13}C difference spectrum (the ^{13}C sample is that of (P_3^B)Fe($NN(^{13}CH_3)_2$)). (E) DFT-calculated N.A.I.–^{13}C difference spectrum. Note that the N–N stretching vibration at 1337 cm^{-1} is mixed with N–C stretching modes.

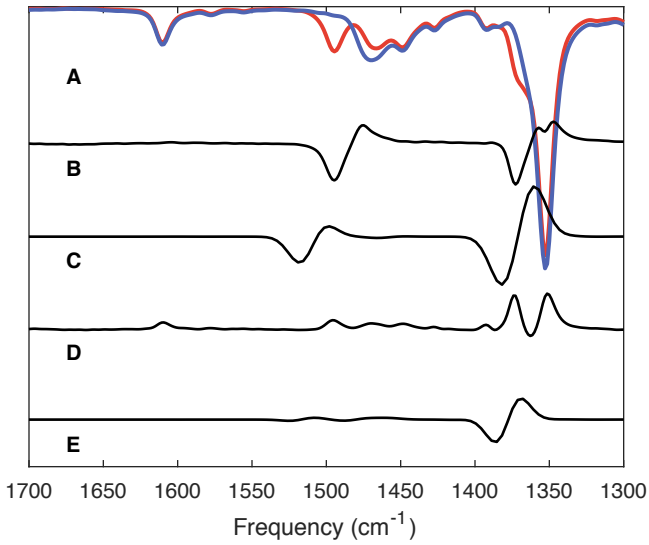

Figure D.25: IR spectra of [(P_3^B)Fe($NNMe_2$)][BAr^F_4] isotopologues. (A) Overlaid spectra of a natural abundance isotope (N.A.I.) sample (red), and that of [(P_3^B)Fe($^{15}N^{15}NMe_2$)]$^+$ (blue). (B) Experimental N.A.I.–^{15}N difference spectrum. (C) DFT-calculated N.A.I.–^{15}N difference spectrum. (D) Experimental N.A.I–^{13}C difference spectrum (the ^{13}C sample is that of [(P_3^B)Fe($NN(^{13}CH_3)_2$)]$^+$). (E) DFT-calculated N.A.I.–^{13}C difference spectrum. The N–N stretching vibration appears at 1495 cm^{-1}. Note that at lower frequencies, the IR spectra are dominated by resonances from the [BAr^F_4]$^-$ counterion, and reliable difference spectra could not be collected.

D.9 UV-vis Spectra

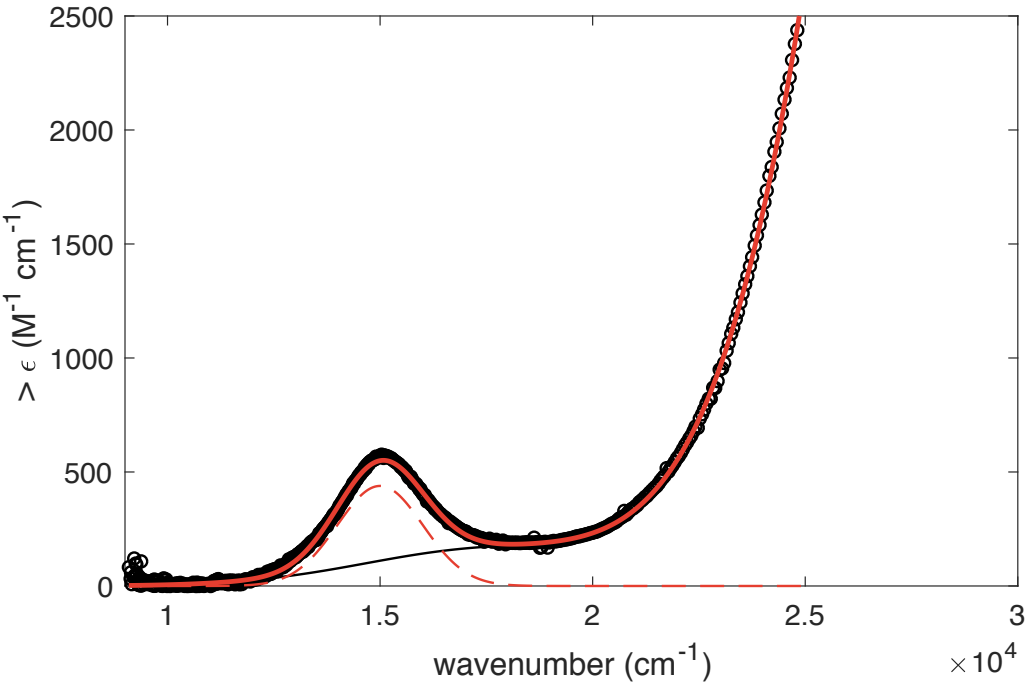

Figure D.26: UV-vis spectrum of ($P_3{}^B$)Fe(NAd) (THF, 298 K). Note that due to the low solubility of ($P_3{}^B$)Fe(NAd) in all common organic solvents, we can only estimate the concentration of this sample to be ca. 0.1 mM, hence the reported molar absorptivity represents a lower limit. The experimental data are shown as open circles, with a Gaussian spectra deconvolution shown in red. Individual sub-components are shown as dashed red and solid black lines. See Table D.5 for the fitting parameters.

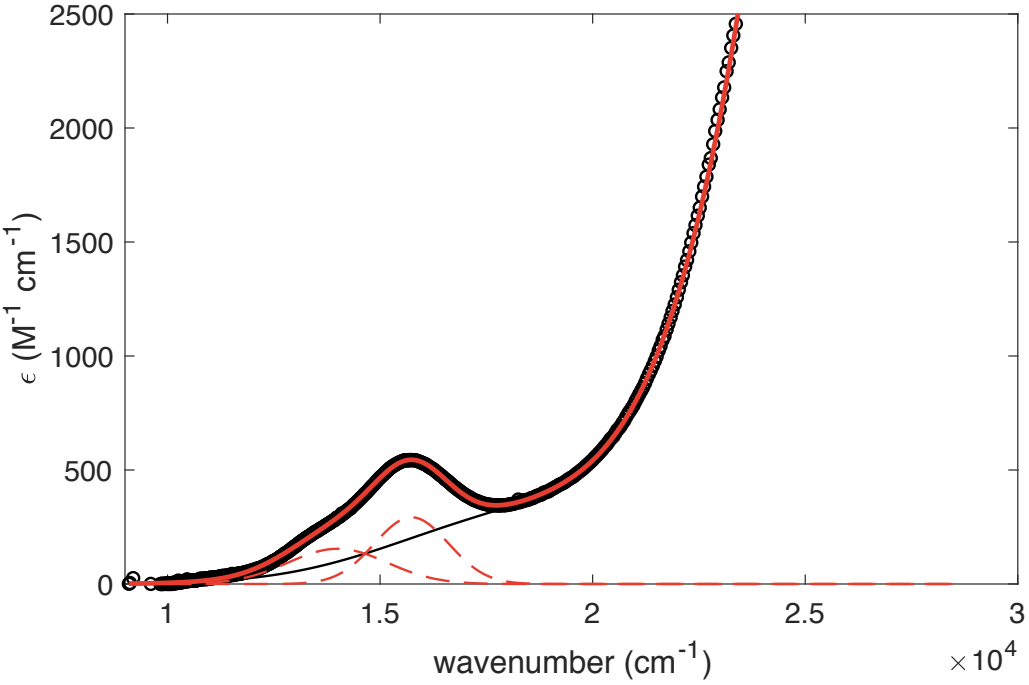

Figure D.27: UV-vis spectrum of (P_3^B)Fe(NN[Si_2]) (2-MeTHF, 153 K). The experimental data are shown as open circles, with a Gaussian spectra deconvolution shown in red. Individual sub-components are shown as dashed red and solid black lines. See Table D.6 for the fitting parameters.

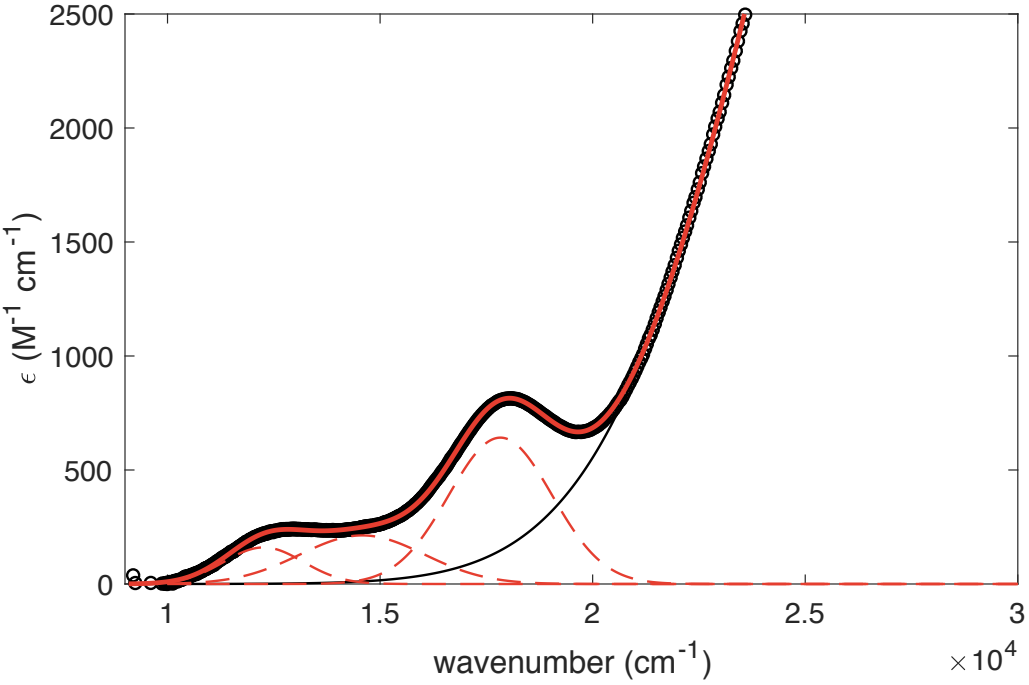

Figure D.28: UV-vis spectrum of (P_3^B)Fe($NNMe_2$) (2-MeTHF, 153 K). The experimental data are shown as open circles, with a Gaussian spectra deconvolution shown in red. Individual sub-components are shown as dashed red and solid black lines. See Table D.7 for the fitting parameters.

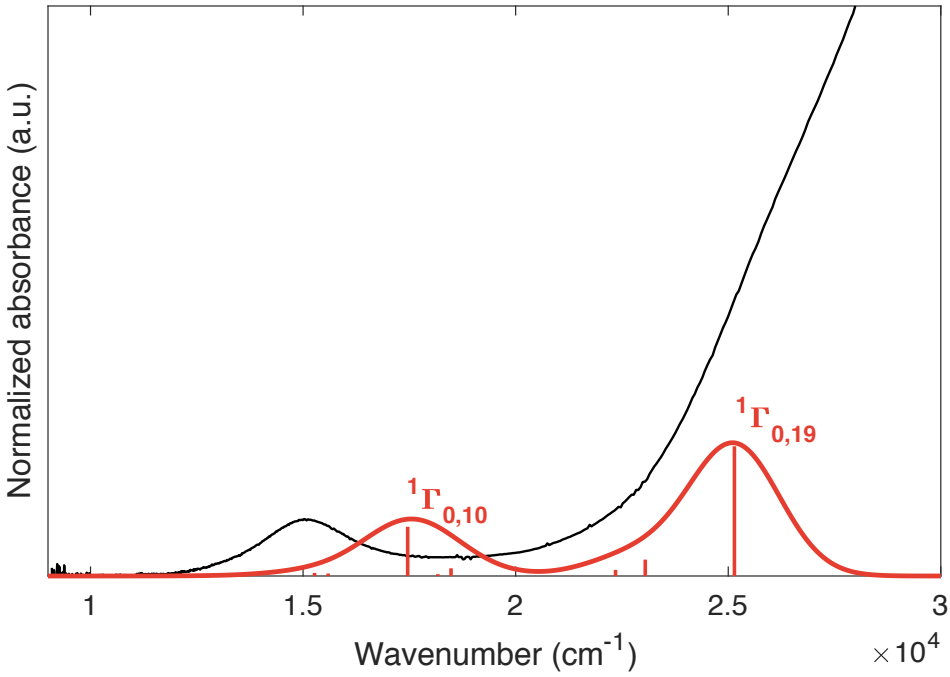

Figure D.29: DFT-based assignment of the optical spectrum of $(P_3{}^B)$Fe(NAd). The experimental spectrum is reproduced in black, while the TD-DFT spectrum is shown in red. As can be seen by the stick spectrum, the optical resonance is due to a single state, $^1\Gamma_{0,10}$; as shown in Figure D.36, this state can be attributed to one-electron excitations from the quasi-degenerate δ-symmetry e orbitals orbitals ($3d_{xy}$, $3d_{x^2-y^2}$) into the quasi-degenerate π*-symmetry e orbitals. The next intense resonance predicted at ca. 25,000 cm^{-1} in the near UV is due to a MLCT transition from the a_1 ($3d_{z^2}$ + B $2p_z$) orbital to the π system of the phenylene linkers of the $P_3{}^B$ ligand.

D.10 Mössbauer Spectra

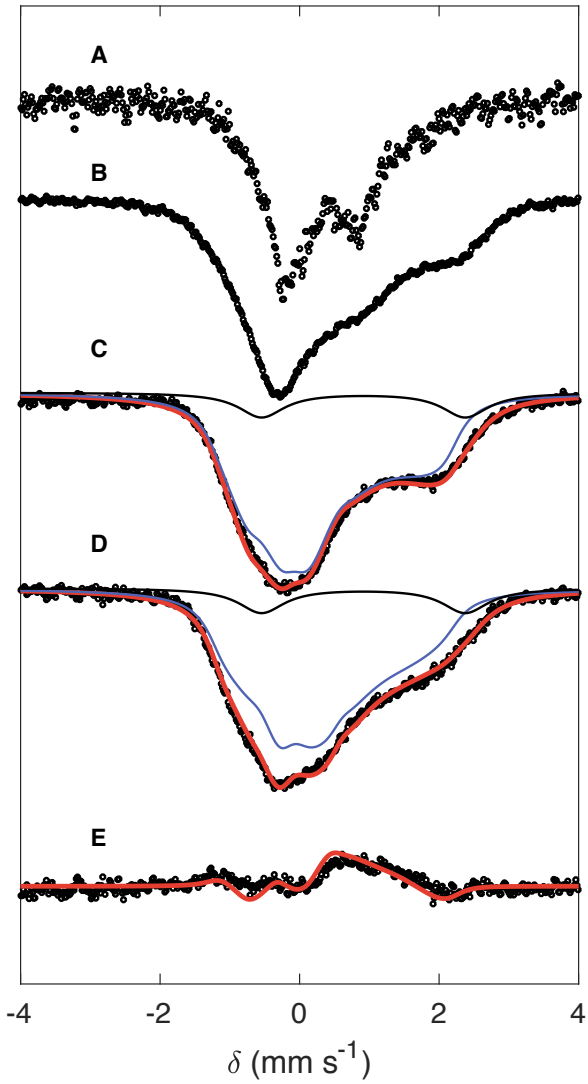

Figure D.30: 80 K Mössbauer spectra of $[(P_3{}^B)Fe(NNMe_2)][BAr^F{}_4]$. Raw data are shown as open circles, with simulations shown as solid red lines; individual sub-components are plotted in blue and black. (A) Polycrystalline sample (natural abundance) collected in a parallel 50 mT field. (B) Frozen solution sample of $[(P_3{}^B)^{57}Fe(NNMe_2)][BAr^F{}_4]$ (4 mM, 2-MeTHF), collected in zero applied field. (C) Frozen solution sample of $[(P_3{}^B)^{57}Fe(NNMe_2)][BAr^F{}_4]$ (4 mM, 2-MeTHF), collected in a parallel 50 mT field. (D) Frozen solution sample of $[(P_3{}^B)^{57}Fe(NNMe_2)][BAr^F{}_4]$ (4 mM, 2-MeTHF), collected in a perpendicular 50 mT field. (E) Difference spectrum (C)−(D). See Table D.8 for fit parameters.

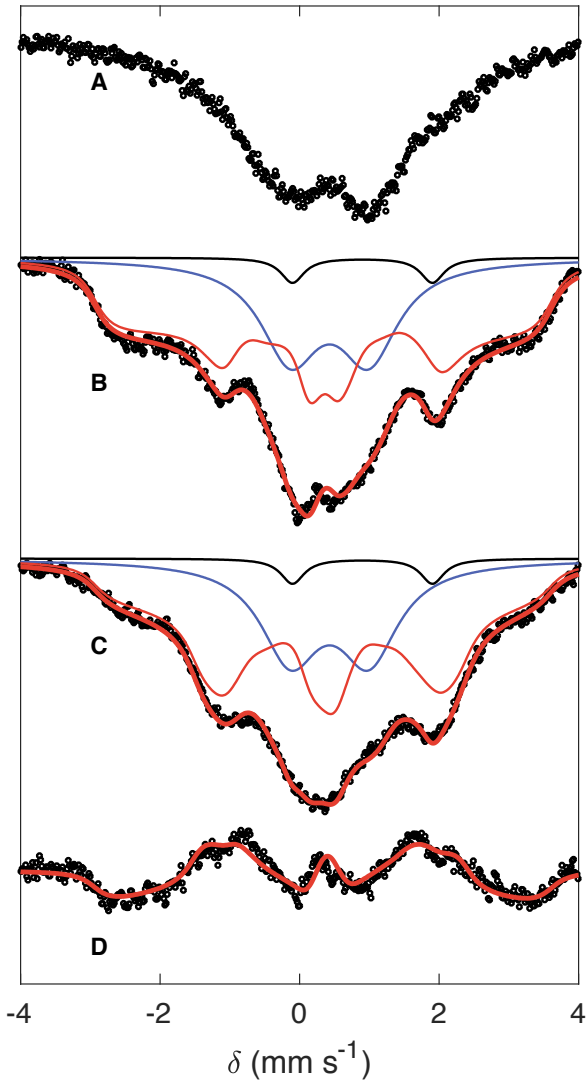

Figure D.31: 80 K Mössbauer spectra of $[(P_3{}^B)Fe(NNMe_2)]^-$. Raw data are shown as open circles, with simulations shown as solid red lines; individual sub-components are plotted in red, blue, and black. (A) Frozen solution sample of $[(P_3{}^B)^{57}Fe(NNMe_2)]^-$ (4 mM, 2-MeTHF), collected in zero applied field. (B) Frozen solution sample of $[(P_3{}^B)^{57}Fe(NNMe_2)]^-$ (4 mM, 2-MeTHF), collected in a parallel 50 mT field. (C) Frozen solution sample of $[(P_3{}^B)^{57}Fe(NNMe_2)]^-$ (4 mM, 2-MeTHF), collected in a perpendicular 50 mT field. (D) Difference spectrum (B)−(C). See Table D.9 for fit parameters.

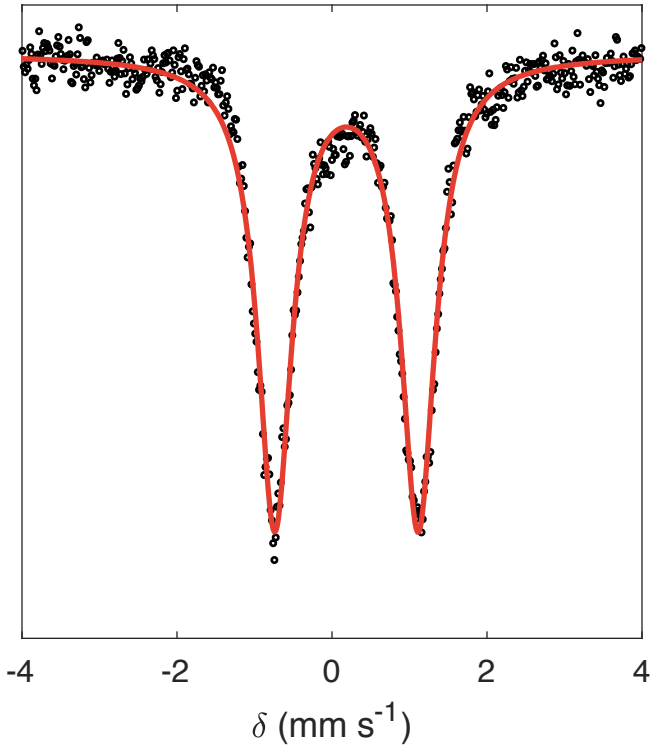

Figure D.32: 80 K Mössbauer spectrum of ($P_3{}^B$)Fe(NN[Si]$_2$) (30 mM, 2-MeTHF, natural abundance). Raw data are shown as open circles, with a simulation shown as a solid red line. Simulation parameters: δ = 0.19 mm s^{-1}; $|\Delta E_Q|$ = 1.85 mm s^{-1}; FWHM = 0.54 mm s^{-1}.

D.11 Cyclic voltammograms

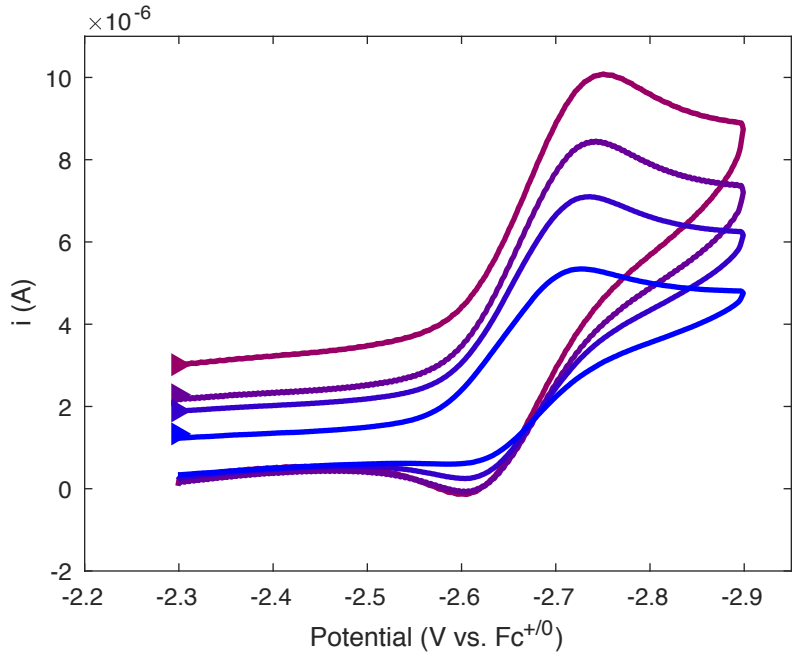

Figure D.33: Cyclic voltammograms of $(P_3{}^B)Fe(NNMe_2)$ (THF, 293 K). Each voltammogram was scanned cathodically through the $[(P_3{}^B)Fe(NNMe_2)]^{0/-}$ couple at ca. −2.6 V. The scan rate was increased in increments of 50 mV s^{-1} from 50 mV s^{-1} (blue) to 200 mV s^{-1} (magenta).

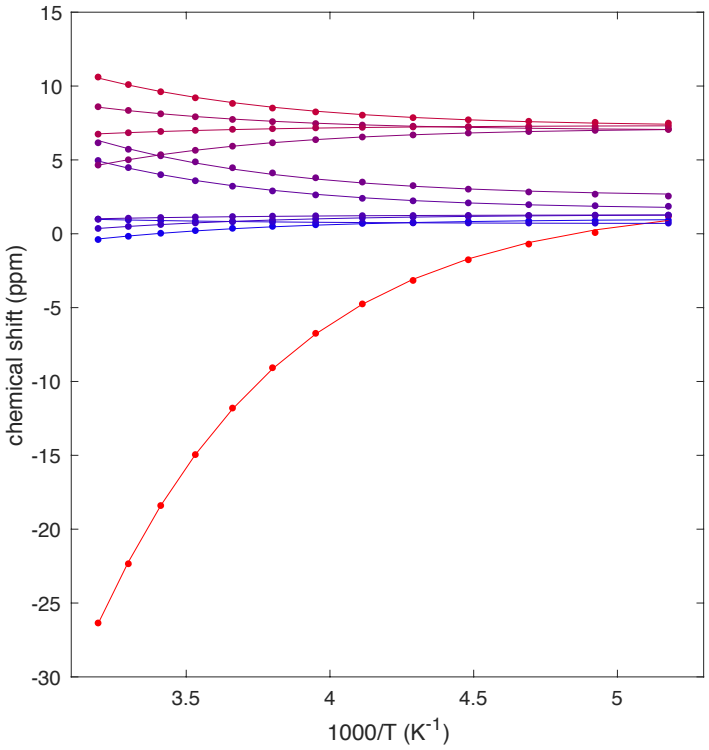

Figure D.34: Simulation of previously-reported variable temperature ^{1}H NMR spectra of (P_3^B)Fe(NNMe$_2$) (500 MHz, d_8-toluene).[5] Circles show the experimental data, while the solid lines show the least-squares fit to the model described in Table D.3. The red curve represents the N-CH$_3$ protons.

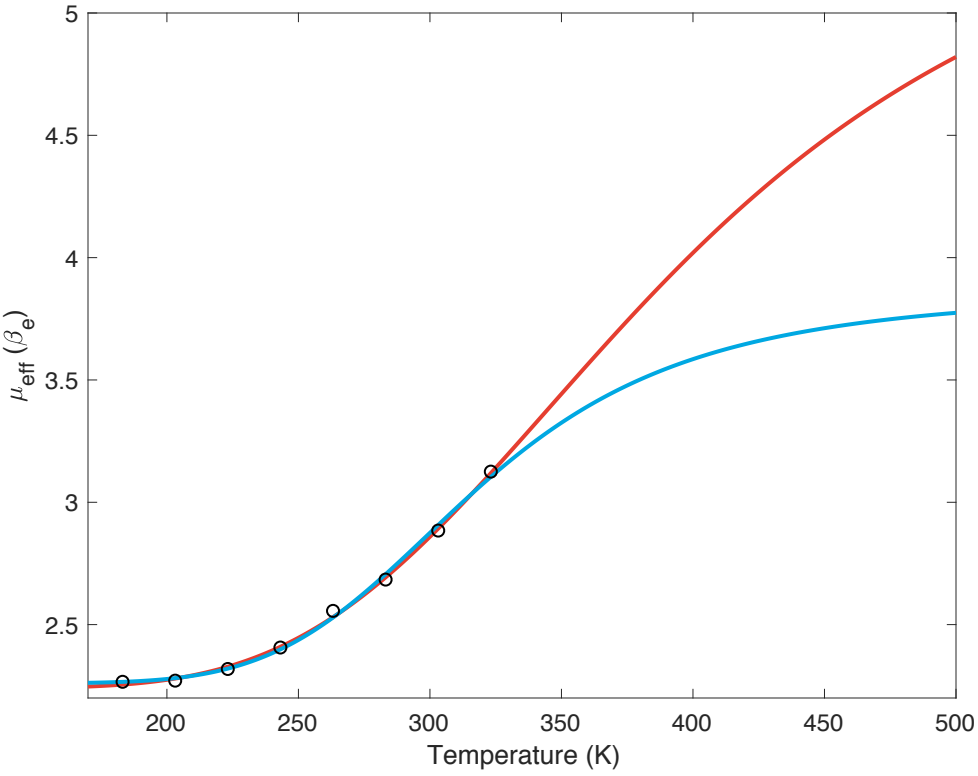

Figure D.35: Simulations of the variable-temperature magnetic susceptibility data of $[(P_3{}^B)Fe(NNMe_2)]^+$. The raw data are plotted as black circles, with simulations assuming the excited state multiplicity is $S = 3/2$ shown in blue, and assuming $S = 5/2$ shown in red. Simulation parameters are shown in Table D.4.

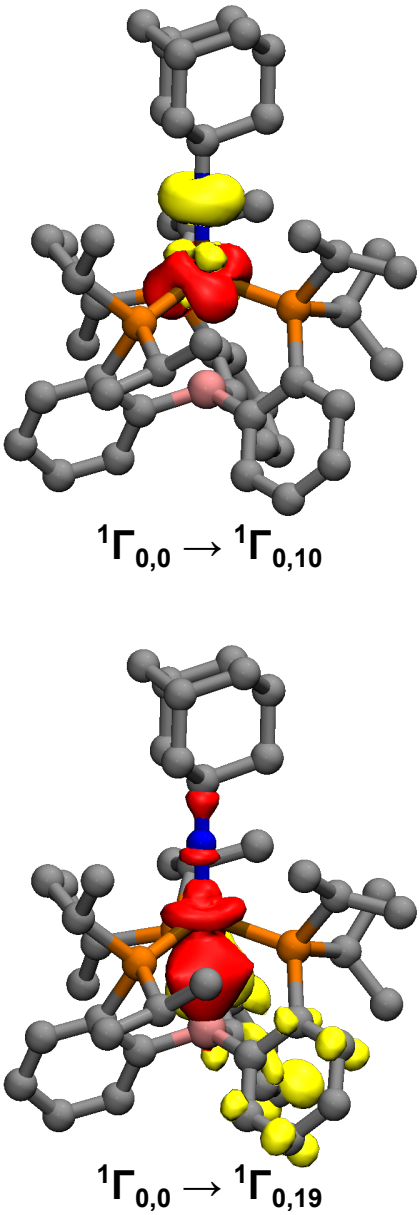

Figure D.36: Difference densities corresponding to the TD-DFT transitions shown in Figure D.29. Negative density is plotted in red, while positive density is plotted in yellow, with an isovalue of 0.003 a.u.

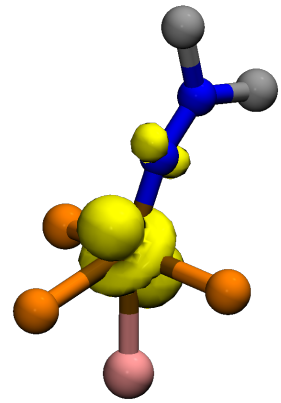

1s → Acceptor state 1

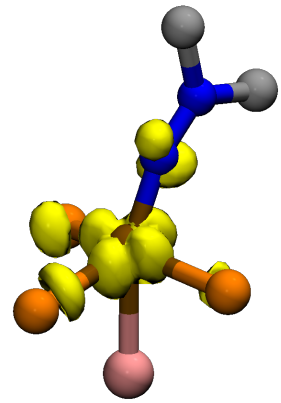

1s → Acceptor state 2

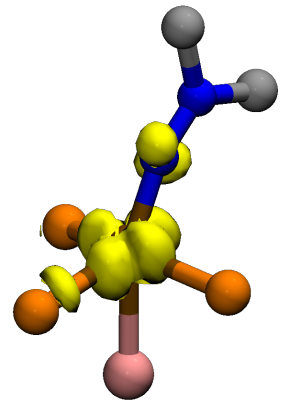

1s → Acceptor state 3

Figure D.37: Difference densities corresponding to the three lowest-energy TD-DFT XANES transitions of $[(P_3{}^B)Fe(NNMe_2)]^+$. Positive density is plotted in yellow, with an isovalue of 0.005 a.u.

D.12 Active Space Orbitals Used in Multireference Calculations

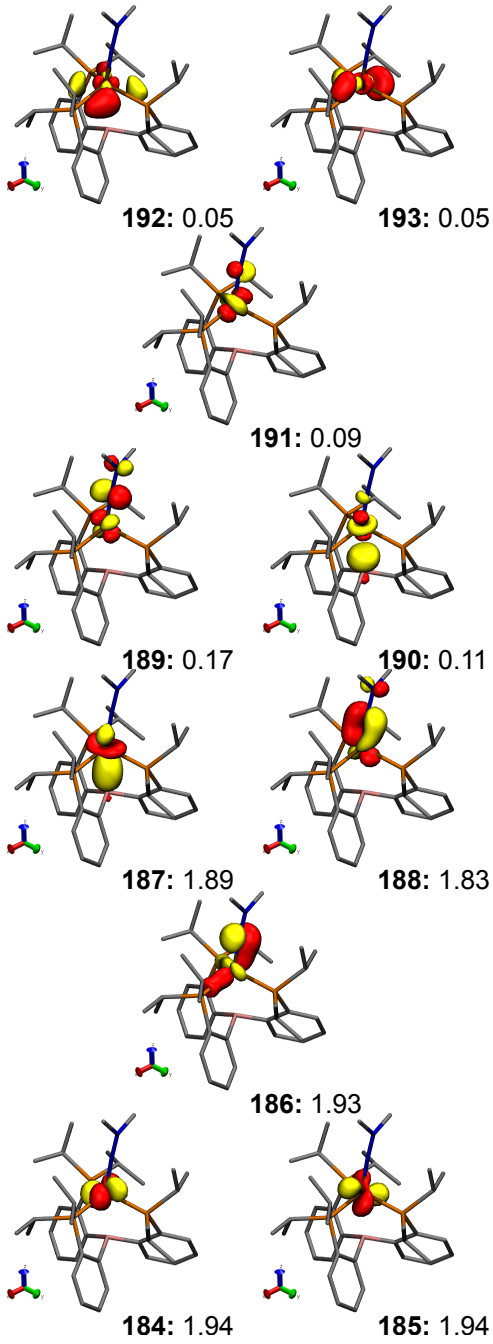

Figure D.38: CAS(10,10) active space natural orbitals from a state-specific calculation of $(P_3{}^B)Fe(NNMe_2)$ in the $^1\Gamma_{0,0}$ state. Orbital labels are given bold, with the corresponding occupation number in normal weight. All surfaces are rendered with an isovalue of 0.075 a.u..

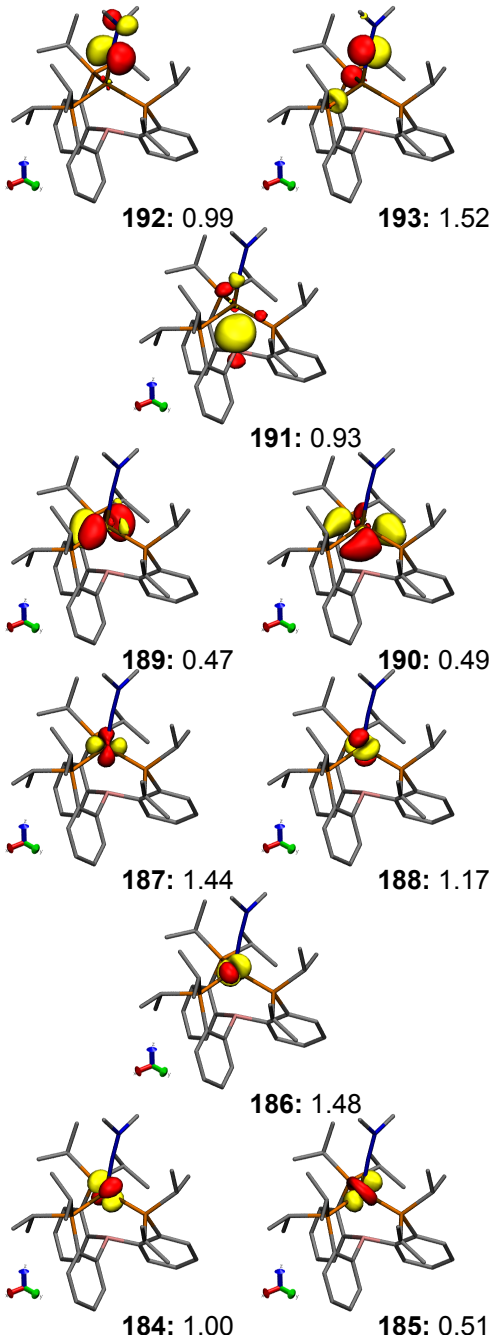

Figure D.39: CAS(10,10) active space orbitals from a state-specific calculation of $(P_3{}^B)Fe(NNMe_2)$ in the $^1\Gamma_{0,0}$ state obtained after Foster-Boys localization. Orbital labels are given bold, with the corresponding occupation number in normal weight. All surfaces are rendered with an isovalue of 0.075 a.u..

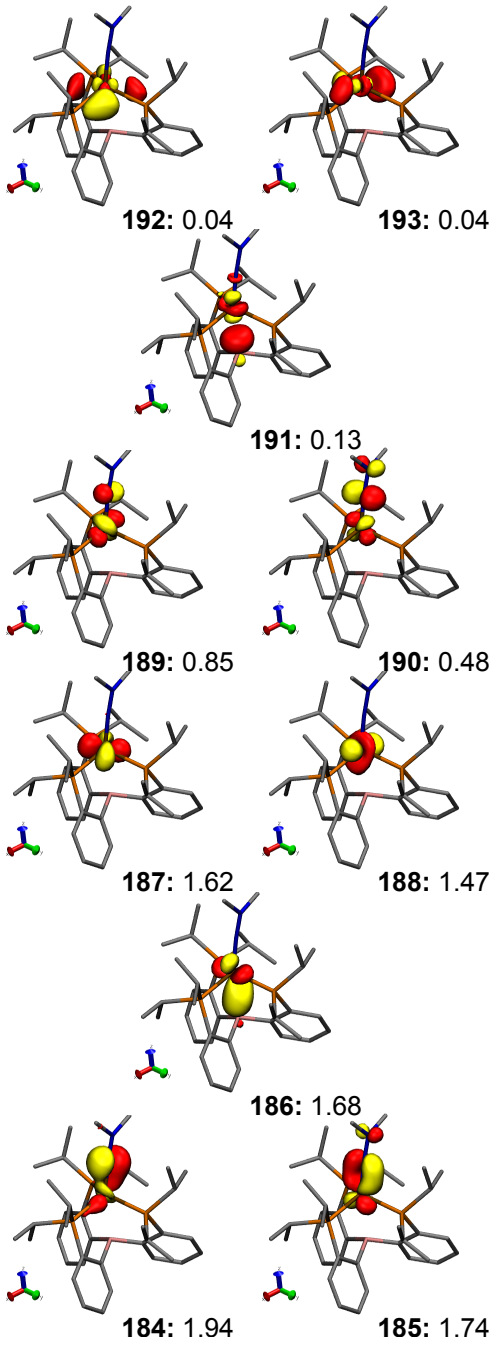

Figure D.40: CAS(10,10) active space natural orbitals from a state-averaged calculation of ($P_3{}^B$)Fe($NNMe_2$) over the 10 lowest-energy singlet states. Orbital labels are given bold, with the corresponding occupation number in normal weight. All surfaces are rendered with an isovalue of 0.075 a.u..

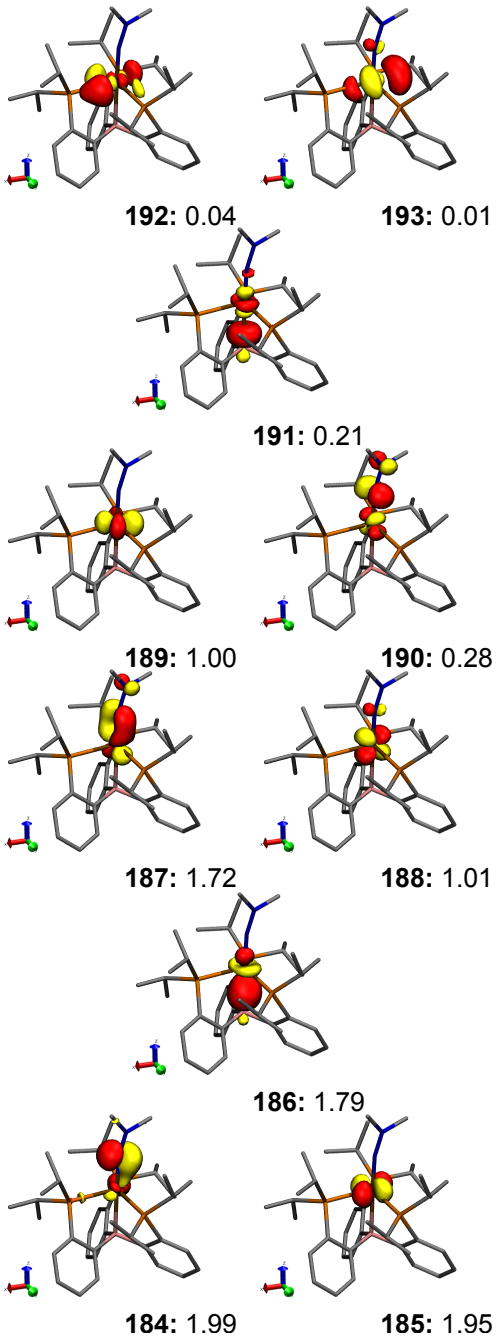

Figure D.41: CAS(10,10) active space natural orbitals from a state-specific calculation of $(P_3{}^B)Fe(NNMe_2)$ in the $^3\Gamma_{0,0}$ state, in the triplet geometry. Orbital labels are given bold, with the corresponding occupation number in normal weight. All surfaces are rendered with an isovalue of 0.075 a.u..

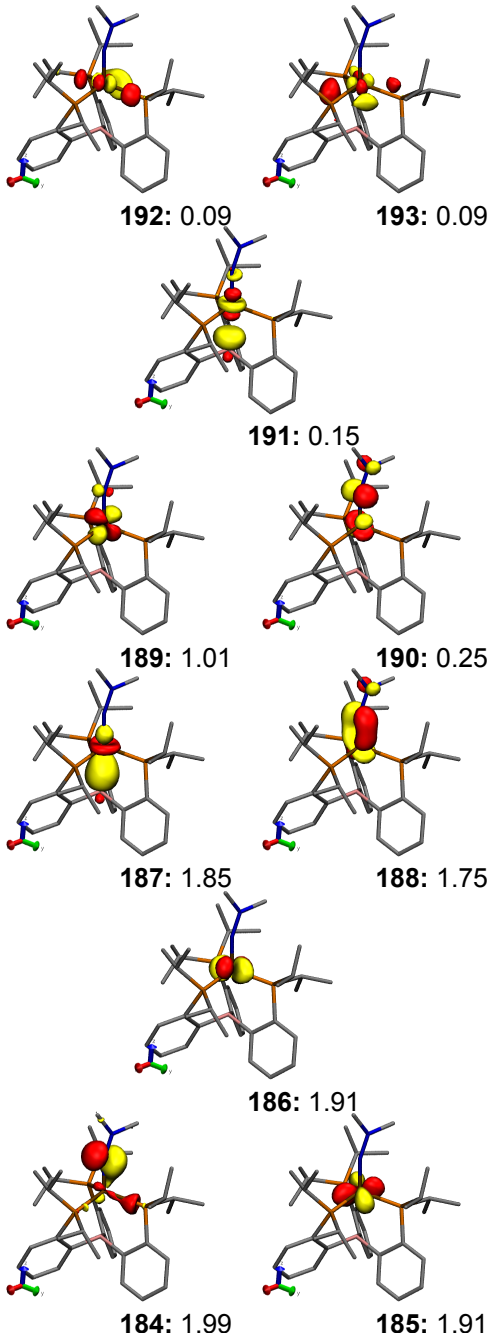

Figure D.42: CAS(11,10) active space natural orbitals from a state-specific calculation of $[(P_3{}^B)Fe(NNMe_2)]^-$ in the $^2\Gamma_{-,0}$ state. Orbital labels are given bold, with the corresponding occupation number in normal weight. All surfaces are rendered with an isovalue of 0.075 a.u..

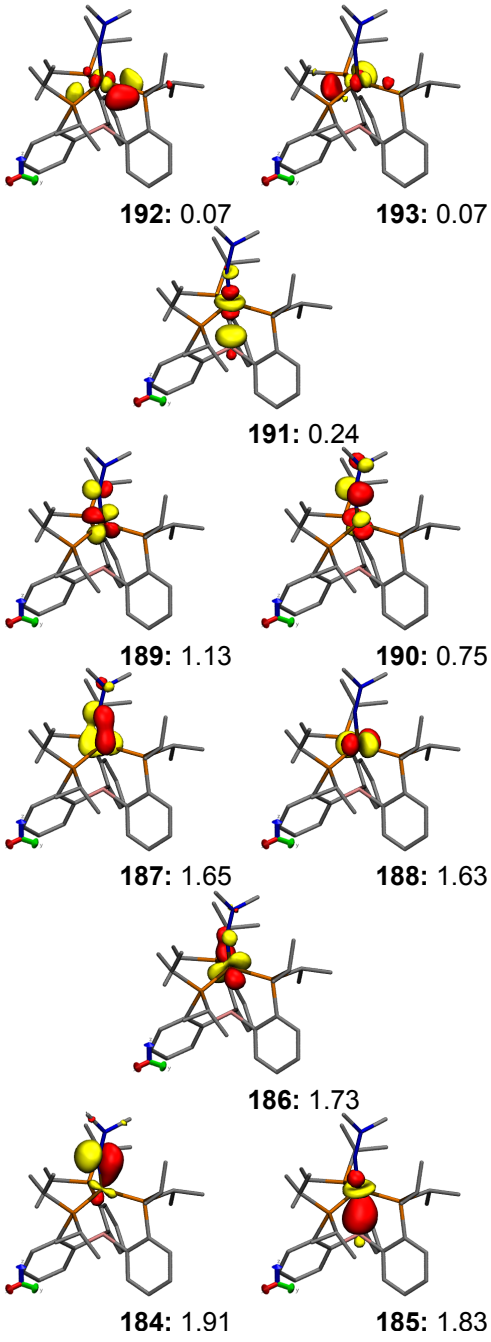

Figure D.43: CAS(11,10) active space natural orbitals from a state-averaged calculation of $[(P_3{}^B)Fe(NNMe_2)]^-$ over the 10 lowest-energy doublet states. Orbital labels are given bold, with the corresponding occupation number in normal weight. All surfaces are rendered with an isovalue of 0.075 a.u..

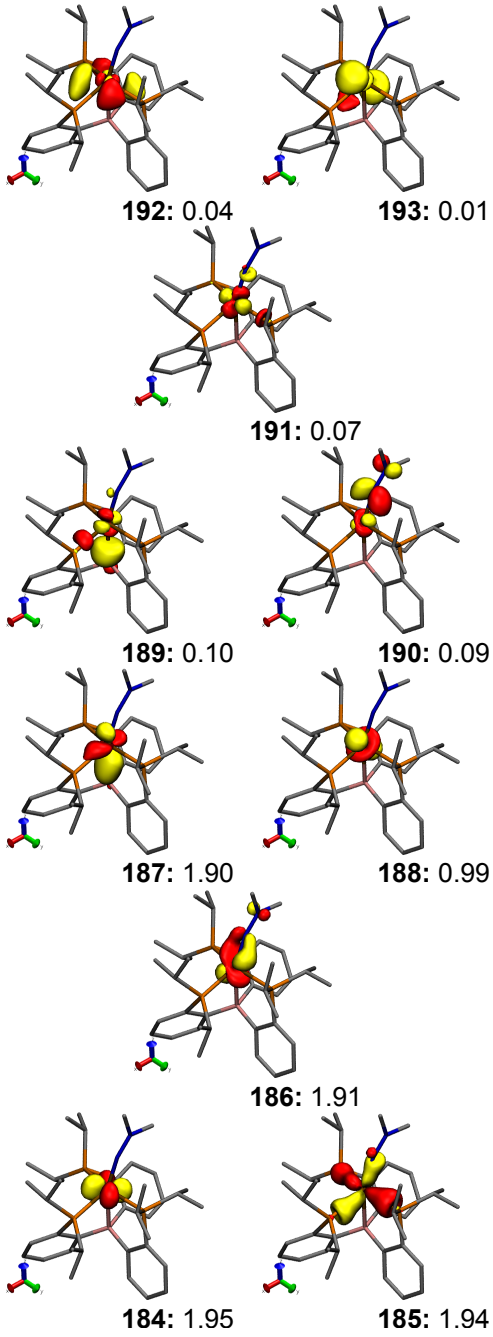

Figure D.44: CAS(9,10) active space natural orbitals from a state-specific calculation of $[(P_3{}^B)Fe(NNMe_2)]^+$ in the $^2\Gamma_{+,0}$ state. Orbital labels are given bold, with the corresponding occupation number in normal weight. All surfaces are rendered with an isovalue of 0.075 a.u.. Note that under the reduced symmetry of this redox state, π_N mixes significantly with a P-based group orbital, and we will refer to this orbital as σ_L. In addition, the Fe 3d orbitals of $3d_{xz}$ and $3d_{x^2-y^2}$ parentage mix significantly, and we will instead label these $3d_{\sigma,1}$ and $3d_{\sigma,2}$.

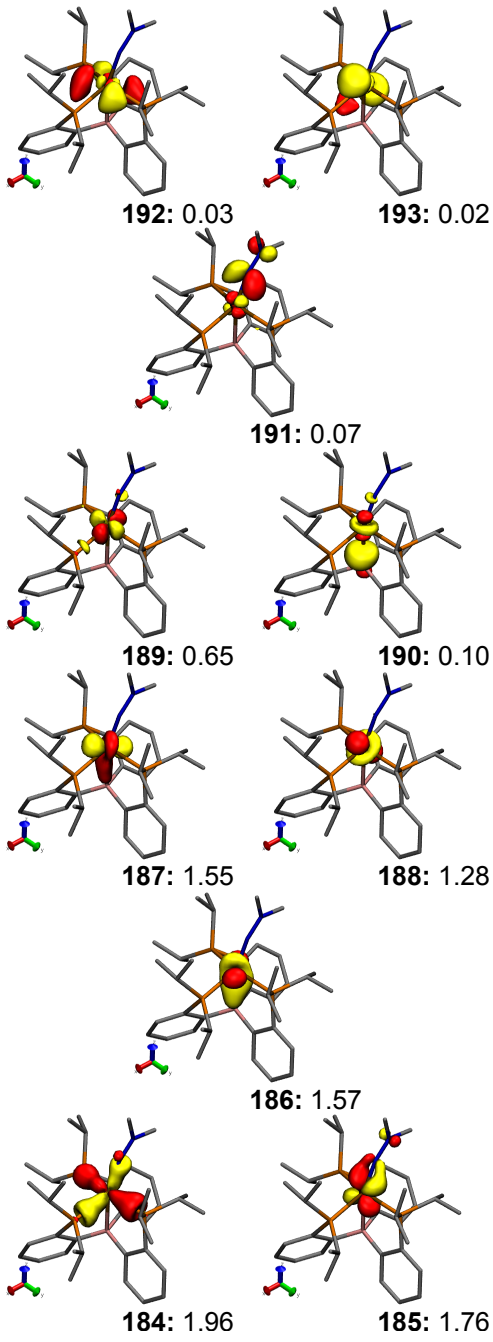

Figure D.45: CAS(9,10) active space natural orbitals from a state-averaged calculation of $[(P_3{}^B)Fe(NNMe_2)]^+$ over the 10 lowest-energy doublet states. Orbital labels are given bold, with the corresponding occupation number in normal weight. All surfaces are rendered with an isovalue of 0.075 a.u..

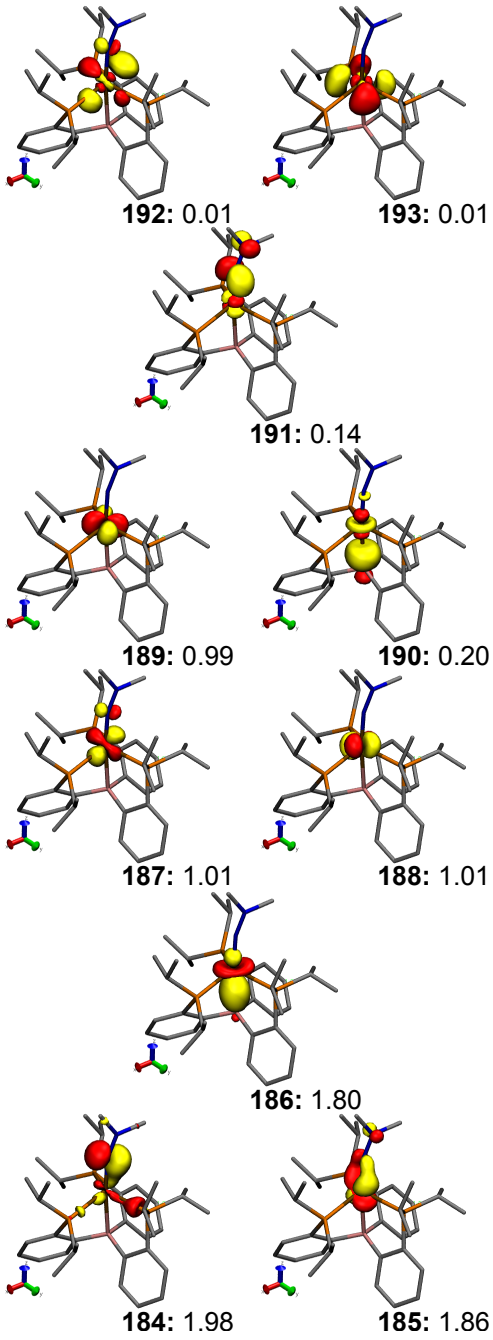

Figure D.46: CAS(9,10) active space natural orbitals from a state-specific calculation of $[(P_3{}^B)Fe(NNMe_2)]^+$ in the $^4\Gamma_{+,0}$ state, in the quartet geometry. Orbital labels are given bold, with the corresponding occupation number in normal weight. All surfaces are rendered with an isovalue of 0.075 a.u..

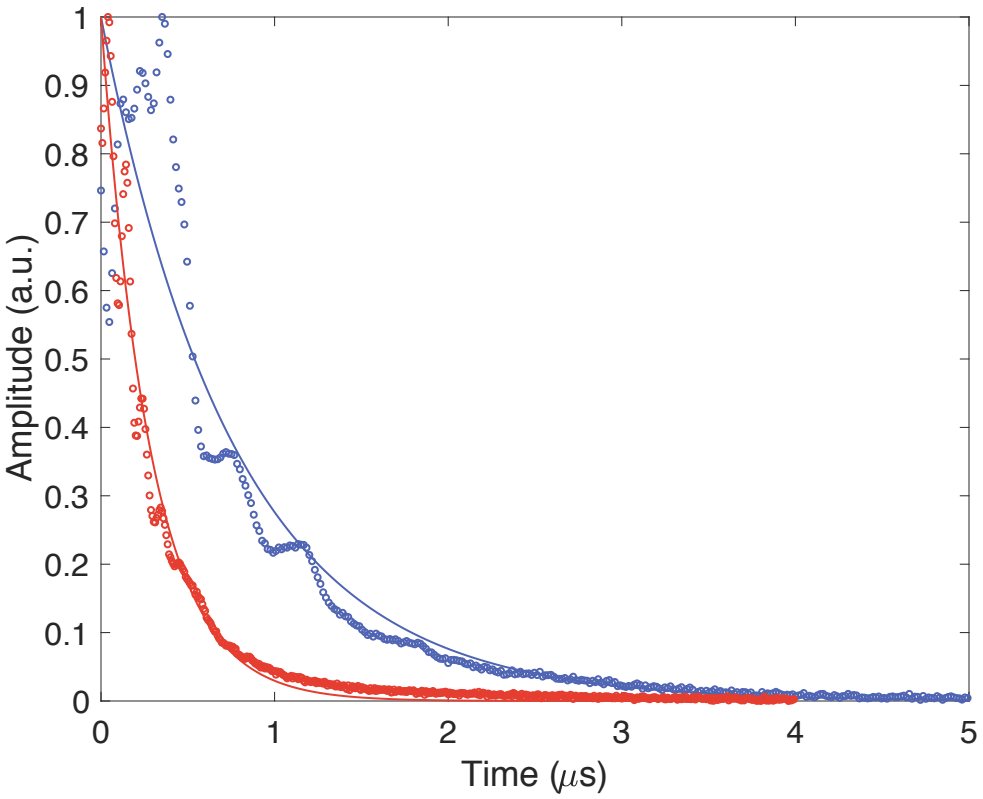

Figure D.47: Determination of the spin-spin relaxation time (T_2) from Hahn spin-echo decay measurements. Raw data are shown as open circles, with monoexponential fits ($A = A_0 \exp(-t/T_2)$) as solid lines. Data for [(P_3^B)Fe($NNMe_2$)][$BAr^F{}_4$] (2 mM, 2-MeTHF, 12 K) are shown in blue, while data for [(P_3^B)Fe(NAd)][$BAr^F{}_4$] (2 mM, 2-MeTHF, 12 K) are shown in red.

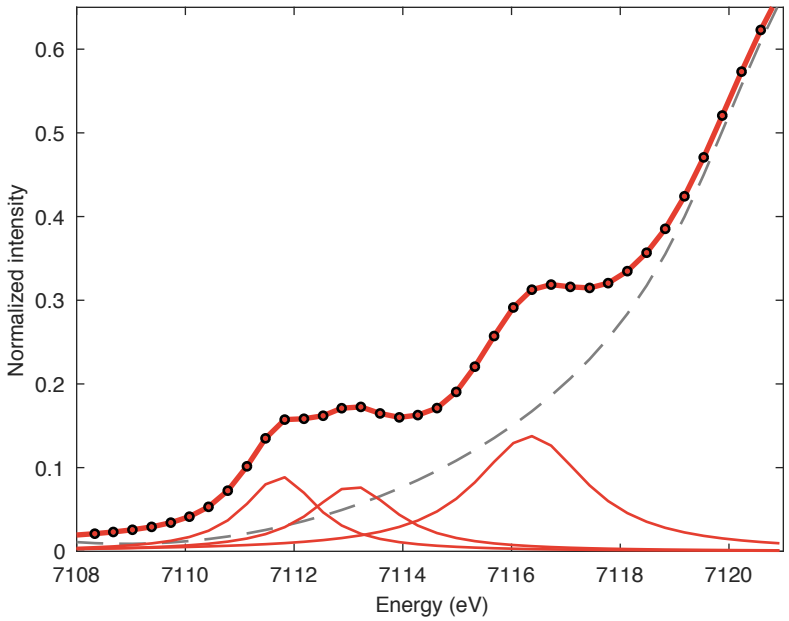

Figure D.48: Pre-edge XANES spectrum of an XAS sample of [(P_3^B)Fe(NNMe$_2$)][BAr^F_4]. Raw data are shown as open circles, simulation as a bold red line, with individual components as thin red lines and the baseline as a dotted grey line. Full simulation parameters are given in Table D.11.

D.13 XRD Tables

Table D.1: Crystal data and structure refinement for $[(P_3{}^B)Fe(NNMe_2)][BAr^F{}_4]\cdot Et_2O$

Empirical formula	$C_{74}H_{82}B_2F_{24}FeN_2OP_3$
Formula weight	1641.79
Temperature (K)	100(2)
Crystal system	Orthorhombic
Space group	$Pca2_1$
a (Å)	21.094(3)
b (Å)	19.460(3)
c (Å)	18.649(3)
α (°)	90
β (°)	90
γ (°)	90
Volume (Å^3)	7655.4(19)
Z	4
ρ_{calc} (g cm^{-3})	1.424
μ (mm^{-1})	0.363
F(000)	3380
Crystal size (mm^3)	$0.1 \times 0.1 \times 0.1$
Radiation	Mo K_α (λ = 0.71073 Å)
2θ range for data collection (°)	2.196 to 30.574
Index ranges	$-30 \leq h \leq 30, -27 \leq k \leq 27, -26 \leq l \leq 26$
Reflections collected	259650
Independent reflections	23383 (R_{int} = 0.0707)
Data/restraints/parameters	23383 / 1 / 980
Goodness-of-fit on F^2	1.034
Final R indexes (I $\geq 2\sigma$(I))	R_1 = 0.0451, wR_2 = 0.1114
Final R indexes (all data)	R_1 = 0.0620, wR_2 = 0.1209
Largest diff. peak/hole (e Å^{-3})	1.827 and −0.462

Table D.2: Crystal data and structure refinement for [K(benzo-15-c-5)$_2$][($P_3{}^B$)Fe(NNMe$_2$)]·4 (2-MeTHF)

Empirical formula	$C_{86}H_{140}BFeKN_2O_{14}P_3$
Formula weight	1624.66
Temperature (K)	100(2)
Crystal system	Triclinic
Space group	P-1
a (Å)	13.2390(5)
b (Å)	18.3254(7)
c (Å)	19.9275(8)
α (°)	87.899(3)
β (°)	75.367(2)
γ (°)	69.520(2)
Volume (Å^3)	4375.0(3)
Z	2
ρ_{calc} (g cm^{-3})	1.233
μ (mm^{-1})	2.812
F(000)	1754
Crystal size (mm^3)	$0.1 \times 0.1 \times 0.1$
Radiation	Cu K_α (λ = 1.54178 Å)
2θ range for data collection (°)	2.578 to 61.165
Index ranges	$-15 \leq h \leq 13, -20 \leq k \leq 20, -22 \leq l \leq 21$
Reflections collected	53935
Independent reflections	12204 (R_{int} = 0.0915)
Data/restraints/parameters	12204 / 577 / 1097
Goodness-of-fit on F^2	1.101
Final R indexes (I $\geq 2\sigma$(I))	R_1 = 0.0884, wR_2 = 0.2176
Final R indexes (all data)	R_1 = 0.1344, wR_2 = 0.2390
Largest diff. peak/hole (e Å^{-3})	0.693 and −0.524

Table D.3: Best fit parameters for the simulation of the VT NMR data of (P_3^B)Fe($NNMe_2$) shown in Figure D.34. The following model was used,

$$\delta_{\text{obs}} = \delta_d + 10^{12} \cdot a_{\text{iso}} \cdot \frac{2hg_e\beta_e}{g_N\beta_N k_B T} \frac{1}{3+\exp(\frac{\Delta E}{RT})}$$

For a derivation, see the supplementary discussion above. The 95% confidence interval is given in brackets below each parameter.

Resonance	δ_d (ppm)	a_{iso} (MHz)	ΔE (kcal mol^{-1})
N-CH_3	2.15 [2.06, 2.25]	−48.4 [−50.5, −46.3]	
*i*Pr-CH_3	1.00 [0.96, 1.06]	−2.3 [−2.5, −2.1]	
*i*Pr-CH_3	0.69 [0.64, 0.74]	0.47 [0.32, 0.64]	
*i*Pr-CH_3	1.30 [1.26, 1.35]	−1.6 [−1.8, −1.4]	
*i*Pr-CH_3	1.29 [1.24, 1.33]	−0.45 [−0.6, −0.3]	
*i*Pr-CH	1.64 [1.60, 1.69]	5.6 [5.3, 5.9]	
*i*Pr-CH	2.52 [2.47, 2.57]	6.4 [6.1, 6.7]	
Ar-CH	7.16 [7.12, 7.21]	−4.3 [−4.5, −4.0]	
Ar-CH	6.99 [6.94, 7.04]	2.7 [2.5, 2.9]	
Ar-CH	7.33 [7.29, 7.39]	−1.0 [−1.1, −0.8]	
Ar-CH	7.27 [7.23, 7.32]	5.5 [5.3, 5.8]	
			3.62 [3.59, 3.65]

Table D.4: Best fit parameters for the simulation of the VT magnetic susceptibility data of $[(P_3{}^B)Fe(NNMe_2)]^+$ shown in Figure D.35. The 95% confidence interval is given in brackets below each parameter.

g_2 ($\mu_2[\beta_e]$)	μ_1	ΔH (kcal mol^{-1})	ΔS (cal mol^{-1} K^{-1})	RMSE
4 (3.87)	2.26 [2.22, 2.30]	4.79 [4.03, 5.55]	13.6 [11.1, 16.1]	0.02
6 (5.92)	2.24 [2.21, 2.27]	3.65 [3.22, 4.09]	6.8 [5.5, 8.2]	0.02

Table D.5: Fit parameters for the Gaussian spectral deconvolution of the UV-vis spectrum of ($P_3{}^B$)Fe(NAd), shown in Figure D.26. The 95% confidence interval is given below each parameter in brackets.

Component	f	$\bar{\nu}_0$ (cm^{-1})	$\sigma_{1/2}$ (cm^{-1})
1	0.0048	15 000	2 376
	[0.0046, 0.0050]	[14 980, 15 010]	[2 321, 2 431]
2 (baseline)	0.0050	17 390	6 721
	[0.0046, 0.0054]	[16 940, 17 840]	[6 217, 7 225]
3 (baseline)	0.88	33 430	10 020
	[0.15, 1.6]	[30 760, 36 100]	[8 570, 11 470]

Table D.6: Fit parameters for the Gaussian spectral deconvolution of the UV-vis spectrum of ($P_3{}^B$)Fe(NN[Si_2]), shown in Figure D.27. The 95% confidence interval is given below each parameter in brackets.

Component	f	$\bar{\nu}_0$ (cm^{-1})	$\sigma_{1/2}$ (cm^{-1})
1	0.0020 [0.0016, 0.0023]	14 000 [13 810, 14 190]	2 751 [2 510, 2 992]
2	0.0028 [0.0023, 0.0032]	15 740 [15 700, 17 790]	2 053 [1 964, 2 141]
3 (baseline)	0.0077 [0.0038, 0.012]	17 910 [16 550, 19 280]	6 569 [5 627, 7 510]
4 (baseline)	1.1 [−5.1, 7.3]	32 640 [14 230, 51 050]	10 030 [712, 19 890]

Table D.7: Fit parameters for the Gaussian spectral deconvolution of the UV-vis spectrum of $(P_3{}^B)Fe(NNMe_2)$, shown in Figure D.28. The 95% confidence interval is given below each parameter in brackets.

Component	f	$\bar{\nu}_0$ (cm^{-1})	$\sigma_{1/2}$ (cm^{-1})
1	0.0016 [0.0009, 0.0023]	12 260 [12 140, 12 380]	2 193 [1 988, 2 398]
2	0.0034 [0.0022, 0.0045]	14 580 [14 420, 14 740]	3 449 [2 457, 4 441]
3	0.0084 [0.0079, 0.0090]	17 830 [17 770, 17 890]	2 864 [2 786, 2 942]
4 (baseline)	0.21 [0.20, 0.22]	28 170 [28 030, 28 310]	9 159 [9 027, 9 292]

Table D.8: Mössbauer simulation parameters for the spectra shown in Figure D.30

Component	**1** ([(P_3^B)Fe($NNMe_2$)]$^+$)	**2**
g_x (= g_{max})	2.192	–
g_y (= g_{mid})	2.089	–
g_z (= g_{min})	2.005	–
δ (mm s^{-1})	0.31	0.92
$\lvert\Delta E_Q\rvert$ (mm s^{-1})	1.16	2.92
η	0	–
A_x (T)	0.04	–
A_y (T)	6.5	–
A_z (T)	17.4	–
β (HFC frame)	26.8°	–
FWHM (mm s^{-1})	0.48	0.80
Relative area	0.96	0.13

Table D.9: Mössbauer simulation parameters for the spectra shown in Figure D.31

Component	**1** ([(**P**$_3^{\mathbf{B}}$)**Fe(NNMe$_2$)**]$^-$)	**2**	**3**
g_x (= $g_{\max}$)	2.068	–	–
g_y (= g_{mid})	2.041	–	–
g_z (= $g_{\min}$)	2.006	–	–
δ (mm s^{-1})	0.39	0.43	0.90
$\lvert\Delta E_Q\rvert$ (mm s^{-1})	1.20	1.13	2.01
η	0.8	–	–
A_x (T)	39.0	–	–
A_y (T)	11.0	–	–
A_z (T)	12.1	–	–
FWHM (mm s^{-1})	0.44	1.03	0.41
Relative area	0.74	0.35	0.04

Table D.10: Fit parameters for T_2 measurments presented in Figure D.47. The 95% confidence interval is given below each parameter.

Compound	T_2 (ns)
$[(P_3{}^B)Fe(NNMe_2)][BAr^F{}_4]$	777 [742, 816]
$[(P_3{}^B)Fe(NAd)][BAr^F{}_4]$	284 [276, 292]

Table D.11: Pre-edge XANES fitting parameters of the spectrum shown in Figure D.48

Baseline							
	Amplitude	*Position (eV)*	*FWHM (eV)*	*Mixing*	*Offset*	*Slope*	*Twist*
	0.738322	7119.89	1.60865	0	0.0407	0.0228	0.0023

Components					
	Amplitude	*Position (eV)*	*FWHM (eV)*	*Mixing*	*LW-ratio*
1	0.09	7111.75	0.82	0	–
2	0.08	7113.08	0.96	0	–
3	0.14	7116.35	1.25	0	–

Table D.12: Comparison of experimental (XRD) and gas-phase optimized core structures of $[(P_3{}^B)Fe(NNMe_2)]^{+/0/-}$.

	$[(P_3{}^B)Fe(NNMe_2)]^+$		$(P_3{}^B)Fe(NNMe_2)$		$[(P_3{}^B)Fe(NNMe_2)]^-$	
	XRD	TPSS	XRD	TPSS	XRD	TPSS
d(Fe–N_α) (Å)	1.738(3)	1.727	1.680(2)	1.667	1.771(7)	1.756
d(Fe–B) (Å)	2.315(3)	2.313	2.534(3)	2.498	2.472(9)	2.447
d(Fe–P1) (Å)	2.2816(9)	2.294	2.2390(8)	2.238	2.280(2)	2.300
d(Fe–P2) (Å)	2.3168(9)	2.356	2.2670(8)	2.298	2.243(2)	2.236
d(Fe–P3) (Å)	2.2626(9)	2.290	2.2469(9)	2.220	2.233(2)	2.234
d(N_α–N_β) (Å)	1.252(4)	1.268	1.293(3)	1.303	1.27(1)	1.303
∠(P2FeP3) (°)	154.93(4)	154.33	125.03(3)	128.75	118.13(9)	118.60
∠(P1FeP3) (°)	96.10(3)	96.06	109.88(4)	108.52	112.22(9)	110.97
∠(P1FeP2) (°)	100.31(3)	100.08	104.28(3)	103.29	115.00(9)	115.88
∠(Fe$N_\alpha N_\beta$) (°)	159.7(3)	159.68	176.1(1)	174.34	161.6(6)	156.11
∠(BFeN_α) (°)	157.36(1)	157.94	168.91(1)	166.08	177.9(3)	175.95
Mean Error (‰)[a]	–	0.589	–	1.22	–	1.13

[a]The mean error is calculated as the mean value of $|p_{exp} - p_{calc}|/p_{exp}$ for each parameter p in the table, multiplied by 100.

Table D.13: Spin state energetics for $[(P_3{}^B)Fe(NNMe_2)]^+$ from geometry optimizations using the TPSS functional

S	ΔH (kcal mol^{-1})	ΔS (cal mol^{-1} K^{-1})
1/2	0	0
3/2	14.5	10.5
5/2	40.7	11.8

Table D.14: Comparison of experimental and DFT-predicted EPR properties of free *N*,*N*-dimethylhydrazyl radicals.

	$[H_2NNMe_2)]^+$		$HNNMe_2$		$[NNMe_2]^-$	
	Expt.[12,13]	DFT	Expt.[13,14]	DFT	DFT (ground state)	DFT (planar)
g_{iso}	2.0035	2.0034	2.0038	2.0037	2.0043	2.0042
$a_{iso}(^{14}N_\alpha)$ (MHz)	26.8	26.6	26.9	25.7	22.0	23.0
$a_{iso}(^{14}N_\beta)$ (MHz)	44.4	40.1	32.2	32.4	26.2	6.9
$a_{iso}(^{1}H_\alpha)$ (MHz)[a]	19.4	−6.6	38.4	−29.8	–	–
$a_{iso}(^{1}H_\gamma)$ (MHz)[b]	39.8	43.3	19.4	18.2	6.3	10.7
$a_{iso}(^{13}C)$ (MHz)	n.d.	−16.6	n.d.	−3.6/5.9	37.1	−21.6

[a]The discrepancy in the experimental and DFT-calculated values of $a_{iso}(^1H_\alpha)$ is likely due to the omission of environmental factors such as hydrogen bonding and other non-covalent interactions.
[b]In the DFT-predicted values, $a_{iso}(^1H_\gamma)$ was averaged over all protons of the N-CH_3 group.

Table D.15: Wavefunction composition (in terms of CI coefficients) from a state-specific CASSCF(10,10) calculation on the $^1\Gamma_{0,0}$ state of $(P_3{}^B)Fe(NNMe_2)$, in terms of the natural orbitals shown in Figure D.38.

	Configuration									
Weight	184	185	186	187	188	189	190	191	192	193
	$3d_{x^2-y^2}$	$3d_{xy}$	$3d_{xz} + \pi_N$	$3d_{z^2} + 2p_z$	$3d_{yz} + \pi^*_{NN}$	$3d_{yz} - \pi^*_{NN}$	$3d_{z^2} - 2p_z$	$3d_{xz} - \pi_N$	$3d'_1$	$3d'_2$
0.79807	2	2	2	2	2	0	0	0	0	0
0.04513	2	2	2	2	0	2	0	0	0	0
0.02251	2	2	2	0	2	0	2	0	0	0
0.01930	2	2	1	2	1	1	0	1	0	0
0.00851	2	2	2	1	1	1	1	0	0	0
0.00633	2	2	0	2	2	0	0	2	0	0
0.00468	2	2	1	1	2	0	1	1	0	0
0.00454	1	2	2	1	2	0	1	0	0	1
0.00438	2	1	2	1	2	0	1	0	1	0
0.00376	1	1	2	2	2	0	0	0	1	1
0.00371	2	1	2	1	2	0	1	0	0	1
0.00308	1	2	2	1	2	0	1	0	1	0
0.00270	2	0	2	2	2	0	0	2	0	0
0.00254	2	1	2	2	1	1	0	0	1	0

Table D.16: Wavefunction compositions (in terms of CI coefficients) from a SA-CASSCF(10,10) calculation on the 10 lowest-energy singlet states of $(P_3{}^B)Fe(NNMe_2)$, in terms of the natural orbitals shown in Figure D.40. Only the first 5 states are listed, with only the largest 4 configurations given.

State	Weight	Configuration									
		184	185	186	187	188	189	190	191	192	193
		$3d_{xz} + \pi_N$	$3d_{yz} + \pi^*_{NN}$	$3d_{z^2} + 2p_z$	$3d_{xy}$	$3d_{x^2-y^2}$	$3d_{xz} - \pi_N$	$3d_{yz} - \pi^*_{NN}$	$3d_{z^2} - 2p_z$	$3d'_1$	$3d'_2$
$^1\Gamma_{0,0}$	0.73869	2	2	2	2	2	0	0	0	0	0
	0.03858	2	0	2	2	2	0	2	0	0	0
	0.02466	2	2	0	2	2	0	0	2	0	0
	0.02102	1	1	2	2	2	1	1	0	0	0
$^1\Gamma_{0,1}$	0.69366	2	2	2	2	1	1	0	0	0	0
	0.04856	2	2	1	2	2	1	0	0	0	0
	0.04618	2	0	2	2	1	1	2	0	0	0
	0.02955	2	2	0	2	2	1	0	2	0	0
$^1\Gamma_{0,2}$	0.61429	2	2	2	1	2	1	0	0	0	0
	0.06375	2	2	2	2	1	0	1	0	0	0
	0.06016	2	2	2	1	2	0	1	0	0	0
	0.04594	2	0	2	1	2	1	2	0	0	0
$^1\Gamma_{0,3}$	0.27517	2	2	2	1	2	0	1	0	0	0
	0.16222	2	2	1	2	2	1	0	0	0	0
	0.10756	2	2	1	2	2	0	1	0	0	0
	0.08747	2	2	2	1	2	1	0	0	0	0
$^1\Gamma_{0,4}$	0.24561	2	2	1	2	2	0	1	0	0	0
	0.23534	2	2	2	2	1	0	1	0	0	0
	0.11832	2	2	2	1	2	0	1	0	0	0
	0.11374	2	2	1	2	2	1	0	0	0	0

Table D.17: NEVPT2 energies from a SA-CASSCF(10,10) calculation on the 10 lowest-energy singlet states of $(P_3{}^B)Fe(NNMe_2)$. Only the first 5 states are listed.

State	Energy (cm^{-1})	
	Expt.	NEVPT2
$^1\Gamma_{0,0}$	0	0
$^1\Gamma_{0,1}$	12 260	13 595.8
$^1\Gamma_{0,2}$	14 580	14915.2
$^1\Gamma_{0,3}$	17 830	17 382.2
$^1\Gamma_{0,4}$		19 278.3

Table D.18: Wavefunction composition (in terms of CI coefficients) from a state-specific CASSCF(10,10) calculation on the $^3\Gamma_{0,0}$ state of $(P_3{}^B)Fe(NNMe_2)$, in terms of the natural orbitals shown in Figure D.41.

	Configuration									
Weight	184	185	186	187	188	189	190	191	192	193
	π_N	$3d_{xy}$	$3d_{z^2} + 2p_z$	$3d_{yz} + \pi^*_{NN}$	$3d_{xz}$	$3d_{x^2-y^2}$	$3d_{yz} - \pi^*_{NN}$	$3d_{z^2} - 2p_z$	$3d'_1$	$3d'_2$
0.69631	2	2	2	2	1	1	0	0	0	0
0.06830	2	2	2	0	1	1	2	0	0	0
0.06280	2	2	2	1	1	1	1	0	0	0
0.04748	2	2	0	2	1	1	0	2	0	0
0.03549	2	2	1	2	1	1	0	1	0	0
0.01548	2	2	1	1	1	1	1	1	0	0
0.00750	2	1	1	2	1	1	0	1	1	0
0.00732	2	2	0	0	1	1	2	2	0	0
0.00603	2	1	2	1	1	1	1	0	1	0
0.00527	2	2	0	1	1	1	1	2	0	0
0.00446	2	2	1	0	1	1	2	1	0	0
0.00445	1	2	2	1	2	1	1	0	0	0
0.00418	2	0	2	2	1	1	0	0	2	0

Table D.19: Wavefunction composition (in terms of CI coefficients) from a state-specific CASSCF(11,10) calculation on the $^2\Gamma_{-,0}$ state of $[(P_3{}^B)Fe(NNMe_2)]^-$, in terms of the natural orbitals shown in Figure D.42.

	Configuration									
Weight	184	185	186	187	188	189	190	191	192	193
	π_N	$3d_{xy}$	$3d_{x^2-y^2}$	$3d_{z^2} + 2p_z$	$3d_{yz} + \pi^*_{NN}$	$3d_{xz}$	$3d_{yz} - \pi^*_{NN}$	$3d_{z^2} - 2p_z$	$3d'_1$	$3d'_2$
0.71930	2	2	2	2	2	1	0	0	0	0
0.06432	2	2	2	2	0	1	2	0	0	0
0.03124	2	2	2	2	1	1	1	0	0	0
0.02818	2	2	2	0	2	1	0	2	0	0
0.01185	2	2	1	1	2	1	0	1	1	0
0.01183	2	1	1	2	2	1	0	0	1	1
0.01154	2	1	2	1	2	1	0	1	0	1
0.00979	2	2	2	1	1	1	1	1	0	0
0.00966	2	2	2	1	2	1	0	1	0	0
0.00885	2	2	0	2	2	1	0	0	2	0
0.00842	2	2	1	2	1	1	1	0	1	0
0.00829	2	0	2	2	2	1	0	0	0	2
0.00778	2	1	2	2	1	1	1	0	0	1
0.00451	1	2	2	2	1	2	1	0	0	0
0.00409	2	2	1	2	2	1	0	0	1	0
0.00347	2	2	2	0	0	1	2	2	0	0
0.00329	2	1	2	2	2	1	0	0	0	1

Table D.20: Wavefunction composition (in terms of CI coefficients) from a state-specific CASSCF(9,10) calculation on the $^2\Gamma_{+,0}$ state of $[(P_3{}^B)Fe(NNMe_2)]^+$, in terms of the natural orbitals shown in Figure D.44.

	Configuration									
Weight	184	185	186	187	188	189	190	191	192	193
	$3d_{xy}$	$3d_{\sigma,1} + \sigma_L$	$3d_{yz} + \pi^*_{NN}$	$3d_{z^2} + 2p_z$	$3d_{\sigma,2}$	$3d_{z^2} - 2p_z$	$3d_{yz} - \pi^*_{NN}$	$3d_{\sigma,1} - \sigma_L$	$3d'_1$	$3d'_2$
0.84932	2	2	2	2	1	0	0	0	0	0
0.02116	2	2	2	0	1	2	0	0	0	0
0.01430	2	2	0	2	1	0	2	0	0	0
0.01321	2	1	1	2	1	0	1	1	0	0
0.01147	2	2	1	1	1	1	1	0	0	0
0.01072	2	1	2	1	1	1	0	1	0	0
0.00722	1	2	2	1	1	1	0	0	1	0
0.00656	1	2	1	2	1	0	1	0	1	0
0.00566	1	1	2	2	1	0	0	1	1	0
0.00541	2	2	1	2	1	0	1	0	0	0
0.00468	2	0	2	2	1	0	0	2	0	0
0.00403	2	2	2	1	1	1	0	0	0	0
0.00397	2	1	2	2	1	0	0	1	0	0
0.00320	0	2	2	2	1	0	0	0	2	0
0.00287	2	2	2	1	0	1	0	0	0	1

Table D.21: Wavefunction composition (in terms of CI coefficients) from a state-specific CASSCF(9,10) calculation on the $^4\Gamma_{+,0}$ state of $[(P_3{}^B)Fe(NNMe_2)]^+$, in terms of the natural orbitals shown in Figure D.46.

	Configuration									
Weight	184	185	186	187	188	189	190	191	192	193
	π_N	$3d_{yz} + \pi^*_{NN}$	$3d_{z^2} + 2p_z$	$3d_{xz}$	$3d_{x^2-y^2}$	$3d_{xy}$	$3d_{z^2} - 2p_z$	$3d_{yz} - \pi^*_{NN}$	$3d'_1$	$3d'_2$
0.77474	2	2	2	1	1	1	0	0	0	0
0.05316	2	2	1	1	1	1	1	0	0	0
0.04719	2	2	0	1	1	1	2	0	0	0
0.03563	2	1	2	1	1	1	0	1	0	0
0.02456	2	0	2	1	1	1	0	2	0	0
0.01859	2	1	1	1	1	1	1	1	0	0
0.00827	1	1	2	2	1	1	0	1	0	0
0.00266	2	1	0	1	1	1	2	1	0	0
0.00261	2	0	1	1	1	1	1	2	0	0

Table D.22: NEVPT2 energies of the doublet excited states of $[(P_3{}^B)Fe(NNMe_2)]^-$, and their contributions to the g-shifts from CASCI.[a]

State	NEVPT2 Energy (cm^{-1})	Δg_1	Δg_2	Δg_3
$^2\Gamma_{-,0}$	0	0	0	0
$^2\Gamma_{-,1}$	10654.9	−0.0129697	−0.0012106	-0.0045002
$^2\Gamma_{-,2}$	11227.1	0.0024437	0.0006445	0.0598511
$^2\Gamma_{-,3}$	11299.4	0.0003412	0.0329346	0.0002667
$^2\Gamma_{-,4}$	16337.2	0.0219329	0.0003345	0.0073102
$^2\Gamma_{-,5}$	18057.5	0.0005674	0.0110975	0.0000371
$^2\Gamma_{-,6}$	21860.3	−0.0004066	0.0006536	−0.0003774
$^2\Gamma_{-,7}$	22084.9	−0.0050565	−0.0078387	−0.0074183
$^2\Gamma_{-,8}$	22123.6	−0.0068105	−0.0000398	−0.0000452
$^2\Gamma_{-,9}$	24520.3	−0.0004940	−0.0001497	−0.0000481

[a]Using a SA-CASSCF(11,10) reference averaging over the first 10 doublet states.

Table D.23: NEVPT2 energies of the doublet excited states of $[(P_3{}^B)Fe(NNMe_2)]^+$, and their contributions to the g-shifts from CASCI.[a]

State	NEVPT2 Energy (cm^{-1})	Δg_1	Δg_2	Δg_3
$^2\Gamma_{+,0}$	0	0	0	0
$^2\Gamma_{+,1}$	7082.5	−0.0001191	0.0002972	0.2501078
$^2\Gamma_{+,2}$	11972.5	0.0000317	0.1221519	0.0008200
$^2\Gamma_{+,3}$	18195.9	0.0006481	0.0002731	0.0018648
$^2\Gamma_{+,4}$	20516.0	−0.0004503	−0.0013382	−0.0036448
$^2\Gamma_{+,5}$	20751.1	0.0048607	−0.0053158	0.0001804
$^2\Gamma_{+,6}$	23678.4	0.0028159	−0.0008443	−0.0019128
$^2\Gamma_{+,7}$	25174.6	−0.0003754	−0.0018492	−0.0006176
$^2\Gamma_{+,8}$	27428.8	−0.0045815	−0.0000001	−0.0001709
$^2\Gamma_{+,9}$	28140.1	−0.0001686	0.0005518	0.0000103

[a]Using a SA-CASSCF(9,10) reference averaging over the first 10 doublet states.

Table D.24: Overlap of magnetic orbitals from BS DFT calculations

State	% HF	$\langle\alpha\|\beta\rangle$	
		$\langle 3d_{z^2}\|B\ 2p_z\rangle$	$\langle 3d_{yz}\|\pi^*_{NN}\rangle$
$^2\Gamma_{+,0}$	0	0.994	0.988
	10	0.988	0.972
	25	0.933	0.903
$^4\Gamma_{+,0}$ [a]	0	0.981	0.962
	10	0.969	0.938
	25	0.906	0.889
$^1\Gamma_{0,0}$	0	–	–
	10	–	–
	25	0.847	0.822
$^3\Gamma_{0,0}$ [b]	0	0.976	0.949
	10	0.948	0.883
	25	0.861	0.743
$^2\Gamma_{-,0}$	0	0.995	0.971
	10	0.985	0.886
	25	0.935	0.702

[a] Computed in the quartet geometry.
[b] Computed in the triplet geometry.

Table D.25: Simulation parameters for HYSCORE spectra of $[(P_3{}^B)Fe(NNMe_2)]^{+/-}$

Charge	Nucleus	e^2qQ/h (MHz)	η	A_1 (MHz)	A_2 (MHz)	A_3 (MHz)	α (°)	β (°)	γ (°)
−	$^{14}N_\alpha$	−5.2	0.4	−3.9	−29.2	11.8	0	0	0
−	$^{15}N_\alpha$	−5.2	0.4	5.4	41.0	−16.5	0	0	0
−	$^{14}N_\beta$	−4.0	0.4	1.6	−5.7	1.6	0	30	30
−	$^{15}N_\beta$	−4.0	0.4	−2.2	8.0	−2.2	0	30	30
+	$^{14}N_\alpha$	−3.2	0.4	−10.7	−5.7	−0.1	10	0	0
+	$^{15}N_\alpha$	−3.2	0.4	15.0	8.0	1	10	0	0
+	$^{14}N_\beta$	−2.8	0.4	−1.5	−7.3	−1.5	0	35	0
+	$^{14}N_\beta$	−2.8	0.4	2.1	10.2	2.1	0	35	0

D.14 Coordinates of DFT-optimized Structures

Table D.26: Optimized coordinates for $(P_3{}^B)Fe(NNMe_2)$ ($S = 0$)

Atom	x (Å)	y (Å)	z (Å)
Fe	0.010810998	0.002966934	-0.001302714
N	-0.390510321	0.01898391	1.616401712
N	-0.827415331	0.030745215	2.843693045
C	-2.217758519	-0.274867715	3.194977816
H	-2.796318257	-0.344237735	2.276363525
H	-2.277763132	-1.227498025	3.737426271
H	-2.625876726	0.520787096	3.829905123
C	0.125689465	0.107068636	3.954449794
H	1.009317938	0.646884551	3.617606441
H	-0.340536458	0.644085961	4.787209705
H	0.419145748	-0.895186612	4.298737703
P	-0.698775353	2.086658112	-0.662662846
P	2.183726055	0.005201533	-0.53718875
P	-0.839837025	-1.981975676	-0.514319181
B	0.011910862	0.006228248	-2.498968646
C	1.355124973	0.808658815	-2.955421833
C	2.496134924	0.87872916	-2.114774737
C	2.608200731	2.105458591	-4.634959336
H	2.63764868	2.595859695	-5.610621927
C	3.731937145	2.145149235	-3.79560697
H	4.640892487	2.661477176	-4.110343221
C	-3.026528744	1.441475452	-4.611453717
H	-3.565292252	1.222216761	-5.536230437
C	1.443238002	1.444927836	-4.217360219
H	0.57186115	1.440904271	-4.876839362
C	-3.380196473	2.563095141	-3.84506715
H	-4.189858533	3.220951746	-4.166854058
C	3.677079762	1.525522836	-2.538273827
H	4.552095142	1.571415559	-1.891800966
C	-1.984991961	0.60001894	-4.190290509
H	-1.724658617	-0.269146707	-4.799174172
C	-0.0069553	-1.522218982	-3.032150923
C	-1.664815664	1.964298402	-2.221530293
C	0.521404793	3.502250432	-1.078255824

Atom	*x* (Å)	*y* (Å)	*z* (Å)
H	1.304418609	2.954672982	-1.618728776
C	-2.691956871	2.827622126	-2.650981748
H	-2.973662659	3.701651146	-2.060171146
C	0.369473573	-1.866191676	-4.352223211
H	0.747502689	-1.0892206	-5.020946587
C	0.305913819	-3.188257521	-4.81705624
H	0.618025174	-3.422703868	-5.837311806
C	-1.950136691	2.972820151	0.462019048
H	-2.128517115	3.940911542	-0.037547463
C	-1.28174303	0.840845908	-2.987761436
C	-0.454099498	-2.572607722	-2.196140624
C	-3.289801381	2.215308177	0.528651453
H	-3.989442669	2.751898567	1.189327955
H	-3.762867343	2.109029519	-0.454207519
H	-3.142321211	1.20759741	0.937677818
C	-0.523289211	-3.904299286	-2.656406285
H	-0.849039301	-4.709010782	-1.9943716
C	-0.141398661	-4.214360784	-3.96929229
H	-0.180008659	-5.246656585	-4.322209934
C	-0.02714879	4.577590603	-2.033945067
H	0.7659002	5.314552233	-2.239278922
H	-0.3483447	4.153379695	-2.991986982
H	-0.875548882	5.126478682	-1.595844536
C	-1.456243606	3.26228948	1.893391391
H	-1.223542164	2.331429326	2.422429689
H	-0.566741569	3.897775801	1.923113071
H	-2.25215694	3.780570842	2.452424581
C	-2.741351387	-2.082094356	-0.411941997
H	-2.955981137	-1.74082789	0.614004777
C	-3.410231778	-1.105619579	-1.388732151
H	-4.499049792	-1.097249294	-1.221189285
H	-3.029674204	-0.086703206	-1.269828936
H	-3.23067521	-1.406745059	-2.429827807
C	-3.345615767	-3.488081485	-0.599595203
H	-3.093901454	-3.895268907	-1.58945581
H	-3.02658587	-4.209142929	0.164440444
H	-4.443757449	-3.418425752	-0.54567529
C	1.183069536	4.182693628	0.136161206

Atom	*x* (Å)	*y* (Å)	*z* (Å)
H	0.522464742	4.941002012	0.580300085
H	1.469827881	3.474019591	0.923871163
H	2.094901945	4.704839076	-0.192722379
C	-0.434850634	-3.493401791	0.564263027
H	-0.953139092	-4.328918779	0.068424728
C	-0.980524849	-3.382561233	1.997575013
H	-0.465608508	-2.58020409	2.542558686
H	-2.060461698	-3.186517266	2.030267219
H	-0.79820139	-4.323985897	2.539620196
C	1.060204525	-3.833014068	0.605233763
H	1.216714438	-4.76662638	1.16889238
H	1.479899926	-3.971155839	-0.398277836
H	1.622338505	-3.036756795	1.11244379
C	2.946297917	0.938915657	0.944685194
H	2.063668974	1.510224431	1.267283347
C	4.082927436	1.953525635	0.720433282
H	5.026817999	1.477914292	0.42237746
H	3.820827456	2.700025576	-0.038706943
H	4.272775887	2.491514568	1.663658997
C	3.27787099	-0.041704333	2.088530631
H	3.427148005	0.516106776	3.027086344
H	2.462479936	-0.761049439	2.245953101
H	4.20089376	-0.605863958	1.899523893
C	3.371925712	-1.477324083	-0.725048179
H	3.177491653	-2.092810554	0.165059165
C	3.067234367	-2.312963001	-1.979754469
H	3.73729491	-3.187041849	-2.007879145
H	2.034808598	-2.670673676	-2.013477795
H	3.243316636	-1.724429239	-2.891186734
C	4.873921076	-1.123223938	-0.744501163
H	5.134867179	-0.555337442	-1.647718217
H	5.207088388	-0.555200472	0.13135129
H	5.456369246	-2.058286869	-0.77068719

Table D.27: Optimized coordinates for $(P_3{}^B)Fe(NNMe_2)$ ($S = 1$)

Atom	x (Å)	y (Å)	z (Å)
Fe	-0.12851598	0.062280363	-0.102780068
N	-0.234364418	0.169677327	1.655626079
N	-0.649450298	0.17454816	2.863959827
C	-2.023939068	-0.199651204	3.258588289
H	-2.522119616	-0.616452181	2.385732061
H	-1.991288604	-0.945423387	4.061912974
H	-2.569684518	0.681815297	3.61797156
C	0.217533277	0.591543768	3.983704175
H	1.1370962	0.993854975	3.564516919
H	-0.289225683	1.358804897	4.582435344
H	0.444818703	-0.264462999	4.632506783
P	-0.807626839	2.225927219	-0.749632016
P	2.283809981	-0.09921249	-0.457036762
P	-0.966868102	-2.052136895	-0.541967282
B	-0.018189098	0.015019443	-2.457683187
C	1.348898587	0.830494928	-2.838543717
C	2.497470084	0.871878518	-1.995188085
C	2.5951055	2.2204177	-4.459766538
H	2.618967008	2.748582858	-5.415800806
C	3.71518295	2.242735879	-3.615395786
H	4.617877241	2.785354117	-3.902908648
C	-3.072036159	1.299953194	-4.669639984
H	-3.589933436	1.02362838	-5.591102932
C	1.440602774	1.524498279	-4.072364252
H	0.572323957	1.535411435	-4.735846031
C	-3.485850021	2.430708979	-3.948271072
H	-4.325299395	3.035298083	-4.296798084
C	3.664892106	1.560812364	-2.390868693
H	4.540077441	1.582167683	-1.742912908
C	-2.002424039	0.517914379	-4.20712089
H	-1.705866039	-0.363975673	-4.779731744
C	-0.006326032	-1.515954165	-3.009773017
C	-1.74986475	1.975329975	-2.299481565
C	0.365271435	3.641060904	-1.212259702
H	0.875204425	3.203087736	-2.082402898
C	-2.817976557	2.769455319	-2.761595338

Atom	*x* (Å)	*y* (Å)	*z* (Å)
H	-3.154925208	3.639363142	-2.193247155
C	0.438593062	-1.836314143	-4.315633495
H	0.842136391	-1.043218323	-4.950062921
C	0.411059985	-3.149267622	-4.808333862
H	0.776939664	-3.361370156	-5.81564963
C	-2.081465535	3.053483849	0.368088359
H	-2.43733516	3.937737959	-0.185293202
C	-1.311262914	0.82919963	-3.012027475
C	-0.49254477	-2.589099217	-2.220301463
C	-3.283267093	2.119153065	0.592870252
H	-4.008200197	2.590988569	1.275123021
H	-3.800420675	1.89036015	-0.347477335
H	-2.958882461	1.169390495	1.038867111
C	-0.524618129	-3.912569473	-2.709296988
H	-0.87983365	-4.731049859	-2.079488433
C	-0.070216795	-4.195852881	-4.004667733
H	-0.080956608	-5.221510975	-4.378436205
C	-0.336178181	4.929589672	-1.675176414
H	0.416824039	5.630895532	-2.068128479
H	-1.060500321	4.739677687	-2.477643915
H	-0.853401872	5.438033287	-0.847250524
C	-1.490204531	3.537739145	1.70489452
H	-0.965458043	2.725649617	2.224915177
H	-0.781983896	4.363811147	1.567298571
H	-2.297446011	3.900904476	2.36070741
C	-2.861491663	-2.201188727	-0.494841955
H	-3.116199364	-1.878191998	0.529022442
C	-3.514659009	-1.217794688	-1.477542358
H	-4.608308669	-1.227281901	-1.346703228
H	-3.157198611	-0.19232524	-1.331137551
H	-3.294841457	-1.496649364	-2.516928787
C	-3.427892108	-3.616485699	-0.715371993
H	-3.154637176	-3.99830873	-1.709565051
H	-3.092161748	-4.340801686	0.038929788
H	-4.528068099	-3.581107337	-0.668902614
C	1.43873714	3.939043187	-0.152880352
H	1.03927259	4.510678756	0.696114811
H	1.879813328	3.015624669	0.23575477

Atom	*x* (Å)	*y* (Å)	*z* (Å)
H	2.244665221	4.537596003	-0.604008469
C	-0.517300153	-3.529974195	0.549710062
H	-0.993505368	-4.399701664	0.069643257
C	-1.075914972	-3.400974639	1.977172108
H	-0.618231787	-2.545346965	2.491693931
H	-2.166873943	-3.274727623	1.998327136
H	-0.836680711	-4.307747522	2.554810615
C	0.994713873	-3.786898109	0.595590479
H	1.20453828	-4.690043792	1.190481719
H	1.414403025	-3.936666786	-0.406535306
H	1.513944604	-2.941401339	1.067031807
C	3.05916538	0.757476873	1.053412226
H	2.197676352	1.356402265	1.389130893
C	4.261260956	1.711380625	0.919331765
H	5.180513096	1.199214296	0.607124097
H	4.064848222	2.522930874	0.208409214
H	4.46283948	2.174033469	1.899815629
C	3.29845033	-0.299347038	2.152933222
H	3.49363018	0.19895618	3.116129751
H	2.419273926	-0.947098592	2.278495446
H	4.167802413	-0.935020581	1.935284898
C	3.478389675	-1.560058991	-0.754897155
H	3.295841497	-2.22533142	0.102622021
C	3.123134694	-2.322988028	-2.041840503
H	3.774320318	-3.206675388	-2.135730642
H	2.082386554	-2.660205242	-2.059629438
H	3.281439526	-1.692058265	-2.927721121
C	4.982232671	-1.221758812	-0.781126625
H	5.225848449	-0.545048987	-1.61169451
H	5.342682389	-0.773011698	0.151981899
H	5.554597266	-2.150258135	-0.940892526

Table D.28: Optimized coordinates for $[(P_3{}^B)Fe(NNMe_2)]^-$

Atom	x (Å)	y (Å)	z (Å)
Fe	-0.005092376	-0.005895153	0.025536424
N	0.083855081	-0.114140551	1.775774862
N	-0.373142023	-0.089207148	2.995472732
C	-1.713276662	0.384299472	3.377686584
H	-2.215514035	0.718371382	2.472723548
H	-1.6446341	1.219588947	4.089735916
H	-2.291928839	-0.42412762	3.848039026
C	0.4833868	-0.456600265	4.127720757
H	1.300878283	-1.073051297	3.755843202
H	-0.099461882	-1.024473683	4.86673922
H	0.898721038	0.433418276	4.62925606
P	-0.964724703	1.961255376	-0.421813696
P	-1.108089586	-1.878977464	-0.499888163
P	2.23044693	0.027460233	-0.51381437
B	-0.016239277	0.014116215	-2.421812863
C	1.33891221	-0.733673884	-2.953037645
C	1.431303198	-1.352273392	-4.223876236
H	0.559788464	-1.342325183	-4.88430435
C	2.58789431	-2.028955796	-4.645727261
H	2.608949136	-2.515272438	-5.625313431
C	3.706208413	-2.104347336	-3.801725459
H	4.600545115	-2.651590123	-4.110675234
C	3.657862795	-1.478584326	-2.545025398
H	4.522225225	-1.553732653	-1.880723138
C	2.49327555	-0.803352831	-2.126742808
C	3.34153525	-0.922716921	0.702759318
H	4.32081521	-1.060392656	0.216144749
C	3.540823546	-0.097115466	1.988228263
H	2.563036562	0.184443274	2.401155092
H	4.112770187	0.824102496	1.810006966
H	4.085176957	-0.686602777	2.74638828
C	2.775845776	-2.312056739	1.028855523
H	3.427528091	-2.829156209	1.755237606
H	2.708858916	-2.937314474	0.129001126
H	1.768325357	-2.218015293	1.456948527
C	3.418547425	1.540488826	-0.756264207

Atom	*x* (Å)	*y* (Å)	*z* (Å)
H	3.247568568	2.151930974	0.143471527
C	3.02638388	2.372311727	-1.986767911
H	3.643638765	3.285854906	-2.036174202
H	1.973594994	2.66828402	-1.973933857
H	3.193983576	1.80119524	-2.911499808
C	4.92844236	1.237080971	-0.849793198
H	5.151941428	0.617720456	-1.730683234
H	5.33621221	0.734989981	0.03790327
H	5.481235928	2.185031533	-0.971972631
C	-1.330207307	-0.79011196	-2.963441651
C	-1.923639208	-0.572632607	-4.230968123
H	-1.52028292	0.207651919	-4.881744487
C	-3.042794728	-1.300861056	-4.666162973
H	-3.48435675	-1.090618756	-5.644626021
C	-3.605579	-2.286068942	-3.840417552
H	-4.48651728	-2.84652843	-4.16386517
C	-3.036468128	-2.52919843	-2.579877636
H	-3.493010197	-3.279104345	-1.929388682
C	-1.919426037	-1.786448235	-2.144456362
C	-0.285795656	-3.634058862	-0.570706099
H	0.268951565	-3.687694531	0.380215445
C	-1.228672014	-4.853700963	-0.655567761
H	-1.841872546	-4.814742422	-1.568182796
H	-1.898923957	-4.962323573	0.207421147
H	-0.622021863	-5.77408688	-0.71411777
C	0.721878157	-3.745118547	-1.723168406
H	1.241419956	-4.71762039	-1.675086056
H	1.473385982	-2.952152114	-1.697482627
H	0.211657583	-3.683499942	-2.695259377
C	-2.570171279	-2.410926379	0.60797145
H	-3.033332822	-3.275226123	0.106751886
C	-3.648452338	-1.324867313	0.711363956
H	-4.439137734	-1.630035713	1.41863355
H	-4.117249023	-1.139416771	-0.263646905
H	-3.220309231	-0.376474159	1.05895624
C	-2.08645233	-2.875875172	1.993838007
H	-1.499931874	-2.093233987	2.488417896
H	-1.450150613	-3.769442073	1.928250876

Atom	*x* (Å)	*y* (Å)	*z* (Å)
H	-2.946850906	-3.12697123	2.638100238
C	-0.066920651	1.557424952	-2.948375854
C	0.338406406	1.936898818	-4.252199385
H	0.750723617	1.177582079	-4.922437726
C	0.274579074	3.266645125	-4.697170022
H	0.616613943	3.523752354	-5.703843617
C	-0.209079535	4.270216344	-3.843218148
H	-0.246073248	5.311459223	-4.173756654
C	-0.626723491	3.924277894	-2.548267445
H	-0.979076291	4.71311643	-1.879343533
C	-0.553295507	2.587272303	-2.103771526
C	-2.879227261	2.21805345	-0.400118427
H	-3.189285471	1.731896609	0.540835341
C	-3.423213863	3.660511774	-0.394851021
H	-3.112757354	4.202258993	-1.30066347
H	-3.110246153	4.244883097	0.481230721
H	-4.527090212	3.636466984	-0.395252447
C	-3.519472363	1.450405281	-1.566793274
H	-4.61756898	1.43536347	-1.460596831
H	-3.160121606	0.417754591	-1.620835558
H	-3.277236453	1.932413327	-2.525200183
C	-0.508680999	3.485404188	0.640793275
H	-1.01289121	4.342167381	0.166476436
C	-1.007361204	3.376251462	2.089353201
H	-0.459355021	2.582221897	2.613108694
H	-2.081598034	3.154514362	2.158040616
H	-0.825816278	4.322258576	2.627942532
C	0.998070469	3.768404548	0.646805598
H	1.215569638	4.666983934	1.250229653
H	1.386168655	3.936966179	-0.36506098
H	1.539011983	2.919279207	1.087455804

Table D.29: Optimized coordinates for $[(P_3{}^B)Fe(NNMe_2)]^+$ ($S = 1/2$)

Atom	x (Å)	y (Å)	z (Å)
Fe	-0.006894038	0.013201438	0.019524574
N	-0.669030577	0.062572307	1.613636964
N	-1.531716342	0.095744476	2.542623167
C	-1.11311518	0.192737019	3.958530905
H	-0.025806948	0.228030086	3.989410912
H	-1.480678524	-0.679835104	4.508144558
H	-1.5367311	1.09865183	4.404901503
C	-2.992384449	0.029399015	2.310066187
H	-3.162056077	-0.165839669	1.253070575
H	-3.456263641	0.977492895	2.602240382
H	-3.41768142	-0.772525078	2.922484229
P	2.190409463	0.008566605	-0.638703931
P	-0.526443769	-2.266914039	-0.262805771
P	-0.343508745	2.259254249	-0.277150008
B	0.016338175	0.022800392	-2.293775753
C	2.330496753	-1.0851379	-2.088245118
C	1.146361345	-0.970382319	-2.856007962
C	1.080959514	-1.677838346	-4.076133369
H	0.179140094	-1.622234287	-4.690306542
C	2.152918017	-2.482067704	-4.498927812
H	2.080410635	-3.036800679	-5.436068918
C	3.317754744	-2.582171773	-3.719620008
H	4.147227357	-3.207766674	-4.052225548
C	3.417100859	-1.869898996	-2.513398976
H	4.334063964	-1.934910025	-1.924612594
C	3.305872752	-0.642863684	0.737115964
H	4.326406587	-0.381096231	0.416561652
C	3.108714135	1.591513607	-1.251326588
H	2.297900053	2.326911415	-1.344261234
C	3.007916448	0.048099007	2.082741702
H	1.987681023	-0.194566021	2.412294848
H	3.094997975	1.140021488	2.037861767
H	3.714711212	-0.310165477	2.845681179
C	3.229885923	-2.165688326	0.920816855
H	3.955420305	-2.475706684	1.687889657
H	3.45410004	-2.716855548	0.001008772

Atom	*x* (Å)	*y* (Å)	*z* (Å)
H	2.232144197	-2.461320653	1.269005869
C	4.185231341	2.170341823	-0.309944125
H	5.048706063	1.498242651	-0.209752733
H	3.819124853	2.405648432	0.696565491
H	4.558458483	3.108318031	-0.746665776
C	3.718963955	1.425715025	-2.658451168
H	4.124129442	2.398259702	-2.976141288
H	2.980167949	1.109005581	-3.402062907
H	4.545231697	0.70145845	-2.662185502
C	-1.491336339	-0.503986352	-2.144416865
C	-1.885592095	-1.559593511	-1.257980452
C	-3.242375374	-1.945152354	-1.159305106
H	-3.54714723	-2.719932966	-0.457587984
C	-4.21334731	-1.361517652	-1.981136644
H	-5.251592421	-1.690146471	-1.914151683
C	-3.838306715	-0.36952461	-2.903672775
H	-4.584291457	0.069100729	-3.568486444
C	-2.512468445	0.069189912	-2.952716477
H	-2.243915272	0.867799938	-3.645739828
C	-1.329504782	-3.058840506	1.246462597
H	-2.066699725	-2.289860248	1.521073149
C	0.215339955	-3.675888977	-1.29477314
H	0.935808436	-3.151861985	-1.931494359
C	1.006256026	-4.728330418	-0.491324841
H	0.356241592	-5.390368214	0.093390961
H	1.743215948	-4.282319561	0.184774298
H	1.556374522	-5.361092012	-1.203230338
C	-0.820514653	-4.339034968	-2.22484654
H	-0.30220217	-5.074699337	-2.858260582
H	-1.302867077	-3.608347341	-2.885559576
H	-1.603193525	-4.873141233	-1.670190822
C	-0.32543544	-3.182838254	2.413175617
H	-0.860548258	-3.45298779	3.336373721
H	0.214997423	-2.243572552	2.587191976
H	0.413356381	-3.973016479	2.225057008
C	-2.095197587	-4.389552754	1.06778123
H	-1.415095735	-5.234597929	0.910198986
H	-2.810122502	-4.378559314	0.237536885

Atom	*x* (Å)	*y* (Å)	*z* (Å)
H	-2.659623303	-4.597231415	1.989657396
C	0.105696211	1.525732731	-2.871215516
C	-0.130313379	2.657753827	-2.044934689
C	-0.178955048	3.960101256	-2.591760255
H	-0.355243895	4.825912392	-1.955602065
C	0.02082878	4.157777774	-3.964242007
H	-0.014195359	5.165686965	-4.379888853
C	0.282641144	3.055239651	-4.792130282
H	0.452322539	3.20305375	-5.860049815
C	0.328881196	1.763927924	-4.247566854
H	0.537338375	0.919082439	-4.90749431
C	0.883854618	3.253694821	0.769794479
H	1.75214632	2.58146586	0.764376586
C	-2.028315545	2.914300723	0.246960942
H	-2.075913888	2.618739515	1.30761449
C	0.425289795	3.349144606	2.238660165
H	1.25660509	3.72597968	2.852566546
H	0.139053848	2.366264025	2.633174181
H	-0.417378059	4.04097829	2.369602002
C	1.363273853	4.615775087	0.23307483
H	0.567811749	5.372301368	0.231681432
H	1.766456915	4.541242433	-0.784611769
H	2.167594029	4.989362722	0.884868319
C	-3.164465147	2.211488102	-0.512646706
H	-4.134377476	2.491900127	-0.074768641
H	-3.073333307	1.119326903	-0.48797935
H	-3.172844924	2.518160696	-1.567038353
C	-2.223101004	4.442523961	0.170226298
H	-2.24597719	4.788629471	-0.871212216
H	-1.453903352	5.006945673	0.709774221
H	-3.195362537	4.699120025	0.617724647

Table D.30: Optimized coordinates for $[(P_3{}^B)Fe(NNMe_2)]^+$ ($S = 3/2$)

Atom	x (Å)	y (Å)	z (Å)
Fe	0.114729567	-0.048266611	0.097517887
N	0.000694085	-0.072180277	1.88515728
N	-0.471935433	0.006753745	3.048818202
C	0.351565176	-0.266512096	4.252986706
H	1.34071064	-0.574455418	3.921696725
H	-0.11873068	-1.059582676	4.843360763
H	0.417875391	0.640288596	4.863506592
C	-1.896105804	0.319771437	3.328442484
H	-2.385041734	0.529542117	2.379455267
H	-1.961152167	1.183854626	3.997709105
H	-2.364981867	-0.540467597	3.81778223
P	2.495497634	0.110013869	-0.568719549
P	-0.949538334	-2.206104715	-0.37295833
P	-0.676410487	2.205675051	-0.320040002
B	0.015729349	0.093060295	-2.295365406
C	2.405947465	-0.994800215	-2.022031679
C	1.174637861	-0.9238431	-2.725712688
C	1.03463273	-1.7248628	-3.885820405
H	0.096638197	-1.693580081	-4.444595007
C	2.070395755	-2.560860139	-4.327799732
H	1.937854369	-3.165311084	-5.226781447
C	3.276228494	-2.627184219	-3.609813533
H	4.081772184	-3.281954333	-3.945040109
C	3.444525633	-1.841729007	-2.460664602
H	4.390004121	-1.889940028	-1.917586922
C	3.721674332	-0.679138749	0.618324826
H	4.708284767	-0.662649388	0.125573818
C	3.351230512	1.654355841	-1.272887466
H	2.503347879	2.195102606	-1.720666838
C	3.809537325	0.093071888	1.952406933
H	2.807133094	0.212589388	2.387498547
H	4.260252144	1.084541328	1.850836173
H	4.4246252	-0.478835205	2.663194754
C	3.322351653	-2.138335658	0.910048453
H	4.061140197	-2.594252177	1.58593616
H	3.265137613	-2.753511433	0.004743408

Atom	*x* (Å)	*y* (Å)	*z* (Å)
H	2.343061856	-2.168225225	1.410037055
C	4.017752726	2.572853514	-0.229828863
H	4.960686713	2.143483007	0.135811855
H	3.379257509	2.787824895	0.636473818
H	4.262464814	3.532734785	-0.707643439
C	4.353082702	1.337236967	-2.400227406
H	4.782052705	2.280605964	-2.770703617
H	3.879177437	0.827416275	-3.246565907
H	5.187370491	0.715212488	-2.042932386
C	-1.505070979	-0.433974683	-2.413530919
C	-2.059467683	-1.512169601	-1.654615735
C	-3.382397323	-1.941831268	-1.883008966
H	-3.810609121	-2.749745811	-1.295375098
C	-4.17707404	-1.342179071	-2.869605081
H	-5.197554128	-1.691632454	-3.032203343
C	-3.646876572	-0.299091747	-3.640876638
H	-4.249560019	0.169584383	-4.420695641
C	-2.342072956	0.150625167	-3.400007202
H	-1.951988052	0.973905411	-3.999775853
C	-2.002878641	-2.905350233	1.028212984
H	-2.666623452	-2.05180043	1.246271904
C	-0.048534243	-3.655303366	-1.18449138
H	0.753083078	-3.147218419	-1.735490044
C	0.616618493	-4.615826952	-0.179444233
H	-0.116288918	-5.259072429	0.324961748
H	1.201090871	-4.089729183	0.584815704
H	1.304711262	-5.275661626	-0.727880634
C	-0.909880045	-4.414977952	-2.211264582
H	-0.284148502	-5.173398249	-2.705575363
H	-1.304084742	-3.747295443	-2.987013874
H	-1.755507084	-4.936248232	-1.743013054
C	-1.131715405	-3.17776053	2.27986635
H	-1.760877192	-3.146634625	3.182034779
H	-0.318120252	-2.452535862	2.391125519
H	-0.684540929	-4.178235273	2.235072095
C	-2.880541178	-4.151641459	0.771847046
H	-2.266964171	-5.035668573	0.557384601
H	-3.60129914	-4.034752214	-0.04313331

Atom	*x* (Å)	*y* (Å)	*z* (Å)
H	-3.454775857	-4.368807299	1.685407083
C	0.171628378	1.599037002	-2.81793406
C	-0.343687821	2.678001028	-2.052742201
C	-0.454559277	3.970616408	-2.608846557
H	-0.855548906	4.79871239	-2.026931928
C	-0.014962337	4.21271088	-3.918492985
H	-0.095672516	5.214902954	-4.341614756
C	0.552808664	3.170022677	-4.667240208
H	0.9165645	3.361248439	-5.67834312
C	0.641740902	1.880521934	-4.121571393
H	1.061063343	1.071677733	-4.723984445
C	0.454552274	3.287531122	0.759881659
H	1.335834197	2.634206231	0.853050822
C	-2.423299931	2.698824686	0.165368514
H	-2.389623844	2.617508833	1.263491028
C	-0.110540801	3.494250702	2.178746722
H	0.675474563	3.916832528	2.822009497
H	-0.443917125	2.555057491	2.634679637
H	-0.951403356	4.201641306	2.183325964
C	0.931637851	4.628712543	0.173170161
H	0.11113981	5.353157566	0.078346886
H	1.403425835	4.513080285	-0.809274026
H	1.675835505	5.067379687	0.855380671
C	-3.463181353	1.68891217	-0.351610007
H	-4.451346707	1.93144608	0.067281935
H	-3.212042068	0.657224702	-0.070127547
H	-3.543664921	1.721383583	-1.445613814
C	-2.835711388	4.139650598	-0.19266897
H	-2.947149046	4.260313836	-1.278325993
H	-2.121870264	4.890507873	0.170846478
H	-3.811779296	4.361056792	0.264970372

Table D.31: Optimized coordinates for $[(P_3{}^B)Fe(NNMe_2)]^+$ ($S = 5/2$)

Atom	x (Å)	y (Å)	z (Å)
Fe	0.267596611	0.060055928	0.106699207
N	0.409586857	-0.241222443	1.918569354
N	0.2800223	0.380567154	3.090200181
C	1.486095262	0.55320657	3.913597815
H	2.249607896	1.061357353	3.323007175
H	1.877281395	-0.414199831	4.260350832
H	1.232425754	1.168765304	4.780397525
C	-0.952628588	0.130803938	3.857810382
H	-1.79537242	0.110028173	3.165357428
H	-1.088985985	0.935397548	4.586015028
H	-0.903563697	-0.827743534	4.392796151
P	2.633757263	-0.085262116	-0.665495207
P	-1.045322408	-2.070617368	-0.448118657
P	-0.9394094	2.192134685	-0.16838588
B	0.014174732	0.054915433	-2.340244367
C	2.417945015	-1.082268306	-2.186101971
C	1.152443891	-0.95751715	-2.827642467
C	0.931999366	-1.741585317	-3.987142245
H	-0.031645018	-1.673955722	-4.49573225
C	1.916673014	-2.597497013	-4.501615666
H	1.715524161	-3.181747246	-5.401043831
C	3.154473279	-2.710254779	-3.851841084
H	3.92232931	-3.383062201	-4.2360101
C	3.400087255	-1.956383195	-2.694521037
H	4.361470249	-2.067712651	-2.19107367
C	3.885180183	-1.04673712	0.343501353
H	4.711247899	-1.260409943	-0.35364899
C	3.522593106	1.455219451	-1.284109669
H	2.870135827	1.752534166	-2.118669623
C	4.467541804	-0.259316067	1.530001704
H	3.677545976	0.070898271	2.214989303
H	5.043402885	0.617425271	1.210929248
H	5.148087421	-0.912240004	2.096080139
C	3.274023988	-2.379976394	0.808625245
H	4.031203066	-2.967509506	1.348735497
H	2.921229895	-2.983179546	-0.03740398

Atom	*x* (Å)	*y* (Å)	*z* (Å)
H	2.428607103	-2.198979118	1.487484534
C	3.533592018	2.614785432	-0.271240454
H	4.204612327	2.425097198	0.576179071
H	2.53057234	2.812123938	0.125584561
H	3.883331299	3.530511032	-0.770059792
C	4.924013301	1.167273889	-1.853434327
H	5.311110536	2.076451124	-2.337349225
H	4.904686713	0.372972277	-2.611240285
H	5.639311231	0.885574061	-1.067891032
C	-1.479721184	-0.439671719	-2.600695804
C	-2.047434042	-1.531598067	-1.889174405
C	-3.273001356	-2.088543412	-2.309347195
H	-3.693051294	-2.954575664	-1.804195249
C	-3.970437361	-1.546022192	-3.398968476
H	-4.920615484	-1.984876986	-3.706386099
C	-3.441710094	-0.44338201	-4.085082672
H	-3.981814986	-0.012239938	-4.929708642
C	-2.208944919	0.095816869	-3.690057466
H	-1.794416993	0.939884915	-4.244843724
C	-2.222430717	-2.491786706	0.970223978
H	-2.668886949	-1.501200417	1.161397922
C	-0.165740756	-3.644073156	-1.034690601
H	0.711477424	-3.220268364	-1.546520503
C	0.341451343	-4.554731552	0.100406458
H	-0.478918201	-5.12774313	0.552664703
H	0.858317662	-4.003833668	0.894509898
H	1.051585325	-5.281515394	-0.321095429
C	-0.951242781	-4.465164724	-2.07567659
H	-0.316770588	-5.29581942	-2.420387269
H	-1.227150335	-3.867776394	-2.952361434
H	-1.865916316	-4.902698862	-1.651894586
C	-1.44591408	-2.903536137	2.243055125
H	-2.086567344	-2.732300953	3.120520618
H	-0.522167206	-2.324747148	2.36867863
H	-1.196774038	-3.970773223	2.229640328
C	-3.372766187	-3.49377359	0.732347362
H	-3.00815784	-4.459398834	0.356802252
H	-4.136796696	-3.112406066	0.047377193

Atom	*x* (Å)	*y* (Å)	*z* (Å)
H	-3.871143459	-3.686938953	1.694634089
C	0.241284345	1.621162781	-2.592055936
C	-0.38059699	2.664270806	-1.842559883
C	-0.440765922	3.976923469	-2.35850867
H	-0.935425275	4.768599196	-1.799170825
C	0.149224319	4.288998471	-3.59134605
H	0.092482203	5.306942027	-3.97888548
C	0.830430424	3.29233402	-4.306137097
H	1.311625647	3.531376532	-5.255978199
C	0.877132441	1.98264564	-3.808200737
H	1.38024182	1.208500463	-4.391081552
C	-0.110463211	3.355353651	1.092227662
H	0.786871415	2.775409013	1.36069866
C	-2.780690611	2.497362523	0.041185327
H	-2.90226873	2.433541445	1.133561131
C	-0.953780008	3.497430773	2.375410458
H	-0.333249843	3.953862327	3.160383699
H	-1.308771183	2.532169417	2.753775615
H	-1.820554773	4.154451085	2.219675153
C	0.360535687	4.738735926	0.606733214
H	-0.483007792	5.403010025	0.37390791
H	1.009749555	4.680827073	-0.274517904
H	0.935077941	5.21445133	1.415975204
C	-3.644343385	1.391923363	-0.588474433
H	-4.699141165	1.57062126	-0.33227461
H	-3.368341767	0.396915597	-0.218834758
H	-3.558457521	1.380014353	-1.682157503
C	-3.245293198	3.892297817	-0.420523304
H	-3.18218878	3.98842964	-1.512778388
H	-2.66833847	4.707193363	0.036415064
H	-4.29895097	4.032328363	-0.1363712

Table D.32: Optimized coordinates for $(P_3{}^B)$Fe(NAd)

Atom	x (Å)	y (Å)	z (Å)
Fe	0.003512004	0.003270525	-0.015312398
P	2.134167241	-0.018373256	-0.745469564
P	-1.072534521	1.855897036	-0.780212243
P	-1.072146288	-1.840624874	-0.79610432
N	0.002358029	0.101070105	1.622345479
C	-2.136449892	-1.444302824	-2.236621922
C	-2.94575275	1.684173854	-1.074698026
H	-3.019100222	0.640847203	-1.406756647
C	-0.109461033	-0.93423581	5.314931005
H	-0.272270926	-1.918946141	5.782059969
C	0.056489717	0.262828056	3.060430727
C	-1.458023733	-0.556434518	-3.106202418
C	-0.400965727	2.541080792	-2.345002369
C	3.343146291	-0.623240872	0.591583562
H	3.211265876	0.198256033	1.311447381
C	1.249193091	-0.926282963	-3.119642256
C	0.785321516	1.900718582	-4.359922809
H	1.247660213	1.133699045	-4.986293396
C	-0.179521534	-1.098839246	3.778940785
H	0.576046847	-1.822045697	3.437252535
H	-1.166315018	-1.486641134	3.490740967
C	-0.979813553	1.414788306	5.094581985
H	-1.766926029	2.120904477	5.404984542
C	-1.036725835	1.255017994	3.557240076
H	-0.875927767	2.232538398	3.082679439
H	-2.025792188	0.888496638	3.241340786
C	-2.268985616	-2.658382826	0.412315008
H	-2.872008017	-3.327118535	-0.222762853
B	0.00300374	-0.007153499	-2.692470552
C	-2.108421851	-0.192987681	-4.306102712
H	-1.616312987	0.49708376	-4.996065899
C	-3.391326498	-0.675405959	-4.617963879
H	-3.879194394	-0.366142504	-5.544879555
C	-0.398546604	3.882229732	-2.776091863
H	-0.86507505	4.662856746	-2.179649387
C	-4.056072645	-1.533549546	-3.730184031

Atom	*x* (Å)	*y* (Å)	*z* (Å)
H	-5.061782083	-1.892087945	-3.957648157
C	0.213557369	4.232855851	-3.990174437
H	0.227413446	5.276440778	-4.310269473
C	1.500658918	0.981057461	5.043014632
H	2.492367929	1.374381615	5.319257694
C	1.445700943	0.808676699	3.506839795
H	2.225964223	0.106161639	3.181976621
H	1.633183119	1.770415338	3.006742835
C	0.809128319	3.239790354	-4.781322697
H	1.292406935	3.508068248	-5.723349086
C	-1.014582429	3.270485089	0.480113452
H	-1.482957976	2.776076104	1.342456349
C	1.296148458	-1.603430508	-4.360425862
H	0.421947929	-1.577034758	-5.016133463
C	1.276419786	-0.388253224	5.720899012
H	1.337336363	-0.284534089	6.816846012
H	2.066396361	-1.095082205	5.417756556
C	2.392060374	-0.987293429	-2.285723306
C	2.910887926	1.682780364	-1.172936016
H	2.017185766	2.259175755	-1.448078262
C	-0.236462978	-3.377555805	-1.566133476
H	0.108295534	-2.958674484	-2.521049527
C	3.538747572	-1.700823266	-2.687802613
H	4.422391297	-1.741488108	-2.054891387
C	2.430608213	-2.329632441	-4.754558023
H	2.437358596	-2.858044714	-5.710414267
C	-1.563817677	-3.530124394	1.466925584
H	-2.283125193	-3.83511464	2.243418157
H	-0.748537187	-2.986396591	1.958614943
H	-1.145586583	-4.444339193	1.028507724
C	0.404423108	1.968728414	5.498452897
H	0.567227318	2.956104564	5.035549366
H	0.452498356	2.111099414	6.590661871
C	-1.208479138	0.048045695	5.774297789
H	-1.185157695	0.160711986	6.870799783
H	-2.203637808	-0.345897803	5.509771033
C	3.553940786	-2.380944868	-3.915344521
H	4.438519737	-2.948089995	-4.211315757

Atom	*x* (Å)	*y* (Å)	*z* (Å)
C	-3.217237962	-1.640166047	1.058785735
H	-3.937644881	-2.156077623	1.713590228
H	-3.785841732	-1.081753172	0.304053049
H	-2.653133783	-0.91660638	1.662341028
C	4.849082768	-0.695808217	0.246197199
H	5.437174647	-0.606108945	1.173405427
H	5.185777202	0.09238231	-0.436643892
H	5.107318896	-1.666034811	-0.199352756
C	0.42918478	3.616143289	0.864339442
H	0.444888736	4.318908574	1.712986755
H	0.957975036	4.092758226	0.025839656
H	0.9760202	2.710879094	1.148707456
C	-3.421583529	-1.928529874	-2.539647261
H	-3.946446783	-2.596685376	-1.853511286
C	3.578376206	2.403187254	0.017145946
H	3.702284316	3.468563453	-0.23144934
H	4.577250761	2.002163029	0.235425473
H	2.98404944	2.349439238	0.937529274
C	2.926409155	-1.915137934	1.313418334
H	3.464818776	-1.993704065	2.271888379
H	3.185505186	-2.80365629	0.722474106
H	1.848236664	-1.931243488	1.515542636
C	-3.765167935	1.806161619	0.226023114
H	-4.775907497	1.402165117	0.059820827
H	-3.881231433	2.84851292	0.551710854
H	-3.312048789	1.239625325	1.049749906
C	3.846163749	1.689680188	-2.397511924
H	4.15357702	2.726067113	-2.609731641
H	3.349064546	1.297172219	-3.29171567
H	4.75865833	1.099025153	-2.231027204
C	-3.529468453	2.550934312	-2.206658437
H	-4.588576484	2.286047454	-2.353355336
H	-3.00608179	2.377095383	-3.154353659
H	-3.483830647	3.626807618	-1.986842962
C	1.009738379	-3.894331458	-0.835944985
H	1.473777321	-4.697004915	-1.430396856
H	0.786470853	-4.301754842	0.159027497
H	1.747912755	-3.096169295	-0.725048228

Atom	*x* (Å)	*y* (Å)	*z* (Å)
C	-1.804412057	4.574845811	0.219604253
H	-1.984501842	5.075189773	1.184512644
H	-2.778134451	4.419499318	-0.256621738
H	-1.231346681	5.27972548	-0.396919649
C	-1.208465876	-4.524984381	-1.901515678
H	-0.686531659	-5.258278738	-2.536492217
H	-2.087905335	-4.17622362	-2.458673014
H	-1.551754646	-5.060952738	-1.004559968
C	0.183152502	1.525853635	-3.138270503

Table D.33: Optimized coordinates for $[H_2NNMe_2]^{\bullet+}$

Atom	*x* (Å)	*y* (Å)	*z* (Å)
N	0.002140723	-0.227830199	0.068113865
N	0.001255257	0.139868521	1.353763862
C	-1.274259026	0.083415953	2.075053543
H	-1.462422508	-0.942081808	2.416163825
H	-2.078770527	0.411157557	1.413273764
H	-1.20370385	0.752161243	2.933219314
C	1.277456616	0.091216667	2.074411659
H	1.201901194	0.756597595	2.934738459
H	2.079061665	0.427546152	1.413382178
H	1.473928561	-0.933843025	2.412133791
H	-0.868056817	-0.092218029	-0.441172901
H	0.871308711	-0.086850626	-0.441481358

Table D.34: Optimized coordinates for $[HNNMe_2]^{\bullet}$

Atom	*x* (Å)	*y* (Å)	*z* (Å)
N	0.068782452	-0.289434885	0.032028036
N	-0.006298886	0.18902767	1.294845964

Atom	x (Å)	y (Å)	z (Å)
C	-1.246197817	0.093800222	2.061525663
H	-1.433319396	-0.93615032	2.407575967
H	-2.078731832	0.411416876	1.427068612
H	-1.192026334	0.753937479	2.932706126
C	1.234747225	0.072717512	2.049685149
H	1.239508164	0.806420848	2.861514276
H	2.061388675	0.267721864	1.365762434
H	1.355180254	-0.935580547	2.477229908
H	-0.901957291	-0.303642103	-0.312817025

Table D.35: Optimized coordinates for $[NNMe_2]^{\bullet-}$ (equilibrium geometry)

Atom	x (Å)	y (Å)	z (Å)
N	0.002653537	0.563092209	0.072917181
N	0.000902085	-0.138168564	1.207758404
C	-1.217959239	-0.07307122	2.051595921
H	-1.214157112	-0.825703569	2.864950203
H	-2.068880836	-0.24401924	1.387367116
H	-1.344574277	0.934766521	2.515460065
C	1.217729397	-0.07423346	2.054642084
H	1.34413564	0.933484521	2.518817054
H	2.070123188	-0.245977259	1.392510179
H	1.211192449	-0.826868451	2.8679725

Table D.36: Optimized coordinates for $[NNMe_2]^{\bullet-}$ (C_{2v} geometry)

Atom	x (Å)	y (Å)	z (Å)
N	0.081217201	-0.524737396	-0.045950265
N	0.01699979	-0.181008715	1.254269798
C	-1.234497399	-0.062367517	1.990770474
H	-1.301349884	-0.75221979	2.868247591

Atom	x (Å)	y (Å)	z (Å)
H	-2.029924566	-0.304376221	1.283294227
H	-1.411757706	0.964826107	2.398404961
C	1.189871946	0.137082484	2.05796805
H	1.169114353	1.173116053	2.480754686
H	2.051039081	0.041156944	1.393852181
H	1.326397185	-0.544781949	2.933718297

References

(1) Spek, A. *Acta Crystallogr. D* **2009**, *65*, 148–155.

(2) La Mar, G. N.; Horrocks, W. D.; Holm, R. H., *NMR of Paramagnetic Molecules: Principles and Applications*; Academic Press: New York, 1973.

(3) Kaupp, M.; Bühl, M.; Malkin, V. G., *Calculation of NMR and EPR Parameters: Theory and Applications*; Wiley-VCH: Weinheim, 2004.

(4) Lemon Christopher, M.; Huynh, M.; Maher Andrew, G.; Anderson Bryce, L.; Bloch Eric, D.; Powers David, C.; Nocera Daniel, G. *Angew. Chem. Int. Ed.* **2016**, *55*, 2176–2180.

(5) Thompson, N. B.; Green, M. T.; Peters, J. C. *J. Am. Chem. Soc.* **2017**, *139*, 15312–15315.

(6) Carvajal, C.; Tölle, K. J.; Smid, J.; Szwarc, M. *J. Am. Chem. Soc.* **1965**, *87*, 5548–5553.

(7) Gütlich, P.; Gaspar, A. B.; Garcia, Y. *Beilstein J. Org. Chem.* **2013**, *9*, 342–391.

(8) Harris, D. C.; Bertolucci, M. D., *Symmetry and Spectroscopy: An Introduction to Vibrational and Electronic Spectroscopy*; Dover Publications: New York, 1989.

(9) De Lorenzi, L.; Fermeglia, M.; Torriano, G. *J. Chem. Eng. Data* **1996**, *41*, 1121–1125.

(10) Del Castillo, T. J.; Thompson, N. B.; Peters, J. C. *J. Am. Chem. Soc.* **2016**, *138*, 5341–5350.

(11) Rittle, J.; Peters, J. C. *J. Am. Chem. Soc.* **2016**, *138*, 4243–4248.

(12) Smith, P.; Stevens, R. D.; Kaba, R. A. *J. Phys. Chem.* **1971**, *75*, 2048–2055.

(13) Hermosilla, L.; Calle, P.; García de la Vega, J. M.; Sieiro, C. *J. Phys. Chem. A* **2006**, *110*, 13600–13608.

(14) Malatesta, V.; Ingold, K. U. *J. Am. Chem. Soc.* **1973**, *95*, 6110–6113.

Appendix E

ISOMER SHIFT TRENDS IN ^{57}FE MÖSSBAUER SPECTRA OF PHOSPHINE IRON COMPLEXES: THE ROLE OF COVALENCY

E.1 Introduction

Mössbauer spectroscopy is an invaluable tool for electronic structure assignment in the organometallic, inorganic, and bioinorganic chemistry of iron. In principle, Mössbauer spectroscopy can be used to extract the electric field gradient ($\boldsymbol{Q}$), the ^{57}Fe hyperfine coupling tensor ($\boldsymbol{A}$) (when relevant), and the electron density at each Fe nucleus in a given sample, the latter of which is given by the isomer shift (δ). A complete determination of the $\boldsymbol{Q}$ and $\boldsymbol{A}$ tensors generally requires low temperature (~4.2 K) and variable field (0 to 10 T) measurements, whereas δ can be conveniently measured at liquid nitrogen temperature (77 K) in low-field ($\leq$ 50 mT). Although δ is a direct measure of a core property of the Fe nucleus, it is sensitive to changes in the electronic structure at the valence level and can be correlated to chemical properties.[1]

Although δ is sensitive to spin state, coordination number, and coordination geometry, perhaps the most widespread use of isomer shift measurements is in the assignment of the formal oxidation state of Fe.[2,3] Even in cases where covalency may obscure the oxidation state, analyses performed on sets of homologous compounds allow for self-consistent assignments to be made within each set. For example, despite the high covalency of the Fe–S bond, the isomer shifts of [FeS] clusters with tetrahedral Fe sites are linearly correlated to the Fe valence determined from crystallographic data.[4] Similarly, the isomer shifts of $\{\mathrm{FeNO}\}^n$ complexes (in the Enemark-Feltham (EF) notation) have been rationalized by a correlation between δ and oxidation state in a family of isostructural compounds,[5] which was used to support an unusual spin-coupling scheme for a low spin $\{\mathrm{FeNO}\}^7$ complex.[5,6]

Phosphine-iron complexes constitute an important class of catalysts for C–C cross cou-

pling and the reduction of a wide variety of unsaturated substrates, including both CO_2 and N_2.[7,8] However, compared with complexes ligated by hard N- and O-atom donors, there are relatively few systematic Mössbauer studies reported for Fe complexes with primary coordination spheres dominated by phosphine ligands. Much of the data in the literature has been collected with chelating bisphosphine ligands (PP), typically of *trans*-$[(PP)_2Fe(L)(L')]^k$ or $[(PP)Fe(L)(L')]^k$ complexes of Fe(II).[9,10] From these studies, the bonding properties of a wide variety of ligands have been analyzed within the theory of partial isomer shifts. However, the simplicity of these ligands generally precludes the isolation of series of isostructural complexes of varying oxidation state,[11,12] which has hampered an analysis of δ in terms of the formal oxidation state of Fe in phosphine complexes.

In recent years, we have prepared a family of isostructural Fe complexes supported by the tetradentate P_3^E ligands (E = B, Si) that enforce pseudo-C_3 symmetry with an equatorial phosphine ligand field. These complexes range over at least four oxidation states and vary in spin state from $S = 0$ to $3/2$, and their Mössbauer data therefore constitute an ideal set for elucidating correlations between δ and the valency of Fe. In this appendix, we analyze a set of 18 such complexes, and determine a semi-empirical correlation between δ and a parameter describing the effective covalency between the Fe and its ligands. As we shall see, the Fe–P covalency proves to be the dominant factor in determining δ.

E.2 Results and Discussion

E.2.1 Preliminary Remarks

The Mössbauer isomer shift, for a given reference sample, is a simple function of the electron density at the nucleus,[1]

$$\delta = \alpha \frac{\Delta R}{R}(\rho_0 - C) \tag{E.1}$$

where α is a positive constant depending upon the identity of the Mössbauer nuclide, $\Delta R/R$ relates to the relative change of the nuclear radius during the transition to its excited state, ρ_0 is the ground state electron density at the nucleus, and C is a constant depending on the

choice of reference. For ^{57}Fe, $\Delta R/R$ is negative, and thus a decrease in δ corresponds to an increase in the electron density at the Fe nucleus. Only electrons with $l = 0$ penetrate the nucleus to a significant extent, and hence ρ_0 may be decomposed into,

$$\rho_0 = \rho_0(1s) + \rho_0(2s) + \rho_0(3s) + \rho_0(val) \tag{E.2}$$

where $\rho_0(n\text{s})$ is the electron density at the nucleus due to the Fe ns electrons and, in complexes, ρ_0(val) (the "valence contribution") is due to the population of the Fe 4s orbital due to mixing with filled, σ-symmetry ligand orbitals. In molecules, the contributions to ρ_0 from the 3s and valence electrons tend to determine δ, as $\rho_0(1s)$ and $\rho_0(2s)$ are approximately constant.[13] Since both of these terms are sensitive to the electronic structure at the valence level, it is possible to correlate δ to chemical properties of the molecule.

It is typically observed that δ correlates inversly with the formal oxidation state of the Fe ion.[2,3] In a previous report, Ye and co-workers analyzed an "unusual" positive correlation between δ and the formal oxidation state in a redox series of $[(P_3{}^{Si})Fe(N_2)]^k$ complexes.[14] In their analysis, the origin of this correlation was determined to be the π-accepting character of the axial N_2 ligand, which results in increasing covalency with reduction of the Fe center. This translates into shorter Fe–N bonds and greater mixing with the vacant Fe 4s orbital, which in turn reduces δ. It was concluded that no correlation existed between δ and the Fe–Si or Fe–P bonding, and, moreover, "that such a positive isomer shift correlation can be observed only for low-valent iron complexes involving strong π-acceptors, whereas for compounds containing σ- and/or π-donors, the isomer shift-oxidation state correlation likely follows the usual trend with a negative slope".[14] As described below, this analysis is essentially correct. However, when considering a larger set of $(P_3{}^{E})$Fe complexes featuring axial ligands that vary in donor properties from strongly π-accepting, to purely σ-donating, and to strongly π-donating, it becomes apparent that the nature of the axial ligand does not adequately explain this positive correlation. Instead, it turns out that it is the π-accepting character of the Fe–P interaction that gives rise to the trend.

E.3 Trends in the Isomer Shifts of (P_3^E)Fe compounds

Table E.1 contains collected characterization data for 18 (P_3^E)Fe complexes for which both crystallographic (or EXAFS) and Mössbauer data are available.[i] To begin our analysis, we consider the simple subset of $[(P_3^{Si})Fe(L)]^k$ (L = CO, N_2; $k = 1+, 0, 1-$) complexes featuring axial ligands generally considered to be redox innocent at the potentials observed for these Fe complexes.[15,16] At the outset, we assign a number n in the EF scheme $\{FeSi\}^n$ to each complex to avoid ambiguities in decomposing the Fe–Si linkage. Correlating δ to n reveals two trends. First, in agreement with previous observations,[14] for a given ligand, δ is inversely proportional to n. Second, within each valence state, δ for the CO complex is systematically reduced by ~0.2 mm s^{-1} from δ for the corresponding N_2 complex (Figure E.1, left).

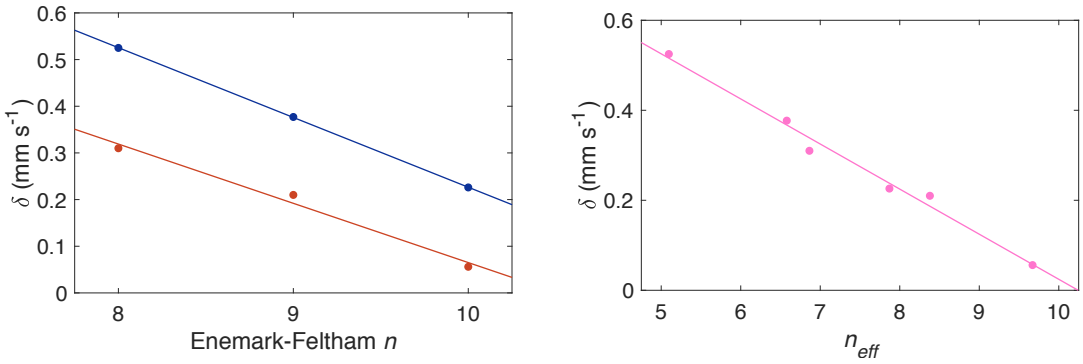

Figure E.1: Plots of δ versus n (left) and n_{eff} (right) for for $[(P_3^{Si})Fe(L)]^k$ (L = CO, N_2; $k = 1+, 0, 1-$).

An intuitive explanation of the second trend is that the Fe–C bond is more covalent than the Fe–N bonds in each set of isoelectronic complexes. Indeed, an examination of the crystallographic bond lengths (Table E.1) reveals that comparing L = N_2 to L = CO within a valence state, the Fi–Si distance lengthens by 0.02(1) Å, the Fe–P distance shortens by 0.01(1) Å, while the Fe–L distance shortens by 0.05(2) Å. The actual increase in the covalency of the Fe–L bond must be even larger than indicated by the crystallographic distances, as C is a larger atom than N (*vide infra*).

[i] With the exception of (P_3^B)Fe(NAd), for which we have calculated a structure using DFT methods.

Table E.1: Collected Characterization Data for $[(P_3{}^E)Fe(L)]^k$ Complexes

Complex	Ligand Type[a]	n[b]	S	Fe–L (Å)	Fe–E (Å)	Fe–P_{avg} (Å)	δ (mm s^{-1})	$\lvert\Delta E_Q\rvert$ (mm s^{-1})	Ref.
$[(P_3{}^{Si})Fe(CO)][BAr^F{}_4]$	σ, π_a	8	1	1.842	2.325	2.390	0.31	4.1	[15]
$(P_3{}^{Si})Fe(CO)$	σ, π_a	9	1/2	1.769	2.294	2.276	0.21	1.3	[15]
$[Na(THF)_3][(P_3{}^{Si})Fe(CO)]$	σ, π_a	10	0	1.733	2.259	2.186	0.056	0.53	[15]
$[(P_3{}^{Si})Fe(N_2)][BAr^F{}_4]$	σ, π_a	8	1	1.913	2.298	2.391	0.53	2.6	[17]
$(P_3{}^{Si})Fe(N_2)$	σ, π_a	9	1/2	1.819	2.271	2.291	0.38	0.71	[16, 17]
$[Na(THF)_3][(P_3{}^{Si})Fe(N_2)]$	σ, π_a	10	0	1.763	2.253	2.203	0.23	0.98	[17]
$(P_3{}^{Si})Fe(CN)$	σ, π_a	8	1	1.973	2.306	2.342	0.44	1.7	[18]
$[Na(12\text{-}c\text{-}4)_2][(P_3{}^{Si})Fe(CN)]$	σ, π_a	9	1/2	1.949	2.242	2.236	0.31	1.4	[18]
$[Na(Solv)_x][(P_3{}^B)Fe(N_2)]$	σ, π_a	9	1/2	1.776	2.31	2.260	0.40	1.0	[19, 20]
$[(P_3{}^B)Fe(N_2)]^{2-}$ [c]	σ, π_a	10	0	1.77	2.34[d]	2.18	0.26	0.82	[21]
$(P_3{}^{Si})Fe(Cl)$	σ, π_d	8	1	2.282	2.305	2.352	0.56	0.34	[16, 22]
$[(P_3{}^B)Fe(N_2H_4)][BAr^F{}_4]$	σ	7	3/2	2.205	2.392	2.448	0.70	2.3	[23, 24]
$[(P_3{}^B)Fe(NH_3)][BAr^F{}_4]$	σ	7	3/2	2.280	2.434	2.449	0.68	1.9	[23, 24]
$(P_3{}^B)Fe(NH_2)$	σ, π_d	7	3/2	1.918	2.449	2.390	0.60	1.5	[23, 24]
$(P_3{}^B)Fe(OTf)$	σ, π_d	7	3/2	2.051	2.386	2.435	0.71	2.62	[21]
$(P_3{}^B)Fe(NAd)$[d]	σ, π_d	6	0	1.641	2.677	2.267	0.04	1.4	[24]
$[(P_3{}^B)Fe(NAd)][BAr^F{}_4]$	σ, π_d	5	1/2	1.660	2.770	2.360	0.15	1.3	[19, 24]
$[(P_3{}^B)Fe(N)][OTf]$[c]	σ, π_d	4	0	1.54	2.75	2.25	−0.15	6.2	[21]

Unless noted otherwise, all distances are from crystallographic data. All Mössbauer parameters were measured at 80 K.
[a] $\sigma = \sigma$-donating; $\pi_a = \pi$-accepting; $\pi_d = \pi$-donating.
[b] EF number for the {FeE} unit.
[c] Distances from EXAFS.
[d] Distances from a DFT-optimized geometry.

There are many ways one might attempt to account for this difference in covalency and obtain a unified correlation. In the theory of partial isomer shifts, δ is given by a sum of δ_{L} due to each ligand, so it should be possible to correct for the differences in axial ligand L by subtracting δ_{L} from the observed isomer shift. Using the values $\delta_{\mathrm{CO}} = -0.13$ mm s^{-1} and $\delta_{\mathrm{N_2}} = 0.09$ mm s^{-1} determined for low-spin O_{h} Fe(II),[10] we find that, while $\delta - \delta_{\mathrm{L}}$ are identical within experimental error for the $\{\mathrm{FeSi}\}^8$ complexes, they still differ by 0.05 mm s^{-1} for the $\{\mathrm{FeSi}\}^{9,10}$ pairs. This deviation may stem from a dependence of δ_{L} on the valence state of Fe. Alternatively, $\chi_P^{\mathrm{Fe}}/\chi_P^{\mathrm{L}}$ (where χ_P is the Pauling electronegativity) can be used as a weighting factor for n to produce an effective valence assignment that corrects for the propensity of the axial ligand atom to donate electrons to Fe. Weighting n by $\chi_P^{\mathrm{Fe}}/\chi_P^{\mathrm{L}}$ results in an excellent linear correlation ($r^2 = 0.97$); however, this weighting factor cannot discriminate between ligands with the same ligating element but differing electronics (e.g., CO vs CN^-; $\mathrm{N_2}$ vs NR^{2-}).

A natural reporter for the metal–ligand covalency is the crystallographic bond distance, but corrected in order to account for size differences between atoms. To this end, we introduce a covalency parameter,

$$\gamma \equiv d_{\mathrm{L}} - r_{W,\mathrm{L}} \tag{E.3}$$

where d_L is the crystallographically-observed Fe–L distance and $r_{W,i}$ is the van der Waals radius of the ligating atom, as tabulated by Bondi.[25] To justify the form of γ, we note that if one assumes a van der Waals radius for Fe, $r_{W,\mathrm{Fe}}(n)$, at a particular valence state n, then for an arbitrary atom i at van der Waals contact with Fe,

$$\gamma_i = (r_{W,i} + r_{W,\mathrm{Fe}}(n)) - r_{W,i} = r_{W,\mathrm{Fe}}(n) \tag{E.4}$$

Thus γ provides a size-consistent covalency scale within valence states, depending on the fact that the Bondi radii accurately reflect non-bonded contact distances in crystal structures.[26] We note that, although we cannot truly normalize γ (as $r_{W,\mathrm{Fe}}(n)$ is not known),

empirically, γ is limited below by 0 and above by 1.[ii] Weighting the EF n by the factor $(1 - \gamma)$ produces an effective Fe valence assignment, n_{eff}, where molecules with a less covalently-bound axial ligand will have higher effective valence. Plotting δ versus n_{eff} for the series above produces a single inverse correlation ($r^2 = 0.97$; Figure E.1, right). Extending this analysis to the full set of $(P_3{}^E)$Fe complexes in Table E.1, with a range of π-accepting, σ-donating, and π-donating axial ligands, preserves the linearity of this correlation ($r^2 = 0.95$), if $[(P_3{}^B)\text{Fe(NAd)}]^{+/0}$ and $[(P_3{}^B)\text{Fe(N)}]^+$ are excluded (Figure E.2). The generality of this inverse correlation demonstrates that the nature of the bonding to the axial ligand is not its primary determinant, contrary to the conclusions of Ye and co-workers.[14]

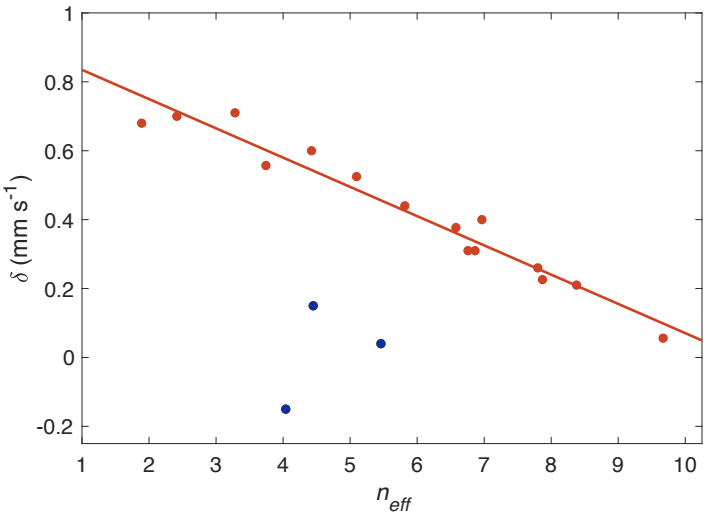

Figure E.2: Plot of δ versus n_{eff}. The data points corresponding to $[(P_3{}^B)\text{Fe(NAd)}]^{+/0}$ and $[(P_3{}^B)\text{Fe(N)}]^+$ are highlighted in blue.

In a previous work, we observed that the spin state S in a variety of $(P_3{}^B)$Fe complexes was linearly correlated with δ.[24] An examination of Table E.1 demonstrates that n and spin multiplicity ($M = 2S + 1$) are related by $M = 9 - n$, suggesting n and M are equivalent reporters of the electron density at the Fe nucleus. Correlating δ to the product γM produces

[ii]For example, from the Cambridge Structural Database,[27] 99.7% of bonded Fe–C distances, 99.9% of bonded Fe–N distances, and 99.9% of bonded Fe–Cl distances fall within this range, regardless of the formal Fe oxidation state.

a single curve (Figure E.3), which is well-modeled by the power law,

$$\delta = \delta_0 + (\gamma M - c)^{\beta} \tag{E.5}$$

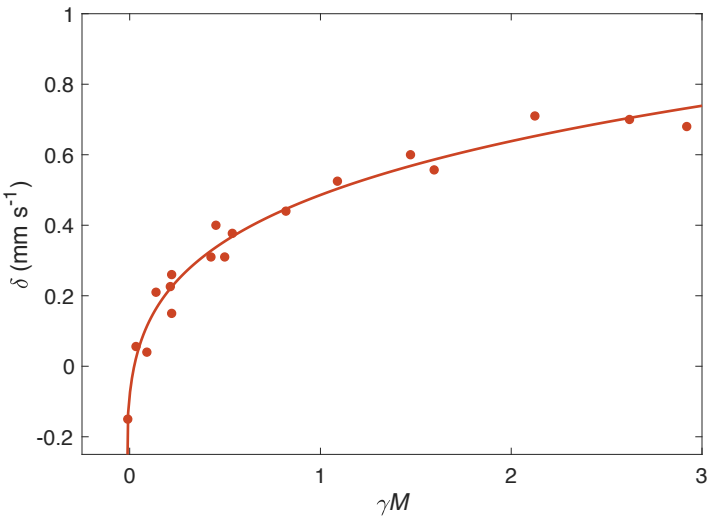

Figure E.3: Plot of δ versus γM. The solid line is a fit to the power law E.5, with $\delta_0 = -0.5179$ mm s^{-1}, $c = -0.01811$, and $\beta = 0.2069$ (RMSE = 0.04 mm s^{-1}).

Gratifyingly, this trend includes the complexes [(P_3^B)Fe(NAd)]$^{+/0}$ and [(P_3^B)Fe(N)]$^+$, which were outliers in the correlation between δ and n_{eff}. The correlation with δ suggests that the term γM is a reporter of the overall metal–ligand covalency in (P_3^E)Fe complexes. Bond strength–bond length relationships have found widespread use in the characterization of solid state materials, where it is assumed that the validity of such correlations relies on the high ionic character of the bonding. In particular, the power law of Brown and Shannon originally introduced for metal oxide materials has been generalized to a wide variety of materials,[28,29] and relationships of a similar form have been extended to systems with a high degree of covalent bonding.[30] As the factor γ, by design, is a measure of the axial ligand covalency, the apparent power law relationship between δ and the product γM implies that M serves as a measure of the Fe–P or Fe–E bond covalency, or both.

Excluding complexes [(P_3^B)Fe(NAd)]$^{+/0}$ and [(P_3^B)Fe(N)]$^+$, the average Fe–P distances tracks closely with the EF n assignment (and hence M), with an average decrease of

0.08 Å per n (r^2 = 0.94; Figure E.4, left). This can be attributed to the electron-accepting nature of phosphine ligands. While both the Si and B atoms tend to accept electron density as well, the size-corrected crystallographic distances are not reliably correlated to n (Figure E.4, right). We conclude that there are two primary determinants of δ in this family of (P_3^E)Fe complexes: (i) across valence states of Fe, δ is primarily determined by the covalency of the Fe–P bonding, and (ii) within a valence state, δ is determined by the covalency of the axial ligand Fe–L bonding. The fact that the isomer shifts of the complexes [(P_3^B)Fe(NAd)]$^{+/0}$ and [(P_3^B)Fe(N)]$^+$ do not correlate well with n_{eff}, but do with γM, indicates that the relative weights of these two factors is reversed for these complexes—i.e., the axial metal ligand interaction dominates the low values of δ for these species.

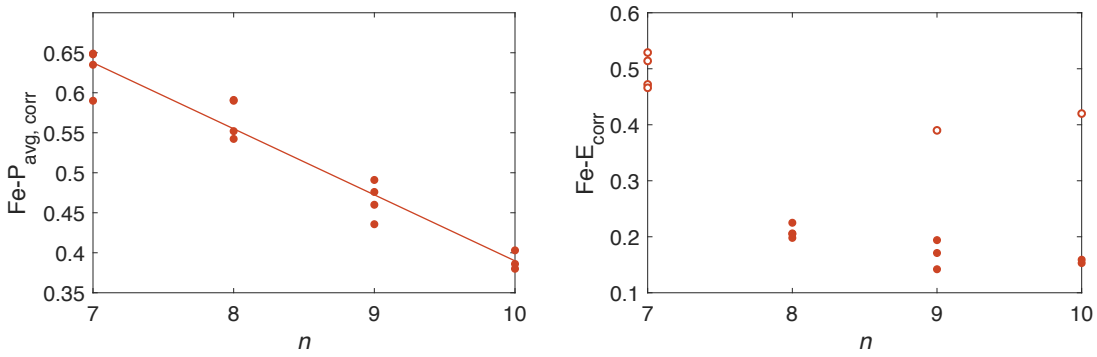

Figure E.4: Correlations between n and the Fe–P/Fe–E bond distances. These distances have been corrected by subtraction of the corresponding van der Waals radii (cf. Equation E.3). In the plot to the right, the Fe–Si complexes are shown as filled circles, while the Fe–B complexes are shown as open circles.

E.4 DFT Analysis of Isomer Shift Trends

In order to support the conclusions made above, DFT calculations have been carried out on a subset of the complexes in Table E.1. DFT methods predict experimental isomer shifts with a great degree of accuracy,[13,21,31] which justifies the analysis of the DFT (Kohn-Sham) wavefunction in terms of the decomposition in Equation E.2.

First, we consider the effects of the axial ligand L within a single valence state by examining the set of complexes [(P_3^{Si})Fe(L)]^k (L = CO, N_2; k = 1+, 0, 1−). As expected,

for a given valence state, the decrease in δ associated with swapping the N_2 ligand for a CO ligand is a result of increases in both ρ_0(3s) and ρ_0(val), with $\Delta\rho_0$(val) accounting for 88(8)% of the observed effect (Table E.2). We can analyze these changes in terms of several factors:[13,14] (i) *d-shielding*: for free ions, it is observed that increases in the metal 3d orbital population screens the s-electrons from the nuclear potential, resulting in more diffuse orbitals, which naturally have lower density at the nucleus; (ii) *4s population*: in complexes, the Fe 4s orbitals become populated as a result of overlap between the filled, totally-symmetric ligand orbitals. Greater metal-ligand covalency should result in an increase of Fe 4s admixture into the filled MOs; (iii) *s-orbital contraction*: complementary to d-shielding, as metal-ligand distances contract, the ligand-based electron density repels the metal s-electrons, resulting in more contracted orbitals with higher density at the nucleus.

From Table E.2, swapping the N_2 ligand for CO results in small but reliable increases in the Fe 3d population, which may account for the small decreases in ρ_0(1s/2s), but rules out d-shielding *(i)* in the observed trend in δ. On the other hand, small increases in the Fe 4s population suggest that *(ii)* may explain the increase in ρ_0(val); in order to extricate *(ii)* from *(iii)*, we have tabulated the covalency-corrected valence contribution, $\rho_0(\text{val})_{\text{corr}}$,[13] which are seen to be essentially identical for each isoelectronic pair. This indicates that the increase in ρ_0(val) is principally due to greater admixture of Fe 4s orbital character in the more covalent Fe–C bond, rather than a contraction of the 4s orbital. However, the increase in ρ_0(3s) can only be explained in terms of a contraction of the 3s orbital *(iii)* as a result of the increased covalency. Thus, the systematic decrease in δ observed for the CO series relative to the N_2 can be interpreted in terms of the greater covalency of the Fe–C bond, in which the dominant effect is greater Fe 4s orbital character in the filled, totally symmetric Fe–L bonding orbital. This is borne out by a population analysis of the L-derived a_1 bonding orbital, which shows significantly lower covalency for the N_2 complex versus the CO complex, and a similar difference in the overall Fe 4s character (Table E.3). In fact, the difference in Fe 4s character between the isoelectronic pairs is remarkably constant

Table E.2: Comparison of ρ_0 and Fe orbital populations for isoelectronic $[(P_3{}^{Si})Fe(L)]^n$ complexes (L = N_2, CO)

	$N_2{}^+$	CO^+	$\Delta(CO-N_2)$	N_2	CO	$\Delta(CO-N_2)$	$N_2{}^-$	CO^-	$\Delta(CO-N_2)$
ρ_0(1s)	10703.878	10703.828	−0.050	10703.831	10703.786	−0.045	10703.779	10703.743	−0.036
ρ_0(2s)	973.950	973.927	−0.023	973.947	973.924	−0.023	973.940	973.928	−0.012
ρ_0(3s)	137.919	138.089	0.170	138.008	138.119	0.111	138.114	138.189	0.074
ρ_0(val)	4.135	4.496	0.360	4.374	4.794	0.420	4.675	5.078	0.403
ρ_0	11819.883	11820.340	0.457	11820.159	11820.623	0.464	11820.508	11820.937	0.429
Fe 3d pop	6.55	6.56		6.68	6.71		6.73	6.80	
Fe 4s pop.	0.38	0.41		0.35	0.38		0.32	0.35	
$\rho_0(val)_{corr}{}^a$	11.0	10.9		12.7	12.6		14.8	14.6	

$^a\rho_0(val)_{corr} = \rho_0(val)/(4s\ pop.)$

Table E.3: Population analysis of the ligand based bonding a_1 orbital in $[(P_3{}^{Si})Fe(L)]^n$ complexes (L = N_2, CO)

	$N_2{}^+$	CO^+	N_2	CO	$N_2{}^-$	CO^-
% L	83.5	68.1	80.4	64.7	77.6	62.3
% Fe	15.1	28.4	17.5	31.1	19.3	31.5
% Fe 4s	2.4	4.8	2.6	4.8	2.5	4.3

across the redox series (2.1(3)%), which tracks well with the nearly constant isomer shift difference. As seen in Figure E.5, this is directly proportional to the difference in the electron density at the Fe nucleus for each MO.

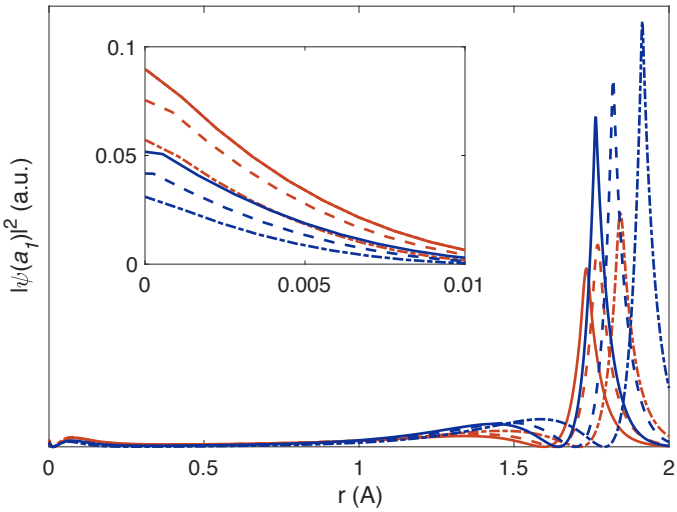

Figure E.5: Plots of the electron density arising from the Fe–L a_1 orbital in $[(P_3{}^{Si})Fe(L)]^n$ complexes (L = N_2, CO). The CO redox series is plotted in red: dash-dotted (cation), dashed (neutral), solid (anion). The N_2 redox series is plotted in blue: dash-dotted (cation), dashed (neutral), solid (anion). The inset shows an expansion of the core region (the Fe nucleus is at $r = 0$).

Before analyzing the trend that occurs across valences states, it is instructive to consider the qualitative picture of metal-ligand bonding in $(P_3{}^{E})Fe$ complexes given by molecular orbital theory. For an idealized trigonal pyramid under C_{3v} symmetry, a d-orbital splitting,

$$|1e(3d_{xz}, 3d_{yz})a_1(3d_{z^2})2e(3d_{xy}, 3d_{x^2-y^2})\rangle$$

is expected, with the precise ordering of the a_1 and 2e sets determined by the relative donor abilities of the axial and equatorial ligands. Introduction of an empty $2p_z$ orbital from an axial E-atom (i.e. trivalent B or Si^+) will mix with the Fe $3d_{z^2}$ orbital, resulting in an overall configuration,

$$|1a_1(3d_{z^2}+2p_z)1e(3d_{xz}, 3d_{yz})2e(3d_{xy}, 3d_{x^2-y^2})2a_1(3d_{z^2}-2p_z)\rangle$$

The Fe-centered frontier orbitals will then consist of the two sets of e-symmetry orbitals, which for a $\{FeE\}^{10}$ configuration will be completely filled. These orbitals all possess Fe–P π character, so sequential de-population should lead to decrease in the Fe–P covalency (Figure E.6).

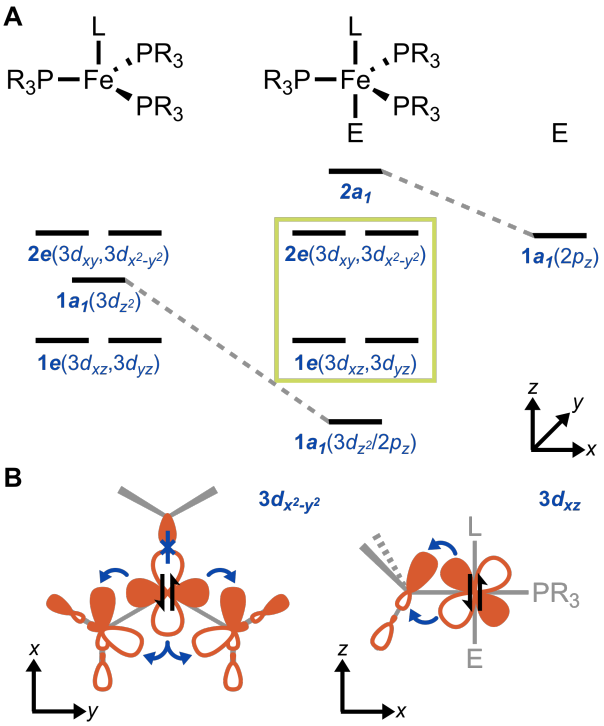

Figure E.6: (A) MO diagram for a generic $(P_3^E)Fe(L)$ complex under idealized C_{3v} symmetry. (B) Representative orbital interactions accounting for the π-accepting character of the Fe–P interaction.

To quantify this effect, DFT calculations were performed on a set of $(P_3^{Si})Fe$ complexes spanning n = 7 to 10. Figure E.7 shows the calculated frontier orbitals for $\{FeSi\}^{10}$ $[(P_3^{Si})Fe(N_2)]^-$ and $\{FeSi\}^7$ $[(P_3^{Si})Fe(Cl)]^+$, which confirm the simple MO picture developed above. The only notable difference is an inversion of the d-orbital character of the two e sets going from n = 10 to 7, owing to the loss of the π-accepting N_2 ligand and introduction of the weakly π-donating Cl ligand.

As shown in Table E.4, with decreasing n the average Fe–P bond order decreases linearly, which is attributable to the de-population of the 1e and 2e π-bonding interactions.

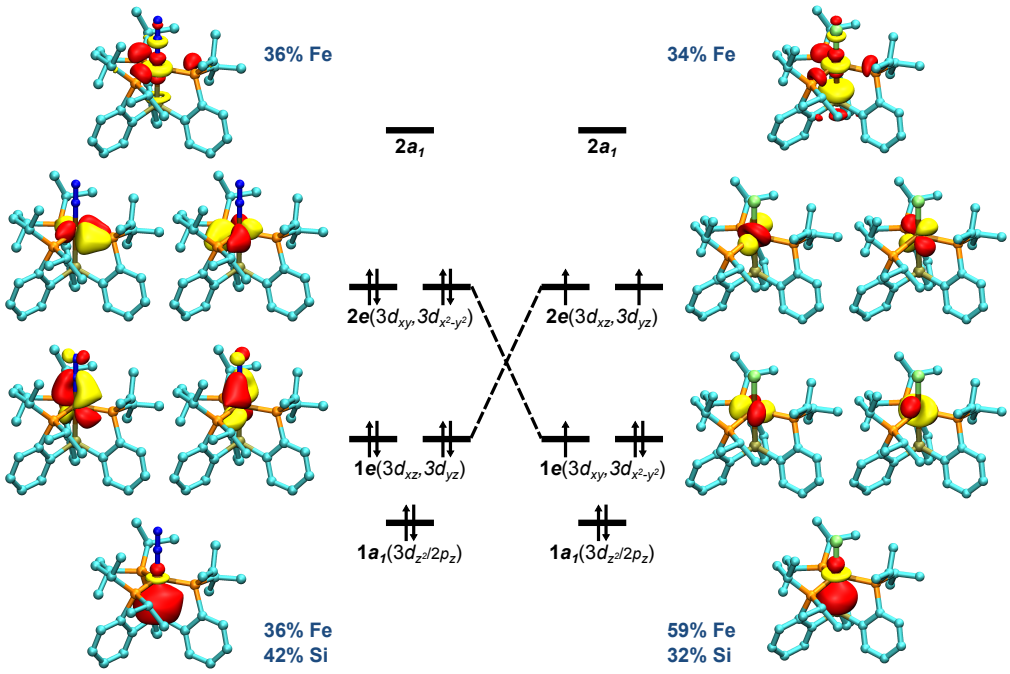

Figure E.7: Qualitative correlation diagram constructed from localized orbitals computed for $[(P_3{}^{Si})Fe(N_2)]^-$ and $[(P_3{}^{Si})Fe(Cl)]^+$. All isosurfaces were plotted with an isovalue of 0.05 a.u., and selected Löwdin orbital populations are shown.

This trend correlates well with $\rho_0(\text{val})_{\text{corr}}$, demonstrating that the effect of enhanced P π backbonding is a radial contraction of the Fe 4s orbital *(iii)*. Across *n*, the Fe–E bonding remains relatively unchanged for $n = 10$ to 8, confirming the experimental finding that *d* is uncorrelated with the Fe–E bond length (*vide infra*). That the changes in the Fe–P bonding dominate the observed changes in δ can be gleaned from the fact that the total 4s population *increases* upon oxidation, counter to the experimental trend in δ. The corresponding (correctly) predicted decreases in $\rho_0(\text{val})$ are thus a result of the increasing diffusivity of the 4s orbital, which overrides its absolute population. In fact, the DFT calculations predict that there is a "turning point" in this trend upon oxidation of the $\{\text{FeSi}\}^8$ complex to the $\{\text{FeSi}\}^7$ complex, such that the predicted change in $\rho_0(\text{val})$ is essentially zero. This presumably reflects the fact that the Fe–Cl interaction becomes increasingly covalent upon oxidation.[9,10]

Finally, we turn to the complexes $[(P_3{}^{B})Fe(NAd)]^{+/0}$ and $[(P_3{}^{B})Fe(N)]^+$, featuring

Table E.4: Comparison of ρ_0 and population analysis for a series of $\{FeSi\}^n$ complexes

	$[(P_3{}^{Si})Fe(N_2)]^-$	$(P_3{}^{Si})Fe(N_2)$	$(P_3{}^{Si})Fe(Cl)$	$[(P_3{}^{Si})Fe(Cl)]^+$
n	10	9	8	7
ρ_0(val)	4.675	4.374	4.000	4.070
Fe 3d pop.	6.729	6.676	6.590	6.361
Fe 4s pop.	0.316	0.346	0.403	0.446
$\rho_0(\text{val})_{\text{corr}}{}^a$	14.802	12.650	9.927	9.133
Avg. Fe–P bond order	0.932	0.759	0.666	0.506
%P (1e + 2e)/e^- ^{b}	15	9.1	7.5	3.4
Fe–Si bond order	0.798	0. 836	0.769	0.627
%Si ($1a_1$)	42	42	41	32

$^a\rho_0(\text{val})_{\text{corr}} = \rho_0(\text{val})/(4\text{s pop.})$
^{b}The % P character in the 1e and 2e orbitals per electron (i.e., normalized by their occupation, $n - 2$).

strongly π-donating ligands. Based on the "turning point" predicted above for the $\{FeSi\}^n$ complexes, the rather low isomer shifts of these complexes can be understood in terms of the highly covalent axial ligand interactions. Taking the nitrido complex $[(P_3{}^B)Fe(N)]^+$ as an instructive case, it is found that it features an average Fe–P bond order (0.756) that is on par with that calculated for the $\{FeSi\}^9$ complex in Table E.4, yet a dramatically increased ρ_0(val) (6.052). This change is not due to to a greater Fe 4s population (0.341 e^-), but rather contraction of the 4s orbital ($\rho_0(\text{val})_{\text{corr}}$ = 17.748). An examination of the orbital contributions to ρ_0(val) for $[(P_3{}^B)Fe(N)]^+$ reveals that a *single* MO is responsible for 27% of the observed value of ρ_0(val), which, as might be expected, is an a_1-symmetry Fe–N bonding orbital (Figure E.8, left). Another MO—of more mixed composition, but retaining the Fe–N σ character—is responsible for another 19% of ρ_0(val). The observed 4s contraction is therefore due to the extremely short Fe≡N bond (1.54 Å), driving s-electron density toward the Fe nucleus (Figure E.8, right). Thus, DFT confirms the interpretation of the experimental data given above.

E.5 Conclusion

To conclude, we have analyzed the isomer shifts of a set of 18 $(P_3{}^E)Fe$ complexes, and developed a semi-empirical model correlating the observed δ with a parameter describing

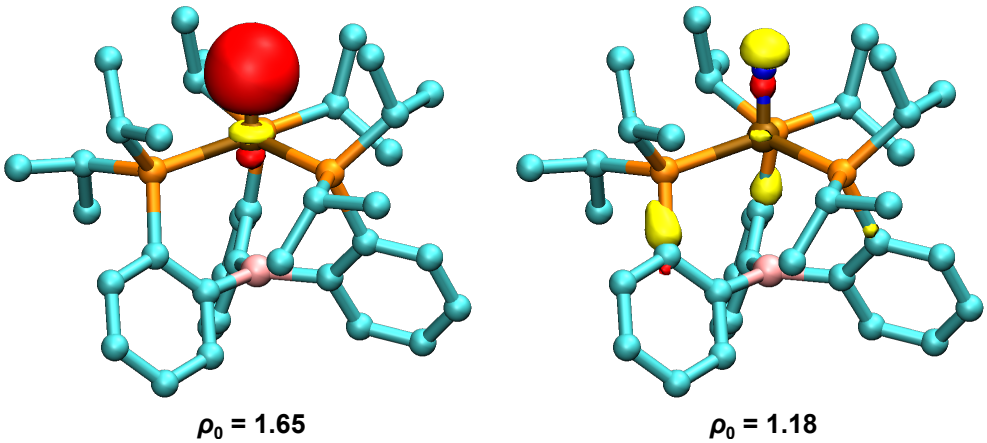

Figure E.8: Selected MOs responsible for the value of ρ_0(val) calculated for $[(P_3{}^B)Fe(N)]^+$ (6.052). Isosurfaces are rendered with an isovalue of 0.075, and the electron density at the Fe nucleus arising from each orbital is given.

the overall metal-ligand covalency (γM). In conjunction with DFT calculations, this analysis reveals that the "unusual" trend in isomer shift noted by Ye and co-workers is not a peculiar feature of $Fe(N_2)$ and Fe(CO) complexes,[14] but can, in fact, be largely attributed to the π-accepting character of the phosphine ligands. Thus, while we agree, in essence, with their analysis, the expanded data set examined here emphasizes the importance of the redox activity of the Fe phosphorous bond.

In a broader context, we wish to emphasize that the concepts developed here do not apply exclusively to phosphine-iron complexes. Indeed, the key concept revealed by our analysis is that the primary determinant of the Mössbauer isomer shift—in molecules—is metal-ligand covalency. The "unusual" trend in the isomer shifts of $(P_3{}^E)Fe$ complexes is only unusual by virtue of the fact that, historically, Mössbauer spectroscopy has been applied to complexes supported by hard donors, which are expected to form stronger bonds with more oxidized Fe centers. By contrast, soft donors, such as phosphines, are expected to form stronger bonds with more reduced Fe centers. As shown by the complexes $[(P_3{}^B)Fe(NAd)]^{+/0}$ and $[(P_3{}^B)Fe(N)]^+$, these effects can compete even within a set of isostructural complexes. On these grounds, we advocate that, to first order, the Mössbauer isomer shift should be interpreted in terms of primary experimental observables, such

as *metal–ligand bond distances*, which are correlated to more nebulous concepts such as covalency or oxidation state.

E.6 Methods

All calculations were carried out using version 3.0.3 of the ORCA package.[32] The calculation of Mössbauer isomer shifts utilized the same methods described in Chapter 4.[21] All calculations were performed on geometries obtained from X-ray crystallography, or, where crystallographic data are not available, using the DFT-optimized structures calculated in Chapter 4 and 5. All population analysis utilized the Löwdin method, except for the calculation of bond orders which utilized the Mayer method. Orbital analyses were performed on the set of localized MOs obtained using the Pipek-Mezey algorithm, which was found to produce sets of orbitals partitioned into a_1-like and e-like interactions. Calculation of real-valued functions of these orbitals was perfomed using Multiwfn.[33]

References

(1) Gütlich, P.; Bill, E.; Trautwein, A. X., *Mössbauer Spectroscopy and Transition Metal Chemistry: Fundamentals and Applications*; Springer: New York, 2011.

(2) Münck, E., *Physical Methods in Bioinorganic Chemistry: Spectroscopy and Magnetism*; Que, L., Ed.; University Science Books: Sausalito, 2000; Chapter 6.

(3) Berry, J. F.; Bill, E.; Bothe, E.; George, S. D.; Mienert, B.; Neese, F.; Wieghardt, K. *Science* **2006**, *312*, 1937–1941.

(4) Hoggins, J. T.; Steinfink, H. *Inorg. Chem.* **1976**, *15*, 1682–1685.

(5) Hauser, C.; Glaser, T.; Bill, E.; Weyhermüller, T.; Wieghardt, K. *J. Am. Chem. Soc.* **2000**, *122*, 4352–4365.

(6) Rodriguez, J. H.; Xia, Y.-M.; Debrunner, P. G. *J. Am. Chem. Soc.* **1999**, *121*, 7846–7863.

(7) Mako, T. L.; Byers, J. A. *Inorg. Chem. Front.* **2016**, *3*, 766–790.

(8) Misal Castro, L. C.; Li, H.; Sortais, J.-B.; Darcel, C. *Green Chem.* **2015**, *17*, 2283–2303.

(9) Barclay, J. E.; Leigh, G. J.; Houlton, A.; Silver, J. *J. Chem. Soc., Dalton Trans.* **1988**, 2865–2870.

(10) Evans, D. J.; Jimenez-Tenorio, M.; Leigh, G. J. *J. Chem. Soc., Dalton Trans.* **1991**, 1785–1787.

(11) Harbron, S. K.; Higgins, S. J.; Levason, W.; Garner, C. D.; Steel, A. T.; Feiters, M. C.; Hasnain, S. S. *J. Am. Chem. Soc.* **1986**, *108*, 526–528.

(12) Harbron, S. K.; Higgins, S. J.; Levason, W.; Feiters, M. C.; Steel, A. T. *Inorg. Chem.* **1986**, *25*, 1789–1794.

(13) Neese, F. *Inorg. Chim. Acta* **2002**, *337*, 181–192.

(14) Ye, S.; Bill, E.; Neese, F. *Inorg. Chem.* **2016**, *55*, 3468–3474.

(15) Lee, Y.; Peters, J. C. *J. Am. Chem. Soc.* **2011**, *133*, 4438–4446.

(16) Whited, M. T.; Mankad, N. P.; Lee, Y.; Oblad, P. F.; Peters, J. C. *Inorg. Chem.* **2009**, *48*, 2507–2517.

(17) Lee, Y.; Mankad, N. P.; Peters, J. C. *Nat. Chem.* **2010**, *2*, 558–565.

(18) Rittle, J.; Peters, J. C. *Angew. Chem. Int. Ed.* **2016**, *55*, 12262–12265.

(19) Anderson, J. S.; Cutsail, G. E.; Rittle, J.; Connor, B. A.; Gunderson, W. A.; Zhang, L.; Hoffman, B. M.; Peters, J. C. *J. Am. Chem. Soc.* **2015**, *137*, 7803–7809.

(20) Moret, M.; Peters, J. C. *Angew. Chem. Int. Ed.* **2011**, *50*, 2063–2067.

(21) Thompson, N. B.; Green, M. T.; Peters, J. C. *J. Am. Chem. Soc.* **2017**, *139*, 15312–15315.

(22) Rittle, J.; Peters, J. C. *J. Am. Chem. Soc.* **2017**, *139*, 3161–3170.

(23) Anderson, J. S.; Rittle, J.; Peters, J. C. *Nature* **2013**, *501*, 84–87.

(24) Del Castillo, T. J.; Thompson, N. B.; Peters, J. C. *J. Am. Chem. Soc.* **2016**, *138*, 5341–5350.

(25) Bondi, A. *J. Phys. Chem.* **1964**, *68*, 441–451.

(26) Rowland, R. S.; Taylor, R. *J. Phys. Chem.* **1996**, *100*, 7384–7391.

(27) Groom, C. R.; Bruno, I. J.; Lightfoot, M. P.; Ward, S. C. *Acta Crystallogr. B* **2016**, *72*, 171–179.

(28) Brown, I. D.; Shannon, R. D. *Acta Crystallogr. A* **1973**, *29*, 266–282.

(29) Gibbs, G. V.; Hill, F. C.; Boisen, M. B.; Downs, R. T. *Phys. Chem. Miner.* **1998**, *25*, 585–590.

(30) Hughes, A. K.; Wade, K. *Coord. Chem. Rev.* **2000**, *197*, 191–229.

(31) McWilliams, S. F.; Brennan-Wydra, E.; MacLeod, K. C.; Holland, P. L. *ACS Omega* **2017**, *2*, 2594–2606.

(32) Neese, F. *WIRES Comput. Mol. Sci.* **2011**, *2*, 73–78.

(33) Tian, L.; Feiwu, C. *J. Comput. Chem.* **2012**, *33*, 580–592.

ABOUT THE AUTHOR

Niklas Bjarne Thompson was born in Ann Arbor, Michigan on October 29th, 1990, to Tullia Lindsten and Craig Thompson, and an older sister, Kajsa. The family soon thereafter moved to Chicago, Illinois, where Nik formed his early memories around the campus of the University of Chicago in Hyde Park. In 1999, they moved again to the suburban Main Line of Philadelphia, Pennsylvania, where Nik completed his primary education before returning, once again, to Hyde Park to attend college at the University of Chicago.

At Chicago, Nik studied chemistry and mathematics, ultimately earning a B.S. in both majors. While at college, Nik performed undergraduate research in the laboratory of Professor Gregory L. Hillhouse, where he attempted the synthesis of terminally-bonded complexes of palladium featuring metal–ligand multiple bonds. After graduation, Nik moved to Pasadena, California to pursue his doctoral studies at the California Institute of Technology under Professor Jonas C. Peters. His graduate work has focused on the mechanistic study of Fe-based catalysts for nitrogen fixation. Upon completion of his dissertation in May, 2018, Nik will move to Cambridge, Massachusetts to pursue postdoctoral studies in the field of bioinorganic chemistry at the Massachusetts Institute of Technology with Professor Daniel L. M. Suess.